

Molecular and Biomolecular Electronics

ADVANCES IN CHEMISTRY SERIES **240**

Molecular and Biomolecular Electronics

Robert R. Birge, EDITOR
Syracuse University

Developed from a symposium sponsored
by the Division of Biochemical Technology
of the American Chemical Society
at the Fourth Chemical Congress of North America
(202nd National Meeting
of the American Chemical Society),
New York, New York,
August 25–30, 1991



American Chemical Society, Washington, DC 1994



Molecular and biomolecular electronics

Library of Congress Cataloging-in-Publication Data

Chemical Congress of North America (4th; 1991; New York, N.Y.)

Molecular and biomolecular electronics; developed from a symposium sponsored by the Division of Biochemical Technology at the Fourth Chemical Congress of North America (202nd National Meeting of the American Chemical Society), New York, New York, August 25-30, 1991 / Robert R. Birge, editor.

p. cm.—(Advances in chemistry series, ISSN 0065-2393; 240).

Includes bibliographical references and index.

ISBN 0-8412-2698-9

1. Molecular electronics. 2. Biochemical engineering. 3. Biomedical materials.

I. Birge, Robert R. II. American Chemical Society. Division of Biochemical Technology. III. Title. IV. Series.

QD1.A355 no. 240


[TK7874.8]

540 s—dc20

[621.381]

94-28455

CIP

The paper used in this publication meets the minimum requirements of American National Standard for Information Sciences—Permanence of Paper for Printed Library Materials, ANSI Z39.48-1984. 

Copyright © 1994

American Chemical Society

All Rights Reserved. The appearance of the code at the bottom of the first page of each chapter in this volume indicates the copyright owner's consent that reprographic copies of the chapter may be made for personal or internal use or for the personal or internal use of specific clients. This consent is given on the condition, however, that the copier pay the stated per-copy fee through the Copyright Clearance Center, Inc., 27 Congress Street, Salem, MA 01970, for copying beyond that permitted by Sections 107 or 108 of the U.S. Copyright Law. This consent does not extend to copying or transmission by any means—graphic or electronic—for any other purpose, such as for general distribution, for advertising or promotional purposes, for creating a new collective work, for resale, or for information storage and retrieval systems. The copying fee for each chapter is indicated in the code at the bottom of the first page of the chapter.

The citation of trade names and/or names of manufacturers in this publication is not to be construed as an endorsement or as approval by ACS of the commercial products or services referenced herein; nor should the mere reference herein to any drawing, specification, chemical process, or other data be regarded as a license or as a conveyance of any right or permission to the holder, reader, or any other person or corporation, to manufacture, reproduce, use, or sell any patented invention or copyrighted work that may in any way be related thereto. Registered names, trademarks, etc., used in this publication, even without specific indication thereof, are not to be considered unprotected by law.

PRINTED IN THE UNITED STATES OF AMERICA

**American Chemical Society
Library**

1155 16th St., N.W.

Washington, D.C. 20036

In Molecular and Biomolecular Electronics; Birge, R.;
Advances in Chemistry, American Chemical Society: Washington, DC, 1994.

1994 Advisory Board

Advances in Chemistry Series

M. Joan Comstock, *Series Editor*

Robert J. Alaimo
Procter & Gamble Pharmaceuticals

Mark Arnold
University of Iowa

David Baker
University of Tennessee

Arindam Bose
Pfizer Central Research

Robert F. Brady, Jr.
Naval Research Laboratory

Margaret A. Cavanaugh
National Science Foundation

Arthur B. Ellis
University of Wisconsin at Madison

Dennis W. Hess
Lehigh University

Hiroshi Ito
IBM Almaden Research Center

Madeleine M. Joullie
University of Pennsylvania

Lawrence P. Klemann
Nabisco Foods Group

Gretchen S. Kohl
Dow-Corning Corporation

Bonnie Lawlor
Institute for Scientific Information

Douglas R. Lloyd
The University of Texas at Austin

Cynthia A. Maryanoff
R. W. Johnson Pharmaceutical
Research Institute

Julius J. Menn
Western Cotton Research
Laboratory, U.S. Department
of Agriculture

Roger A. Minear
University of Illinois
at Urbana-Champaign

Vincent Pecoraro
University of Michigan

Marshall Phillips
Delmont Laboratories

George W. Roberts
North Carolina State University

A. Truman Schwartz
Macalaster College

John R. Shapley
University of Illinois
at Urbana-Champaign

L. Somasundaram
DuPont

Michael D. Taylor
Parke-Davis Pharmaceutical Research

Peter Willett
University of Sheffield (England)

FOREWORD

The **ADVANCES IN CHEMISTRY SERIES** was founded in 1949 by the American Chemical Society as an outlet for symposia and collections of data in special areas of topical interest that could not be accommodated in the Society's journals. It provides a medium for symposia that would otherwise be fragmented because their papers would be distributed among several journals or not published at all.

Papers are reviewed critically according to ACS editorial standards and receive the careful attention and processing characteristic of ACS publications. Volumes in the **ADVANCES IN CHEMISTRY SERIES** maintain the integrity of the symposia on which they are based; however, verbatim reproductions of previously published papers are not accepted. Papers may include reports of research as well as reviews, because symposia may embrace both types of presentation.

ABOUT THE EDITOR



ROBERT R. BIRGE is professor of chemistry, director of the W. M. Keck Center for Molecular Electronics, and research director of the New York State Center for Advanced Technology in Computer Applications and Software Engineering at Syracuse University. His research interests include the application of nonlinear laser spectroscopy and quantum theory to the study of light-transducing proteins and the development of protein-based molecular electronic devices. Birge serves on the editorial boards of *Nanotechnology*, *BioSpectroscopy*, and *Supramolecular Science*, and has cochaired advisory panels for the National Institutes of Health and the National Academy of Sciences.

Birge received his B.S. degree in chemistry from Yale University in 1968, his Ph.D. in chemical physics from Wesleyan University in 1972, and was a National Institutes of Health postdoctoral fellow at Harvard University from 1973 to 1975. He was an assistant and associate professor of chemistry at the University of California, Riverside (1975–1984) and served as professor and head of the Chemistry Department at Carnegie Mellon University (1984–1987). He joined the faculty at Syracuse University in 1988.

PREFACE

MOLECULAR ELECTRONICS not only represents the final technological stage in the miniaturization of computer circuitry, but it also provides promising new methodologies for high-speed signal processing and communication, novel associative and neural architectures, as well as linear and nonlinear devices and memories. This volume is the first in this series to examine the relatively new field of molecular electronics. Chapters 1–6 provide overviews and fundamentals, Chapters 7–12 cover linear and nonlinear molecular photonics, Chapters 13–18 discuss systems based on self-assembly, and Chapters 19–23 cover protein-based systems and devices.

The contents are based in part on the subject areas covered by the International Symposium on Molecular and Biomolecular Electronics held during the American Chemical Society National Meeting in New York City, August 25–29, 1991. The goal of the four-day symposium was to provide experimentalists and theoreticians working on quantum semiconductor and molecular devices with an opportunity to discuss current research problems in an interdisciplinary environment.

Participants from 11 countries with expertise in quantum electronics, nanoscale semiconductor fabrication, organic chemistry, genetic engineering, molecular biophysics, and nonlinear optics made enthusiastic attempts to communicate their progress to an audience largely unfamiliar with the field under discussion. Sometimes a talk succeeded in bridging the gap of background and experience, but often many members of the audience had trouble understanding the terminology, the techniques, and even the relevance of a given presentation.

In some respects, these failures were more important to the development of this volume than the successful talks, because the failures convinced the conference organizers of the need for an *Advances in Chemistry* volume to provide a perspective on the interdisciplinary international research effort in molecular electronics. The contributors to this volume were chosen from among the leaders in the principal research areas considered by the conference organizers to be part of, or highly relevant to, recent advances in the field. Contributors were asked to provide an overview of the fundamental methods and procedures of their specialties, followed by a review of recent research with an emphasis on their own contributions.

Each chapter was examined by at least three external reviewers, with at least one reviewer having no research expertise in the field covered by the chapter. Although this approach caused a delay in publication, it improved the clarity of the chapters, particularly for those readers unfamiliar with the topics. We thus hope to have achieved the principal goal of providing a book that will help readers to appreciate and comprehend the terminology, methods, procedures, and issues involved in the principal research areas that combine to advance the field of molecular electronics.

Acknowledgments

It is a pleasure to acknowledge the many people whose contributions made this volume, and the symposium that prompted its preparation, successful. First, I thank Connie Birge, the conference coordinator, for the many hours she spent contacting participants, organizing the sessions to minimize conflicts with other symposia, and helping some of our international participants with the unique visa problems that Glasnost produced. Without her persistence, and the help of Senator Daniel Moynihan's office, a number of key participants would have missed the conference. The symposium would not have achieved the degree of international and interdisciplinary participation were it not for the time and effort of the symposium session chairs: A. Aviram, E. Greenbaum, S. Marder, J. Michl, R. Potember, and H. Ti Tien. I also thank Michael Marron and the Office of Naval Research for their generous support of the conference. Additional support was provided by the Division of Biochemical Technology of the American Chemical Society, Digital Equipment Corporation, Biological Components Corporation, Syracuse University, and the Industrial Affiliates Program of the W. M. Keck Center for Molecular Electronics. Finally, I want to thank Margaret Brown, Steven Powell, and Colleen Stamm of the American Chemical Society Books Department for monitoring the submission of manuscripts, encouraging authors to stay on schedule, overseeing the refereeing process, and for editorial and publication supervision.

ROBERT R. BIRGE

W. M. Keck Center for Molecular Electronics
Syracuse University
Syracuse, NY 13244-4100

May 19, 1993

Introduction to Molecular and Biomolecular Electronics

Robert R. Birge

W. M. Keck Center for Molecular Electronics and Department of Chemistry, Syracuse University, 111 College Place, Syracuse, NY 13244

This chapter provides a brief introduction to the field of molecular and biomolecular electronics. The advantages and disadvantages of implementing molecular electronics are discussed in terms of selected characteristics including size, speed, architecture, quantum statistics, nanoscale engineering, stability, nonlinear properties, and reliability.

MOLECULAR ELECTRONICS IS AN INTERDISCIPLINARY FIELD that lies at the interface of chemistry, electrical engineering, optical engineering, and solid-state science. There are two schools of thought regarding molecular electronics. One school emphasizes nanotechnology as the driving force and views molecular electronics as one avenue for achieving nanoscale devices (1). The second school emphasizes the properties of molecules and the unique architectures and capabilities that molecular systems provide as the principal motivation (2). The difference is one of emphasis rather than of direction, and most recent conferences (3) and books (including this volume) have sought an accommodation of both perspectives.

For the purposes of this discussion, molecular electronics is defined as the encoding, manipulation, and retrieval of information at a molecular or macromolecular level. This approach contrasts with current commercial techniques, fast approaching their practical limits, in which these functions are accomplished via lithographic manipulation of bulk materials to generate integrated circuits. Molecular electronics not only represents the final technological stage in the miniaturization of computer circuitry, but it also provides promising new methodologies for high-speed signal processing and communication, novel associative and neural architectures, as well as linear and nonlinear devices and mem-

0065-2393/94/0240-0001\$08.00/0
© 1994 American Chemical Society

ories. The ability to explore new architectures unique to molecular-based systems has a potential equal to that provided by molecular scale engineering and miniaturization.

Biomolecular electronics is a subfield of molecular electronics that investigates the use of native as well as modified biological molecules (chromophores, proteins, etc.) in place of the organic molecules synthesized in the laboratory. Because natural selection processes have often solved problems of a nature similar to those that must be solved in harnessing organic compounds and because self-assembly and genetic engineering provide sophisticated control and manipulation of large molecules, biomolecular electronics has shown considerable promise. There is no clear dividing line separating molecular from biomolecular electronics. For example, if a synthetic chemist incorporates a porphyrin molecule into a synthetic organic logic gate, is this an example of biomolecular electronics? Such examples are commonplace, and for simplicity we will typically use the adjective "molecular" to cover both synthetic and natural sources of organic compounds.

The preceding discussion conveys some of the advantages but few of the problems inherent in the implementation of molecular electronics. One of the best ways to introduce this field is to examine the potential advantages and disadvantages as outlined in Table I. The list presented in Table I is neither exhaustive nor orthogonal. First, many additional characteristics could have been included. Those listed in Table I are selected to provide the broadest coverage with a minimum number of categories. Second, the characteristics are in some cases overlapping. For example, the reliability of a device is a function of the size and stability of the component molecules, the speed of the device and the quantum mechanical properties of the molecule or molecular ensemble. Nevertheless, the characteristics listed in Table I serve to represent the principal issues that not only encourage but also challenge scientists seeking to implement molecular electronics. We will discuss each separately.

Size and Speed

Molecules are synthesized from the "bottom up" by carrying out additive synthesis starting with readily available organic compounds. Bulk semiconductor devices are generated "from the top down" via lithographic manipulation of bulk materials. A synthetic chemist can selectively add an oxygen atom to a chromophore with a precision that is far greater than a comparable oxidation step facilitated by using electron-beam or X-ray lithography. Figure 1 shows molecular-based gates, which are typically 1000 times smaller than their semiconductor equivalents (3-7). At the same time, such gates have yet to approach a comparable

Table I. Characteristics, Potential Advantages, and Current Disadvantages of Implementing Molecular Electronics

<i>Characteristic</i>	<i>Potential Advantages</i>	<i>Current Disadvantages</i>
Size-speed	Small size of molecular scale offers high intrinsic speed. Picosecond switching rates are common.	Small size makes connection to control, input, and output circuitry difficult.
Architecture	Neural, associative, and parallel architectures can be implemented directly.	Three terminal devices and standard logic designs are difficult to implement.
Quantized behavior	The quantum mechanical properties can be engineered with high precision.	Quantized behavior limits electron current densities and architectural flexibility.
Nanoscale engineering	Synthetic organic chemistry, self-assembly, and genetic engineering provide nanometer resolution.	Nanolithography provides higher scale factors and flexibility than current molecular techniques.
Stability	Some molecules and proteins offer thermal and photochemical stabilities comparable to bulk semiconductors.	Most molecules and proteins are photochemically or thermally labile precluding general application.
Nonlinear properties	Intrinsic second- and third-order properties of molecules can be synthetically optimized.	Lifetimes and damage thresholds of molecular-based nonlinear optical devices are not yet competitive.
Reliability	Ensemble averaging via optical coupling or state assignment averaging provides high reliability.	Thermal or photochemical stress, impurity effects, and quantum statistics limit reliability of many systems.

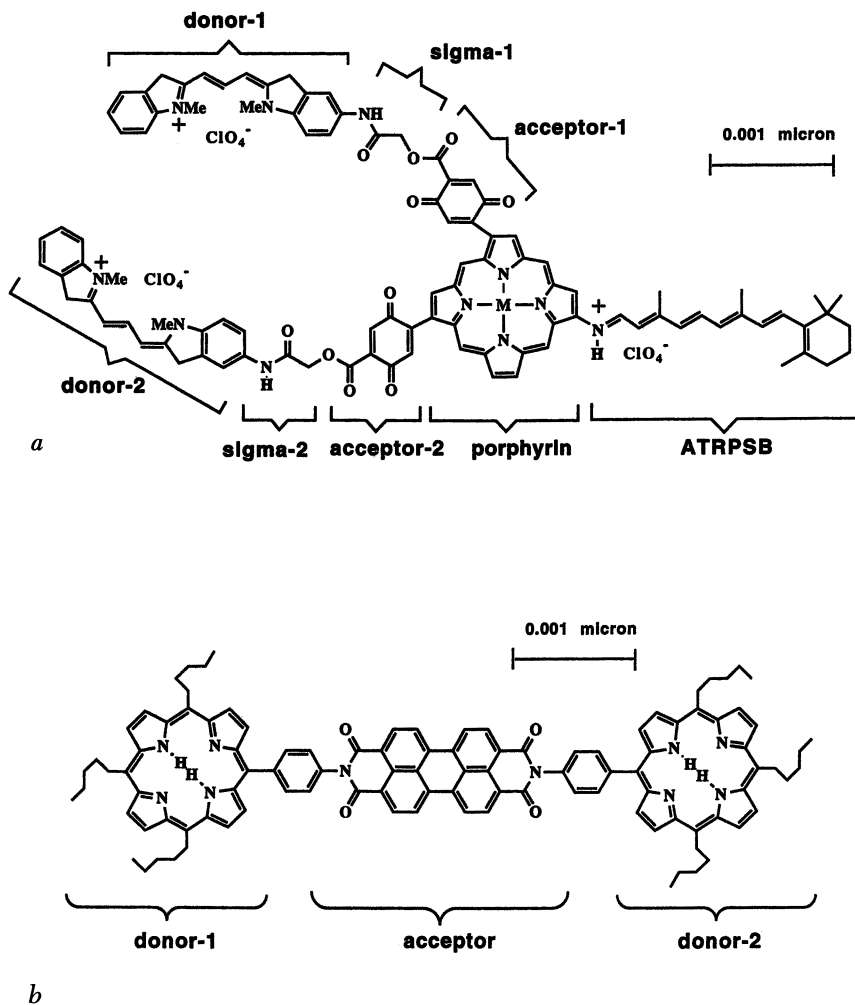


Figure 1. Examples of optically coupled charge-transfer molecular gates currently under investigation. The top gate (a) operates through light activation of an electron from the donor(s) to acceptor(s) and generates an electrostatic shift of the output chromophore absorption maximum from 520 to 590 nm if both inputs have been activated simultaneously (4). The sigma separators are used to increase the back-tunneling time to ~ 3 ps. The bottom gate (b) also operates via electron-transfer reactions and results in single or double reduction of the acceptor depending on the light intensity or wavelength (6). The size bars are approximate.

level of reliability or to interconnect capability compared to their semiconductor counterparts.

The signal propagation times of molecular gates are due in large part to their small sizes. Whether the gate is designed to operate via electron transfer, electron tunneling, or conformational photochromism, a decrease in size will yield a comparable increase in speed. This effect is due to the fact that all gates in use, under study, or envisioned are activated by the shift in the position of a charge carrier, and all charge carriers have mass. Whether the device is classical or relativistic, the mass of the carrier places a limit on how rapidly the conformational change can take place. Thus, size and speed are intimately related. One can criticize this view as arbitrarily restrictive in that electrostatic changes can be generated via optical excitation, and the generation of an excited electronic state can occur within a large chromophore in less than 1 fs (1 fs = 10^{-15} s, the time it takes light to travel $\sim 0.3 \mu\text{m}$). Nevertheless, the reaction of the system to the charge shift is still a size-dependent property, and the relationship between the total size of the device and the response time remains valid. A detailed discussion of electron motion and current densities in molecules is provided by Nafie (8).

The ultimate speed of a device is determined by other factors as well. As noted by Lawrence and Birge (9), Heisenberg uncertainty limits the maximum frequency of operation, f_{max} , of a monoelectronic or monomolecular devices on the basis of the following relationship:

$$f_{\text{max}} \cong \frac{0.00800801 \tilde{\nu}_s \pi^2}{hN \left[2\pi + 2 \tan^{-1}(-2) + \ln \left(\frac{\tilde{\nu}_s^2}{4} \right) - \ln \left(\frac{5\tilde{\nu}_s^2}{4} \right) \right]} \quad (1a)$$

$$f_{\text{max}}(\text{GHz}) \approx \frac{0.963\tilde{\nu}_s}{N} \quad (1b)$$

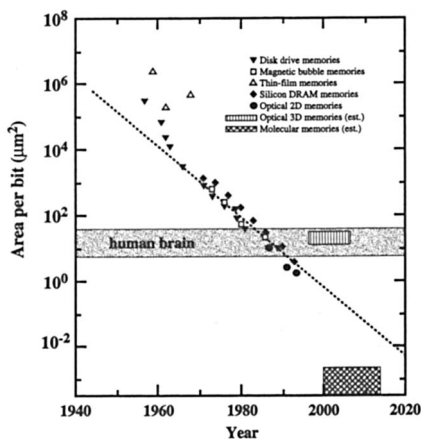
where ν_s is the energy separation of the two states of the device in wavenumbers, and N is the number of state assignments that must be averaged to achieve reliable state assignment. This equation applies only to monoelectronic or monomolecular devices; Heisenberg's uncertainty principle permits higher frequencies for ensemble averaged devices. For example, if a device requires 1000 state assignment averages to achieve reliability and $\nu_s \cong 1000 \text{ cm}^{-1}$, it will have a maximum operating frequency of $\sim 960 \text{ MHz}$. The concept of state assignment averaging is defined and quantitatively examined in reference 9. Virtually all monomolecular or monoelectronic devices require $N > 500$ at ambient temperature, but cryogenic devices operating at 1.2 K can approach $N = 1$. Thus, although molecular devices have an inherent advantage with re-

spect to speed, quantum mechanics places constraints on the maximum operating frequency that can have a significant impact at ambient temperatures.

It is interesting to examine the trends in bit size that have characterized the past few decades of memory development. The results are shown in Figure 2 and indicate that the area per bit has decreased logarithmically since the early 1970s (10). For comparison Figure 2 also shows the cross-sectional area per bit calculated for the human brain (assuming one neuron is equivalent to one bit) and for proposed three-dimensional memories and proposed molecular memories. Although current technology has surpassed the cross-sectional density of the human brain, the major advantage of the neural system of the brain is that information is stored in three dimensions. At present, the mind of a human being can store more "information" than the disk storage allocated to the largest supercomputers. Of course, the human brain is not digital, and such comparisons are tenuous. Nevertheless, the analogy underscores the fact that current memory technology is still anemic compared to the technology that is inherent in the human brain. It also demonstrates the rationale for, and potential of, the development of three-dimensional memories (11, 12).

We can also conclude from an analysis of Figure 2 that the trend in memory densities will soon force the bulk semiconductor industry to address some of the same issues that confront scientists who seek to implement molecular electronics.

Figure 2. Analysis of the area in square micrometers required to store a single bit of information as a function of the evolution of computer technology in years. The data for magnetic disk, magnetic bubble, thin-film, and silicon dynamic random access (DRAM) memories are taken from Keyes (10). These data are compared with the cross-sectional area per bit (neuron) for the human brain as well as anticipated areas and implementation times for optical three-dimensional memories (9, 11, 12) and molecular memories. The optical three-dimensional memory, the brain, and the molecular memories are three-dimensional, and therefore the cross-sectional area per bit is plotted for comparison. The area (A) is calculated in terms of the volume per bit, V/bit, by the formula $A = (V)^{2/3}$.



Architecture

Molecular electronics offers significant potential for exploring new architectures (2, 13). Many of the chapters in this volume examine new architectures that are based on self-assembly (14–19). Other chapters explore architectures that, although not unique to molecular systems, can be implemented with greater flexibility or performance by using molecular materials (7, 11, 20–28). The opportunity to explore new architectures is one of the key aspects of molecular electronics that has prompted the enthusiasm of researchers.

This enthusiasm is somewhat tempered, however, by the recognition that the three-terminal transistor that represents the fundamental building block of current computer gates and signal processing circuitry is difficult to implement using molecules. This problem, which also applies to Josephson junction devices, has one of two potential consequences. It could limit the role that molecular electronics will play in enhancing current computer and signal processing systems. Alternatively, it could encourage the investigation and development of new designs based on neural, associative, or parallel architectures and lead to hybrid systems with enhanced capabilities relative to current technology. The latter alternative is far more likely. For example, optical associative memories and three-dimensional memories can be implemented with unique capabilities based on molecular electronics (9, 11, 12). Implementation of these memories within hybrid systems is anticipated to have near-term application. Furthermore, the human brain, a computer with capabilities that far exceed the most advanced supercomputer, is a prime example of the potential of molecular electronics. The development of an artificial neural computer is beyond our current technology, but it would be illogical to assume that such an accomplishment is impossible. Thus, we should view molecular electronics as opening new architectural opportunities that will lead to advances in computer and signal processing systems.

Quantized Behavior

As noted in the chapter by Reed and Seabaugh (29), band-gap engineering and nanofabrication techniques have made possible a new class of quantum devices with unique functionalities. Quantum devices have the potential for greatly reducing the complexity of circuits while simultaneously increasing the maximum frequency of operation. The fact that scientists and engineers working on bulk semiconductor gates have endorsed the potential of quantum devices is an indirect endorsement of molecular electronics. This position follows from a recognition that the quantum mechanical properties of molecules can be optimized for particular applications with considerable precision and with growing

sophistication. A majority of the candidate molecules and devices discussed in this book function in a quantized rather than in a classical format (7–9, 11, 13–27, 30). Quantized behavior is not always advantageous, however. Molecules invariably respond to the addition or subtraction of an electron with reorganization of the core electrons and the movement of the atoms in response to bonding changes. This characteristic limits the electron current a molecule can carry and complicates the design of three-terminal devices that provide amplification. Thus, quantized behavior can limit architectural flexibility.

Nanoscale Engineering

The feature size of high-speed semiconductor devices has decreased dramatically during the evolution of computer technology (*see* Figure 2). Driven by the demand for higher speeds and densities, micrometer and even submicrometer feature sizes are now commonplace. Ultraviolet lithography can provide modest improvement over current densities, but the evolution toward nanoscale feature sizes will require electron-beam or X-ray lithography. Although such lithography is well understood, it is very expensive to implement. As noted, organic synthesis provides a “bottom up” approach that offers a 100- to 1000-fold improvement in resolution relative to the best lithographic methods (6, 7, 20, 21). Organic synthesis has been developed to a high level of sophistication in large part as a result of the efforts of natural product synthetic chemists to recreate a priori the complex molecules that nature has developed via billions of years of natural selection. A sophisticated synthetic effort already exists within the drug industry, and thus a commercially viable molecular electronic device could likely be generated in large quantities using present commercial facilities.

Two alternatives to organic synthesis have had a significant impact on current efforts in molecular electronics: self-assembly and genetic engineering. The use of the Langmuir–Blodgett technique to prepare organized structures is the best known example of self-assembly (16, 18, 19). However, self-assembly can also be used in the generation of membrane-based devices (14, 17), microtubule-based devices (15), and liquid-crystal holographic films (28). Genetic engineering offers a unique approach to the generation and manipulation of large biological molecules (12, 22, 23, 26, 30–33). The current methods and procedures of site-directed mutagenesis are reviewed in the chapter by Stayton et al. (26), and a number of chapters examine the application of this technique to bacteriorhodopsin-based devices (22, 23, 25, 30).

Thus, molecular electronics provides at least three discrete methods of generating nanoscale devices: organic synthesis, self-assembly, and site-directed mutagenesis. The fact that the latter two methods currently

offer access to larger and often more complicated structures has been responsible in part for the early success of biomolecular electronics. All three techniques offer resolutions significantly better than those possible via bulk lithography.

High resolution is not the only criterion in examining the quality of nanoscale engineering. Lithography offers an advantage that none of the techniques available to molecular electronics can duplicate. Lithography can be used to construct very large scale integrated (VLSI) devices involving more than 100,000 discrete components with complex interconnections. This ability can be quantitatively analyzed by defining the scale factor, a ratio defined as the overall area of the device divided by the size of the discrete gates or transistors that make up the device. A typical VLSI circuit has a scale factor of approximately 10^5 . Despite the fact that organic synthesis offers convenient access to a three-dimensional structure, the preparation of extremely large molecules is a significant challenge. A comparable scale factor for large organic molecules is approximately 10^3 – 10^4 . Genetic engineering provides access to much larger structures, and scale factors of 10^5 and even 10^6 are common. Nevertheless the use of amino acid building blocks limits flexibility. Self-assembly expands the size still further, but at present, the scale factors are small due to the use of identical molecules. In conclusion, nanoscale semiconductor engineering still provides the best combination of scale factor and flexibility.

Stability

One of the commonly stated advantages of bulk semiconductor materials relative to organic molecules is thermal stability. Silicon and gallium arsenide can operate at temperatures that exceed those which most molecules can withstand for extended periods of time. However, many molecules and proteins can operate at very high temperatures, and some have thermal stabilities that exceed those evidenced by silicon and gallium arsenide. Furthermore, the use of ensemble averaging, in which many molecules are used to simultaneously represent a single bit of information, enhances system stability by allowing some molecules to decompose without adversely affecting system reliability. Similar observations apply to photochemical stability, an issue relevant to optical computing and optical memories. For example, the protein bacteriorhodopsin, which is the light-transducing protein in the salt marsh bacterium *Halobacterium halobium*, exhibits outstanding thermal and photochemical stability (5, 9, 12, 22, 23, 25, 30–33). This feature is due in part to natural selection and the in vivo requirement that this protein operate within a bacterium inhabiting a hot salt marsh under intense solar radiation. The chromophore phthalocyanine, which has many de-

vice applications, has even greater stability (27). In summary, thermal and photochemical stability is an important issue in implementing molecular electronics, but organic and biological molecules can be designed with stabilities more than adequate for device applications.

Nonlinear Properties

Many optical and electronic devices make use of the nonlinear properties of the constituent materials (9, 11, 12, 21, 24, 32). A majority of the recent work in this area has concentrated on nonlinear optical properties because of the importance of these properties to the design of optical communication systems, optical computing, and optical memories. Four chapters of this book are devoted to this important area (11, 20, 21, 24). One of the principal advantages of using organic molecules in nonlinear optical applications is the ability to tailor the properties of the molecules to suit specific applications. Synthetic organic chemistry offers a level of flexibility in optimizing the dipole moment, transition moments, electronic symmetry, and conjugation length of a candidate material that exceeds that inherent in manipulation of bulk inorganic materials.

The principal problems encountered with present-day nonlinear optical molecular materials are associated with transparency, damage threshold, and lifetime. Thus, although organic materials have been prepared with second-order hyperpolarizabilities much higher than lithium niobate, the latter inorganic material has found greater commercial application in second-harmonic generation. Organic materials, however, are rapidly closing the gap (20, 21), and commercial viability is fast approaching reality.

Reliability

The issue of the reliability of molecular electronic devices is discussed in detail in a separate chapter in this book (9), and therefore the present discussion will be brief and selective. The topic is extremely important, however, and has been used repeatedly by semiconductor scientists and engineers as a reason to view molecular electronics as impractical. Indeed, an article by Birge et al. (4) has been referenced by others to argue (incorrectly) that the need to use ensemble averaging in optically coupled molecular gates and switches demonstrates the inherent unreliability of molecular electronic devices. This point of view is comparable to suggesting that transistors are inherently unreliable because more than one charge carrier must be used to provide satisfactory performance. The majority of ambient-temperature molecular and bulk semiconductor devices use more than one molecule or charge carrier to represent a bit for two reasons: (1) ensemble averaging improves reliability, and (2) ensemble averaging permits higher speeds (34). The

nominal use of ensemble averaging does not, however, rule out reliable monomolecular or monoelectronic devices. We explore the issue of reliability in ensemble averaged and monomolecular devices briefly.

The probability of correctly assigning the state of a single molecule, p_1 , is never exactly unity. This less than perfect assignment capability is due to quantum effects as well as inherent limitations in the state assignment process. The probability of an error in state assignment, P_{error} , is a function of p_1 and the number of molecules, n , within the ensemble used to represent a single bit of information. P_{error} can be approximated by the following equation (9):

$$P_{\text{error}}(n, p_1) \cong -\text{Erf} \left[\frac{(2p_1 + 1)\sqrt{n}}{4\sqrt{2p_1(1 - p_1)}}; \frac{(2p_1 - 1)\sqrt{n}}{4\sqrt{2p_1(1 - p_1)}} \right] \quad (2)$$

where Erf [Z_0 ; Z_1] is the differential error function defined by

$$\text{Erf} [Z_0; Z_1] = \text{Erf} [Z_1] - \text{Erf} [Z_0] \quad (3)$$

where

$$\text{Erf} [Z] = \frac{2}{(\pi)^{1/2}} \int_0^Z \text{Exp} (-t^2) dt \quad (4)$$

Equation 2 is approximate and neglects error associated with the probability that the number of molecules in the correct conformation can stray from their expectation values on the basis of statistical considerations. Nevertheless it is sufficient to demonstrate the issue of reliability and ensemble size. First, we define a logarithmic reliability parameter, ξ , which is related to the probability of error in the measurement of the state of the ensemble (device) by the function, $P_{\text{error}} = 10^{-\xi}$. A value of $\xi = 10$ is considered a minimal requirement for reliability in non-error-correcting digital architectures.

If we assume that the state of a single molecule can be assigned correctly with a probability of 90% ($p_1 = 0.9$), then equation 1 indicates that 95 molecules must collectively represent a single bit to yield $\xi > 10$ [$P_{\text{error}}(95, 0.9) \cong 8 \times 10^{-11}$]. We must recognize that a value of $p_1 = 0.9$ is larger than is normally observed, and some examples of reliability analyses for specific molecular-based devices is provided in Chapter 6 (9). In general, ensembles larger than 10^3 are required for reliability unless fault-tolerant or fault-correcting architectures can be implemented.

The question then arises whether or not we can design a reliable computer or memory that uses a single molecule to represent a bit of information. The answer is yes provided one of two conditions apply. The first condition is architectural. It is possible to design fault-tolerant

architectures that either recover from digital errors or simply operate reliably with occasional error due to analog or neural-like environments. An example of digital error correction is the use of additional bits beyond the number required to represent a number. This approach is common in semiconductor memories, and under most implementations these additional bits provide for single-bit error correction and multiple-bit error detection. Such architectures lower the required value of ξ to values less than 4. An example of analog error tolerance is embodied in many optical computer designs that use holographic or Fourier architectures to carry out complex functions.

The second condition is more subtle. It is possible to design molecular architectures that can undergo a state reading process that does not disturb the state of the molecule. For example, an electrostatic switch could be designed that can be "read" without changing the state of the switch. Alternatively, an optically coupled device can be read by using a wavelength that is absorbed or diffracted but that does not initiate state conversion. Under these conditions, the variable n that appears in equation 1 can be defined as the number of nondestructive read "operations" rather than the ensemble size. Thus our previous example indicating that 95 molecules must be included in the ensemble to achieve reliability can be restated as follows: A single molecule can be used provided we can carry out 95 nondestructive measurements to define the state. Multiple-state measurements are equivalent to integrated measurements and should not be interpreted as a start-read-stop cycle repeated n number of times. A continuous read with digital or analog averaging can achieve the same level of reliability.

Conclusions

This discussion has outlined the advantages and disadvantages of implementing molecular electronics. We have chosen to examine this issue with reference to the selected characteristics of size, speed, architecture, quantum statistics, nanoscale engineering, stability, nonlinear properties, and reliability. The key conclusions are summarized in Table I. If one ignores the issue of commercial viability, an enthusiastic endorsement of molecular electronics is justified on the basis of the exciting basic research that has characterized this field. Commercial viability, however, remains an open question in many areas of proposed implementation. Nevertheless, molecular-based biosensors and chiral photonic materials have already achieved commercial status. Molecular-based holographic and nonlinear optical materials, microwave assemblies, and optical memories have also been demonstrated to have commercial viability. Liquid-crystal displays (LCDs), one of the first commercially successful molecular electronic devices, are now common. When first introduced,

LCDs were slow, thermally labile, inefficient and exhibited poor contrast and limited viewing angles. The dramatic improvement in characteristics and the resulting current commercial success of LCDs are due to an extensive research and development effort. We should not expect similar levels of success from the current molecular electronic device candidates without similar time and effort. Those companies willing to invest in molecular electronics research now may soon represent the dominant growth companies in biomedical, photonic, signal processing, communications, and computer technology.

References

1. *Nanotechnology: Research and Perspective*; Crandall, B. C.; Lewis, J., Eds.; Massachusetts Institute of Technology: Cambridge, MA, 1992.
2. *Computer* (Special issue on Molecular Computing; Conrad, M., Ed.) 1992, 25, 6–67.
3. *Molecular Electronics—Science and Technology*; Aviram, A., Ed.; American Institute of Physics: New York, 1992; Vol. 262, p 334.
4. Birge, R. R.; Ware, B. R.; Dowben, P. A.; Lawrence, A. F. In *Molecular Electronics—Science and Technology*; Aviram, A., Ed.; Engineering Foundation: New York, 1989; pp 275–284.
5. Birge, R. R. In *Nanotechnology: Research and Perspective*; Crandall, B. C.; Lewis, J., Eds.; Massachusetts Institute of Technology: Cambridge, MA, 1992; p 381.
6. O’Neal, M. P.; Niemczyk, M. P.; Svec, W. A.; Gosztola, D.; Gaines, G. L.; Wasielewski, M. R. *Science (Washington, D.C.)* 1992, 257, 63–65.
7. Metzger, R. M. Chapter 5 in this volume.
8. Nafie, L. A. Chapter 4 in this volume.
9. Lawrence, A. F.; Birge, R. R. Chapter 6 in this volume.
10. Keyes, R. W. *AIP Conf. Proc.* 1992, 262, 285–297.
11. Dvornikov, A. S., Rentzepis, P. M. Chapter 7 in this volume.
12. Birge, R. R. *Computer* 1992, 25, 56–67.
13. Conrad, M. Chapter 3 in this volume.
14. Ottova-Leitmannova, A.; Martynski, T.; Warkak, A.; Ti Tien, H. Chapter 17 in this volume.
15. Shashidar, R.; Schnur, J. M. Chapter 18 in this volume.
16. Marx, K. A.; Samuelson, L. A.; Kamath, M.; Sengupta, S.; Kaplan, D.; Kumar, J.; Tripathy, S. Chapter 15 in this volume.
17. Fendler, J. H. Chapter 16 in this volume.
18. Albrecht, O.; Sakai, K.; Takomoto, K.; Matsuda, H.; Eguchi, K.; Nakagiri, T. Chapter 13 in this volume.
19. Fujihira, M. Chapter 14 in this volume.
20. Di Bella, S.; Fragala, I. L.; Ratner, M. A.; Marks, T. J. Chapter 9 in this volume.
21. Gorman, C. B.; Van Doremale, G. H. J.; Marder, S. R. Chapter 8 in this volume.
22. Hampp, N.; Thoma, R.; Zeisel, D.; Bröchle, C.; Österheld, D. Chapter 21 in this volume.
23. Hong, F. T. Chapter 22 in this volume.
24. Pierce, B. M. Chapter 10 in this volume.
25. Rayfield, G. Chapter 23 in this volume.

26. Stayton, P. S.; Olinger, J. M.; Wollman, S. T.; Bohn, P. W.; Sligar, S. G. Chapter 19 in this volume.
27. Wada, T.; Hosoda, M.; Sasabe, H. Chapter 11 in this volume.
28. Zhang, J.; Sponsler, M. B. Chapter 12 in this volume.
29. Reed, M.; Seabaugh, A. C. Chapter 2 in this volume.
30. Lanyi, J. K. Chapter 20 in this volume.
31. Schick, G. A.; Lawrence, A. F.; Birge, R. R. *Trends Biotechnol.* **1988**, *6*, 159–163.
32. Birge, R. R. *Annu. Rev. Phys. Chem.* **1990**, *41*, 683–733.
33. Oesterhelt, D.; Brauchle, C.; Hampp, N. *Quart. Rev. Biophys.* **1991**, *24*, 425–478.
34. Birge, R. R.; Lawrence, A. F.; Tallent, J. A. *Nanotechnology* **1991**, *2*, 73–87.

RECEIVED for review March 25, 1993. ACCEPTED revised manuscript May 11, 1993.

Prospects for Semiconductor Quantum Devices

Mark A. Reed¹ and Alan C. Seabaugh²

¹ Department of Electrical Engineering and Applied Physics,
Yale University, New Haven, CT 06520

² Central Research Laboratories, Texas Instruments Inc., Dallas, TX 75265

Presented is a review of several semiconductor device approaches in which the electronic transport is dominated by quantum mechanical resonant tunneling. These approaches, which are a blend of heteroepitaxial thin-film growth and nanofabrication techniques, are candidates for an integrated circuit technology based on revolutionary device mechanisms. The detailed transport physics in these approaches is presented and discussed. Quantum devices have the potential to scale beyond the limits of conventional transistor approaches, and the prospects for these and other potential approaches are addressed.

THE DOWNSCALING OF MINIMUM GEOMETRIES of transistor-based integrated circuits (ICs) will eventually be brought to an end by a combination of problems related to device technology, interconnections, noise, and reliability. Scaling has heretofore provided exponential improvements in device speed and power dissipation, which has led to substantial enhancement of system performance. The resulting saturation of circuit densities almost certainly implies a saturation of the historical exponentially downward trend in cost and volume per bit or function.

Estimates based on abstract physical switching device models that are independent of specific device technologies indicate that several orders of magnitude in downscaling of device power is theoretically permitted in devices with minimum geometries of a few hundred angstroms, if an appropriate device technology can be found. The key to this search is to employ electronic phenomena that are characterized by dimensions much smaller than the depletion layer widths and diffusion lengths that provide the basis for conventional transistor function.

0065-2393/94/0240-0015\$09.44/0
© 1994 American Chemical Society

A step can be taken in this direction by employing heterojunctions rather than p–n junctions to introduce potential barriers for the purposes of carrier confinement. This approach is currently limited to compound semiconductors such as gallium arsenide (GaAs) and indium phosphide (InP), because of the absence of an adequate heterojunction technology for silicon. Nevertheless, as we shall see, this approach can be carried to the limit of completely unipolar devices employing only heterojunctions for confinement, completely eliminating all p–n junctions and their associated space-consuming depletion layers from the device.

The advent of molecular beam epitaxy (MBE) and similar thin-film growth technologies, as well as the blending with nanofabrication techniques, permits the fabrication of semiconductor heterostructures with features on the scale of nanometers. The ability to control the solid state in dimensional extremes has been a compelling attraction to researchers for more than three decades. The demonstration of two-dimensional electron gas (2DEG) systems initiated research that has continued unabated to present. The progress in this field increased dramatically with the arrival of atomically precise heterojunction epitaxial technology, allowing the realization of heretofore *gedankenexperiment* (thought experiment) structures (such as quantum wells) that exhibit manifest quantum effects. Today, we have reached a level of solid-state structural sophistication where we commonly design and fabricate devices based primarily on quantum mechanical phenomena. We now have available the tools to create and explore novel physical phenomena within nanoscale heterostructures. In these semiconductor nanostructures, having dimensions comparable to the de Broglie wavelength of electrons in materials, quantum mechanical effects are being engineered to produce potentially revolutionary device mechanisms.

More than a decade ago, nonclassical electron tunneling was demonstrated in “bandgap-engineered” heterojunction epitaxial structures (1). The importance of this result was not the specific realization of the tunneling structure, but a realization that artificially structured heterojunction devices could indeed demonstrate predominantly quantum transport.

Quantum mechanical tunneling is an electron-transport mechanism that, in semiconductors, becomes important when the thickness of potential barriers to carrier transport becomes very small, on the order of 10 nm. From a device standpoint, electrical control of quantum mechanical tunneling has been sought after for its potential use in three-terminal devices operating at sizes too small to operate as conventional transistors. Three-terminal devices based on tunneling would provide a means of continuing the historical exponential downward trend in minimum device geometries and in switching power and delay beyond the limits of transistors (2).

Beyond this, we also have the capability to fabricate structures that are truly “mesoscopic” in nature by nanofabrication. Here, we can observe not only tunneling and quantum confinement in three dimensions, but also single-electron charging effects. If schemes can be identified to create structures with large energy separations (i.e., to permit room temperature operation) and concurrently with gain, then another path is presented by which quantum device technology could extend beyond the limits of conventional transistor approaches. Presented here is a review of several semiconductor device approaches that are candidates for an IC technology based on quantum mechanical resonant tunneling.

Resonant Tunneling Transistors

Introduction. Within the past decade, heteroepitaxial technology has allowed researchers to explore a wide array of superlattice, quantum-well, and resonant-tunneling structures. The first proposals and investigations of the resonant-tunneling diode (RTD) were reported by Chang et al. (2) and subsequently were given impetus by Sollner et al. (3), who first observed large (from a technology standpoint) negative differential resistance (NDR). The RTD is in essence the electrical analog of a Fabry–Perot resonator, that is, a quantum well with thin electrically leaky barriers. The barriers are formed epitaxially by the judicious placement of semiconductors to produce band discontinuities to the majority charge carrier.

Since the initial demonstrations of the RTD (1, 3), many resonant-tunneling devices have been proposed and demonstrated (4, 5). Early experience with Esaki diodes showed that although diodes exhibiting NDR can be used for switching, large-scale ICs based on such threshold logic devices have not been commercially successful. Three-terminal devices providing current gain and fan-out are desired, and the fabrication process must be suitable for high levels of integration. A particularly intriguing concept has been to incorporate an RTD into one or another of the terminals of an otherwise conventional transistor (4–8). These crossbred transistor–RTD devices, particularly the resonant-tunneling bipolar transistor (RTBT) and the resonant-tunneling hot electron transistor (RHET), exhibit a serpentine transconductance characteristic that can be used to perform Boolean logic operations with a reduced device count. These semi-analog (although purely digital to the external user) “compressed-function” logic circuits promise to increase speed by reducing the total number of gates in a circuit (some approximately 1 order of magnitude). A broader review of the physics and applications of resonant-tunneling transistors (RTTs) can be found in references 4 and 5.

Resonant Tunneling. Resonant-tunneling devices are voltage-controlled. In the RTD, the current increases monotonically until a voltage, the resonant peak voltage, is reached. Resonance corresponds to the condition that electrons in the emitting (high-energy) side of the device are energetically aligned with the allowed transverse states of the quantum well. Quantum-well states are determined by the shape of the potential well, particularly the well width and the barrier potential height, but also weakly on the tunnel barrier thickness. Just beyond the resonant peak voltage the current abruptly diminishes forming a region of NDR, which is then followed by a region of monotonic current increase. If additional RTDs are combined in series or parallel, this characteristic can be repeated again. The energy band structures and characteristics of a typical RTD structure is shown in Figure 1. The most widely investigated heterojunction material is the lattice-matched GaAs–AlGaAs system, where the highly doped contacts and central quantum well are GaAs, and the barriers are Al_xGa_{1-x}As. The two Al_xGa_{1-x}As layers that define the central GaAs quantum well serve as partially transparent barriers to electron transport through the device. Resonant tunneling occurs when the bias voltage across the outer electrodes is such that one of the quantum-well bound states is monoenergetic with the input electrode Fermi level. The structure is the electrical analog of a Fabry–Perot resonator. Leakage (inelastic tunneling current) is determined by the quality of the interface and electron–phonon scattering. Improvements in epitaxial growth techniques have been responsible for the enhanced performance of these structures. The measured current–

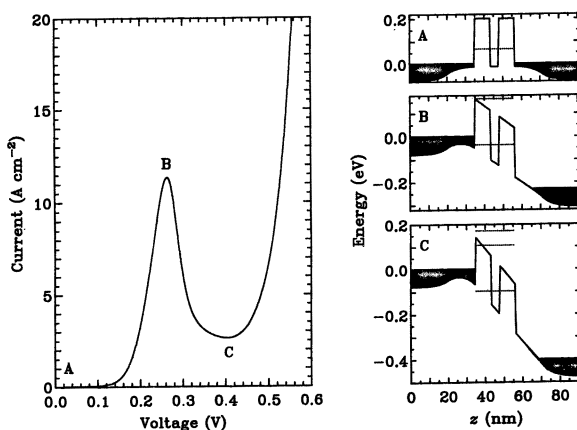


Figure 1. Measured current–voltage characteristics of an AlGaAs–GaAs RTD at 77 K and the corresponding computed energy and diagram as function of applied bias. (Reproduced with permission from reference 9. Copyright 1989 Academic.)

voltage (I - V) characteristic of the AlGaAs–GaAs RTD is shown in Figure 1. Alongside the I - V curve is a set of computed energy band diagrams for the structure for three separate positions on the measured I - V characteristic: at zero bias (A), biased at resonance (B), and biased beyond resonance (C) (9).

A common figure of merit for the RTD is the ratio of peak current at resonance to the lowest current after resonance, called the valley current. This ratio is termed the peak-to-valley current ratio (PVR). Double-barrier RTDs operating at room temperature, (see Figure 2) are readily obtained; PVRs as high as 50:1 (10) have been reported at 300 K. A wide design flexibility is available for development of high-speed, high-current applications (e.g., switching and logic) or low-current, low-power (e.g., memory and again, logic) applications. High-current densities (exceeding 2×10^5 A/cm²) at the current peak are obtained with PVR exceeding 4 and with approximately symmetric I - V behavior. At these current densities, comparable to those achieved in bipolar transistors, there is clearly sufficient current to drive subsequent stages with fan-out.

Device Physics of Resonant Tunneling Transistors. To make a three-terminal quantum device, we need a way to control the current through the device with a voltage or current supplied to the control electrode. The current through the device may be presumed to be conducted by resonant tunneling of electrons. The obvious transistor approach (an alternative to the crossbred transistor–RTD approaches) is to directly manipulate the potential of the quantum well. If this is to be done through the electrostatic potential, then mobile charges must be added to or removed from the quantum well by the control electrode, which acts as a source of the perturbation in the potential. The nature and behavior of these charges present the fundamental challenges.

Let us first consider what happens in a unipolar structure when electrons are used to control the tunneling current. The problem with such schemes is that the equilibrium electrons in the base are still quan-

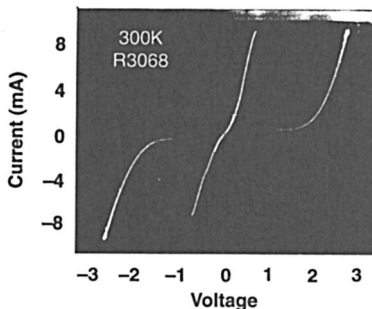


Figure 2. Current–voltage (I - V) characteristics for an AlAs–In_{0.53}Ga_{0.47}As–InAs–In_{0.53}Ga_{0.47}As–AlAs (2/1/2/1/2 nm) RTD exhibiting peak-to-valley current ratio near room temperature (25°C).

tum mechanical particles and have to occupy allowed quantum states in the quantum well. The lowest state is typically the state through which the electrons tunnel, for example in the RTD. In the RTD case with electrical contact to the quantum well, there exists no distinction between controlling and current-carrying electrons of the structure as required for transistor operation. In addition, as illustrated in Figure 3a, the base–collector tunnel barrier is insufficient to confine the electrons to the base if it is thin enough to permit resonant tunneling. This condition leads to an excessive base–collector leakage current, of sufficient magnitude to effectively short circuit the base–collector junction and make transistor action impossible.

A device called the quantum-well excited-state tunneling transistor (QuESTT), independently invented by Frensley and Reed (11), Schulman and Waldner (12), and Haddad et al. (13, 14) overcomes this problem. This structure uses a narrower band-gap quantum-well layer to “hide” the lowest-lying electron state from the tunneling electrons, thus making it available to the control electrons, as shown in Figure 3c. The control electrons are injected into and extracted from the base by a contact to the central layer of narrow-band-gap material. The quantum well, and thus the bound states in the quantum well, can then be modulated with respect to the contact potentials, providing a tunable tunneling mechanism. Resonant tunneling occurs when the quantum-well bound states become monoenergetic with the emitter electrode Fermi level, now created by applying a base voltage. The problem now becomes technological instead of fundamental; that is, overcoming the obvious fabrication difficulties of exposing and contacting a thin (~ 10 nm) quantum-well base. Though a number of attempts have been made, a QuESTT exhibiting both gain and negative transconductance has yet to be realized.

As with the unipolar device described, the most obvious bipolar quantum-well transistor structure suffers from a similar leakage problem. The leakage path becomes apparent if we consider the energy band diagram of the resonant-tunneling structure. Such a band diagram is shown in Figure 3b. To achieve resonant tunneling, the potential of the bottom of the quantum well must be biased below the bottom of the conduction band in the source electrode. Therefore, the emitter–base bias must be greater than the band-gap potential of the quantum-well base. Now we have to have some way to make contact to the majority carrier holes in the quantum well, and this implies a bulk region that is doped p-type. If this p-type region is in contact with the n-type emitter, a dominant nonresonant parasitic current results.

As with the QuESTT, leakage currents can be suppressed through appropriate choice of heterostructures. Such a bipolar analog of the QuESTT has been proposed and demonstrated (15–18). A schematic

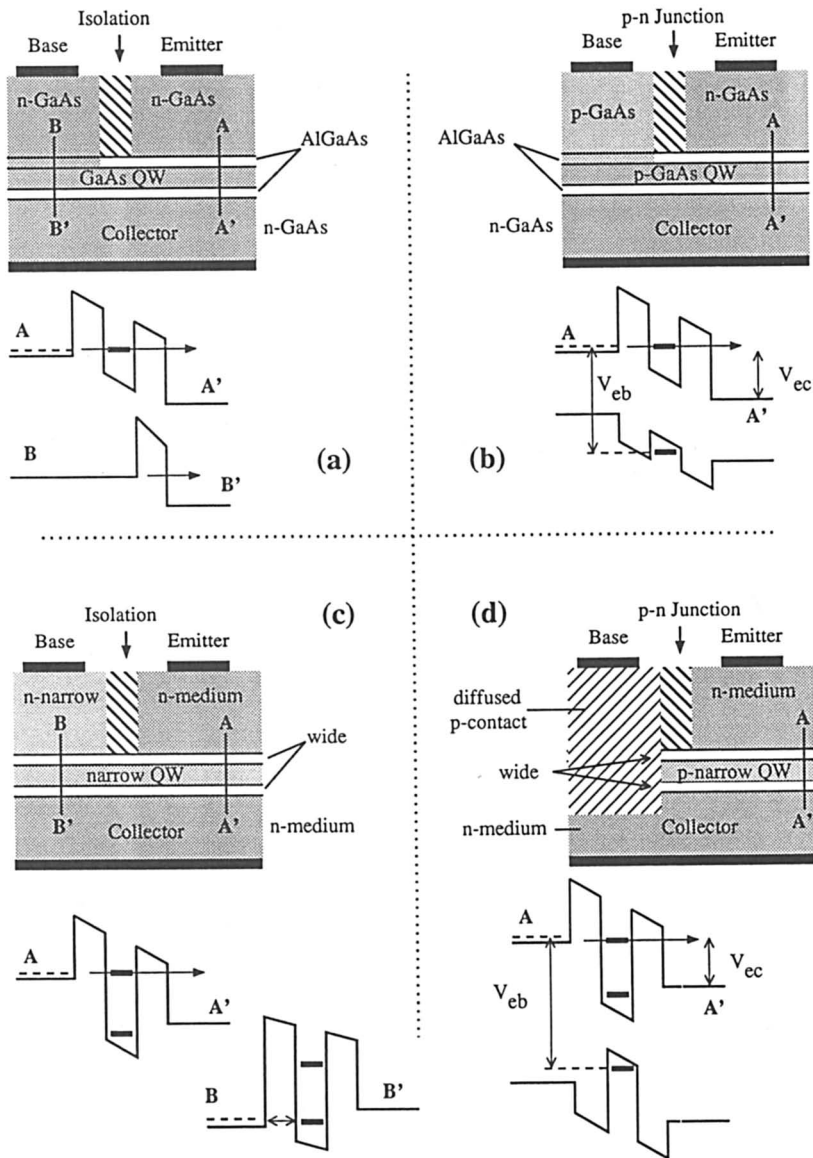


Figure 3. (a) Hot electron tunneling transistor. The band diagram through AA' shows tunneling behavior, but that through BB' shows parasitic base current. (b) A bipolar tunneling transistor. The energy band diagram through section AA' illustrates the large forward bias required for this device to operate. (c) The quantum-well excited-state tunneling transistor (QuESTT). Collector current is derived from tunneling through the excited (upper) quantum-well state, while control carriers are supplied to the ground state by the base contact and confined by the medium-gap collector. (d) The bipolar quantum-well resonant-tunneling transistor (BiQuaRTT). The energy band diagram through section AA' illustrates the reduced forward bias voltage due to the narrow-bandgap quantum well.

band diagram for this device is shown in Figure 3d. Like the QuESTT, the quantum well is made of a narrower band-gap material than the emitter, which reduces the bias voltage required to turn on the device and introduces a barrier to holes, thereby suppressing hole injection into the emitter. In this case the base is heavily p-doped to provide for ohmic contact to the well; thus the device has been called the bipolar quantum-well resonant-tunneling transistor (BiQuaRTT). Contact to the quantum-well base of this device is achieved by either ion implantation or diffusion of acceptors, and a number of device embodiments have been realized (15–18). Though both current gain and negative transconductance (NTC) at room temperature have been observed in this device, simultaneous NTC and gain have not yet been achieved, due to the large base scattering rate from both the quantum confinement and the base doping. However, recently, a remarkable resonant transmission effect in the BiQuaRTT has been observed in transistors in which the quantum-well base is both widened and structured. In these BiQuaRTTs, a multiple room temperature NDR characteristics is obtained with simultaneous current gain (19).

An alternative approach to the quantum-well base transistor is to integrate RTDs into conventional transistor heterostructures. By comparing their band diagrams, the differences between the crossbred RTD–transistor approach and the quantum-well RTT approach can be seen for the bipolar transistor case in Figure 4. The RTBT approaches are shown on the periphery and the BiQuaRTT in the center. Each of the energy band diagrams was recalculated [by solution of Poisson's equation (20)] from published material descriptions and plotted on the same horizontal scale. The npn transistor structure and resonant-tunneling double-barrier can be seen in each of the energy diagrams. The initial approaches of Capasso et al. (21) and Futatsugi et al. (22) are shown at the top of the figure. Futatsugi et al. placed the RTD at the emitter–base junction (Figure 4, upper left), but Capasso et al. (upper right) put the undoped RTD just inside the p-type base. The effect in both devices is approximately the same. Improved PVR and current gain in the RTBT have been obtained by spacing the RTD back from the p-type base dopants. Transistors based on the InAlAs–InGaAs system and lattice-matched to InP have been demonstrated and are also shown in Figure 4, for both a single RTD (lower left) (23) and a stack of two RTDs (24) (lower right). Using the same basic approach, similar improvement has been obtained in the GaAs–AlGaAs RTBT (25).

The BiQuaRTT, shown in the center of Figure 4, differs from the RTBTs in that the p-dopants are located within the quantum well; thus the entire base is two-dimensional (2D) with transport proceeding from three-dimensional (3D) emitter to 2D base to 3D collector. Again, the resonant-tunneling double-barrier quantizes the allowed energies at

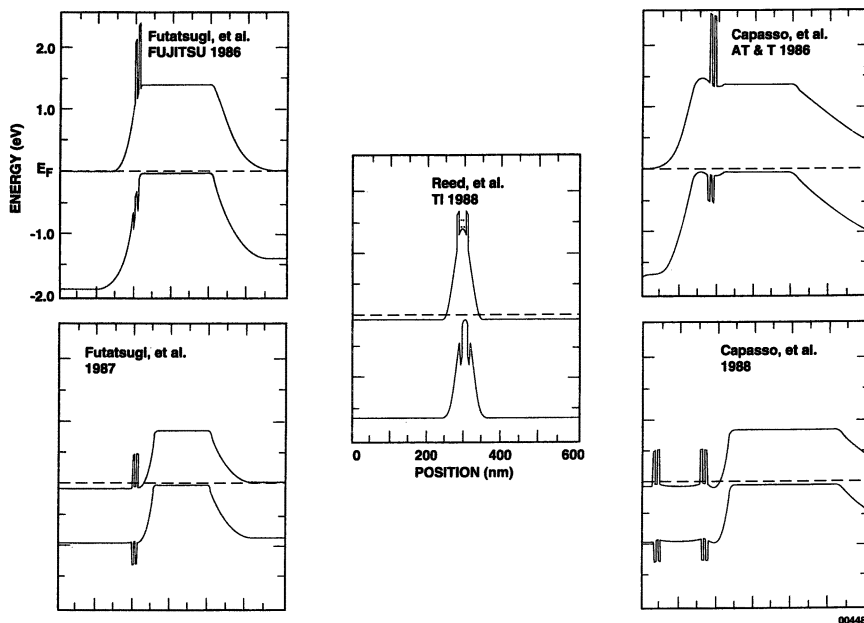


Figure 4. Energy band profile comparison of bipolar resonant-tunneling transistors. The literature references are, in counterclockwise order starting in the upper right, Capasso et al. (21), Futatsugi et al. (22), Futatsugi et al. (23), and Capasso et al. (24), and in the center, Reed et al. (15). The top two and center structures are GaAs–AlGaAs materials on GaAs substrates, and the lower structures are InGaAs–InAlAs materials grown on InP. (Reproduced with permission from reference 5. Copyright 1994 Academic.)

which the electron can transverse the 2D base (in the growth direction). To inhibit hole injection into the emitter at resonance, the quantum-well base is comprised of a lower band-gap semiconductor than the emitter. An ohmic contact to the quantum well is used to control the base potential relative to the emitter and thereby set the condition for tunneling transmission across the base.

Unlike the conventional transistor–RTD combination, the quantum-well RTT is scalable, that is, further reduction in the dimensionality of the device is possible, through the introduction of lateral confinement. In the RTD–conventional transistor approach where the RTD is essentially in series combination, series resistance and size quantization between elements become a problem with lateral scaling. Further, the quantum-well RTT has a more compact vertical layer sequence than its counterpart, the RTBT, because the resonant-tunneling double barrier is an integral part of the structure. For integration with conventional transistors, a greater process flexibility is allowed, because additional

epitaxy can be added for integration of conventional transistors or other circuit elements with less increase in the surface topography.

The transfer characteristic for the RTT can be understood as a simple extension of RTD principles. For example, in the BiQuaRTT, illustrated in Figure 5a, for applied base voltage steps, the transmission from emitter to collector is controlled by the energetic position of the emitter electrons with respect to the quantized base states. When energetic alignment is achieved, the current transport through the transistor is enhanced. For biases off resonance, the current decreases, but increases again because of inelastic processes and resonant transmission through higher lying base states. Thus, the collector current has an oscillatory response (alternately positive and negative), and therefore, an oscillatory transconductance for a monotonically increasing base-emitter voltage.

The idealized transfer characteristic for the RTT is shown in Figures 5b and 5c. As with the RTD, the transistor is voltage-controlled with the base-emitter voltage determining the collector current. As shown in Figures 5b and 5c, the collector current increases, then decreases, then increases again for a monotonically increasing base-emitter voltage. Generally equivalent characteristics are expected for all the vertical RTTs described here: RTBT, RHET, QuESTT, and the narrow-base BiQuaRTT.

Recent Device Results. The quantum-well version of a resonant-tunneling transistor has been realized in a number of embodiments (15–18). The first structure realized (15) utilized a band-gap-engineered superlattice contact region as an alternative to the InGaAs quantum-well embodiment (16) to create a wider band-gap material. By varying the dimensions of the components of the superlattice, the effective band-gap of the superlattice can be continuously “tuned” anywhere between that of the components. This solution actually simplifies technical dif-

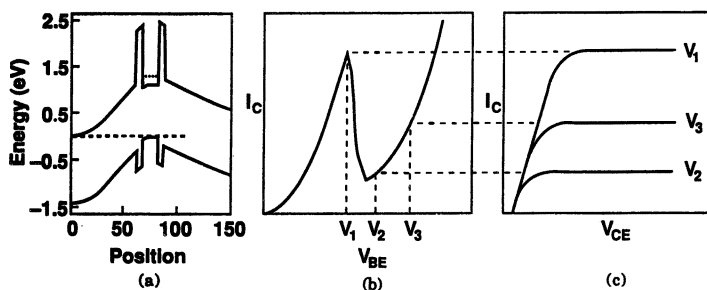


Figure 5. Computed NpN BiQuaRTT energy band profile (a) and the idealized common-emitter transistor characteristics (b) collector current versus base-emitter voltage V_{BE} , and (c) collector current versus collector-emitter voltage, V_{CE} .

difficulties in the growth of such structures and permits extensive future modifications of the device band structure by simple dimensional modulation.

Strong room-temperature size-quantization effects can be obtained in the BiQuaRTT with high current gain at resonance and with wide quantum wells (19). This new transistor effect arises from the alteration of quantum-well-base shape with base-collector bias. Changes in the quantum-well shape lead to large modulations of the transmission coefficient for quasi-thermalized minority electrons crossing the base.

The computed energy band diagram for the wide quantum-well BiQuaRTT device is shown in Figure 6. This BiQuaRTT has a quantum-well width of 120 nm, with doping confined to the central 80 nm of the well. As a result of the undoped layer preceding the collector tunnel barrier, a triangular potential well forms at the base-collector junction (Figure 6), thereby making the quantum-well base asymmetric. The shape of the triangular well, particularly its depth, is controlled by the base-collector bias.

A set of four transistors was fabricated on the basis of the structure in Figure 6, and their resulting characteristics are shown in Figure 7. These transistors differ by the presence or absence of one or both of the AlAs tunnel barriers. Specifically, the first transistor utilized the BiQuaRTT structure of Figure 6. A second transistor excluded both tunnel barriers, thereby forming a conventional In(GaAl)As-InGaAs heterojunction bipolar transistor (HBT). A third transistor omitted the collector tunnel barrier, thus forming a tunnel-barrier-emitter HBT, and the final structure omitted the emitter tunnel barrier, thereby forming an HBT with a tunnel barrier at the base-collector junction. In this

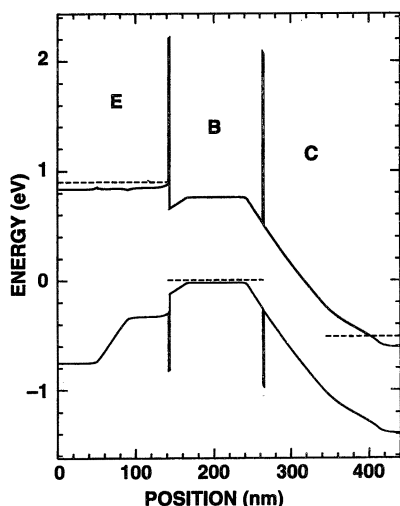


Figure 6. Computed potential profile for the BiQuaRTT at room temperature with $V_{BE} = 0.95$ V and $V_{CB} = 0.5$ V. The dashed lines indicate the quasi-Fermi level energies that are set by the applied voltages.

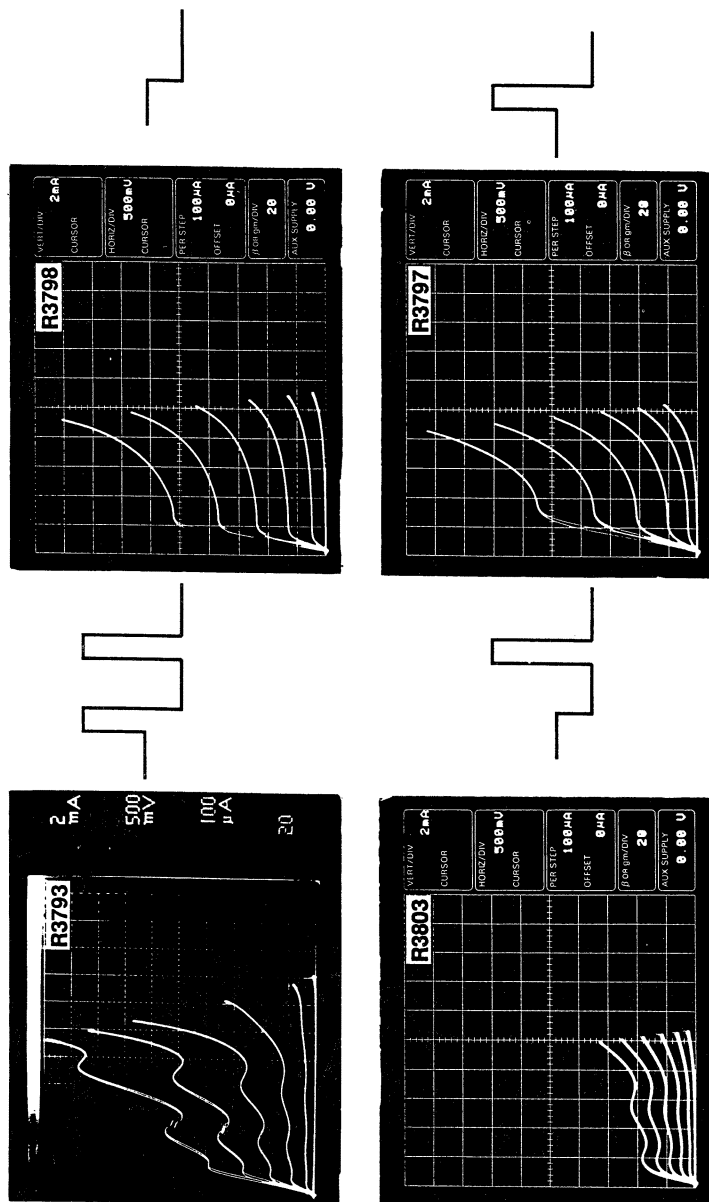
(625 μm^2 Emitter)

Figure 7. Comparison of four different bipolar transistors heterostructures differing by the presence or absence of AlAs tunnel barriers at the emitter-base or base-collector heterojunctions. Starting from the upper left and proceeding clockwise, the common emitter transistor characteristics correspond to the wafers: (R3793) BiQuaRTT, including both tunnel barriers as in Figure 6; (R3798) heterojunction bipolar transistor (HBT), no tunnel barriers; (R3797) tunnel emitter HBT, a tunnel barrier in the emitter-base junction only; and (R3803) BiQuaRTT with a tunnel barrier in the base-collector only. A schematic band diagram illustrating the heterojunction alignments are drawn next to each photo.

latter BiQuaRTT the base is quantized by the emitter–base heterojunction and the base–collector tunnel barrier. Strong multiple NDR regions are observed in the two transistors, which include the base–collector tunnel barrier, although in the conventional HBT and tunnel-emitter HBT structures, no NDR is observed. The biases, current gain, and collector current magnitude are comparable for the entire set of transistors.

This set of four structures shows that the NDR is independent of the emitter tunnel barrier and requires the base–collector tunnel barrier. These observations are explained as follows: Minority electrons injected into the base have an energetic distribution exceeding the separation of quantized base states. As the injected electrons diffuse across the base, they quasi-thermalize and thereby assume a narrow distribution near the triangular potential well at the base–collector junction. As the base–collector bias increases, the lowest lying quantum-well base state with wave vector normal to the base–collector tunnel barrier is successively dropped into the triangular potential well and is then below the energy of the narrow electron distribution at the emitter side of the triangular potential well. When this lowest-lying state is dropped into the triangular well, the transmission probability is reduced for electrons across the triangular potential well. This modulation of the transmission probability as states are dropped into the triangular potential well produces the NDR.

These results are indicative of the rich device physics and complex phenomena that can be found in band-gap-engineered tunneling transistor structures. Exploration of quantum-well base transistors is still in its early stages. The advent of selective etchants for the InGaAs–AlAs heterojunction system (26) is making possible the fabrication of quantum-well RTTs with minimized quantum-well base widths and further exploration of alternative charge control mechanisms.

RTT Circuits. For function in a logic application, resonant-tunneling transistors must possess current gain, input–output isolation, threshold voltage uniformity, and fan-in and -out, as required for digital circuits (27). Room-temperature operation is generally preferred to achieve broad application.

The motivation for realizing these devices is not simply device speed: A detailed modeling of these devices shows that the speed is at best equivalent to that of a well-designed HBT or HET. Instead, the increase in speed occurs at the circuit level, due to a decrease in the number of gates needed. The serpentine transfer characteristic of the NTC devices described gives us the ability to implement complex logic functions, which would normally require many transistors, with a circuit containing fewer devices. The recent book chapters by Capasso et al. (4), Seabaugh

and Reed (5), and the work of Takatsu et al. (28) give a review of recent developments in RTD and RTT circuits.

Using transfer characteristics such as illustrated ideally in Figure 5 and obtained in the RHET and RTBT, compressed function logic is possible. The classic example of this feature is shown in Figure 8 for the RHET. By using a resistive summing network at the base terminal of the device and using the intrinsic NTC characteristic of the RHET, the XNOR (exclusive not-OR) function can be realized in a single device. The number of transistors is reduced by a factor of approximately 5 over existing transistor technologies to achieve the same function. In this way a logic function requiring many transistors is performed with a single RTT. The amount of logic performed per unit area is thereby increased, and the delay caused by multiple transistor stages and their interconnects is reduced.

Referring to Figure 8a, the resistive summing network is used at the base terminal of the device to convert the binary inputs at A and B to a quasi-analog signal at the base terminal. When both A and B inputs are low, the base voltage is low and the collector current through the RHET is low. If either A or B inputs are high (1), the resonant bias is presented at the base and the collector current is high. If both A and B inputs are high the device is biased off resonance and the current through the RHET is low. The exclusive-NOR gate then has binary input and output signals, but performs the additional logic through the use of the analog summing node and novel device transfer characteristic. The measured output characteristics of the RHET is shown in Figure 8b, confirming the expected truth table.

The serpentine transfer characteristic of RTT devices gives us the ability to implement complex logic functions, which would normally

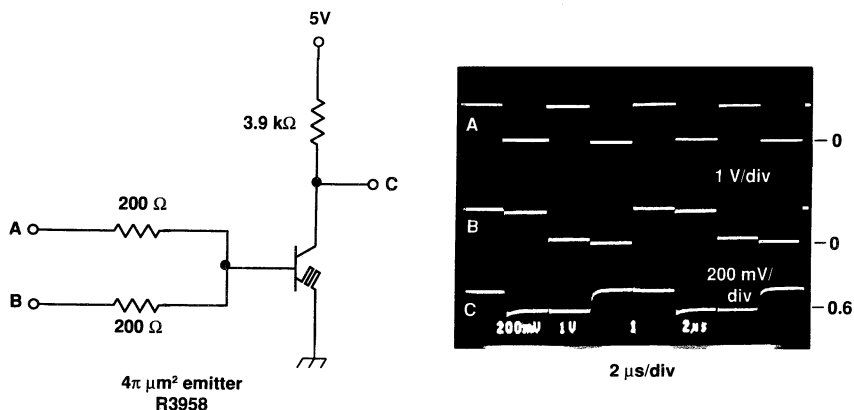


Figure 8. Room-temperature RHET exclusive-NOR gate.

require many transistors, with a circuit containing only a few RTTs. Let us assume the characteristics of the ideal RTT; that is, NTC but positive output conductance, as illustrated in Figure 9a. Four states are identifiable if one includes the rising current at large base voltage. The sequence of states fits very well with the truth table of a full adder (except that the output is inverted). A complete full adder could be realized with the circuit approach shown in Figure 9b, using one RTT and a few other transistors. In this circuit the addend (A), augend (B), and carry (C_n) inputs are algebraically added in a summing node that drives the base of the RTT. The RTT produces an inverted sum that is restored by an inverter. The carry output (C_{n+1}) is generated from the same summing node by a saturating (or latching) amplifier. The inverter and the noninverting amplifier could be implemented with either RTTs or HBTs. The circuit design using HBTs would be quite straightforward and would require at most three more transistors. If RTTs are used, the carry function could be generated using a simple latching circuit and the inverter function could be obtained from an exclusive NOR gate with one input biased high.

It has been about 5 years since the initial reports of RTTs, yet ICs are only now being realized. Three major reasons for the slow progress in this field are as follows: (1) the lack of a detailed understanding of device transport in quantum-well devices, (2) circuit designs that utilized NTC devices are still in their infancy, and (3) immaturity of growth and process technology. Critical dimension control and uniformity of quantum-well and tunnel barrier thickness, and the resultant fluctuations in threshold voltages and current densities to first order, should not be a limitation with proper design of materials, fabrication, and device. RTT compressed function logic circuits should become competitive with improvements in processes and innovations in circuit technology, thus providing a vehicle for device and circuit scaling beyond the conventional transistor limit.

Quantum Dots

Introduction. In the previous section, we discussed the ability to make quantum devices by heteroepitaxial means. Recently, microfabrication technology has progressed to the point that researchers can now controllably impose additional lateral dimensions of quantum confinement on 2D systems with length scales approaching those of epitaxial confinement (29–31). The achievement of one-dimensional (1D) quantum wires and zero-dimensional (0D) quantum dots have demonstrated that electronic systems with different dimensionality are now available to the experimentalist.

How does one fabricate these structures of low dimensionality? The obvious approach is to utilize the existing technology of MBE or metal-

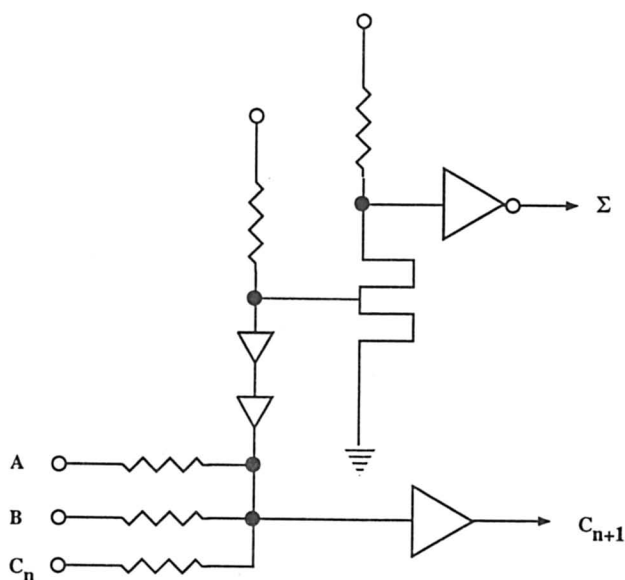
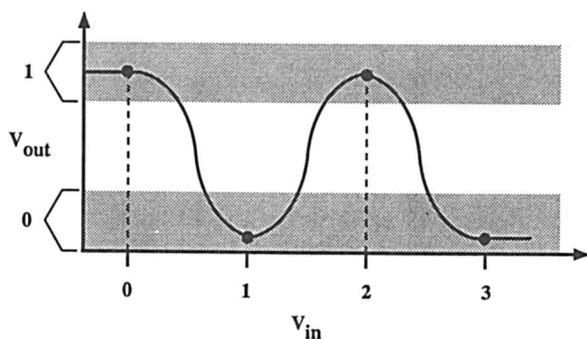


Figure 9. A full adder using RTTs: (a) serpentine transfer characteristics of the RTT with logic levels assigned and (b) a complete full adder realized with one RTT and a few other transistors. In this circuit the inputs are the addend (A), augend (B), and carry (C_n). The carry output (C_{n+1}) is generated from the same summing node by a saturating (or latching) amplifier. The circuit design using HBTs for the conventional transistors would require approximately three additional transistors.

organic chemical vapor deposition (MOCVD) to define a 2D system, and impose additional lateral confinement with nanometer lithographic techniques. State-of-the-art in electron-beam lithography can define dimensions in the 15-nm regime, with pattern-transfer techniques in the same dimensional regime, clearly sufficient to observe large quantum size effects.

An obvious technique that comes to mind in creating a quantum confining potential is to use nanometer-size electrostatic gates on the epitaxial structure, which confine the underlying 2D system (often a 2DEG). By applying a negative potential, the underlying 2DEG is depleted underneath the gates and confined to the region between the gates. This approach results in a smooth electrostatic confinement that has the advantage of a continuously tunable confining potential. This technique also has the coincident advantage that nanometer-size imperfections in the definition of the gate structures are not transferred to the confining potential, because the electrostatic screening of the 2D electrons smooths out the confining potential to a length scale significantly larger than these imperfections. However, the screening also means that the dimensional size of the confining potential is large (>100 nm) and energetically shallow (relatively, when compared to heterojunction confinement), resulting in quantum confined states spaced by ~ 1 meV. Electronic transport that reveals quantum size effects in these systems thus only occurs for low temperatures (<1 K). Yet even with these limitations, this technique has proven to be sufficiently successful to demonstrate quantum confinement.

A more interesting (and thus, more complex) situation is when one can create quantum confinement with large energetic barriers, so that one can enter the nonequilibrium quantum transport regime. In this regime, achieving transistor structures with gain can be done by imposing structural confinement on the 2D system by anisotropic dry etching, which some call the "neolithic" approach. The basic principle is to use energetic ions to either erode or chemically react with the epitaxial material structure. By using a reactive gas species that forms volatile compounds with the material, semiconductor structures as small as 20 nm have been demonstrated. Thus, hard wall potentials can be formed by etching either partially or completely through the epitaxial structure. However, two serious drawbacks are seen with this approach. First, a serious side effect of dry etching is damage to the semiconductor by the energetic ions. The extent of the damage is poorly understood and has shown large process variability. Second, the resulting free surfaces (in the compound semiconductor systems) result in a large concentration of nonradiative recombination sites. Additionally, the free surfaces "pin" the Fermi level; that is, large depletion layers extend from the surface into the electron system. These depletion layers result in making the

lithographically defined dimension different from the desired region of quantum confinement of the electron system. Thus, both optical and electronic transport studies are problematic. Only in special arrangements has this technique yielded conclusive results. One of these arrangements and the resultant transport studies is presented in the following section.

Transport in Quantum Dots. The creation of 0D electronic systems ("quantum dots") (32–38) is intriguing because these structures are analogous to semiconductor atoms, with energy levels tunable by the confining potentials. A configuration is adopted in which structural lateral confinement is imposed onto a heteroepitaxial resonant tunneling structure; that is, the quasi-bound momentum component (the transport direction) is epitaxially defined, and additional confinement is fabrication-imposed. Tunneling spectroscopy then probes the low-dimensional states. Because of this configuration, the behavior of a system operated far from equilibrium can be examined.

1D–0D Tunneling. The fabrication of these structures was previously reported (32, 33). The approach essentially embeds a quasi-bound quantum dot between two quantum wire contacts. Creation of dots less than 500 Å is possible, although we will show that the appropriate range for the typical epitaxial structure and process used is in the range 1000–2500 Å in diameter. A scanning electron micrograph of a collection of these etched structures is seen in Figure 10. Contact is made to just a single structure, so that the resulting transport is tunneling spectroscopy of a single dot.

The current–voltage–temperature characteristics of these structures typically exhibit a clear series of additional NDR peaks at low temperatures (Figure 11). Variation of the lateral diameter by more than 1 order of magnitude verifies an approximate R^{-1} energy splitting dependence, indicating energy quantization by the lateral potential instead of single-electron charging, which would have a R^{-2} dependence (39). The observed quantum dot spectrum may be explained as resonances when the quantum dot states are biased through the emitter subband states with increasing device bias (40). To determine if this mechanism quantitatively explains the spectrum, the 3D self-consistent screening quantum dot model is solved at applied bias to determine the variation of the emitter and quantum dot energy levels with applied voltage. The model self-consistently obtains the electrostatic potential in a zero-current theory from Poisson's equation utilizing a Thomas–Fermi approximation for the electron density (41). The solution of the electrostatic problem then provides the potential responsible for lateral quantization of electron states. The radial bound states in the contacts provide

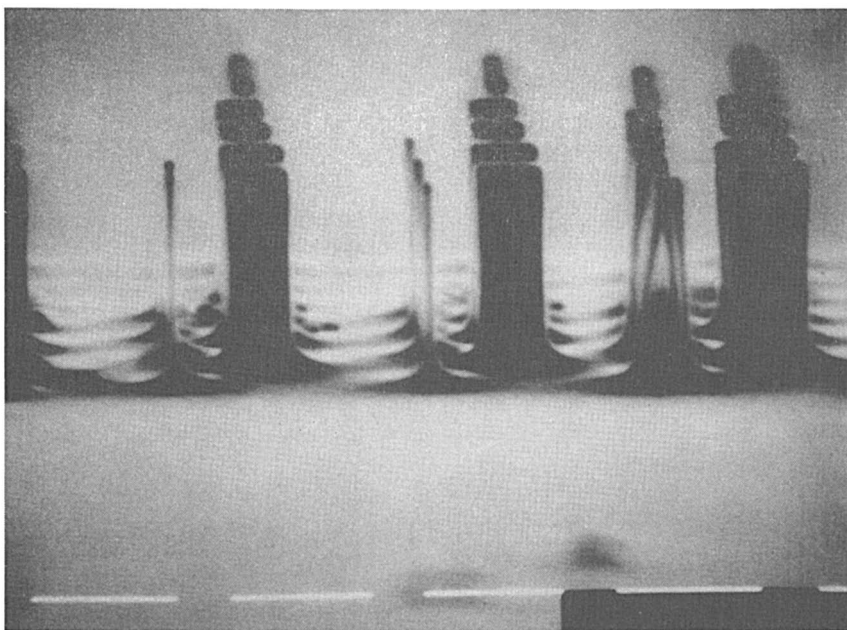


Figure 10. Scanning electron micrograph of an array of anisotropically etched columns containing a quantum dot. The horizontal white marker is 0.5 μm .

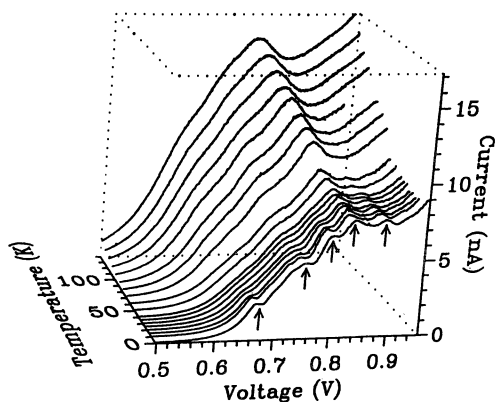


Figure 11. Current–voltage characteristics of the 1000 Å single quantum-dot nanostructure (32) as a function of temperature, indicating resonant tunneling through the discrete states of the quantum dot. The arrows indicate peak positions for the $T = 1.0\text{ K}$ curve. (Reproduced with permission from reference 32. Copyright 1988.)

the minima of the emitter and collector subbands. Likewise the discrete quantum-well levels are obtained from a solution of the radial Schrödinger equation.

The solution to the 3D screening problem of the experimental situation of Reed et al. (32) under applied bias is displayed in Figure 12. The electron potential energy surface is plotted as a function of radius and epitaxial dimensions. The energy scale is defined relative to the Fermi energy; thus, the potential at the external radius equals 0.7 V (the Fermi level pinning value). Clearly, the lateral depletion has a dominant effect on energetically lifting the double-barrier structure significantly above the level previously determined only by the z-doping profile. The relevant quantum dot states, determined by solving the radial Schrödinger equation, arise from the previous quantum-well ground state ($n = 1$). The excited state ($n = 2$) quantum dot states are virtual (above the barriers).

We can now calculate the energies of the 1D emitter (and collector) and 0D quantum dot states under arbitrary applied bias. Figure 13 shows the crossings of the emitter subband level (n') with the quantum dot levels (n) as a function of applied bias, transposed onto the 1.0 K experimental spectra of reference 32. The relevant dot states all have the same $n_z (=1)$ quantum number ($n_2 =$ two dot states are virtual), which is hereafter suppressed. General agreement is seen between the experimental and predicted peak voltage positions, especially the anomalously

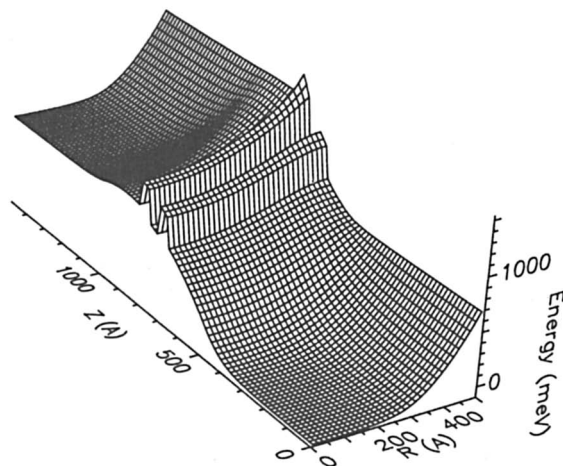


Figure 12. The electron potential energy surface is plotted as a function of radius and epitaxial dimensions (solution to the 3D screening problem) of the experimental situation of reference 32 (data are from Figure 11), under applied bias. The energy scale is defined relative to the Fermi energy. (Reproduced with permission from reference 32. Copyright 1988.)

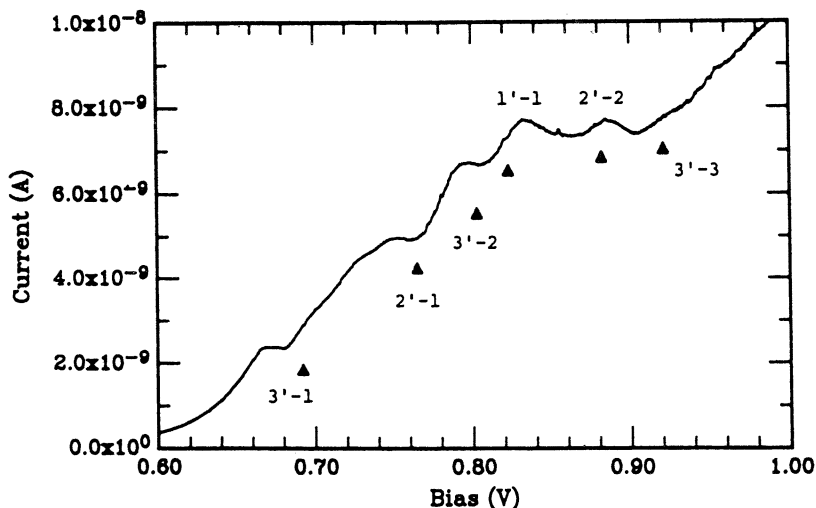


Figure 13. The crossings of the emitter subband level (n') with the quantum dot levels (n) as a function of applied bias, transposed onto the 1.0 K experimental spectra of Figure 11.

large splitting of the first resonance. The experimental measurement is current, which implies that an integration over the density of emitter states should be done for a strict comparison. The predicted 3'-3 transition appears to be absent in the spectrum, except for a very weak structure at 0.92–0.93 V. However, this absence is expected because the collector barrier becomes sufficiently low such that this state becomes virtual at ~ 0.95 V. This low collector barrier has an important implication and is verification that the observed resonances are due to states localized in the quantum dot.

The 1D density of states in the emitter becomes thermally smeared when $3k_B T > \Delta E$ (the emitter subband spacing), and thus at high temperatures the only surviving transition is the 1'-1. This indeed occurs when $3k_B T \sim 21$ meV, in good agreement with the subband spacing of 25 meV. In the high-temperature limit, the structure emulates an unconfined 1D resonant tunneling diode.

The observation of the momentum-nonconserving transitions ($n' \neq n$) shows that k -perpendicular is not a good quantum number in this system, due to the hourglass topography of the electron constant energy surface. This absence of a n, n' (radial) selection rule is natural from the radially changing, cylindrically symmetric geometry that breaks translational symmetry.

0D-0D Tunneling. An intriguing situation would be to examine the case of 0D-0D tunneling, compared to the 1D-0D situation. The

fabrication of such structures is relatively straightforward, using a double-well, triple-barrier initial epitaxial structure. The structure was designed so that state overlap is small (with respect to the lateral splitting energy), so that the 1D–0D and 0D–0D transitions can be compared. Lateral fabrication is similar to that already described.

Figure 14 shows the 4.2 K current–voltage characteristics of this structure. A similar modeling of the state crossings as described was performed, and the spectra of the transitions are superimposed on the figure. The notation used here is 1 (emitter subband)-(final state), for either the first (n') or second (n'') (i.e., further downstream from the emitter) dot.

The spectra is well-fit by resonances occurring for crossings of the 0D states with the lowest 1D subband in the contact. The agreement is good for the major ($1-n'$) resonances, significantly stronger than the n'' states due to the thinner tunnel barrier. The position of the minor second set, $1-n''$, predicts the structure below the $1-1'$ peak. The peaks are not apparent at higher voltages, probably due to overlap with the $1-n'$ resonances.

The predicted 0D–0D crossing spectra gives bad agreement both qualitatively (spacings and number of peaks) and quantitatively (peak

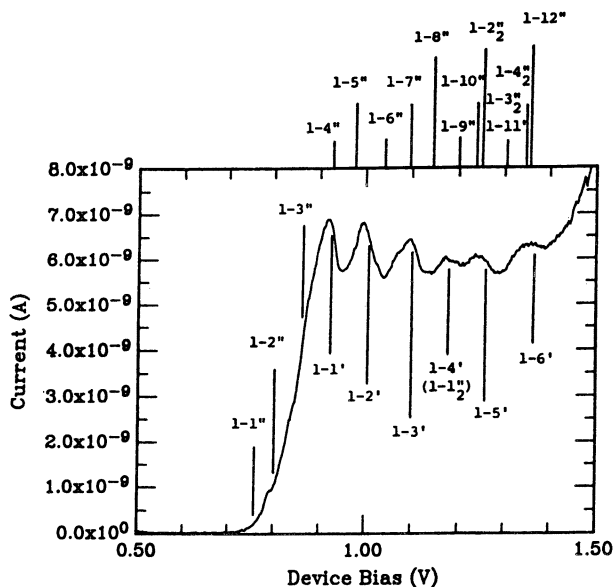


Figure 14. Current–voltage characteristic at $T = 4.2$ K of the “0D–0D” sample, with predicted resonant peak positions superimposed. The notation is 1 (emitter subband)-(final state), for either the first (n') or second (n'') dot. The subscript (i.e., n''_2) denotes the $n_s = 2$ excited state.

positions); the predicted spacing of 0D–0D crossings are approximately 5 mV throughout the region examined. However, because the lateral potential of the adjacent dots is nearly identical, k -perpendicular is a good quantum number in the 0D–0D transitions, compared to the dramatic lateral potential variation in the 1D–0D transitions. Thus, the 0D–0D transitions would only occur for $n' = n''$, which is not experimentally accessible in this structure. Thus, we observe only the 1D–0D transitions (each separately), and not the 0D–0D transitions (the selection rule holds for $n' = n''$ and not for $n = n', n''$) because the lateral potential changes from the contact-to-dot region but not for the dot-to-dot region. Observation of these transitions will require a delicately designed structure in the AlGaAs system, although there exist other candidate systems where this may be easier.

Summary. Quantum dot structures provide a unique laboratory for the exploration of quantum transport through nanostructured semiconductors, such as electronic transitions and selection rules involving those states. The epitaxial design freedom allows a highly complex electronic state structure to be examined. Additionally, these nanostructures provide clues to systems with possible technological impact, because they can operate at high temperature (NDR in these have been observed even at room temperature) and far from equilibrium, implying that multiterminal devices can operate with gain. The exploration of these structures is very new, and the interplay between size- and charge-quantization, as well as identifying alternate materials and fabrication methods, could lead to a technologically important device technology scalable to the mesoscopic regime.

Future Quantum Device Prospects

On the horizon are a number of enticing physical systems to be explored. We have discussed here quantum confinement involving heterojunctions and electrostatic confinement by free surface pinning. An alternative, also mentioned, is to control the potential of 2DEG systems with gate potentials.

At present, the degree of quantum confinement in gate-confined systems is relatively weak and uncontrolled. Confinement is presently achieved by “soft” potentials that give rise to subband splittings of only a few millielectron volts. Exploration of the simplest configuration utilizing this technique, a point-like constriction of a 2DEG, has shown fascinating results (42, 43). Simply, the conductance of the point contacts will be quantized, in units of e^2/h per spin, in the limit of a few ballistic electron channels. Such systems provide a fascinating laboratory for exploring the limit of electronic transport, of exploring

the ballistic transport regime, and of demonstrating nonlocal quantum interference. Additionally, in these systems the contacts to such a system are nontrivial, intimately affecting the measurement (44). If structures are created where the interference of electron waves are a dominant effect, how is the system measured? In such systems, the “contacts” to the system are no longer ideal—they are now by definition part of the entire (interacting and interfering) electron wave system. Thus, electrical leads become intractably invasive. This device issue is serious, as the ability to create an isolated gate circuit architecture is now problematic.

The field awaits the technological achievement of a confining heterojunction technology that allows low-dimensional confinement equal to that presently done in only the epitaxial dimension. Once a lateral heterojunction technology is achieved, subband spacings of tens, perhaps hundreds of millielectron volts will be realized, with resulting quantum transport that is dominant and perhaps technologically useful. This degree of control, which has been achieved in the epitaxial dimension, may give rise to a host of new, promising electron devices that could find use in high-speed and novel transfer characteristics applications. Additionally, we concentrated on electron device technology, although one should be cognizant of similar advances in low-dimensional optoelectronic devices that may benefit from the same advances.

An exciting contender for advances in this regime is the achievement of low-dimensional structures by in situ epitaxial growth. A number of approaches exist for the realization of such structures. The most intriguing recent approach is the technique of “cleaved edge overgrowth”, where 2D MBE heteroepitaxial material is cleaved in situ, rotated, and subsequent growth occurs directly onto a 2D interface. These approaches promise the realization of 3D heterojunction confinement, an important prerequisite for useful low-dimensional electron devices. Likewise, the spectrum of material systems that have been explored is relatively sparse and is driven by those systems in which there are technological applications. Other promising material systems, too numerous to list here, exist on the horizon. Materials technology has continued to be the enabler for the exciting physics one sees today; it seems reasonable that this perspective will not change.

Within the last few years, it has been realized that charge quantization as well as energy quantization may well be an important consideration in low-dimensional structures. In fact, structures have been fabricated where the presence or absence of a single electron dominantly affects the transport (45, 46). This effect has been termed “Coulomb blockade”, and manifests itself when the capacitance of the structure is so small that the charging energy of a single electron is the dominant

energy in the system. This effect has led to the suggestion that single electron devices can be realized; indeed, an electron “turnstile” has been realized (47). Such effects will become dominant for electron devices on the nanoscale.

To gain an appreciation of the technological possibilities of these technologies, with regard to room temperature operation and gain (i.e., large operating voltage), Figure 15 presents a comparison of different quantum device technologies, plotted as a function of their experimentally observed operating temperature and voltage. At this time, only the technologies that utilize heterojunction barriers for charge separation and tunneling provide the requisite requirements. Yet even these are substantially inferior from a fabrication and reliability standpoint and do not attack the issue of interconnection limitations. These technologies provide only a direction in which to direct research; significant advances await materials and fabrication issues and an approach that limits interconnects.

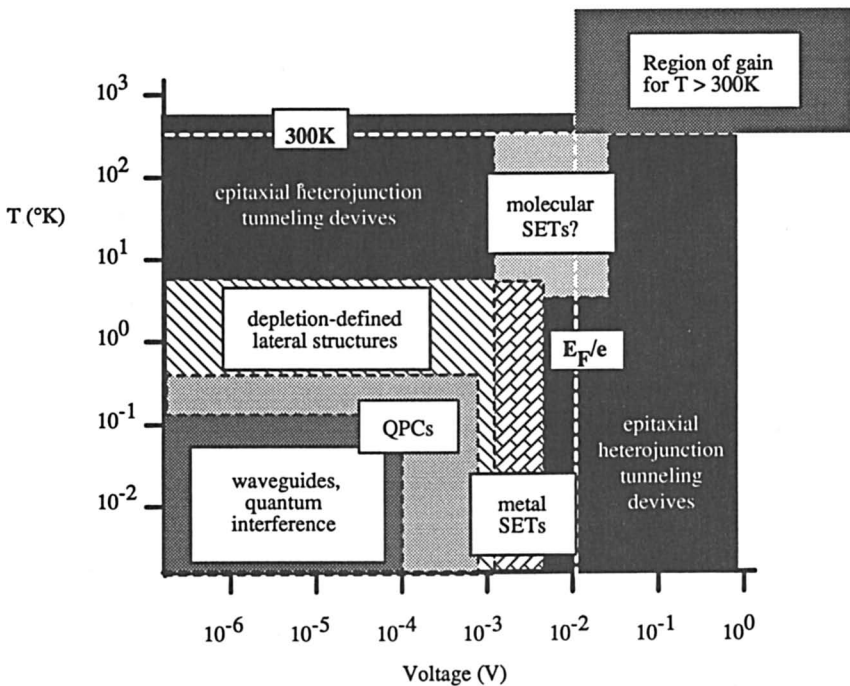


Figure 15. Comparison of different quantum device technologies, plotted as a function of their experimentally observed operating temperature and voltage. QPCs, quantum point contact structures; SETs, single-electron transistors. Room temperature and voltage equal to the Fermi level voltage are noted.

Summary

Presented here is a review of relevant recent quantum device results that may direct research in solid-state and other device technologies. The important lessons are that dominant quantum mechanical transport phenomena can be achieved and controlled and that devices with sufficient gain–fan-out and room temperature operation may likely be realized, although interconnections remain an issue. Significant progress awaits innovative developments in materials and fabrication. Precision in fabrication is a requirement, and this constraint may necessitate fabrication techniques and materials quite different from present ones.

Acknowledgments

We are grateful to Bill Frensley and Jim Luscombe for theoretical support, to Yung-Chung Kao and Rich Matyi for epitaxial growth, to John Randall for fabrication, and we are indebted to Bob Bate for seminal ideas on quantum device technology.

This work was supported in part by the Air Force Wright Laboratory, the Office of Naval Research, and the Defense Advanced Research Projects Agency.

References

1. Chang, L. L.; Esaki, L.; Tsu, R. *Appl. Phys. Lett.* **1974**, *24*, 593.
2. Keyes, R. W. *Science (Washington, D.C.)* **1985**, *230*, 138.
3. Sollner, T. C. L. G.; Goodhue, W. D.; Tannenwald, P. E.; Parker, C. D.; Peck, D. D. *Appl. Phys. Lett.* **1983**, *43*, 588.
4. Capasso, F.; Sen, S.; Beltram, F.; In *High Speed Semiconductor Devices*; Sze, S. M., Ed.; John Wiley & Sons: New York, 1990; pp 465–520.
5. Seabaugh, A. C.; Reed, M. A.; In *Heterostructure and Quantum Devices*; Einsbruch, N. G.; Frensley, W. R., Eds.; Academic: Orlando, FL, 1994.
6. Yokoyama, N.; Imamura, K.; Ohnishi, H.; Mori, T.; Muto, S.; Shibatomi, A. *Solid State Electron.* **1988**, *31*, 577.
7. Woodward, T. K.; McGill, T. C.; Burnham, R. D. *Appl. Phys. Lett.* **1987**, *50*, 451.
8. Capasso, F.; Sen, S.; Cho, A. Y. *Appl. Phys. Lett.* **1987**, *51*, 526.
9. Frensley, W. R. In *Nanostructure Physics and Fabrication*; Reed, M. A.; Kirk, W. P., Eds.; Academic: Orlando, FL, 1989; pp 231–240.
10. Smet, J.; Broekaert, T. P. E.; Fonstad, C. G. *J. Appl. Phys.* **1991**, *71*, 2475.
11. Frensley, W. R.; Reed, M. A. U.S. Patent 4,959,696, 1986.
12. Schulman, J. N.; Waldner, M. J. *Appl. Phys.* **1988**, *63*, 2859.
13. Haddad, G. I.; Reddy, U. K.; San, J. P.; Mains, R. K. *Superlattices Microstructures* **1989**, *5*, 437–441.
14. Haddad, G. I.; Reddy, U. K.; San, J. P.; Mains, R. K. *Superlattices Microstructures*, **1990**, *7*, 369.
15. Reed, M. A.; Frensley, W. R.; Matyi, R. J.; Randall, J. N.; Seabaugh, A. C. *Appl. Phys. Lett.* **1989**, *54*, 1034.
16. Seabaugh, A. C.; Frensley, W. R.; Randall, J. N.; Reed, M. A.; Farrington, D. L.; Matyi, R. J. *IEEE Trans. Electron Devices* **1989**, *ED-36*, 2328.

17. Seabaugh, A. C.; Frensley, W. R.; Kao, Y.-C.; Randall, J. N.; Reed, M. A. *IEEE/Cornell Conference on Advanced Concepts in High Speed Semiconductor Development and Circulation*; The Institute of Electrical and Electronics Engineers, Inc.: New York, 1989; pp 255–264.
18. Waho, T.; Maezawa, K.; Mizutani, T. *Proceedings on GaAs and Related Compounds*; Institute of Physics Series 120; Institute of Physics: Bristol, England, 1992; pp 601–606.
19. Seabaugh, A. C.; Kao, Y.-C.; Frensley, W. R.; Randall, J. N.; Reed, M. A. *Appl. Phys. Lett.* **1991**, *59*, 3413–3415.
20. Luscombe, J. H.; Frensley, W. R. *Nanotechnology* **1990**, *1*, 131.
21. Capasso, F.; Sen, S. S.; Gossard, A. C.; Hutchinson, A. L.; English, J. H. *IEEE Electron Device Lett.* **1986**, *EDL-7*, 573–576.
22. Futatsugi, T.; Yamaguchi, Y.; Ishii, K.; Imamura, K.; Muto, S.; Yokoyama, N.; Shibatomi, A. *Jpn. J. Appl. Phys.* **1987**, *26*, 431.
23. Futatsugi, T.; Yamaguchi, Y.; Muto, S.; Yokoyama, N.; Shibatomi, A. *IEDM Tech. Dig.* **1987**, *1987*, 877–878.
24. Capasso, F.; Sen, S.; Cho, A. Y.; Sivco, D. L. *Appl. Phys. Lett.* **1988**, *53*, 1056.
25. Wu, J.-S.; Chang, C.-Y.; Lee, C.-P.; Chang, K.-H.; Liu, D.-G.; Liou, D.-C. *Jpn. J. Appl. Phys.* **1991**, *30*, L160–L162.
26. Broekaert, T. P. E.; Fonstad, C. G. *IEDM Tech. Dig.* **1990**, 339.
27. Keyes, R. W. *Rev. Mod. Phys.* **1989**, *61*, 279–287.
28. Yokoyama, N.; Ohnishi, H.; Mori, T.; Takatso, M.; Muto, S.; Imamura, K.; Shibatomi, A. In *Hot Carriers in Semiconductor Nanostructures: Physics and Applications*; Shaw, J., Ed.; Academic: Orlando, FL, 1992; pp 443–467.
29. *Physics and Technology of Submicron Structures*; Heinrich, H.; Bauer, G.; Kuchar, F., Eds.; Springer-Verlag: New York, 1988.
30. Reed, M. A.; Kirk, W. P. *Nanostructure Physics and Fabrication*; Academic: Orlando, FL, 1989.
31. Kirk, W. P.; Reed, M. A. *Nanostructures and Mesoscopic Systems*; Academic: Orlando, FL, 1992.
32. Reed, M. A.; Randall, J. N.; Aggarwal, R. J.; Matyi, R. J.; Moore, T. M.; Wetsel, A. E. *Phys. Rev. Lett.* **1988**, *60*, 535.
33. Reed, M. A.; Randall, J. N.; Luscombe, J. H.; Frensley, W. R.; Aggarwal, R. J.; Matyi, R. J.; Moore, T. M.; Wetsel, A. E. In *Festkörperprobleme*; Rößler, Ü., Ed.; Braunschweig/Wiesbaden: Vieweg, Germany, 1989; Vol. 29, pp 267–283.
34. Tarucha, S.; Hirayama, Y.; Saku, T.; Kimura, T. *Phys. Rev. B* **1990**, *41*, 5459; *Appl. Phys. Lett.* **1991**, *58*, 1623.
35. Ramdane, A.; Faini, G.; Launois, H. *Z. Phys.* **1991**, *B85*, 389.
36. Su, B.; Goldman, N. J.; Santos, M.; Shayegan, M. *Appl. Phys. Lett.* **1991**, *58*, 747.
37. Tewordt, M.; Law, V. J.; Kelley, M. J.; Newbury, R.; Pepper, M.; Peacock, D. C.; Frost, J. E. F.; Ritchie, D. A.; Jones, G. A. C. *J. Phys.: Condens. Matter* **1990**, *2*, 8969.
38. Dellow, M. W.; Beton, P. H.; Langerak, C. J. G. M.; Foster, T. J.; Main, P. C.; Eanes, L.; Henini, M.; Beaumont, S. P.; Wilkinson, C. D. W. *Electron. Lett.* **1991**, *27*, 134.
39. Groshev, A.; *Proceedings of the 20th International Conference on the Physics of Semiconductors*; Anastassakis, E. M.; Joannopoulos, J. D., Eds.; World Scientific: Singapore, 1990, p 1238.
40. Bryant, G. W. *Phys. Rev. B* **1989**, *39*, 3145.

41. Luscombe, J. H. In *Nanostructures and Mesoscopic Systems*; Kirk, W. P.; Reed, M. A., Eds.; Academic: Orlando, FL, 1992; p 357.
42. van Wees, B. J.; van Houten, H.; Beenakker, C. W. J.; Williamson, J. G.; Kouwenhoven, L. P.; van der Marel, D.; Foxon, C. T. *Phys. Rev. Lett.* **1988**, *60*, 848.
43. Wharam, D. A.; Thornton, T. J.; Newbury, R.; Pepper, M.; Ahmed, H.; Frost, J. E. F.; Hasko, D. G.; Peacock, D. C.; Ritchie, D. A.; Jones, G. A. J. *Phys. C.* **1988**, *21*, L209.
44. Buttiker, M. *Phys. Rev. Lett.* **1986**, *57*, 1761.
45. Fulton, T. A.; Dolan, G. J. *Phys. Rev. Lett.* **1987**, *59*, 807.
46. Kuzmin, L. S.; Delsing, P.; Claeson, T.; Likharev, K. K. *Phys. Rev. Lett.* **1989**, *62*, 2539.
47. Geerligs, L. J.; Anderegg, V. F.; Holweg, P. A. M.; Mooij, J. E.; Pothier, H.; Esteve, D.; Urbina, C.; Devoret, M. H. *Phys. Rev. Lett.* **1990**, *64*, 2691.

RECEIVED for review March 12, 1992. ACCEPTED revised manuscript March 24, 1993.

The Fitness of Carbon for Computing

Michael Conrad

Department of Computer Science, Wayne State University,
Detroit, MI 48202

The Henderson thesis that among the elements only carbon can serve as the basis for life is contemplated from the standpoint of molecular computer design. The analysis suggests that the powerful information-processing capabilities of biological organisms, like life itself, depend on the shape properties of carbon polymers and could not easily be duplicated with silicon or any other material. The role of macromolecular shape is illustrated by a hypothetical device that uses self-assembly for pattern recognition. Signals reaching the external membrane of the device along different input lines release specifically shaped proteins. Different input signal patterns thus yield different self-assembled mosaics, which in turn are linked to output actions by adaptor molecules. Each adaptor protein groups together all the input patterns that give rise to the shape features of the mosaic that it recognizes. The self-organizing dynamics is incompatible with effectively programmable structure-function relations, but it affords higher efficiency and adaptive capacity than can be achieved by digital computers.

Intelligent Particles versus Digital Switches

Molecular computers are natural or artificial systems in which individual macromolecules play a critical information-processing role. Biological organisms clearly fit this definition. Their stunning information-processing capabilities are ultimately based on the specific interactions of proteins, lipids, and nucleic acids. Today's computer technology is based instead on switching actions of macroscopic aggregates of atoms, most commonly silicon. The two modes of computing are radically different. Biological information processing is largely mediated by intricate macromolecular particles that utilize shape complementarity to recognize other molecular objects. My purpose here is to take a new look at the relative virtues of carbon and silicon from the point of view of computing. I will argue that carbon is indeed uniquely suited to the type of

0065-2393/94/0240-0043\$08.00/0
© 1994 American Chemical Society

information processing at which biological systems excel. Whether it is possible to construct digital molecular computers, using either carbon or noncarbon molecules, is also a pertinent question. Our analysis of these issues suggests some of the many problems that will require contributions from scientists with a variety of disciplinary skills.

Carbon versus Silicon

A perennial question is whether carbon is the only possible basis for life. Henderson (1) and later Sidgwick (2) presented strong arguments to the effect that carbon is indeed uniquely suited to support the life process. The main points (as summarized in reference 3) are the octet of four electron pairs in carbon and the multiplicity of carbon compounds that are possible. The octet of four electron pairs confers high stability on covalently bonded carbon compounds because of the fact that the saturated carbon atom cannot serve either as an electron donor or acceptor. Silicon is more reactive because its covalency can rise to six. The second virtue of carbon, the combinatorial variety of structures that it affords, is facilitated by the fact that the energy required for the formation of C–C bonds is about the same as for other bonds (such as C–H and C–O), whereas for silicon only about half as much energy is required to break Si–Si bonds as Si–H and Si–O bonds. Long-chain silicon polymers would not be nearly as stable as long-chain carbon polymers, with evident implications for the repertoire of folded shapes that could be obtained.

The relatively low reactivity of carbon is useful from the standpoint of conserving information and function. It is also useful for energy transduction processes, because the proteins of the electron-transfer system must release energy in small, controlled steps. The combinatorial variety of structures allows for high specificity as well as for a great range of more general physical–chemical properties. The relation between carbon compounds and water, in particular the relation between carbon dioxide and the stability of hydrogen ion concentrations, is also a crucial consideration apropos the homeostatic requirements of organisms and ecosystems. Factors such as the latter greatly strengthen the argument that carbon is uniquely suited to life. They do not, however, bear in the same way on the relative merits of carbon and silicon as supports for artificial information-processing systems.

Henderson's thesis preceded the discovery of the transistor. Here the dominant role is played not by carbon, but by silicon and silicon-like compounds. Let us therefore turn the analysis around, by asking whether inorganics are especially well-suited to the implementation of the simple switching operations that mediate digital computing.

Electronic switches—whether light switches, vacuum tubes, or transistors—are three terminal devices comprising a source of electrons,

a sink for electrons, and a knob that controls the flow of electrons. The action of the control terminal induces a slight shift in the concentration of electrons (or holes) away from equilibrium. The return to equilibrium is accompanied by the flow of electrons. Movements of the atomic nuclei are not functionally relevant, in distinct contrast to the nuclei of biological polymers. The only exception is superconducting switches, because superconductivity is based on slight lattice distortions induced by the motion of electrons. The pattern recognition capabilities of all such switches are vested in the control terminal, and consequently are extremely simple (inasmuch as the control is an applied potential). This feature again is in sharp contrast to biological macromolecules, in which shape complementarity can serve as a control. We could further elaborate this picture by considering two (or multiple) state devices that involve magnetism, optical bistability, or molecular conformation, but then we would be deviating from the predominant feature of present-day digital computing.

Now let us make the discussion more specific by considering semiconducting switches (cf. reference 4). The semiconducting property means that the material can undergo a transition from insulating to conducting states. Thus it should have some properties of a metal. This feature is illustrated most clearly by crystals of elemental silicon and germanium because these are covalent insulators, but have a spatial distribution of electronic charge similar to that of metals. To act as a switch, however, the semiconductor must be inhomogeneous. The inhomogeneity property means that the concentration of donor and acceptor impurities varies with position. This property allows the application of an external potential (at the control terminal) to create a temporary disequilibrium in the distribution of charge carriers.

For example, suppose that two input lines impinge on the control terminal. The input is coded as a 1 if the line carries an electric pulse and as a 0 if the line carries no pulse. If the semiconductor is organized so that the transition from an insulating to a conducting state occurs when the potential change equals or exceeds a threshold corresponding to the arrival of a single pulse, it is an "or" gate (i.e., recognizes 10, 01, 11). If it is organized so that the transition occurs only when two pulses arrive it is an "and" gate (i.e., recognizes only 11). The pattern recognition capability of such threshold devices is severely limited by the fact that they always respond to an average value (or some weighted average) of their inputs. Implementing nonlinearities that would enable a semiconductor to recognize more specific features of the input (e.g., to perform an "exclusive or" operation) is difficult. As noted, this condition is in sharp contrast to biological macromolecules, which recognize objects in a manner that is better analogized to the fitting together of pieces of a jigsaw puzzle.

Numerous materials and processes can support threshold switching, so obviously we cannot argue that silicon is uniquely suited for this purpose in the same sense that carbon appears to be uniquely suited to life. We can, however, see why macroscopic aggregates of silicon and congener materials dominate, at least at the present time. First, the fact that they are macroscopic means that switching properties can reliably conform to formal specifications (because the alternative states are coded by ensembles of particles with sharply peaked average values). Second, the high reactivity of silicon becomes an advantage because it is favorable for coordination with donor and acceptor impurities. Third, replicability of the samples is all-important. The combinatorial variety of individual organic structures is irrelevant in the context of a macroscopic aggregate and even disadvantageous to the extent that it would militate against uniformity.

Might donor–acceptor processes at an individual-molecule level serve as a basis for reliable switching? Much of the work in “molecular electronics” is motivated by this question, in particular in connection with carbon molecules. The electron-transfer proteins (5), nonbiological conjugated polymers that have metallic properties (6), and optically sensitive molecules (7) have all inspired interest in this question. Possibly, the organic chemists will create a new class of electronically or solitonically conducting polymers with exploitable switching properties. To use these for digital computing on an individual-molecule basis, it would be necessary to suppress side effects (such as tunneling, diffusion, and fluctuation) without relying on statistical averaging or without requiring so much redundancy that the advantage of individual molecules is lost. It would also be necessary to establish interconnects among the switches to allow for significant processing to occur at the mesoscopic level before excursions to the macroscopic level are required. We cannot exclude the possibility of progress in these directions in the future, especially in connection with optical links (because silicon is not well-suited for interaction with photons). However, we will argue that this is not the mode of information processing that has an existence proof in biological nature and that implementing modes of information processing more akin to those that occur in cells and organisms would have far greater impact on the problem domains that could be addressed by artificial computers than would duplicating a conventional computer architecture in an organic key.

Shape-Based Information Processing

We carry Henderson’s thesis yet a step further, by looking at carbon from the point of view of the powerful information-processing capabilities of biological polymers. The important point is to identify these

capabilities and not mask them by trying to force carbon into a digital switching framework suitable to silicon. The following are some of the most prominent of these capabilities, but by no means a comprehensive list.

1. *Shape-based pattern recognition.* The specific shapes of proteins and other macromolecules allow them to recognize object molecules (called substrates) or to self-assemble into larger molecular mosaics. The pattern recognition function of enzymes is on a slower (millisecond) time scale as compared to conventional silicon switches; but the number of conventional switching operations required to duplicate the pattern recognition function would be enormous.
2. *Conformational switching.* Proteins and other macromolecules undergo shape changes (including electronic-conformational interactions) in conjunction with the recognition process (8, 9). Shape can also change in response to milieu. This ability allows for a form of memory storage and also for precise control over recognition and effector action. The issue of switching speed is dependent on what feature of the molecular motion is being utilized. Significant shifts in nuclear configuration are usually slower than silicon switching speeds, but are useful for exerting sensitive control over delicate sensing and modulating functions. Electronic transitions can occur on an extremely fast time scale that could potentially match or possibly exceed those achievable with conventional inorganic materials, but these transitions are generally part of an ultrahighly integrated system of multiple nuclear and electronic motions, together with various quasi-particle modes.
3. *High stability and reliability.* The usual view is that individual molecular switches are less stable than silicon switches. Silicon switches, however, are statistical aggregates of atoms and consequently subject to entropic degradation. This is not the case for single molecules, because these can retain their form and function as long as the constituent covalent bonds are not altered or the weak bonds disrupted in an irreversible way. The self-assembly property also provides an intrinsic self-repair capability.
4. *Combinatorial variability of structure-function relations.* Proteins and other macromolecules have levels of structure. The primary structure of a protein is the sequence

of amino acids; the tertiary structure is the folded shape, and this shape largely determines the functional properties. The number of different amino acid sequences is enormous (for proteins comprising 400 amino acids it is 20^{400}). The possibilities for engineering proteins with particular specificity (or molecular pattern recognition) properties are myriad. The possibilities for engineering nuclear configurations that allow for subtle controls over electron motions are vastly greater than that possible with inorganic compounds.

5. *Low dissipation.* Protein enzymes, as catalysts, act reversibly. Consequently their pattern recognition functions are performed with zero energy dissipation. Energy dissipation is required if the catalytic activity is to leave a macroscopic trace. This condition typically requires from 10 to 100 kT per catalytic step, much better than the roughly 10^5 kT of energy dissipation associated with each switching operation in a present-day silicon computer.
6. *Optical interfacing.* Pigmented biomolecules in many cases provide excellent possibilities for interacting with light (10, 11). Silicon, by contrast, is ineffective in this respect.
7. *Membrane-based biosensing.* Proteins and other biomolecules can form ultrahighly integrated membrane components capable of controlling the electrochemical signal-processing capabilities of membranes. Macromolecules in this type of environment can serve as sensitive sensing components (11, 12).
8. *Network dynamics.* Membranes, antigen–antibody networks, cytoskeleton, and hydrogen bond networks interpenetrating with lipid and protein structures allow for the properties noted above to be linked into extended but highly integrated polymacromolecular structures. The extended structures probably allow for a wide variety of informationally significant dynamic processes, including collective vibrations, quasi-particle signal transmission involving solitons (13) or phonons (14), mechanical (15) or conformational (16) information transmission, coherent dipole oscillations (17), collective hydrogen bond dynamics (18), structural changes created by self-assembly and disassembly (19) or by polymerization–depolymerization processes (20), and spatiotemporal structure formation through nonlinear biochemical interactions (21, 22).

I have not included information storage functions in this list, such as the storage and retrieval capability afforded by the covalent linking of nucleotides in DNA and the hydrogen bonds that contribute to the maintenance of base pairing. This type of function is obviously extremely important in biology, and technologically significant for directed evolution of proteins (23) and ribozymes (24). I have omitted it, however, because I want to avoid superficial analogies to bit-by-bit string-processing operations and to digital computer programs. Such analogies are misleading because the sequence of bases in DNA codes for the sequence of amino acids in proteins. The protein folds up to yield the three-dimensional shape and dynamics responsible for recognition, control, binding, and catalytic functions. This folding is dependent on the interactions among numerous amino acids. It is as if a program written in Pascal were coded into a sequence of magnetized beads, which then aggregated into a three-dimensional tool on the basis of free energy minimization. All such self-organizing processes are rigorously excluded from digital computers; if they were not excluded, the user could not communicate desired rules to the computer by using a simple user's manual that specifies the computational function of each element in a definitive and context-limited manner, and therefore in a manner that can be influenced only by a restricted number of interactions with other elements.

DNA would thus be entirely disanalogous to a digital computer program even if it were transcribed and translated in an entirely bit-by-bit fashion. But in fact even the string-processing analogy breaks down, because DNA, by itself and in conjunction with genomic proteins, has shape properties that are utilized in readout, especially in the control of gene expression (25).

Macroscopic–Microscopic Communication Links

How do the properties of integrated molecular complexes contribute to the computational capabilities of organisms, and how might they be best utilized in technological devices? To address these questions, it is necessary to consider the larger scale architectural requirements of molecular computers. The key requirement is an interface with the macroscopic world. And the key question is how much computational work can be performed at the mesoscopic and microscopic levels before conversion to a macroscopic representation is necessary.

The basic scheme, to be referred to as the M-m architecture, is illustrated in Figure 1 (26). Signal patterns impinging on the external membrane of a cell are transduced to internal chemical or molecular events. In this way macroscopic (M) representations of information are converted to microscopic (m) representations at the molecular level,

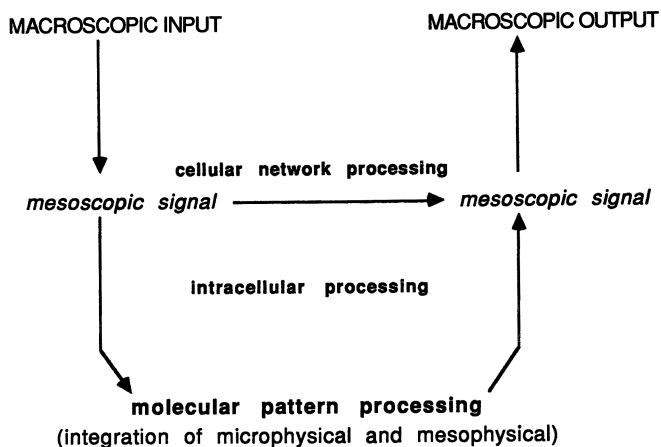


Figure 1. M-m architecture. Information is transduced from macroscopic to microscopic representations, processed at the microscopic level, and then amplified to a macroscopic effector signal. For tactilizing processors, the input signal patterns are transduced to a form that can exploit the powerful shape-based recognition properties of proteins and other macromolecules. The microscopic dynamics are generally mixed with meso-scale phenomena, with extremely close integration in the case of shape-based computing.

processed at this level, and then amplified to macroscopic (M) output actions. Actually the scheme would be more accurately described as an M-m-m organization, where *m* represents mesoscopic levels of processing. This is because the microphysical electronic and quasi-particle dynamics of proteins and other biological macromolecules are wrapped into “particulate organizations” that are large enough to have dynamic shape features, yet small enough to explore each others’ shapes through Brownian motion. It would be impossible for individual electrons or protons, or even small molecules, to have dynamic shape features and impossible for truly macroscopic systems to have Brownian motion. This “wrapping together” is of enormous importance, because it allows quantum features of the microphysical entities to contribute to the computation.

The adenosine cyclic 3',5'-phosphate (cAMP) cascade is a biological instantiation (27, 28). Here hormones and mediators bind with receptors on the external membrane. These interact with regulatory proteins that in turn activate enzymes that produce cAMP, the second messenger, from ATP. The cAMP migrates to a target protein from some large family of target proteins (the kinases), which in turn activate an effector protein. Effector proteins might control DNA readout, microtubule action, or ion channel activity. The transduction need not be through the second-messenger mechanism, however. Steroid hormones enter directly into

the cell. Some signals, such as mechanical distortions, may be transduced via direct alterations of the cytoskeletal structure. Information processing can occur at each stage of the process, starting with the regulatory proteins at the input, proceeding through integration of cAMP or cytoskeletal signals, and culminating in the specific readout actions of the kinase and effector proteins. Membrane dynamics and propagating distortions in the hydrogen bond structure that are adjacent to the multiple membranes in a cell and that envelop the vast majority of proteins provide another potential medium for integrating signals in space and time. Such distortions would be induced by changes in the distribution of ions, especially bivalent ions and polyvalent proteins.

The essence of the M-m scheme is tactilization. The input signals to a cell (or device) could be in the form of light signals, electric pulses, chemicals, or mechanical deformations. The transduction process converts these to a form recognizable by individual macromolecules with dynamic shape properties. The term "tactile" refers to the fact that shape-based interactions play an important role in the recognition process. The transduction process is a tactilization process because it converts the input signal pattern into a "touchable" form that can be recognized by intricately shaped particulate organizations.

The Self-Assembly Model

The role of shape-based interactions in the tactilization scheme is illustrated in an unadulterated manner by the self-assembly device in Figure 2 (19, 29–31). In this case patterns of input signals impinging on the external membrane release specifically shaped macromolecules that self-assemble into a polymacromolecular mosaic. Adaptor molecules that control the output of the device recognize shape features that represent different groups of signal input patterns. In this way a symbolic pattern recognition problem is converted into a free energy minimization problem. Such a device might operate on a neural impulse (or millisecond) time scale, or faster if only subtle conformational changes are involved. But if the basins of attraction are appropriately set up, it could address pattern recognition problems that would consume more time if measured in terms of the total number of conventional switching operations.

Patterns with an ambiguous space–time structure fall into this computationally difficult class. Spatial distortion can be handled by arranging the distribution or "region of reactivity" of the releasable shapes. Input patterns with different spatial orderings will lead to the same output action as long as the assembly process groups them into some recognizable feature of the mosaic. The temporal ambiguity is easily handled by using macromolecules that undergo conformation change upon release and by choosing appropriate decay times for these conformations. Tem-

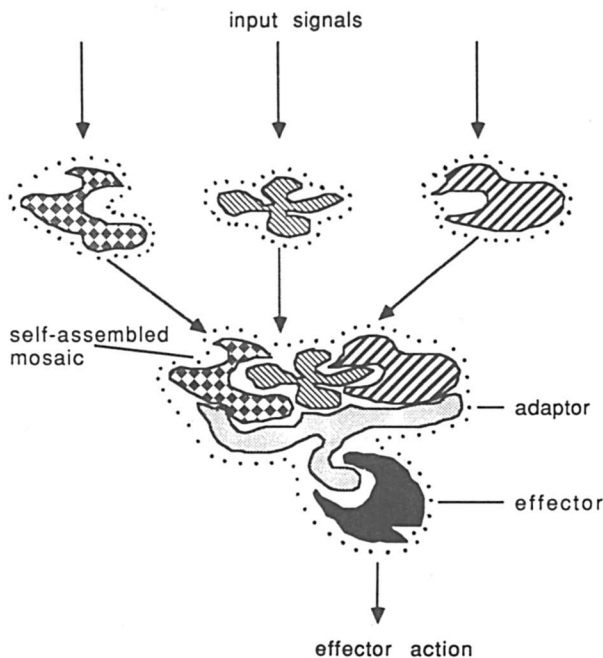


Figure 2. Schematic of tactilizing processor operating on the basis of the self-assembly principle. Signals arriving at the different input lines release differently shaped macromolecules. Consequently different patterns of input signals yield polymacromolecular mosaics with distinctive shape features. Adaptor enzymes pick out shape features associated with different subsets of input patterns. The number of possible sets of input patterns that can be recognized depends on the number of adaptor enzymes. The second specificity of the adaptor activates an effector protein that controls the output of the cell or device (for example, by creating a membrane potential change). The dotted envelopes around the shapes schematically represent the fact that the self-assembly process is in part guided by the electronic wave functions and hence occurs faster than would be expected on the basis of a purely classical model. Tactilizing processors may be viewed as models of cellular pattern recognition or as designs for advanced biosensors.

porally distorted or rearranged input patterns that release the same collection of macromolecules will be grouped together if there is some common time at which these are all in active conformations. The device will reset automatically if conformationally decayed macromolecules rebind to their original sites of attachment. This rebinding can occur rapidly if the released molecules do not have to travel far to form a mosaic, a feature that is also important for the time delay between input and output. The reassembly in the initial configuration would be speeded up by the imposition of a gradient, such as an electric field or a pH gradient.

The self-assembly design highlights the manner in which micro-physical (quantum level) dynamics increases computational power beyond that which can be obtained with a classical system using a comparable number of time or processor resources. The docking of molecules that are candidates for self-assembly generally involves shifts in the nuclear configuration. This shifting means a significant mutual interaction involving the electronic as well as the nuclear wave functions. The action associated with the electronic wave functions is sufficiently small in comparison to Planck's constant to allow barrier penetration at the electronic level to speed up the search for the self-assembled configuration. A purely classical system would never be able to penetrate a barrier to find a minimum. The type of nuclear-electronic interactions required would be possible whenever the Born-Oppenheimer assumption of random electronic phases becomes inapplicable, because conformational changes then necessarily accompany the electronic motions.

The self-assembly processor may be viewed as an advanced biosensor design that, if fabricated, could be used for preprocessing or effector control. Many variations are possible, including variations that use antibody-antigen interactions for self-assembly, reaction-diffusion patterns to represent external input patterns, networks of macromolecules (such as reconstituted microtubules) to integrate signals in space and time, or tunneling pathways in proteins (32) to integrate influences impinging on an individual macromolecule.

Our hypothesis is that transduction cascades such as this play a major role in biological cells, including neurons. The second-messenger mechanism is known to influence the firing activity of some central nervous system neurons (15, 27, 28), and a number of lines of evidence indicate that the cytoskeleton may serve as an internal nervous system in neurons, in analogy to its well-known role as micro-skeleton and micromuscle (15, 20, 33, 34). The role of self-assembly per se is more speculative at the present time. Clearly, specific interactions, including the self-assembly of antigen-antibody networks, play a major information-processing role on the external membrane, at the stage of first-messenger reception. Self-assembly and disassembly are ubiquitous inside the cell. So far these processes have been viewed primarily from a pattern formation point of view rather than as a means of fast pattern recognition. The vast majority of macromolecular interactions are accompanied by conformational changes, and whenever these occur, the possibility exists that different macromolecules are affected by different specific influences and that the conformations emerging from their interaction can be used to control the internal or external actions of the cell in a manner appropriate to the pattern (or context) of influences.

Learning Algorithms

How could cells (or artificial tactilizing devices) processing information on the basis of self-assembly be educated to perform a desired task? Because of the cell's self-organizing dynamics, desired programs cannot be communicated to it by setting the states of the components and the connections among them in the same manner that programs can be implanted in a network of simple switches. Evolution by variation and natural selection plays an important role in nature. A cell with elaborate tactilization dynamics will transduce different impinging influences into a large variety of distinct local conformational representations. The control and information-processing capabilities of the cell will depend on the repertoire of adaptor molecules that can associate these local conformational features with effector actions. The adaptors are tuned by variation and natural selection. With artificial devices, directed evolution through protein engineering would replace variation and natural selection. An additional adaptive process, involving cyclic regeneration of self-assembled structure, could conceivably also play an important role. If the pattern of influences alters the internal structure of the cell, this in turn will alter the self-assembled conformational representations and hence the internal or external effector actions. The representations will continue to change until the resulting effector actions correct for any variations in the pattern of external influences. The stabilization of the system will thus automatically be associated with the emergence of a tactilization dynamics that transforms inputs to outputs in a functionally useful manner.

Networks of tactilizing processors are computation universal, which means that they are capable of performing any computational process that can be performed by a digital computer. This is obvious because digital computers are constructed from networks of simple pattern recognizers (e.g., "and," "or," and "not" gates). The advantage of using a large repertoire of powerful special purpose pattern recognizers is that more efficient implementations are possible. The implication is that networks of tactilizing processors would in practice be able to compute a larger class of functions than would digital machines. Our hypothesis is that the dramatic disparities in human and machine capabilities are in part due to this difference in efficiency; in part they are also due to the malleability of biomolecular structure–function relations and to the enhanced capacity for evolutionary learning and other forms of adaptation that this affords. For models comprising large numbers of tactilizing processors to correlate with the capabilities of the brain, it is necessary to add many higher level controls, including synaptic facilitation mechanisms that allow for different processors to be orchestrated into func-

tionally useful combinations and that allow for memory storage and retrieval (35, 36).

Carbon Switches Reconsidered

Conventional silicon computers may be viewed as special cases of the M-m architecture in which microscopic (*m*) and mesoscopic (*m*) scale information processing are completely absent. Serial machines are an extreme special case in which only a small number of processors are active at any given time. For this reason, such systems are effectively programmable. Parallel systems utilize the services of many processors simultaneously. All existing parallel systems are structurally programmable because the processors conform to precise user's manual specifications. They are not effectively programmable, however, because the global program generating the system's state-to-state behavior (its execution sequence) is in general not known in advance. If constraints are introduced that ensure that conflicts among processors will never occur, the system will in most cases degenerate to a serial mode (unless restricted to a highly restricted class of problems).

The difference between existing technical parallel systems and biomolecular systems is that the number and type of interactions that a component is allowed to engage in is strictly limited by the user's manual in the former case, but not in the latter. This limitation is the reason that the structure-function relations in a tactilizing processor are nonprogrammable. The high efficiency is due to the fact that many more interactions can contribute to the problem-solving behavior of the system. The second important difference is that relaxing the constraints required for programmable structure-function relations allows high structure-function malleability. Structurally nonprogrammable parallel systems, such as the tactilizing designs, thus have the additional advantage that it is easier to educate them through structure modification procedures (such as directed evolution) than it is to educate parallel systems built up from components with definitively specified switching behavior.

The question inevitably arises whether it might be possible to replace the silicon switches with carbon switches and whether this might afford any advantages. It should be clear, from the preceding discussion, that a carbon-based implementation of a structurally programmable computer would have no advantages from the point of view of mode of computation even if it operated on the mesoscopic (*m*) or microscopic (*m*) scale. It would then be a special case of an M-m architecture in which the engineer would attempt to freeze out all interactions (including quantum effects) that could conceivably interfere with programmable structure-function relationships, just as in a conventional computer. Such a shift

from a silicon to a carbon realization could not alter the trade-off between programmability, computational efficiency, and evolutionary plasticity and therefore could not introduce any new computing concepts. Any potential benefits would have to be based on size, speed, reliability, functionality in unusual environments, and cost of fabrication.

Most of the proposals currently in the air for implementing conventional switches in carbon fall into four main categories: carbon analogues of silicon switches, optomolecular switches, conformational switches used for memory storage and retrieval, and carbon–silicon hybrids. The use of self-organizing dynamics must be restricted to the self-fabrication of circuits; it cannot contribute to the computation per se as long as structure–function programmability is retained as a requirement. The main problem is implementing enough connections among units to support a significant amount of micro-level computation before an excursion to the macro-level is required. This requirement would mean establishing extremely precise connections, either using self-assembly properties of proteins attached to switching elements or using nanotechnological techniques such as scanning tunnelling or atomic force microscopy. If small size is achieved, tunneling side effects and other macroscopic parasitics would be difficult to exclude. Redundancy schemes would be necessary to counteract these effects. If macroscopic interfaces must be incorporated in relatively high proportion, the size advantage would be completely obliterated.

Whether such proposals can feasibly extend the size and speed limits that conventional silicon switches are incrementally approaching is an open question. Pigmented macromolecules afford the possibility of utilizing photon interconnects in a manner that should have advantages for parallel computing and that could allow increased density of memory storage. Silicon–carbon interfaces are another promising line of development. The important point is that to duplicate conventional designs, it is necessary to tease switching operations out of the ultrahighly integrated recognition, control, catalytic, and energy-transfer dynamics of macromolecules. The main difficulty is that the teasing out must be complete enough to suppress side effects if the objective is to implement a system with programmable structure–function relations. The same problem arises with synthetic organic polymers because such polymers must possess hooks that enable the formation of precise networks without disabling the switching function. These difficulties are transformed into opportunities if the objective is to implement a tactilizing processor because the side effects then contribute to the computational function and consequently become desirable features.

Carbon–Silicon Synergy

The foregoing discussion may be summarized in terms of the trade-off cube illustrated in Figure 3 (37, 38). The *x*-axis represents the size scale

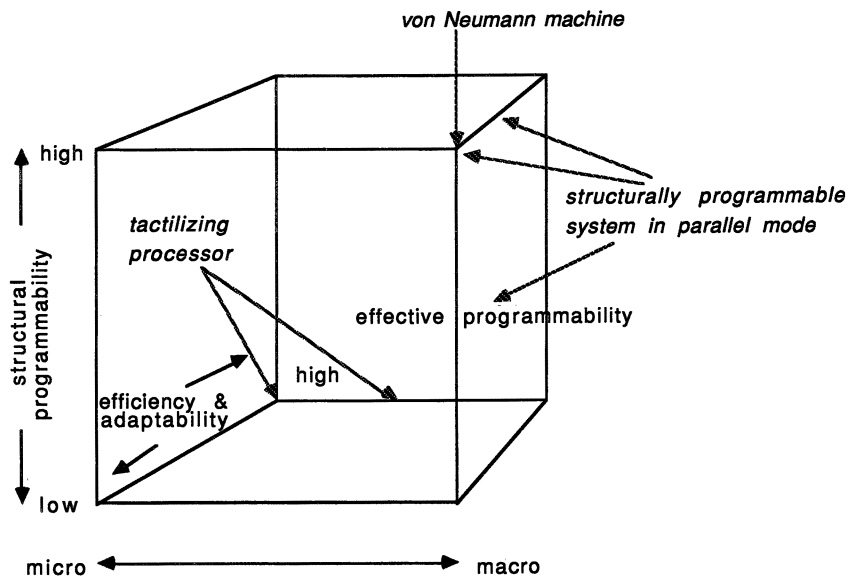


Figure 3. Trade-off cube. The “axes” of the cube represent structural programmability, efficiency, adaptability, and scale of operation. For visual convenience efficiency and adaptability are assigned a common axis because both are potentially high when structural programmability is low. The trade-off principle implies that not all loci in the cube are feasible.

at which the most significant computing activity takes place and runs from microscopic to mesoscopic to macroscopic. The y -axis represents structural programmability, and the z -axis is used to represent both potential efficiency and evolutionary adaptability because in biomolecular systems these are both high. (This double use of the z -axis is, however, more a matter of pictorial than logical necessity because a structurally programmable computer could have high evolutionary adaptability if it allocated sufficient computational resources to simulate nonprogrammable structure–function relations).

Not all loci in the cube are feasible. As indicated, the conventional serial digital computer (or von Neumann machine) is completely macroscopic, completely programmable, and low in efficiency and evolutionary adaptability. Running such a structurally programmable system in a parallel mode increases efficiency somewhat, but generally compromises effective programmability without increasing evolutionary adaptability (except for some designs, such as connectionist neural nets that exploit natural structure–function relations). Tactilizing processors have low structural programmability, but potentially high efficiency and high adaptability. Some of the significant information processing occurs at the meso-level and some at the micro-level. Purely macroscopic re-

alizations are impossible, except for simulations that entail an enormous cost in terms of efficiency. The extent to which it is feasible or economical to use carbon switches (with their biologically relevant properties suppressed) to implement structurally programmable designs with significant information processing at the meso- or micro-level is an open question. As silicon switches become smaller, side effects become inevitable. Utilizing these side effects for information processing, for example in the context of a cellular automaton architecture, could allow for enhanced efficiency and adaptability, at the expense of substantial loss in programmability. But the efficiency and adaptability achieved would be very much less than is possible through shape-based macromolecular pattern recognition.

The trade-off cube illustrates the difference between the mode of computing most natural to carbon and the mode most natural to silicon and reveals the synergies afforded by these differences. The application domains are complementary. Formal computing, whether implemented through silicon switches or “suppressed” carbon polymers, allows a programmer to communicate rules to a computer in an intentional manner; but this is feasible only if the task to be performed can be specified in an unambiguous manner and if the intentionality property is not counterproductively costly in terms of information-processing efficiency and adaptability. If the problem to be addressed is inherently serial (nonparallelizable), it is inherently refractory to efficient solution. If it is parallelizable, more efficient use of processors is possible, but in general intentional programming must be replaced by learning algorithms. If the demand for formally specified switching operations is relaxed, the number of interactions that can be used for computing can grow faster than the number of processors, affording yet greater computational efficiency and adaptability. Carbon, used in its natural mode, is by far the material of choice here, for the same reason that it is the material of choice (or of necessity) for life itself.

The self-assembly device described earlier provides a concrete example. We have already seen how a system operating in this mode can exploit the natural physics and chemistry of proteins to efficiently recognize patterns that are too ambiguous to be managed in real time by digital techniques. Such self-assembly processors could serve as pre-processors that precode visual inputs into a form rigid enough to be efficiently managed by conventional computer vision systems. Other feasible computational synergies include the following: implementation of digitally refractory input–output transforms, use of tactilizing processors for intrinsic timing, use of self-organizing dynamics for pattern categorization, allocation of adaptive computing tasks to systems with malleable structure–function relations, and expanded sensor and effector capabilities. Fabrication synergies that in practice would also be domain-

expanding include the following: facilitation of multiple optical interconnects for realizing highly parallel designs, self-organization of functional networks via self-assembly, construction of transduction–amplification cascades for macro–micro communication links, and use of dense optomolecular electronic media to manipulate distributed memory structures.

The most important domain synergy is omnipresent in the human–machine interface. Digital computers are completely dependent on human beings for their design, fabrication, and programming. Artificial intelligence is completely parasitic on human intelligence. The latter is a product of evolution, operating in the biomolecular mode. The extension of Henderson’s thesis is that carbon provides the substrate not only for life, but ultimately for silicon computing as well.

Molecular Computing Viewed from the Future

I have presented a conception of computing based on the self-organizing properties of particulate organizations, mainly proteins and protein–membrane complexes. Self-organization takes place at several levels. The lowest level is the emergence of three-dimensional structure and dynamics, in the case of proteins through the folding process. Use of the term “tactile information processing” is motivated by the importance of shape for the recognition, control, and effector properties of proteins. The next level is the emergence of polymacromolecular mosaics and networks through self-assembly. Self-assembly plays a well-known role in structure formation. The formation and modulation of such structures in biological cells is responsive to milieu (input) and influences milieu (output). A fortiori the structure formation process serves an information-processing function. My hypothesis is that the pattern recognition–effector control activities of biological cells is in significant measure mediated by such self-assembly dynamics and that this is also true for neurons in the brain.

What are the prospects for developing pattern-processing devices that operate on the basis of the self-assembly principle, of using these as preprocessors for silicon computers, and eventually of linking them up into networks capable of performing complex functions? To address this question, I would like to take the liberty of doing the impossible: projecting myself into the future and surveying the historical development of the field from now till then (say 50 years from now).

One process that certainly took place (because it is taking place now) is infrastructure development. The biotechnological infrastructure of the 1990s is certainly primitive in comparison to the silicon infrastructure, but almost certainly any future historian would record an expansion of biotechnological capabilities in this period, with ac-

celeration in the 21st century. Protein engineering, immunoglobulin-structuring techniques, membrane technologies, biosensor design, modeling techniques, and automation supportive of directed evolution and fabrication are all advancing. The linking together of components into molecular functional systems will become increasingly manageable.

One possibility is that a point will be reached at which molecular computing devices begin to proliferate, and at this point attention will turn to shaping the infrastructure for molecular computer design. A second possibility is that precursor architectures that integrate a variety of modes of computing, some through simulation, will be used to guide molecular computer design. The integration might be concrete or conceptual. In either case the idea would be to infiltrate the precursor with carbon components in a step-by-step way, assessing at each stage the relative computational and economic merits of carbon and silicon. My strong suspicion is that our future historian will write that those organizations and regions that combined infrastructure development with a concerted effort to develop devices for industrial and automation purposes were the ones that dominated the field in the 21st century.

More detailed comments of our future historian were unfortunately blurred in the process of transmitting them from the future to the present. I am sure he or she discerned that the precursor-guided development comprised two competing approaches. One, traveling on the flow of the electronics industry, emphasized enhancement of formal switches and also a variety of related electronic and optoelectronic functions that are currently performed by conventional materials. The second, returning to the biomolecular roots of computing, emphasized shape-based molecular recognition. The two developments called for the same infrastructural supports and utilized similar technologies, and I hope that the molecular computing community took advantage of this synergy. I also hope that the larger society effectively utilized the synergies afforded by the domain complementarities of formal and biomolecular modes of computing, but I have the impression that many unnecessary failures and costs were incurred due to lack of understanding on this point. I do not have the impression that our historian took any special note of the multidisciplinary nature required to achieve the advances in molecular computing. From his vantage point it was probably seen as such a foregone necessity that he failed to note it, just as a fish might fail to note the water in which it swims. Such are the pitfalls of historiography. How little he understood the great efforts his 1990s forebears had to exert to support multidisciplinary teams.

Acknowledgments

This research was supported in part by the U.S. National Science Foundation (Grant ECS-9109860).

References

1. Henderson, L. J. *The Fitness of the Environment*; Macmillan: New York, 1913.
2. Sidgwick, N. V. *The Chemical Elements and Their Compounds*, 2 Vols.; Oxford University: New York, 1950.
3. Edsall, J. T.; Wyman, J. *Biophysical Chemistry*; Academic: Orlando, FL, 1958.
4. Ashcroft, N. W.; Mermin, N. D. *Solid State Physics*; Saunders College: Philadelphia, PA, 1976.
5. Gilmanshin, R. I.; Lazarev, P. W. *Biotekhnologiya* 1987, 3, 421–432.
6. MacDiarmid, A. G.; Epstein, A. J. *Proceedings of the 11th Annual International IEEE Engineering in Medicine and Biology Society Conference*; Institute of Electrical and Electronics Engineers: New York, 1989; Vol. 11, p 1299.
7. Potember, R. S.; Hoffman, R. C.; Kim, S. H.; Speck, K. R.; Stetyick, K. A. *J. Mol. Electron.* 1988, 4, 5–16.
8. Volkenstein, M. V. *Physics and Biology*; Academic: Orlando, FL, 1982.
9. Conrad, M. *Phys. Lett. A* 1978, 68, 127–130.
10. Birge, R. R. *Annu. Rev. Biophys. Bioeng.* 1981, 10, 315–354.
11. Hong, F. T. In *Molecular Electronics: Biosensors and Biocomputers*; Hong, F. T., Ed.; Plenum: New York, 1989; pp 105–114.
12. Tien, H. T.; Salamon, Z.; Kochev, A.; Ottova, A.; Zviman, M. In *Molecular Electronics: Biosensors and Biocomputers*; Hong, F. T., Ed.; Plenum: New York, 1989; pp 259–267.
13. Carter, F. L. In *Computer Applications in Chemistry*; Heller, S. R.; Potenzzone, R., Jr., Eds.; Elsevier Science Publishers: Amsterdam, The Netherlands, 1983; pp 225–261.
14. Conrad, M.; Liberman, E. A. *J. Theor. Biol.* 1983, 45, 931–968.
15. Liberman, E. A.; Minina, S. V.; Mjakotina, O. L.; Shklovsky-Kordy, N. E.; Conrad, M. *Brain Res.* 1985, 338, 33–44.
16. Conrad, M. *Proceedings of the 12th Annual International Conference of the IEEE Engineering in Medicine and Biology Society*; The Institute of Electrical and Electronics Engineers, Inc.: New York, 1990; Vol. 12, pp 1776–1777.
17. Fröhlich, H. *Int. J. Quantum Chem.* 1983, 23, 1589–1595.
18. Conrad, M. *J. Molec. Electron.* 1988, 4, 57–65.
19. Conrad, M. *Proceedings of the 11th Annual International Conference of the IEEE Engineering in Medicine and Biology Society*; The Institute of Electrical and Electronics Engineers, Inc.: New York, 1989; Vol. 11, pp 1154–1355.
20. Matsumoto, G.; Sakai, H. *J. Membr. Biol.* 1979, 50, 1–14.
21. Nicolis, G.; Prigogine, I. *Self-Organization in Nonequilibrium Systems*; Wiley-Interscience: New York, 1977.
22. Rössler, O. E. *Z. Naturforsch. A* 1983, 38a, 788–801.
23. Ni, B.; Chang, M.; Puschl, A.; Lange, J.; Needleman, R. *Gene* 1990, 169–172.
24. Robertson, D. L.; Joyce, G. F. *Nature (London)* 1990, 344, 467–468.
25. Conrad, M.; Brahmachari, S.; Sasisekharan, V. *BioSystems* 1986, 19, 123–126.
26. Conrad, M. In *Advances in Computers*; Yovits, M. C., Ed.; Academic: Orlando, FL, 1990; pp 235–324.
27. Greengard, P. C. *Cyclic Nucleotides, Phosphorylated Proteins and Neuronal Function*; Raven: New York, 1978.
28. Liberman, E. A.; Minina, S. V.; Shklovsky-Kordy, N. E.; Conrad, M. *BioSystems* 1982, 15, 127–132.

29. Conrad, M. *IEEE Spectrum* **1986**, *23*, 55–60.
30. Conrad, M. In *Real Brains, Artificial Minds*; Casti, J.; Karlqvist, A., Eds.; North-Holland: Amsterdam, The Netherlands, 1987; pp 197–226.
31. Conrad, M. *Biomed. Biochim. Acta* **1990**, *49*, 743–755.
32. Beratan, D. N.; Onuchic, J. N.; Hopfield, J. J. In *Molecular Electronics: Biosensors and Biocomputers*; Hong, F. T., Ed., Plenum: New York, 1989; pp 353–360.
33. Hameroff, S. *Ultimate Computing*; North-Holland: Amsterdam, The Netherlands, 1987.
34. Koruga, D. *BioSystems* **1990**, *23*, 297–303.
35. Conrad, M. *BioSystems* **1989**, *22*, 197–213.
36. Conrad, M.; Kampfner, R. R.; Kirby, K. G.; Rizki, E. N.; Schleis, G.; Smalz, R.; Trenary, R. *BioSystems* **1989**, *23*, 175–218.
37. Conrad, M. *Comm. ACM* **1985**, *28*, 464–480.
38. Conrad, M. In *The Universal Turing Machine: A Half Century Survey*; Herken, R., Ed.; Oxford University: New York, 1988; pp 285–307.

RECEIVED for review March 12, 1992. ACCEPTED revised manuscript December 22, 1992.

Molecular Electronic Transition Current Density Simple Orbital Transitions

Laurence A. Nafie

Department of Chemistry and Center for Molecular Electronics,
Syracuse University, Syracuse, NY 13244-4100

The theory of molecular electronic transition current density (TCD) is presented. It is shown that nonzero TCD is associated with any pair of quantum mechanical stationary states of an atomic or molecular system. Under the influence of an appropriate external perturbation, two stationary states can become coupled as linear components of the same nonstationary state and TCD appears at the difference frequency of the original states. TCD is also shown to obey the equation of continuity for the conservation of overlap probability density between the two participating stationary states. Three examples of TCD are presented for simple electronic transitions: the $1s \rightarrow 2p_x$ transition in atomic hydrogen and two $\pi \rightarrow \pi^$ transitions associated with frontier molecular orbitals in ethylene and butadiene. The theory of TCD provides a quantum mechanical basis for understanding the generation of electronic current in materials at the level of individual molecules and is therefore relevant to the emerging field of molecular electronics.*

ELECTRON PROBABILITY DENSITY (1, 2) in molecules, the absolute square of the molecular electronic wave function, is a well-known and often used function in the quantum mechanical description of the electronic structure of molecules. This density function is often used to illustrate the spatial forms of surfaces of constant electron probability density, which we hold in our minds as representations of the shapes of orbitals in atoms and molecules (2, 3).

By contrast, electron current density (1) is a much less utilized density function of the molecular electronic wave function. The principal reason is that electron current density vanishes everywhere in space for

0065-2393/94/0240-0063\$08.00/0
© 1994 American Chemical Society

a single nondegenerate, stationary-state electronic wave function. Electron current density represents a dynamic action that is simply absent for a molecule in a nondegenerate time-independent stationary state. However, as we demonstrate later, nonzero electron current density can be associated with pairs of stationary states and, in particular, as they appear in nonstationary states. In molecules whose stationary states have been perturbed by an external perturbation, nonstationary states arise that contain pairwise mixtures of the stationary states. Nonstationary-state wave functions can describe transitions between stationary states and can support nonzero electron current density.

For simplicity, we focused our attention on nondegenerate, stationary states. In the case of degenerate stationary states, nonzero electron current density may be present in the individual substates, and when it is present, it is manifested as nonzero orbital angular momentum. Nevertheless, the current density and angular momentum associated with the sum of all of the degenerate substates is zero, and these substates can only be observed in isolation by the presence of some symmetry-lowering perturbation.

Property density functions such as the electron probability density, the electron current density, and the electric-dipole moment density, to name just a few, which are associated with a single molecular stationary state, provide information regarding the contributions from various locations in a molecule to the total integrated value of the property associated with the density function. For each such property density it is possible to extend its definition to a pair of molecular eigenstates and to refer to the resulting density function as a transition density function (4). For the three preceding examples, we then have, first, the transition probability density, which is more commonly referred to as the overlap density; second, the transition current density, the subject of this chapter; and finally, the transition electric-dipole moment density. The integral of a transition density function is the transition matrix element associated with the pair of participating stationary states. The transition matrix element associated with transition current density is the velocity form of the electric-dipole transition moment, as demonstrated in the last section of this chapter. The density associated with the position form of the electric-dipole transition moment can be studied in terms of changes of electron density between the initial and final electronic states (5).

Transition current density (TCD) is represented by a vector field. At every point in the space occupied by the molecule, a vector with magnitude and direction represents the TCD at that point. On the other hand, the probability density of a single electronic state and the overlap (transition) probability density of a pair of electronic states are examples of scalar fields. At every point in space, scalar fields can be represented

simply by a magnitude. TCD is, therefore, inherently more complex than probability density and contains more information. It represents the electron density pathways by which one probability density function is related to another one.

There are two major classifications of electronic TCD in molecules. The one described in this chapter involves transitions between orthogonal pairs of electronic eigenstates. The TCD in this case describes the current associated with the oscillation of the overlap density between the two states, but because the states are orthogonal, it does not describe the continuous transformation of one state into the other. The other class of TCD involves transitions within a single electronic state due to nuclear motion within that state, such as that associated with vibrational or rotational transitions. TCD in the second class is induced by nuclear velocities and is non-Born–Oppenheimer in origin (6–8). In this case TCD represents the electron density pathways by which the electron probability density of a single electronic state is transformed to a new electron probability density by nuclear motion. Vibrationally induced TCD is directly responsible for magnetic-dipole transitions between vibrational eigenstates and hence for vibrational circular dichroism intensities in molecules (6–8). The class of TCD considered in this chapter applies to pure electronic transitions in molecules with spatially fixed and stationary nuclei and therefore is within the Born–Oppenheimer approximation.

A principal motivation for investigating all forms of molecular electronic TCD is to gain a better understanding of electron-transition-density pathways in individual molecules. It is believed that this information will be important in understanding the role of individual molecules in the conduction of current in molecular electronic devices, whether in isolation or collectively in some larger ensemble of molecular structure.

Theory

Stationary States. We begin by considering the general stationary state (g), time-dependent electronic wave function, $\psi_g(\mathbf{r}, t)$, for the eigenstate with energy E_g equal to $\hbar\omega_g$, which satisfies the time-dependent Schrödinger equation,

$$\psi_g(\mathbf{r}, t) = \psi_g(\mathbf{r}) \exp(iE_g t/\hbar) = \psi_g(\mathbf{r}) \exp(i\omega_g t) \quad (1)$$

where \hbar is Planck's constant divided by 2π , ω_g is the radial frequency associated with state g , and where $\psi_g(\mathbf{r})$ is assumed to be real and is a solution of the time-independent Schrödinger equation. The definition of the electron probability density (ρ) for the wave function in equation 1 is

$$\rho_g(\mathbf{r}, t) = \psi_g^*(\mathbf{r}, t)\psi_g(\mathbf{r}, t) = \psi_g^2(\mathbf{r}) \quad (2)$$

Although the probability density is defined with the potential to be a time-dependent function, the time dependence cancels because of the complex conjugation of the one wave function relative to the other in equation 2. Thus, the probability density of a stationary-state wave function is time-independent. The corresponding electron current density (\mathbf{j}) is defined as (1)

$$\mathbf{j}_g(\mathbf{r}, t) = (\hbar/2mi)[\psi_g^*(\mathbf{r}, t)\nabla\psi_g(\mathbf{r}, t) - \psi_g(\mathbf{r}, t)\nabla\psi_g^*(\mathbf{r}, t)] \quad (3a)$$

$$\mathbf{j}_g(\mathbf{r}, t) = (\hbar/2mi)[\psi_g(\mathbf{r})\nabla\psi_g(\mathbf{r}) - \psi_g(\mathbf{r})\nabla\psi_g(\mathbf{r})] = 0 \quad (3b)$$

where m is the mass of the electron, i is the square root of -1 , and ∇ is the vector gradient operator. Equation 3b shows that the time dependence is lost for the same reason as in the equation for the probability density earlier, leaving two terms that are identical except for their sign, and therefore they cancel. This represents a simple proof that the current density for every point in space is zero for the general nondegenerate stationary-state wave function given in equation 1.

Nonstationary States. We next consider a simple time-dependent, nonstationary-state wave function, $\psi_{g(e)}(\mathbf{r}, t)$, where we assume that an external perturbation mixes, or has mixed, some character of a single stationary-state wave function, ψ_e , into the original wave function, ψ_g . We write the nonstationary-state wave function as

$$\psi_{g(e)}(\mathbf{r}, t) = c_g\psi_g(\mathbf{r}) \exp(i\omega_g t) + c_e\psi_e(\mathbf{r}) \exp(i\omega_e t) \quad (4)$$

and we assume that the coefficients c_g and c_e are real and are either time independent or very slowly varying on the time scale of the difference frequency, $\omega_g - \omega_e$. In the case of time-independent coefficients, equation 4 represents a pure quantum state and is a solution of the time-dependent Schrödinger equation. Also, if the coefficients are constant, external perturbation no longer acts on the system to change the relative populations of the system between the states e and g . It is also reasonable to assume that c_g is much larger than c_e if the influence of state e is due to only a small perturbation; however, the form of the nonsteady expressions given here does not depend on the relative values of the mixing coefficients and is equally valid for a small perturbative mixing of the state g into the state e . Finally, we also assume that the sum of the squares of the coefficients is unity to ensure the normalization of the nonstationary-state wave function. For this wave function, the electron probability density is given by

$$\rho_{g(e)}(\mathbf{r}, t) = \psi_{g(e)}^*(\mathbf{r}, t)\psi_{g(e)}(\mathbf{r}, t) \quad (5a)$$

$$\rho_{g(e)}(\mathbf{r}, t) = c_g^2\psi_g^2(\mathbf{r}) + c_e^2\psi_e^2(\mathbf{r}) + 2c_g c_e \psi_g(\mathbf{r})\psi_e(\mathbf{r}) \cos \omega_{eg}t \quad (5b)$$

$$\rho_{g(e)}(\mathbf{r}, t) = c_g^2\rho_g(\mathbf{r}) + c_e^2\rho_e(\mathbf{r}) + 2c_g c_e O_{ge}(\mathbf{r}) \cos \omega_{eg}t \quad (5c)$$

where $\omega_{eg} = \omega_e - \omega_g$. The first two terms on the right-hand sides of equations 5b and 5c are the individual contributions of the participating stationary-state wave functions and are time independent, whereas the time-dependent term represents an oscillation at the difference frequency of the two states and depends on the product of the two coefficients and the two wave functions. The wave-function product is the overlap probability density or the transition probability density, $O_{ge}(\mathbf{r})$, and is a time-independent quantity that we have defined as

$$O_{ge}(\mathbf{r}) \equiv \psi_g(\mathbf{r})\psi_e(\mathbf{r}) \quad (6)$$

The electron current density that arises for this nonsteady-state wave function follows from the general definition just described:

$$\mathbf{j}_{g(e)}(\mathbf{r}, t) = (\hbar/2mi)[\psi_{g(e)}^*(\mathbf{r}, t)\nabla\psi_{g(e)}(\mathbf{r}, t) - \psi_{g(e)}(\mathbf{r}, t)\nabla\psi_{g(e)}^*(\mathbf{r}, t)] \quad (7a)$$

$$\mathbf{j}_{g(e)}(\mathbf{r}, t) = (-\hbar/2m)c_g c_e [\psi_g(\mathbf{r})\nabla\psi_e(\mathbf{r}) - \psi_e(\mathbf{r})\nabla\psi_g(\mathbf{r})] \sin \omega_{eg}t \quad (7b)$$

$$\mathbf{j}_{g(e)}(\mathbf{r}, t) = -2c_g c_e \mathbf{J}_{ge}(\mathbf{r}) \sin \omega_{eg}t \quad (7c)$$

The contributions of the individual stationary states vanish, as previously described for a single stationary state, leaving only one time-dependent term. This term does not vanish because the two wave functions play different roles with respect to the ∇ -operator. This term, like the overlap probability density discussed earlier, is sinusoidal at the transition frequency and depends on the product of the two mixing coefficients. For convenience, we have extracted a time-independent vector field from equation 7b, which we define as $\mathbf{J}_{ge}(\mathbf{r})$, the electron transition current density, TCD, namely

$$\mathbf{J}_{ge}(\mathbf{r}) \equiv (\hbar/2m)[\psi_g(\mathbf{r})\nabla\psi_e(\mathbf{r}) - \psi_e(\mathbf{r})\nabla\psi_g(\mathbf{r})] \quad (8)$$

where the antisymmetry associated with the two participating eigenstates is apparent from the form of this expression. The TCD is a time-independent expression for the current density associated with the quantum mechanical transition from state g to e , or vice versa, in the molecule.

Conservation of Probability Density. To gain a deeper appreciation of the function \mathbf{J}_{ge} and its relation to the overlap density O_{ge} , we consider the equation of continuity in quantum mechanics that relates the gradient of the current density to changes in the probability density for every point in space associated with molecule. For the nonstationary-

state wave function defined previously, the continuity equation is given by (1)

$$-\nabla \cdot \mathbf{j}_{g(e)}(\mathbf{r}, t) = \partial \rho_{g(e)}(\mathbf{r}, t) / \partial t \quad (9)$$

This equation states that the net flow of current density into or out of an infinitesimally small volume element in space is exactly balanced by the change with time of the probability density in that volume element. From equations 5c and 7c we can write

$$\partial \rho_{g(e)} / \partial t = -2c_g c_e \omega_{eg} O_{ge} \sin \omega_{eg} t \quad (10)$$

$$-\nabla \cdot \mathbf{j}_{g(e)} = 2c_g c_e \nabla \cdot \mathbf{J}_{ge} \sin \omega_{eg} t \quad (11)$$

From these two equations it is possible to express the continuity equation without reference to the mixing coefficients and in terms of the time-independent fields that we defined in equations 6 and 8, namely,

$$-\nabla \cdot \mathbf{J}_{ge} = \omega_{eg} O_{ge} \quad (12)$$

This equation can be regarded as a general transition continuity equation. Its validity can be verified directly by the following series of relationships:

$$-\nabla \cdot \mathbf{J}_{ge} = (-\hbar/2m)[\nabla \psi_g \cdot \nabla \psi_e + \psi_g \nabla^2 \psi_e - \nabla \psi_e \cdot \nabla \psi_g - \psi_e \nabla^2 \psi_g] \quad (13a)$$

$$-\nabla \cdot \mathbf{J}_{ge} = (1/\hbar)\{\psi_g[(-\hbar^2/2m)\nabla^2 + V]\psi_e - \psi_e[(-\hbar^2/2m)\nabla^2 + V]\psi_g\} \quad (13b)$$

$$-\nabla \cdot \mathbf{J}_{ge} = (1/\hbar)(E_e - E_g)\psi_g \psi_e \quad (13c)$$

$$-\nabla \cdot \mathbf{J}_{ge} = \omega_{eg} O_{ge} \quad (13d)$$

Equation 13a follows from the definition of \mathbf{J}_{ge} in equation 8 and two of its terms cancel. In equation 13b the same appropriate potential energy term, V , has been added and subtracted to yield two opposite-signed Hamiltonians of an electron in the molecule. For simplicity, we have considered only one electron, but extension to many electrons is straightforward if desired. Equation 13c follows from the action of the Hamiltonian on the wave function of state e in the first term and state g in the second. The last equation is then obtained with two simple substitutions and confirms the transition continuity equation given in equation 12.

Orbital Transition Densities

In this section we illustrate the density functions developed in the preceding section for three simple electronic transitions between three pairs of states that are represented by orbital wave functions. In the first and simplest case, we consider the $1s$ to $2p_x$ transition of atomic hydro-

gen. We then consider the frontier orbitals associated with the $\pi \rightarrow \pi^*$ molecular transition of a double bond, a simple example being the molecule ethylene. Finally, we consider a $\pi \rightarrow \pi^*$ transition for a conjugated pair of such double bonds, such as would be found in butadiene. All calculations of property densities and the three-dimensional graphical presentations of the scalar fields were carried out using the program *Mathematica*, version 2.0 (9). The graphs of the TCD vector fields were constructed element by element from the numerical data with the word-processing program *Chemtext* (10).

The normalized $1s$ and $2p_x$ orbital wave functions for atomic hydrogen are given by

$$\psi_{1s} = \pi^{-1/2} e^{-r} \quad (14)$$

$$\psi_{2p_x} = (32\pi)^{-1/2} x e^{-r/2} \quad (15)$$

where the unit of distance is chosen to the Bohr radius, 0.528 \AA . Figure 1 displays the probability densities and the overlap density for the two atomic states in the xz -plane that passes through the atomic center. The x -axis is in the lengthwise dimension across the figure and the z -axis is depthwise toward and away from the viewer. A pictorial representation of these two wave functions, with regions of positive and negative amplitude, is given at the top of the figure. For conformity with the notation established in the previous section, we associate the initial state, $1s$, with the state g , and the final state, $2p_x$, with the state e . The density plots depict a square planar surface of two Bohr radii on a side. The familiar spatial dependence of the s - and p -states is clearly seen in the two probability density plots, and the shape of the overlap density surface can be recognized as that associated with the product of the orbital wave functions.

In Figure 2 we present plots of the TCD. The two surfaces in three dimensions are scalar plots of the x - and z -components of the TCD vector field in the xz -plane, given by

$$\mathbf{J}_{ge} = J_{ge,x} \hat{x} + J_{ge,z} \hat{z} \quad (16)$$

where \hat{x} and \hat{z} are unit vectors in the x - and z -directions. For simplicity, we have omitted the factor of $\hbar/2m$ in the definition given in equation 8. At the bottom of Figure 2, we show the two scalar-field components as merged into a single low-resolution representation of the vector-field density, \mathbf{J}_{ge} . The scalar field $J_{ge,x}$ has an appearance that is similar to the $1s$ probability density plot, although it has an elliptical profile with the major axis in the x -direction. It represents positive TCD in the x -direction and is the primary component of the TCD vector field. The z -component, $J_{ge,z}$, on the other hand is smaller in magnitude and

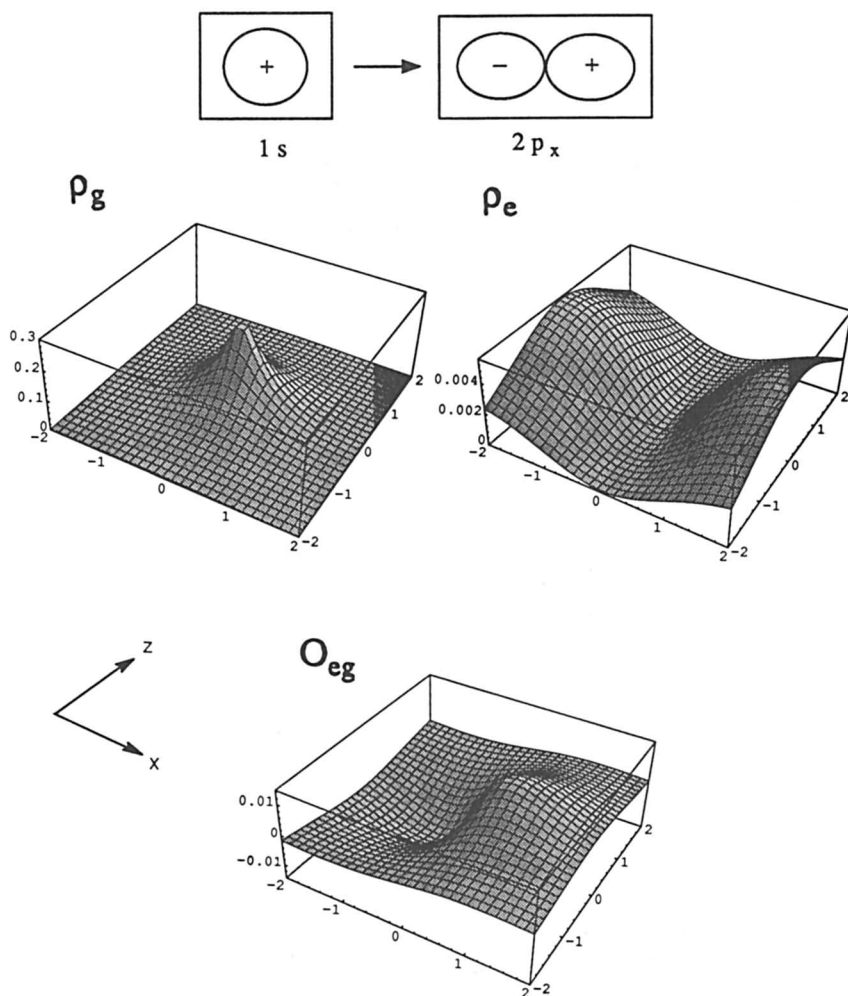
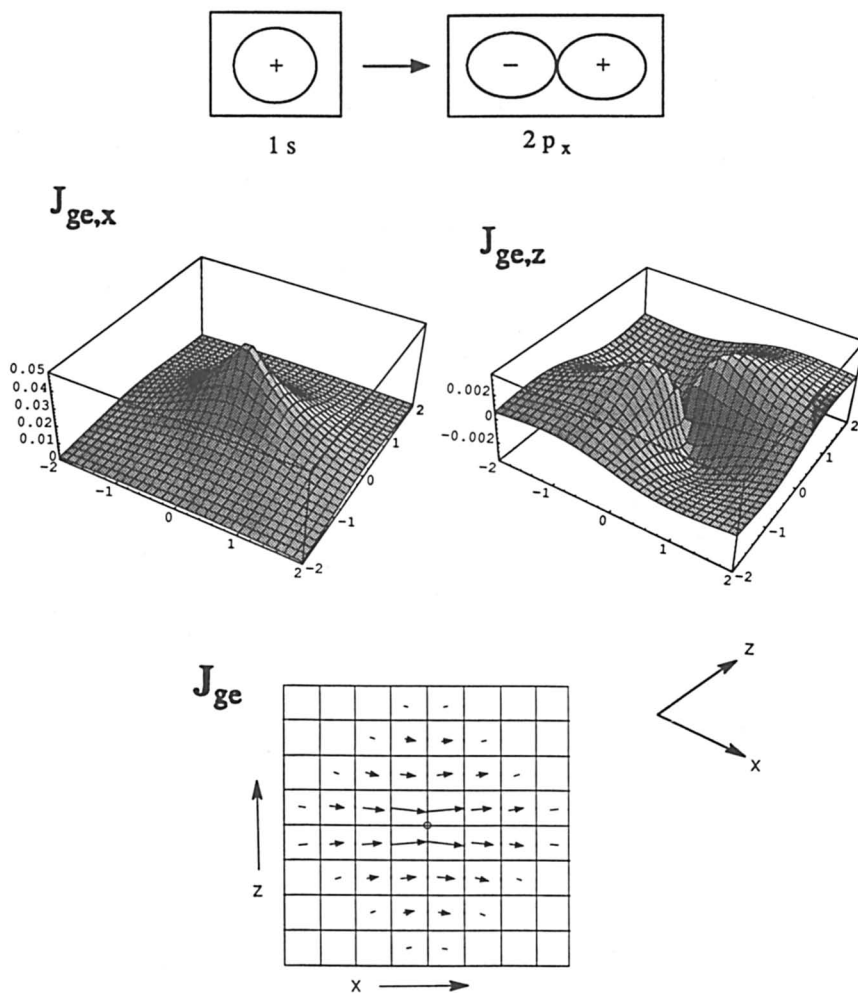


Figure 1. Electron probability densities for the $1s$ (initial, ρ_g) and $2p_x$ (final, ρ_e) orbital wave functions of atomic hydrogen, and the overlap probability density (O_{ge}). The form of the wave functions in the plane of the density functions is shown at the top of the figure.

has regions of positive and negative TCD. The z -component is responsible for the slight channeling or narrowing effect as current density passes near the atomic center and then spreads out again afterward. The x -dipole allowed character of this transition is reflected by the overall net flow of TCD along the x -axis and only along the x -axis.



The frontier molecular orbitals for the $\pi \rightarrow \pi^*$ transition of an isolated double bond are constructed from normalized atomic hydrogen $2p_z$ orbitals as given by

$$\psi_{\pi} = 2^{-1/2}[\psi_{2p_z}(r_1) + \psi_{2p_z}(r_2)] \quad (17)$$

$$\psi_{\pi^*} = 2^{-1/2}[-\psi_{2p_z}(r_1) + \psi_{2p_z}(r_2)] \quad (18)$$

where r_1 and r_2 designate the locations of the origin of the $2p_z$ atomic orbitals. We choose a separation distance of 2.66 Bohr radii, which corresponds to a bond distance of approximately 1.41 Å. The origins of the r_1 - and r_2 - $2p_z$ orbitals lie at the (x,y,z) coordinates $(-1.33,0,0)$ and $(1.33,0,0)$, respectively, along the x -axis. The wave function expressed in equation 17 may be regarded as a π -bonding molecular orbital and the corresponding wave function 18 as an antibonding π -orbital. The probability and overlap densities for these orbitals are presented in Figure 3 in the same format as in Figure 1 where again the orbital wave functions of state g (initial) and e (final) are given at the top of the figure for reference. The plots, covering a larger area, are again in the xz -plane, and the origin of coordinates is at the center of the interatomic axis. Both the upper and lower regions of the π -bonds lie in the xz -plane.

The plots of the TCD for this transition are given in Figure 4. The x -component of the TCD depicts current flowing in the positive x -direction above and below the interatomic axis. The z -component again contains regions of positive and negative TCD and is smaller in magnitude than the x -component. The x -dipole character of this transition is again evident from the full-vector-field representation at the bottom of the figure. In this case, however, the influence of the z -component is both opposite and larger than that for the $1s$ to $2p_x$ transition in Figure 2. The overall pattern is one of bowing out rather than of channeling in as the TCD passes along the bonding region from the region of one atomic center to the other.

In the final example, the frontier orbitals associated with the $\pi \rightarrow \pi^*$ transition of a conjugated pair of double bonds are considered. The spatial forms of the bonding and antibonding orbitals are presented at the top of Figure 5. An xz -plane is shown passing through the upper lobes of the atomic $2p_y$ -orbitals used to construct molecular orbitals. This plane is chosen to be 2 Bohr radii above the plane of the four atomic centers that comprise the bonding framework. The first two centers are the same distance apart as those for the isolated double bond considered in the previous transition, and the third and fourth centers are also separated by this distance. The second and third centers are separated by a bond length of 1.54 Å, and the 123- and 234-center bond angles are 120° , typical for sp^2 -hybridization. The orbital wave functions have the form

$$\psi_\pi = 4^{-1/2}[\psi_{2p_y}(r_1) + \psi_{2p_y}(r_2) - \psi_{2p_y}(r_3) - \psi_{2p_y}(r_4)] \quad (19)$$

$$\psi_{\pi^*} = 4^{-1/2}[-\psi_{2p_y}(r_1) + \psi_{2p_y}(r_2) + \psi_{2p_y}(r_3) - \psi_{2p_y}(r_4)] \quad (20)$$

where the coordinates for the orbital centers r_1 , r_2 , r_3 , and r_4 in Bohr radii are $(-3.387,0,1.258)$, $(-0.726,0,1.258)$, $(0.726,0,-1.258)$, and $(3.387,0,-1.258)$, respectively.

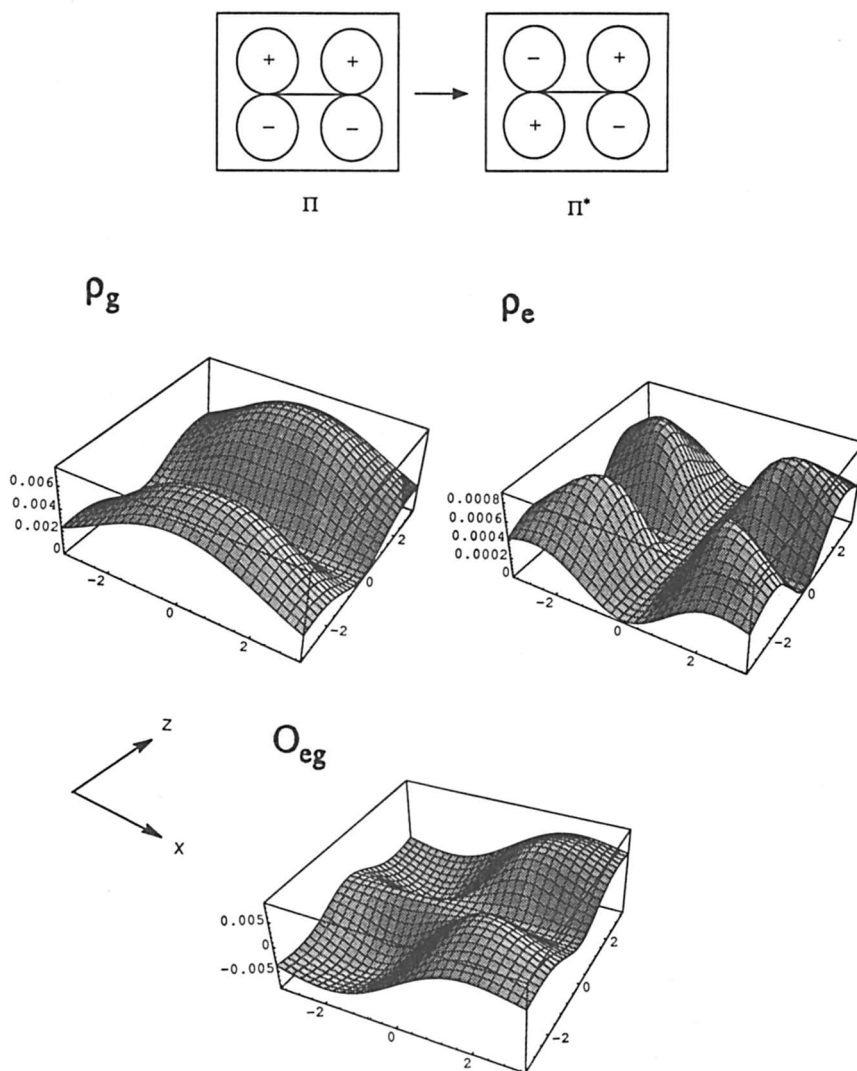


Figure 3. Electron probability densities for the frontier orbitals of π (initial, ρ_g) and π^* (final, ρ_e) orbital wave functions of an isolated double bond, as in ethylene, and the overlap probability density (O_{eg}) of these orbitals. The form of the orbital wave functions in the plane plotted is shown at the top of the figure.

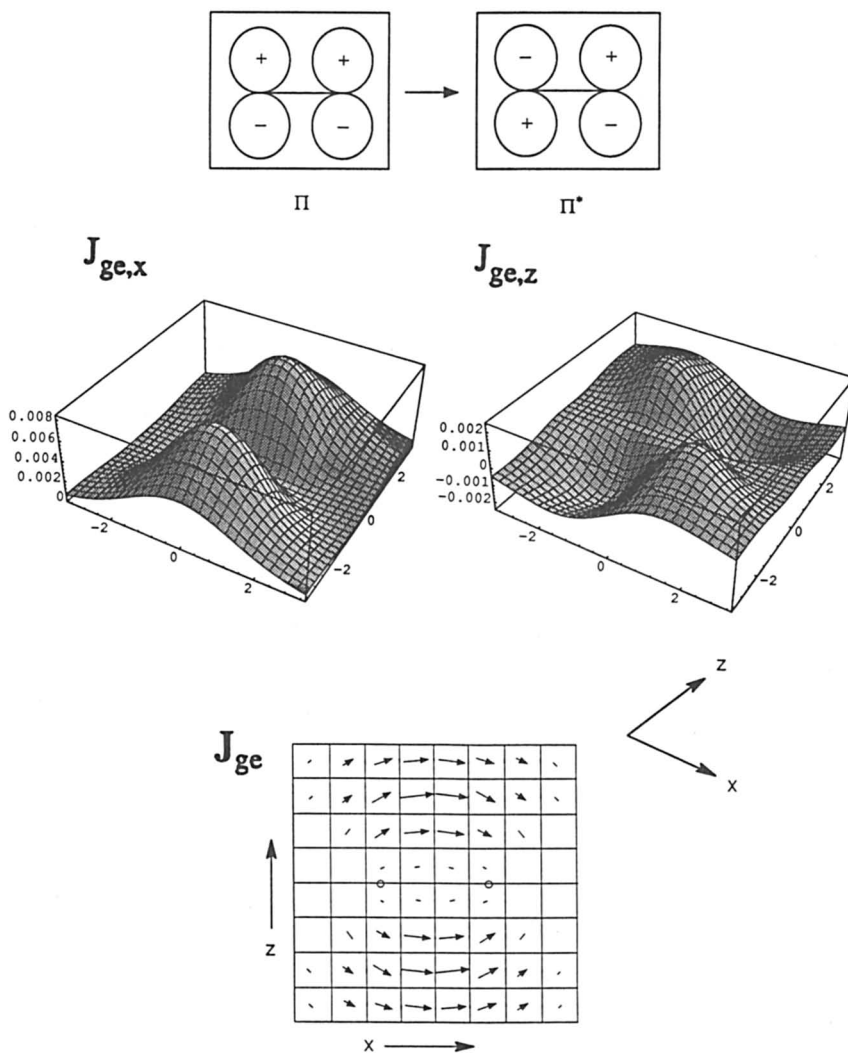


Figure 4. The x- and z-components of the electron TCD for the π to π^* transition of an isolated double bond are presented as three-dimensional scalar surface plots (above) and their combined two-dimensional vector field plot (below).

The probability density of the bonding orbital shown in Figure 5 exhibits two regions of π -bonding that become greatly diminished in the probability density plot of the π -antibonding orbital. By contrast, in the antibonding orbital, π -bonding is seen along the 2,3-center axis, which in the bonding orbital corresponds to a single bond with no π -bonding. In terms of the constituent orbital wave functions, the bonding

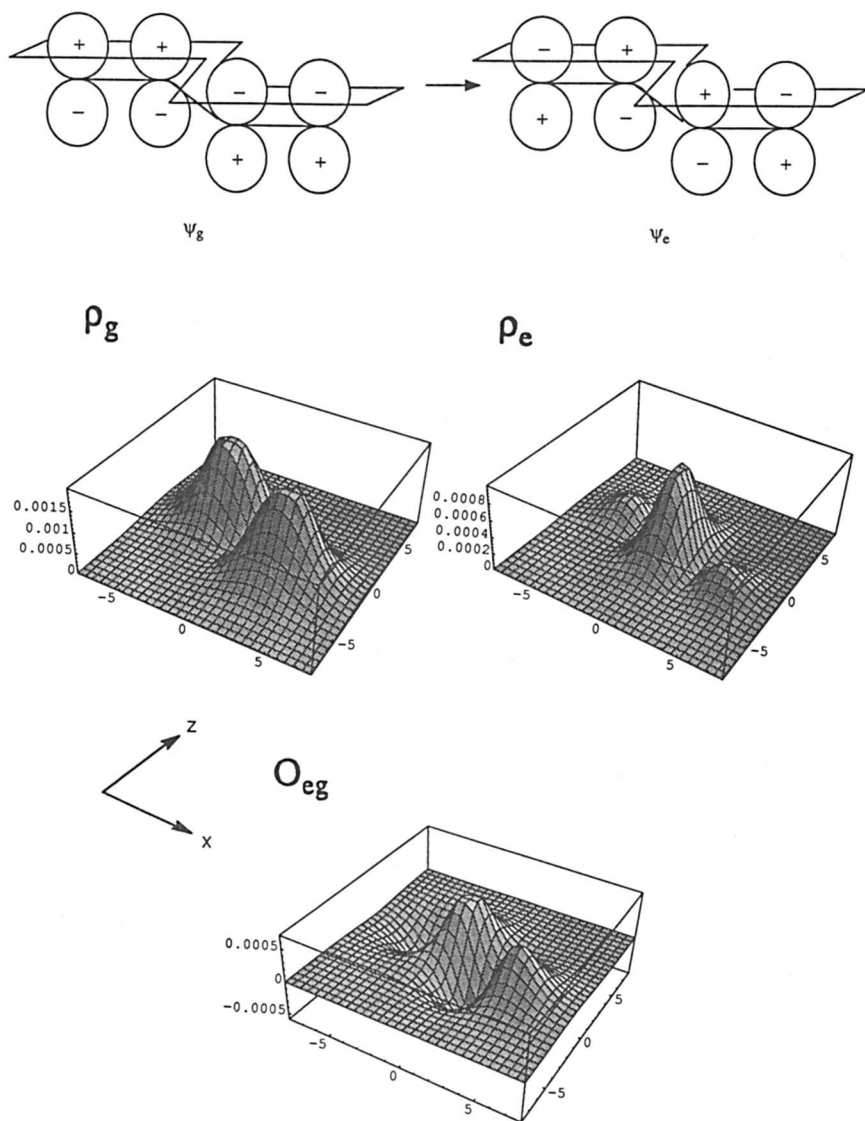


Figure 5. *Electron probability densities for the frontier orbitals of π (initial, ρ_g) and π^* (final, ρ_e) orbital wave functions for a pair of conjugated double bonds, as in butadiene, and the overlap probability density (O_{ge}) of these orbitals. The form of the orbital wave functions in the plane plotted is shown at the top of the figure.*

orbital has two regions of constructive overlap and one node between atoms 2 and 3, whereas the antibonding state has one region of constructive overlap and two nodes, between atoms 1 and 2 and between atoms 3 and 4. The overlap density shows two regions of alternating positive and negative overlap corresponding to the multiplication of the π - and π^* -orbital wave functions in these regions.

The plots of the TCD for this transition are presented in Figure 6 in the same manner as for the previous transitions. The direction of the dipole-allowed character of this transition for the phase chosen in the coordinate frame described previously is positive x and negative z . The x -component of TCD shows two maxima associated with the bonding regions in the π -bonding orbital corresponding to TCD flowing in the positive x -direction. Strong TCD between these two regions flows in the positive x -direction. The z -component of the TCD show two relatively weak regions of TCD flowing in the positive z -direction, and an intense negative TCD region with a global minimum between atoms 2 and 3. The combined TCD field at the bottom of the figure shows a pattern of current density that is similar to two single-bond TCD patterns joined together, although there is very strong current all along the bond axis of atoms 2 and 3 and, as a result, all along the conjugated π -bonding backbone of the molecule.

Discussion

Although the general concept of transition property density has been advanced previously, the theoretical derivation presented in this chapter represents the first identification of transition current density as general quantum mechanical property of any pair of quantum mechanical stationary states. This derivation not only demonstrates that nonvanishing TCD can be expected for any pair of quantum states, but that TCD obeys the equation of continuity for the conservation of the overlap density at all points in the space of the two quantum states. By the introduction of nonstationary states, the origin of TCD is illustrated as part of a time-dependent quantum mechanical interference term oscillating at the difference frequency of the pair of quantum stationary states.

In a dynamical sense, the oscillating TCD term is responsible for the absorption and emission of radiation through the resonance interaction of the radiation field with an atom or molecule. The radiation field usually serves as the source of the perturbation that is necessary to create nonstationary states, and the oscillating time-dependent terms responsible for TCD. Under special conditions it is possible to directly observe phenomena representing these oscillating time-dependent terms. This occurs in the fluorescence associated with a single pair of

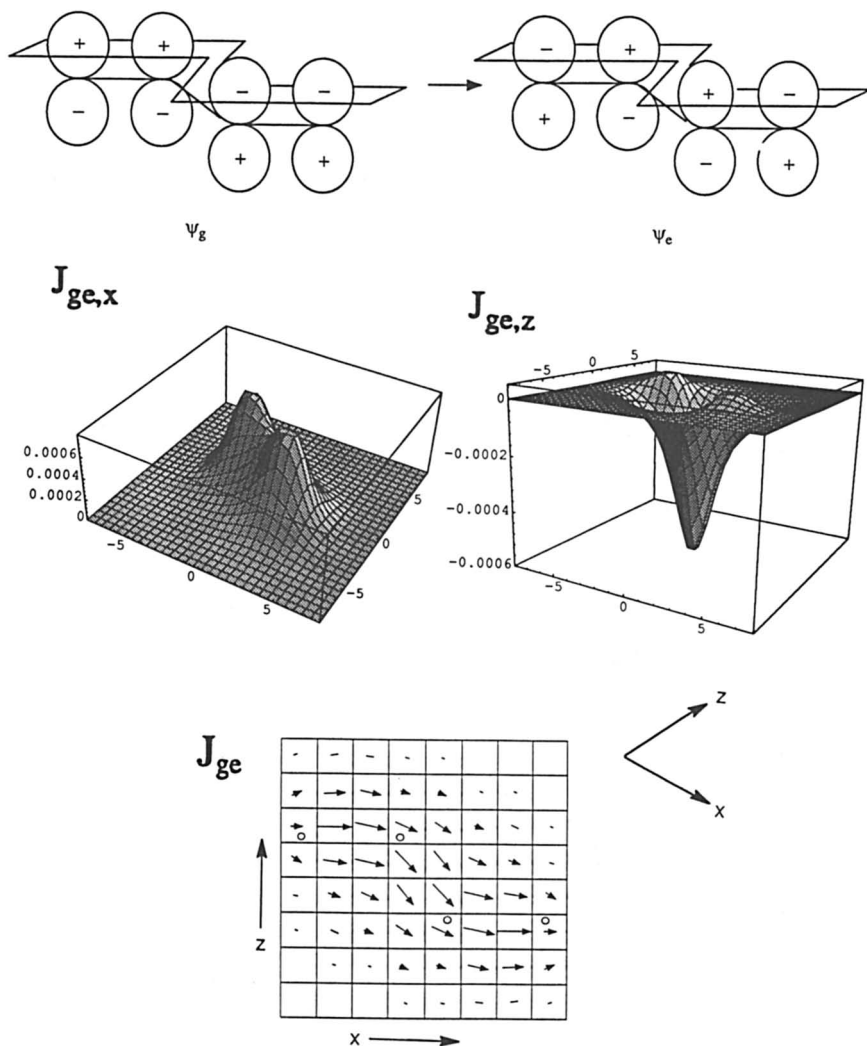


Figure 6. The x- and z-components of the electron TCD for the π to π^* transition of a pair of conjugated double bonds are presented as three-dimensional scalar surface plots (above) and their combined two-dimensional vector field plot (below).

isolated, excited states in a gas-phase atom or molecule, where the phenomenon is referred to as quantum beats (11). In general, however, many such pairs of interfering states are present and interfere destructively with one another. A radiation field, however, is able to selectively isolate individual pairs through direct resonance and the conservation of energy.

The definition of TCD in equation 8 is a general definition free of the circumstances that give rise to the occurrence of TCD in real quantum systems. In particular it is independent of the difference frequency or the values of the mixing coefficients. The definition applies equally well to both members of the pair of quantum mechanical states, although as previously noted the relationship of the definition to the two states is one of opposite sign. The sign, however, is of no particular consequence because it merely reflects a choice of phase with respect to the oscillation of the TCD at the transition frequency. For the transitions illustrated in this chapter, the density plots would apply equally well if we exchanged the identities of the initial and final states and multiplied one of the wave functions by -1 .

In this chapter the examples of orbital transitions chosen to illustrate electronic TCD all represent electric-dipole-allowed transitions. In the first case of $1s$ to $2p_x$ orbitals of atomic hydrogen, the transition is x -dipole allowed. The integral over the plane (or entire space) of the TCD is proportional to the velocity form of the electric-dipole transition moment, as follows:

$$\int J_{ge}(\mathbf{r})d\mathbf{r} = (\hbar/2m) \int [\psi_g(\mathbf{r})\nabla\psi_e(\mathbf{r}) - \psi_e(\mathbf{r})\nabla\psi_g(\mathbf{r})]d\mathbf{r} \quad (21a)$$

$$\int J_{ge}(\mathbf{r})d\mathbf{r} = -(\hbar/m) \int \psi_e(\mathbf{r})\nabla\psi_g(\mathbf{r})d\mathbf{r} \quad (21b)$$

$$\int J_{ge}(\mathbf{r})d\mathbf{r} = -i \int \psi_e(\mathbf{r})(\mathbf{p}/m)\psi_g(\mathbf{r})d\mathbf{r} \quad (21c)$$

where the anti-Hermitian property of the integral (1, 6) is used to obtain equation 21b, and equation 21c follows from the definition of the quantum mechanical momentum operator. The entire contribution of the $1s$ to $2p_x$ TCD to the velocity transition moment is due to the x -component of the TCD, the integral of the z -component for this transition being zero. Although the z -component contributes nothing to the integrated velocity dipole, because it has canceling regions of positive and negative TCD, it nevertheless, in general, has nonzero TCD at arbitrary points throughout the plane and gives the TCD vector field its particular form as illustrated in Figure 2. A similar situation is encountered in the second example of the $\pi \rightarrow \pi^*$ transition where the principal direction of the TCD is in the x -direction, and the transverse, nondipole component of the field is in the z -direction. In the final example both the x - and z -directions carry dipole allowed contributions as well as nondipole allowed transverse TCD contributions.

The TCD associated with simple electronic orbitals in atoms and molecules is the simplest form of electronic current in isolated molecules. Current density due to nuclear motion can be described in terms of

electronic TCD associated with the complete set of excited electronic states through Rayleigh–Schrödinger perturbation theory (6). Any detailed quantum mechanical description of electronic current involving molecular-level components, that is, molecular electronics, must be grounded at some point in the generation electronic TCD in molecules. In more complex arrangements of molecules involving aggregates of molecules or macromolecules, the descriptions of the electronic states become more complex and large sums over TCDs must be carried out to describe the current density in such systems. In the limit of extended solid-state structure, the interaction between local subunits leads to the usual electronic description of band structure encountered in standard treatments of current density and conductivity in matter (12).

Descriptions of long-range electron transfer in biological molecules, corresponding to the intermediate level in the preceding discussion, have been carried out (13–15). These studies are relevant to molecular electronics because they represent examples of individual macromolecules transporting charge over significant distances. The immediate object of one type of description (13, 14) is to calculate the probability of electron transfer involving an initial state prior to electron transfer and a final state following transfer. Although the pathways of electron transfer are of interest, the formalism at most yields differences in scalar fields associated with probability density differences. A second type of description uses a quantum-path integral approach to describe the single path of an excess electron migrating from one location near a molecule to another under the influence of electrostatic forces (15). This formalism differs in concept from the one presented here because a single electron path is generated and not a vector field associated with electronic current density. Using the formalism introduced in this chapter and the specifications of initial and final quantum mechanical states, the electronic TCD could be calculated for long-range electron-transfer transitions, and current density pathways could be visualized.

Acknowledgments

The author gratefully acknowledges support from the Industrial Affiliates Program of the Center for Molecular Electronics.

References

1. Schiff, L. I. *Quantum Mechanics*, 3rd ed.; McGraw-Hill: New York, 1968.
2. Levin, I. N. *Quantum Chemistry*, 3rd ed.; Allyn and Bacon: Boston, MA, 1983.
3. Hout, R. F., Jr.; Pietro, W. H.; Hehre, W. J. *A Pictorial Approach to Molecular Structure and Reactivity*; Wiley: New York, 1984.
4. McWeeny, R. *Methods of Molecular Quantum Mechanics*, 2nd ed.; Academic: Boston, MA, 1989.

5. Theiste, D.; Jones, R. D.; Callis, P. R. *Chem. Phys. Lett.* 1987, 133, 14.
6. Nafie, L. A. *J. Chem. Phys.* 1983, 79, 4950.
7. Nafie, L. A.; Freedman, T. B. *J. Phys. Chem.* 1986, 90, 763.
8. Nafie, L. A. *J. Chem. Phys.* 1992, 96, 5687.
9. *Mathematica*; Version 2.0; Wolfram Research Inc.: Champaign, IL, 1991.
10. *Chemtext*; Molecular Design Ltd.: San Leandro, CA, 1990.
11. Chaiken, J.; McDonald, J. D. *Adv. Laser Spectrosc.* 1982, 1, 177.
12. Ziman, J. M. *Principles of the Theory of Solids*; Cambridge University: Cambridge, England, 1965.
13. Bertran, D. N.; Onuchic, J. N.; Hopfield, J. J. *J. Chem. Phys.* 1985, 83, 5325.
14. Bertran, D. N.; Onuchic, J. N.; Hopfield, J. J. *J. Chem. Phys.* 1987, 86, 4488.
15. Wheeler, R. A.; McCammon, J. A. *Chem. Phys. Lett.* 1990, 174, 369.

RECEIVED for review March 12, 1992. ACCEPTED revised manuscript February 2, 1993.

The Quest for D- σ -A Unimolecular Rectifiers and Related Topics in Molecular Electronics

Robert M. Metzger

Department of Chemistry, University of Alabama,
Tuscaloosa, AL 35487-0336

Progress is being made toward unimolecular devices, whose function relies on the manipulation of the energy levels or conformations of either a single molecule or a small cluster of molecules. These devices, at the forefront of "molecular electronics", should leapfrog conventional microelectronics, for which a 100-Å lower limit in "design rules" is predicted. Fast organic rectifiers and transistors should be addressable by scanning tunneling microscopy. The quest for the proposed Aviram-Ratner D- σ -A unimolecular rectifier is reviewed, where D is a good one-electron donor (but poor acceptor), σ is a covalent, saturated "sigma" bridge, and A is a good one-electron acceptor (but poor donor). D- σ -A should more easily form the zwitterion $D^+-\sigma-A^-$ (followed by fast intramolecular electron transport $D^+-\sigma-A^- \rightarrow D-\sigma-A$) than the zwitterion $D^--\sigma-A^+$. Many candidate D- σ -A molecules form Langmuir-Blodgett films and Schottky barrier rectification have been seen, but intramolecular electron tunneling through D- σ -A has not yet been confirmed.

MOLECULAR ELECTRONICS (ME) (1) has two current definitions as follows.

1. the "wider" definition, which includes the interesting electrical behavior (conductivity, superconductivity, etc.) of all known lower dimensional systems, Langmuir-Blodgett (LB) films, and clusters
2. the "stricter and narrower" definition, which focuses on the properties of the single molecule

0065-2393/94/0240-0081/\$13.04/0
© 1994 American Chemical Society

This chapter presents these definitions, followed by a discussion of a few “bulk” molecular devices. The next sections present ideas for external connections to single molecules, several proposals for unimolecular electronic devices, and a review of efforts to harness intramolecular electron transfer.

The last two sections chronicle the progress made toward the realization of the organic rectifier, a proposal advanced in 1974 by Ari Aviram, Mark A. Ratner, and co-workers (2–4) that a single organic molecule of the type D– σ –A could be a rectifier of electrical current. This molecule D– σ –A would act as a rectifier, because the D end is a good organic one-electron donor (but poor acceptor), σ is a covalent saturated (“sigma”) bridge, and A is a good organic one-electron acceptor (but poor donor). The Organic Rectifier Project (ORP) at the Universities of Mississippi (1981–1991) and Alabama (1986–1991) has been the combined effort of a synthetic chemist (Charles A. Panetta) and a physical chemist (Robert M. Metzger) to put to a practical test the Aviram–Ratner Ansatz (5–34). The impetus for the ORP, one of the key experiments in ME, has been that the working thickness promised by such a D– σ –A device is of the order of one or two molecular lengths, that is, about 5 nm. The rosiest forecast is that a working length (“design rule”) of 100 Å = 10 nm is the smallest conceivable for silicon or gallium arsenide technology; present limits are well above 100 nm.

As discussed in the last section, the rectification by a single organic molecule or by an organized LB (35–41) monolayer of such molecules has not been achieved by the ORP. However, Sambles (University of Exeter) and co-workers have observed rectification by an LB monolayer (42, 43), but this is ascribed (44, 45) to a Schottky barrier rather than to the Aviram–Ratner mechanism (this is not surprising, given the specific D– σ –A and D⁺– π –A[–] molecules used). The revolutionary scanning tunneling microscope (STM) (46) shows promise for confirming the Aviram–Ratner Ansatz (22, 23, 31, 32), but difficulties exist in measuring currents through molecules in an unambiguous manner.

Broad and Narrow Definitions of Molecular Electronics

The term ME was popularized by the late Forrest L. Carter, who organized three international workshops on ME devices starting in 1981 (47–49); these were followed by similar conferences in Varna (50), Hawaii (51), and St. Thomas (52). In 1983, an unscientific proposal about self-assembling biological “computers” (“biochips”) received undeserved and uncritical worldwide media attention; the understandable reaction to such exaggerations almost drowned the infant field of ME! A very sobering note outlined what technical accomplishments were still needed (53, 54). Since then, more conservative chemists, physicists,

and materials scientists have broadened the definition of ME and relabeled some of their research areas as ME, and thus have restored respectability to the field.

At present, two interpretations of ME exist. In its first, broader, definition, ME encompasses the studies of all molecule-based electronic processes in lower dimensional systems, to wit, in approximate historical order:

- (A1) intercalated graphites (C_8K , etc.) (55)
- (A2) intercalated two-dimensional chalcogenides (TaS_2 , etc.) (56)
- (A3) charge-transfer salts (organic conductors and superconductors) (57)
- (A4) conducting low-dimensional polymers (57, 58)
- (A5) inorganic linear-chain compounds (59)
- (A6) LB multilayers (35–41)

These research areas have been studied worldwide for almost two decades, and relabeling them as ME may be a convenient shorthand, an attention-getting method for funding research proposals, or just a current fad.

In the second, more narrow definition, ME devices (“zero-dimensional devices”) utilize the electronic properties of single molecules or clusters. Examples of proposals are as follows:

- (B1) Aviram and Ratner’s rectifier, which is the main subject of this chapter (2–4)
- (B2) Aviram and Ratner’s hydrogen atom switch (3, 4)
- (B3) Mitani’s proton transfer system (60)
- (B4) Carter’s soliton switch (61)
- (B5) Fujihira’s LB monolayer photodiode (62)

The following proposals have been brought forth for “passive” molecular connectors that may one day be useful to interrogate unimolecular ME devices:

- (C1) molecular wires and antennas, for example, carotenes and other polyenes (63)
- (C2) Aviram’s linked thiophene “connects” (64) realized by Tour et al. (65)
- (C3) Miller’s “molecular lines” (66)
- (C4) molecular inclusions in urea, thiourea, cyclodextrins (67), calixarenes (68), or zeolites (69)

It is imperative that these potential devices utilize fast intramolecular electron transfer speeds (faster than 1 GHz, that is, electron per molecule

per nanosecond). Indeed, ME will enjoy a substantial margin over present-day semiconductor electronics only if ME can couple the advantages of molecular size (<2 nm) and fast intramolecular electron transfer (>1 GHz). There is little use in making a small but slow device.

Bulk Molecular Devices

First, we discuss some known “bulk” molecular devices, even though they are molecular devices only in the larger sense (i.e., because of the band structure of the solids or because of phase change properties or other bulk effects).

Bulk Organic Rectifiers. After the discovery of the *pn* junction diode (*p* is hole-rich region, *n* is electron-rich region) and the *npn* transistor, it was of interest to see whether macroscopic films of organic molecules could function as bulk *pn* rectifiers (diodes) or as *npn* transistors. The *pn* rectifiers would occur if a film or crystal of an organic electron donor (which becomes a *p* region) were brought in contact with that of an organic electron acceptor (*n* region). This was indeed verified in the 1960s (70).

Pockels–Langmuir, Langmuir–Blodgett, and Langmuir–Schaefer Films. Before discussing organic rectifiers based on LB films, we define (Figure 1) the terms Pockels–Langmuir (PL) (17), LB, and Langmuir–Schaefer (LS) films (37–39). The self-assembly of one-molecular thick “monolayers” at the air–water interface was studied scientifically by Agnes Pockels, Lord Rayleigh, and Irving Langmuir (39). PL films may be a convenient term (17) for stable self-assembling monolayers at the air–water interface (37) (Figure 1a). A few studies have used mercury as a subphase (71). Kathleen Blodgett found that PL monolayers could be transferred quantitatively to a solid substrate by dipping the substrate vertically through the PL monolayer: These monolayers are then LB monolayers or (by repeated dipping) LB multilayer films (35, 36) (Figure 1b and 1d). Schaefer found that horizontal dipping of a substrate could also transfer films that otherwise did not transfer well by the LB method: These are LS films (72) (Figure 1c).

An early study of electrical conductivity between an Al electrode and a mercury drop through *N* Y-type LB monolayers of cadmium arachidate [CA = Cd(C₁₉H₃₈COO)₂] (73), as a sandwich Al|(CA)_N|Hg (here, vertical bar denotes an interface), claimed that, beyond a background through-film current density j_a (due to defects), the intrinsic current density j_i depended upon the number of layers and followed the Bethe–Sommerfeld tunneling equation: $\log j_i \propto V^{1/2}$, where *V* is the tunneling barrier. There were other similar studies (74); groups in the United Kingdom found instead $\log j \propto V^{1/4}$, which favored an interpre-

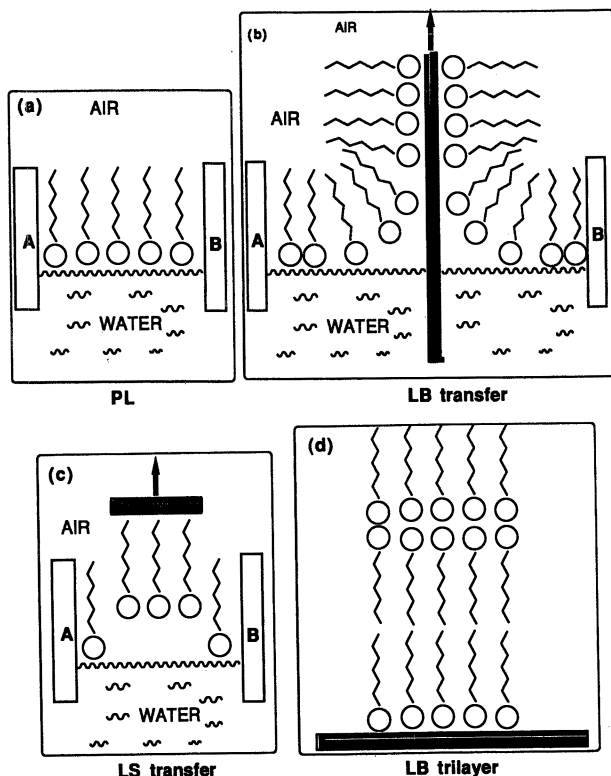


Figure 1. a, Structure of Pockels–Langmuir (PL) film at air–water interface; A and B are solid barriers that minimize the monolayer surface area (A_c) at the collapse surface pressure (Π_c); the tadpole-shaped structure represents an amphiphilic molecule: The circle is its polar “head” group; the zig-zag is its hydrophobic “greasy tail,” for example, a long saturated alkane chain. b, Vertical transfer of Langmuir–Blodgett (LB) film (35, 36) onto a hydrophilic solid substrate (e.g., Al). c, Horizontal transfer of Langmuir–Schaefer (LS) film (72) onto a hydrophobic solid substrate (e.g., graphite). d, Structure of LB Y-type trilayer on hydrophilic substrate.

tation of a defect-limited process (75, 76). Because they are somewhat disordered within the plane of the film, LB multilayers have more electrical defects than may be expected naively (77).

Multilayer Langmuir–Blodgett Organic Rectifiers. Kuhn and co-workers (78) showed that one can obtain a “pn” (or DA) rectifier in a LB multilayer sandwich Al|(CA-D)_q|(CA)_r|(CA-A)_s|Al. Here (CA-D)_q denotes the electron-donor system D (=q LB monolayers of CA randomly doped in the ratio 5:1 with suitable organic π -electron donors D), whereas (CA)_r denotes a spacer layer of r undoped monolayers of CA, and (CA-A)_s denotes the electron-acceptor system A (=s LB monolayers

of CA randomly doped with suitable organic π -electron acceptors A). This work was repeated and confirmed by Sugi and co-workers (79), who observed rectification properties, but only if $q \geq 3$, $r \geq 1$, and $s \geq 3$, that is, if there are at least seven monolayers (below that, irreproducible data resulted). In these LB films, the registry and intermolecular approach between D and A dissolved in adjacent CA monolayers cannot be controlled.

A Phase-Change Organic Switch. In 1979 a fast switch was discovered by Potember (80) in CuTCNQ, where TCNQ is 7,7,8,8-tetracyanoquinodimethane. This was due to the thermodynamic metastability (in crystals or amorphous powders) of the violet, low-conductivity ionic state (IS) $\text{Cu}^+ \text{TCNQ}^-(c)$, relative to the yellow, low-conductivity, neutral state (NS) $\text{Cu}^{(0)} \text{TCNQ}^{(0)}(c)$, with, presumably, an intermediate, mixed-valent, higher conductivity state (CS); one could switch between the two states $\text{IS} \leftrightarrow \text{CS}$ either with an applied voltage over a certain threshold value, or by a moderate laser beam, while heat will restore the IS. This is found also in AgTCNQ and in a few other related systems (81). The switching rate is quite fast and can be even used for optical data storage (82), but has not been incorporated in commercial devices. This work has been carried out also with a scanning tunneling microscope (83).

A Molecule-Based Transistor Using Conducting Polymers. Wrighton and co-workers (84, 85) developed a "molecule-based transistor" that uses conducting polymers, either chemically doped polyaniline layers deposited on Au interdigitated electrodes (84) or a 50- to 100-nm "gate" polyaniline polymer between two Au electrodes shadowed with SiO_2 ; this device still has a gain of almost 1000, but also a slow switching rate (10 kHz), limited by ionic conduction rates (85). Stubb and co-workers (86) showed that a single LB monolayer can be used in a molecule-based transistor.

Phase-Change Optical Memories. There are four established technologies for mass-information storage and retrieval (87–89):

1. magnetic memories (MM), disks and tapes, based on ferrite, iron oxide, chromium oxide and pure iron (coated with alumina or silica): These are erasable or write-many, read-many (WMRM) media.
2. Si- and GaAs-based semiconductor computer memories (SM): These can be considered as very-fast write-many, read-many (FWMRM) media.
3. Al pits (melted regions, or crystalline-to-amorphous tran-

sition) on polycarbonate-based laser-readable compact-disk (CD) technology: This is a permanent or write-once, read-many (WORM) medium.

4. magneto-optical media (WORM)

The present limitations in storage density, access time, and cost of the above four techniques have spurred an extensive search for alternative storage strategies. Alternative methods of storing WORM data on CD-type surfaces depend on phase-change systems (opaque to transparent, etc.) that can use inorganic substrates (e.g., Te) or organic substrates, or systems that depend on local melting and moving aside an organic film [e.g., phthalocyanines (90)]. Organic systems may show a cost advantage in optically addressable nonmagnetic WORM media.

Highly Conducting Langmuir–Blodgett Films. Barraud (Commissariat à l’Energie Atomique, Saclay) and Kawabata (National Chemical Laboratory for Industry, Tsukuba) have worked on many LB multilayer films that are highly anisotropic in their conductivity; they are insulators in the direction normal to the film plane, but conductors in the plane of the film, with anisotropies of the order of 10^{10} (91–93). This is caused by partial charge transfer in the film plane (e.g., between TCNQ⁰ and TCNQ⁻, or between TTF⁰ and TTF⁺, where TTF is tetrathiafulvalene) and by the formation of partially crystalline π -stacks in the plane of the film, very similar to those exhibited in anisotropic quasi-one-dimensional conducting crystals like TTF TCNQ. The only difference is the much higher anisotropy.

Spin Transitions in Langmuir–Blodgett Films. The groups of Barraud and Kahn (University of Paris) have demonstrated hysteretic bistability in an LB film of 200 monolayers of Fe(tris-alkylated-1,10-phenanthroline)₂(isothiocyanate)₂ (94).

Connections to a Unimolecular Electronic Device

Before we review the currently active proposals for truly unimolecular devices, we should discuss ideas for how to “talk” to such single molecules or clusters, that is, how to get signals to and from the macroscopic world of electronics ($>1 \mu\text{m}$) to the “nanoscopic” world of single molecules (perhaps through an intermediate “mesoscopic” world of sizes of the order of $1 \mu\text{m}$ – 100 nm).

To address a single molecule electrically, one needs a “molecular wire” (63) (e.g., a polyacetylene strand) or a “molecular antenna” (95) (e.g., the conjugated portion of β -carotene), neither of which can be easily connected to an external potential source, at present. Until the recent advent of the STM (46), one could not connect a single molecule

to an external circuit. Therefore, when the ORP was initiated, in about 1981, to realize the Aviram–Ratner rectifier, one had to content oneself with one-molecule-thick planar assemblies of molecules.

The three techniques that showed promise were as follows: (1) the LB technique (35–41), and the technique of covalently bonding molecules to electrode surfaces, either by (2) silanizing a hydroxyl-coated electrode and then attaching molecules covalently (96), or (3) by silanizing the molecule and attaching it directly by spin-coating by the oleophobic method (97) to a hydroxyl-coated electrode (98). As discussed previously, good monolayer coverage is claimed for methods 2 and 3 (98), but not for method 1 (96).

Macroscopic Connections: Langmuir–Blodgett and Langmuir–Schaefer Films. If one cannot address a single molecule, one can perhaps address a monolayer of identical molecules transferred to a suitable (metal) substrate by the LB (vertical transfer) or LS (horizontal transfer) methods. If the support is electrically conducting and a metal probe is gently lowered atop the LB monolayer or multilayer, then many identical molecules can be addressed electrically, provided that electrical short circuits through defects do not occur. However, LB monolayers are only weakly physisorbed to surfaces, and thus can reorder, recrystallize, or even desorb with time. This difficulty can be circumvented if a photopolymerizable [e.g., diacetylene (99)] group is included in the monolayer-forming molecule and if the molecular geometry is so engineered as to yield topotactic polymerization; this can result in a very robust, yet electroactive, polymer. In some cases, polymers at the air–water interface transfer well onto solid supports.

One should also remember the free-standing bilayer lipid membranes (BLM), pioneered by Mueller (100) and Montal (101). A very delicate and ephemeral BLM is formed when a thin hydrophobic support with a 1- to 10-mm hole is lowered into water and a monolayer is transferred to it on both sides of the support, and also across the hole. The BLM will have the hydrophobic parts of the two monolayers touching across the hole, so that an artificial bilayer membrane similar to that of cell walls is obtained, which is useful for electron-transport studies.

Macroscopic Connections: The Silyl Bridge. An alternate connection strategy, devised by Murray (96) to study the electrochemistry at the electrode surface more closely, consists of derivatizing an oxide-coated metal-electrode surface with trichlorosilyl groups and then reacting this surface with the desired molecule that has a terminal alcohol group; this, however, does not usually give full monolayer coverage on the metal. The reverse strategy, advanced by Sagiv (97), starts with the self-assembling “oleophobic” membranes of Zisman (98) and silanizes

the molecule and attaches it to an oxide and hydroxyl-group-covered metal surface, thereby achieving full monolayer coverage. An interesting variant of Sagiv's technique allows the sequential assembly of well-designed multilayers covalently attached to each other and to a hydroxyl-coated surface (102). Thiols and other S-containing compounds chemisorb well onto Au (103, 104).

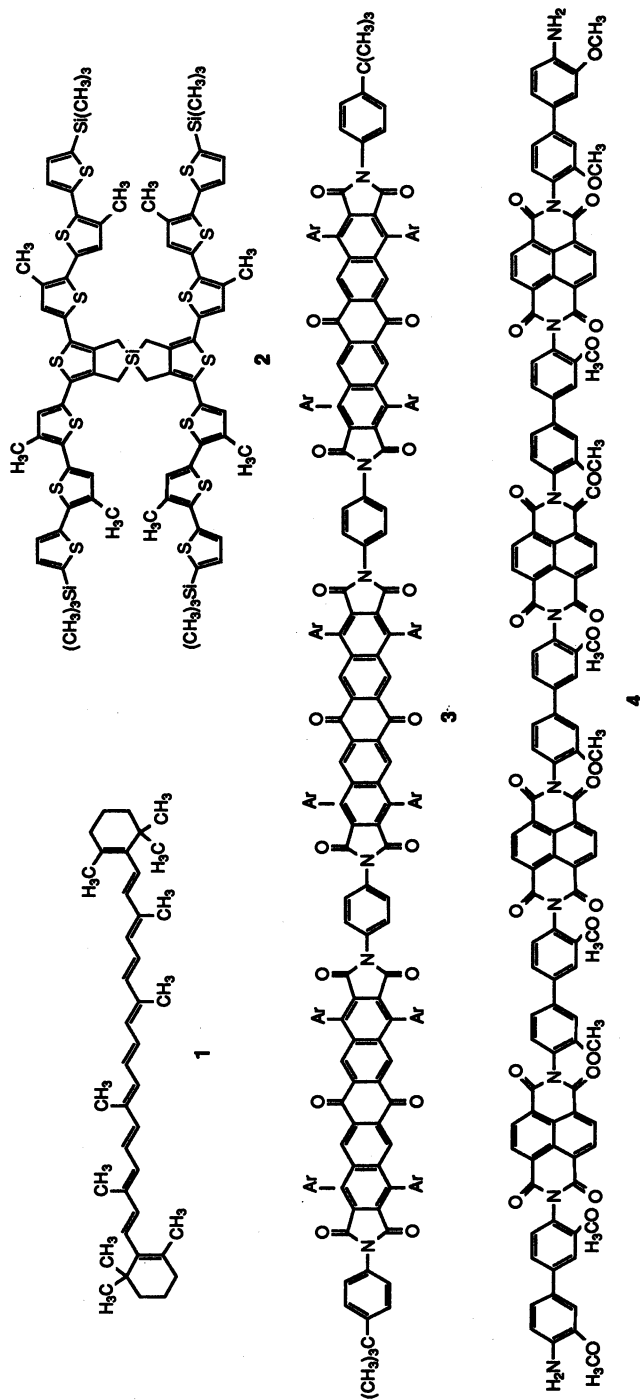
Macroscopic Connections: Cyclodextrins, Calixarenes, and Zeolites. The existence of cavities of precisely controlled size within cyclodextrins and calixarenes allows the inclusion of small electroactive molecules within these cavities and yet provides well-formed macroscopic crystals with the desired inclusions precisely oriented within them (67, 68). Similarly, the cavities inside zeolites have been exploited by Enzel and Bein (69) to produce strands of conducting polymers inside the channels of zeolites (however, the zeolite-conducting polymer adduct is overall insulating). The connections of such matrices to an external circuit have not been addressed so far.

Mesoscopic Connections: Anchoring onto Quantum Dots. By ion-beam lithography "quantum dots" have been produced on Si that are only 100 nm across (but there is hope to make them about 10 nm across) (105). Wrighton has proposed that adjacent quantum dots A and B, coated by different metals, for example, Au and Al, could be bridged by a designed molecular rectifier molecule $X-D-\sigma-A-Y$, where the X end will chemisorb on dot A but not on B, whereas the Y end will chemisorb on quantum dot B, but not on A. Then a potential across the quantum dots will enable directed currents through the molecule (Wrighton, M., private communication).

Proposed Nanoscopic Connection: Molecular Wires. The natural sacrificial antioxidant β -carotene (1) has been touted as a molecular wire (63) or as a molecular antenna (95) and certainly will provide fast electronic access to single molecules. Such polyenes are, unfortunately, very susceptible to air oxidation (as is doped polyacetylene, the simplest conducting polymer).

Nanoscope Connection: Spiro-Linked Thiophene Intercircuit Connections. Aviram proposed (64) a spiro-linked polythiophene system to interconnect two mutually perpendicular conducting molecular wires, both of which consist of *n*- or *p*-doped polythiophene. Such a molecule (2) has been synthesized (65).

Nanoscope Insulators: Molecular Lines. Several successive Diels–Alder condensation reactions can yield insulating, yet sturdy, LB film-forming oligomers of controlled length (3, 4) (66).



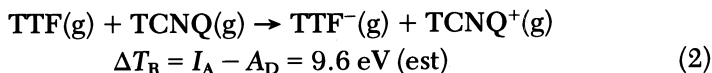
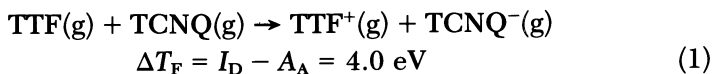
Nanosopic Connection: Scanning Tunneling Microscopy. The recent advent of STM (46) as an affordable research technique should allow the electronic addressing of a single molecule. If this becomes easily controllable and reproducible, then a real revolution in ME devices should be “just around the corner”. Indeed, an STM has been used to demonstrate tunnel diode behavior (106). However, as experience with STM accumulates, one must learn to beware of false images [“seeing what one wants to believe,” e.g., DNA on graphite (107, 108)], to account for reconstructions of the conducting surface by the tip (109), and to understand the force applied by the atomically sharp tip onto a weakly chemisorbed species like an LB or LS film; this force may burrow the tip rather deeply within the LB monolayer or may create artificial furrows within it (Hansma, P. K., private communication).

Truly Unimolecular Devices

We next consider ideas to achieve unimolecular or zero-dimensional electronic devices.

Proposed *D*- σ -*A* Rectifier. The Ansatz of Aviram and Ratner (2-4) starts from the discovery of highly conducting lower dimensional organic charge-transfer (CT) systems based on good one-electron donors (*D*) such as TTF (5) and good organic one-electron acceptors (*A*) such as TCNQ (6).

Good donor molecules (i.e., molecules with relatively low gas-phase first-ionization potentials I_D) are, at the same time, poor acceptors (they have low electron affinity A_D); good acceptors (i.e., molecules with a relatively high first-electron affinity A_A) are, at the same time, rather poor donors (have high I_A); thus the gas-phase energy ΔT_F required for charge transfer (both components at infinite separation) is about 4 eV (electronvolt) (eq 1), whereas the energy ΔT_R required for the reverse reaction would need over 9 eV (eq. 2):



Thus, the “Gedankenmolkül” *D*- σ -*A* (7), if assembled between two metal electrodes M_1 and M_2 , as in Figure 2b (discussed as $M_1 | \text{D}-\sigma-\text{A} | M_2$ in the section, “The Aviram-Ratner Organic Unimolecular Rectifier”), will exhibit easy electron transfer from M_1 to M_2 because the relatively accessible zwitterionic state $\text{D}^+-\sigma-\text{A}^-$ is used (while the electron flow from M_1 to M_2 would be inefficient, because the barrier to form the

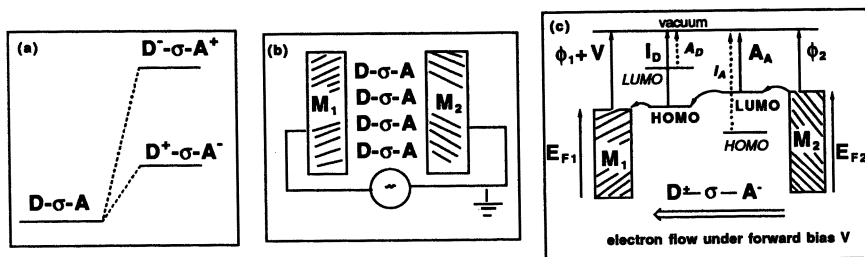
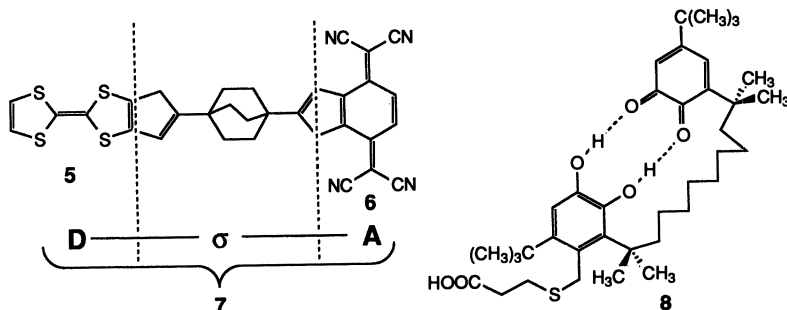
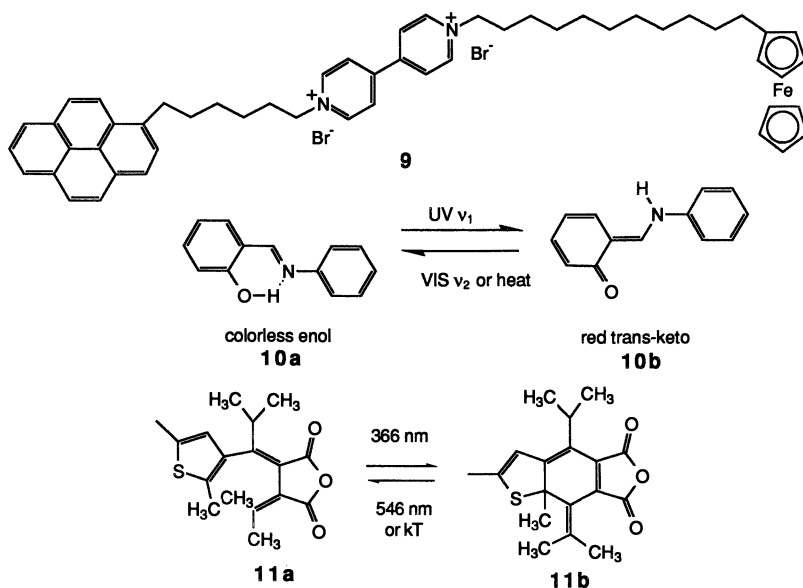


Figure 2. The Aviram-Ratner Ansatz. a, Reason for electronic asymmetry: The zwitterion $D^+ - \sigma - A^-$ is many electron volts lower in energy than the other zwitterion $D^- - \sigma - A^+$. b, Connection of an oriented monolayer between two macroscopic metal electrodes M_1 and M_2 ; this is the device $M_1 | D - \sigma - A | M_2$, grounded at M_2 . c, If, under moderate forward electrical bias applied to the device $M_1 | D - \sigma - A | M_2$, the work function ϕ_2 of the grounded macroscopic metal electrode M_2 matches in energy the electron affinity A_A of the lowest unoccupied molecular orbital (LUMO) of the A side of $D - \sigma - A$ (equal distance from the vacuum level to the LUMO of A), and if the work function ϕ_1 , plus the applied voltage V , of metal electrode M_1 matches the ionization potential I_D of the highest unoccupied molecular orbital (HOMO) of the D side of $D - \sigma - A$ (equal distance from the vacuum level to the HOMO of D), then, since I_D is typically larger than A_A , the tunneling through the barrier is assisted only in the direction shown, and rectification of electrical current is achieved. (In italics are shown the HOMO of the acceptor and the LUMO of the donor, and the energies I_A and A_D .)

zwitterion $D^- - \sigma - A^+$ would be several eV higher). The Aviram-Ratner device will work if the tunneling of electrons from A to D is assisted “through the bond system” (110) and will fail if the electron transfer between the metal electrodes M_1 and M_2 is predominantly by direct, unassisted, ordinary “through space” tunneling. Molecule 7 was never synthesized, and the idea languished until the ORP started in earnest, as is chronicled later in this chapter.





Proposed H Atom and Proton Transfer Switches. Aviram has also proposed an intramolecular hydrogen atom transfer switch, based on H bonding in ortho-quinone-catechol systems (3, 4); there is intramolecular H-atom transfer in such a system (8) (111, 112). Mitani is working toward a proton transfer switch (60).

Proposed Soliton Switch. The late Forrest L. Carter (61) proposed that soliton motion in polyacetylenes could be harnessed in various switches, gates, and logic circuits. However, apart from the difficulties of synthesizing or addressing such molecules, soliton switches are expected to be relatively slow devices.

Fujihira's Langmuir-Blodgett Photodiode. Fujihira and co-workers (62) have demonstrated that a single LB monolayer can function as a photodiode, probably the first truly unimolecular device. They synthesized a $D-\sigma_1-A-\sigma_2-S$ molecule (9), where D is electron donor, ferrocene; σ_1 is the $(CH_2)_{11}$ chain; A is the final electron acceptor, viologen; σ_2 is the $(CH_2)_6$ chain; S is sensitizer, pyrene. This molecule was transferred as an LB monolayer onto a semitransparent Au electrode (with the viologen or A part of molecule closest to Au). The electrode was the side of an electrochemical cell containing a 0.1-M KCl solution

and a Pt counter electrode. Under bias, an electron is transferred from solution to the ferrocene end of the LB film and then to the ground state of the pyrene molecule. Ultraviolet light at 330 nm excited the pyrene radical cation from the ground state to an excited state, from which the electron is transferred to the viologen, thus completing the circuit. A photocurrent of 2 nA at 0.0 V versus the standard calomel electrode (SCE) was observed only whenever the light was turned on (62).

Light-Induced Intramolecular Rearrangements. Sixl (113) suggested using the photochromism of *N*-salicylideneaniline (10), where the enol configuration can be converted to the *trans*-keto conformation by using light of frequency ν_1 , and converted back by either heat or by light of frequency ν_2 . Keto–enol tautomerism is accompanied by an intramolecular rotation. Another light-induced rearrangement in a fulgide (11) has been studied recently (114).

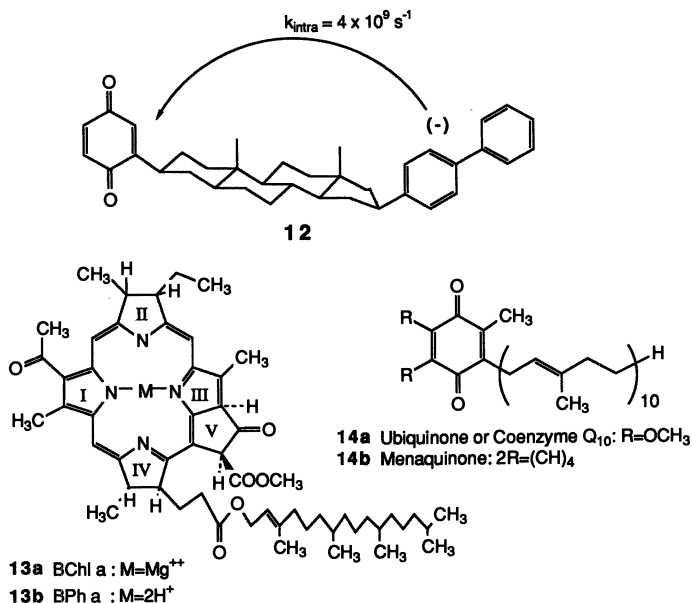
Conductivity Change in Langmuir–Blodgett Films Due to Light-Induced Conformational Change. The late Yasujiro Kawabata and co-workers (115) showed that a light-induced *cis*–*trans* conformational change in azobenzene affects the in-plane electrical conductivity of an LB film.

Potential Conformational Change Systems. The idea of using organic molecules that undergo conformational changes in optical storage devices is widespread. Birge (116) studied the primary step in the photocycle of bacteriorhodopsin (the light-harvesting protein of *Halo-bacterium halobium*), in which the bacteriorhodopsin containing all-*trans* retinal (bR568) can be converted (at 77 K), with two-photon illumination at 540 and 635 nm, into K610 or bathorhodopsin; at lower laser powers, the same two-photon illumination scheme can interrogate which molecules have converted to K610 and which remain in the bR568 state. The K610 state may consist of a *cis*–retinal segment. The harnessing of such *cis*–*trans* isomerizations (also involved in the physiology of the visual pigments) may yield interesting molecular devices.

At room temperature, holographic recording of images can be obtained by whole cell membranes (but not the isolated enzyme) deposited on a glass plate (Hampp, N., private communication).

Other D– σ –A and D– π –A Electron Transfer Molecules

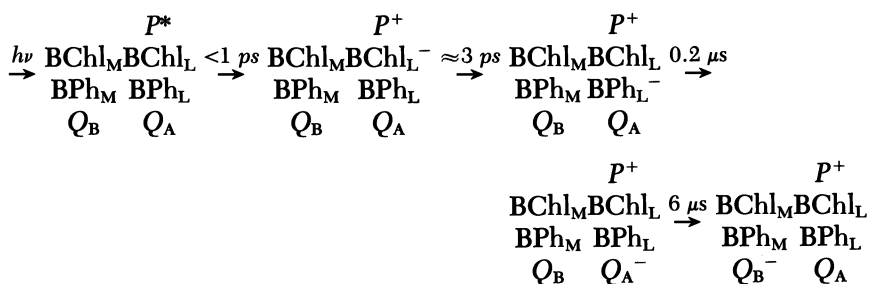
Before discussing the progress toward the Aviram–Ratner D– σ –A unimolecular rectifier, one should mention related molecules of the D– σ –A and D– π –A type, which have been synthesized for studies of intramolecular electron transfer, photosynthesis, organic conductivity, and for new nonlinear optical devices.



Understanding Intramolecular Electron Transfer. Taube pioneered (117) the understanding of intramolecular electron transfer in solution involving binuclear transition metal complexes, both *D*- σ -A and *D*- π -A. More recently, efforts have been made to control the electron transfer in solution between *D*- σ is Creutz-Taube ion [Ru(bpy)₃]²⁺ (bpy is 2,2'-bipyridine), and A is methylviologen (118). Miller, Closs, and co-workers (119, 121) showed that the intramolecular electron transfer rate through molecules *D*- σ -A such as 12, at first increases steadily with an increasing $I_D - A_A$ (where I_D is the ionization potential of the donor moiety D, A_A is the electron affinity of the acceptor moiety A). Then, if $I_D - A_A$ is increased further, the electron transfer rate decreases, because of an increase in the Franck-Condon reorganization (because the geometries of D⁺ and A⁻ are quite different from the geometry of D and A, respectively) (119-121) [Marcus "inverted region" (122)]. In the experiment, performed in a low-temperature glass, the electron "donor" is really the biphenyl radical anion (which initially captures an electron from a linear accelerator; thus biphenyl radical anion acts as the initial acceptor A'; the ultimate electron acceptor A is varied (A is benzoquinone in 12). Thus the system is really A'- σ -A, instead of *D*- σ -A, and the intramolecular electron transfer rates correlate with differences in the electron affinities of A' and A or of their

solution electrochemical reduction potentials. An obvious analogy remains between **12** and D- σ -A systems.

Structure of Bacterial Photosynthetic Reaction Center. A dramatic advance in understanding natural photosynthesis was the crystal structure determination of the photosynthetic reaction centers (RC) of *Rhodospseudomonas viridis* (RV) (123) and of *Rhodobacter sphaeroides* (RS) (124). This RC consists of six tetrapyrrole subunits: a dimeric "special pair" (*P*) of bacteriochlorophyll (BChl, **13a**) molecules, two "accessory" BChl's, two bacterio-pheophytins (BPh, **13b**), and a quinone acceptor *Q* (ubiquinone, **14a** for RV, menaquinone, **14b** for RS). A light photon $h\nu$ is absorbed by *P*, exciting it to *P**; then an electron is transferred by an irreversible CT process from *P* to *Q*_A within 200 ps and to *Q*_B after a further 6 μ s (125-130), as follows:



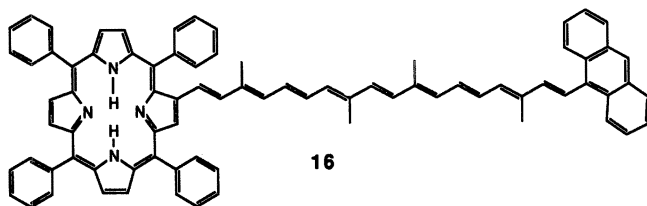
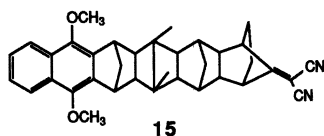
The natural photosynthetic system exhibits a crucial asymmetry: The forward CT converts the initial state D- σ -A into a long-lived charge-separated state D⁺- σ -A⁻ (i.e., in nature the back charge transfer (BCT) is much less likely or much slower); thus D⁺- σ -A⁻ persists long enough to enable oxidation and reduction chemistry at the physically well-separated D⁺ and A⁻ sites.

Progress toward a Biomimetic D- σ -A Photosynthetic Reaction Center. For an artificial D- σ -A photosynthetic system, the goal is to stabilize the charge-separated state, perhaps by adapting Mother Nature's trick of using several exoergic electron transfers to the ultimate quinone (BCT becomes statistically unlikely because of the number of "uphill" steps involved). Many model D- σ -A systems have been prepared and studied; a partial list of active research groups and their interesting molecules would include the groups of Bolton (University of Western Ontario) (131), Dervan and Hopfield (California Institute of Technology) (132), Mataga (Osaka University) (133, 134), Mauzerall (Rockefeller University) (135, 136), Staab (Max-Planck-Institute for Medical Research, Heidelberg) (137), Verhoeven (University of Amsterdam) and Paddon-Row (University of Sydney) (15) (138, 139), Effenberger and Wolf (University of Stuttgart) (16) (140), Gust and Moore

(Arizona State University) (17) (141, 142), and Wasielewski (Argonne National Laboratory) (18) (95). For 17 the charge-separated final state ($\pi-D^+-\sigma-D'-\sigma-A-\sigma-A'^-$) has the impressively long lifetime of 55 μ s (142).

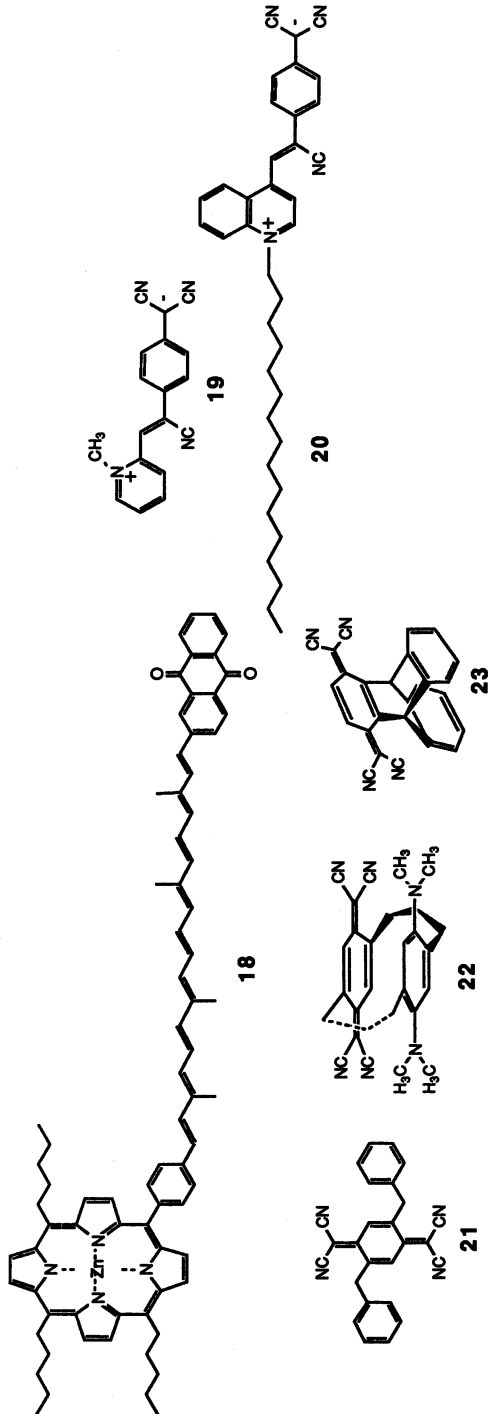
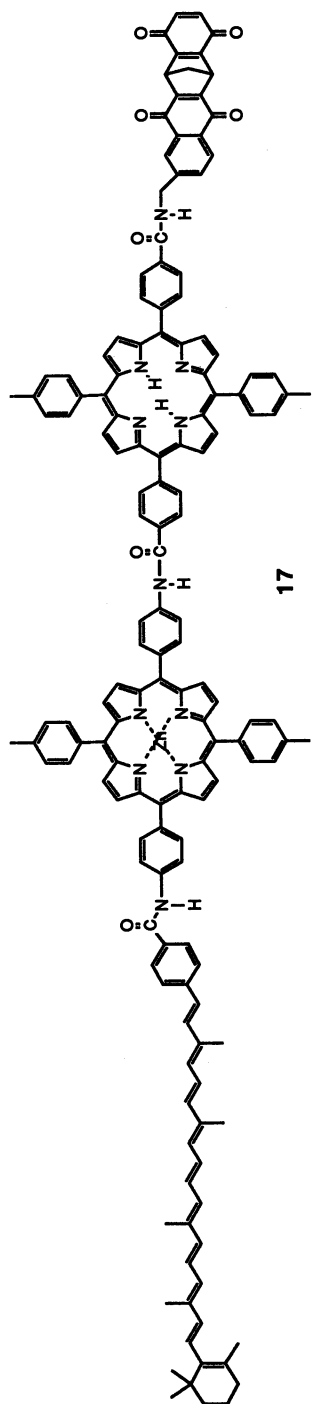
Nonlinear Optical $D-\sigma-A$ and $D-\pi-A$ Molecules. $D-\sigma-A$ and $D-\pi-A$ molecules can also exhibit large second-order nonlinear optical coefficients [β (molecular) or $\chi^{(2)}$ (bulk)]; which become large when the electron-donating group D and the accepting group A are separated by a large distance, because this increases the molecular dipole in both ground and excited states (143). The potential application is for frequency doubling (second-harmonic generation). Powerful and inexpensive primary lasers are not available in the visible and ultraviolet regions of the spectrum, and the output of IR lasers is usually frequency-doubled with expensive inorganic nonlinear optical crystals such as lithium niobate and potassium dihydrogen phosphate (143). An interesting set of zwitterionic molecules, were derived from P3CNQ (19) (144, 145), for example, $C_{16}H_{33}-Q3CNQ$ (20), which has a very high calculated β (146, 147).

Unusual $D-\sigma-A-\sigma-D$ and $D=\sigma=A$ Molecules. Becker et al. (148) (University of the Negev, Beersheba) prepared 21, ($D-\sigma-A-\sigma-D$) where A, which is TCNQ, is linked to two benzyl groups ($D-\sigma$ are weak donors), whereas the group of Staab (149) attempted to make a TTF-TCNQ plane ($D=\sigma=A$) as a potential new organic conductor, but achieved the synthesis of 22 instead. In studies of Mulliken intramolecular CT, Murata's group (150) (Osaka University) synthesized 23 and several methoxy derivatives thereof.



The Aviram-Ratner Organic Unimolecular Rectifier

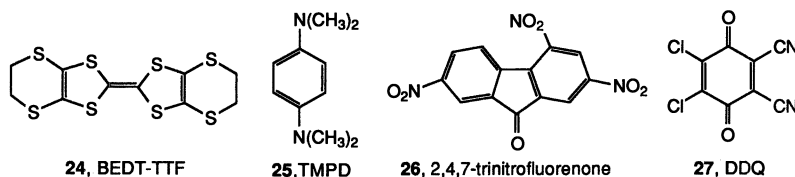
We can now review the progress made toward the synthesis and characterization of the Aviram-Ratner rectifier $M_1|D-\sigma-A|M_2$ (Figure 2b).



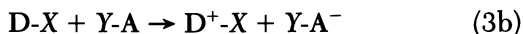
Given that STM was not available when the project started, an initial commitment was made to the LB technique.

Electronic and Synthetic Criteria. Several interlocking criteria must be satisfied for the rational synthesis of suitable *D*- σ -*A* systems:

1. I_D for the donor end *D* must be as small and as close as possible to the work function ϕ of the metal layer M_1 . Typical values are given in Table I and Figure 3. BEDT-TTF, **24**, is the strong donor bis-ethylenedithiolene-tetrathiafulvalene, while TMPD, **25**, is the strong donor *N,N,N',N'*-tetramethyl-*para*-phenylenediamine.



2. A_A for the acceptor end *A* must be as small and as close as possible to the work function ϕ of the metal layer M_2 . Table I and Figure 3 show that requirements 1 and 2 can be met only approximately. DDQ, **27**, is the very strong acceptor 2,3-dichloro-5,6-dicyano-1,4-benzoquinone.
3. In a molecule in which the “sigma” bridge σ has already been built, it is extremely difficult to chemically convert a weak donor into a strong donor or to convert a weak acceptor into a strong acceptor. Therefore, one must first synthesize a monosubstituted strong donor (call it *D*-*X*) and a monosubstituted strong acceptor (call it *Y*-*A*) and then join them by a coupling reaction (eq 3a) that, somehow, avoids the undesirable but likely formation of ionic CT complexes (eq 3b):



4. The molecules must pack efficiently into self-assembling monolayers or bind covalently to a substrate. If the designed *D*- σ -*A* molecule does not form PL (**17**, **26**) self-assembling monolayers at the air-water interface, then either long aliphatic “greasy tails” must be added to form a hydrophobic tail or an ionic, hydrophilic “head” should be added to either the *D* end or the *A* end. The molecules

Table I. Experimental Ionization Potentials and Electron Affinities for Selected Donors Acceptors, and Work Functions for Selected Metals

<i>Donor</i>	I^a	<i>Ref.</i>	<i>Acceptor</i>	A^a	<i>Ref.</i>	<i>Metal</i>	ϕ (eV)	<i>Ref.</i>
Benzene (W)	9.38	151	<i>p</i> -benzoquinone (W)	1.9	155	Mg	3.66	158
BEDT-TFF (24, M)	7.6	152	2,4,7-trinitrofluorenone (26, M)	2.2	156	Al(111)	4.24	159
TTF (5, S)	6.83	153	TCNQ (6, S)	2.8	157	Au(111)	5.31	162
TMPD (25, S)	6.25	154	DDQ (27, S)	3.13	156	Pt(111)	5.7	161

^a Values are expressed in electron volts; reference numbers in parentheses.

NOTE. I , ionization potentials; A , electron affinities; ϕ , work functions; W, weak; M, medium; S, strong. For other abbreviations, see text.

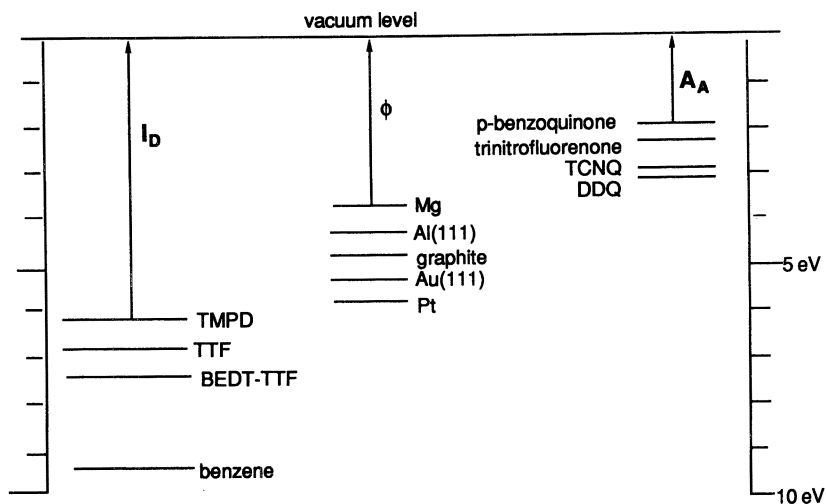


Figure 3. Energy level diagram for donors (I_D), metals (ϕ), and acceptors (A_A).

should be fairly flat, so as to form compact PL films, yet flexible enough, so as to transfer well as LB films (by the vertical or LB dipping method, or by the horizontal or LS method).

5. The electron transfer through the *D*- σ -*A* molecule and through its hydrophobic or hydrophilic tails must be fast: A molecular device that is small but slow is predicted to be useless. That electron transfer is fast through properly designed molecules (e.g., the photosynthetic reaction center) is well known. The work of Miller, Closs, and co-workers (119–121), reviewed previously, shows that $I_D - A_A$ values must not be too large, to avoid the reduction in electron transfer rates caused by a large Franck–Condon reorganization.
6. The device will have a limited tolerance for high voltages or for heating. A monolayer 2–3-nm thick probably tolerates no more than 1-V external bias across it before dielectric breakdown should occur (2–4, 7)

Practical Criteria for Good Donors and Acceptors. In practice, ionization potentials for all-organic donors range from 6.25 eV for a “strong” donor like TMPD (25) to 9.38 eV for a “weak” donor such as benzene; electron affinities have a much more limited range, from

1.9 eV for a relatively weak acceptor (*p*-benzoquinone) to 3.2 eV for the strongest acceptor (DDQ, 27). The match with metal work functions is not optimal. A long time ago, Matsen (162) and Hush and Pople (163) noted that the ionization potentials (electron affinities) of condensed aromatic hydrocarbons decrease (increase) with increasing molar mass, to meet “at infinity” the work function of graphite, which can be considered as an “infinite” hermaphroditic two-dimensional ideal donor and acceptor: $I_D = A_A = \phi = 4.40$ (164), 4.45 (165), or 4.62 eV (166).

For the Aviram–Ratner unimolecular rectifier, one needs $\Delta T_F = I_D - A_A > 0$ to ensure that “down-hill” through-bond assisted inelastic electron tunneling from A^- to D^+ ; this condition is trivially realized. From Table I, one sees $\Delta T_F = 3.1$ eV (for TMPD and DDQ), 4.0 eV (for TTF, 5 and TCNQ, 6), 5.2 eV (for pyrene and 2,4,7-trinitrofluorenone, 26), 7.6 eV (for the “weak” electron donors and acceptors benzene and *p*-benzoquinone). However, if ΔT_F is too large, then the Franck–Condon factor becomes too small (or the molecular reorganization energy becomes too large), and through-bond electron transfer rates will become too slow. In fact, the work of Miller, Closs, and co-workers (119–121) suggests that maximum electron transfer rates (faster than $10^9/s$) through androstane σ -skeletons are obtained when $\Delta T_F \approx 1.25$ eV (estimated from solution half-wave reduction potentials) and will become slow if ΔT_F approaches either 0 or 2.5 eV. Confronted by the large size of ΔT_F Aviram and Ratner argued that, by formation of mixed-valent stacks of TTF donors and TCNQ acceptors in the LB film, the energy barriers to ionization and electron capture would be reduced in the film state.

The energy levels shown in Figure 3 suggest that a good combination for the device $M_1 | D-\sigma-A | M_2$ is $M_1 = Pt$, $D = TMPD$, $A = DDQ$, $M_2 =$ (either Mg or Al): Mg should allow the zwitterion $D^+ - \sigma - A^-$ to form at about 0.5-V bias and Al at 1-V bias. As a rough guide for the synthetic chemist, one would prefer $I_D < 7$ eV and $A_A > 2.5$ eV. Because gas-phase ionization potentials, and particularly gas-phase electron affinities are not easily accessible to the organic chemist, a convenient, if more approximate, measure of electronic activity may be the voltammetric half-wave oxidation or reduction potential $E_{1/2}$. Suitable target values are discussed in the section “Cyclic Voltammetry”.

One may also define an asymmetry parameter ΔE :

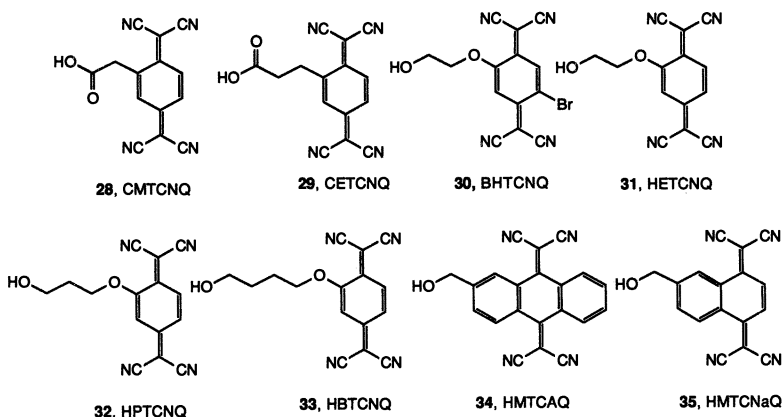
$$\Delta E = \Delta T_F - \Delta T_R = (I_D - A_A) - (I_A - A_D) = (I_D + A_D) - (I_A + A_A) \quad (4)$$

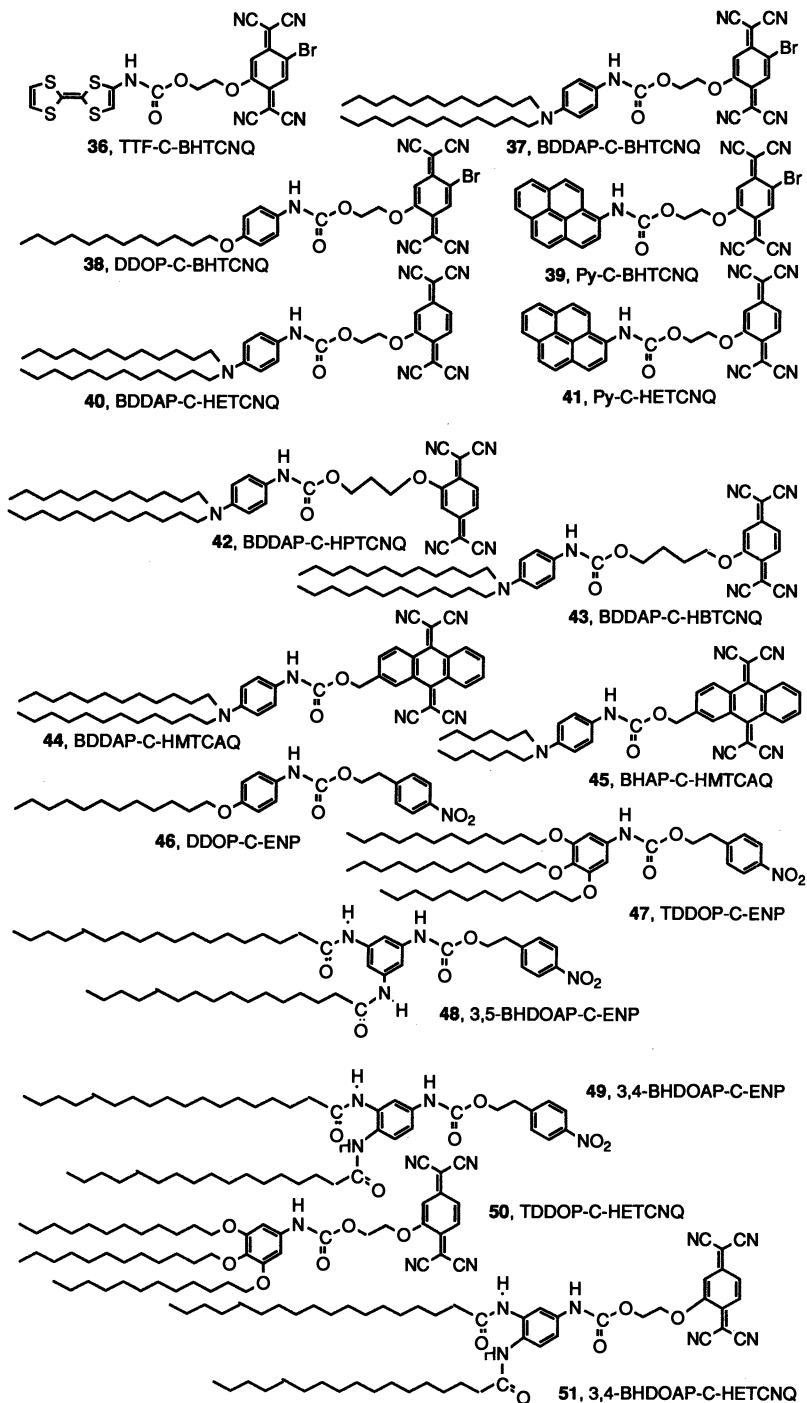
which should help to quantify the electronic asymmetry required in a $D-\sigma-A$ molecule.

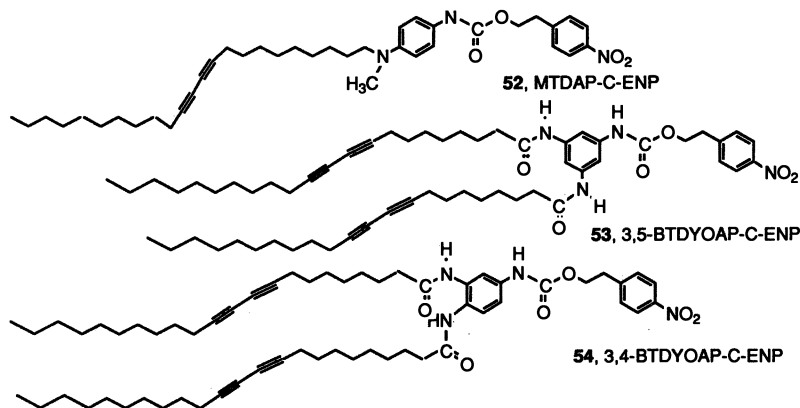
Synthesis. Monofunctionalized TTF compounds, such as TTF-Li, TTFCH₂OH, and TTF-COOH, were pioneered by Green (167). Hertler (168) had coupled a bifunctional TTF to a bifunctional TCNQ alcohol

via the urethane, or carbamate coupling reaction, yielding a semiconducting copolymer $(-\sigma\text{-TTF}-\sigma\text{-TCNQ-})_x$ and had also prepared a monofunctional alcohol (168).

The monofunctional TCNQ compounds carboxymethylene TCNQ (CMTCNQ, 28) and carboxyethylene TCNQ (CETCNQ, 29) were prepared, but would not couple with TTF-CH₂OH (5). The monofunctional TCNQ alcohol 2-bromo-5-hydroxyethoxy TCNQ (BHTCNQ, 30) (168) was found to couple to TTF isocyanate (TTF-NCO, generated from TTF-Li), to yield a TTF-carbamate-BHTCNQ (TTF-C-BHTCNQ) (6–8), and to carboxy TTF (TTF-COOH), to yield a TTF-ester-BHTCNQ (TTF-E-BHTCNQ) (8). Both of these products were obtained in low yield, and in two phases, one of which was ionic, the other neutral. Then the attention was turned to carbamates obtained by coupling BHTCNQ to phenyl, 1-pyrenyl, and *N,N*-dialkyl-aminophenyl isocyanates (9–33) (the latter can be thought of as modifications of TMPD). The synthesis of BHTCNQ (168, 169) contained a very inefficient, low-yield step; a new, monofunctionalized acceptor, prepared in higher yield, was hydroxyethoxyTCNQ (HETCNQ, 31) (19). Two other acceptors, hydroxypropoxy TCNQ (HPTCNQ, 32) and hydroxybutoxyTCNQ (HBTCNQ, 33) were also prepared by similar routes (170). An easily synthesized acceptor was 2-hydroxymethyl-11,11,12,12-tetracyano-9,10-anthraquinodimethane (HMTCAQ, 34), but both HMTCAQ and its underivatized parent molecule (171) are both weak two-electron acceptors: The *peri* hydrogens force them into a butterfly-shaped configuration. A final acceptor was 2-hydroxymethyl-9,10-tetracyano-5,8-naphthoquinodimethane (HMTcNaQ, 35), whose crystal structure has been determined (34); however, it decomposed instead of coupling with phenyl, 4-(dimethylamino)phenyl or 1-pyrenyl isocyanates (34).







Carbamates and esters were thus obtained with BHTCNQ, HETCNQ, HPTCNQ, HBTCNQ, and HMTCAQ as acceptors. The various *D*- σ -A molecules that form LB films were the carbamates 36–54. Of these, 46–54 were prepared to incorporate *D*- σ -A molecules into polymerizable diacetylenes, which may yield promising nonlinear optical materials, primarily for frequency doubling: 46–51 were “trial molecules” without diacetylenes, mostly with the weak ethoxynitrophenyl (ENP) acceptor group. To explain the acronyms used for structures 42–54, BDDAP-C-BHTCNQ is the *N,N*-bis-dodecyl-*p*-aminophenyl carbamate of 2-bromo-5-hydroxyethoxyTCNQ, whereas MTDAP-C-ENP is the *N*-methyl-*N*-triseikosi-10,12-diyl-*p*-aminophenyl carbamate of ethoxy-*p*-nitrobenzene (not the world’s most systematic name!).

One can speculate why carbamate coupling reactions failed with CMTCNQ, CETCNQ, and HMTCAQ, but succeeded (eq 3a) with BHTCNQ, HETCNQ, HPTCNQ, HBTCNQ, and HMTCAQ. The planned σ bridge length is the number of C, O, or N atoms between *D* and *A* ends: 4, CMTCNQ and HMTCAQ; 5, CETCNQ; 6, BHTCNQ and HETCNQ; 7, HPTCNQ; and 8, HBTCNQ. Because the carbonyl group provides partial conjugation within the bridge, up to two atoms from the donor, one can surmise that, at least for the strong acceptor TCNQ, a four to five atom bridge length is too short for a coupling reaction to occur. Naturally, if the bridge is too long (say, >8 atoms) and flexible, then conformational freedom may allow the *D* and *A* ends to move to within intramolecular overlap, thereby creating a horseshoe-shaped molecule with internal CT, which may not function as a rectifier.

Cyclic Voltammetry. Donors, acceptors, and several *D*- σ -A molecules were characterized by cyclic voltammetry (CV). Table II summarizes the results and also contains literature data about related donors and acceptors 55–70, which should be useful for future *D*- σ -A syntheses. Figure 4 shows the CV for BDDAP-C-HETCNQ, 40.

Table II. Solution Cyclic Voltammetric Half-Wave Potentials, (V vs. SCE), Gas-Phase Vertical Ionization Potentials, and Electron Affinities for Donors, Acceptors, and D-σ-A Molecules

Molecule	Note	Oxid. (1)		Oxid. (2)		Red. (1)		Red. (2)		Ref.	I (eV)	Oxid. D → D ⁺	Red. A → A ⁻	Ref.
		E _{1/2} (V)	D → D ⁺	E _{1/2} (V)	D ⁺ → D ²⁺	E _{1/2} (V)	A → A ⁻	E _{1/2} (V)	A ⁻ → A ²⁻					
Donors														
TMPD (25)	a	0.10	—	0.66	—	—	—	—	—	14	6.25	—	—	154
	a	0.01	—	—	—	—	—	—	—	153	—	—	—	173
TTF (5)	a	0.35	—	0.75	—	—	—	—	—	172	6.83	—	—	152
	a	0.37	—	0.75	—	—	—	—	—	152	6.70	—	—	174
BEDT-TTF (24)	a	0.54	—	0.96	—	—	—	—	—	172	≈6.7	—	—	152
	a	0.54	—	0.85	—	—	—	—	—	152	—	—	—	176
Pyrene (55)	a	1.16	—	—	—	—	—	—	—	175	7.41	0.58	—	127
Anthracene (56)	a	1.09	—	—	—	—	—	—	—	175	7.55	0.60	—	151
Benzene	a	2.30	—	—	—	—	—	—	—	175	9.38	-1.0	—	178
TTFCOCl (57)	a	0.602	—	0.936	—	—	—	—	—	179	—	—	—	—
DMAP-C-Me (58)	a	0.55	—	—	—	—	—	—	—	14	—	—	—	—
BDDABA (62)	b	1.09i	—	—	—	—	—	—	—	180	—	—	—	—
Acceptors														
TCNQ (6)	a	—	0.127	—	—	—	—	-0.291	—	181	—	2.8	—	157
	a	—	0.17	—	—	—	—	-0.37	—	182	—	—	—	—
	a	—	0.19	—	—	—	—	-0.35	—	183	—	—	—	—
	a	—	0.151	—	—	—	—	-0.403	—	32	—	—	—	—
	c	—	0.54	—	—	—	—	-0.13	—	186	—	—	—	—
	d	—	0.53	—	—	—	—	0.02	—	182	—	—	—	—
TCNQF ₄ (63)	e	—	0.51	—	—	—	—	-0.30	—	185	—	—	3.22	184
DDQ (27)	a	—	0.54	—	—	—	—	-0.13	—	186	—	—	3.13	156
DCNQI (64)	d	—	—	—	—	—	—	-1.030	—	185	—	—	≈2.87	190
p-Benzoquinone (65a)	a	—	-0.481	—	—	—	—	—	—	185	—	—	1.91	155
	a	1.21	-0.98	—	—	—	—	-1.50	—	187	—	—	1.98	177
9,10-Anthraquinone (66)	a	—	-0.98	—	—	—	—	-1.50	—	188	—	—	1.59	155
Chloranil (65b)	a	—	+0.01	—	—	—	—	-0.71	—	189	—	—	2.76	177
Bromanil (65c)	a	—	0.00	—	—	—	—	-0.72	—	189	—	—	—	—
Fluoranil (65d)	a	—	-0.04	—	—	—	—	-0.82	—	189	—	—	2.92	177
2,4,7-Trinitrofluorenone (26)	a	—	-0.42	—	—	—	—	-0.67	—	190	—	—	2.2	156
C ₆₀	d	—	-0.18	—	—	—	—	-0.58, -1.07	—	191	—	—	2.6	192
													2.8	193

TCNE (67)	<i>a</i>	—	0.152	-0.568	181	2.3
CMTCNQ (28)	<i>a</i>	—	0.236	-0.267	32	194
CEHCNQ (29)	<i>a</i>	—	0.222	-0.275	32	195
BHTCNQ (30)	<i>a</i>	—	0.305	-0.170	9	196
HETCNQ (31)	<i>a</i>	—	0.107	-0.398	19	
	<i>c</i>	—	0.101	-0.400	32	
HMTCAQ (34)	<i>a</i>	—	—	-0.333	11	
	<i>c</i>	—	—	-0.334	32	
TCAQ (68)	<i>g</i>	—	—	-0.390	171	
HMTCN ₂ Q (35)	<i>c</i>	—	-0.025	-0.491	34	
TCNaQ (69)	<i>g</i>	—	0.060	-0.425	171	
<i>D-σ-A</i> molecules						
TTF-C-BHTCNQ (36)	<i>a</i>	0.75i	0.298	—	179	
DDOP-C-BHTCNQ (38)	<i>h</i>	1.21	0.25	-0.07	9	
BDDAP-C-HETCNQ (40)	<i>b</i>	0.97i	-0.08	-0.20i	30	
Py-C-HETCNQ (41)	<i>b</i>	1.01	0.08	-0.35	30	
BHAP-C-HMTCAQ (45)	<i>b</i>	0.60	—	-0.36	30	
DDOP-C-HETCNQ (50)	<i>b</i>	0.99i	0.07	-0.47	26	
DDOP-C-ENP (46)	<i>b</i>	1.39	-1.13	—	26	
BDDOP-C-ENP (61)	<i>b</i>	1.66i	-1.09	—	26	
TTDOP-C-ENP (47)	<i>b</i>	1.14i	-1.15	—	26	
MTDAP-C-ENP (52)	<i>b</i>	0.54	-1.06	—	30	

^a Solvent: CH₃CN. Reference electrode: SCE.

^b Solvent: CH₂ClCH₂Cl. Reference electrode: Ag/AgCl. An offset correction of 0.15 V (26) has been added to the measured values to convert them to V vs. SCE.

^c Solvent: CH₃CN. Reference electrode: Ag/AgNO₃. An offset correction of 0.291 V [see HETCNQ (32)] has been added to the measured values to convert them to V vs. SCE.

^d Solvent: CH₂Cl₂. Reference electrode: Ag/AgCl. An offset correction of 0.15 V (26) has been added to convert them to V vs. SCE.

^e Solvent: BuCN. Reference electrode: SCE.

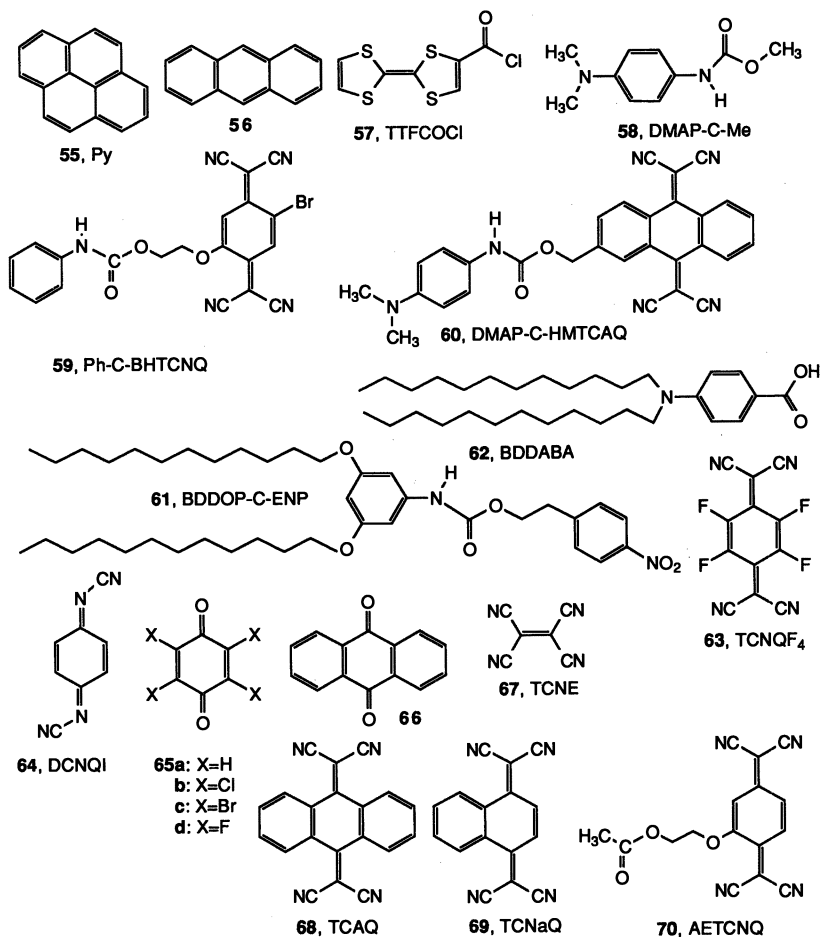
^f Similar to A₁ (TCNQ (160)), because $E_{1/2}$ (DCNQI) $\approx E_{1/2}$ (TCNQ) (189).

^g Solvent: CH₂ClCH₂Cl. Reference electrode: Ag/AgNO₃. An offset correction of 0.320 V (9) has been added to the measured values to convert them to V vs. SCE.

^h Solvent: BuCN. Reference electrode: Ag|0.01 M AgNO₃. An offset correction of 0.320 V (9) has been added to the measured values to convert them to V vs. SCE.

ⁱ Solvent: CH₃CN. Reference electrode: Ag/AgNO₃. An offset correction of 0.320 V (9) has been added to the measured values to convert them to V vs. SCE.

NOTE: $E_{1/2}$, half-wave potentials; V, volts; SCE, standard calomel electrode; I, ionization potentials; A, electron affinities; D, donor; A, acceptor; Oxid., oxidation; Red., reduction; i, irreversible;



It is quite clear from Table II that the solution half-wave potentials ($E_{1/2}$) of the D- σ -A molecules reflect well the reducing and oxidizing properties of the D and A ends, respectively; that is, the carbamate linkages are, in fact, reasonable σ -bridges, and the donor and acceptor functions have been preserved, as planned.

For future work, it may be useful to rephrase the requirements for donors and acceptors in D- σ -A rectifier molecules in terms of approximate limits on solution $E_{1/2}$ potentials, because most organic chemists are unfamiliar with work functions, gas-phase ionization potentials, and gas-phase electron affinities. Several correlations between gas-phase I_D and solution $E_{1/2}$ exist (197–200), and one between A_A and $E_{1/2}$ (156). Naturally, these are only approximate correlations; they do not include the dependence of $E_{1/2}$ on solvent or on the varying size of the solvent cage around molecules of different shapes (152, 201).

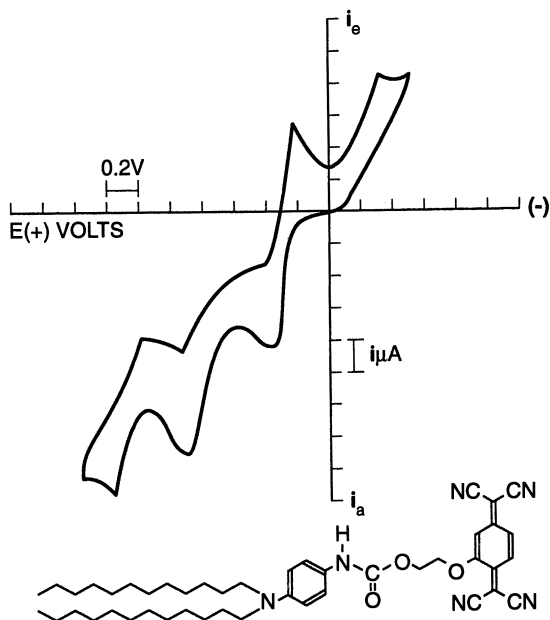


Figure 4. Cyclic voltammogram of BDDAP-C-HETCNQ, 40. (After reference 30).

Using the $E_{1/2}$ values in CH_3CN solution, relative to the standard calomel electrode (SCE), for the donors in Table II a satisfactory approximate correlation (to within ± 0.2 V) is (197) as follows:

$$E_{1/2} = 0.89I_D - 5.70$$

whereas for the strong acceptors DDQ, TCNQ, chloranil, *p*-benzoquinone, and 9,10-anthraquinone an acceptable correlation (to within ± 0.2 V) is

$$E_{1/2} = A_A - 2.62$$

Finally, the criteria for a “good” donor ($I_D < 7$ eV: TMPD, TTF, BEDT-TTF) and a “good” acceptor, ($A_A > 2.5$ eV: TCNQ, TCNQF_4 , DCNQI, chloranil, bromanil, fluoranil, and maybe TCNE or C_{60}), proposed in the section, “Practical Criteria for Good Donors and Acceptors,” become $E_{1/2} < 0.50$ V versus SCE for the donor D and $E_{1/2} > -0.12$ V versus SCE for the acceptor A.

Pockels–Langmuir and Langmuir–Blodgett Films. Table III displays an updated catalog of molecules (13–22) prepared by the ORP, which form PL monolayers at the air–water interface and which transfer

Table III. Pressure-Area Isotherm Data for Pockels–Langmuir Films

Molecule	No.	Type	T/K	Π_c (mN/m)	A_c (\AA^2)	Ref.
TTF-C-BHTCNQ	36	Strong D Strong A	292	12.7	134 ± 50	7
DDOP-C-BHTCNQ	38	Weak D Strong A	292	20.2	50 ± 1	9
BDDAP-C-BHTCNQ	37	Medium D Strong A	293	47.3	57 ± 1	17
Py-C-BHTCNQ	39	Medium D Strong A	283	28.2	53 ± 1	9
BDDAP-C-HETCNQ	40	Medium D Strong A	293	40.0	44 ± 1	30
Py-C HETCNQ	41	Medium D Strong A	293	46	—	30
BDDAP-C-HMTCAQ	44	Medium D Weak A	293	22.3	58 ± 1	17
BHAP-C-HMTCAQ	45	Medium D Weak A	293	35.8	42 ± 1	18
DDOP-C-ENP ^a	46	Weak D Weak A	278	23.7	38 ± 1	26
TDDOP-C-ENP ^a	47	Weak D Weak A	278	34.0	76 ± 1	26
TDDOP-C-HETCNQ ^a	50	Weak D Strong A	283	47.5	54 ± 1	26
3,5-BHDOAP-C-ENP	48	Weak D Weak A	299	49.6	39 ± 2	204
3,4-BHDOAP-C-ENP	49	Weak D Weak A	300	54.5	35.8 ± 0.5	31
3,4-BHDOAP-C-HETCNQ	51	Weak D Strong A	300	55.2	51 ± 2	31
MTDAP-C-ENP ^a	52	Weak D Weak A	278	16.5	63 ± 1	25
3,5-BTDYOAP-C-ENP	53	Weak D Weak A	298	18.7	58 ± 2	31
3,4-BTDYOAP-C-ENP	54	Weak D Weak A	300	49.4	50 ± 1	31

NOTE Π_c and A_c , the pressure and molecular area, respectively, at the collapse point.

^a The film makes Z-type Langmuir–Blodgett multilayers (substrate at 22 °C, film at 5 °C).

well onto Al or glass or other slides as LB monolayers. TTF-C-BHTCNQ, 36, was difficult to purify; the “neutral” form seemed to deposit “pancake-style” onto the water, and synthetic difficulties forced its abandonment. The strongest films (highest collapse pressure and most vertical pressure-area isotherm) were obtained with BDDAP-C-BHTCNQ, 37 (Figure 5).

The acceptor HMTCAQ used in 44 and 45 was easy to prepare (11), but is well-known to be a weak two-electron acceptor, with a highly nonplanar geometry (24). For D- σ -A systems where A is HMTCAQ, PL films were obtained when the alkyl substituent was bis-hexyl (44) or

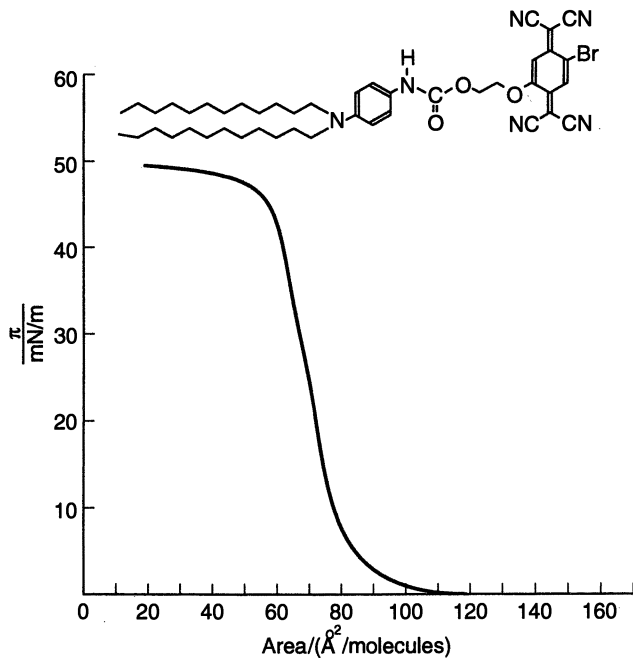


Figure 5. Pressure-area isotherm of BDDAP-C-BHTCNQ, 37, at 293 K. (Reproduced with permission from reference 16. Copyright 1988.)

bis-dodecyl (45), but not bis-methyl (60): For 60 crystals were obtained instead, whose structure is discussed below.

Molecules 46–51 are model systems for a related project that aims to incorporate *D*- σ -A systems into LB-film-forming diacetylenes, which may be polymerized in situ on the film balance, for the purpose of preparing new systems with promise as nonlinear optical devices. Interestingly, 46, 47, 50, and 52 form *Z*-type multilayers on a glass substrate (the film subphase is held at 5 °C, but the slide is at room temperature).

Crystal Structures of Model Donor, Acceptor, and *D*- σ -A Molecules. A few crystal structures have been solved: for the donor DMAP-C-Me, 58 (13) (Figure 6), for the acceptor BHTCNQ, 30 (15) (Figure 7), and for the methyl ester (AETCNQ, 70) of the acceptor HETCNQ, 31 (16) (Figure 8), and for HMTCNQ, 35 (34). Here ACETCNQ is the acronym for acetyloxy TCNQ. The small difference in conformation between AETCNQ and BHTCNQ can be attributed to crystal packing forces, rather than to intramolecular effects. Amphiphilic molecules that form LB films will not usually crystallize, because of the usual aliphatic “tails” added to them. The structures of two *D*- σ -A molecules, which do not form PL or LB films, were solved: Ph-C-

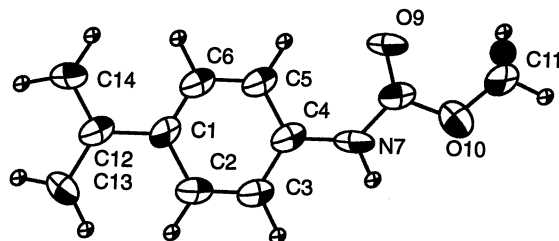


Figure 6. ORTEP-II plot of the crystalline structure of DMAP-C-Me, **58**. Space group *Pbca* (#61), $a = 13.926$, $b = 9.999$, $c = 14.854$ Å, $Z = 8$, $R = 5.9\%$ for 786 reflections. (Reproduced with permission from reference 13. Copyright 1988.)

BHTCNQ, **59** (8) (Figure 9) and DMAP-C-HMTCAQ, **60** (24) (Figure 10). Both structures show an extended carbamate linkage; in Ph-C-BHTCNQ, the dihedral angle between the phenyl ring and the six-membered central ring of BHTCNQ is only 8° (8). This gives hope that in LB films of related D- σ -A molecules the carbamate linkage will also be extended.

Molecular Orbital Calculations. As reported previously (22) semiempirical molecular orbital (MO) calculations, using the MNDO

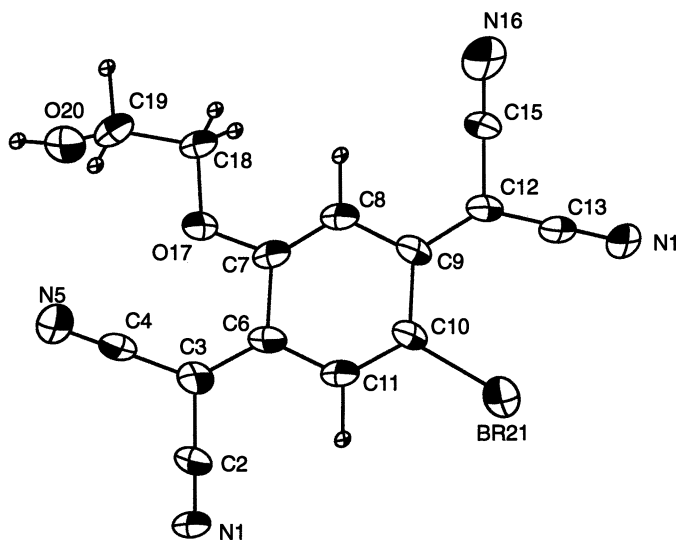


Figure 7. ORTEP-II plot of BHTCNQ, **30**. Space group *P2₁/n* (#14), $a = 9.258$, Å, $b = 13.618$ Å, $c = 10.947$ Å, $\beta = 92.14^\circ$, $Z = 4$, $R = 3.9\%$ for 1395 reflections. (Reproduced with permission from reference 15. Copyright 1988.)

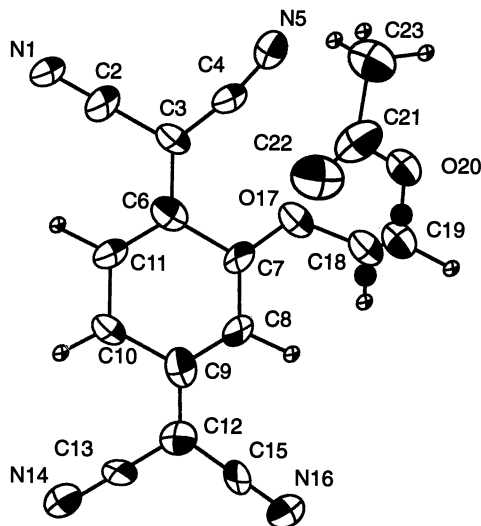


Figure 8. ORTEP-II plot of AETCNQ, 70. Space group *P*-1 (#2), $a = 7.165$ Å, $b = 9.058$ Å, $c = 13.244$ Å, $\alpha = 70.06^\circ$, $\beta = 87.14^\circ$, $\gamma = 68.22^\circ$, $Z = 2$, $R = 3.4\%$ for 1143 reflections. (Reproduced with permission from reference 16. Copyright 1988.)

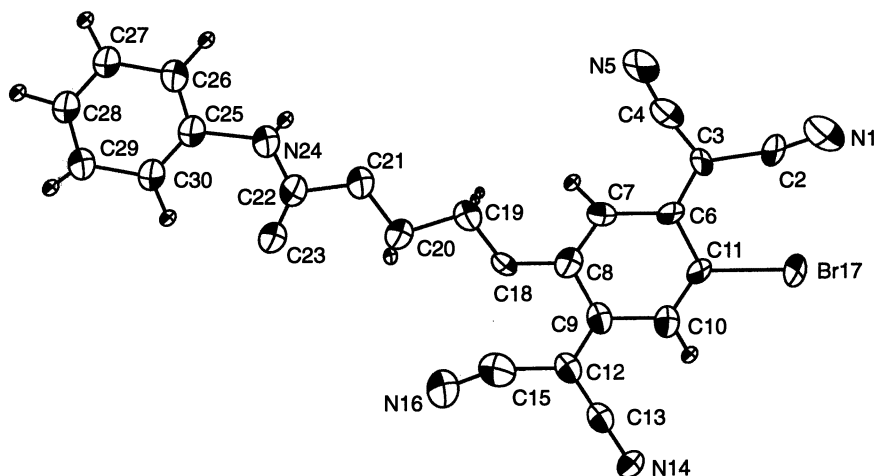


Figure 9. ORTEP-II plot of the crystalline structure of Ph-C-BHTCNQ, 59. Space group *P*₂/*n* (#14), $a = 8.310$ Å, $b = 9.278$ Å, $c = 25.383$ Å, $\beta = 96.15^\circ$, $Z = 4$, $R = 7.9\%$ for 2229 reflections. (Reproduced with permission from reference 8. Copyright 1984.)

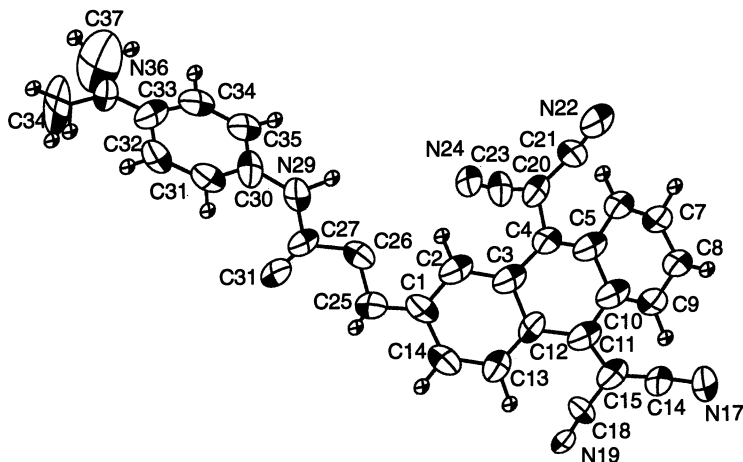


Figure 10. ORTEP-II plot of the crystalline structure of DMAP-C-HMTCAQ, 60. Space group $P-1$ (#2), $a = 8.748$ Å, $b = 10.989$ Å, $c = 13.541$ Å, $\alpha = 90.67^\circ$, $\beta = 99.15^\circ$, $\gamma = 98.62^\circ$, $Z = 2$, $R = 12.7\%$ for 1839 reflections. (Reproduced with permission from reference 24. Copyright 1989.)

(moderate neglect of differential overlap) algorithm, with full geometry optimization, in computer program MOPAC, have been performed on D- σ -A molecules, to predict their geometry, and also their HOMO and LUMO energies. The Br atom in BHTCNQ was replaced by F for simplicity of calculation. The structures, as drawn by computer program ORTEP-II using typical van der Waals atomic radii (1.2 Å for H, 1.7 Å for C, 1.5 Å for O, 1.35 Å for F, and 1.65 Å for S) are shown in Figures

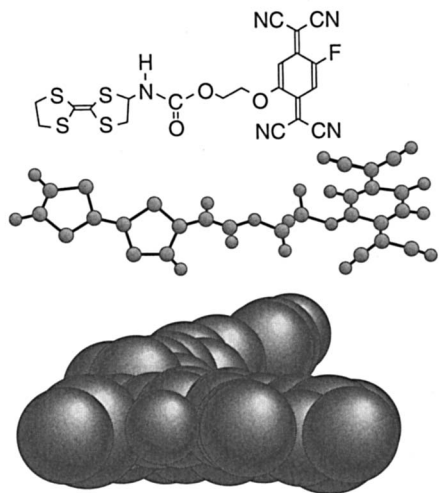


Figure 11. Structure (top), MNDO conformation (middle), and MNDO van der Waals shape, viewed from the acceptor end (bottom) for TTF-C-FHTCNQ, 36; $I_D = 8.197$ eV, $A_A = 2.975$ eV, $I_A = 9.581$ eV, $A_D = 0.134$ eV, $\Delta T_F = I_D - A_A = 5.222$ eV, $\Delta T_R = I_A - A_D = 9.447$ eV; $\Delta E = \Delta T_F - \Delta T_R = 4.225$ eV. (Reproduced with permission from reference 22. Copyright 1988.)

11–15 (the van der Waals shape is viewed from the A end of the molecule). Also given are the HOMO ($-I_D$) and LUMO ($-A_A$) energies, and also the differences $I_D - A_A$ and $I_A - A_D$ discussed in equations 1, 2, and 4.

Overall, the MNDO structures are extended, as expected, and as favored by the MNDO parametrization, but there are a few small surprises: (1) whereas the data of Table III suggest that in a PL film Py-C-BHTCNQ is a relatively flat molecule, Figure 14 introduces a twist in the carbamate linkage; (2) whereas the data of Table III suggest a well-packed BDDAP-C-BHTCNQ molecule, Figure 13 shows a conformer in which the bis-hexyl “tails” are not well-aligned with each other; (3) whereas the crystal structure of BMAP-C-HMTCAQ (24) shows that both dicyanomethylene substituents on the anthracene ring deviate from the plane in the same direction, Figure 15 shows that MNDO gave them a “corkscrew” twist. The MNDO ionization energies I_D are probably 1–2 eV high, as expected from a Koopmans’ theorem calculation; the size of the difference $\Delta E = (I_D - A_A) - (I_A - A_D)$ is large, as expected. The calculated barrier for forward tunneling in BDDAP-C-FHTCNQ is

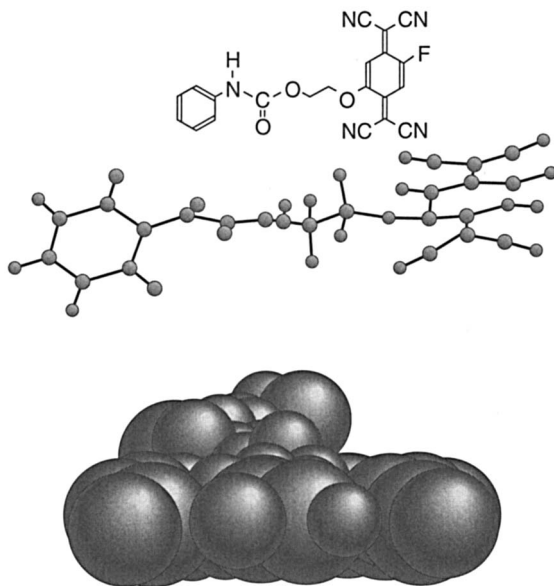


Figure 12. Structure (top) MNDO conformation (middle), and MNDO van der Waals shape, viewed from the acceptor end (bottom) for Ph-C-FHTCNQ, a variant of Ph-C-BHTCNQ, **59**; $I_D = 9.141$ eV, $A_A = 2.941$ eV, $I_A = 9.555$ eV, $A_D = 0.062$ eV, $\Delta T_R = I_D - A_A = 6.200$ eV, $\Delta T_R = I_A - A_D = 9.493$ eV; $\Delta E = \Delta T_F - \Delta T_R = 3.293$ eV. (Reproduced with permission from reference 22. Copyright 1988.)

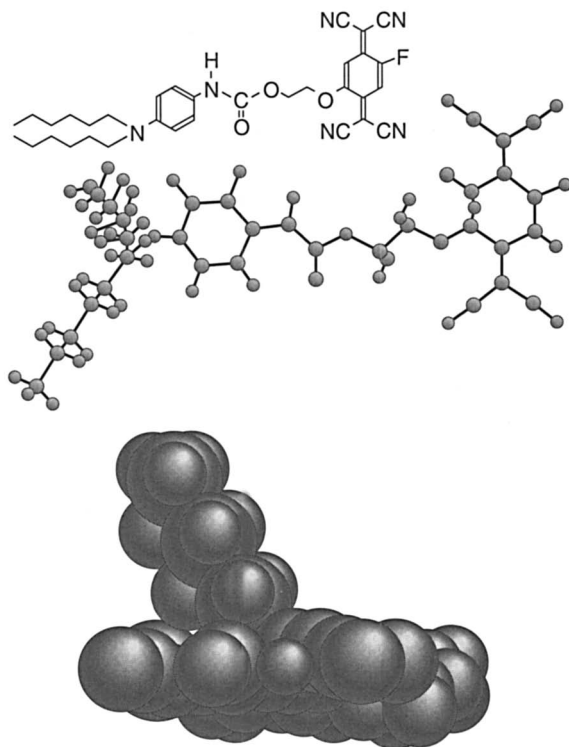


Figure 13. Structure (top), MNDO conformation (middle), and MNDO van der Waals shape, viewed from the acceptor end (bottom) for BHAP-C-FHTCNQ, a variant of BDDAP-C-BHTCNQ, 37; $I_D = 8.767$ eV, $A_A = 2.936$ eV, $I_A = 9.560$ eV, $A_D = 0.099$ eV; $\Delta T_F = I_D - A_A = 5.831$ eV, $\Delta T_R = I_A - A_D = 9.461$ eV; $\Delta E = \Delta T_F - \Delta T_R = 3.630$ eV. (Reproduced with permission from reference 22. Copyright 1988.)

a very large $\Delta T_F \approx 5.8$ eV, whereas for a real Aviram–Ratner rectifier one hopes $\Delta T_F \approx 1\text{--}3$ eV.

Fourier Transform Infrared Spectra of D- σ -A Monolayers. Grazing-angle Fourier transform infrared spectra of monolayers of BDDAP-C-HMTCAQ, BDDAP-C-BHTCNQ, and TDDOP-C-HETCNQ have been measured and reported previously (21–23, 25). The C–H stretch bands are well-resolved, even for a single monolayer, and a broad structure at about 3500 cm^{-1} is seen for “fresh” samples, but disappears for samples older than about 60 days; this may be water trapped between the LB film layer and the aluminum substrate.

Nonlinear Optical Data on D- σ -A Systems. An attempt was made to see whether any second-harmonic signals could be detected

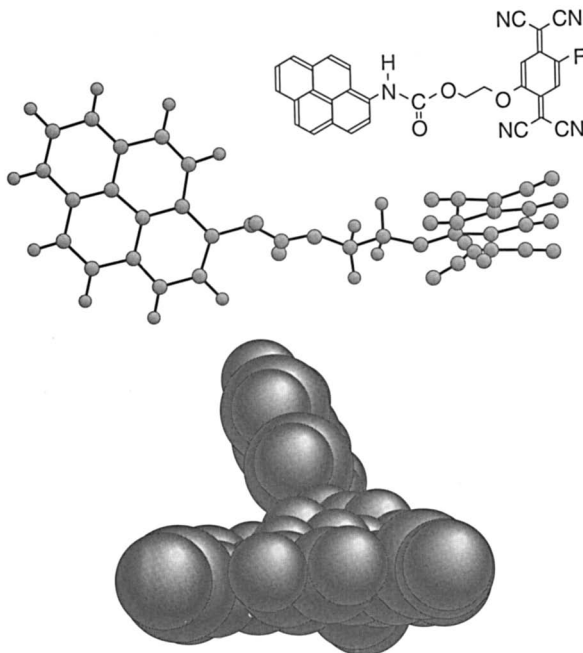


Figure 14. Structure (top), MNDO conformation (middle), and MNDO van der Waals shape, viewed from the acceptor end (bottom), for Py-C-FHTCNQ, a variant of Py-C-BHTCNQ; **39**; $I_D = 8.192$ eV, $A_A = 2.957$ eV, $I_A = 8.986$ eV, $A_D = 1.175$ eV; $\Delta T_F = I_D - A_A = 5.235$ eV; $\Delta T_R = I_A - A_D = 8.347$ eV; $\Delta E = \Delta T_F - \Delta T_R = 3.112$ eV. (Reproduced with permission from reference 22. Copyright 1988.)

from Z multilayers of **50**, but the result was negative, maybe because the Z-type multilayers may have reorganized with the time elapsed between deposition and measurement (Cephalas, A. C., personal communication).

The third-order nonlinear optical susceptibility $\chi^{(3)}$ was measured (very crudely) for dilute chloroform solutions of **42**, **48**, **49**, and **51** by the self-trapping of an Ar ion laser beam ($\lambda = 514.5$ nm). For two of them, the concentrations were measured, so that the molecular γ could also be measured. The results are as follows: **42**, $\chi^{(3)} = 2.5 \times 10^{-7}$ cm⁴ statC⁻²; **48**, $\chi^{(3)} = 6.8 \times 10^{-8}$ cm⁴ statC⁻²; **49**, $\chi^{(3)} = 1.1 \times 10^{-7}$ cm⁴ statC⁻², $\gamma = 1.45 \times 10^{-26}$ cm⁷ statC⁻²; and **51**, $\chi^{(3)} = 2.5 \times 10^{-6}$ cm⁴ statC⁻², $\gamma = 3.36 \times 10^{-24}$ cm⁷ statC⁻² (31). The values are quite large and probably incorporate solution heating effects and resonant enhancements due to molecular absorption bands. In particular, the ratio $\gamma(\mathbf{51})/\gamma(\mathbf{49}) = 231$ seems to be due to the presence of TCNQ in **51**, but not in **49**. In fact, a later experiment of degenerate

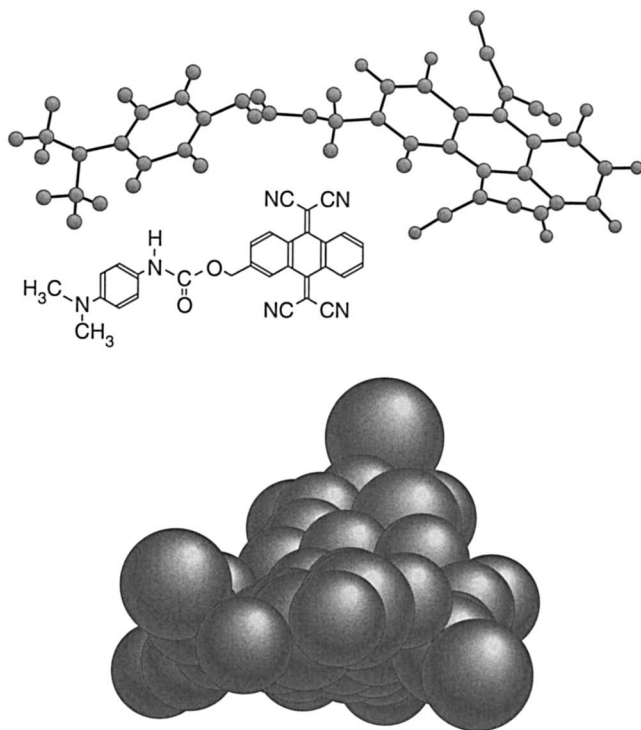


Figure 15. MNDO conformation (top), structure (middle), and MNDO van der Waals shape, viewed from the acceptor end (bottom) of DMAP-C-HMTCAQ, 60; $I_D = 9.052$ eV, $A_A = 2.627$ eV; $I_A = 9.364$ eV, $A_D = 0.144$ eV; $\Delta T_R = I_D - A_A = 6.425$ eV, $\Delta T_R = I_A - A_D = 9.220$ eV; $\Delta E = \Delta T_F - \Delta T_R = 2.795$ eV. (Reproduced with permission from reference 22. Copyright 1988.)

four-wave mixing using frequency-doubled Nd-YAG beam ($\lambda = 532$ nm) and the same solution of **51** destroyed the sample, because of absorption, obviously due to the TCNQ chromophore (205).

Rectification Experiments

Here we discuss seven attempts, by the ORP and by others, to detect rectification.

Macroscopic Test: Metal|Langmuir–Blodgett monolayer|Hg. In the first experiment (9), a 2-mm diameter droplet of Hg was used to probe the conductivity across a single monolayer LB film deposited on top of either Pt or conducting tin oxide (ITO) glass; three sandwiches were thus tested:

1. Pt|DDOP-C-BHTCNQ|Hg
2. Pt|Py-C-BHTCNQ|Hg
3. ITO|DDOP-C-BHTCNQ|Hg

In all cases the background conductivity of the solid support was measured, presumably because of microscopic pinholes in the LB film or because of damage to the film by the Hg drop (9).

Macroscopic Test: Al|BDDAP-C-BHTCNQ|Al Fingers with Low Overlap. In the hope that maybe defects may be avoided, statistically, in a domain of the order of about 0.5×0.5 mm, if one searched through enough samples, the left-hand half of 15 glass microscope slides was coated (using a mask) with five parallel fingers of Al at least 500-nm thick, 3.5-mm long, and 1.6-mm wide (21). Then the 15 slides were coated with a single LB monolayer of BDDAP-C-BHTCNQ, 37, at room temperature. Finally, the slides were coated again with five fingers of Al, but this time on the right-hand side of the slide, so that the vertical overlap Al|BDDAP-C-BHTCNQ|Al would be in an area of only about 0.5×0.5 mm. Of the 75 junctions thus prepared, many were open circuits; the rest were short circuits. Thus, a defect-free domain of BDDAP-C-BHTCNQ was not found (21).

Nanosopic Test: STM on H Atom Switch. In 1988 (111) it was reported that rectification had been observed in a modified Digital Instruments Nanoscope I STM, for molecule 8, which had been originally designed as internal hydrogen atom transfer switch (and not as a rectifier). The claim for molecular rectification was later retracted (112).

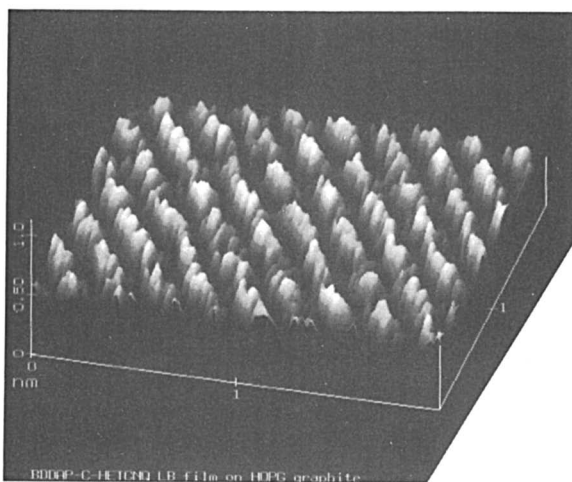
Nanosopic Test: STM on BDDAP-C-BHTCNQ. Pomerantz also kindly studied with his modified STM, an LB monolayer of BDDAP-C-BHTCNQ, 37, deposited on a Au|Ag|mica substrate, using an atomically sharp *W* tip, as the couple *W*|BDDAP-C-BHTCNQ|Au. Large “rectification” currents were observed (22, 23), but later control experiments by Pomerantz showed that this “rectification effect”, with very large currents, could also occur in the absence of any molecule. Disclaimers were issued (22, 23).

Macroscopic Test: Pt|DDOP-C-BHTCNQ|Mg|Al. Sambles and co-workers (42) at the University of Exeter found that a monolayer of DDOP-C-BHTCNQ, 38, sandwiched between Pt and Mg electrodes, behaved as a rectifying LB film. The great merit of this work was to have made defect-free LB monolayers, but the molecule used does not contain a strong donor moiety, that is, I_D is probably too high for an Aviram–Ratner rectifier. Indeed the rectifying behavior has been ascribed to Schottky barrier formation between Mg and TCNQ (44, 45).

Macroscopic Test: Pt|C₁₆H₃₃-Q3CNQ|Mg|Al. Later, Sambles' and Ashwell's group found that an LB film of *Z*-*b*-(1-hexadecyl-4-quinolinium)- α -cyano-4-styryldicyanometanide (C₁₆H₃₃-Q3CNQ, **20**) similarly sandwiched between Pt and Mg electrodes (the Mg shadowed with Ag) also showed macroscopic rectification behavior (43). However, the observed current–voltage (*I*–*V*) curves may also be due to a Schottky barrier (Mg 3CNQ salt) (44).

Nanosopic Test: STM on BDDAP-C-HETCNQ, Py-C-HETCNQ, and C₁₆H₃₃-Q3CNQ. With a Digital Instruments Nanoscope II STM, we have studied samples of BDDAP-C-HETCNQ (**40**) (31), Py-C-HETCNQ (**41**) (31), and C₁₆H₃₃-3CNQ (**20**) (the latter kindly supplied by G. J. Ashwell) (205). The samples were transferred onto highly oriented pyrolytic graphite (Union Carbide grade ZYA and ZYH) by the *LS* horizontal transfer lifting technique and were studied in air at room temperature using Pt–Ir “nanotips” (Digital Instruments) and the “A” head. At low set-point currents, some asymmetries in the *I*–*V* plots could be seen. In preliminary work with BDDAP-C-HETCNQ and Py-C-HETCNQ, the image of graphite is replaced by what seems to be an image of the film (31). The images are shown in Figures 16–18. The substrate does not allow for easy transfer by the LB method, so the *LS* (horizontal lift) technique was used.

The images are not of graphite, and, in particular, the data of Figure 18 provide atomic resolution. It is likely that in Figures 16 and 17 the



*Figure 16. STM image (X, Y scan width 2 nm; Z height 1 nm) of BDDAP-C-HETCNQ, **40**, on HOPG graphite; Pt–Ir tip. (Reproduced with permission from reference 31. Copyright 1991.)*

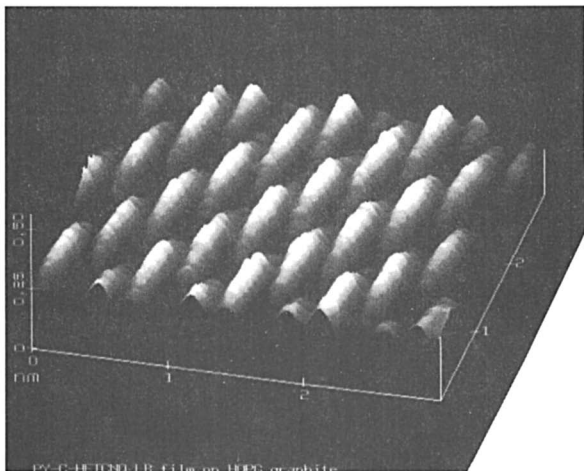


Figure 17. STM image (X, Y scan width 2 nm; Z height 1 nm) of Py-C-HETCNQ, 4I, on HOPG graphite. Pt-Ir tip. (Reproduced with permission from reference 31. Copyright 1991.)

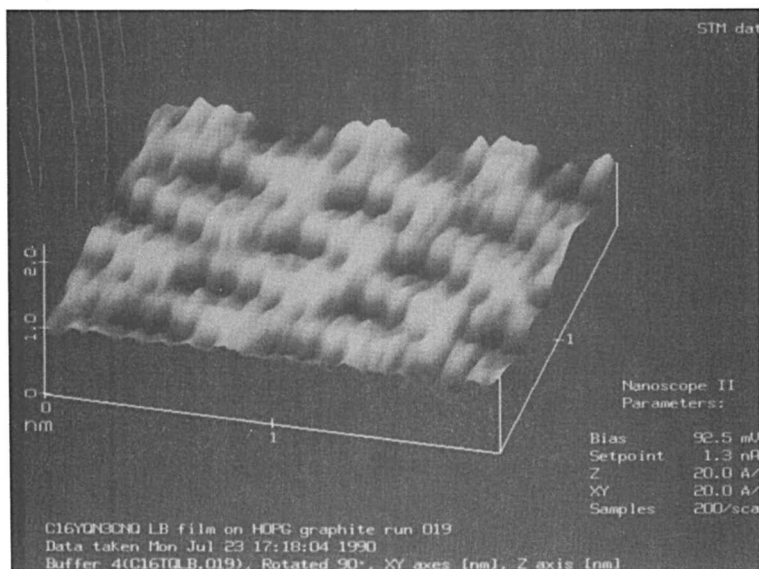


Figure 18. STM image (X, Y scan width 2 nm; Z height 1 nm) of $C_{16}H_{33}-3CNQ$, 20, on HOPG graphite. Pt-Ir tip (205).

Pt–Ir tip has penetrated partially through the monolayer, but it is not quite clear what molecular features are seen. Figure 18 can be interpreted by assuming that the hexadecyl “tail” of $C_{16}H_{33}$ -Q3CNQ, **20**, is closest to the graphite, while the Pt–Ir tip “sees” the cyano atoms at the opposite end of the zwitterionic molecule. However, the LS transfer was not successful in a later experiment with **20**, and only the graphite surface was seen. Atomic resolution was not seen on a large-single-crystal-Au (111) surface, even after Ar^+ ion milling and annealing at 500 °C. The same bad luck was had with Au on mica samples.

When the LS transfers of **20**, **21**, and **40** were successful, attempts were made to detect the rectification curve by using this capability in the STM software: The scan is interrupted, and a series of voltage pulses and increases in the tunneling current are collected and displayed; then the tunneling scan is resumed. Interesting hints of rectification were seen at different times, with all manner of asymmetric curves, but the effect was not seen reproducibly enough to inspire any confidence. Efforts are still continuing, with modifications to the STM head, new preparations of Au on mica (206), and so on.

Conclusion

The progress toward the organic rectifier has been reviewed, also in the broader perspective of other related issues in unimolecular electronics. Schottky barrier rectification has been seen in LB films of D– σ –A and D⁺– π –A[–] molecules, but the goal of Aviram–Ratner rectification through an oriented D– σ –A molecule has not yet been achieved. Guidelines for future synthetic efforts and experimental tests have been discussed.

Acknowledgment

A great debt of gratitude is owed to my former colleagues at the University of Mississippi: Charles A. Panetta, Norman E. Heimer, Daniel L. Mattern, and Charles L. Hussey, their students (Jamil Baghdadchi, Epifanio Torres, and Hossain Nadizadeh), and postdoctoral fellows (Amjad Bhatti and Yozo Miura) for a decade of collaboration, support, and encouragement. I am also grateful to my graduate students (Richard K. Laidlaw, Mohammad A. Takassi, and Xiang-Li Wu), postdoctoral fellows (Robert R. Schumaker and Alan J. McKinley), and undergraduates (Dawn C. Wisner and James T. Singleton) for their diligence. Geoffrey J. Ashwell (Cranfield), Sukant K. Tripathy (Lowell), Ari Aviram and Melvin Pomerantz (IBM Yorktown Heights) have helped with measurements, samples, advice, and psychological support.

The U.S. National Science Foundation supported this work (the latest grant is DMR–88–01924). I am very grateful to Fred E. Stafford (now at the University of Chicago), John A. Tossell, Kenneth J. Wynne, and

David R. Nelson for their patient supervision. Support was also given by the Office of Naval Research (Kenneth J. Wynne) and by the Naval Air Development Command. The present support of JVC America (for research in nonlinear optics) is acknowledged.

References

1. Metzger, R. M. In *Lower-Dimensional Systems and Molecular Electronics*; Metzger, R. M.; Day, P.; Papavassiliou, G. C., Eds.; NATO ASI Series; Plenum: New York, 1991; Vol. B248, p 691.
2. Aviram, A.; Freiser, M. J.; Seiden, P. E.; Young, W. R. U.S. Patent 3 953 874, April 27, 1976.
3. Aviram, A.; Ratner, M. A. *Chem. Phys. Lett.* **1974**, *29*, 277.
4. Aviram, A.; Seiden, P. E.; Ratner, M. A. In *Molecular Electronic Devices*, Carter, F. L., Ed.; Dekker: New York, 1982; p 5.
5. Bagdadchi, J.; Panetta, C. A. *J. Org. Chem.* **1983**, *48*, 3852.
6. Metzger, R. M.; Panetta, C. A. *J. Phys. (Les Ulis, Fr.) Colloque* **1983**, *44*, C3-1605.
7. Metzger, R. M.; Panetta, C. A. In *Molecular Electronic Devices*, Carter, F. L., Ed.; Dekker: New York, 1987; Vol. 2, p 1.
8. Panetta, C. A.; Baghdadchi, J.; Metzger, R. M. *Mol. Cryst. Liq. Cryst.* **1984**, *107*, 103.
9. Metzger, R. M.; Panetta, C. A.; Heimer, N. E.; Bhatti, A. M.; Torres, E.; Blackburn, G. F.; Tripathy, S. K.; Samuelson, L. A. *J. Mol. Electron.* **1986**, *2*, 119.
10. Metzger, R. M.; Panetta, C. A.; Miura, Y.; Torres, E. *Synth. Metals* **1987**, *18*, 797.
11. Torres, E.; Panetta, C. A.; Metzger, R. M. *J. Org. Chem.* **1987**, *52*, 2944.
12. Metzger, R. M.; Panetta, C. A. In *Proceedings of the Eighth Winter Conference on Low-Temperature Physics*; UNAM: Mexico City, Mexico, 1987; p 81.
13. Laidlaw, R. K.; Miura, Y.; Panetta, C. A.; Metzger, R. M. *Acta Cryst.* **1988**, *C44*, 2009.
14. Laidlaw, R. K.; Miura, Y.; Grant, J. L.; Cooray, L.; Clark, M.; Kispert, L. D.; Metzger, R. M. *J. Chem. Phys.* **1987**, *87*, 4967.
15. Laidlaw, R. K.; Baghdadchi, J.; Panetta, C. A.; Miura, Y.; Torres, E.; Metzger, R. M. *Acta Cryst.* **1988**, *B44*, 645.
16. Miura, Y.; Laidlaw, R. K.; Panetta, C. A.; Metzger, R. M. *Acta Cryst.* **1988**, *C44*, 2007.
17. Metzger, R. M.; Schumaker, R. R.; Cava, M. P.; Laidlaw, R. K.; Panetta, C. A.; Torres, E. *Langmuir* **1988**, *4*, 298.
18. Metzger, R. M.; Panetta, C. A. In *Organic and Inorganic Lower-Dimensional Materials*; Delhaès, P.; Drillon, M., Eds.; NATO ASI Series; Plenum: New York, 1988; Vol. B168, p 271.
19. Miura, Y.; Torres, E.; Panetta, C. A.; Metzger, R. M. *J. Org. Chem.* **1988**, *53*, 439.
20. Miura, Y.; Panetta, C. A.; Metzger, R. M. *J. Liq. Chrom.* **1988**, *11*, 245.
21. Metzger, R. M.; Panetta, C. A. *J. Mol. Electron.* **1989**, *5*, 1.
22. Metzger, R. M.; Panetta, C. A. *J. Chim. Phys.* **1988**, *85*, 1125.
23. Metzger, R. M.; Panetta, C. A. *Synth. Met.* **1989**, *28*, C807.
24. Metzger, R. M.; Laidlaw, R. K.; Torres, E.; Panetta, C. A. *J. Cryst. Spectr. Res.* **1989**, *19*, 475.

25. Metzger, R. M.; Panetta, C. A. In *Molecular Electronics—Science and Technology*; Aviram, A.; Bross, A., Eds., New York Engineering Foundation: New York, 1990; p 293.
26. Metzger, R. M.; Wisner, D. C.; Laidlaw, R. K.; Takassi, M. A.; Mattern, D. L.; Panetta, C. A. *Langmuir* **1990**, *6*, 1515.
27. Metzger, R. M.; Panetta, C. A. In *Lower-Dimensional Systems and Molecular Electronics*; Metzger, R. M.; Day, P.; Papavassiliou, G. C., Eds.; NATO ASI Series; Plenum: New York, 1991; Vol. B248, p 641.
28. Metzger, R. M.; Panetta, C. A. In *Advanced Organic Solid State Materials*; Chiang, L. Y.; Cowan, D. O.; Chaikin, P., Eds.; Materials Research Society Symposium Proceedings Series; Materials Research Society: Philadelphia, PA, 1990; Vol. 173, p 531.
29. Metzger, R. M.; Panetta, C. A. In *Condensed Systems of Low Dimensionality*; Beeby, J. L., Ed.; NATO Advanced Study Institute Series; Plenum: New York, 1991; Vol. B253, p 779.
30. Metzger, R. M.; Panetta, C. A. *New J. Chem.* **1991**, *15*, 209.
31. Metzger, R. M.; Panetta, C. A. *Synth. Met.* **1991**, *42*, 1407.
32. Panetta, C. A.; Heimer, N. E.; Hussey, C. L.; Metzger, R. M. *Synlett* **1991**, 301.
33. Metzger, R. M., In *Molecular Electronics—Science and Technology*; Aviram, A., Ed.; American Institute of Physics Conference Proceedings; American Institute of Physics: New York, 1992; Vol. 262, p 85.
34. Torres, E.; Heimer, N. E.; Clark, B. J.; Hussey, C. L. *J. Org. Chem.* **1991**, *56*, 3737.
35. Blodgett, K. B. *J. Am. Chem. Soc.* **1935**, *57*, 1007.
36. Blodgett, K. B.; Langmuir, I. *Phys. Rev.* **1937**, *51*, 964.
37. Gaines, G. L., Jr.; *Insoluble Monolayers at Liquid-Gas Interfaces*; Interscience: New York, 1966.
38. Kuhn, H.; Möbius, D.; Bücher, H. In *Physical Methods of Chemistry*, Vol. I, Part IIIB; Weissberger, A.; Rossiter, B. W., Eds.; Wiley: New York, 1972; p 577.
39. *Langmuir-Blodgett Films*; Roberts, G., Ed.; Plenum: New York, 1990.
40. Kuhn, H. *Pure Appl. Chem.* **1979**, *51*, 341.
41. Kuhn, H. *Pure Appl. Chem.* **1981**, *53*, 2105.
42. Geddes, N. J.; Sambles, J. R.; Jarvis, D. J.; Parker, W. G.; Sandman, D. J. *Appl. Phys. Lett.* **1990**, *56*, 1916.
43. Ashwell, G. J.; Sambles, J. R.; Martin, A. S.; Parker, W. G.; Szablewski, M. *J. Chem. Soc. Chem. Commun.* **1990**, 1374.
44. Sandman, D. J.; Laski, J.; Geddes, N. J.; Sambles, J. R.; Jarvis, D. J.; Parker, W. G. *Synth. Metals* **1991**, *42*, 1415.
45. Geddes, N. J.; Sambles, J. R.; Jarvis, D. J.; Parker, W. G.; Sandman, D. J. *J. Appl. Phys.*, in press.
46. Binnig, G.; Rohrer, H.; Gerber, Ch.; Weibel, E. *Phys. Rev. Lett.* **1982**, *49*, 57.
47. *Molecular Electronic Devices*; Carter, F. L., Ed.; Dekker: New York, 1982.
48. *Molecular Electronic Devices*; Carter, F. L., Ed.; Dekker: New York, 1987; Vol. II.
49. *Molecular Electronic Devices, Proceedings of the 3rd International Symposium*; Carter, F. L.; Siatkowski, R. E.; Wohltjen, H., Eds.; North-Holland: Amsterdam, The Netherlands, 1988.
50. *Molecular Electronics—IVth International School on Condensed Matter*; Borissov, M., Ed.; World Scientific: Singapore, 1987.

51. *Molecular Electronics—Science and Technology*; Aviram, A.; Bros, A., Eds.; New York Engineering Foundation: New York, 1990.
52. *Molecular Electronics—Science and Technology*; Aviram, A., Ed.; American Institute of Physics: New York, 1992; Vol. 262.
53. Haddon, R. C.; Lamola, A. C. *Proc. Natl. Acad. Sci. U.S.A.* **1985**, *82*, 1874.
54. Swalen, J. D.; Allara, D. L.; Andrade, J. D.; Chandross, E. A.; Garoff, S.; Israelachvili, J.; McCarthy, T. J.; Murray, R.; Pease, R. F.; Rabolt, J. F.; Wynne, K. J.; Yu, H. *Langmuir* **1987**, *3*, 932.
55. *Graphite Intercalation Compounds*; Davidov, D.; Selig, H., Eds.; Synthetic Metals Series; 1988; Vol. 23.
56. Acrivos, J. V. NATO ASI Series, 1984; Vol. C130, p 479.
57. For the proceedings of three recent conferences, see (a) *Advanced Organic Solid State Materials*; Chiang, L. Y.; Cowan, D. O.; Chaikin, P., Eds.; Materials Research Society Symposium Proceedings Series, MRS: Philadelphia, PA, 1990; Vol. 173; (b) *Lower-Dimensional Systems and Molecular Electronics*; Metzger, R. M.; Day, P.; Papavassiliou, G. C., Eds.; NATO ASI Series; Plenum: New York, 1991; Vol. B248; (c) *Synth. Met.* **1991**, *41–43*.
58. *Handbook of Conducting Polymers*, Skotheim, T. A., Ed.; Dekker: New York, 1986; Vol. I and II.
59. Relevant articles in *Extended Linear-Chain Compounds*; Miller, J. S., Ed.; Plenum: New York, 1982, 1982, 1983; Vols. I, II, and III.
60. Inabe, T.; Hoshino, N.; Mitani, T.; Maruyama, Y. *Bull. Chem. Soc. Jpn.* **1989**, *62*, 2245.
61. Carter, F. L. In *Molecular Electronic Devices*; Carter, F. L., Ed.; Dekker: New York, 1982; p 51.
62. Fujihira, M.; Nishiyama, K.; Yamada, H. *Thin Solid Films* **1985**, *132*, 77.
63. Lehn, J.-M. *Angew. Chem. Intl. Ed. Engl.* **1988**, *27*, 89.
64. Aviram, A. *J. Am. Chem. Soc.* **1988**, *110*, 5687.
65. Tour, J. M.; Wu, R.; Schumm, J. S. *J. Am. Chem. Soc.* **1991**, *113*, 7064.
66. Kenny, P. W.; Miller, L. L.; Rak, S. F.; Jozefiak, T. R.; Christophel, W. C.; Kim, J. H.; Uphaus, R. A. *J. Am. Chem. Soc.* **1988**, *110*, 4445.
67. Szejtli, J. *Cyclodextrin Technology*; Kluwer: Dordrecht, Holland, 1988.
68. *Calixarenes, a Versatile Class of Macrocyclic Compounds*; Vicens, J.; Böhrner, V. Eds.; Kluwer: Dordrecht, Holland, 1990.
69. Enzel, P.; Bein, T. In *Lower-Dimensional Systems and Molecular Electronics*; Metzger, R. M.; Day, P.; Papavassiliou, G. C., Eds.; NATO ASI Series, Plenum: New York, 1991; Vol. B248, p 421.
70. Meinhard, J. E. *Appl. Phys. Lett.* **1964**, *35*, 3059.
71. Kinzig, B. J. In *Molecular Electronic Devices*; Carter, F. L., Ed.; Dekker: New York, 1982; p 223.
72. Langmuir, I.; Schaefer, V. J. *J. Am. Chem. Soc.* **1938**, *60*, 1351.
73. Mann, B.; Kuhn, H. *J. Appl. Phys.* **1971**, *42*, 4398.
74. Handy, R. M.; Scala, L. C. *J. Electrochem. Soc.* **1966**, *113*, 109.
75. Roberts, G. G.; Vincett, P. S.; Barlow, W. A. *J. Phys. C* **1978**, *11*, 2077.
76. Thredgold, R. H.; Vickers, A. J.; Allen, R. A. *J. Phys. D* **1984**, *17*, L5.
77. Peterson, I. R. *J. Chim. Phys.* **1988**, *85*, 997.
78. Polymeropoulos, E. E.; Möbius, D.; Kuhn, H. *Thin Solid Films* **1980**, *68*, 173.
79. Sugi, M.; Sakai, K.; Saito, M.; Kawabata, Y.; Iizima, S. *Thin Solid Films* **1985**, *132*, 69.

80. Potember, R. S.; Poehler, T. O.; Cowan, D. O. *Appl. Phys. Lett.* **1979**, *34*, 405.
81. Potember, R. S.; Hoffmann, R. C.; Hu, H. S.; Cocchiario, J. E.; Viands, C. A.; Murphy, R. A.; Poehler, T. O. *Polymer* **1987**, *28*, 574.
82. Potember, R. S.; Hoffman, R. C.; Benson, R. C.; Poehler, T. O. *J. Phys. (Les Ulis) Colloque* **1983**, *44*, C3-1597.
83. Yamaguchi, S.; Viands, C. A.; Potember, R. S. *J. Vac. Sci. Technol. B* **1991**, *9*, 1129.
84. White, H. S.; Kittleston, G. P.; Wrighton, M. S. *J. Am. Chem. Soc.* **1984**, *106*, 5375.
85. Turner Jones, E. T.; Chyan, O. M.; Wrighton, M. S. *J. Am. Chem. Soc.* **1987**, *109*, 5526.
86. Paloheimo, J.; Kuivalainen, P.; Stubb, H.; Vuorimaa, E.; Yli-Lahti, P. *Appl. Phys. Lett.* **1990**, *56*, 1157.
87. Ryu, H.; Akagane, K.; Kori, H. *Chem. Econ. Eng. Rev.* **1986**, *18(12)*, 26.
88. Slonim, J.; Mole, D.; Bauer, M. *Library Hi-Tech* **1985**, *3(4)*, 27.
89. Kalanaraman, P. S.; Kuder, J. E.; Jones, R. S. In *Functional Polymers*; Bergbreiter, D. E.; Martin, C. R., Eds.; Plenum: New York, 1989; p 173.
90. Nikles, D. E.; Forbes, C. E.; Goldberg, H. A.; Johnson, R. E.; Kohn, R. S.; Onorato, F. J. *Proc. Soc. Photo-optical Instrum. Eng.* **1989**, *107B*, 43.
91. Ruaudel-Teixier, A.; Vandevyver, M.; Barraud, A. *Mol. Cryst. Liq. Cryst.* **1985**, *120*, 319.
92. Vandevyver, M. In *Lower-Dimensional Systems and Molecular Electronics*; Metzger, R. M.; Day, P.; Papavassiliou, G. C., Eds.; NATO ASI Series; Plenum: New York, 1991; Vol. B248, p 503.
93. Nakamura, T.; Tachibana, H.; Matsumoto, M.; Tanaka, M.; Kawabata, Y. In *Lower-Dimensional Systems and Molecular Electronics*; Metzger, R. M.; Day, P.; Papavassiliou, G. C., Eds.; NATO ASI Series; Plenum: New York, 1991; Vol. B248, p 519.
94. Coronel, P.; Barraud, A.; Claude, R.; Kahn, O.; Ruaudel-Teixier, A.; Zarembovitch, J. *J. Chem. Soc. Chem. Commun.* **1989**, 193.
95. Wasielewski, M. R.; Johnson, D. G.; Svec, W. A.; Kersey, K. M.; Cragg, D. E.; Minsek, D. W. In *Photochemical Energy Conversion*; Norris, J. R., Jr.; Meisel, D., Eds.; Elsevier: New York, 1989; p 135.
96. Murray, R. W. *Acc. Chem. Res.* **1980**, *13*, 135.
97. Maoz, R.; Netzer, L.; Gun, J.; Sagiv, J. *J. Chim. Phys.* **1988**, *85*, 1059.
98. Bigelow, W. C.; Pickett, D. L.; Zisman, W. A. *J. Colloid Sci.* **1946**, *1*, 513.
99. Wilson, E. G. *Mol. Cryst. Liq. Cryst.* **1985**, *121*, 271.
100. Mueller, P.; Rubin, D. O.; Tien, H. T.; Wescott, W. C. *Nature (London)* **1962**, *194*, 979, and *J. Phys. Chem.* **1963**, *67*, 534.
101. Montal, M. *Annu. Rev. Biophys. Bioeng.* **1976**, *5*, 116.
102. Li, D.-Q.; Ratner, M. A.; Marks, T. J.; Zhang, C.-H.; Yang, J.; Wong, G. K. *J. Am. Chem. Soc.* **1990**, *112*, 7389.
103. Porter, M. D.; Bright, T. B.; Allara, D. L.; Chidsey, C. E. D. *J. Am. Chem. Soc.* **1987**, *109*, 3559.
104. Bain, C. D.; Troughton, E. B.; Tao, Y.-T.; Evall, J.; Whitesides, G. M. *J. Am. Chem. Soc.* **1989**, *111*, 321.
105. Graff, G. *Science (Washington, D.C.)* **1991**, *254*, 1306.
106. Bedrossian, P.; Chen, D. M.; Mortensen, K.; Golovchenko, J. A. *Nature (London)* **1989**, *342*, 258.
107. Dunlap, D. D.; Bustamante, C. *Nature (London)* **1989**, *342*, 204.

108. Clemmer, C. R.; Beebe, Jr., T. P. *Science (Washington, D.C.)* 1991, 251, 640.
109. Ohmori, T.; Hashimoto, K.; Fujishima, A. *Jpn. J. Appl. Phys.* 1991, 30, 1826.
110. Hoffmann, R. *Acc. Chem. Res.* 1971, 4, 1.
111. Aviram, A.; Joachim, C.; Pomerantz, M. *Chem. Phys. Lett.* 1988, 146, 490.
112. Aviram, A.; Joachim, C.; Pomerantz, M. *Chem. Phys. Lett.* 1989, 162, 416.
113. Sixl, H.; Higelin, D. In *Molecular Electronic Devices*; Carter, F. L., Ed.; Dekker: New York, 1987; Vol. II, p 27.
114. Ulrich, K.; Port, H.; Wolf, H. C.; Wonner, J.; Effenberger, F.; Ilge, H.-D. *Chem. Phys.* 1991, 154, 311.
115. Tachibana, H.; Nakamura, T.; Matsumoto, M.; Komizu, H.; Manda, E.; Niino, H.; Yabe, A.; Kawabata, Y. *J. Am. Chem. Soc.* 1989, 111, 3080.
116. Birge, R. R.; Cooper, T. M. *Biophys. J.* 1983, 42, 61.
117. Taube, H. *Pure Appl. Chem.* 1975, 44, 25.
118. Meyer, T. J. In *Photochemical Energy Conversion*, Norris, J. R., Jr.; Meisel, D., Eds.; Elsevier: New York, 1989; p 75.
119. Calcaterra, L. T.; Closs, G. L.; Miller, J. R. *J. Am. Chem. Soc.* 1983, 105, 670.
120. Miller, J. R.; Calcaterra, L. T.; Closs, G. L. *J. Am. Chem. Soc.* 1984, 106, 3047.
121. Liang, N.; Miller, J. R.; Closs, G. L. *J. Am. Chem. Soc.* 1990, 112, 5353.
122. Marcus, R. A.; *Disc. Faraday Soc.* 1960, 29, 21.
123. Deisenhofer, J.; Epp, O.; Miki, K.; Huber, R.; Michel, H. *J. Mol. Biol.* 1984, 180, 385.
124. Arnoux, B.; Ducruix, A.; Reiss-Husson, F.; Kutz, M.; Norris, J.; Schiffer, M.; Chang, C. H. *FEBS Lett.* 1989, 258, 47.
125. Kirmaier, C.; Holten, D. *Biochemistry* 1991, 30, 609.
126. Kirmaier, C.; Holten, D.; Bylina, E. J.; Youvan, D. C. *Proc. Natl. Acad. Sci. U.S.A.* 1988, 85, 7562.
127. Breton, J.; Martin, J.; Fleming, G. R.; Lambay, J. *Biochemistry* 1988, 27, 8276.
128. Petrich, J. W.; Martin, J. L.; Houde, D.; Poyart, C.; Orszag, A. *Biochemistry* 1987, 26, 7914.
129. Kirmaier, C.; Holten, D.; Parson, W. W. *Biochim. Biophys. Acta* 1985, 810, 33.
130. Woodbury, N. W.; Becker, M.; Middendorf, D.; Parson, W. M. *Biochemistry* 1985, 24, 7516.
131. McIntosh, A. R.; Bolton, J. R.; Connolly, J. S.; Marsh, K. L.; Cook, D. R.; Ho, T.-F.; Weedon, A. C. *J. Phys. Chem.* 1986, 90, 5640.
132. Joran, A. D.; Leland, B. A.; Geller, G. G.; Hopfield, J. J.; Dervan, P. B. *J. Am. Chem. Soc.* 1984, 106, 6090.
133. Nishitani, S.; Kurata, N.; Sakata, Y.; Misumi, S.; Karen, A.; Okada, T.; Mataga, N. *J. Am. Chem. Soc.* 1983, 105, 7771.
134. Osuka, A.; Nagata, T.; Maruyama, K.; Mataga, N.; Asahi, T.; Yamazaki, I.; Nishimura, Y. *Chem. Phys. Lett.* 1991, 185, 88.
135. Lindsay, J.; Mauzerall, D.; Linschitz, H. *J. Am. Chem. Soc.* 1983, 105, 6528.
136. Delaney, J. K.; Lindsay, J. S.; Mauzerall, D. C. *J. Am. Chem. Soc.* 1990, 112, 957.
137. Krieger, C.; Weiser, J.; Staab, H. A. *Tetrahedron Lett.* 1985, 26, 6050.

138. Hush, N. S.; Paddon-Row, M. N.; Cotsaris, E.; Oevering, H.; Verhoeven, J. W.; Heppener, M. *Chem. Phys. Lett.* **1985**, *117*, 8.
139. Kroon, J.; Verhoeven, J. W.; Paddon-Row, M. N.; Oliver, A. M. *Angew. Chem. Int. Ed. Engl.* **1991**, *30*, 1358.
140. Effenberger, F.; Wolf, H. C. *New. J. Chem.* **1991**, *15*, 117.
141. Moore, T. A.; Gust, D.; Mathis, P.; Mialocq, J.-C.; Chachaty, C.; Bensasson, R. V.; Land, E. J.; Doizi, D.; Liddell, P. A.; Lehman, W. R.; Nemweth, G. A.; Moore, A. L. *Nature (London)* **1984**, *307*, 630.
142. Gust, D.; Moore, T. A.; Moore, A. L.; Lee, S.-J.; Bittersman, E.; Luttrull, D. K.; Rehms, A. A.; DeGraziano, J. M.; Ma, X. C.; Gao, F.; Belford, R. E.; Trier, T. T. *Science (Washington, D.C.)* **1990**, *248*, 199.
143. Prasad, P. N.; Williams, D. J. *Introduction to Nonlinear Optical Effects in Molecules and Polymers*; Wiley: New York, 1991; Chapters 7 and 10.
144. Metzger, R. M.; Heimer, N. E.; Ashwell, G. J. *Mol. Cryst. Liq. Cryst.* **1984**, *107*, 133.
145. Akhtar, S.; Tanaka, J.; Metzger, R. M.; Ashwell, G. J. *Mol. Cryst. Liq. Cryst.* **1986**, *139*, 353.
146. Ashwell, G. J. U.K. Patent Appl. 9007230.7, 1990.
147. Ashwell, G. J.; Dawnay, E. J. C.; Kuczynski, A. P.; Szablewski, M. In *Advanced Organic Solid State Materials*; Chiang, L. Y.; Cowan, D. O.; Chaikin, P., Eds.; Materials Research Society Symposium Proceedings Series; Materials Research Society: Philadelphia, PA, 1990; Vol. 173, p 507.
148. Becker, J. Y.; Bernstein, J.; Bittner, S.; Levi, N.; Shaik, S. *J. Am. Chem. Soc.* **1983**, *105*, 4468.
149. Staab, H. A.; Hintz, R.; Knaus, G. H.; Krieger, C. *Chem. Ber.* **1983**, *116*, 2827.
150. Murata, I. *Pure Appl. Chem.* **1983**, *55*, 323.
151. (a) Wacks, M. E.; Dibeler, V. H. *J. Chem. Phys.* **1959**, *31*, 1557; (b) Wacks, M. E. *J. Chem. Phys.* **1964**, *41*, 1661.
152. Lichtenberger, D. L.; Johnston, R. L.; Hinkelmann, K.; Suzuki, T.; Wudl, F. *J. Am. Chem. Soc.* **1990**, *112*, 3302.
153. Dvorak, V.; Nemek, I.; Zyka, J. *Mikrochem. J.* **1967**, *12*, 324.
154. Batley, M.; Lyons, L. E. *Mol. Cryst.* **1968**, *3*, 357.
155. Kebarle, P.; Chowdhury, S. *Chem. Rev.* **1987**, *87*, 513.
156. Chen, E. C. M.; Wentworth, W. E. *J. Chem. Phys.* **1975**, *63*, 3183.
157. Compton, R. N.; Cooper, C. D. *J. Chem. Phys.* **1977**, *66*, 4325.
158. Garron, R. C. *Rend. Acad. Sci. Paris* **1964**, *258*, 1458.
159. Grepstad, J. K.; Garland, P. O.; Slagsvold, B. *J. Surf. Sci.* **1976**, *57*, 348.
160. Potter, H. C.; Blakeley, J. M. *J. Vac. Sci. Technol.* **1975**, *12*, 635.
161. Demuth, J. E. *Chem. Phys. Lett.* **1977**, *45*, 12.
162. Matsen, F. A. *J. Chem. Phys.* **1956**, *24*, 602.
163. Hush, N. S.; Pople, J. A. *Trans. Faraday Soc.* **1955**, *51*, 600.
164. Pope, M. *J. Chem. Phys.* **1962**, *37*, 1001.
165. Kluge, W. In *Landolt-Börnstein Physikalische Tabellen*, 6th ed.; Springer: Berlin, Germany, 1959; Vol. 2, Part 6, p 909.
166. Jain, S. C.; Krishnan, K. S. *Proc. Roy. Soc. London* **1952**, *A213*, 143.
167. Green, D. C. *J. Org. Chem.* **1979**, *44*, 1476.
168. Hertler, W. R. *J. Org. Chem.* **1976**, *41*, 1412.
169. Baghdadchi, J. Ph.D. Dissertation, University of Mississippi, Dec. 1982.
170. Heimer, N. E., University of Mississippi, Unpublished results.
171. Kini, A. M.; Cowan, D. O.; Gerson, F.; Möckel, R. *J. Am. Chem. Soc.* **1985**, *107*, 556.

172. Chen, W.; Cava, M. P.; Takassi, M. A.; Metzger, R. M. *J. Am. Chem. Soc.* **1988**, *110*, 7903.
173. Gleiter, R.; Schmidt, E.; Cowan, D. O.; Ferraris, J. P. *J. Electron. Spectrosc.* **1973**, *2*, 207.
174. Berlinsky, A.; Carolan, J. F.; Weiler, L. *Can. J. Chem.* **1973**, *52*, 3373.
175. Pysh, E. S.; Yang, N. C. *J. Am. Chem. Soc.* **1963**, *85*, 2125.
176. Clar, E.; Robertson, J. M.; Schloegl, R.; Schmidt, W. *J. Am. Chem. Soc.* **1981**, *103*, 1320.
177. Cooper, C. D.; Naff, W. T.; Compton, R. N. *J. Chem. Phys.* **1975**, *63*, 2752.
178. Gutmann, F.; Lyons, L. E. *Organic Semiconductors*; Wiley: New York, 1967; p 698.
179. Hussey, C. L.; Baghdadchi, J.; Panetta, C. A.; Metzger, R. M., Unpublished results.
180. Takassi, M. A. Ph.D. Dissertation, University of Mississippi, Aug. 1989.
181. Acker, D. S.; Hertler, W. R. *J. Am. Chem. Soc.* **1962**, *84*, 3370.
182. Wheland, R. C.; Gilsson, J. L. *J. Am. Chem. Soc.* **1976**, *98*, 3916.
183. Anderson, J. R.; Jorgensen, O. *J. Chem. Soc. Perkin Trans. 1* **1979**, 3095.
184. Emge, T. J.; Maxfield, McR.; Cowan, D. O.; Kistenmacher, T. J. *Mol. Cryst. Liq. Cryst.* **1981**, *65*, 161.
185. Eggins, B. R. *Chem. Commun.* **1969**, 1267.
186. Aumüller, A.; Hünig, S. *Liebigs Ann. Chem.* **1986**, 165.
187. Ashraf, M.; Headridge, J. B. *Talanta* **1969**, *16*, 1439.
188. Jeftic, L.; Manning, G. *J. Electroanal. Chem.* **1970**, *26*, 195.
189. Peover, M. E. *J. Chem. Soc.* **1962**, 4540.
190. Kuder, J. K.; Pochan, J. M.; Turner, S. R.; Hinman, D. F. *J. Electrochem. Soc.* **1978**, *125*, 1750.
191. Allemand, P. M.; Koch, A.; Wudl, F.; Rubin, Y.; Diederich, F.; Alvarez, M. M.; Anz, S. J.; Whetten, R. L. *J. Am. Chem. Soc.* **1991**, *113*, 1050.
192. Yang, S. H.; Pettiette, C. L.; Conceicao, J.; Chesnovsky, O.; Smalley, R. E. *Chem. Phys. Lett.* **1987**, *139*, 233.
193. Peover, M. E. *Trans. Faraday Soc.* **1962**, *58*, 2370.
194. Lyons, L. E.; Palmer, L. D. *Austr. J. Chem.* **1976**, *29*, 1919.
195. Farragher, A. L.; Page, F. M. *Trans. Faraday Soc.* **1967**, *63*, 2369.
196. Chowdhury, S.; Kebarle, P. *J. Am. Chem. Soc.* **1986**, *108*, 5453.
197. Miller, L. L.; Nordblum, G. D.; Mayeda, E. A. *J. Org. Chem.* **1972**, *37*, 916.
198. Parker, V. D. *J. Am. Chem. Soc.* **1976**, *98*, 98.
199. Ebbertsen, L. In *Advances in Physical Organic Chemistry*; Gold, V.; Bethell, D., Eds.; Academic: Orlando, FL, 1982; Vol. 18, p 79.
200. Nelsen, S. F. *Isr. J. Chem.* **1979**, *18*, 45.
201. Bechgaard, K.; Andersen, J. R. In *The Physics and Chemistry of Low-Dimensional Solids*; Alcácer, L., Ed.; NATO ASI Series, Reidel: Dordrecht, Holland, 1980; Vol. C56, p 247.
202. Wu, X.-L.; Parakka, J. L.; Metzger, R. M., Unpublished results.
203. Nadizadeh, H.; Mattern, D. L.; Singleton, J.; Wu, X.-L.; Metzger, R. M., Unpublished results.
204. Chandra Sekhar, P., Unpublished results.
205. Wu, X.-L.; Shamsuzzoha, M.; Metzger, R. M.; Ashwell, G. J., Submitted for publication in *Adv. Mater.*
206. Holland-Moritz, E.; Gordon, J., II; Borges, G.; Sonnenfeld, R. *Langmuir* **1991**, *7*, 301.

RECEIVED for review March 12, 1992. ACCEPTED revised manuscript January 27, 1993.

Fundamentals of Reliability Calculations for Molecular Devices and Photochromic Memories

Albert F. Lawrence¹ and Robert R. Birge

Department of Chemistry and W. M. Keck Center for Molecular Electronics,
Syracuse University, Syracuse, NY 13244

Although molecular electronics offers significant promise, the issue of reliability remains a critical component to the analysis of potential commercialization. This chapter examines the mathematical foundations and the methods and procedures associated with calculating the reliability of a molecular-based device. The principal sources of error and their effects on the probability of correctly setting or reading the state of a binary device are defined. These results are used to derive formulas to determine the minimum number of molecules that must be used to define a binary state. In addition we examine the reliability of selected molecular devices currently proposed or under development for application as optically coupled gates and memories. In addition to accounting for sources of error such as quantum uncertainty, imperfect absorption, or measurement error, we also identify error sources arising from the dynamics of the read and write operations. These latter types of error can be described by using the mathematics of chaos in the statistics of ensembles.

THE PATH TO MOLECULAR ELECTRONICS presents some formidable technical problems, although systems based on molecular transformations offer great potential for achieving the ultimate limits in speed and density of processing components. Because the relevant physics on the nanometer scale is fundamentally different than the physics on the micrometer scale, it is probably unlikely that we will build exact molecular analogs to the devices that are familiar to the electronics engineer. Thus,

¹ Alternative address: Biological Components Corporation, Menlo Park, CA 94025

0065-2393/94/0240-0131\$09.80/0
© 1994 American Chemical Society

such devices as transmission lines, amplifiers, gates, and switches will probably not be available to a hypothetical circuit designer who works with structures composed of a few atoms. Nevertheless, it should still be desirable to build devices like digital computers, if only because of the rich and powerful computational theory that a Turing machine embodies. As a result, we require devices that embody basic logical functions such as “and,” “not,” and “or” and that perform their functions with adequate and well-defined reliability.

Numerous molecular systems found in nature exhibit the transmission and control of signals through modulation of an effective potential. Often, the fundamental mechanics also include (1) a conformational switch from one metastable state to another, (2) the motion of a charged particle via a combination of tunneling and escape processes along a periodic potential, and (3) the direct coupling of the conformational switch to the transport process (1–4). A binding event or absorption of a photon of energy represents common mechanisms for initiating this chain of events. In both natural and synthetic molecular systems, movement of charge or mass in multiple potential wells represent the dominant mode of state change.

This chapter describes the calculations that must be performed to estimate the reliability of a device. We will consider the barest of essentials: setting a switch and reading the state of a switch. In the physical world, both of these operations require the input of energy to change the state of a system of atoms. This is the primary or basic event. Whether the switch is a single molecule or a semiconductor structure containing more than 10^{12} atoms, both of these operations are subject to error. We will discuss the theory that applies to a single read–write event and to the average of many read–write events.

Dynamics of a Molecular Switch

The underlying mechanics of a molecular switch can be quite complex and subtle. Our present investigation emphasizes photochromic molecular switches. One of the most well-studied examples is bacteriorhodopsin, the light-harvesting component in the purple membrane of the halophilic microorganism *Halobacterium halobium* (4, 5). The photo-physical properties of this protein are discussed in detail in Chapters 20–23 in this book. Thus, our discussion will be limited to a very brief overview relevant to the bacteriorhodopsin-based devices that will be examined at the end of this chapter.

The light-adapted form of bacteriorhodopsin undergoes a photochemical cycle that is responsible for transporting protons from the inside (cytoplasm) to the outside (extracellular) of the membrane. The primary molecular event is a *trans* to *cis* photoisomerization around the $C_{13}=C_{14}$

double bond. The initial phototransduction event provides the motive force for the proton transport.

At liquid nitrogen temperature, the native protein photochemically interconverts between a green absorbing state (**bR**, $\lambda_{\max} = 577$ nm) and a red absorbing state (**K**, $\lambda_{\max} = 620$ nm). At near ambient temperature, the native protein photochemically interconverts between a green absorbing state (**bR**, $\lambda_{\max} = 568$ nm) and a blue absorbing state (**M**, $\lambda_{\max} = 412$ nm). These photochromic transformations occur with high-quantum efficiency (4, 5) and at liquid nitrogen temperatures, picosecond reaction times (6–8).

The retinyl chromophore exhibits multiple metastable configurations in both the excited and ground states. The primary event involves a change in the shape of the conformational potential energy surface (due to the excitation of the electrons) followed by a conformational change and a nonradiative decay to the ground state (9). Because the barrier to conformational change in the excited state is small, or negative, absorption of light leads to the exceedingly rapid photoisomerization. In a sense, conformational motion in the excited state acts to effectively gate conformational changes in the ground state.

The dynamics of the initial phototransduction in bacteriorhodopsin exhibit a number of features that complicate the mathematical analysis. First, the rapidity of the conformational change eliminates the assumption of adiabaticity. The nuclear motion must be analyzed as occurring in a changing potential. Many of the standard analyses of tunneling in a double well potential assume weak coupling between the tunneling motion and the other degrees of freedom of the system. This is not the case with bacteriorhodopsin. Finally, as the potential wells become more shallow, states other than those occupying the lowest level in each well must be taken into account. Because of these difficulties, a rigorous mathematical analysis is not yet available. Nevertheless, attempts to solve various special cases of this problem have led to a number of mathematical developments (9–11). At one time or another, analyses involving several areas of pure mathematics have entered the picture (12–21). The difficulty of the mathematical analysis of the double well potential underscores the need for a simplified picture of the dynamics. For this reason and for reasons of quantum uncertainty that will be described in the next section, we must limit ourselves to a probabilistic analysis.

Origins of Error

Although the dynamics of a molecule are deterministic in principle, statistics play a major role in determining the interaction of a molecule with an external perturbation. In the case of photonic events, this result follows from the collapse of the wave function that occurs upon the

absorption of a quantum of light. Previously, we described an example of a switch that is activated via the absorption of a photon of light by a chromophore from a flux of photons. This event has a certain quantum amplitude. That amplitude corresponds to a probability of observation that is never unity, and thus, a highly reliable device based on optical coupling will usually require more than one molecule to participate in the transformation of interest. Another important example is the transfer of an electron from one site to another. The observation of electron transfer from one part of a molecule to another is also governed by quantum statistics. Accordingly, single electron devices, which exploit the motion of a single charge, must also exploit the properties of an ensemble, but in a more subtle way (12–14). Exceptions to this statement are only possible when the write operation is carried out with a stimulus and a barrier to interconversion that far exceeds kT , and when the read operation is nondestructive. The former requirement has typically required extremely low temperatures to be realized (<4 K). Nondestructive read operations are more common in the implementation of certain semiconductor- and molecular-based devices, and we will investigate the reliability of such devices later.

Heisenberg's Uncertainty Principle and State Assignment Error. The time interval allocated to the measurement of the state of a molecular or semiconductor switch is called the aperture time. As the aperture time approaches picosecond intervals, it contributes to the uncertainty in reading the state of a device. Heisenberg's uncertainty principle states that the product of the energy uncertainty and the time uncertainty is equal to or larger than $h/(4\pi)$, where h is Planck's constant ($h \cong 6.6261 \times 10^{-34}$ J s). For example, a device operating with a 1-ps aperture time ($\Delta t = 10^{-12}$ s) will introduce a minimum energy uncertainty of about 3 cm^{-1} . This uncertainty will reduce the probability of correct state assignment, which we denote as $P_{\langle 1 \rangle}$. Birge et al. (21) have described the relation between the time uncertainty and the aperture time for state assignment for a two-state system with Lorentzian state distributions characterized by full-widths at half-maxima of $\check{\nu}_f$. The energy separation of the maxima in the two distributions is represented by $\check{\nu}_s$. This approach describes the minimum error encountered and sets upper limits on the effect of aperture time on reliability. The following equations provide an approximate measure of the effect of aperture time on $P_{\langle 1 \rangle}$ based on Heisenberg's uncertainty principle:

$$P_{\langle 1 \rangle}^h = \frac{2 - \min(1, 2 - 2P_{\langle 1 \rangle}) + \Delta P^h}{2} \quad (1a)$$

$$\Delta P^h = \frac{\alpha_1}{\beta_1} - \frac{\alpha_2}{\beta_2} \quad (1b)$$

where $P_{\langle 1 \rangle}^h$ represents the probability of a correct determination of the state of the device containing a single molecule or a single charge carrier corrected for Heisenberg energy broadening, $P_{\langle 1 \rangle}$ is analogously defined but neglecting the Heisenberg correction; ΔP^h is the Heisenberg correction factor and the remaining terms are defined as follows:

$$\alpha_1 = \tilde{\nu}_f^2 \left[\tilde{\nu}_s \pi + \tilde{\nu}_s \tan^{-1} \left(\frac{-2\tilde{\nu}_s}{\tilde{\nu}_f} \right) + \frac{1}{2} \left[\tilde{\nu}_f \ln \left(\frac{\tilde{\nu}_f^2}{4} \right) \right] - \frac{1}{2} \left[\tilde{\nu}_f \ln \left(\frac{\tilde{\nu}_f^2}{4} + \tilde{\nu}_s^2 \right) \right] \right] \quad (2a)$$

$$\beta_1 = \tilde{\nu}_s \pi (\tilde{\nu}_f^2 + \tilde{\nu}_s^2) \quad (2b)$$

$$\alpha_2 = 2\tilde{\nu}_f^2 \Delta t \left\{ \pi \delta + \delta \tan^{-1} \left(\frac{-2\delta}{\tilde{\nu}_f} \right) + \frac{1}{2} \left[\tilde{\nu}_f \ln \left(\frac{\tilde{\nu}_f^2}{4} \right) - \frac{1}{2} \left[\tilde{\nu}_f \ln \left(\frac{\tilde{\nu}_f^2}{4} + \delta^2 \right) \right] \right] \right\} \quad (2c)$$

$$\beta_2 = (2\tilde{\nu}_s \pi \Delta t + 2\pi \hbar) (\tilde{\nu}_f^2 + \delta^2) \quad (2d)$$

$$\delta = \tilde{\nu}_s + \frac{\hbar}{\Delta t} \quad (2e)$$

where $\hbar = h/(2\pi) \cong 5.3087$ ps cm⁻¹ and the units of the constants assume that the full-width at half-maximum, $\tilde{\nu}_f$, and the energy preparation of the two distributions, $\tilde{\nu}_s$, are in wave numbers (cm⁻¹). Note that α_1 and β_1 depend only on $\tilde{\nu}_s$ and $\tilde{\nu}_f$, whereas α_2 and β_2 are functions of all three variables ($\tilde{\nu}_s$, $\tilde{\nu}_f$, Δt). The correction factor, ΔP^h , is always greater than zero because α_1/β_1 is always greater than α_2/β_2 . Thus, the Heisenberg correction will always lower the probability of correct state determination. However, ΔP^h goes to zero for large separations and large aperture times due to the following limiting behavior:

$$\lim_{\substack{\tilde{\nu}_f \rightarrow 0 \\ \tilde{\nu}_s \rightarrow \infty \\ \Delta t \rightarrow \infty}} \left(\frac{\alpha_1}{\beta_1} \right) = \frac{\alpha_2}{\beta_2}$$

which is physically realistic. That is, for infinite aperture times and infinite energy separations between the two states, Heisenberg's uncertainty principle makes no observable contribution to the state assignment process. In contrast, ΔP^h goes to unity when $\Delta t \rightarrow 0$ and $\tilde{\nu}_s \rightarrow 0$, because under these conditions, $\alpha_1/\beta_1 \rightarrow 1$ and $\alpha_2/\beta_2 \rightarrow 0$. The latter limiting behavior is also physically realistic. As the state assignment aperture

time decreases to zero, energy uncertainty increases to infinity and precludes the differentiation of state. (The limiting case $\tilde{\nu}_s \rightarrow 0$ is essentially a null condition. If there is no energy difference between the two states, it is impossible to differentiate between the two states and therefore $\Delta P^h = 1$.)

The nature of the full-width at half-maximum term, $\tilde{\nu}_f$, requires further discussion. This term has origins in two separate physical parameters. The first involves the distribution of energies that define the observed states of the two-level device. For example, a photochromic switch has an absorption spectrum associated with each state. In this case, $\tilde{\nu}_f$ is equal to the full-width at half-maximum of the absorption spectrum, $\tilde{\nu}_{\text{abs}}$. For an electronic gate, $\tilde{\nu}_f$ is given by

$$\tilde{\nu}_f \cong \frac{\Delta\Delta P\Delta\tau}{hc} \cong 50341 \text{ (cm}^{-1}\text{)} \Delta\Delta P \text{ (}\mu\text{W)}\Delta t \text{ (ps)} \quad (3)$$

where $\Delta\Delta P$ is the error in the output power in microwatts and Δt is the aperture time in picoseconds. The second contribution to $\tilde{\nu}_f$ is relevant in those systems that probe the state of the device with an external electromagnetic field with an energy bandwidth of $\tilde{\nu}_\lambda$. This contribution is folded into the total full-width at half-maximum by taking the square root of the sum of the squares of the two contributions (i.e., $\tilde{\nu}_f = \sqrt{\tilde{\nu}_{\text{abs}}^2 + \tilde{\nu}_\lambda^2}$). This latter contribution can usually be ignored if narrow bandwidth lasers are used to probe the device state. In contrast, capacitance effects in microwave semiconductor circuits often generate appreciable energy bandwidths that dominate the calculation of $\tilde{\nu}_f$ and limit the frequency of digital microwave circuits. Although it is not the principal subject of this chapter, it is worth noting that the previous equations apply equally well to the analysis of Heisenberg aperture effects on high-frequency semiconductor devices.

The Probabilistic Analysis. Our basic assumption is that we are given a system that changes state upon the absorption of energy. If this system is embodied by an ensemble of molecules, state changes can be detected by a shift in absorption lines. In many of the systems to be examined later, our ensemble is a sample of photochromic molecules that exist in two conformations: state A or state B, absorbing photons primarily at wavelengths λ_0 and λ_1 , respectively. Given that the change in state does not reverse spontaneously with a high probability, such an ensemble may be characterized as a switch. Absorption of light at wavelength λ_0 will change some of the molecules in conformation A to conformation B and exposure to light at wavelength λ_1 will change molecules in conformation B to conformation A. This is the write operation. We can characterize the write operation by means of two matrices:

$$M_0 = \begin{pmatrix} p_{AA}^0 & p_{AB}^0 \\ p_{BA}^0 & p_{BB}^0 \end{pmatrix}, \quad (4a)$$

$$M_1 = \begin{pmatrix} p_{AA}^1 & p_{AB}^1 \\ p_{BA}^1 & p_{BB}^1 \end{pmatrix} \quad (4b)$$

where p_{AB}^1 represents the probability that a molecule in state A will shift to state B when it absorbs a photon of light at wavelength λ_i . In physical systems these probabilities are dependent on a number of factors; we assume that they are fixed in advance. The entries in each row of the two matrices sums to unity. We will take our sample to have N molecules and designate exposure of the sample to light at wavelength λ_0 as writing a 0 to the sample. The first source of error is due to conversions failing to take place or going the wrong way; for example, if p_{AA}^0 or p_{BA}^0 is nonzero, then it is possible that the write operation will fail. When this is so, the state of the ensemble is subject to random variation. Generally such an ensemble will have two distinct probability distributions. In particular we define $P_{0,s}(M)$ to be the probability that the ensemble contains M molecules in state A after writing a 0 to the ensemble and $P_{1,s}(M)$ similarly gives the probability of M molecules in state A after writing a 1 to the ensemble. The letter "s" refers to the setting operation. We assume that the write operation is sufficient to bring the ensemble to an equilibrium distribution, that is, that the state before the write has negligible effect. The notion of a distribution of states generalizes to a variety of systems, so we can take it as basic to the mathematical analysis of the read and write operations.

The read operation is the measurement of the absorption of light in the sample. The state of the ensemble (i.e., the relative fractions of molecules in A and B states) is to be inferred by observing the absorption at λ_0 or λ_1 or both. In this case we are measuring a population, and the absorption is subject to random variation. Thus, a second source of error is intrinsic to the measurement process, independent of the measurement apparatus. This situation is illustrated in Figure 1.

Generally, we will make one or more measurements on the ensemble. Referring to Figure 1, if the measurements are on one side of a preassigned threshold (for example, if the measured absorption places the ensemble in the 0 region), we will assign the nominal value 0 to the ensemble; otherwise, we will assign the nominal value 1. It is desirable that the two probability distributions of measurements be well separated. To be more precise, we want the operation of writing a value $i = 0$ or 1 on our sample to produce a well-distinguished distribution of ensemble states, $P_{i,s}(x)$. Assume the value 0 has been written to the sample. Referring again to Figure 1, we require that the integral of $P_{0,s}(x)$ over the 0 region, R_0 , should be very close to unity, the integral of $P_{0,s}(x)$ over

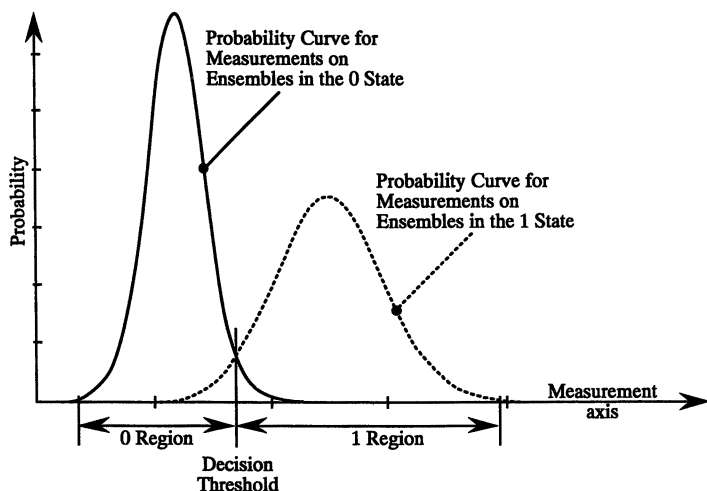


Figure 1. Measurement probabilities for ensembles to which a 0 or a 1 has been previously written. The decision threshold is chosen to optimize reliability while simultaneously providing a symmetric error. If this is a photochromic system, the measurement axis is in wavelength and the vertical axis represent the probability of light absorption for the ensemble. The figure assumes complete interconversion.

the 1 region should also be close to zero, and that reverse conditions hold for $P_{1,s}$. Because of errors in measurement we also require that the peaks of the distributions $P_{0,s}$ and $P_{1,s}$ be well separated.

The possibility that our measurement process changes the state of the ensemble is implicit in the previous discussion. This is always true for photochromic read processes. Thus, we must often write after a read operation to restore the state of the switch. As we will show later, a random sequence of reads and writes on a large sample may produce one of several well-separated states. A determination of the ensemble dynamics, that is, the change of state following exposure to various mixtures of light requires, in addition, the determination of a number of transition probabilities. Finally, to give some realism to the model, we can assume that a certain small fraction of the molecules may degrade to an unresponsive state upon exposure to light. We will discuss the consequences of this in the final section.

Analysis of Probabilities

The Discrete Case. We will begin with a simple case in which we assume all molecules can be read either in state A or state B and we will develop a formula for the error that can be attributed to either the

first or second cause described earlier. We will ignore errors in the measurement apparatus in this section. In the case of the system of photochromic molecules as described in the previous section, this corresponds to reading the state of an ensemble with one wavelength of light, say λ_i . We can assume that the ensemble contains N molecules and that N_A are in state A. The probability for an absorption event for a single molecule is $k_{A,a}^i$ if the molecule is in state A and $k_{B,a}^i$ if the molecule is in state B. For future reference we define the absorption probability matrix:

$$M_{0,1,a} = \begin{pmatrix} k_A^0 & k_B^0 \\ k_A^1 & k_B^1 \end{pmatrix} \quad (5)$$

In the remainder of this section we will assume our read operation involves the use of a single wavelength. We will treat the general case in a later section.

We use the convention that the conditional probability, $P_a(M_0 | N_0)$, is the probability that attenuation due to absorption indicates that M_0 molecules are in state A, given that N_0 molecules are actually in state A. The total absorption is due to contributions from two processes. The first process reads some portion, say $M_0 - K$ of the A molecules, as A. The second process reads some portion, say K of the B molecules as A. The joint probability of reading the two populations in this way is defined as $P_{ae}(K)$. Because the returns from the two populations are independent events the probability $P_{ae}(K)$ is given by the product:

$$P_{ae}(K) = \binom{N_0}{M_0 - K} (k_A^i)^{(M_0 - K)} (1 - k_A^i)^{(N_0 - M_0 + K)} \\ \times \binom{N - N_0}{K} (1 - k_B^i)^K (k_B^i)^{(N - N_0 - K)} \quad (6)$$

where the first term is given by the binomial probability distribution for the return from reading the A population and the second term from the binomial probability distribution for the return from the B population. This formula is obtained by elementary techniques in probability theory (16). Note that the values of $M_0 - K$ and K are limited to be less than N and $N - N_0$, respectively, and that $P_{ae}(K)$ does not represent the probability of K errors. The actual number of read errors in the measurement of the state of the ensemble is $N_0 - M_0 + 2K$.

To obtain the conditional probability, we have to sum over all possibilities for errors.

$$P_a(M_0|N_0) = \sum_{K_1 \leq K \leq K_2} P_{ae}(K) = \sum_{K_1 \leq K \leq K_2} \binom{N_0}{M_0 - K} (k_A^i)^{(M_0 - K)} \\ \times (1 - k_A^i)^{(N_0 - M_0 + K)} \times \binom{N - N_0}{K} (1 - k_B^i)^K (k_B^i)^{(N - N_0 - K)} \quad (7)$$

In equation 7 $K_1 = M_0 - N_0$ and $K_2 = N - N_0$. This expression is exact.

The calculation of error rates requires the introduction of the distribution of ensemble states, $P_{0,s}(K)$. Because assignment to a state depends upon the relation of an absorption value to a preassigned threshold, we must sum over the possibilities for an error in assignment. We assume that we make one perfect absorption measurement on the ensemble and compare it with a threshold value T . We assign the value 0 or 1 depending on whether the absorption is greater or less than T . The probability of making an error in reading the preset state of the ensemble is obtained by summing over all possibilities for exceeding the threshold. Specifically,

$$P_{0,e} = \sum_{M > T} P_a(M|N_0) P_{0,s}(N_0) \quad (8)$$

where $P_{0,s}(N_0)$ is the probability that N_0 molecules are in state A after writing a 0 to the ensemble. This formula represents only those errors intrinsic to the absorption process and does not take errors in the measurement apparatus into account.

The Continuous Case. To proceed further with the analysis, we must consider errors due to the measurement apparatus. Although we could continue with our analysis of the discrete case, it is more appropriate to study the continuous case. This is because most measurements would be done with large ensembles. Furthermore, we can simplify the expressions somewhat without losing sight of the essentials. If the ensemble is large, then the normal distribution is a good approximation for the binomial distribution. The normal distribution, P_g , is written

$$P_g(x) = \frac{1}{\sigma\sqrt{2\pi}} \text{Exp}\left[-\left(\frac{x - \mu}{2^{1/2}\sigma}\right)^2\right] \quad (9)$$

where μ is the mean and σ is the standard deviation of the distribution. If we define the binomial probability distribution, $P_{b,p,N}$ via

$$P_{b,p,N}(K) = \binom{N}{M} p^{(M)} (1 - p)^{(N - M)} \quad (10)$$

replacing the mean, μ , by pN and the standard deviation, σ , by $\sqrt{Np(1 - p)}$ in equation 9 gives a good approximation.

For intermediate values of N a correction factor is sometimes used (17):

$$P_{b,p,N}(K) \approx \frac{1}{\sigma\sqrt{2\pi}} \text{Exp}\left[-\left(\frac{K-\mu}{2^{1/2}\sigma}\right)^2\right] \times \left[1 + \frac{N(p-3p^2+2p^3)}{3!\sigma^3} \left(\frac{K^3}{\sigma^3} - \frac{3K}{\sigma}\right)\right] \quad (11)$$

Thus, to obtain the normal approximation to the binomial distribution, we need only compute the mean and standard deviation for the binomial distributions and substitute these values into an integral of a product of Gaussians representing the sum in equations 7 and 8.

We can generalize the discussion of equations 7 through 10 to multiple measurements of samples that return values in a continuous region. We will, therefore, consider the case in which two measurements are made. We will consider the measurement process. We will use small letters to denote fractions, that is, we will consider the case where some fraction, say x_0 is in state A and a second fraction, say x_1 is in state B. Although there is the possibility of a remainder $1 - (x_0 + x_1)$ being in an unresponsive state (perhaps through degradation), we will not consider it, so $x_1 = 1 - x_0$. We will say that the sample is in state (x_0, x_1) . The expression $P_a[(z_0, z_1)|(x_0, x_1)]$ represents the probability density that some fraction, z_0 , of light at wavelength λ_0 and some fraction z_1 of light at wavelength λ_1 is absorbed in the sample, given that the sample is in state (x_0, x_1) . We will also consider errors in the measurement process. The conditional distribution $P_m[(y_0, y_1)|(z_0, z_1)]$ gives the probability that absorptions are measured as (y_0, y_1) when the actual absorptions are (z_0, z_1) . We can express the conditional probability arising from the read operation as an integral:

$$P_r[(y_0, y_1)|(x_0, x_1)] = \int_0^1 \int_0^1 P_m[(y_0, y_1)|(z_0, z_1)] P_a[(z_0, z_1)|(x_0, x_1)] dz_0 dz_1 \quad (12)$$

In most cases the light measurement process is independent of absorption in the sample, so we can write

$$P_m[(y_0, y_1)|(z_0, z_1)] = P_m[(y_0 - z_0, y_1 - z_1)] \quad (13)$$

Next we define some integrals that reflect the results of measurements on the random ensembles $P_a[(y_0, y_1)|i]$:

$$E_{0,0} = \int_{R_0} P_r[(y_0, y_1) | 0] dy_1 dy_2 \quad (14a)$$

$$E_{0,1} = \int_{R_1} P_r[(y_0, y_1) | 0] dy_1 dy_2 \quad (14b)$$

$$E_{1,0} = \int_{R_0} P_r[(y_0, y_1) | 1] dy_1 dy_2 \quad (14c)$$

$$E_{1,1} = \int_{R_1} P_r[(y_0, y_1) | 1] dy_1 dy_2 \quad (14d)$$

The values $E_{i,j}$ constitute the entries of the confusion matrix for reading the state of the sample after writing either a 0 or a 1. In particular $E_{0,1}$ and $E_{1,0}$ give the error rates for reading ensembles in the 0 and 1 states, respectively.

Equilibrium Conditions. We will assume, for the moment, that our ensemble is very large, that is, σ is very close to zero. We will also assume that the operation of writing allows the sample to come to equilibrium. We will also assume that none of the molecules in the sample degrade to an unreactive state. In this case the distribution $P_{i,s}$ can be represented by a δ -function:

$$P_{i,s}(x_0, x_1) = \delta_{\mu_{i,s}}(x_0) \delta_{1-\mu_{i,s}}(x_1) \quad (15)$$

where the value $\mu_{i,s}$ gives the expected proportion of molecules in state A. In order to track the state of the ensemble, we must introduce some transition matrices. We define

$$M_{i,t} = \begin{pmatrix} p_{AA,t}^i & p_{AB,t}^i \\ p_{BA,t}^i & p_{BB,t}^i \end{pmatrix} \quad (16)$$

where the entries of the matrix $M_{i,t}$ are the probabilities that the transitions will occur upon exposure to light at wavelength λ_i . The entries of these matrices are related to the entries of the matrices M_i via

$$p_{AA,t}^i = 1 - k_A^i + k_A^i p_{AA}^i \quad (17a)$$

$$p_{AB,t}^i = k_A^i p_{AB}^i \quad (17b)$$

$$p_{AB,t}^i = k_A^i p_{AB}^i \quad (17c)$$

and

$$p_{BB,t}^i = 1 - k_B^i + k_B^i p_{BB}^i \quad (17d)$$

We are assuming that multiple absorptions are negligible. Referring to the matrices $M_{i,t}$, we have the normalized expectations:

$$\mu_{i,s} = \frac{p_{BA,t}^i}{1 + p_{BA,t}^i - p_{AA,t}^i} \quad (18)$$

The expression for $\mu_{i,s}$ is obtained by solving the equation

$$\begin{pmatrix} p_{AA,t}^i & p_{BA,t}^i \\ p_{AB,t}^i & p_{BB,t}^i \end{pmatrix} \begin{pmatrix} \mu_{i,s} \\ 1 - \mu_{i,s} \end{pmatrix} = \begin{pmatrix} \mu_{i,s} \\ 1 - \mu_{i,s} \end{pmatrix} \quad (19)$$

and using the relations $p_{AA,t}^i + p_{AB,t}^i = 1$ and $p_{BA,t}^i + p_{BB,t}^i = 1$.

Calculations for Ensembles with Known Starting States. Both the assumptions of long writing times and large ensembles must be relaxed for practical calculations. We will examine the situation for smaller ensembles. The basic question we wish to answer is what is the distribution, P_s , of our ensemble after repeated exposures to light at various wavelengths. The probabilities for molecular transitions as the result of repeated writes can be described as matrix products:

$$\begin{pmatrix} p_{AA,t} & p_{BA,t} \\ p_{AB,t} & p_{BB,t} \end{pmatrix} = \begin{pmatrix} p_{AA,t}^{i_k} & p_{BA,t}^{i_k} \\ p_{AB,t}^{i_k} & p_{BB,t}^{i_k} \end{pmatrix} \begin{pmatrix} p_{AA,t}^{i_{k-1}} & p_{BA,t}^{i_{k-1}} \\ p_{AB,t}^{i_{k-1}} & p_{BB,t}^{i_{k-1}} \end{pmatrix} \cdots \begin{pmatrix} p_{AA,t}^{i_1} & p_{BA,t}^{i_1} \\ p_{AB,t}^{i_1} & p_{BB,t}^{i_1} \end{pmatrix} \quad (20)$$

Here, we are not assuming that the sample comes to equilibrium during each exposure. Because the transition probabilities for repeated writes can be treated in the same way as single writes, we can write the probability distribution P_s for an ensemble of N molecules as the convolution of Gaussians:

$$\begin{aligned} P_s[(z, 1-z)|(x, 1-x)] &\approx \int_0^z dy \frac{1}{\sigma_A \sqrt{2\pi}} \text{Exp} \left[- \left(\frac{y - p_{AA,t}x}{2^{1/2}\sigma_A} \right)^2 \right] \\ &\quad \times \frac{1}{\sigma_B \sqrt{2\pi}} \text{Exp} \left[- \left(\frac{z - \frac{xy}{(1-x)} + p_{BA,t}(1-x)}{2^{1/2}\sigma_B} \right)^2 \right] \\ &= \frac{1}{\sigma_t \sqrt{2\pi}} \text{Exp} \left[- \left(\frac{z - \mu_t}{2^{1/2}\sigma_t} \right)^2 \right] \quad (21) \end{aligned}$$

The last equality follows from the well-known fact that the convolution of two Gaussian distributions is a Gaussian distribution (18). We can calculate the mean and standard deviation from the moment generating function (19) and the discussion following equation 10. In particular we have:

$$\sigma_{A,t} = \frac{\sqrt{p_{AA,t}(1 - p_{AA,t})}}{\sqrt{xN}} \quad (22a)$$

$$\sigma_{B,t} = \frac{\sqrt{p_{BA,t}(1 - p_{BA,t})}}{\sqrt{(1-x)N}} \quad (22b)$$

$$\mu_t = p_{AA,t}x + p_{BA,t}(1 - x) \quad (22c)$$

$$\sigma_t = \sqrt{x^2(\sigma_{A,t})^2 + (1-x)^2(\sigma_{B,t})^2} \quad (22d)$$

Equation 21 is analogous to equation 8 for the discrete case. Before we consider the general case of finite ensembles and short exposures, we note that repeated exposures to a single wavelength, no matter how short each individual exposure, cause a sample to converge to an equilibrium state. This is because the eigenvalues of the matrices M_t are 1 and $p_{AA,t} - p_{BA,t}$ with corresponding eigenvectors $(\mu_{i,s}, 1 - \mu_{i,s})$ and $(\mu_{i,s}, -\mu_{i,s})$, respectively. Because $p_{AA,t} - p_{BA,t}$ is less than unity, the eigenspace associated with $p_{AA,t} - p_{BA,t}$ collapses to zero. Furthermore, the product of matrices converges to a definite value, so each of the distributions $P_{i,s}(x_1, x_2)$ will tend to a limit that depends on the initial state of the ensemble. Thus, to make some estimate of error, we must make a maximum uncertainty assumption to obtain an upper estimate on the error rates $E_{0,1}$ and $E_{1,0}$ in equation 14. We will return to this point after discussing the other distributions that enter into the error calculation.

The situation is much more complicated if we are exposing the sample to several different types of exposure with more than one wavelength of light. If we are not careful in limiting the admissible sequences of operations, it is possible that the sample will cycle between several intermediate states or even will behave chaotically. More precisely, it has been shown that a sequence of linear transforms, chosen at random from almost any finite set of two-dimensional transforms and then applied to any starting vector in the plane will generate a fractal pattern (19). Equation 19 shows that the parameters μ_t and σ_t can inherit that chaotic behavior, because they depend upon an (arbitrary) starting point. Put another way μ_t and σ_t may fluctuate chaotically as we add successive transforms to the chain described by equation 20. Because this is the typical case, the possibility of chaotic processes entering into the operation of a device composed of a large ensemble of switches should be considered in the design of that device.

We now assume an arbitrary sequence of light exposures, which may be associated with both read and write operations, followed by a final read operation. If the read and write operation are at a single wavelength, then the photon absorption probabilities for wavelengths λ_0 are given as the top row and the photon absorption probabilities for wavelength λ_1 are given as the bottom row in a product of matrices as follows:

$$\begin{pmatrix} k_{A0} & k_{B0} \\ k_{A1} & k_{B1} \end{pmatrix} = \begin{pmatrix} k_{A,a}^0 & k_{B,a}^0 \\ k_{A,a}^1 & k_{B,a}^1 \end{pmatrix} \begin{pmatrix} p_{AA,t}^{i_k} & p_{BA,t}^{i_k} \\ p_{AB,t}^{i_k} & p_{BB,t}^{i_k} \end{pmatrix} \begin{pmatrix} p_{AA,t}^{i_{k-1}} & p_{BA,t}^{i_{k-1}} \\ p_{AB,t}^{i_{k-1}} & p_{BB,t}^{i_{k-1}} \end{pmatrix} \\
 \dots \begin{pmatrix} p_{AA,t}^{i_1} & p_{BA,t}^{i_1} \\ p_{AB,t}^{i_1} & p_{BB,t}^{i_1} \end{pmatrix} \quad (23)$$

where the transition matrices are associated with the read and write operations. As with the analysis of distribution functions given by equations 21 and 22, the absorption probabilities are Gaussian distributed with mean μ_a^0 and standard deviation σ_a^0 . These quantities depend on the initial ensemble state. Assume we start with state $(x_0, 1 - x_0)$. Then the following equations give the mean and standard deviation for the λ_0 absorption probability distribution.

$$\sigma_{A,a}^0 = \frac{\sqrt{k_{A0}(1 - k_{A0})}}{\sqrt{x_0 N}} \quad (24a)$$

$$\sigma_{B,a}^0 = \frac{\sqrt{k_{B0}(1 - k_{B0})}}{\sqrt{(1 - x_0) N}} \quad (24b)$$

$$\mu_a^0 = k_{A0}x_0 + k_{B0}(1 - x_0) \quad (24c)$$

$$\sigma_a^0 = \sqrt{x^2(\sigma_{A,a}^0)^2 + (1 - x)^2(\sigma_{B,a}^0)^2} \quad (24d)$$

Similar formulas hold for λ_1 absorption probabilities.

Read Operations at Multiple Wavelengths. If some of the read operations are via multiple wavelengths, then the analysis in the equations still holds, but the transition probability matrices and absorption probability matrices are more difficult to define. The ensemble state transitions associated with such reads do not generally have the same simple relationship with the single molecule transition probabilities that the ensemble state transitions associated with single wavelength exposures have with single molecule transition probabilities. One problem is that multiple absorptions become more likely when several wavelengths are administered simultaneously. A more serious problem arises from the noncommutativity of operations. The result of exposure to wavelength λ_0 followed by exposure to wavelength λ_1 is not the same as the result of exposure to λ_1 followed by exposure to wavelength λ_0 . For this reason, there is no easy way to assign a transition matrix to simultaneous exposure. We may subdivide the interval of exposure and take the result of exposure to several wavelengths as the product of the results over the subintervals. Formally, if we define

$$M_{i,t,n} = \begin{pmatrix} -\frac{k_A^i}{n} + \frac{k_A^i}{n} p_{AA}^i & \frac{k_B^i}{n} p_{BA}^i \\ \frac{k_A^i}{n} p_{AB}^i & -\frac{k_B^i}{n} + \frac{k_B^i}{n} p_{BB}^i \end{pmatrix} \quad (25)$$

then the transition matrix for simultaneous exposure is given by

$$M_{0+1,t} = \lim_{n \rightarrow \infty} (I + M_{0,t,n} + M_{1,t,n})^n \quad (26)$$

We can write similar expressions for the absorptions. If we define

$$M_{0+1,a,n} = \begin{pmatrix} \frac{k_A^0}{n} & \frac{k_B^0}{n} \\ \frac{k_A^1}{n} & \frac{k_B^1}{n} \end{pmatrix} \quad (27)$$

then y_0 photons of wavelength λ_0 and y_1 photons of wavelength λ_0 are absorbed. In particular:

$$\begin{pmatrix} y_0 \\ y_1 \end{pmatrix} = N \lim_{n \rightarrow \infty} \left(\sum_{k=1}^n M_{0+1,a,n} (M_{0+1,t,n})^k \right) \begin{pmatrix} x_0 \\ x_1 \end{pmatrix} \equiv M_{0+1,a} \begin{pmatrix} x_0 \\ x_1 \end{pmatrix} \quad (28)$$

where N is a suitable normalization constant, (x_0, x_1) is the state of the ensemble, and $M_{0+1,t,n}$ is defined in a similar way to $M_{i,t,n}$.

The matrices $M_{0+1,t}$ and $M_{0+1,a}$ can be written in terms of matrix exponentials and integrals of matrix exponentials. Specifically,

$$M_{0+1,t}(u) = \text{Exp}[u \cdot (M_{0,t} + M_{1,t} - 2I)] \quad (29a)$$

$$M_{0+1,a} = \int_0^1 M_{0,1,a} M_{0+1,t}(u) du \quad (29b)$$

where u is the "time" parameter. Equations 20 through 22 and equations 24 hold with some of the $M_{i,t}$ replaced by $M_{0+1,t}$ or $M_{0,1,a}$ replaced by $M_{0+1,a}$.

The next step in our analysis of probabilities is to consider errors in the measurement apparatus. We will assume that measurement errors are Gaussian distributed. Then by equation 13,

$$P_m[(y_0, y_1) | (z_0, z_1)] \approx \frac{1}{\sigma_m^0 \sqrt{2\pi}} \text{Exp} \left[-\left(\frac{y_0 - z_0}{2^{1/2} \sigma_m^0} \right)^2 \right] \\ \times \frac{1}{\sigma_m^1 \sqrt{2\pi}} \text{Exp} \left[-\left(\frac{y_1 - z_1}{2^{1/2} \sigma_m^1} \right)^2 \right] \quad (30)$$

Furthermore, from equation 9

$$P_r[(y_0, y_1) | (x_0, x_1)] \approx \int_0^1 \frac{1}{\sigma_m^0 \sqrt{2\pi}} \text{Exp} \left[- \left(\frac{y_0 - z_0}{2^{1/2} \sigma_m^0} \right)^2 \right] \frac{1}{\sigma_a^0 \sqrt{2\pi}} \text{Exp} \left[- \left(\frac{z_0 - \mu_a^0}{2^{1/2} \sigma_a^0} \right)^2 \right] dz_0 \times \int_0^1 \frac{1}{\sigma_m^1 \sqrt{2\pi}} \text{Exp} \left[- \left(\frac{y_1 - z_1}{2^{1/2} \sigma_m^1} \right)^2 \right] \frac{1}{\sigma_a^1 \sqrt{2\pi}} \text{Exp} \left[- \left(\frac{z_1 - \mu_a^1}{2^{1/2} \sigma_a^1} \right)^2 \right] dz_1 \quad (31)$$

Each integral is the convolution of Gaussians, so the joint conditional probability is the product of Gaussian distributions

$$P_r[(y_0, y_1) | (x_0, x_1)] \approx \frac{1}{\sigma_r^0 \sqrt{2\pi}} \text{Exp} \left[- \left(\frac{y_0 - \mu_r^0}{2^{1/2} \sigma_r^0} \right)^2 \right] \frac{1}{\sigma_r^1 \sqrt{2\pi}} \text{Exp} \left[- \left(\frac{y_1 - \mu_r^1}{2^{1/2} \sigma_r^1} \right)^2 \right] \quad (32)$$

where the parameters σ_r^0 and μ_r^0 are derived via equation 24 and the rules for convolutions. In particular,

$$\mu_r^0 = \mu_a^0 \quad (33a)$$

$$\sigma_r^0 = \sqrt{(\sigma_m^0)^2 + (\sigma_a^0)^2} \quad (33b)$$

Similar equations hold for σ_r^1 and μ_r^1 .

Ensembles with Unknown Starting States. The final step in our analysis is to consider the effect of uncertainty as to the initial state (x_0, x_1) of the ensemble. We take this into account by considering the probabilities on the molecular level. For an ensemble set to state 0 we assume that an individual molecule has probability p_{0A} of being in state A and probability p_{0B} of being in state B, where we can take $p_{0A} = \mu_{0,s}$, and so on. The terms p_{1A} and p_{1B} denote the corresponding probabilities for an ensemble in state 1. Then the photon absorption probabilities are as follows

$$p_{0,a}^0 = P_{0A} k_{A,a}^0 + p_{0B} k_{B,a}^0 \quad (34a)$$

$$p_{0,a}^1 = p_{0A} k_{A,a}^1 + p_{0B} k_{B,a}^1 \quad (34b)$$

and similarly for ensembles in state 1. Then we can approximate the absorption probability for an ensemble in state 0:

$$P_a[(y_0, y_1) | 0] = \frac{1}{\sigma_{0,a}^0 \sqrt{2\pi}} \text{Exp} \left[- \left(\frac{y_0 - \mu_{0,a}^0}{2^{1/2} \sigma_{0,a}^0} \right)^2 \right] \frac{1}{\sigma_{0,a}^1 \sqrt{2\pi}} \text{Exp} \left[- \left(\frac{y_1 - \mu_{0,a}^1}{2^{1/2} \sigma_{0,a}^1} \right)^2 \right] \quad (35)$$

where

$$\sigma_{0,a}^0 = \frac{\sqrt{p_{0,a}^0(1-p_{0,a}^0)}}{\sqrt{N}} \quad (36a)$$

$$\mu_{0,a}^0 = p_{0,a}^0 \quad (36b)$$

and

$$\sigma_{0,a}^1 = \frac{\sqrt{p_{0,a}^1(1-p_{0,a}^1)}}{\sqrt{N}} \quad (37a)$$

$$\mu_{0,a}^1 = p_{0,a}^1 \quad (37b)$$

Similar formulas hold for an ensemble in state 1. Read probabilities can be calculated as in equations 12, 13, and 31:

$$P_r[(y_0, y_1) | i] = \int_0^1 \int_0^1 P_m[(y_0, y_1) | (z_0, z_1)] P_a[(z_0, z_1) | i] dz_0 dz_1 \quad \text{and so on} \quad (38)$$

Recall that the values $E_{i,j}$ defined by equation 14 constitute the entries of the confusion matrix for reading the state of the sample after writing either a 0 or a 1. In particular $E_{0,1}$ and $E_{1,0}$ give the error rates for reading ensembles in the 0 and 1 states, respectively.

The error terms may be calculated by substitution of equations 30, 36, 37, and 38 into equations 14. To make definite calculations we need a parametric description of the regions R_0 and R_1 . If an optimal decision criteria is desired, that is, a threshold curve that minimizes $E_{0,1}$ and $E_{1,0}$ then the regions R_0 and R_1 will be separated by a curve which is a conic section. This is because the minimal error is associated with the threshold curve. This can be seen by observing that moving the threshold curve away from C increases the error. In particular, C is the curve on which

$$C = \{(y_1, y_2) | P_r[(y_1, y_2) | 0] = P_r[(y_1, y_2) | 1]\} \quad (39)$$

$$\begin{aligned} & \frac{1}{\sigma_{0,r}^0 \sqrt{2\pi}} \text{Exp} \left[- \left(\frac{y_1 - \mu_{0,r}^0}{2^{1/2} \sigma_{0,r}^0} \right)^2 \right] \frac{1}{\sigma_{0,r}^1 \sqrt{2\pi}} \text{Exp} \left[- \left(\frac{y_2 - \mu_{0,r}^1}{2^{1/2} \sigma_{0,r}^1} \right)^2 \right] \\ &= \frac{1}{\sigma_{1,r}^0 \sqrt{2\pi}} \text{Exp} \left[- \left(\frac{y_1 - \mu_{1,r}^0}{2^{1/2} \sigma_{1,r}^0} \right)^2 \right] \frac{1}{\sigma_{1,r}^1 \sqrt{2\pi}} \text{Exp} \left[- \left(\frac{y_2 - \mu_{1,r}^1}{2^{1/2} \sigma_{1,r}^1} \right)^2 \right] \quad (40) \end{aligned}$$

The fact that this is a conic section can be seen by taking the logarithm of both sides. Also note that the $\mu_{j,r}^i$ and $\sigma_{j,r}^i$ are derived from the $\mu_{j,a}^i$ and $\sigma_{j,a}^i$ via an equation similar to equation 33.

Specific Devices

These calculations are applied to some specific examples by Birge et al. (20, 21). The parameters used in the exposition in this section are derived

from references 20 and 21 and the references cited therein. We summarize some of the results of the second paper and add a new discussion of the reliability of three-dimensional optical memories. In reference 21 Birge et al. make the basic assumption that the ensemble state assignments for the "0" and "1" states are given in terms of a probability for the correct assignment of the state of a single switch. This probability is denoted $P_{\langle 1 \rangle}$. To simplify the calculations, quantum yield ratios are arbitrarily assigned to be 0.25 for the 0 state and 0.75 for the 1 state, so that the expected ensemble yields μ_0 and μ_1 are taken to be

$$\mu_0 = N(0.75 - 0.5P_{\langle 1 \rangle}) \quad (41a)$$

$$\mu_1 = N(0.25 + 0.5P_{\langle 1 \rangle}) \quad (41b)$$

Here, N is the number of switches in the ensemble. Because of the uncertainties in prior state, the two extreme values for the standard deviation are given as follows:

$$\sigma_{\min} = [NP_{\langle 1 \rangle}(1 - P_{\langle 1 \rangle})]^{1/2} \quad (42)$$

$$\sigma_{\max} = [N(0.25 + 0.5P_{\langle 1 \rangle})(0.75 - 0.5P_{\langle 1 \rangle})]^{1/2} \quad (43)$$

The values of σ_{\min} and σ_{\max} apply to both the 0 state and the 1 state. Error probabilities are defined in terms of the error function:

$$P_{\min}^{\text{error}} = \text{Erf} \left[\frac{N/2 - \mu_1}{(2)^{1/2} \sigma_{\min}} ; -\frac{\mu_1}{(2)^{1/2} \sigma_{\min}} \right] = 10^{-\xi_{\min}} \quad (44)$$

$$P_{\max}^{\text{error}} = \text{Erf} \left[\frac{N/2 - \mu_1}{(2)^{1/2} \sigma_{\max}} ; -\frac{\mu_1}{(2)^{1/2} \sigma_{\max}} \right] = 10^{-\xi_{\max}} \quad (45)$$

The error functions are as usually defined:

$$\text{Erf} [Z] = \frac{2}{(\pi)^{1/2}} \int_0^Z \text{Exp}(-t^2) dt \quad (46a)$$

$$\text{Erf} [Z_0; Z_1] = \text{Erf} [Z_1] - \text{Erf} [Z_0] \quad (46b)$$

Electrostatic Switches. Electrostatic molecular switches operate by undergoing a conformational or configurational rearrangement that changes the magnitude and direction of the static dipole moment (20, 21, 23–25). Switching is initiated by applying a field in the direction of the dipole moment of the desired final state. The generic molecular switch described in reference 20 yields a unit component reliability of $P_{\langle 1 \rangle} = 0.702$, which is relatively high for molecular-based devices and comparable to solid-state devices, assuming one molecule is equivalent

to a single charge carrier. The reliability curve shown in Figure 2 indicates that approximately 1600 molecules must be included in the ensemble to generate adequate reliability ($\xi \geq 10$), ensemble sizes that are comparable to the number of charge carriers required for high-reliability, high-frequency semiconductor devices (25–28).

Optically Coupled Not And (NAND) Gates. Optically coupled molecular gates have the potential of operating at subpicosecond switching times with excellent reliability due to optical ensemble averaging. Prototype gates under investigation are activated by picosecond laser pulses and have chromophoric outputs that are monitored via continuous-wave monochromatic light (28–30). The charge-transfer tunneling-reset design proposed in reference 20 has a unit component reliability of $P_{\langle 1 \rangle} = 0.525$, which is significantly lower than the electrostatic switch described previously due primarily to the use of optical coupling to activate and monitor the state of the device. This use of optical coupling also leads to an estimated limiting reliability factor of $\xi = 22$, a value three orders of magnitude lower (in absolute scale) relative to the electrostatic gate. The reliability versus ensemble size curve for the optically coupled Not And (OCNAND) gate shown in Figure 2 indicates that approximately 130,000 molecules must be included in the ensemble to generate adequate reliability ($\xi \geq 10$).

Optical Random Access Memory Based on Bacteriorhodopsin. Bacteriorhodopsin has been investigated for use in optically coupled random access memories (RAMs) (29), picosecond photodetectors (31, 32), optical disk storage (33), spatial light modulators (34), various types of holography (35–42), and in Fourier-transform optical associative memories (34). Applications of this protein to optical memories and

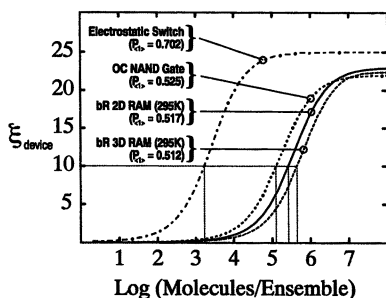


Figure 2. The effect of ensemble size on the reliability of selected molecular devices represented by plotting ξ as a function of \log_{10} (molecules/ensemble). The reliability parameter, ξ , is related to the probability of error in the measurement of the state of the ensemble (device) by the function, $P_{\text{device error}} = 10^{-\xi}$. Note that as ξ increases, reliability increases logarithmically. The error probability, $P_{\text{device error}}$, derives from statistical error in the measurement of state as well as the probability that the number of molecules in the correct conformation A versus conformation B can stray from their expectation values based on statistical considerations.

optical computing have been reviewed recently by Birge (4, 5). Chapters 21–23 in this volume are also relevant to device applications involving bacteriorhodopsin.

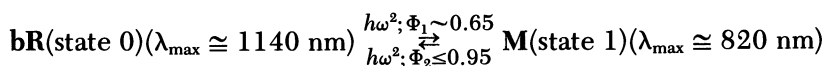
A reliability analysis has been carried out for a bacteriorhodopsin optical memory operating at ambient temperature. According to the information presented in references 20 and 21, this device has a unit component reliability of $P_{\langle 1 \rangle} = 0.517$, which is low primarily because photostationary states with relatively similar concentrations of the two species are used to represent the 0 and 1 states (*see* discussion in references 5 and 30). Birge et al. (21) calculate that $10^{5.5}$ ($\sim 316,000$) molecules must be included in the ensemble (irradiated volume) to generate a reliability of $\xi \geq 10$. The current design of the optical RAM uses an optical design and spin-coated polymer thin films, which leads to approximately 10^7 molecules in the irradiated volume, which leads to a reliability that is limited primarily by $\xi = 23$ (Figure 2).

The issue of aperture time uncertainty arises because of the rapidity of the transitions in bacteriorhodopsin. We can apply equations 1 and 2 to this system. Let state 0 be defined as **BR** ($\lambda_{\max} = 568$ nm; $\tilde{\nu}_0 = 17,600$ cm^{-1}) and state 1 be defined as **K** ($\lambda_{\max} = 620$ nm; $\tilde{\nu}_1 = 16,130$ cm^{-1}). Thus, $\tilde{\nu}_s = |\tilde{\nu}_1 - \tilde{\nu}_0| = 1470$ cm^{-1} . A reasonable value for $\tilde{\nu}_f$ is 3000 cm^{-1} . Solution of equation 1b as a function of selected apertures listed in parentheses gives $\Delta P^h = 0.00000136$ ($\Delta t = 1$ ns), 0.00135 ($\Delta t = 1$ ps), 0.0133 ($\Delta t = 0.1$ ps), 0.112 ($\Delta t = 0.01$ ps), and 0.373 ($\Delta t = 1$ fs). Only for aperture times shorter than 1 ps does Heisenberg broadening have a significant impact on the reliability. Indeed, for virtually all systems that involve ensemble averaging, this source of error is of little if any consequence until one approaches aperture times in the subpicosecond regime. This follows from the fact that the probability for a single molecule correct assignment, $P_{\langle 1 \rangle}$, is well below unity. Thus, ΔP^h will not have a large influence on the overall reliability until it reaches values greater than 0.01. This statement does not apply to the monoelectronic or monomolecular devices described in a subsequent section.

Three-Dimensional Optical Memories. Two-photon three-dimensional (3D) optical addressing architectures offer significant promise for the development of a new generation of ultra-high density RAMs (*see* reference 5 and Chapter 7 by Dvornik and Rentzepis in this volume). These memories read and write information by using two orthogonal laser beams to address an irradiated volume ($1\text{--}50$ μm^3) within a much larger volume of a nonlinear photochromic material. A two-photon process is used to initiate the photochemistry, and this process involves the unusual capability of some molecules to capture two photons simultaneously to populate an energy level within the molecule with an energy equal to the sum of the energies of the two photons absorbed.

Because the probability to a two-photon absorption-process scales as the square of the intensity, photochemical activation is limited to a first approximation to regions within the irradiated volume. (Methods to correct for photochemistry outside the irradiated volume are described in reference 5.) The 3D addressing capability derives from the ability to adjust the location of the irradiated volume in three dimensions. Two-dimensional (2D) optical memories have a storage capacity that is limited to $\sim 1/\lambda^2$, where λ is the wavelength, which yields approximately 10^8 bits/cm². In contrast, 3D memories can approach storage densities of $1/\lambda^3$, which yields densities in the range 10^{11} to 10^{13} bits/cm³. The design described subsequently is designed to store 18 GBytes (1 Gbyte = 10^9 bytes) within a data storage cuvette with dimensions of $1.6 \times 1.6 \times 2$ cm. Our current storage capacity is well below the maximum theoretical limit of ~ 512 GBytes for the same ~ 5 cm³ volume.

Bacteriorhodopsin has four characteristics that combine to enhance its comparative advantage as a nonlinear optical photochromic medium (4, 5). First, it has a large two-photon absorptivity due to the highly polar environment of the protein binding site, and the large change in dipole moment that accompanies excitation. Second, bacteriorhodopsin exhibits large quantum efficiencies in both the forward and reverse direction. Third, the protein gives off a fast electrical signal when light-activated that is diagnostic of its state (*see* Chapter 22 in this volume). Fourth, the protein can be oriented in optically clear polymer matrices permitting photoelectric state interrogation. The two-photon induced photochromic behavior is summarized in the scheme below:



Photochemistry is initiated by using a two-photon process and laser wavelengths twice those used to initiate normal (i.e., one-photon) photochemistry. We arbitrarily assign **bR** to binary state 0 and **M** to binary state 1. The chromophore in **bR** has an unusually large two-photon absorptivity ($\delta = 290 \times 10^{-50}$ cm⁴ s molecule⁻¹ photon⁻¹), a value that is approximately 10 times larger than absorptivities observed for other polyene chromophores (4). This permits the use of much lower intensity laser excitation to induce the forward photochemistry. The above wavelengths are correct to only ± 40 nm, because the two-photon absorption maxima shift as a function of temperature and polymer matrix water content.

The optical design of the two-photon 3D optical memory is shown in Figure 3. The bacteriorhodopsin is contained in a cuvette and is oriented by using electric fields prior to polymerizing the polyacrylamide gel matrix. This orientation is required to use the photoelectric signal

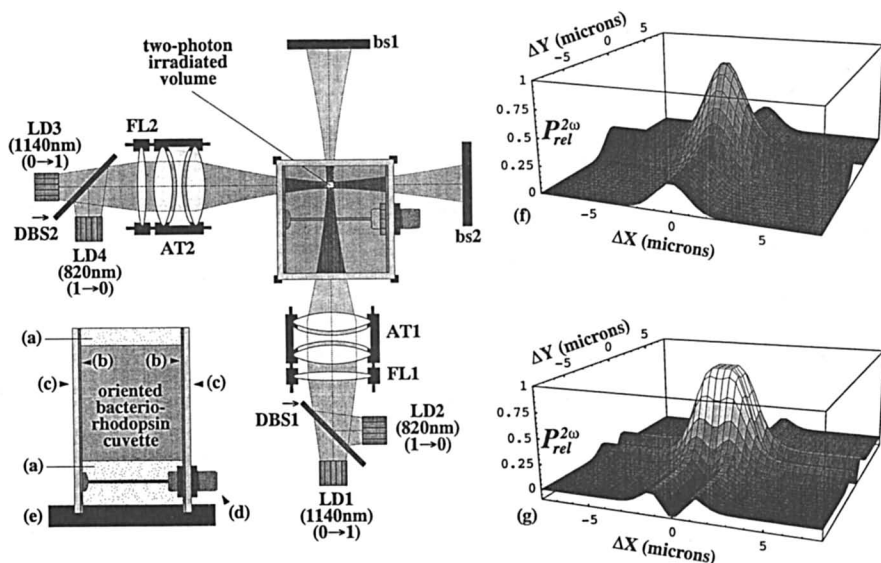


Figure 3. Schematic diagram of the principal optical components of a two-photon three-dimensional optical memory based on bacteriorhodopsin. The write operation involves the simultaneous activation of LD₁ and LD₃ (0 → 1) or LD₂ and LD₄ (1 → 0) to induce two-photon absorption within the irradiated volume and partially convert either bR to M (0 → 1) or M to bR (1 → 0). The write operation uses a 10-ns pulse and a pulse simultaneously of 1 ns. The protein is oriented within the cuvette by using an electric field prior to polymerization of the polyacrylamide gel. A polymer sealant is then used to maintain the correct polymer humidity. The SMA connector is attached to the indium–tin–oxide conducting surfaces on opposing sides of the cuvette and is used to transfer the photoelectric signal to the external amplifiers and box-car integrators. Symbols and letter codes are as follows: (a) sealing polymer, (b) indium–tin–oxide conductive coating, (c) BK7 optical glass; (d) SMA or OS50 connector; (e) Peltier temperature controlled base plate (0–20 °C); AT (achromatic focusing triplet); bs (beam stop); DBS (dichroic beam splitter); LD (laser diode); FL (adjustable focusing lens). Computer simulations of the probability of two-photon-induced photochemistry (vertical axis) as a function of location relative to the center of the irradiated volume (ΔX_{focus} and ΔY_{focus}) in microns are shown in (f) and (g). The top right contour plot (f) shows the probability after two 1140-nm laser beams have been simultaneously directed along orthogonal axes crossing at the center of the irradiated volume. The bottom right contour plot (g) shows the probability after two 820-nm “cleaning pulses” have been independently directed along the same axes. The maximum conversion probability at $x = 0, y = 0$ is normalized to unity for both contour plots.

to monitor the state of the proteins occupying the irradiated volume. A write operation is carried out by firing simultaneously the two 1140-nm lasers (to write a 1) or the two 820-nm lasers (to write a 0). To eliminate unwanted photochemistry along the laser axes, nonsimultaneous firing of the lasers not used in the original write operation is carried out immediately following the write operation. The methods and procedures of this "cleaning" operation are described in reference 5, and the results are shown in the contour plots shown in Figure 3. The position of the cuvette is controlled in three dimensions by using a series of actuators that independently drive the cuvette in the x , y , or z direction. For slower speed maximum density applications, piezoelectric-stepper motor micrometers are used. For higher speed, lower density applications, voice-coil actuators are used. Parallel addressing of large data blocks can also be accomplished by using holographic lenses or other optical architectures.

A key requirement of the two-photon memory is to generate an irradiated volume that is reproducible in terms of xyz location over lengths as large as 2 cm. In the present case, our memory cuvettes are typically ~ 1.6 cm in the x and y dimension and ~ 2 cm in the z direction (see Figure 3). These dimensions are variable up to 2 cm on all sides and can be as small as 1 cm on a side depending upon the desired storage capacity of the device. By using a set of fixed lasers and lenses and by moving the cuvette by using orthogonal translation stages, excellent reproducibility can be achieved ($\pm 1 \mu\text{m}$ for piezoelectric micropositioners and $\pm 3 \mu\text{m}$ for voice-coil actuators). Refractive inhomogeneities that develop within the protein-polymer cuvette as a function of write cycles adversely affect the ability to position the irradiated volume with reproducibility. This problem is due to the change in refractive index associated with the photochemical transformation. The problem is minimized by operating with a relatively large irradiated volume ($\sim 30 \mu\text{m}^3$) and by limiting the photochemical transformation to 60:40 versus 40:60 in terms of relative **bR:M** percentages.

A detailed examination of the reliability of 3D memories has not been published, in part because each design has unique aspects that mediate the analysis. A reliability analysis based on a preliminary analysis of the experimental results obtained for the optical 3D memory shown in Figure 3 suggests that this memory has a unit component reliability of $P_{\langle 1 \rangle} = 0.512$, which is one of the lowest unit reliabilities encountered in our studies to date. The relatively low value is due to a number of characteristics unique to volumetric memories, which must be designed to measure the state of an ensemble within a larger volumetric medium (5). The curve shown in Figure 2 indicates that $10^{5.7}$ ($\sim 501,000$) molecules must be included in the ensemble (irradiated volume) to generate a reliability of $\xi \geq 10$. The following equation estimates the concentra-

tion, C , of protein necessary to achieve reliable operation as a function of linear bit separation, S :

$$C(\text{mol/l}) = (1.66 \times 10^{-9}) \frac{N(\text{molecules/bit})}{[S(\mu\text{m})]^3} \quad (47)$$

For example, a 3D memory operating with a linear bit separation of $3 \mu\text{m}$, requires a concentration of 3.1×10^{-5} mol/l of protein to achieve reliability ($\xi \geq 10$; $N = 5 \times 10^5$). This concentration is difficult to achieve for oriented memory media, and the largest concentration we have achieved to date while maintaining high homogeneity and orientation is 1.3×10^{-5} mol/l. This result suggests one of two scenarios. A reliable 3D memory based on bacteriorhodopsin will either require larger linear bit separations ($S > 4 \mu\text{m}$) or error-tolerant designs. The error-tolerant approach has been adopted in our prototypes, where we store 10-bits-per-8-bit character (data byte), thereby providing single bit error correction and double bit error detection. The above observations should not be used to argue that 3D optical memories do not offer high density and high reliability, simultaneously. A very conservative design based on $S = 6 \mu\text{m}$ will still provide a projected 200-fold improvement in storage density based on overall package size.

Monoelectronic and Monomolecular Devices. The possibility of constructing monomolecular (21, 23, 24, 42–44) and single electron devices (12–14, 45, 46) is the subject of active experimental and theoretical study. For convenience, we will refer to any device that relies on a single molecule or single charge carrier as a single quantized entity (SQE) device. One might conclude from the previous discussion that such devices are unrealistic, because the device having an ensemble of only one quantized entity will require an unrealistically high value of $P_{\langle 1 \rangle}$ (~ 1) to yield reliable operation. The probability of correctly assigning the state of an SQE, $P_{\langle 1 \rangle}$, is never exactly unity. Based on equation 44, we can write the best-case probability of an error in state assignment as follows:

$$P_{\min}^{\text{error}}(N, P_{\langle 1 \rangle}) \cong -\text{Erf} \left[\frac{(2P_{\langle 1 \rangle} + 1)\sqrt{N}}{4\sqrt{2P_{\langle 1 \rangle}(1 - P_{\langle 1 \rangle})}}; \frac{(2P_{\langle 1 \rangle} - 1)\sqrt{N}}{4\sqrt{2P_{\langle 1 \rangle}(1 - P_{\langle 1 \rangle})}} \right] \quad (48)$$

where N , the ensemble size is defined later for an SQE and $\text{Erf}[Z_0; Z_1]$ is defined in equations 46a and b). Equation 48 neglects error associated with thermal state interconversion. (We leave N in this equation for reasons outlined later.) A minimal condition for reliable SQE devices is that the barrier to unactivated state interconversion be sufficiently high to prevent thermal randomization. As previously noted, a value of P_{\min}^{error}

$= 10^{-10}$ is considered a minimal requirement for reliability in non-error-correcting digital architectures.

Provided the state of the SQE device is not altered during the assignment process, we can reinterpret the N term that appears in equation 48 as the number of measurements rather than as the number of quantized entities in the ensemble. The correspondence is not exact, but if each measurement is truly independent and the state of the device is assigned based on the linear average of all state assignment measurements, then the correspondence is nearly exact. Thus, P_{\min}^{error} is to a good approximation identical for a device with an ensemble of size N or an SQE device with a state assignment based on N linearly averaged measurements. This observation dramatically decreases the $P_{\langle 1 \rangle}$ requirement as shown in the following list giving $P_{\langle 1 \rangle}$ to achieve $P_{\min}^{\text{error}} \leq 10^{-10}$ as a function of N : 0.8956 ($N = 100$), 0.6894 ($N = 10^3$), 0.5642 ($N = 10^4$), 0.5204 ($N = 10^5$), and 0.5065 ($N = 10^6$).

The next question that must be answered is how fast a given number of measurements can be carried out to assign the device state. This assignment is, of course, highly dependent upon the architecture of the system, but it is possible to use Heisenberg's uncertainty principle to assign the maximum frequency that the system can sustain and still carry out the required averaging. If we make the assumption that $\tilde{\nu}_f = \tilde{\nu}_s$, the following equation can be derived based on the Lorentzian distribution functions introduced in the derivation of equations 1 and 2:

$$f_{\max} \cong \frac{0.00800801 \tilde{\nu}_s \pi^2}{hN \left[2\pi + 2 \tan^{-1}(-2) + \ln \left(\frac{\tilde{\nu}_s^2}{4} \right) - \ln \left(\frac{5\tilde{\nu}_s^2}{4} \right) \right]} \quad (49a)$$

$$f_{\max} \text{ (GHz)} \approx \frac{0.963 \tilde{\nu}_s}{N} \quad (49b)$$

where f_{\max} is the maximum frequency of operation, $\tilde{\nu}_s$ is the energy separation of the two states of the SQE device in wavenumbers, and N is the number of state assignments that must be averaged to achieve reliable state assignment. This equation only applies to SQE devices; Heisenberg's uncertainty principle permits higher frequencies for ensemble averaged devices. It is also important to note that equation 49 gives an upper limit. For example, an SQE device with $P_{\langle 1 \rangle} \cong 0.7$ ($N \sim 10^3$) and $\tilde{\nu}_s \cong 1000 \text{ cm}^{-1}$ will have a maximum frequency of $\sim 960 \text{ MHz}$.

Conclusions

We have presented a reliability theory based on receiver operational characteristic theory and binomial probability theory. Our analysis requires the assignment of a threshold level, and we make the assumption

that there is a single-level decision threshold, T , that is defined symmetrically relative to the two distribution functions. Thus, the threshold is optimized for determining the state of the device as accurately as possible while yielding symmetrical error.

Our mathematical treatment accounts for several sources of error in setting and reading a switch. In addition to the usually discussed sources, such as quantum uncertainty, imperfect absorption, and measurement error, the dynamics of operating a switch introduce another source of error. This error arises because the shape of the probability curves for outcome of changing the state of an ensemble can depend upon the starting state of the ensemble. Thus the dynamics may become chaotic, as is indicated in the discussion following equations 21 and 22. This chaos adds an indeterminacy to the operation of a switch that can be controlled only through careful design.

We also address the problem of reading and writing via multiple wavelengths simultaneously. We have indicated how to compute the statistics of read and write operations via multiple wavelengths from a knowledge of the statistics of single wavelength operations. This is of significance when, because of speed considerations, the ensemble is not permitted to come to equilibrium.

Three variables are required to assign the reliability of a device. The first variable, $P_{\langle 1 \rangle}$, is the probability of determining the state of the device if only one molecule (or information carrier) is present. The second variable, N , is the number of molecules (or information carriers) operating to assign the state of the device (i.e., the number of quantized entities within the ensemble). The third variable, ξ , is the limiting logarithmic reliability factor, which is a function of the entire system and the environment in which it must operate.

The first variable, $P_{\langle 1 \rangle}$, is often difficult to assign experimentally. If we can measure the reliability of the device for a known ensemble size, our procedures can be used to define reliability as a function of smaller and larger ensembles.

Sample reliability analyses are carried out on four devices to determine the minimum number of molecules, N , that must be included in the ensemble to achieve an error probability of less than 10^{-10} . The devices studied include a molecular electrostatic gate ($N \cong 1600$), an optically coupled molecular NAND gate ($N \cong 130,000$), a 2D optical RAM based on bacteriorhodopsin ($N \cong 320,000$), and a 3D (volumetric) RAM based on bacteriorhodopsin ($N \cong 500,000$).

Although optical coupling will typically require larger ensembles, optical coupling provides the most convenient method of generating the ensemble averaging that is often required for device reliability while maintaining the speed advantages inherent in molecular or nanoscale ballistic devices.

Heisenberg's uncertainty principle places constraints on the speed with which the state of a device can be assigned and for typical molecular devices an observable diminution in the probability of correct state assignment occurs for aperture (state assignment) times less than 1 ps. For virtually all systems that involve ensemble averaging, "Heisenberg energy broadening" is of little physical consequence until one approaches aperture times in the subpicosecond regime.

Monomolecular or one-electron devices will require a $P_{\langle 1 \rangle}$ value of 0.9985 to achieve reliability in the absence of assignment averaging. Averaging can be used, however, to achieve reliability with a concomitant reduction in speed. For example, if 1000 assignment averages are taken, a $P_{\langle 1 \rangle}$ value of ~ 0.7 is sufficient. Quantum effects limit the maximum frequency of operation of monomolecular and one-electron devices to approximately f_{\max} (GHz) $\approx 0.96 \tilde{\nu}_s/N$ where $\tilde{\nu}_s$ is the energy separation of the two states of the device in wavenumbers, and N is the number of state assignments that must be averaged to achieve reliable state assignment.

Acknowledgments

This work was supported in part by grants from the W. M. Keck Foundation, The U.S. Air Force Rome Laboratory (F30602-91-C-0084), the National Institutes of Health (GM-34548), the Office of Naval Research (N00014-88-K-0359), and the Industrial Affiliates Program of the W. M. Keck Center for Molecular Electronics at Syracuse University. The authors thank A. Aviram, P. A. Dowben, R. W. Keyes, K. K. Likharev, L. A. Nafie, M. Reed, and B. Ware for interesting and helpful discussions.

References

1. Birge, R. R.; Findsen, L. A.; Pierce, B. M. *J. Am. Chem. Soc.* **1987**, *109*, 5041-5043.
2. Kobilka, B. W.; Kobilka, T. S.; Daniel, K.; Regan, J. W.; Caron, M. G.; Lefkowitz, R. J. *Science (Washington, D.C.)* **1988**, *240*, 1310-1318.
3. Pnevmatikos, S. *Phys. Rev. Lett.* **1988**, *60*, 1534-1537.
4. Birge, R. R. *Annu. Rev. Phys. Chem.* **1990**, *41*, 683-733.
5. Birge, R. R. *Computer* **1992**, *25*, 56-67.
6. Pollard, H. J.; Franz, M. A.; Zinth, W.; Kaiser, W.; Kolling, E.; Oesterhelt, D. *Biophys. J.* **1986**, *49*, 651-662.
7. Mathies, R. A.; Brito Cruz, C. H.; Pollard, W. T.; Shank, C. V. *Science (Washington D.C.)* **1988**, *240*, 777-779.
8. Mathies, R. A.; Lugtenburg, J.; Shank, C. V. In *Biomolecular Spectroscopy*; Birge, R. R.; Mantsch, H. H., Ed.; The International Society for Optical Engineering: Bellingham, WA, 1989; pp 138-145.
9. Birge, R. R. *Biochim. Biophys. Acta* **1990**, *1016*, 293-327.
10. Miller, W. H.; George, T. F. *J. Chem. Phys.*, **1972**, *56*, 5637.

11. Legett, A. J.; Chakravarty, S.; Dorsey, A. T.; Fisher, M. P. A.; Garg, A.; Zwerger, W. *Rev. Mod. Phys.* **1987**, *59*, 1.
12. Fulton, T. A.; Dolan, G. J. *Phys. Rev. Lett.* **1987**, *59*, 109–112.
13. Likharev, K. K. *IEEE Trans. Magn.* **1987**, *23*, 1142.
14. Likharev, K. K. *IBM J. Res. Dev.* **1988**, *42*, 144.
15. Loève, M. *Probability Theory I*; Springer-Verlag: New York, 1977; pp 8–24.
16. Papoulis, A. *Probability, Random Variables and Stochastic Processes*; McGraw-Hill: New York, 1965; pp 270–272.
17. Folland, G. B. *Harmonic Analysis in Phase Space*; Princeton University: Princeton, NJ, 1989.
18. Hogg, R. V.; Craig, A. T. *Introduction to Mathematical Statistics*; MacMillan: New York, 1959; p 23.
19. Barnsley, M. F.; Demko, S. *Proc. Roy. Soc. London* **1985**, *A399*, 243–275.
20. Birge, R. R.; Ware, B. R.; Dowben, P. A.; Lawrence, A. F. In *Molecular Electronics—Science and Technology*; Aviram, A., Ed.; Engineering Foundation: New York, 1988; pp 275–284.
21. Birge, R. R.; Lawrence, A. F.; Tallent, J. R. *Nanotechnology* **1991**, *2*, 73–87.
22. Hong, F. T. *Molecular Electronics—Biosensors and Biocomputers*; Plenum: New York, 1989; pp 1–454.
23. Aviram, A. *Molecular Electronics—Science and Technology*; Engineering Foundation: New York, 1989; pp 1–416.
24. Launay, J. P. In *Molecular Electronics—Science and Technology*; Aviram, A., Ed.; Engineering Foundation: New York, 1989; pp 237–246.
25. Keyes, R. W. *Science (Washington, D.C.)* **1985**, *230*, 138–144.
26. Keyes, R. W. In *Advances in Electronics and Electron Physics*; Hawkes, P., Ed.; Academic: Orlando, FL, 1988; pp 159–214.
27. Keyes, R. W. In *Molecular Electronics—Science and Technology*; Aviram, A., Ed.; Engineering Foundation: New York, 1989; pp 197–204.
28. Birge, R. R.; Lawrence, A. F.; Finsen, L. A. In *Proceeding of the International Congress on Technology and Technology Exchange*; International Technology Institute: Pittsburgh, PA, 1986; pp 3–8.
29. Birge, R. R.; Zhang, C. F.; Lawrence, A. F. In *Molecular Electronics*; Hong, F., Ed.; Plenum: New York, 1989; pp 369–379.
30. Schick, G. A.; Lawrence, A. F.; Birge, R. R. *Trends Biotech.* **1988**, *6*, 159–163.
31. Rayfield, G. In *Molecular Electronics*; Hong, F. T., Ed.; Plenum: New York, 1989; pp 361–368.
32. Simmeth, R.; Rayfield, G. W. *Biophys. J.* **1990**, *57*, 1099–1101.
33. Lawrence, A. F.; Birge, R. R. In *Nonlinear Electrodynamics in Biological Systems*; Adey, W. R.; Lawrence, A. F., Eds; Plenum: New York, 1984; pp 207–218.
34. Gross, R. B.; Izgi, K. C.; Birge, R. R. *Proc. SPIE* **1992**, *1662*, 186–196.
35. Hampp, N.; Bräuchle, C.; Österhelt, D. *Biophys. J.* **1990**, *58*, 83–93.
36. Bazhenov, V. Y.; Soskin, M. S.; Taranenko, V. B. *Sov. Tech. Phys. Lett.* **1987**, *13*, 382–384.
37. Bazhenov, V. Y.; Soskin, M. S.; Taranenko, V. B.; Vasnetsov, M. V. In *Optical Processing and Computing*; Arsenault, H. H.; Szoplik, T.; Macukow, B., Eds.; Academic: Orlando, FL, 1989; pp 103–144.
38. Bunkin, F. V.; Vsevolodov, N. N.; Druzshko, A. B.; Mitsner, B. I.; Prokhorov, A. M.; Savranskii, V. V.; Tkachenko, N. W.; Shevchenko, T. B. *Sov. Tech. Phys. Lett.* **1981**, *7*, 630–631.

39. Burykin, N. M.; Korchemskaya, E. Y.; Soskin, M. S.; Taranenko, V. B.; Dukova, T. V.; Vsevolodov, N. N. *Opt. Commun.* **1985**, *54*, 68–70.
40. Ivanitskiy, G. R.; Vsevolodov, N. N. *Photosensitive Biological Complexes and Optical Recording of Information*; USSR Academy of Sciences, Biological Research Center, Institute of Biological Physics: Pushchino, Russia, 1985; pp 1–209.
41. Vsevolodov, N. N.; Poltoratskii, V. A. *Sov. Phys. Tech. Phys.* **1985**, *30*, 1235–1247.
42. Launay, J. P. In *Molecular Electronics—Science and Technology*; Aviram, A., Ed.; Engineering Foundation: New York, 1989; pp 237–246.
43. Farazdel, A.; Dupuis, M.; Clementi, E.; Aviram, A. *J. Am. Chem. Soc.* **1990**, *112*, 4206–4214.
44. Hush, N. S.; Wong, A. T.; Bacskay, G. B.; Reimers, J. R. *J. Am. Chem. Soc.* **1990**, *112*, 4192–4197.
45. Kuzmin, L. S.; Likharev, K. K. *Pis'ma Zh. Eksp. Teor. Fiz.* **1987**, *45*, 389.
46. Fulton, T. A.; Gammel, P. L.; Bishop, D. J.; Dunkleberger, L. N.; Dolan, G. J. *Phys. Rev. Lett.* **1989**, *63*, 1307–1310.

RECEIVED for review March 12, 1992. ACCEPTED revised manuscript March 24, 1993.

Two-Photon Three-Dimensional Optical Storage Memory

A. S. Dvornikov and P. M. Rentzepis*

Department of Chemistry, University of California, Irvine, Irvine, CA 92664

We present a means for constructing three-dimensional optical memory devices that operate by two-photon interaction. Photochromic molecules and semiconductors have been studied as materials for writing and reading information within the volume of a solid matrix. The mechanism for writing and reading the information, bit density, cycle times, and stability of the materials under various experimental conditions are the topics addressed.

COMPUTER TECHNOLOGY has progressed to such an extent that it has created an even larger need for high-performance devices that must store, retrieve, and process huge volumes of data at extremely high speeds (1). Improvements in silicon technology are bringing computer usage to a critical point where the memory capacity and input-output speed are the limiting factors. Therefore, the major component that will modulate the practical limits of high-speed computing is thought to be the memory. Owing to the huge data storage requirements, the need for the parallel execution of tasks and necessity of a compact, very high capacity, low-cost memory is becoming almost mandatory.

The necessity, therefore, for the search to find means to store large amounts of information in small volumes cannot be overstated, nor can the requirement for these memories to be capable of large bandwidths and parallel access be overemphasized. Three-dimensional (3D) storage may provide a desirable solution to these needs. Research efforts that may lead to 3D information storage include persistent hole burning (2), phase holograms (3), and two-photon processes, especially using organic materials (4-6), semiconductors, and biomolecules such as bacteriorhodopsin (7-10). In this chapter we will restrict discussion to the last

* Corresponding author.

0065-2393/94/0240-0161\$08.00/0
© 1994 American Chemical Society

topic, namely 3D storage by means of two-photon absorption and particularly in the utilization of organic photochromic materials (11).

To make a quantum increase in the information density available and the input–output of information be suitable for parallel processing, an all-optical storage device must be advanced and utilized and a means for storing more information per unit volume must be found (12, 13). In the case of optical systems, the density of information stored is dependent upon the reciprocal of the wavelength λ to the power of the dimension used to store information. For example, if the information is stored in one dimension, then the density is proportionally $1/\lambda$. This relationship also suggests that the information storage density is much higher at UV wavelengths and 3D devices than when visible light is used to store information in a two- (2D) or 3D medium. In a 2D memory, the theoretical storage density for a device that operates at 200 nm is 2.5×10^9 bits/cm², whereas for a similar 3D storage memory the density may be as high as 1.2×10^{14} bits/cm³.

In the following sections we will discuss the basis for a two-photon process, the means for writing and reading information within a volume storage device; describe the materials and methods used; and present a status report on their relevant molecular and spectroscopic properties.

Two-Photon Mechanism

The theoretical bases for two-photon processes were established in the early 1930s (14). The probability for a two-photon transition to occur may be expressed as a function of three parameters: line profile, transition probability for all possible two-photon processes, and light intensity. These factors are related by

$$P_{if} \cong \frac{\gamma_{if}}{[\omega_{if} - \omega_1 - \omega_2 - \bar{v} \cdot (\mathbf{K}_1 + \mathbf{K}_2)]^2 + (\gamma_{if/2})^2} \times \left| \sum_k \frac{\mathbf{R}_{ik} \cdot \mathbf{e}_1 \cdot \mathbf{R}_{kf} \cdot \mathbf{e}_2}{(\omega_{ki} - \omega_1 - \mathbf{K}_1 \cdot \bar{v})} + \frac{\mathbf{R}_{ik} \cdot \mathbf{e}_2 \cdot \mathbf{R}_{kf} \cdot \mathbf{e}_1}{(\omega_{ki} - \omega_2 - \mathbf{K}_2 \cdot \bar{v})} \right|^2 \cdot I_1 I_2 \quad (1)$$

where γ_{if} is the spectral width; i , k , and f are the initial, intermediate, and final states, respectively; 1 and 2 refer to the two laser beams; R_{ik} and R_{fk} are matrix elements; I_1 and I_2 are the intensities of the two laser beams; K_1 and K_2 are wave vectors; e_1 and e_2 are polarization vectors; ω_{if} is the center frequency; and P_{if} is the two-photon transition probability.

According to this postulate, two-photon transitions may also allow for the population of molecular levels that are forbidden for one-photon processes such as $g \rightarrow g$ and $u \rightarrow u$ in contrast to the $g \rightarrow u$ and $u \rightarrow g$ transitions that are allowed for one-photon processes. The first factor

describes the spectral profile of a two-photon transition. The first factor corresponds to a single-photon transition at a center frequency $\omega_{if} = \omega_1 + \omega_2 + \bar{v}(\mathbf{K}_1 + \mathbf{K}_2)$ with a homogeneous width γ_{if} . The second factor describes the transition probability for the two-photon transition. This second factor is the sum of products of matrix elements $\mathbf{R}_{ik}\mathbf{R}_{kf}$ for transitions between the initial state i and the intermediate molecular levels k or between k and the final state f . Often a virtual level is introduced to describe the two-photon transition. The frequencies of ω_1 and ω_2 can be selected in such a way that the virtual level is close to a real molecular state. This greatly enhances the transition probability, and it is, therefore, generally advantageous to populate the final level E_f by means of two different energy photons with $\omega_1 + \omega_2 = (E_f - E_i)/\hbar$ rather than by two equal photons. The third factor shows that the transition probability depends upon the product of the intensities I_1 and I_2 . In the case where the photons are of the same wavelength, then the transition probability depends upon I_2 . It will therefore be advantageous to utilize lasers emitting high-intensity light such as picosecond and subpicosecond pulses.

Such a two-photon absorption process makes it possible to preferentially excite molecules inside a volume in preference to the surface. This is possible because the wavelength of each beam alone is longer and has less energy than the energy gap between the ground state and first allowed electronic level. However, if two beams are used and the energy sum of the two laser photons is equal to or larger than the energy gap of the transition, then absorption will take place. It is also important to note that there is no real level at the wavelength of either beam; therefore, neither photon may be absorbed alone. When two such photons collide within the volume, absorption occurs only at the place of pulse overlap. Theoretically the ratio of the signal to the background is 3:1; however, there are several means for increasing this ratio such as using a weak beam that can induce by itself a two-photon process and an intense laser pulse that cannot populate any allowed excited state by means of two photons. Another means for reducing the background intensity has been discussed by Birge (15). This two photon virtual process is in sharp contrast to the sequential two-photon process where the first step involves the absorption of a single photon by a real spectroscopic level and therefore is not capable of volume storage. The principal difference in the two cases as far as their suitability for 3D volume memory is that the virtual case avails itself to writing and reading in any place within the 3D volume, whereas the sequential excitation is restricted in writing and reading first at the surface. At the point where the two beams interact, the absorption will induce a molecular change that will distinguish this microvolume from the unexcited space. The two molecular structures, that is, the original and the one created by

the two-photon absorption, are used as the write and read forms of a 3D optical storage memory, respectively.

Writing and Reading in a 3D Memory

A 3D memory provides several desirable properties that may not be found in today's electrooptic devices. The major advantages of a 3D storage device are as follows: (1) immense information storage capacity, $\sim 10^{13}$ bits/cm³; (2) random and parallel access; (3) nanosecond or faster writing and reading speed; (4) small size and low cost; (5) absence of mechanical or moving parts; (6) minimal cross talk between adjacent bits; and (7) high reading sensitivity.

The operations that enable one to store, retrieve, and erase information within a 3D volume are as follows:

1. **Writing:** information is recorded at any place within the 3D medium.
2. **Reading:** information is retrieved from the memory.
3. **Erasing:** information recorded in any part of the memory is removed.

Currently, information for a digital computer is stored in the form of binary code. The two stages of the binary code, zero, 0 and one, 1, may be thought of as the photochemical changes that lead to two distinct structures of the particular molecular species used as the storage medium. An example is provided by the changes in molecular structure occurring in photochromic materials such as spirobenzopyrans (SP) after the simultaneous absorption of two photons. The structure of a typical SP molecule is shown in Figure 1. SP has two distinct forms: the spiropyran or closed form and the merocyanine or open form. These two distinct forms provide the two states necessary for storage information in a binary format. Specifically the original closed form designates zero, whereas the open form designates one.

To write information in a 3D device that contains SP requires excitation in the UV region of the spectrum because SP absorbs at ~ 260 and 355 nm (see Figure 2). Excitation to this state is provided by the two-photon absorption of either a 1064-nm photon and a 532-nm photon equivalent to a 355-nm photon, or two 532-nm photons, corresponding to a 266-nm photon. The background to signal ratio for two collinear beams propagating at opposite directions is 1:3.

Figure 1 displays the energy level diagram along with the molecular structures of the write and read forms of SP. By using laser beams with wavelengths shown in Figure 1 and by translating the beams along the axes of the memory device, which in this case is in the form of a cube,

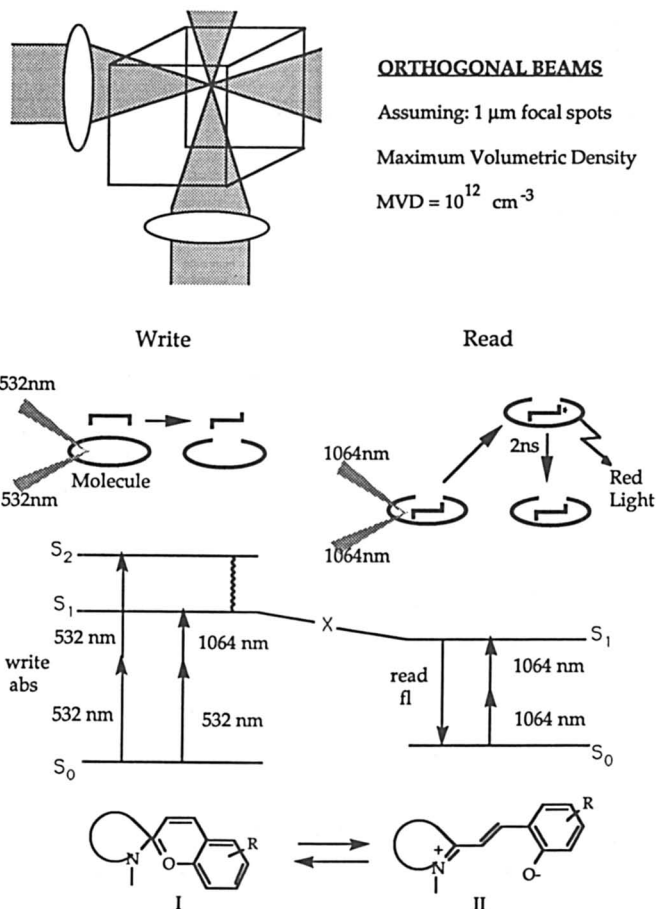


Figure 1. Top, Schematic representation of writing and reading in 3D by two-photon processes. Middle, Energy level diagram and shape of SP in the write and read forms. Bottom, Structure of the SP in the write (I) and read (II) form.

the required spatial pattern is achieved in the form of colored spots within the volume of the memory. The information can be stored in a page format with several pages superimposed within a memory volume. A complication can arise from the presence of fluorescence from the excited, closed zero form which, if absorbed by adjacent molecules, would subsequently transform them to the read form and thus introduce cross talk between adjacent bits. To avoid such effects, molecules are chosen that do not fluoresce in the write form. No fluorescence from the write form of the SP molecules used in our experiments has been observed even at liquid nitrogen temperatures (5).

The read cycle operates similarly to the write cycle except that the read form absorbs at longer wavelengths than the write form; therefore, one or both laser beam wavelengths must be longer than the ones used for writing. The result of absorption by the written molecule is fluorescence. This fluorescence is detected by a photodiode or charge-coupled device (CCD) and is processed as 1 in the binary code. The longer wavelengths assure that only the written molecules will absorb this radiation, which induces fluorescence to be emitted only from the written volume of the memory. The fluorescence spectrum of a written bit is shown in Figure 2. Self-absorption of the fluorescence by adjacent written SP molecules does not affect the reading process because the largest segment of the fluorescence is emitted at longer wavelengths than the ab-

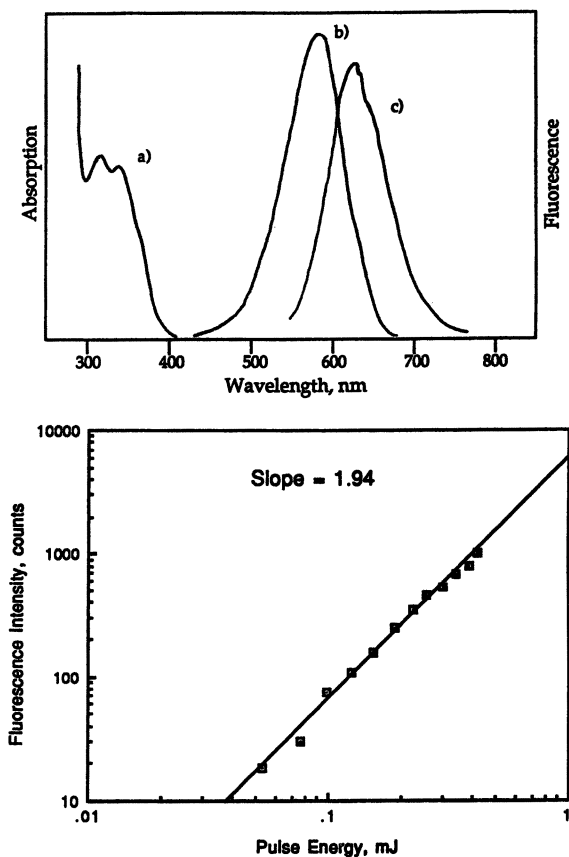


Figure 2. Top, Absorption spectra of write form (a); read form (b), and fluorescence of read form (c) of 1SP in polymethyl methacrylate. Bottom, Laser power vs. fluorescence intensity (proof of two-photon process).

sorption band. The small amount of fluorescence that may be absorbed by adjacent written bits will yield signals that are either too weak in intensity to be detected or that can be easily eliminated by means of electronic discriminators. Because the reading is based on fluorescence, a zero background process, this method has the advantage of a high reading sensitivity. Light detection by means of photomultipliers or CCDs makes possible single-photon detection measurements. The fluorescence was found to decay with ~ 5 -ns lifetime, which in essence is the speed of the reading process.

Erasing the information may be achieved either by increasing the temperature of the memory device to ~ 50 °C or by irradiation with infrared light. By increasing the temperature, the written molecules achieve more energy than barrier separating write and read, causing the written molecules to revert to the original form.

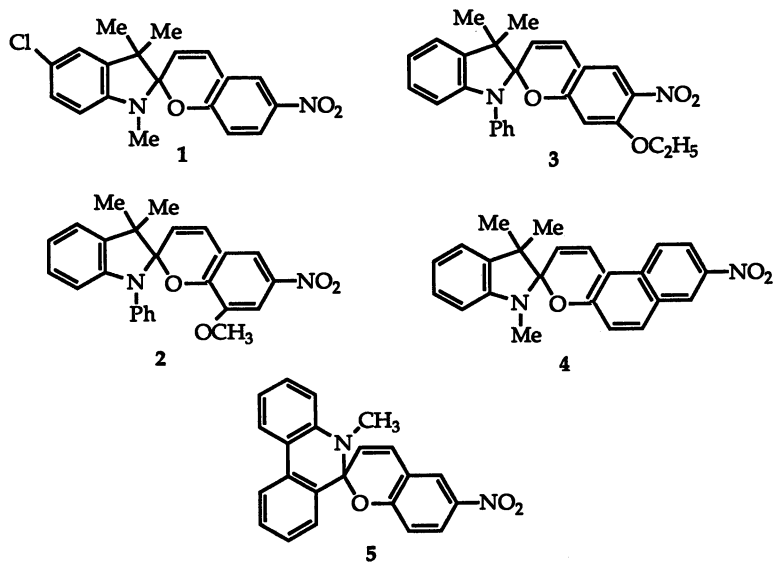
Materials

A vast number of molecules may be used as materials for 3D devices, including photochromic materials, phosphors, photoisomers, and semiconductors. One rather promising class of molecules that has been used in research on 3D storage are the spiropyrans. Spiropyrans are molecules of the general structure shown in Figure 1 and Table I. The photochromism, namely their change in molecular structure after light absorption, of spiropyrans is attributed to the photoinduced cleavage of the C–O bond of the pyran ring formed by isomerization to another form referred to as merocyanine dye (16). We designate this initial orthogonal structure as the write form, 0, in the binary code. Light at 350 nm or less induces absorption that initiates the photochemical opening of the pyran ring (see Figure 1) forming an isomer that, in turn, rearranges to a planar form as a result of thermal isomerization. This planar form designated as the read form, 1, in the binary code, is colored in appearance and absorbs intensely in the 550-nm region as shown in Figure 2. The intermediate state, between the orthogonal and planar species, has been identified by means of time resolved spectroscopy (17, 18). The final, colored species of SP is formed with a quantum yield that varies from ~ 10 to 98% (16). This variation depends in part on the structure of the original molecule and the host, that is, polymer or solvent. Generally, 6-NO₂, 8-OCH₃-substituted compounds such as 1SP and 2SP are more sensitive than other types of spiropyrans and have coloration quantum yields of about 50 to 70% in nonpolar solvents. The coloration quantum yield usually decreases with increasing of solvent polarity (19). The energy levels of the photochromic components depend upon the substituents and the nature of the matrix. Therefore, the choice of the molecule has a profound effect upon the operation, speed, and performance of

Table I. Spectra and Decay Kinetics of Read Form of Spiroprans in Polystyrene and Poly (methyl methacrylate)

SP	Absorption of Merocyanine Form (nm)		Fluorescence of Merocyanine Form (nm)		$k_1; k_2$ (s^{-1})	
	PS	PMMA	PS	PMMA	PS	PMMA
1	609	580	645	625	$4 \times 10^{-3}; 2 \times 10^{-4}$	$1 \times 10^{-3}; 3 \times 10^{-4}$
2	630	615	690	670	$1 \times 10^{-2}; 6 \times 10^{-4}$	$5 \times 10^{-3}; 2 \times 10^{-4}$
3		580		620		$3 \times 10^{-2}; 2 \times 10^{-3}$
4		585		605		
5		565		610		

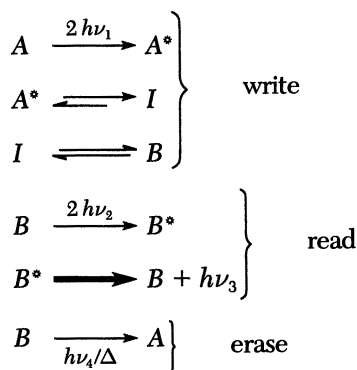
NOTE: k_1 and k_2 , thermal decay constants; SP, spirobenzopyrans; PS, polystyrene; PMMA, poly(methyl methacrylate).



the overall memory device. The polymer matrix usually decreases the rate of molecular transformation and its quantum yield compared to liquids because of increase in viscosity. In addition solid devices are frequently preferable to liquids.

The mechanism that drives the write and read process in these photochromic molecules may be presented by the following equation, where A represents the original closed form, 0, in binary code; A^* designates the electronic excited state of A ; I is an intermediate species of very-short lifetime; $h\nu_1$, $h\nu_2$, $h\nu_3$, and $h\nu_4$ are photon energies; $\nu_1 \neq \nu_2 \neq \nu_3$ and usually $\nu_1 > \nu_2 > \nu_3$. B is the colored, open form binary code 1; B^*

designates the excited state of *B* that is formed after absorption of two photons; Δ is heat; and $h\nu_3$ designates fluorescence.



Other materials that are highly photochromic and that may be used for 3D devices are fulgides. Fulgides also undergo photoinduced ring opening. The quantum yields for the read and write forms have been measured (20, 21), and the lifetime of the process including the intermediate states and kinetics are shown in Figure 3. Because of the lack of fluorescence, these materials are not considered suitable for applications where the reading process relies on the detection of fluorescence emitted by the written bits. For the case of nonfluorescing materials, reading can be realized by detection of the two-photon absorption of the written molecules.

Another distinct set of materials that have some very interesting inherent properties for optical memories are the infrared phosphors (22, 23). These materials emit in the visible region of the spectrum when irradiated with near-IR light. The Quantex Q-phosphors that we studied are semiconductor materials doped with rare earth electron traps. The writing process is achieved by the promotion of an electron from the valence to the conduction band by means of UV irradiation. The electron is trapped and remains there indefinitely because the potential energy well of the trap is much deeper than 1000 T. Reading of the information is achieved by irradiating the phosphor with near-IR light ~ 1 eV, which is of sufficient energy to excite the electron over the barrier. Subsequently the electron decays back into the valence band followed by visible light emission. Presently, two disadvantages are associated with the commercially available phosphors. The information may be read only once and the phosphor is not soluble in any polymer that we know. Therefore, a 3D block composed of these materials suffers from excessive light scattering. These materials however have the advantages of being stable at room temperature and because a very large number of electrons

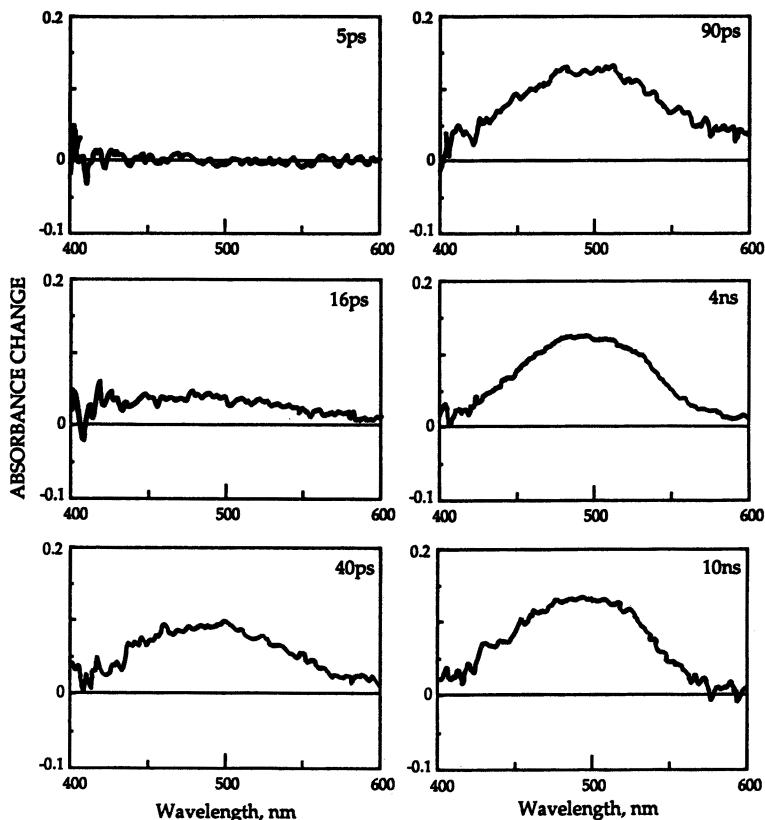


Figure 3. Transient absorption spectra (ΔA) of photochromic fulgides as a function of time (ps).

may be excited into the conduction band, the storage of very large numbers of bits of information may be possible.

Presently, we favor the use of photochromic materials such as spiropyrans over other materials for 3D memory devices because they possess most of the characteristics needed for writing and reading within a 3D device, such as high absorption cross-section, high photocoloration efficiency, intense fluorescence of the read form, and the possibility to repeat the write-read-erase cycle more than 10^6 times.

Stability

Several critical characteristics must be examined before materials may be considered suitable for 3D memory devices. These properties may include among others the stability at room temperature, fatigue as a function of the number of cycles performed, laser power requirements

for writing and reading, cross talk, absorption cross-section, and fluorescence quantum yield. Studies are currently performed in all of these areas. The closed form of SP materials that correspond to 0 in the binary or write form are stable. However, the open, read form is rather unstable and was found to revert to the original write form after a few hours at room temperature. The information in the SP read form was found to disappear via a multiexponential thermal decay. Such a nonexponential behavior is expected because of the many types of isomers and the many nonequivalent sites in the polymer matrix. However, the thermal decay kinetics may be satisfactorily approximated as a sum of two exponentials. The decay constants calculated under this approximation are shown in Table I. Replacement of one polymer by another with higher polarity may cause the decrease in the rate of dark decay of the merocyanine forms. Apparently, this effect can be attributed to relative stabilization of the polar structure of the merocyanine form by the polar environment of the matrix. The effect of the thermal decay processes on the stored information is obviously very detrimental to any device because it causes the information stored to be deleted. To alleviate this, the material is kept at low temperatures, that is, $-40\text{ }^{\circ}\text{C}$ or lower, where the decay of the read form is negligible. Because the open form is essentially a dianion with a positive charge located on the nitrogen and a negative on the oxygen (Figure 1), an ionic species such as an acid could bind these groups and anchor the molecule permanently onto the open, written structure. This was achieved by the use of HCl and a variety of organic and inorganic acids. Reaction of SP with HCl shifts the equilibrium from the closed form to the open form and renders the open form stable indefinitely at room temperature. It was possible to drive it back to the closed form by irradiation with UV light. The use of polar polymers such as poly(hydroxyethyl methacrylate) (PHEMA) for anchoring the two ends of written SP molecules has also improved the stability and lifetime of the read form. For example, while in the original molecule, the information decayed to $1/e$ of its value within 70 min; at $20\text{ }^{\circ}\text{C}$ the bridged material was found to have a lifetime of $1.6 \times 10^6\text{ s}$ or $3 \times 10^4\text{ min}$ at $3\text{ }^{\circ}\text{C}$ (see Figure 4). As a consequence of this chemical binding, the activation energy of the bridged species has increased to 40 kcal as shown in the Arrhenius plot of Figure 4.

We have measured the decay kinetics from 77 to 273 K with an accuracy of $\pm 2\text{ K}$, keeping the sample in a cryostat, thus allowing us to measure the photostability of the read form as a function of temperature. The sample was kept at a particular temperature, irradiated with 532-nm photons, and then the fluorescence intensity of the read form was recorded as a function of the number of laser reading pulses. The decay of fluorescence intensity as a function of laser irradiation, at 0.5 mJ, at various temperatures is shown in Figure 5 (top). These experiments

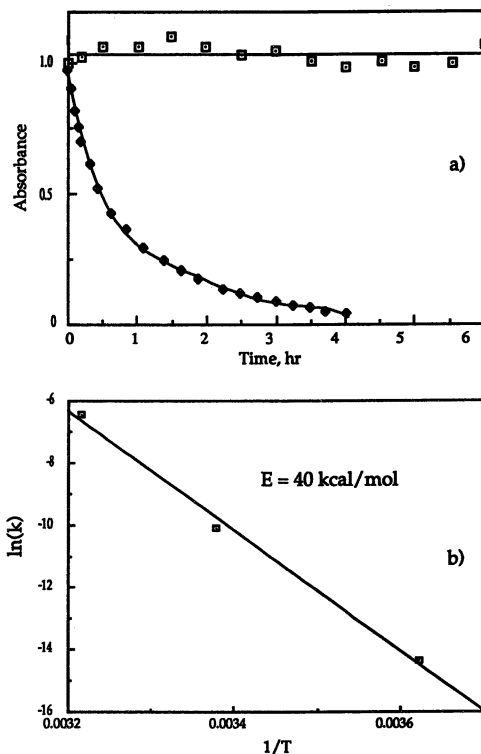


Figure 4. a, Decay of read form of ISP in polymethyl methacrylate; top trace: at 77 K; bottom trace: at room temperature. b, Activation energy plot of bridged read form of ISP in poly(hydroxyethyl methacrylate). k is thermal decay rate constant and T is temperature in kelvins.

showed that the lifetime of the read form of SP, dissolved in a poly(methyl methacrylate) (PMMA) solid block, increase with decrease in temperature (Table II).

Fatigue

Fatigue, which for a photochromic molecule is defined as the gradual loss of information after repeated write and read cycles, is a very important property of the device. Fatigue places a limit on the maximum number of write and read cycles that can be performed with a particular single 3D memory unit. Fatigue, therefore, may be measured by the decrease in the fluorescence intensity of the written form as a function of the cycles performed. The effect of temperature and laser power on fatigue may also be important and has been studied extensively. In the studies presented here, we used a 1-cm PMMA cube in which 10^{-2} M

1 SP was homogeneously dispersed. A set of $\sim 30\text{-}\mu\text{m}$ spots were written inside this PMMA-SP cube. The material was maintained at $\sim 77\text{ K}$ throughout the experiment. The reason for this low temperature was to ascertain that any decay measured was due to the reading process rather than to temperature. In these experiments, the written spot was illuminated with a laser light having the preselected energies shown in Figure 5 (bottom), and the change in the fluorescence intensity of the written spot was measured as a function of reading cycles. The data show that the energy of the beam plays a dominant role on the fatigue and the number of cycles that may be performed before the stored

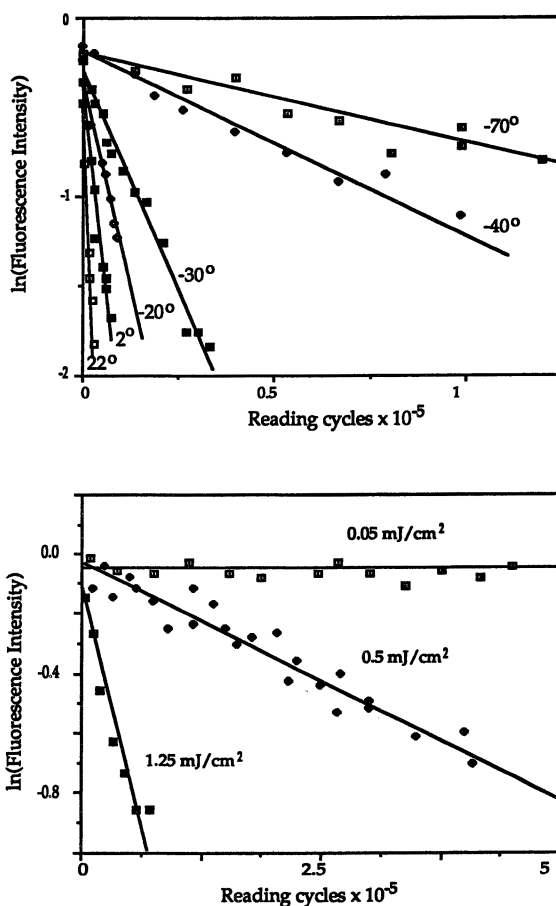


Figure 5. Top, Fatigue of 1SP in poly(methyl methacrylate) as a function of temperature; shown as fluorescence intensity versus number of cycles at various temperatures at 0.5 mJ/cm^2 . Bottom, Fatigue as a function of laser energy for 1SP.

Table II. Photostability of ISP in Various Polymers

Polymer	20 °C	0 °C	-20 °C	-30 °C	-40 °C	-60 °C	-70 °C	-80 °C	ΔE (kcal/mol)
PMMA	1.3×10^{-2} (76)	5.2×10^{-3} (190)	2.7×10^{-3} (370)	1.2×10^{-3} (850)	2.4×10^{-4} (4100)		1.2×10^{-4} (8400)		6.4
PS	4.9×10^{-3} (200)	6.1×10^{-3} (160)	7.2×10^{-4} (1400)		3.3×10^{-4} (3000)	2.7×10^{-4} (3700)			5.0
PVA	5.8×10^{-2} (17)	3.5×10^{-2} (28)	2.3×10^{-3} (430)		1.4×10^{-3} (715)	2.9×10^{-4} (3450)		2.5×10^{-5} (40000)	8.7

NOTE: Values are thermal decay constant expressed in s^{-1} with τ value in parentheses, expressed in s. 1 SP, 1 spirobenzopyran; ΔE , change in energy; PMMA, poly(methyl methacrylate); PS, polystyrene; PVA, poly(vinyl alcohol).

information fades. The fatigue expressed as decrease in fluorescence intensity shows that one-half of the information is lost after 10^5 cycles when the energy of the beam is 1.25 mJ/cm^2 . The same intensity decrease occurred after $\sim 10^6$ cycles when the power of the reading laser was 0.5 mJ/cm^2 . Practically no change was observed when a 0.05-mJ/cm^2 energy laser beam was used to read the stored information. These results suggest that to utilize the SP material for the construction and utilization of a memory device, the energy of the laser should be $\sim 50 \mu\text{J}$ if the information is to read more than 10^6 times.

Effect of Polymer on Stability

The stability of the written form was also measured as a function polarity and hardness of the host medium. The measurements were based on the decrease in the fluorescence intensity of the read form as a function of the polarity and hardness of the polymer matrix while keeping all other parameters, such as temperature, wavelength, and intensity of the laser beam constant throughout the experiment. The fluorescence quantum yields of SP solutions in methyl methacrylate (MMA), in 2-hydroxyethyl methacrylate (HEMA), and in the corresponding polymers are listed in Table III.

We have shown previously that polar solvents stabilize the written polar structure and attenuate the rate of isomerization. Similarly hard polymer matrices limit the ability for molecular group movement, thus making isomerization slower and consequently increase the fluorescence quantum yield. The data in Table III show that the fluorescence quantum yield of SP increases from HEMA to PHEMA from 3.0×10^{-3} to 5.0×10^{-2} . A similar increase on the fluorescence quantum yields is found for MMA and PMMA. The higher fluorescence quantum yield for the read form of SP was observed in PHEMA polymer matrices, which are both hard and polar. These data show that the choice of polymer has a strong influence in the stability of the read form. It follows, therefore,

Table III. Kinetic and Spectroscopic Properties of ISP

<i>ISP desolved in</i>	<i>Fluorescence Quantum Yield</i>	<i>Thermal Decay Constant (s^{-1})</i>	<i>Lifetime (s)</i>
MMA	$<1 \times 10^{-3}$	7.2×10^{-3}	14
HEMA	3.0×10^{-3}	8.6×10^{-4}	1200
PMMA	1.6×10^{-2}	4.0×10^{-4}	2500
PHEMA	5.0×10^{-2}	3.0×10^{-5}	33000

NOTE: ISP, 1 spirobenzopyran; MMA, methyl methacrylate; HEMA, 2-hydroxyethyl methacrylate; PMMA, poly(methyl methacrylate); PHEMA, poly(hydroxyethyl methacrylate).

that the period of time during which the written information is retained is a function of both the hardness and the polarity of the polymer used. This, of course, holds for the SP molecules studied and is not necessarily a condition for other materials that may be utilized for 3D storage.

We have presented a rather short description of the studies performed on two-photon 3D memory. The data show that it is possible to write and read information in a 3D format.

It is evident, however, that much more research and in-depth studies must be performed to understand the molecular characteristics of these materials, their nonlinear properties, and the parameters that influence the stability of the write and read forms before a practical device may be constructed. In addition, the background noise during the reading and writing processes and many optical and engineering requirements still need to be addressed. Many difficulties are encountered when one attempts to construct even a prototype 3D optical system. Our studies indicate that photochromic materials are promising candidates for utilization in 3D optical-storage memory devices. We trust that continuing research pursued on 3D memory devices by means of two-photon, and the other promising areas mentioned briefly in the opening paragraphs of this chapter will result in a 3D optical-storage memory that will make, eventually, optical computing and large-scale parallel data processing a reality.

Acknowledgment

This work was supported in part by the U.S. Air Force, Rome Laboratories, and DARPA under contract F 30602-90-C0014.

References

1. Gaylord, T. K. *Opt. Spectra* 1972, 6, 25.
2. *Persistent Hole Burning: Science and Applications*; Moerner, W. E., Ed.; Springer: Berlin, Germany, 1987.
3. D'Auria, L.; Huignard, J. P.; Slezak, C.; Spitz, E. *Appl. Opt.* 1974, 13, 808.
4. Parthenopoulos, D. A.; Rentzepis, P. M. *Science (Washington, D.C.)* 1989, 245, 843.
5. Parthenopoulos, D. A.; Rentzepis, P. M. *J. Appl. Phys.* 1990, 68, 814.
6. Stickler, J. H.; Webb, W. W. *Optics Lett.* 1991, 16, 1780.
7. Birge, R. R. *Annu. Rev. Phys. Chem.* 1990, 9, 683.
8. Birge, R. R.; Fleitz, P. A.; Gross, R. A.; Izgi, J. C.; Laurence, A. F.; Stuart, J. A.; Tallert, J. R. *IEEEFMBS* 1990, 12, 1788.
9. Brauchle, C.; Hampp, N.; Oesterhelt, D. *Adv. Mater.* 1991, 3, 420.
10. Thoma, R.; Hampp, N.; Brauchle, C.; Oesterhelt, D. *Optics Lett.* 1990, 16, 651.
11. Hunter, S.; Kiamilev, F.; Esener, S.; Parthenopoulos, D. A.; Rentzepis, P. M. *Appl. Opt.* 1990, 29, 2058.
12. DeCegama, A. L. *Parallel Processing Architecture and VLSI Hardware*, Prentice Hall: Englewood Cliffs, NJ, 1989.

13. Robinson B. *Electron. Eng. Times* **1989**, September 18.
14. (a) Goeppert-Mayer, M. *Ann. Phys.* **1931**, 9, 273; (b) Demtröder W. *Laser Spectroscopy*; Springer-Verlag: New York, 1988.
15. Birge, R. R. *Computer* **1992**, 25, 56.
16. Bertelson, R. C. In *Techniques of Chemistry: Photochromism*; Brown, G. M., Ed.; Wiley-Interscience: New York, 1971; Vol. 3, p 45.
17. Krysanov, S. A.; Alfimov, M. V. *Chem. Phys. Lett.* **1982**, 91, 77.
18. Dvornikov, A. S.; Malkin, Y. N.; Kuzmin, V. A. *Bull. Ac. Sci. USSR Div. Chem.* **1982**, 31, 1355.
19. *Photochromism. Molecules and Systems*; Durr, H.; Bouas-Laurent, H., Eds.; Elsevier: New York, 1990.
20. Heller, H. G.; Oliver, S. J. *Chem. Soc. Perkin Trans.* **1981**, 1, 197.
21. Horie, K.; Hirao, K.; Keumochi, N.; Mita, I. *Macromol. Chem. Rapid Comm.* **1988**, 9, 267.
22. Lindmayer, J. *Sensors* **1986**, 3, 37.
23. Lindmayer, J. *Solid State Technol.* **1988**, August, 135.

RECEIVED for review March 12, 1992. ACCEPTED revised manuscript March 2, 1993.

Optimization of Materials for Second-Order Nonlinear Optical Applications

Christopher B. Gorman,^{1,2} Gerard H. J. VanDoremaele,²
and Seth R. Marder^{*,1,2}

¹ Jet Propulsion Laboratory, California Institute of Technology, 4800 Oak Grove Drive, Pasadena, CA 91109

² Molecular Materials Resource Center, The Beckman Institute, California Institute of Technology, Pasadena, CA 91125

This chapter outlines the approaches to the design and fabrication of organic nonlinear optical materials. First, the relationships between chemical structure and the first molecular hyperpolarizability (β) are described. Then, issues related to incorporation of these molecules into bulk materials with useful second-order susceptibilities, ($\chi^{(2)}$) are reviewed, in particular, crystalline and thin-film materials. We describe advantages and disadvantages of the various approaches in light of recent results.

A VARIETY OF ORGANIC COMPOUNDS containing loosely held electrons (typically in π -bonds) could give rise to very large nonlinear optical (NLO) responses relative to those of inorganic materials was an observation made by several research groups in the early 1970s. Furthermore, most organic NLO materials exhibit ultrafast response times compared to inorganic materials because the polarization response is purely electronic and has virtually no nuclear component. The realization that these large, fast nonlinearities could lead to efficient optoelectronic devices provided the impetus for substantial research on organic materials for NLO applications.

In contrast to inorganic materials, the NLO response of organic materials has been found to be molecular in origin. As a result, there is the potential for development of a systematic understanding of how molecular structure relates to the molecular first hyperpolarizability, β , a tensor quantity used to characterize the efficacy of a molecule in generating a

* Corresponding author.

0065-2393/94/0240-0179\$12.32/0
© 1994 American Chemical Society

second-order response. It can be shown that second-order NLO effects only occur in noncentrosymmetric molecules (i.e., those lacking inversion symmetry). Likewise, for the potentially large molecular hyperpolarizability of an organic molecule to lead to a macroscopic susceptibility (e.g., $\chi^{(2)}$), it is necessary for the molecules to be in a noncentrosymmetric arrangement within the bulk. In this chapter, we attempt to outline briefly some of the issues pertaining to second-order NLO materials and try to summarize the present state of understanding regarding these issues. As much as possible, we try to illustrate important concepts using examples from the literature. We emphasize that this chapter is not intended to be a comprehensive review of current NLO research. Numerous recent reviews and volumes describing the state-of-the-art are available to provide the reader with more detailed information (1).

This chapter is organized in two sections. In the first section, molecular nonlinearities are discussed. First basic computational techniques for calculating hyperpolarizabilities and experimental techniques for measuring hyperpolarizabilities are outlined. Then basic design strategies for achieving asymmetric polarization are presented, highlighting the effects of donor–acceptor strength and conjugation length. With the aid of a simple molecular orbital analysis of a simplified quantum chemical expression for the first hyperpolarizability, β , the shortcomings of existing approaches are discussed and alternative approaches for the optimization of β are presented.

In the second part of the chapter, materials issues are addressed. The need to consider materials issues other than optimization of nonlinearity is noted and various mechanisms to achieve noncentrosymmetric bulk materials are reviewed. First crystalline materials are discussed as are approaches to engineer noncentrosymmetric crystals via hydrogen bonding or by the use of organic salts. Then the concept of electric field poling of molecules within a polymer matrix is introduced. Factors that control the degree and stability of molecular alignment in the polymer are highlighted. New approaches to improve upon these factors are reviewed, and alternative methods including self assembly and Langmuir–Blodgett (LB) film are briefly discussed. Finally, our perspective on the future outlook for second-order NLO research is presented.

Structure–Property Relationships for the NLO Response in Organic Chromophores

Computational and Experimental Methods. It is essential to understand how chemical structure relates to β if we are to develop guidelines for the synthesis of highly nonlinear molecules and materials. To develop this understanding, it is necessary to formulate theoretical

models for the relationship between structure and β and to test these models by obtaining experimental values of β for carefully chosen series of compounds. Several theoretical methods have been developed to calculate hyperpolarizabilities (2, 3), two of which have been most routinely applied. The first, termed finite-field (FF), calculates the dipole moment of a molecule in its ground state in the presence of a direct current (dc) electric field. Zero-frequency polarizability and hyperpolarizability tensor components are computed by taking the derivatives (first derivative for α , second derivative for β , etc.) of this dipole moment with respect to the field (4). The second method, sum-over-states (SOS) uses an expression for the hyperpolarizabilities derived from perturbation theory:

$$\beta_{ijk} \propto \sum_e \sum_{e'} \frac{\mu_{ge}^i \mu_{ee'}^j \mu_{e'g}^k}{E_{eg} E_{e'g}} \quad (1)$$

In this expression the terms in the numerator are transition dipole moments (μ) between the states (here g is the ground state and e and e' are excited states) of the molecule, and the terms in the denominator are the transition energies (E) between these states. Thus, the hyperpolarizability is expressed in terms of a mixing between the ground and excited states of the molecule (5). A simplified version of this formula in which only two states are taken into account has been proven to be helpful when rationalizing structure–property relationships in NLO chromophores. This two-state formula is expressed as follows:

$$\beta \propto (\mu_{ee} - \mu_{gg}) \left(\frac{\mu_{ge}^2}{E_{ge}^2} \right) \quad (2)$$

Although reservations exist for its general adequacy in extended molecules, the two-state approximation captures the qualitative spectroscopic dependencies of β for molecules with strong charge-transfer (CT) transitions. The two-state expression for β predicts that chromophores with large extinction coefficients (related to the transition dipole moment between the ground and excited state, μ_{ge}) and low-energy absorptions (i.e., $1/E_{ge}^2$) will have large β values. The term, $\mu_{ee} - \mu_{gg}$, the difference in dipole moments between the ground and excited states of the molecule, indicates that a large change in dipole moment upon excitation causes a large β .

Experimental β values can be obtained by the electric field-induced second-harmonic generation (EFISH) technique. In this experiment, the vectorial projection of β is measured along the molecular dipole direction, denoted β_μ (6–8). Because β_μ is frequency-dependent, comparison of values measured for different molecules must account for dispersion,

typically by using a model. An alternative approach is to perform measurements with sufficiently low-frequency radiation to directly obtain an estimate of the limiting nonresonant value. If the ground-state dipole is oriented in a direction along which the projection of β contains the dominating components, then analysis of data from the EFISH experiment provides a meaningful measure of the second-order optical nonlinearity of the molecule.

This section outlines our current understanding of the relationship between molecular structure and β . Many results cited here are taken from extensive structure–property studies conducted by Cheng et al. (9–11). Although some of the molecules described in these studies have been examined in the past and because the magnitude of the NLO response is dependent upon a number of factors, including the wavelength of the light employed and the environment in which the molecule resides (e.g., solvent in the EFISH experiment), a consistent set of experimental conditions must be maintained if meaningful comparisons are to be made. When such measurements are reported, we attempt to provide references to earlier studies on the molecule of interest.

Basic Features of the NLO Chromophore. Organic second-order NLO molecules have delocalized (polarizable) electrons that respond asymmetrically to electric fields (such as those associated with light). So, the ease of polarization depends upon the direction of polarization. The polarizability of the π -electron system can be biased by attaching electron-donors and -acceptors at the ends. Thus, as the electrons interact with the oscillating electric field in light, they will show a preference to shift from donor toward acceptor and a reluctance to shift in the opposite direction. Two prototypical examples of NLO chromophores are *p*-nitroaniline (PNA, Figure 1) (12) and 4-dimethylamino-

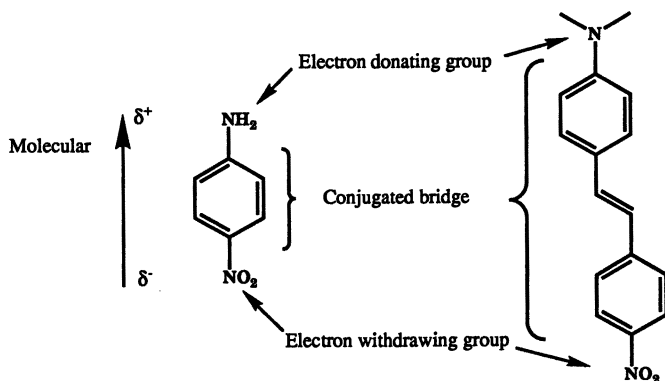


Figure 1. PNA (left) and DANs (right).

4'-nitrostilbene (DANS, Figure 1) (13). In PNA, the benzene ring π -system provides the polarizable electrons, the amine and dialkylamino groups act as the donor, and the nitro acts as the acceptor inducing directionally asymmetric polarizability. In DANS, the two benzene rings and the double bond are all conjugated, providing a longer π -system. This increased conjugation length, in general, leads to increased linear and nonlinear polarizability.

Asymmetry—Donors and Acceptors. The notion of donors and acceptors has been well developed by physical organic chemists to aid in understanding reactivity and spectroscopy. Hammett first tabulated the relative electronic influence of a substituent by examining its effect on reactivity (14). These Hammett parameters have been tabulated for a number of groups (15) and have been applied to the relationship between donor and acceptor strength and NLO response. For donor-acceptor substituted benzenes, NLO response is seen to scale almost linearly with donor-acceptor strength as indicated by the Hammett parameters σ^+ and σ^- (Figure 2) (10). Similar results are observed for 4,4'-disubstituted stilbenes (16). Accordingly, substantial efforts have been devoted to searching for better donors and acceptors. To this end, Katz

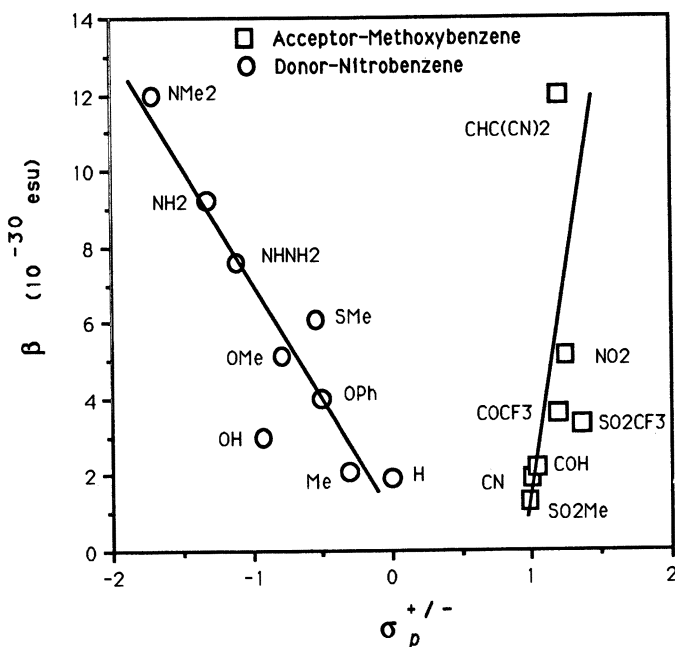


Figure 2. β versus $\sigma^{+/-}$ for p-disubstituted benzenes (Reproduced with permission from reference 10.)

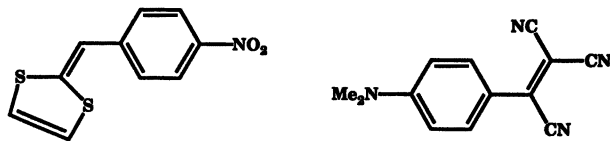


Figure 3. Strong donors and acceptors. Dithiolyldenemethyl is a donor (left) and a tricyanovinyl group is an acceptor (right).

et al. (17, 18) have prepared chromophores containing donors such as dithiolyldenemethyl (19) and acceptors such as dicyanovinyl and tricyanovinyl (Figure 3). These molecules show higher β_μ values than benzene molecules substituted with conventional donors (e.g., dimethylamino) and acceptors (e.g., nitro). It is difficult, however, to separate the effect of these groups as donor–acceptor and their role in increasing the effective conjugation length of the chromophore, another effect that has been shown to increase β (17, 18).

For donor–acceptor-substituted benzenes and stilbenes, strong donors and acceptors correlate with increased λ_{\max} and β (even accounting for dispersion, Figure 4). This transparency–nonlinearity trade-off is expected within the context of the two-state model. Examination of the two-state equation (eq 2) reveals that there should be an inverse quadratic relationship between the intrinsic nonlinearity (β_0) and the energy of the CT transition (10, 20). This relationship assumes that the transition dipole moment and the change in dipole moment between the CT states are independent of donor–acceptor strength. However, it has been

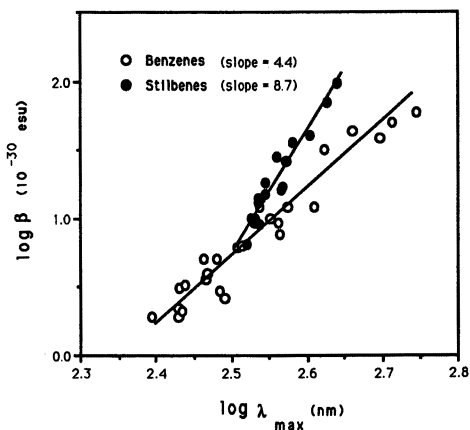


Figure 4. Logarithmic plot of β versus λ_{\max} for p-disubstituted benzenes and 4,4'-disubstituted stilbenes. (Reproduced from reference 10. Copyright 1991 American Chemical Society.)

pointed out that in these weakly polarized systems, these latter two terms might also be correlated with combined donor–acceptor strength. These factors could lead to further enhancement of β (10).

Organic salts are also excellent candidates for NLO chromophores because charged groups in a molecule may be expected to be excellent electron donors or acceptors (21). For example, Meredith has estimated that β for 4'-dimethylamino-*N*-methyl-4-stilbazolium salt is roughly equivalent to that of DANS ($\beta_{\mu} = 72 \times 10^{-30}$ esu) (10).

In addition to conventional organic donors and acceptors, transition-metal moieties have been examined as donors and acceptors (22). Preliminary studies on ferrocene (23), pentacarbonyltungsten-pyridine (24), and bisphosphinehaloplatinum aryl complexes (22) indicate that donor–bridge–acceptor molecules with organometallic end groups are useful for engineering molecular hyperpolarizabilities. In several cases, the organometallic compounds exhibited nonlinearities comparable to those found in some of the better organics. Many of the same chemical factors that influence the magnitude of hyperpolarizabilities of organic materials (i.e., nature of the π -electron bridge and donor–acceptor strength are operative in the metal-containing systems as well). Visible absorption bands may limit the utility of many metal organic compounds for harmonic generation of UV or visible light. However, they may have utility for telecommunication applications that utilize 0.8-, 1.3-, or 1.5- μm radiation.

Effect of the Length and Nature of the Electron System on the Optical Nonlinearity. As we have seen, the perturbation of the π -system resulting from substitution with donors and acceptors plays an important role in determining the magnitude and sign of β . However the majority of the polarization response lies within the π -system itself, therefore, it is important to consider how the details of the π -system affect β . Researchers have investigated a variety of systems containing delocalized π -electrons. Some types of π -electron bridged systems are shown in Figure 5. Structure–property studies for some of these systems, including the stilbenes (11, 25) and tolans (11, 26) have been performed. Donor–acceptor polyenes (with the donor and acceptor attached directly to the vinylic group as opposed to diphenylpolyenes, which resemble stilbenes) have been the subject of great theoretical interest (3, 27–32) and only recently have experimental results been reported (33–36). Although other more exotic chromophores illustrate some of the unusual structural features that can give rise to a measurable hyperpolarizability, none represent approaches toward optimal chromophores and thus will not be discussed in detail.

Another important consideration is the planarity of the π -system and its effect upon the optical nonlinearity. A nonplanar π -system results

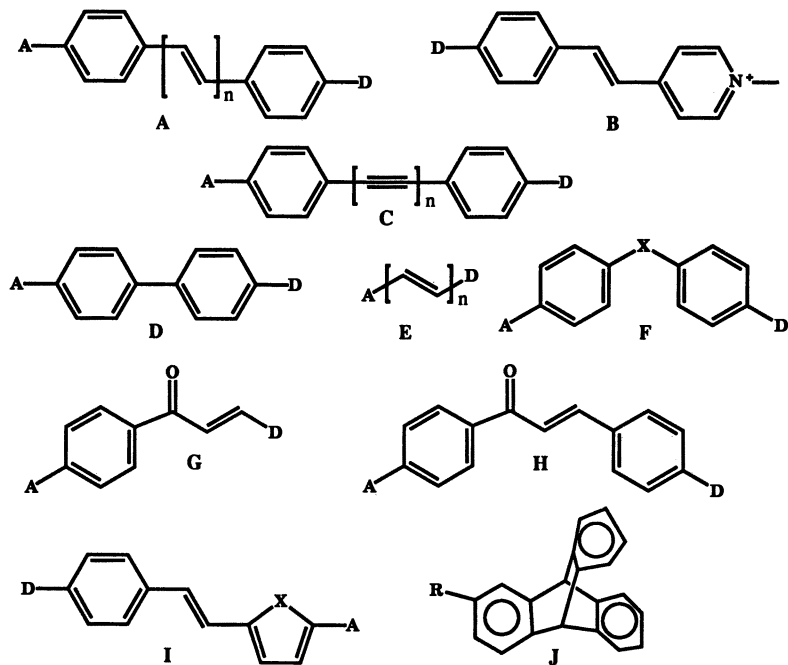


Figure 5. Some systems studied for their NLO properties include (A) stilbenes and longer α,ω -diphenyl polyenes (9, 10, 13, 16, 25, 37–40), (B) stilbazolium salts (21, 41–46), (C) tolanes (diphenyl acetylenes) and longer α,ω -diphenyl polyynes (11, 26, 35, 47–49), (D) biphenyls (11, 25, 50), (E) polyenes (3, 27–36), (F) diphenyl chalcogens ($X = O, S, Se, Te$) (51–53) and benzophenones ($X = CO$) (54) and sulfones ($X = SO_2$) (52, 53), (G) enones (55), (H) chalcones (54, 55), (I) systems containing heterocycles such as thiophenes ($X = S$), furans ($X = O$), and pyrroles ($X = NH$) (11, 54, 55), and even the three-dimensional (J) triptycenes (56).

in reduced effective conjugation and reduced β . This consideration has been studied computationally on donor–acceptor diphenylacetylenes (Figure 5C) by Barzoukas et al. (35) and experimentally in a comparison of donor–acceptor biphenyls and fluorenes by Cheng et al. (11). For example, donor–acceptor biphenyls have lower β_μ values relative to their fluorene analogues (Figure 6) due to this nonplanarity, but as donor and acceptor strength increases, the β_μ values for the biphenyl- and fluorene-derivatives converge, presumably because the biphenyl becomes less twisted, enabling CT.

Usually, β is increased by lengthening a molecule (Figure 7). In general, an increase in conjugation length results in a larger transition dipole moment and lower energy absorption in the molecule, which leads to larger β according to the two-state expression. This is true for polyenes and diphenylpolyenes (Table I) that have been studied both

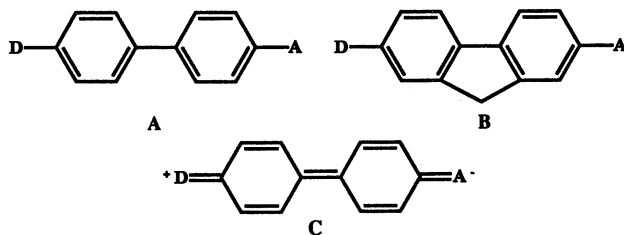


Figure 6. The constitution of donor-acceptor (A) biphenyls, (B) fluorenes, and (C) the resonance structure representing the charge-transfer form of the chromophore.

computationally (28, 29, 31) and experimentally (33, 34, 57, 58). Here, β_μ was related to conjugation length with power law expressions of the form ($\beta_\mu \propto n^m$) where n is the (often somewhat ill-defined) conjugation length. The value of the exponent, m , varies with the experimental conditions or computational method, but it gives some indication of the relationship between conjugation length and β for these chain lengths. As the molecules become sufficiently long, the communication between the donor and the acceptor eventually drops to zero, and β saturates or possibly decreases. Intuitively one may expect that this saturation length will be π -system dependent with more polarizable systems saturating at a greater length. This behavior has been observed both theoretically and experimentally.

Upon increasing the conjugation length (n), rapid saturation of the hyperpolarizability is observed in polyynes and polyphenylenes (Figure 8) (11, 26, 29). These results suggest that these chromophores contain more localized electrons, both in the bridge and in the donor and acceptor, thus limiting their hyperpolarizability. This result is not surprising given the limitations of these molecular units in a π -system,

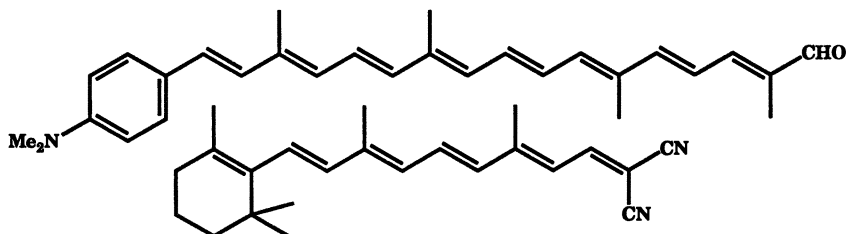
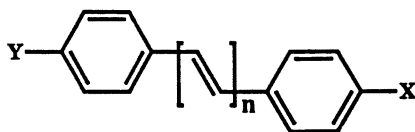


Figure 7. Examples of some long polyenes based upon carotenes that have been synthesized by (top) Lehn (33, 34) and (bottom) Kawabe and Ikeda (36, 59) that show substantial β . The value of $\mu\beta_0$ ($1.34 \mu\text{m}$ in chloroform, corrected for dispersion) of the top molecule is 3400×10^{-48} esu, approximately two orders of magnitude higher than that of PNA.

Table I. Results on Distributed α,ω -Diphenylpolyene Oligomers of the Form:



n	X	Y	Solvent	λ_{max} (nm)	$\mu \times 10^{18}$ (esu)	$\beta \times 10^{30}$ (esu)
1	NO ₂	MeO	CHCl ₃	376	4.5	34
2	NO ₂	MeO	CHCl ₃	397	4.8	47
3	NO ₂	MeO	CHCl ₃	414	5.1	76
4	NO ₂	MeO	CHCl ₃	430	5.8	101
1	NO ₂	NMe ₂	CHCl ₃	430	6.6	73
2	NO ₂	NMe ₂	CHCl ₃	442	7.6	107
3	NO ₂	NMe ₂	CHCl ₃	458	8.2	131
4	NO ₂	NMe ₂	CHCl ₃	464	9 ± 1	190 ± 50

namely the increase in bond-length alternation in the polyynes and the high energy of the quinoid form compared to the aromatic form in the polyphenyls.

Molecular Orbital Analysis of β . In an attempt to formulate generalized structure–property relationships for second-order NLO chromophores, Marder et al. (60) performed a theoretical analysis of a two-state model (61–63) for generic molecules consisting of a donor, acceptor, and two bridge orbitals. It was shown that an optimal combination of donor and acceptor strengths for a given bridge maximizes β . At the time this analysis was performed, molecules with sufficiently strong donors and acceptors to reach the peak of the β -curve have not been synthesized.

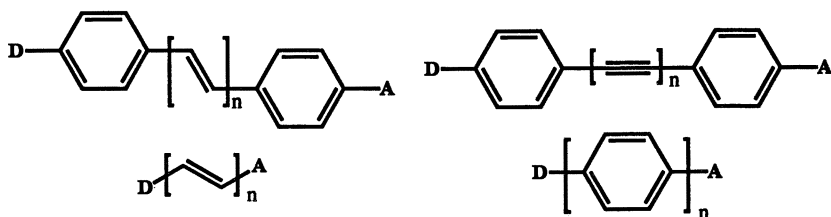
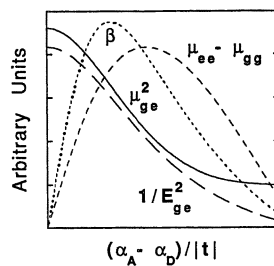


Figure 8. Based upon computation and experiment, the second-order hyperpolarizability in donor–acceptor polyenes and diphenyl-capped polyenes (left) is observed to increase with increasing conjugation length whereas that for diphenyl-capped acetylenes and phenylenes (right) does not increase or quickly saturates at a low conjugation (n).

Figure 9. The dependence of $(\mu_{ee} - \mu_{gg})$, μ_{ge}^2 , $1/E_{ge}^2$, and β on $(\alpha_D - \alpha_A)/|t|$ derived from molecular orbital calculations on the 4-orbital system described in the text. The Coulomb energies are denoted with α and the coupling matrix element between bridge orbitals is $|t|$. (Reproduced with permission from reference 60. Copyright 1991 American Association for Advancement of Science.)



The peaked dependence of β on the difference in Coulomb energies of the end groups (α_A and α_D), normalized by the coupling within the bridge orbitals (t) for a generic 4-orbital π -system is shown in Figure 9. Several qualitative features emerge from this 4-orbital analysis and the two-level model for β in bridged donor–acceptor molecules (60, 64, 65).

In Figure 9, small $(\alpha_A - \alpha_D)/|t|$ represents strong mixing of donor (D) and acceptor (A) orbitals via the bridge, whereas large $(\alpha_A - \alpha_D)/|t|$ represents the decoupling of these orbitals from the bridge. Thus, qualitatively, strong donors and acceptors are on the left and weak donors and acceptors are on the right. When $(\alpha_A - \alpha_D)/|t| = 0$ the π -electrons are symmetrically distributed in both the highest occupied molecular orbital (HOMO) and lowest unoccupied molecular orbital (LUMO), a condition in which both μ_{ge}^2 and $1/E_{ge}^2$ are maximized but the change in dipole moment, $(\mu_{ee} - \mu_{gg})$, is zero (Figure 10). This description corresponds to a symmetrical cyanine chromophore (66, 67) with symmetric π -electron population or to a neutral chromophore substituted with strong donors and acceptors, such that the π -electron density is equally shared between the donor and the acceptor. For neutral asymmetric molecules, large but equal ground- and excited-state dipole moments are expected.

With increasing $(\alpha_A - \alpha_D)/|t|$, the HOMO takes on added donor and reduced acceptor character, whereas the LUMO does the opposite. As a result, the π -electron distribution becomes increasingly asymmetric, leading to reduced μ_{ge}^2 and $1/E_{ge}^2$, but increased $(\mu_{ee} - \mu_{gg})$. This descrip-

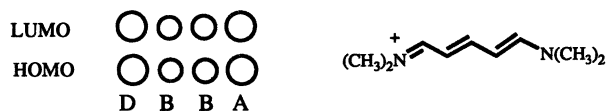


Figure 10. (left) Schematic representation of the magnitudes of the orbital coefficients in the HOMO and LUMO from the 4-orbital calculation, where $(\alpha_A - \alpha_D)/|t| = 0$. (right) Symmetrical cyanine molecule for which $(\alpha_A - \alpha_D)/|t| = 0$.

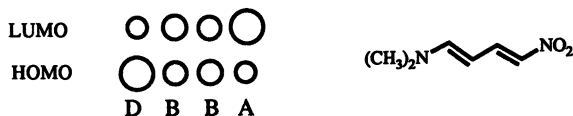


Figure 11. (left) Schematic representation of the magnitudes of the orbital coefficients in the HOMO and LUMO from the 4-orbital calculation where $(\alpha_A - \alpha_D)/|t|$ is relatively small and positive. (right) A polyene molecule with a strong donor and acceptor corresponding to a relatively small value of $(\alpha_A - \alpha_D)/|t|$.

tion corresponds to a somewhat asymmetrical cyanine (68), or to a chromophore with donor and acceptor substituents of moderate strength (Figure 11).

For large $(\alpha_A - \alpha_D)/|t|$, the bridge-mediated donor-acceptor orbital mixing decreases, and the HOMO and LUMO are largely bridge orbital in character. This decoupling leads to a further reduction of μ_{ge}^2 and $1/E_{ge}^2$ as well as a vanishing $(\mu_{ee} - \mu_{gg})$ because the symmetrical bridge orbitals are largely unperturbed by the donor and acceptor. This description corresponds to chromophores with very weak donor and acceptor groups. The optical transition in the UV-visible spectrum with most of the oscillator strength in such a molecule would be dominantly $\pi-\pi^*$ with little CT character (Figure 12).

Because β_{xxx} (the component of β along the CT axis) is the product of these three peaked functions, it also has a maximum on the low $(\alpha_A - \alpha_D)/|t|$ side of the $(\mu_{ee} - \mu_{gg})$ peak. However, for most molecules where β_μ was determined by EFISH (6, 7, 10), β_μ was found to increase with increasing donor- and acceptor-strengths (10). If the optimal combination of donors and acceptors was achieved, using stronger donors and acceptors would lead to too much CT in the ground state, thus decreasing $(\mu_{ee} - \mu_{gg})$ and resulting in smaller β . Because this has not been observed, we believe the examined molecules have values of $(\alpha_A - \alpha_D)/|t|$ that are too large. It is clearly necessary to decrease $(\alpha_A - \alpha_D)/|t|$; this decrease corresponds to an increase in the degree of ground-state CT. Most of the molecules examined by EFISH have dominantly aromatic ground states. The corresponding CT states have predominantly quinonal ring structures. Electronic polarization, arising from an applied electric

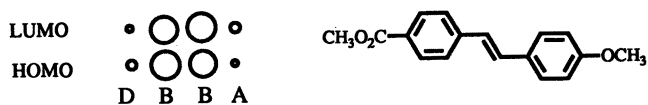


Figure 12. (left) Schematic representation of the magnitudes of the orbital coefficients in the HOMO and LUMO from the 4-orbital calculation, where $(\alpha_A - \alpha_D)/|t|$ is relatively large. (right) Stilbene molecule with a weak donor and acceptor corresponding to a large value of $(\alpha_A - \alpha_D)/|t|$.

field, results in a perturbed ground-state wave function with increased quinonal character and decreased resonance stabilization energy (Figure 13a). Thus, ground-state aromaticity reduces electronic polarizability. As a result, the effective donor and acceptor strengths of a given pair connected by an aromatic bridge will be lower than when they are attached to a degenerate π -electron bridge. Here, a degenerate π -electron bridge is defined as one that has equivalent resonance energies in both the neutral and polarized forms, where terminal π -orbital energy differences are ignored (Figures 13b and 13c). Such a bridge will neither assist nor impede CT. Compounds with somewhat quinonal ground states and aromatic excited states can be synthesized and tend to assist charge polarization (Figure 13d) (69). Based on the energetic considerations detailed previously, we suggest that the choice of an aromatic ground state is the predominant factor that has limited the magnitude of β for a given chain length. Molecules having degenerate π -electron bridges, such as polyenes or molecules with equal ground-state aromatic and quinonal character, will not lose aromaticity upon CT. This greatly diminishes the effective $(\alpha_A - \alpha_D)/|t|$ and may allow one to optimize β .

To test this hypothesis, dimethylindoaniline (DIA, Table II, 1), a commercially available dye with a π -system as in Figure 13c was examined (60). In the ground state, one ring of this π -system is aromatic, and the other ring is quinonal. In the charge-separated state, the aromatic–quinonal nature of each ring is reversed, preserving the π -electron degeneracy. EFISH measurements in chloroform at 1.907

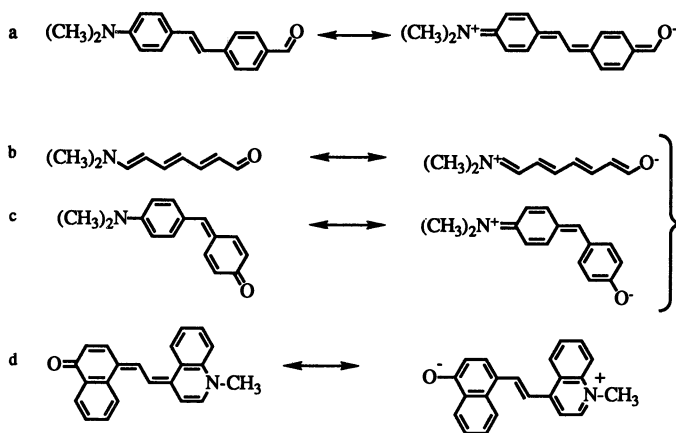


Figure 13. Limiting resonance forms for molecules (a) with an aromatic ground state where resonance energy is lost in the CT state, (b) with polyene and (c) with aromatic–quinonal ground states where resonance energy does not change in the CT states (d) with a quinonal ground state where resonance energy is gained in the CT state.

Table II. Optical Data for Compounds 1-5

Compound Structure	No.	λ_{max} (nm)	$\beta \times 10^{30}$ (esu)	$\beta_0 \times 10^{30}$ (esu)
	1	590	190	106
	2	430	73	55
	3	610	91	48
	4	412	52	40
	5	487	266	183

μm yielded a very large $\beta_\mu = 190 \times 10^{-30}$ esu and $\beta_\mu(0)$ of 106×10^{-30} esu after correcting for dispersion (Table II) (61, 63). In contrast, for DANS (Table II, 2) $\beta_\mu = 73 \times 10^{-30}$ esu and $\beta_\mu(0) = 55 \times 10^{-30}$ esu. Thus, even though DIA is two atoms shorter than DANS and lacks coplanar rings, β_μ is roughly a factor of three greater, and $\beta_\mu(0)$ is almost a factor of two greater.

It was hypothesized that breaking the degeneracy of the π -system while keeping the overall length of the molecule constant would in general result in a lower hyperpolarizability. To test this hypothesis ω -(4-*N,N*-dimethylaminophenyl)penta-2,4-dien-1-al (Table II, 4) was examined. This molecule is structurally similar to 1 but lacks the ring critical for the degeneracy of the π -system. The value of β for this compound (52×10^{-30} esu) is more than three times smaller than that of 1. Similarly, one might expect that loss of aromaticity in the nitrophenyl ring of DANS would lead to a large enhancement of β . Accordingly, 6-(4-*N,N*-dimethylaminophenyl)-1-nitrohexa-1,3,5-triene (Table II, 5) was synthesized and its hyperpolarizability was measured. A factor 3.3 enhancement of β for 5 versus DANS was realized (Table II). These results strongly suggest that the enhanced nonlinearity of 1 is due largely to the degenerate π -electron bridge.

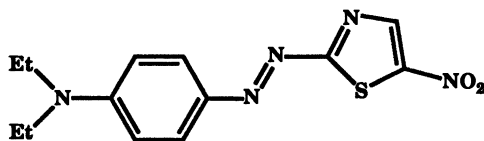


Figure 14. One of the thiazole chromophores explored by Dirk et al. (70).

Further support for this hypothesis comes from the work of Dirk et al. (70) who examined chromophores using the less aromatic thiazole ring (Figure 14). They noted an enhanced β relative to the DANS and attributed the improvement to the lowered aromaticity of the heterocyclic thiazole ring. Cheng et al. (11) also explored the use of heterocyclic rings in NLO chromophores. Both groups observed red shifts in the optical absorption spectra of the chromophores compared to aromatic analogs. Enhanced hyperpolarizabilities were also observed. Replacement of a benzene ring with a furan or thiophene ring resulted in enhanced hyperpolarizability.

Some groups have investigated structures with quinoidal ground states. Brédas (71) examined 2-methylene-2H-pyrrole derivatives (Figure 15), but found no increase in hyperpolarizability compared to PNA. Lalama (69) investigated structures, such as that in Figure 15 (right) and found large negative values for β ($\beta_x = -240 \pm 60 \times 10^{-30} \text{ cm}^5/\text{esu}$). According to the two-state expression, β is negative if there is a decrease or change in sign in the dipole moment upon excitation. This result suggests that the charge-separated resonance structure is the main contributor to the ground state of this molecule, which is plausible because it is aromatic in this form. Li et al. (31) computationally studied molecules of this type and also found large β values. Although this chap-

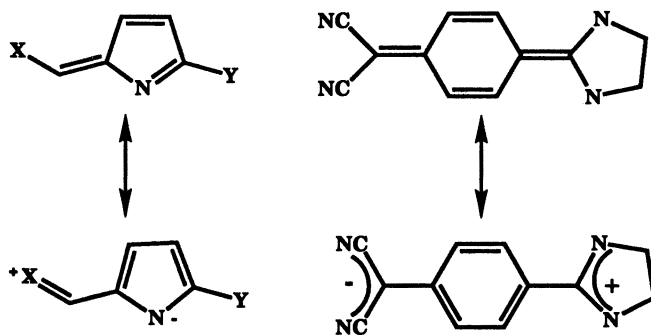


Figure 15. The two resonance structures of the 2-methylene-2H-pyrrole derivatives studied by Brédas (71) (left) and a dicyanoquinodimethane derivative studied by Lalama (69) (right).

ter indicates that the sign of β was computed, only its magnitude was reported.

Recently, Ikeda et al. reported β for several Brooker dyes (72, 73) based upon thiobarbituric acid derivatives (74, 75). These compounds can pick up some aromatic stabilization in the charge-separated resonance structure. These dyes exhibited large negative β values [$\mu_0\beta_0 = -5400 \times 10^{-48}$ esu for Figure 16 (left) and $-12,000 \times 10^{-48}$ esu for Figure 16 (right)].

Optimization of Materials for Nonlinear Optics

We have reviewed some of the strategies employed to prepare molecules with large second-order optical nonlinearities. We now turn our attention to the optimization of materials, which is far more complex due to the variety of requirements that must be fulfilled for a given application. The remainder of this chapter focuses on the optimization of materials that utilize two common NLO effects, electrooptic (EO) switching and frequency generation [e.g., second-harmonic generation (SHG), and third-harmonic generation (THG)]. Many applications utilize these effects, and each application has unique requirements, the details of which are beyond the scope of this chapter. However, there are general material requirements that all second-order NLO materials must fulfill. In particular, the bulk material must be noncentrosymmetric to exhibit second-order NLO effects. Thus, it is not sufficient to incorporate a

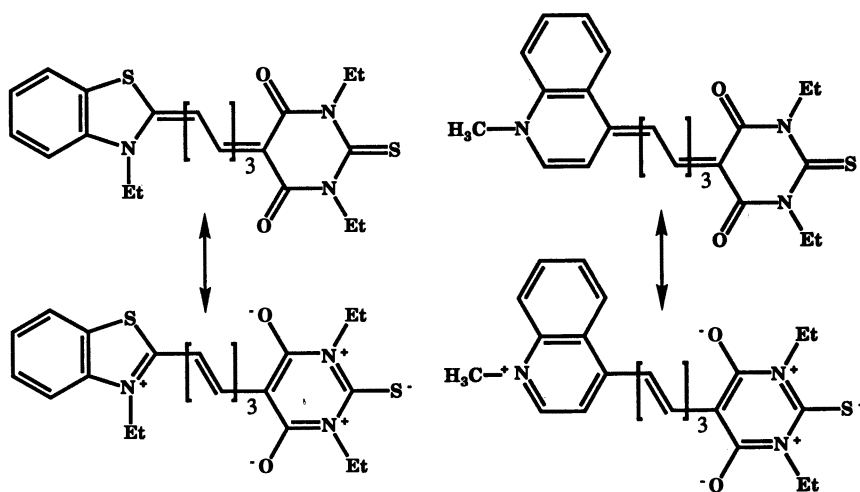


Figure 16. Resonance structures of some of the thiobarbituric acid-based cyanines showing the gain in aromaticity in the end groups upon charge separation.

molecule with a large β isotropically in a medium. Furthermore, the materials must exhibit low optical losses from either absorption or scattering, and they must be orientationally, environmentally, and photochemically stable. In addition, if the materials are to be incorporated into devices, it is necessary for them to be processable (76). In general, two basic materials classes have been examined as second-order NLO materials: single crystals and thin films. In the sections that follow, we will examine the solutions to the problems associated with each of these materials classes.

Crystalline Materials. Initial studies of organic materials for NLO applications focused on single crystals. One serious problem with this approach is that $\sim 75\%$ of all achiral molecules crystallize in centrosymmetric space groups and thus have vanishing $\chi^{(2)}$ (20). In addition, it is often difficult to grow optical quality single crystals. Often the crystals exhibit poor mechanical properties that complicate device fabrication and can limit their range of operating conditions (76). On the other hand, if an optimal or nearly optimal alignment of chromophores in the crystal lattice can be found, then barring a phase transition, that orientation will be indefinitely stable (i.e., the chromophores will not become unaligned with time). Furthermore, single crystals typically have the highest number density of active chromophores possible.

Proper alignment of chromophores in the bulk is a major impediment to achieving the goal of large $\chi^{(2)}$. "Proper" alignment itself is application-dependent. For EO applications, it is generally desirable to have all of the chromophores aligned in parallel so that $\chi^{(2)}$ is the largest possible. Thus, the most desirable space group for electrooptics applications is P1, which has only translational symmetry elements. For sum- and difference-frequency mixing applications, of which SHG is the most common example, the situation is more complex because optimization of the $\chi^{(2)}$ tensor is only one of several optical constraints. To combine polarization waves efficiently, conditions must be met so that the fundamental and the second-harmonic polarization waves reinforce each other (i.e., they remain in phase as they propagate through the medium) (77). If this "phase matching" requirement is met, then the second-harmonic intensity increases as the light propagates through the crystal. Zyss and Oudar (78) determined the optimal orientation of the chromophores within the crystal lattice for various crystal classes. In general, they found that the optimal geometry for phase-matched SHG had the chromophores oriented in a herringbone pattern in which the optimal angle between the chromophores was dependent upon the particular symmetry operations of the space group.

Characterization of Second-Order NLO Crystals. It is worth digressing to discuss how the NLO properties of crystalline materials are

often characterized before examining strategies for isolating optimized crystals. Usually a candidate material is first subjected to the Kurtz powder test (79). In this technique, a sample of crystalline material is illuminated with laser radiation, and, if the material has an appreciable $\chi^{(2)}$, a signal at the second harmonic will be generated. This signal is isolated from the fundamental light and other spurious radiation either by use of narrow bandpass filters or of a monochromator, or both. The isolated second-harmonic light is collected and its intensity is compared to some reference compound (e.g., quartz or urea) of which $\chi^{(2)}$ is well-characterized. The magnitude of the SHG signal obtained from the Kurtz powder test is largely determined by the orientation of the chromophores in the crystal lattice, linear optical, and dispersive factors.

After initial screening by the powder technique, a single crystal of the promising compound is typically grown and characterized by crystallography. A variety of detailed linear and nonlinear optical measurements are then performed to determine the dielectric constants, the frequency-dependent refractive indices, the EO coefficients, and the SHG coefficients (related to the $\chi^{(2)}$ tensor). EO coefficients are frequently denoted as r_{ijk} (80) and form a tensor, as do the coefficients of β . The first subscript refers to the resultant polarization of the material along a defined axis and the following subscripts refer to the orientations of the polarization of the applied electric fields. Because the EO effect involves two fields mixing to give rise to a third, r_{ijk} is a third-rank tensor. The SHG efficacy is characterized by the d coefficients (80), which are determined by careful SHG studies and which also form a third-rank tensor. In general, characterization of thin films uses similar techniques.

What Controls the Crystal Structure? Numerous energetic factors influence crystal packing making it extremely difficult to predict a priori the crystal structure of a compound (81, 82). These factors include dispersion (van der Waals), dipole–dipole, dipole-induced dipole, quadrupole, ion–ion, and possibly hydrogen bonding interaction energies. In general, the observed crystal structure will have an arrangement of molecules or ions where the sum of all of these energies is minimized or nearly minimized. It is still under debate which of the factors dominates this sum (which is, of course, different for different systems) but it is generally agreed that the dispersion forces are always important. Near the equilibrium geometry, the attractive dispersion forces vary as $1/r^6$. As a result, the molecules attempt to crystallize most densely to maximize stabilization due to the dispersion forces. This implies that molecular shape plays an important role in determining the crystal structure (81).

Because NLO chromophores often have appreciable dipole moments (4–7 Debye is common), it is possible that dipole–dipole interactions

play a more important role in influencing crystal packing than in the set of all organic molecules. As a result, many researchers have speculated that cancellation of the destabilizing dipole–dipole interactions upon crystallization of dipolar chromophores in centrosymmetric space groups provides a strong driving force for centrosymmetric crystallization. This notion has had a major influence on attempts to “engineer” crystals for NLO applications. Recent independent studies by Whitesell et al. (83) and by Hurst and Munn (84) question the validity of this concept. Whitesell et al. (83) performed a survey of the Cambridge crystallographic database and found no correlation between incidence of non-centrosymmetry and magnitude of molecular dipole moments as calculated via the AM1 Hamiltonian in AMPAC. Such a lack of correlation observed for a relatively random set of molecules does not necessarily imply that for relatively two-dimensional (2D) molecules with rather large dipole moments, such as PNA and DANS, dipole–dipole interactions are not important. Hurst and Munn (84) performed a series of calculations on PNA (which crystallizes in a centrosymmetric space group) and 2-methyl-4-nitroaniline (MNA, which crystallizes in a non-centrosymmetric space group) and found that the dipole energy was stabilizing in both cases and, in fact, was larger in the MNA. Nevertheless, several attempts have been made to synthesize materials in which dipole–dipole interactions are minimized, with the hope that these molecules would crystallize in noncentrosymmetric space groups. In the following paragraphs we examine various approaches to isolate useful NLO crystals.

Chirality. The simplest strategy for avoiding centrosymmetric crystal packings is to work with resolved, chiral molecules because they cannot crystallize in space groups containing mirror planes or an inversion center. Thus, one can take advantage of the naturally occurring chiral materials as building blocks for NLO crystals and noncentrosymmetry is guaranteed. Unfortunately, the problem is not so straightforward because, frequently, orientation of the chromophores in the lattice is far from optimized, and small bulk hyperpolarizabilities are observed. Thus, although chirality can prevent centrosymmetry, it cannot prevent pseudocentrosymmetry wherein all of the large coefficients of the β -tensor are nearly cancelled. Furthermore, incorporation of chiral auxiliaries into the molecule typically dilutes the chromophore, leading to a lower number density in the material and ultimately a smaller achievable signal. Nonetheless, numerous studies used this approach and in some instances promising compounds were identified. In particular Velsko (85) found that amino acid salts were, statistically, good candidates for high-power UV generation. In the late 1970s researchers began synthesizing nitroaromatic derivatives with chiral amines, some of which

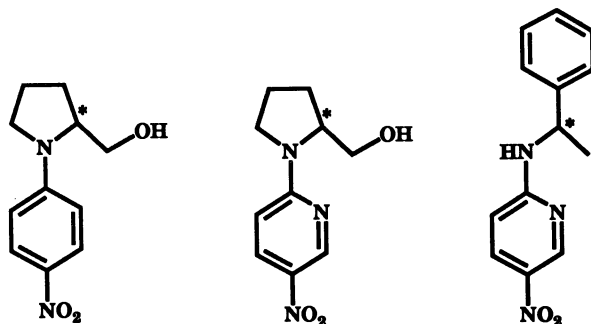


Figure 17. Optically active nitroaromatics that exhibit efficient SHG: from left to right, (4-nitrophenyl)-(1) prolinol (NPP) (86), prolinolnitropyridine (PNP) (87), and α -methylbenzylaminonitropyridine (MBANP) (88).

may be useful for generation of light at 532 nm by frequency doubling the 1.064 μm fundamental of a Nd:YAG laser (Figure 17).

Hydrogen Bonding. Another strategy employed to encourage dipolar molecules to crystallize in noncentrosymmetric space groups is to find a force to overwhelm the potentially deleterious dipole–dipole interactions. Dipole–dipole interaction energies in crystals are estimated to be in the range of ~ 1 –2 kcal/mol (81, 89). Intermolecular hydrogen bonding interactions can range from 3 to 6 kcal/mol and thus are stronger than dipole–dipole interactions. In most of the early studies using this approach, researchers did not design the molecule to facilitate specific intermolecular hydrogen bonding interactions. Rather, they worked under the premise that hydrogen bonding interactions exhibit no particular preference for centrosymmetric or noncentrosymmetric crystallization, and thus should statistically improve the probability of isolating noncentrosymmetric crystals. Crystals of several nitroanilines such as NPP⁸⁶ and 3-acetamido-4-dimethylaminobenzene (DAN) (Figure 18) were identified in which the molecular orientation was quite favorable for SHG.

More recent studies by Etter (90–92) and Lehn (93, 94), in particular, have focused on using rationally designed specific hydrogen bonding

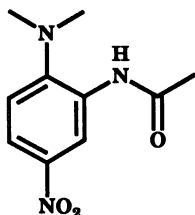


Figure 18. Molecular structure of 3-acetamido-4-dimethylaminobenzene (DAN) (54).

interactions. Etter has examined a series of nitroanilines and found a high occurrence of acentric hydrogen bond aggregates. Furthermore, it was noted that the relatively high occurrence of noncentrosymmetric crystal structures in this class of materials may, in part, be due to the formation of these acentric aggregates. In a very-elegant experiment it was shown that crystals of *p*-aminobenzoic acid and 3,5-dinitroaniline form a 2D acentric sheet (Figure 19) (91). In related studies, Lehn (93) has shown that substituted barbituric acids and substituted 1,3,5-triaminopyrimidines can form polar tapes (93, 94). Although none of the hydrogen bonded aggregates reported by Etter or Lehn have SHG efficiencies of any technological significance, systematic studies of such well-defined intermolecular interactions are the critical first steps toward the rational design of crystalline materials.

Inclusion Complexes. Incorporation of chromophores into a chiral host or a host containing polar channels is another approach to isolate noncentrosymmetric materials. Tomaru (95) and later Wang (96) synthesized β -cyclodextrin (β -CD) inclusion complexes of several chromophores that normally crystallize centrosymmetrically. Cocrystallization of PNA with β -CD yielded a microcrystalline material with a powder SHG efficiency (fundamental at 1.064 μm) 4 times that of urea where β -CD alone gave a negligible signal. It was later shown that various organic and organometallic chromophores form SHG active complexes

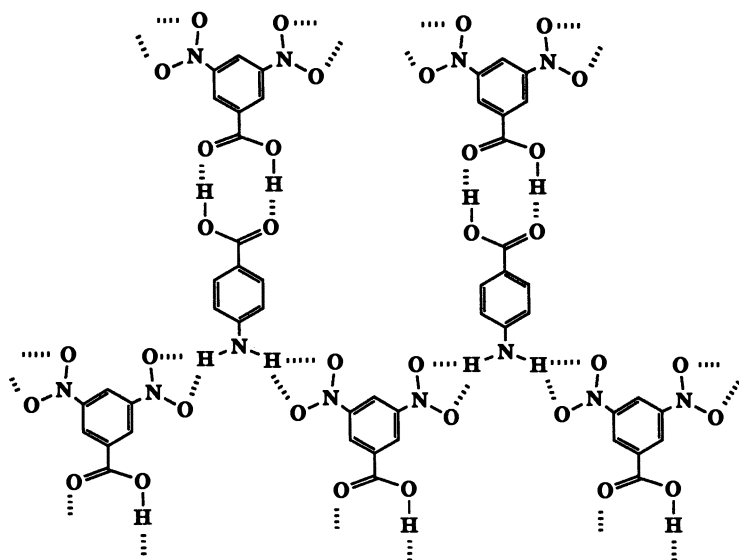


Figure 19. Hydrogen bonded network formed by cocrystallization of 3,5-dinitrobenzoic acid and 4-aminobenzoic acid (91).

with tris-*o*-thymotide and with thiourea. X-ray crystallography revealed that several thiourea complexes were arranged with the thiourea in polar hexagonal channels around the guest molecules. Although several of the complexes had excellent alignment, the largest SHG signal observed (benzenechromiumtricarbonyl tris-thiourea) was 2.3 times that of urea (fundamental at 1.064 μm) (97, 98). In another study, Stucky et al. (99) demonstrated that incorporation of organic molecules into inorganic hosts gave rise to appreciable SHG efficiencies.

Salts. In 1983 Meredith (21) suggested that in organic salts, Coulombic interactions could override the deleterious dipolar interactions that provide a strong driving force for centrosymmetric crystallization. To test this hypothesis salts of the form $(\text{CH}_3)_2\text{NC}_6\text{H}_4\text{-CH=CH-C}_5\text{H}_4\text{N}(\text{CH}_3)^+\text{X}^-$ were examined and most of the counterions gave materials that exhibited relatively large powder SHG efficiencies. In particular, it was found that $(\text{CH}_3)_2\text{NC}_6\text{H}_4\text{-CH=CH-C}_5\text{H}_4\text{N}(\text{CH}_3)^+\text{CH}_3\text{OSO}_3^-$ (DASM) had a large SHG efficiency roughly 220 times that of urea (fundamental at $\lambda = 1.907 \mu\text{m}$) (21). Subsequent studies by Marder et al. (46, 100, 101) and Nakanishi et al. (44, 102–105) provided compelling evidence that variation of counterions in organic and organometallic salts is a simple and highly successful approach to create materials with very large $\chi^{(2)}$. Marder (46) synthesized a series of *N*-methyl-stilbazolium salts with various donor groups and various counterions, many of which exhibited large powder SHG efficiencies. Furthermore, both Nakanishi (44, 102–105) and Marder (46, 100, 101, 106, 107) found that the tosylate ion in particular tended to strongly favor polar arrangements of chromophores in the crystal lattice. For example, dimethylamino stilbazolium tosylate (DAST) (Figure 20) gave a signal 1000 times the urea standard (fundamental at $\lambda = 1.907 \mu\text{m}$) (46). Single crystal studies on several salts revealed that these materials have unprecedented $\chi^{(2)}$. Okada (105) showed that hydroxystilbazolium tosylate (Figure 20) has a d_{11} of 500 pm/V for 1.064- μm fundamental radiation. Similarly, d_{11} of ~ 600 pm/V for 1.907- μm fundamental radiation was measured for DAST (106). An EO figure of merit (FOM) for

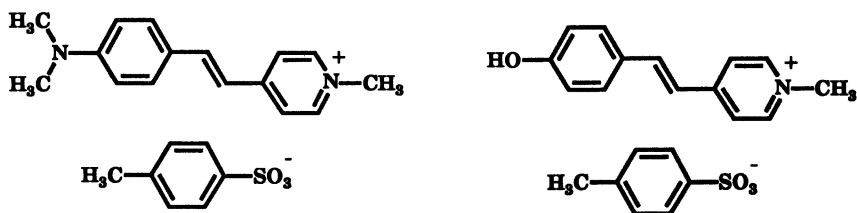


Figure 20. Molecular structures of dimethylamino stilbazolium tosylate (DAST) and hydroxystilbazolium tosylate.

a material is $n^3r/2$ where n is the refractive index of the materials and r is the EO coefficient as discussed before. The FOM for DAST is 2100 pm/V and is 650 pm/V for DASM, which compare favorably to other materials such as MNA (320 pm/V), the ceramic lead lanthanum zirconate titanate (PLZT) (1150 pm/V), and LiNbO_3 (200 pm/V) (106, 107). Furthermore, DAST shows exceptional thermal stability for an organic material: It is stable up to over 250 °C. These preliminary measurements indicate the tremendous potential of this material for providing a highly nonlinear, thermally stable organic for optical signal processing, communications, and interconnect applications.

N-Oxides. Another relatively successful approach to minimize the effects of dipole–dipole interactions was pioneered by Zyss et al. (108), who examined pyridine *N*-oxide compounds. By synthesizing molecules with very small ground-state dipole moments, it was hoped that there would be a higher probability of crystallization in noncentrosymmetric space groups. It was found that β -scales with the change of dipole moment between the ground and excited states and therefore a large ground-state dipole moment was not necessary. Thus, these workers set out to synthesis molecules with a mesomeric dipole in one direction and a more localized dipole in the opposite direction, such that the resultant dipole moment would sum to roughly zero. The *N*-oxide group can act as both a donor or an acceptor (Figure 21) so this system was a potential candidate to exhibit both large changes in dipole moment between the ground and excited state and also to maintain a small ground-state dipole moment. Accordingly, it was discovered that 3-methyl-4-nitropyridine-1-oxide (POM) exhibited excellent SHG properties.

Organic Photorefractive Crystals. The photorefractive effect is well-known in inorganic crystals and is used for the storage of infor-

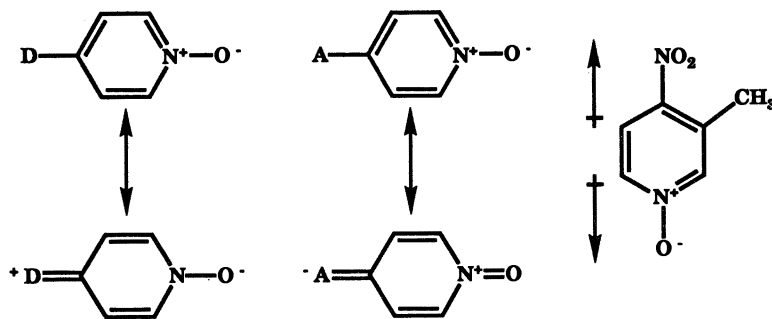


Figure 21. The *N*-oxide group acting as a donor (left), acceptor (center), and in 3-methyl-4-nitropyridine-1-oxide (POM) (right) with arrows illustrating the partial cancellation of the molecular dipole moment.

mation, for optical phase conjugation, and for a variety of optical image-processing techniques. In inorganic solids, both an EO response and photoconductivity can be observed. Very recently, it was observed for the first time in an organic crystal. Günter et al. (109, 110) doped single crystals of 2-cyclooctylamino-5-nitropyridine (COANP) (Figure 22, left) with ~ 0.2 mol% of 7,7,8,8-tetracyanoquinodimethane (TCNQ) (Figure 22, right) (109, 110). The TCNQ generated and transported charge carriers in the COANP crystal, which possesses a reasonable EO coefficient of about 10–20 pm/V (20). The material was formed by supercooling a melt of the two compounds. Diffraction efficiencies of between 0.1 and 1% were observed by using illumination intensities of roughly 1 W/cm^2 . These efficiencies are much lower than those observed in inorganic materials and the rise time for the effect, between 100 and 1000 s, is much slower as well. However, this initial system is not in any way optimized and the choice of different guest dopants and hosts could lead to materials competitive with inorganic crystals.

Poled Polymer Films. A promising method that avoids some of the problems associated with single crystal materials is the fabrication of organic polymeric thin films (111). A fundamental advantage of thin films is that a large electric field (E) can be achieved per applied volt (V), since $E = V/L$, where L is the thickness of the film. This approach also offers flexibility in choosing the chromophore, because the size and shape of the chromophore is largely decoupled from the ability to achieve reasonable orientational order. Achieving processability, however, is the main driving force for the research on polymeric NLO materials. For example, large area thin films ($>1 \text{ cm}^2 \times 1\text{-}\mu\text{m}$ thick) can be routinely prepared. These films can be used as wave guides (112) in either SHG or EO devices. If reasonable care is taken in the fabrication of the films, the resulting wave guides can exhibit relatively small losses

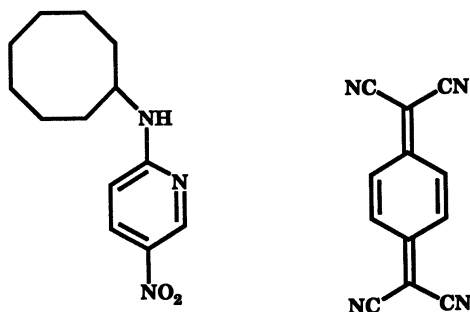


Figure 22. Molecular structures of 2-cyclooctylamino-5-nitropyridine (COANP) and 7,7,8,8-tetracyanoquinodimethane (TCNQ).

(i.e., <0.5 dB/cm) (113). Other advantages in processability not always available in crystalline materials include flexible dimensions and low dielectric constant, with consequently shorter response times to applied electric-switching fields. Moreover, the optical, chemical, physical, and mechanical properties of the polymers can be tailored so that glass-transition temperature (T_g), hardness, transparency, and so on, meet the requirements for specific applications.

Poled polymers are the most widely studied class of organic thin films. To form a poled polymer, a thin-film polymeric host containing a dissolved NLO chromophore is heated above its T_g and an electric field is applied across the film, which couples to and aligns the dipolar chromophores. Alternatively, the noncentrosymmetric order can be “spontaneously” achieved by carefully tailoring the chemical structure of the chromophores (L-B films and other self-assembled structures). All organic thin films must meet several stringent requirements in addition to high nonlinearity. To minimize optical losses due to scattering, high homogeneity of refractive index in the material is required. Accordingly, care is usually taken to avoid phase separation, chromophore aggregation, or formation of other microcrystalline regions. High transparency (for SHG at both fundamental and second-harmonic frequencies), high orientational order per applied field strength, photochemical and thermal stability in ambient and operating environments, dimensional stability, thickness control, and processability are all important as well.

Poling Procedure. Research on poled polymers has focused mainly on increasing noncentrosymmetric order and on the stability of the induced orientation of the chromophores. In the poled polymer concept, one attempts to noncentrosymmetrically incorporate a high number density of NLO active molecules as shown in Figure 23. An NLO chro-

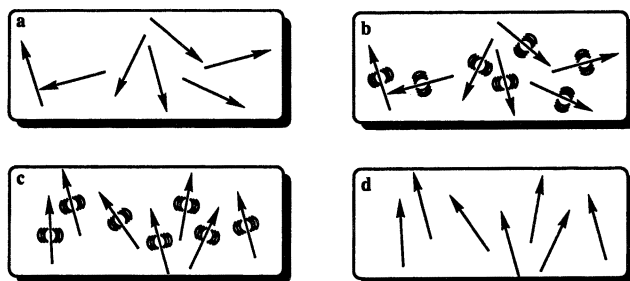


Figure 23. Schematic representation of the poling procedure. A polymer matrix containing (a) initially randomly oriented chromophores is (b) heated above its glass transition temperature, allowing the chromophores to move. Application of an electric field orients the chromophores (c). Cooling of the film fixes this orientation. After cooling, the field is removed (d).

mophore and a glassy polymer are dissolved in an organic solvent and spin-coated onto a substrate. The film is then heated above or around its glass transition temperature. At this temperature, the molecules can rotate in the rubbery matrix. An intense dc electric field as high as 10^6 V/cm is applied and this field creates a force on the dipole moments of the chromophores, aligning them. Thus, the polymers and chromophores must be nonconducting to support these large fields. With the electric field still applied, the film is cooled below the T_g of the polymer, restricting the motions of the chromophores. The resulting noncentrosymmetric structure contains the molecular units oriented on the average normal to the film ($C_{\infty v}$ symmetry). In this state, the electric field of an optical beam propagating through the film can be maximally modified when the field is parallel to the orientated molecular units. As such, the films are ideally suited for wave guide applications.

The magnitude of the second-order NLO effect in a poled polymer film is related to several factors. Using a noninteracting oriented molecular gas model, equation 3 has been derived to describe the second-order susceptibility in the direction of the poling field ($\chi_{333}^{(2)}$).

$$\chi_{333}^{(2)} = NF\beta_{\mu}\langle\cos^3\phi\rangle \quad (3a)$$

where

$$\langle\cos^3\phi\rangle = \mu_z E_p / ckT \quad (3b)$$

Here, N is the number density of chromophores in the materials, k is the Boltzman constant, T is the temperature in Kelvin, and c is a system-dependent factor equal to 5 for isotropic systems and to 1 for ideal liquid crystalline systems (Ising systems). The term $\langle\cos^3\phi\rangle$ is the induced polar order, which is an average angular orientation where ϕ is the angle between the poling axis and the molecular dipole moment of the chromophores. The brackets indicate the Boltzman thermal average. This equation is valid at low field, $\mu_z E_p < kT$. As shown experimentally (114) and derived theoretically (115), at higher fields the linear relation of E versus χ levels off (saturates). Equation 3 suggests that a lower poling temperature will lead to a higher degree of orientation. This is due to the inevitable Boltzman distribution of orientation around the poling axis. However, often the opposite is observed and can be explained on the basis of the mobility of the chromophores, which increases with temperature. Order parameters ($\langle\cos^3\phi\rangle$) of 10–20% have typically been obtained (116). In addition, $\chi^{(2)}$ depends on additional parameters such as the number density of chromophore moieties (N), macroscopic local field factors (F), the applied electric poling field (E_p), and the chromophore molecular ground-state dipole moment (μ_z) (64, 117–119). The direction of the dominant component of β is not necessarily exact along

the direction of μ (both are vectors), and the poling process will align the chromophores according to the direction of the dipole moment. Consequently, β_μ is the important parameter, therefore, chromophores in which β and μ are most closely coincident are optimal. The local field factors (F) account for the influence of the surroundings, with respect to the NLO effect. They relate the value of the external field to the local field experienced by the molecule as a result of contributions from neighboring molecules (e.g., charges and dipoles induced by electronic motions).

Poling Methods. Figure 24 shows the two common poling techniques. The first is conventional contact poling wherein two electrodes are placed in contact with the two flat sides of the film. Application of a voltage across the two electrodes creates an electric field in the film. Contact poling is advantageous because relatively low voltages and well-defined electric fields can be employed. The ability to precisely define electric fields can be exploited by using patterned electrodes. For example, a quasi-phased matched polymer wave guide can be constructed by using periodic poling or periodic finger electrodes above the film surface (120–122). The periodic grating or modulation in the value of $\chi^{(2)}$ that results from this poling technique equalizes the effective indices at the fundamental and second-harmonic wavelengths. A disadvantage of contact poling is the tendency toward physical and catastrophic electric breakdown. Breakdown arises from inhomogeneities in the film that allow current to flow between the two plates. Because the electrodes conduct very well (in the horizontal direction), the first leak in the film will discharge the electrodes immediately.

The second method is corona poling. Here, ions are discharge-generated at a sharp (tungsten) needle at high static potential (123) and then are accelerated toward the polymer film surface connected to a grounded electrode. The field in the film is created by the bias due to the ions on its surface relative to the ground. The most important ad-

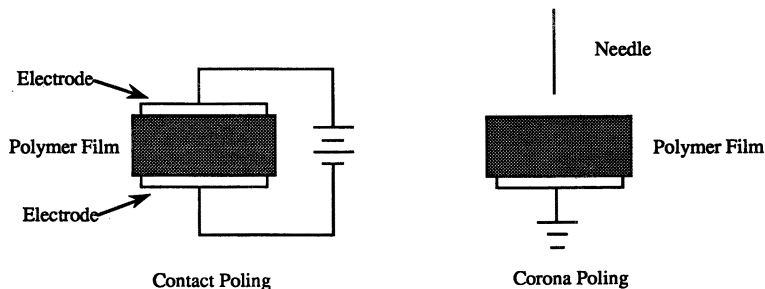


Figure 24. Contact and corona polings.

vantage of corona poling is that a higher field is achievable because the relative immobility of the ions on the surface avoids destructive electric breakdown. Other advantages that arise from the absence of electrodes in contact with both sides of the film are the easy access to secondary chemistry during poling and the important possibility of in situ NLO measurements that can be performed. However, corona poling requires a high voltage, and it is difficult to define and reproduce the electric field.

Developments. During the last 10 years, many investigations have been undertaken to develop the poled polymer concept. Many researchers have tried to increase SHG by maximizing the chromophore order and by using high $\mu \cdot \beta$ chromophores. Moreover, much attention has been focused on increasing the orientational stability of the chromophores in the film.

Guest-Host Systems. The simplest form of the poled polymer approach is doping, wherein the chromophore molecules are dissolved in a polymer without any chemical binding (guest–host system). This approach was first applied to second-order NLO by Meredith et al. (124). They described a system with DANS dissolved up to 2% by weight in a thermotropic nematic liquid crystalline copolymer. Other initial doped polymer experiments often employed 4-(4-nitrophenylazo)-4-ethyl-N-(2-hydroxyethyl)aniline (Disperse Red) (a commercially available dye, Figure 25) dissolved in poly(methyl methacrylate) (PMMA) (125–128). It was shown that these materials were suitable for guided-wave EO devices (129). Guest–host systems suffer from several drawbacks. For most systems it appears to be difficult to increase the chromophore concentration above 10 mol% before the onset of phase separation (i.e.,

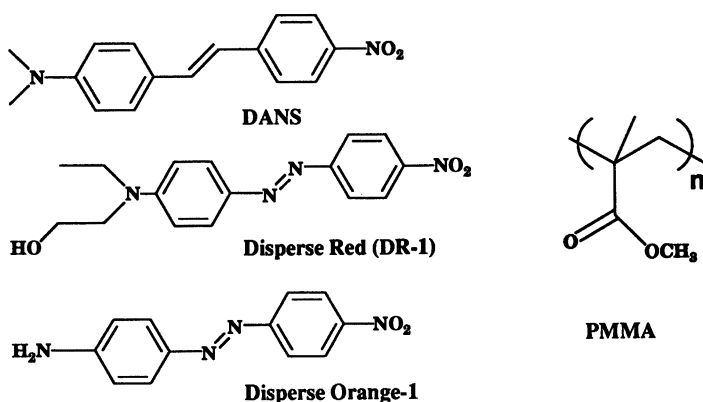


Figure 25. Representative chromophores and polymer used in poling.

chromophore aggregation). Also, when the chromophore moieties are forced into a nonequilibrium configuration, they tend to randomize their orientations over time. In addition to the thermally induced relaxation, these materials will be subject to large oscillating fields, typically 5×10^4 V/cm, only an order of magnitude less than the poling fields. Thus the relaxation time scale of guest–host systems is typically in the order of several days at room temperature (130).

Covalent Attachment of the Chromophores to the Polymer. Alignment stability may be improved by covalently attaching chromophores to polymer chains, reducing their mobility. Acrylate polymers incorporating NLO active dyes in the chain have been extensively studied (131–135). Other polymers prepared by radical polymerization have been explored (136), as have condensation polymers (137) such as polyesters (138), polyurethanes (139, 140), and epoxies (141). The most common approach to attaching the chromophores has been to incorporate them as side groups of the main polymer chains. This covalent attachment was expected to lead to materials with good orientational stability, because reorientation of the chromophores would require reorientation of large block segments of the polymer chain (142).

Liquid Crystalline Polymers. Liquid crystal hosts have been used to achieve a higher order parameter and improved temporal stability. As mentioned before, the increased order parameter is related to c in equation 3 (1 for a perfect liquid crystalline system and 5 for isotropic systems). At high poling fields the obtainable alignment saturates in both the isotropic and the liquid crystalline case to the same value. Liquid crystalline polymers often have liquid crystalline active (mesogenic) units attached to the polymer backbone. Spacer units that decouple the motions between the polymer backbone and the mesogens are commonly used to facilitate formation of nematic mesophases. The liquid crystalline polymer host can show nematic behavior above its T_g , as well as homogeneous and homotropic alignment in response to externally applied electric fields. The chromophores can be frozen in the nematic structure (124, 143, 144). If the structure of the chromophore is similar to the mesogenic units of the polymer, the chromophore will tend to adopt the same anisotropic orientation as the mesophase (Figure 26).

Relaxation Behavior and Thermal History of the Film. In situ corona poling has been used to determine the orientation kinetics and relaxation behavior (subsequent loss of orientation) of the chromophores in the film. It was found that the rise of the second-harmonic (SH)-signal upon applying the field and the decay after the poling field has been removed are not single exponential time functions. It is generally accepted that

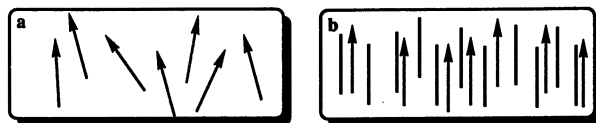


Figure 26. Schematic representation of chromophore orientation in (a) an isotropic poled polymer and (b) a nematic liquid crystalline poled polymer.

the excess free volume at molecular level and the thermal motion play a role on the stability of alignment (114, 130, 145). For instance, the thermal history of the film appears to be an important aspect for maintaining the induced chromophore orientation. Sub- T_g annealing of the films prior to poling enhances the stability of the SHG and allows poling at higher fields, because it reduces the tendency for electric breakdown (114, 146). The higher stability can be explained by the decrease in free volume during the annealing process, leading to a decreased rotational freedom and mobility of the chromophores (147, 148).

Chromophore Modification. Strategies for enhanced electric field-induced order propose to increase the ground-state dipole moment of the chromophore either by oligomerization of the chromophore moieties (149, 150) or incorporating them into larger zwitterionic molecules (150). Many problems are inherently associated with the use of zwitterions. Because they were insoluble in all but very polar solvents μ and β could not be measured, and the polymer films doped with the zwitterions had sufficiently high conductivities that a large electric field could not be created within the film. Head-to-tail oligomers appeared to be a more promising approach to increase the effective dipole moment of the chromophore. Katz et al. (149, 150) demonstrated that μ increased with oligomer length, although the additivity was not yet optimal because the directions of the dipoles of the various segments were not collinear. These initial experiments indicate that oligomeric guest–host systems can be more stable than the comparable guest–host systems with monomeric chromophores. It is expected that covalent incorporation of these oligomers into polymers will further improve the temporal stability.

Cross-Linking. Cross-linking a dye–polymer system either during or after the poling process can greatly restrict the mobility of the chromophores within the medium (Figure 27), leading to improved temporal stability, although it is generally hard to achieve as high polar order parameters as in non-cross-linked systems. Marks et al. (146, 151) have prepared films containing chromophores such as DANS or 4-(4-nitrophenylazo)diphenylamine (Disperse Orange-1) (Figure 25) in combi-

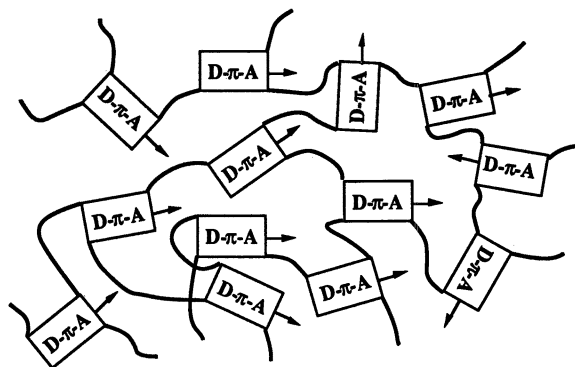


Figure 27. Schematic of cross-linked NLO-polymers. D- π -A stands for donor and acceptor substituted π -system as covalently incorporated nonlinear optical unit. The arrows denote the ground state dipole moments. (Modified from reference 76. Copyright 1991 American Chemical Society.)

nation with EPO-TEK 301, a commercially available, two-component optical-grade epoxy resin. Partial curing appeared to be necessary to prevent electric breakdown, before a poling field could be applied. After precuring, the film was poled and a highly cross-linked film containing oriented chromophores was obtained. In comparison to non-cross-linked guest-host systems, a significantly longer-lived chromophore orientation at ambient temperature (on the order of many days) was achieved. Robello (152) explored photo-cross-linking of (meth)acrylic systems with the rationale that the film could be cross-linked and poled at lower temperature, possibly leading to improved order parameters (eq 3). Higher number densities of chromophores and improved orientational order can be achieved by covalently incorporating chromophores into the cross-linked polymer matrix. For example, amorphous linear polyethylene containing PNA sidegroups exhibited a decay in SHG intensity from an initial EO coefficient $d_{33} = 31$ pm/V to 19 pm/V after 5 days at room temperature (153, 154). Similar behavior was observed in the linear epoxy polymer of PNA and diglycidyl ether of bisphenol A. The coefficient d_{33} decreased from 31 to 22 pm/V in 28 days (155). A heavily cross-linked system provided by reacting 4-nitro-1,2-phenylenediamine and bisphenol-A diglycidylether appeared to be stable ($d_{33} = 14$ pm/V for long periods even at elevated temperatures (85 °C) (155, 156). Temporal stability at elevated temperatures is a critical materials property for numerous applications.

A related method has been reported in which a linear side-chain polymer (poly(*p*-hydroxy)styrene with 16% functionalization with *N*-(4-nitrophenyl)-(S)-prolinol as the NLO active side groups) was cross-linked with a diepoxy during poling. This procedure also led to en-

hanced stability (157). Limited success was achieved by using photo-cross-linkable acrylic chromophores as monomers. Unfortunately, low obtainable cross-linking resulted in a low T_g and the d_{33} of these materials showed a considerable decay with time (158). Better orientational stability was obtained when the chromophores were covalently attached to a polymer backbone containing photo-cross-linkable groups, but this resulted in lower second-order NLO effects, attributed to photoinduced *cis-trans* isomerization of the azo unit in the NLO chromophore (159). Polyurethanes are an alternative to epoxy systems and have been reported as linear (139, 140) and cross-linked NLO systems (160, 161). Reaction of diisocyanates such as hexamethylene-diisocyanate or 4,4'-methylenebisphenylisocyanate and chromophores with two hydroxyl functionalities such as 4-(4-nitrophenylazo)-bis(*N*-(2-hydroxyethyl)aniline (Disperse Red 17) gave a linear polymer, and a cross-linked polymeric system could be prepared with trifunctional isocyanates and bifunctional chromophores.

Photorefractive Polymers. Recently, the photorefractive effect was observed in a poled polymer system (162, 163). In this case, an epoxy polymer bisphenol-A diglycidylether 4-nitro-1,2-phenylenediamine was used as the EO material. The polymer was doped with compounds based upon *p*-diethylaminobenzaldehydehydrazone (DEH) as hole transport agents. Diffraction efficiencies of up to 0.1% were observed. The authors point out that the important limitation in this and other organic systems is the relatively low carrier mobility that leads to rather slow responses. It was suggested that addition of charge-generation units could enhance the response as could the use of conductive polymers.

Langmuir-Blodgett Films. There have been several reports of high second-order nonlinear optical activity in LB films (77, 164), which allow control of the symmetry and alignment of the molecules and might be suitable for wave guide fabrication. Approximately 500 layers must be deposited to achieve sufficient thickness (0.1–1 μm) for single-mode propagation of optical waves, and, unfortunately, it is difficult to obtain this many layers while simultaneously maintaining the noncentrosymmetric structure. Formation of such a structure must be done carefully and it is inconvenient and time-consuming. Films often exhibit poor thermal and mechanical stability and poor optical quality due to light scattering from microcrystalline domains that form.

Initial SHG experiments were performed on a single-layer LB film (165). Adding fatty acids increased the SHG intensity of monolayers of hemicyanine chromophores, the opposite to what one would expect considering dilution. This effect was attributed to increased order and the lower level of undesired aggregate formation (166). Successive de-

position to form multilayers of NLO moieties often results in centrosymmetric (head-to-head, tail-to-tail, so called Y-type) structures with each successive layer aligned opposite in direction to the previous layer. Deposition of intermediate nonlinear-inactive layers of fatty acids can be used to form a noncentrosymmetric (ABAB) configuration of the nonlinear molecules (167), but dilutes the NLO active moieties. By selecting a spacer in which the donor-acceptor groups are oppositely arranged, an alternate LB film structure can be built in which the nonlinearities derived from these alternate layers are additive. It is also possible to make head-to-tail (Z-type) films by using diamide amphiphiles (168). Amide groups in the chains make it more hydrophilic and increase the tendency to make Z-type layers. As expected for perfectly ordered films, these films showed quadratic dependence of the SHG intensity on the number of layers.

SHG active arrangements can also be made with two different active components, that form a (head-to-head) Y-type structure in which the amphiphiles in each of the opposing pairs of layers have their acceptor and donor groups (and thus β) in the opposite direction with respect to each other. Thus, the individual second-order activities should be additive. This approach has been demonstrated on bilayers of a hemicyanine and a nitrostilbene (Figure 28) (169, 170) and on bilayers of two different hemicyanines with opposite β s (171). Later it was shown that ordered films up to 10 layers could be prepared, but the SHG intensity did not grow quadratically with the number of layers (172). Another noncentrosymmetric structure involves a Y-type, herringbone-like structure, where all layers tilt in the same direction (173).

Cross-links between neighboring groups (i.e., polymer formation) might solve some of the problems associated with LB films, including domain-induced light scattering and poor stability. Polymerization of LB films or the use of prepolymers in the preparation of LB films has

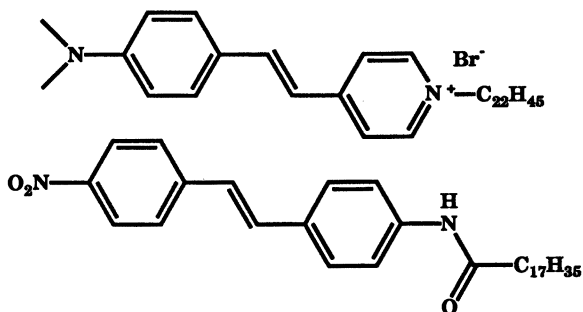


Figure 28. A hemicyanine (top) and a nitrostilbene (bottom) for SHG active LB films (169).

been explored. Multilayers of unsaturated carboxylic acids have been polymerized with UV light (174), and the use of preformed polymers in monolayers has been reported (175–178). SHG in this type of monolayer was first demonstrated on a monolayer of a polysiloxane partly functionalized with an azochromophore containing a hydroxyl group (175). Multilayers up to 8 layers were prepared by interleaving two different polyethers partly substituted with hemicyanine in which one polymer contained the dipole pointing toward the backbone, and the other contained the dipole pointing away from the backbone (179).

A comparable system with alternating polymer layers exhibited (180) stable SHG properties and order up to 40 layers as demonstrated from the quadratic dependence of the SHG signal on the number of layers. The high stability was achieved by using a fluorocarbon chain as the hydrophobic part. Compared to hydrocarbons, fluorocarbon chains are stiffer and more hydrophobic and can thus be shorter (180).

Other Methods. Self-assembly of structures based on trichlorosilane derivatives (181, 182) is a novel and promising approach for the preparation of highly ordered and stable films (183, 184). Layers of oriented chromophores are assembled sequentially on a glass slide and the chains within a layer are cross-linked. Subsequent layers are covalently attached to the prior layers. Multilayer structures have been built up with a repeating reaction sequence giving alternating stilbazolium chromophore layers and soft polysiloxane layers that connect the molecules transverse to the stacking direction thus providing stability (Figure 29). Results on up to five layers indicate that this technique has potential, and it is expected that such systems will show a high degree of order

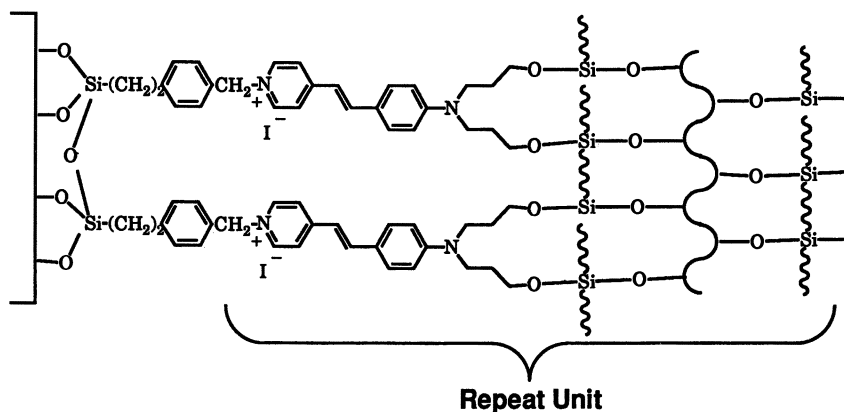


Figure 29. Scheme of self-assembled multilayers. (Modified from reference 183. Copyright 1990 American Chemical Society.)

and an improved orientational stability. However, it has yet to be demonstrated that micrometer-thick films can be fabricated with this new methodology. The novel self-assembled layer systems are still in the initial stages of development, but are very promising especially when higher chromophore densities can be achieved.

Katz et al. (185) have developed an alternative and perhaps simpler methodology involving assembly of zirconium phosphonate layers. Silicon and glass substrates phosphorylated and then reacted with $ZrOCl_2$, followed by reaction with 4-(4-{*N,N*-bis(2-hydroxyethyl)-amino}phenylazo) phenylphosphonic acid, generated the first monolayer. This layer could then be phosphorylated with $POCl_3$ and the previous reaction sequence starting with $ZrOCl_2$ could then be repeated (Figure 30). Twenty-five layers were readily assembled. Furthermore, plots of the thickness, absorbance, and square root of SHG intensity versus number of layers all gave straight lines, indicating that the layers were well-ordered. The films showed good thermal stability, showing only a diminution of the second-harmonic intensity above 150 °C at which point the spectroscopic evidence suggests that the chromophores began to decompose (185).

Outlook for the Future

Our understanding of the factors that determine the behavior of second-order NLO materials has advanced dramatically over the past several years. In particular, strategies now exist for the optimization of molecular second-order nonlinearities. However, most molecules with very large nonlinearities are strongly absorbing in the visible region of the spectrum, lowering their utility for frequency doubling of diode and Nd:YAG lasers. New strategies for enhancing molecular nonlinearities while maintaining transparency are still needed. Great strides have been made toward optimization of macroscopic nonlinearities as well. Crystalline materials now exist with nonlinearities much greater than inorganic materials such as $LiNbO_3$. If these materials are to become the active elements in devices, issues related to crystal growth and processing will have to be addressed. Poled polymers and self-assembled multilayers with nonlinearities as large as state-of-the-art inorganic materials have now been reported. Given the current level of understanding regarding optimization of molecular nonlinearities, it is clear that nonlinearities much larger than those realized to date will be achievable. A real concern for the future of thin-film materials is not obtaining large nonlinearities, but rather developing materials that are environmentally, photochemically, and orientationally stable. If these issues can be successfully addressed, the great promise of organic NLO materials will be realized.

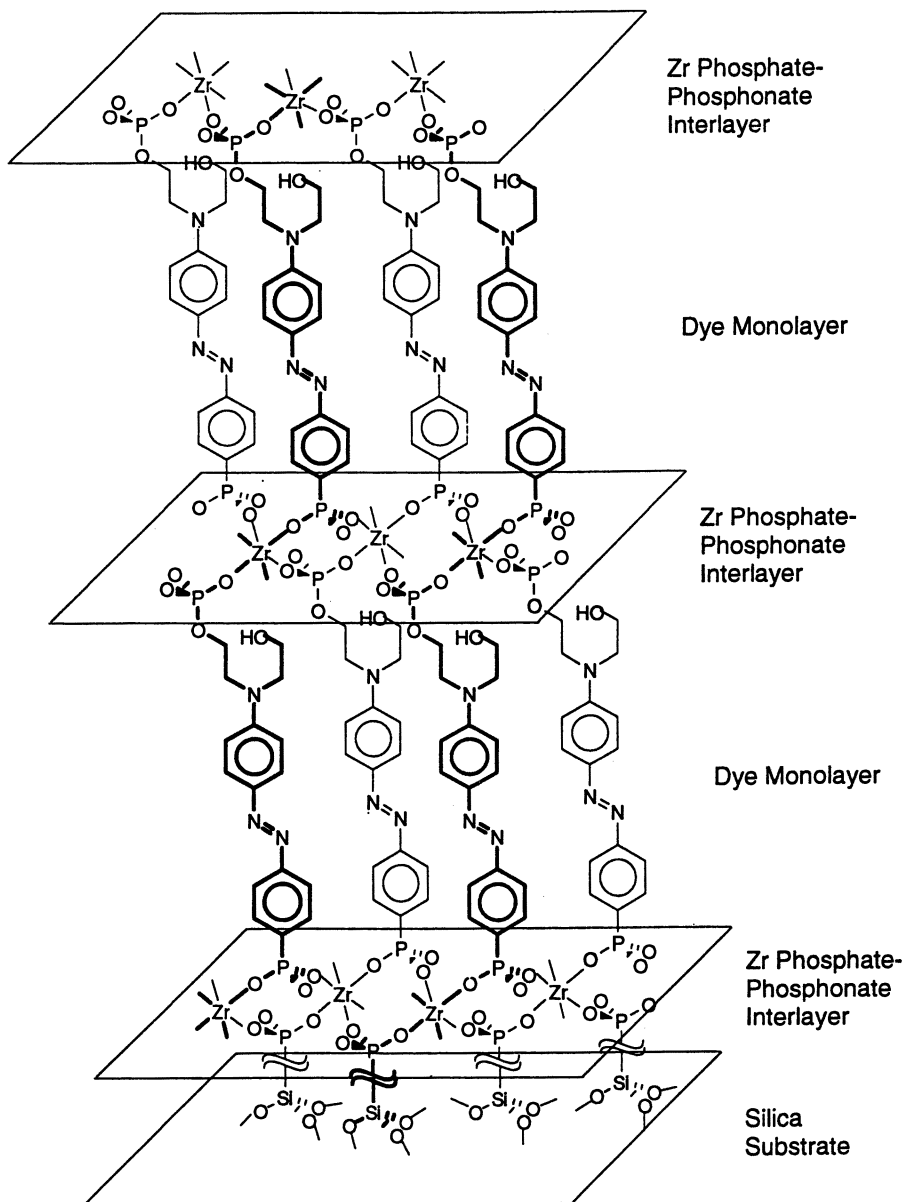


Figure 30. Zirconium phosphonate-based multilayers (185).

Acknowledgments

Part of this paper was written at the Center for Space Microelectronics Technology, Jet Propulsion Laboratory (JPL), California Institute of Technology under contract with the National Aeronautics and Space Administration (NASA). The work was sponsored by The Defense Advanced Research Projects Agency through Contract No. 91-NC-146 administered by the Air Force Office of Scientific Research. Support from the National Science Foundation through Grant CHE-9106689 is also gratefully acknowledged. C. B. Gorman thanks the JPL directors office for postdoctoral fellowship. The authors thank Bruce Tiemann, Sandra Gilmour, Andrienne Friedli, and Chin-Ti Chen for a critical reading of this manuscript.

References

1. *Materials for Nonlinear Optics: Chemical Perspectives*; Marder, S. R.; Sohn, J. E.; Stucky, G. D., Eds.; ACS Symposium Series 455; American Chemical Society: Washington, DC, 1991.
2. Beratan, D. N. In *Materials for Nonlinear Optics: Chemical Perspectives*; Marder, S. R.; Sohn, J. E.; Stucky, G. D., Eds.; ACS Symposium Series 455; American Chemical Society: Washington, DC, 1991; pp 89-102.
3. André, J.-M.; Delhalle, J. *Chem. Rev.* **1991**, *91*, 843-865.
4. Kurtz, H. A.; Stewart, J. J. P.; Dieter, K. M. *J. Comput. Chem.* **1990**, *11*, 82-87.
5. Pugh, D.; Morley, J. O. In *Nonlinear Optical Properties of Organic Molecules and Crystals*; Chemla, D. S.; Zyss, J., Eds.; Academic: Orlando, FL, 1987; Vol. 1, pp 192-224.
6. Oudar, J. L.; Person, H. L. *Opt. Commun.* **1975**, *15*, 258.
7. Levine, B. F.; Bethea, C. G. *Appl. Phys. Lett.* **1974**, *24*, 445.
8. Singer, K. D.; Garito, A. F. *J. Chem. Phys.* **1981**, *75*, 3572-3580.
9. Cheng, L.-T.; Tam, W.; Meredith, G. R.; Rikken, G. L. J. A.; Meijer, E. W. *Proc. SPIE* **1989**, *1147*, 61-72.
10. Cheng, L.-T.; Tam, W.; Stevenson, S. H.; Meredith, G. R.; Rikken, G.; Marder, S. R. *J. Phys. Chem.* **1991**, *95*, 10631-10643.
11. Cheng, L.-T.; Tam, W.; Marder, S. R.; Steigman, A. E.; Rikken, G.; Spangler, C. W. *J. Phys. Chem.* **1991**, *95*, 10643-10652.
12. Teng, C. C.; Garito, A. F. *Phys. Rev. B.* **1983**, *28*, 6766-6773.
13. Oudar, J. L. *J. Chem. Phys.* **1977**, *67*, 446-457.
14. Hammett, L. P. *J. Am. Chem. Soc.* **1937**, *59*, 96.
15. Jaffé, H. H. *Chem. Rev.* **1953**, *53*, 191.
16. Ulman, A. *J. Phys. Chem.* **1988**, *92*, 2385-2390.
17. Katz, H. E.; Dirk, C. W.; Schilling, M. L.; Singer, K. D.; Sohn, J. E. In *Nonlinear Optical Properties of Polymers*; Heeger, A. J.; Orenstein, J.; Ulrich, D. R., Eds.; Materials Research Society Symposium Proceedings 109; Materials Research Society: Pittsburgh, PA, 1988; pp 115-125.
18. Katz, H. E.; Singer, K. D.; Sohn, J. E.; Dirk, C. W.; King, L. A.; Gordon, H. M. *J. Am. Chem. Soc.* **1987**, *109*, 6561-6563.
19. Nogami, T.; Nakano, H.; Shirota, Y.; Umegaki, S.; Shimizu, Y.; Uemiya, T.; Yasuda, N. *Chem. Phys. Lett.* **1989**, *155*, 338-340.

20. Nicoud, J. F.; Twieg, R. J. In *Nonlinear Optical Properties of Organic Molecules and Crystals*; Chemla, D. S.; Zyss, J., Eds.; Academic: Orlando, FL, 1987; Vol. 1, pp 227–296.
21. Meredith, G. R. In *Nonlinear Optical Properties of Organic and Polymeric Materials*; Williams, D. J., Ed.; ACS Symposium Series 233; American Chemical Society: Washington, DC, 1983; pp 27–56.
22. Cheng, L.-T.; Tam, W.; Meredith, G. R.; Marder, S. R. *Mol. Cryst. Liq. Cryst.* **1990**, *189*, 137.
23. Calabrese, J. C.; Cheng, L.-T.; Green, J. C.; Marder, S. R.; Tam, W. *J. Am. Chem. Soc.* **1991**, *113*, 7227–7232.
24. Cheng, L.-T.; Tam, W.; Eaton, D. F. *Organometallics* **1990**, *9*, 2856–2857.
25. Wang, Y.; Tam, W.; Stevenson, S. H.; Clement, R. A.; Calabrese, J. *Chem. Phys. Lett.* **1988**, *148*, 136–141.
26. Steigman, A. E.; Graham, E.; Perry, K. J.; Khundkar, L. R.; Cheng, L.-T. *J. Am. Chem. Soc.* **1991**, *113*, 7658–7666.
27. Hurst, G. J. B.; Dupuis, M.; Clementi, E. *J. Chem. Phys.* **1988**, *89*, 385–395.
28. Kurtz, H. A. *Int. J. Quant. Chem. Quant. Chem. Symp.* **1990**, *24*, 791–798.
29. Morley, J. O.; Docherty, V. J.; Pugh, D. *J. Chem. Soc. Perkin Trans. II* **1987**, 1351–1355.
30. Papadopoulos, M. G.; Waite, J. *THEOCHEM* **1989**, *61*, 121–128.
31. Li, D.; Ratner, M. A.; Marks, T. J. *J. Am. Chem. Soc.* **1988**, *110*, 1707–1715.
32. Yoshimura, T. *Appl. Phys. Lett.* **1989**, *55*, 534–536.
33. Barzoukas, M.; Blanchard-Desce, M.; Josse, D.; Lehn, J.-M.; Zyss, J. *Chem. Phys.* **1989**, *133*, 323–329.
34. Blanchard-Desce, M.; Ledoux, I.; Lehn, J.-M.; Malthête, J.; Zyss, J. *J. Chem. Soc. Chem. Commun.* **1988**, 737–739.
35. Barzoukas, M.; Fort, A.; Boeglin, A.; Serbutoviez, C.; Oswald, L.; Nicoud, J. F. *Chem. Phys.* **1991**, *153*, 457–464.
36. Kawabe, Y.; Ikeda, H.; Sakai, T.; Kawasaki, K. In *Nonlinear Optics of Organics and Semiconductors*; Kobayashi, T., Ed.; Springer Proceedings in Physics 36; Springer-Verlag: New York, 1989; pp 120–123.
37. Fouquey, C.; Lehn, J.-M.; Malthête, J. *J. Chem. Soc. Chem. Commun.* **1987**, 1424–1426.
38. Kanis, D. R.; Ratner, M. A.; Marks, T. J.; Zerner, M. C. *Chem. Mater.* **1991**, *3*, 19–22.
39. Tiemann, B. G.; Marder, S. R.; Perry, J. W.; Cheng, L.-T. *Chem. Mater.* **1990**, *2*, 690–695.
40. Zyss, J. *J. Chem. Phys.* **1979**, *71*, 909–916.
41. Bruce, D. W.; Dunmur, D. A.; Esteruelas, M. A.; Hunt, S. E.; Le Lagadec, R.; Maitlis, P. M.; Marsden, J. R.; Sola, E.; Stacey, J. M. *J. Mater. Chem.* **1991**, *1*, 251–254.
42. Kajzar, F.; Girling, I. R.; Peterson, I. R. *Thin Solid Films* **1988**, *160*, 209–215.
43. Ziolo, R.; Gunther, W.; Meredith, G. R.; Williams, D. J. *Acta Cryst. B* **1982**, *38*, 341.
44. Okada, S.; Masaki, A.; Matsuda, H.; Nakanishi, H.; Kato, M.; Muramatsu, R.; Otsuka, M. *Jpn. J. Appl. Phys.* **1990**, *29*, 1112–1115.
45. Neal, D. B.; Kalita, N.; Pearson, C.; Petty, M. C.; Lloyd, J. P.; Roberts, G. G.; Ahmad, M. M.; Feast, W. J. *Synth. Met.* **1989**, *28*, D711–D719.

46. Marder, S. R.; Perry, J. W.; Schaefer, W. P. *Science (Washington, D.C.)* **1989**, *245*, 626–628.
47. Kurihara, T.; Tabei, H.; Kaino, T. *J. Chem. Soc. Chem. Commun.* **1987**, 959–960.
48. Zhang, Y.; Wen, J. *J. Chem. Res. (S)* **1991**, *1*, 20–21.
49. Brédas, J. L.; Dehu, C.; Meyers, F. *J. Am. Chem. Soc.* **1993**, *115*, 6198.
50. Combellas, C.; Gautier, H.; Simon, J.; Thiebault, A.; Torunilhac, F.; Barzoukas, M.; Josse, D.; Ledoux, I.; Amatore, C.; Verpeaux, J.-N. *J. Chem. Soc. Chem. Commun.* **1988**, 203–204.
51. Robinson, D. W.; Abdel-Halim, H.; Inoue, S.; Kimura, M.; Cowan, D. O. *J. Chem. Phys.* **1989**, *90*, 3427–3429.
52. Barzoukas, M.; Josse, D.; Zyss, J.; Gordon, P.; Morley, J. O. *Chem. Phys.* **1989**, *139*, 359–367.
53. Wnek, G. E.; Kitipichai, P.; Frysinger, G.; Korenowski, G. M.; Gorodisher, I.; Uhlmann, D. R.; Wei, Y. In *Nonlinear Optical Properties of Polymers*; Heeger, A. J.; Orenstein, J.; Ulrich, D. R., Eds.; Materials Research Society Symposium Proceedings 109; Materials Research Society: Pittsburgh, PA, **1988**; pp 139–141.
54. Itoh, Y.; Oono, K.; Isogai, M.; Kakuta, A. *Mol. Cryst. Liq. Cryst.* **1989**, *170*, 259–272.
55. Tweig, R. J.; Jain, K. In *Nonlinear Optical Properties of Organic and Polymeric Materials*; Williams, D. J., Ed.; ACS Symposium Series 233; American Chemical Society: Washington, DC, **1983**; pp 57–80.
56. Norvez, S.; Barzoukas, M. *Chem. Phys. Lett.* **1990**, *165*, 41–44.
57. Huijts, R. A.; Hesselink, G. L. *J. Chem. Phys. Lett.* **1989**, *156*, 209–212.
58. Dulcic, A.; Flytzanis, C.; Tang, C. L.; Pépin, D.; Fétizon, M.; Hoppillard, Y. *J. Chem. Phys.* **1981**, *74*, 1559–1563.
59. Ikeda, H.; Kawabe, Y.; Sakai, T.; Kawasaki, K. *Chem. Lett.* **1989**, 1285–1288.
60. Marder, S. R.; Beratan, D. N.; Cheng, L.-T. *Science (Washington, D.C.)* **1991**, *252*, 103–106.
61. Oudar, J. L.; Chemla, D. S. *J. Chem. Phys.* **1977**, *66*, 2664.
62. Levine, B. F.; Bethea, C. G. *J. Chem. Phys.* **1977**, *66*, 1070.
63. Lalama, S. J.; Garito, A. F. *Phys. Rev. A* **1979**, *20*, 940–942.
64. Williams, D. In *Electronic and Photonic Applications of Polymers*; Bowden, M. J.; Turner, S. R., Eds.; Advances in Chemistry 6; American Chemical Society: Washington, DC, **1988**; pp 297–329.
65. Choy, M. M.; Siraci, S.; Byer, R. L. *IEEE J. Quantum Electron.* **1975**, *QE-11*, 40.
66. Brooker, L. G. S.; White, F. L.; Keyes, G. H.; Smyth, C. P.; Oesper, P. F. *J. Am. Chem. Soc.* **1941**, *63*, 3192–3202.
67. Brooker, L. G. S.; Sprague, R. H. *J. Am. Chem. Soc.* **1941**, *63*, 3203–3213.
68. Brooker, L. G. S.; Keyes, G. H.; Williams, W. W. *J. Am. Chem. Soc.* **1942**, *64*, 199–210.
69. Lalama, S. J.; Singer, K. D.; Garito, A. F.; Desai, K. N. *Appl. Phys. Lett.* **1981**, *39*, 940–942.
70. Dirk, C. W.; Katz, H. E.; Schilling, M. L.; King, L. A. *Chem. Mater.* **1990**, *2*, 700–705.
71. Meyers, F.; Adant, C.; Brédas, J. L. *J. Am. Chem. Soc.* **1991**, *113*, 3715–3719.
72. Brooker, L. G. S.; Keyes, G. H.; Sprague, R. H.; VanDyke, R. H.; VanLare, E.; VanZandt, G.; White, F. L. *J. Am. Chem. Soc.* **1951**, *73*, 5326–5332.

73. Brooker, L. G. S.; Keyes, G. H. *J. Am. Chem. Soc.* **1951**, *73*, 5356–5358.
74. Ikeda, H.; Kawabe, Y.; Sakai, T.; Kawasaki, K. *Chem. Lett.* **1989**, 1803–1806.
75. Ikeda, H.; Sakai, T.; Kawasaki, K. *Chem. Phys. Lett.* **1991**, *179*, 551–554.
76. Bjorklund, G. C.; Ducharme, S.; Fleming, W.; Jungbauer, D.; Moerner, W. E.; Swalen, J. D.; Twieg, R. J.; Willson, C. G.; Yoon, D. Y. In *Materials for Nonlinear Optics: Chemical Perspectives*; Marder, S. R.; Sohn, J. E.; Stuckey, G. D., Eds.; ACS Symposium Series 455; American Chemical Society: Washington, DC, 1991; pp 216–225.
77. Prasad, P. N.; Williams, D. J. *Introduction to Nonlinear Optical Effects in Molecules and Polymers*; John Wiley & Sons: New York, 1991; pp 160–174.
78. Zyss, J. S.; Oudar, J. L. *Phys. Rev. A* **1982**, *26*, 2028.
79. Kurtz, S. K.; Perry, T. T. *J. Appl. Phys.* **1968**, *39*, 3798–3823.
80. Yariv, A. *Quantum Electronics*, 3rd ed.; John Wiley & Sons: New York, 1989; p 676.
81. Kitaigorodsky, A. I. *Molecular Crystal and Molecules*; Physical Chemistry 29; Academic: Orlando, FL, 1973; p 553.
82. Wright, J. D. *Molecular Crystals*; Cambridge University: Cambridge, England, 1987; p 178.
83. Whitesell, J. K.; Davis, R. E.; Saunders, L. L.; Wilson, R. J.; Feagins, J. P. *J. Am. Chem. Soc.* **1991**, *113*, 3267–3270.
84. Hurst, M.; Munn, R. W. In *Organic Materials for Non-Linear Optics*; Hann, R. A.; Bloor, D., Eds.; Royal Society of Chemistry Special Publication No. 69; Royal Society of Chemistry, Burlington House: London, 1989; pp 3–15.
85. Velsko, S. P. In *Materials for Nonlinear Optics: Chemical Perspectives*; Marder, S. R.; Sohn, J. E.; Stuckey, G. D., Eds.; ACS Symposium Series 455; American Chemical Society: Washington, DC, 1991; pp 343–359.
86. Zyss, J.; Nicoud, J. F.; Coquillay, M. *J. Chem. Phys.* **1984**, *81*, 4160.
87. Twieg, R. J.; Dirk, C. W. *J. Chem. Phys.* **1986**, *85*, 3539.
88. Twieg, R. J.; Azema, A.; Jain, K.; Cheng, Y. Y. *Chem. Phys. Lett.* **1982**, *92*, 208.
89. Zyss, J.; Chemla, D. S. In *Nonlinear Optical Properties of Organic Molecules and Crystals*; Chemla, D. S.; Zyss, J., Eds.; Academic: Orlando, FL, 1987; Vol. 1, p 76.
90. Etter, M. C. *J. Phys. Chem.* **1991**, *95*, 4601–4610.
91. Etter, M. C.; Frankenbach, G. M. *Chem. Mater.* **1989**, *1*, 10–12.
92. Etter, M. C.; Huang, K. S.; Frankenbach, G. M.; Admond, D. A. In *Materials for Nonlinear Optics: Chemical Perspectives*; Marder, S. R.; Sohn, J. E.; Stucky, G. D., Eds.; ACS Symposium Series 455; American Chemical Society: Washington, DC, 1991; pp 457–471.
93. Lehn, J.-M.; Mascal, M.; Cian, A. D.; Fischer, J. *J. Chem. Soc. Chem. Commun.* **1990**, 479.
94. Lehn, J.-M. In *Materials for Nonlinear Optics: Chemical Perspectives*; Marder, S. R.; Sohn, J. E.; Stuckey, G. D., Eds.; ACS Symposium Series 455; American Chemical Society: Washington, DC, 1991; pp 436–445.
95. Tomaru, S.; Zembutsu, S.; Kawachi, M.; Kobayashi, M. *J. Inclusion Phenom.* **1984**, *2*, 885–890.
96. Wang, Y.; Eaton, D. F. *Chem. Phys. Lett.* **1985**, *120*, 441–444.
97. Tam, W.; Eaton, D. F.; Calabrese, J. C.; Williams, I. D.; Wang, Y.; Anderson, A. G. *Chem. Mater.* **1989**, *1*, 128–140.

98. Eaton, D. F.; Anderson, A. G.; Tam, W.; Wang, Y. J. *Am. Chem. Soc.* **1987**, *109*, 1886–1888.
99. Cox, S. D.; Gier, T. E.; Bierlein, J. D.; Stucky, S. D. *J. Am. Chem. Soc.* **1989**, *110*, 2986.
100. Marder, S. R.; Perry, J. W.; Schaefer, W. P.; Tiemann, B. G.; Groves, P. C.; Perry, K. J. *Proc. Soc. Photo Opt. Instrum. Eng.* **1989**, *1147*, 108–115.
101. Marder, S. R.; Perry, J. W.; Tiemann, B. G.; Schaefer, W. P. *Organometallics* **1991**, *10*, 1896–1901.
102. Koike, T.; Ohmi, T.; Umegaki, S.; Okada, S.; Masaki, A.; Matsuda, H.; Nakanishi, H. *CLEO Tech. Dig.* **1990**, *7*, 402.
103. Nakanishi, H.; Kagami, M.; Hamazaki, N.; Watanabe, T.; Sato, H.; Miyata, S. *Proc. Soc. Photo Opt. Instrum. Eng.* **1989**, *1147*, 84–89.
104. Okada, S.; Matsuda, H.; Nakanishi, H.; Kato, M.; Muramatsu, R. Japanese Patent 63-348265, 1988.
105. Okada, S.; Masaki, A.; Matsuda, H.; Nakanishi, H.; Koike, T.; Ohmi, T.; Yoshikawa, N.; Umegaki, S. *Proc. Soc. Photo Opt. Instrum. Eng.* **1990**, *1337*, 178.
106. Perry, J. W.; Marder, S. R.; Perry, K. J.; Sleva, E. T.; Yakmyshyn, C.; Stewart, K. R.; Boden, E. P. *Proc. Soc. Photo Opt. Instrum. Eng.* **1991**, *1560*, 302–309.
107. Yakmyshyn, C. P.; Marder, S. R.; Stewart, K. R.; Boden, E. P.; Perry, J. W.; Schaeffer, W. P. In *Organic Materials for Non-Linear Optics II*; Hann, R. A.; Bloor, D., Eds.; Royal Society of Chemistry Special Publication No. 91; Royal Society of Chemistry, Burlington House: London, 1991; pp 108–114.
108. Zyss, J.; Chemla, D. S.; Nicoud, J. F. *J. Chem. Phys.* **1981**, *74*, 4800.
109. Sutter, K.; Hulliger, J.; Günter, P. *Solid State Commun.* **1990**, *74*, 867–870.
110. Sutter, K.; Hulliger, J.; Günter, P. *Proc. Soc. Photo Opt. Instrum. Eng.* **1991**, *1560*, 290–295.
111. Williams, D. J. *Angew. Chem. Int. Ed. England* **1984**, *23*, 690–703.
112. Thackara, J. L.; Lipscomb, G. F.; Stiller, M. A.; Ticknor, A. J.; Lytel, R. *Appl. Phys. Lett.* **1988**, *52*, 1031–1033.
113. Lytel, R.; Lipscomb, G. F. In *Multifunctional Materials*; Buckley, A.; Gallagher-Daggitt, G.; Karasz, F. E.; Ulrich, D. R., Eds.; Materials Research Society Symposium Series 175; Materials Research Society: Pittsburgh, PA, 1990; pp 41–50.
114. Ye, C.; Minami, N.; Marks, T. J.; Yang, J.; Wong, G. K. *Macromolecules* **1988**, *21*, 2899–2901.
115. Willand, C. S.; Williams, D. J. *Ber. Buns. Phys. Chem.* **1987**, *91*, 1304–1310.
116. Haas, D.; Yoon, H.; Man, H.; Cross, G.; Mann, S.; Parsons, N. *Proc. Soc. Photo Opt. Instrum. Eng.* **1989**, *1147*, 222–232.
117. Le Grange, J. D.; Kuzyk, M. G.; Singer, K. D. *Mol. Cryst. Liq. Cryst.* **1987**, *150b*, 567–605.
118. Williams, D. J. In *Nonlinear Optical Properties of Organic Molecules and Crystals*; Chemla, D. S.; Zyss, J., Eds.; Academic: Orlando, FL, 1987; Vol. 1, pp 405–435.
119. Meredith, G. R.; VanDusen, J. G.; Williams, D. J. In *Nonlinear Optical Properties of Organic and Polymeric Materials*; Williams, D. J., Ed.; ACS Symposium Series 233; American Chemical Society: Washington, DC, 1983, pp 109–133.

120. Khanarian, G.; Norwood, R.; Landi, P. *Proc. Soc. Photo Opt. Instrum. Eng.* **1989**, *1147*, 129–133.
121. Khanarian, G.; Norwood, R. A.; Haas, D.; Feuer, B.; Karim, D. *Appl. Phys. Lett.* **1990**, *57*, 977–979.
122. Khanarian, G.; Norwood, R. *Proc. Soc. Photo Opt. Instrum. Eng.* **1990**, *1337*, 44–52.
123. Comizzoli, R. B. *J. Electrochem. Soc.* **1987**, *13*, 424–429.
124. Meredith, G. R.; VanDusen, J. G.; Williams, D. J. *Macromolecules* **1982**, *15*, 1385–1389.
125. Singer, K. D.; Lalama, S. J.; Sohn, J. E. *Proc. Soc. Photo Opt. Instrum. Eng.* **1985**, *578*, 130–136.
126. Singer, K. D.; Sohn, J. E.; Lalama, S. J. *Appl. Phys. Lett.* **1986**, *49*, 248–250.
127. Singer, K. D.; Kuzyk, M. G.; Sohn, J. E. *J. Opt. Soc. Am. B* **1987**, *4*, 968–975.
128. Sohn, J. E.; Singer, K. D.; Kuzyk, M. G.; Holland, W. R.; Katz, H. E.; Dirk, C. W.; Schilling, M. L. *Polym. Eng. Sci.* **1989**, *29*, 1205–1208.
129. Lalama, S. J.; Sohn, J. E.; Singer, K. D. *Proc. Soc. Photo Opt. Instrum. Eng.* **1985**, *578*, 168.
130. Hampsch, H. L.; Yang, J.; Wong, G. K.; Torkelson, J. M. *Macromolecules* **1988**, *21*, 526–528.
131. Singer, K. D.; Kuzyk, M. G.; Holland, W. R.; Sohn, J. E.; Lalama, S. J.; Comizzoli, R. B.; Katz, H. E.; Schilling, M. L. *Appl. Phys. Lett.* **1988**, *53*, 1800–1802.
132. Matsumoto, S.; Kubodera, K.; Hurihara, T.; Kaino, T. *Appl. Phys. Lett.* **1987**, *51*, 1–2.
133. Hill, J. R.; Pantelis, P.; Abbasi, F.; Hodge, P. J. *Appl. Phys.* **1988**, *64*, 2749–2751.
134. Zhao, M.; Bautista, M.; Ford, W. T. *Macromolecules* **1991**, *24*, 844–849.
135. Henry, R. A.; Hoover, J. M.; Knoesen, A.; Kowel, S. T.; Lindsay, G. A.; Mortazavi, M. A. *Mat. Res. Soc. Symp. Proc.* **1990**, *173*, 601–606.
136. Ye, C.; Marks, T. J.; Yang, J.; Wong, G. K. *Macromolecules* **1987**, *20*, 2322–2324.
137. Dai, D. R.; Marks, T. J.; Yang, J.; Lundquist, P. M.; Won, G. K. *Macromolecules* **1990**, *23*, 1891–1894.
138. DeMartino, R. N.; Wayne, N. J. U.S. Patent 4 757 130, 1988.
139. Kitipichai, P.; LaPerota, R., Jr.; Korenowski, G. M.; Wnek, G. E.; Gorodisher, I.; Uhlmann, D. R. *Polym. Prepr.* **1989**, *30*, 176.
140. Meyrueix, R.; Mignani, G.; Tapolsky, G. In *Organic Molecules for Nonlinear Optics and Photonics*; Messier, J., Ed.; Kluwer Academic: Dordrecht, The Netherlands, 1991; pp 161–176.
141. Jungbauer, D.; Teraoka, I.; Yoon, D. Y.; Reck, B.; Swalen, J. D.; Twieg, R.; Willson, C. G. *J. Appl. Phys.* **1991**, *69*, 8011–8017.
142. Willand, C. S. Presented at the American Chemical Society National Meeting, Denver, CO, 1987.
143. Finklemann, H.; Ringsdorf, H.; Wendorf, J. H. *Makromol. Chem.* **1979**, *179*, 273.
144. Finklemann, H.; Naegele, D.; Ringsdorf, H. *Makromol. Chem.* **1979**, *180*, 203.
145. Hampsch, H. L.; Yang, J.; Wong, G. K.; Torkelson, J. M. *Macromolecules* **1990**, *23*, 3640–3647.

146. Hubbard, M. A.; Minami, N.; Ye, C.; Marks, T. J.; Yang, J.; Wong, G. K. *Proc. Soc. Photo Opt. Instrum. Eng.* **1988**, *971*, 136–141.
147. Hampsch, H. L.; Yang, J.; Wong, G. K.; Torkelson, J. M. *Polym. Commun.* **1989**, *30*, 40–43.
148. Hampsch, H. L.; Yang, J.; Wong, G. K.; Torkelson, J. M. *Macromolecules* **1990**, *23*, 3648–3654.
149. Katz, H. E.; Schilling, M. L. *J. Am. Chem. Soc.* **1989**, *111*, 7554–7557.
150. Katz, H. E.; Schilling, M. L.; Holland, W. R.; Fang, T. In *Materials for Nonlinear Optics: Chemical Perspectives*; Marder, S. R.; Sohn, J. E.; Stuckey, G. D., Eds.; ACS Symposium Series 455; American Chemical Society: Washington, DC, 1991; pp 267–278.
151. Hubbard, M. A.; Marks, T. J.; Yang, J.; Wong, G. K. *Chem. Mater.* **1989**, *1*, 167–169.
152. Robello, D. R.; Ulman, A.; Willand, C. S. U.S. Patent 4 796 971, 1989.
153. Eich, M.; Sen, A.; Looser, H.; Bjorklund, G. C.; Swalen, J. D.; Twieg, R.; Yoon, D. Y. *J. Appl. Phys.* **1989**, *66*, 2559–2567.
154. Eich, M.; Sen, A.; Looser, H.; Yoon, D. Y.; Bjorklund, G. C.; Twieg, R.; Swalen, J. D. *Proc. Soc. Photo Opt. Instrum. Eng.* **1988**, *971*, 128–135.
155. Reck, G.; Eich, M.; Jungbauer, D.; Twieg, R. J.; Willson, C. G.; Yoon, D. Y.; Bjorklund, G. C. *Proc. Soc. Photo Opt. Instrum. Eng.* **1989**, *1147*, 74–83.
156. Eich, M.; Reck, B.; Yoon, D. Y.; Willson, C. G.; Bjorklund, G. C. *J. Appl. Phys.* **1989**, *66*, 3241–3247.
157. Park, J.; Marks, T. J.; Yang, J.; Wong, G. K. *Chem. Mater.* **1990**, *2*, 229–231.
158. Robello, D. R.; Willand, C. S.; Scozzafava, M.; Ulman, A.; Williams, D. J. In *Materials for Nonlinear Optics: Chemical Perspectives*; Marder, S. R.; Sohn, J. E.; Stuckey, G. D., Eds.; ACS Symposium Series 455; American Chemical Society: Washington, DC, 1991; pp 279–293.
159. Chen, M.; Yu, L.; Dalton, L. R.; Shi, Y.; Steier, W. H. *Macromolecules* **1991**, *24*, 5421–5428.
160. Mignani, G.; Barthelemy, P.; Meyrueix, R. U.S. Patent 2 636 745, 1990.
161. Mignani, G.; Barthelemy, P.; Meyrueix, R. U.S. Patent 4 985 528, 1991.
162. Ducharme, S.; Scott, J. C.; Twieg, R. J.; Moerner, W. E. *Phys. Rev. Lett.* **1991**, *66*, 1846–1849.
163. Moerner, W. E.; Walsh, C.; Scott, J. C.; Ducharme, S.; Burland, D. M.; Bjorklund, G. C.; Twieg, R. J. *Proc. Soc. Photo Opt. Instrum. Eng.* **1991**, *1560*, 278–289.
164. Roberts, G. G. In *Langmuir-Blodgett Films*; Roberts, G. G., Ed.; Plenum: New York, 1990; pp 351–368.
165. Aktsipetrov, O. A.; Akhmediev, E. D.; Mishina, E. D.; Novak, V. R. *JETP Lett.* **1983**, *37*, 207–209.
166. Girling, I. R.; Cade, N. A.; Kolinsky, P. V.; Jones, R. J.; Peterson, I. R.; Ahmad, M. M.; Neal, D. B.; Petty, M. C.; Roberts, G. G.; Feast, W. J. *J. Opt. Soc. Am. B* **1987**, *4*, 950–955.
167. Girling, I. R.; Kolinsky, P. V.; Cade, N. A.; Earls, J. D.; Peterson, I. R. *Opt. Commun.* **1985**, *55*, 289–292.
168. Popovitz-Biro, R.; Hill, K.; Landau, E. M.; Lahav, M.; Leiserowitz, L.; Sagiv, J.; Hsiung, H.; Meredith, G. R.; Vanherzeele, H. *J. Am. Chem. Soc.* **1988**, *110*, 2672–2674.
169. Neal, D. B.; Petty, M. C.; Roberts, G. G.; Ahmad, M. M.; Feast, W. J.; Girling, I. R.; Cade, N. A.; Kolinsky, P. V.; Peterson, I. R. *Electron. Lett.* **1986**, *22*, 460–462.

170. Ahmad, M. M.; Feast, W. J.; Neal, D. B.; Petty, M. C.; Roberts, G. G. J. *Mol. Elect.* **1986**, *2*, 129–133.
171. Cross, G. H.; Peterson, I. R.; Girling, I. R.; Cade, N. A.; Goodwin, M. J.; Carr, N.; Sethi, R. S.; Marsden, R.; Gray, G. W.; Lacey, D.; McRoberts, A. M.; Scrowston, R. M.; Toyne, K. J. *Thin Solid Films* **1988**, *156*, 39–52.
172. Cresswell, J. P.; Tsibouklis, J.; Petty, M. C.; Feast, W. J.; Carr, N.; Goodwin, M.; Lvov, Y. M. *Proc. Soc. Photo Opt. Instrum. Eng.* **1990**, *1337*, 358–363.
173. Bosshard, C.; Kupfer, M.; Gunter, P.; Pasquier, C.; Zahir, S.; Seifert, M. *Appl. Phys. Lett.* **1990**, *56*, 1204–1206.
174. Laschewsky, A.; Ringsdorf, H.; Schmidt, G. *Thin Solid Films* **1985**, *134*, 153–172.
175. Carr, N.; Goodwin, M. J.; McRoberts, A. M.; Gray, G. W.; Marsden, R.; Scrowston, R. M. *Makromol. Chem. Rapid. Commun.* **1987**, *8*, 487–493.
176. Tredgold, R. H.; Winter, C. S. *J. Phys. D.* **1982**, *15*, L55–58.
177. Mumby, S. J.; Swalen, J. D.; Rabolt, J. F. *Macromolecules* **1986**, *19*, 1054–1059.
178. Tredgold, R. H. *Thin Solid Films* **1987**, *152*, 223–230.
179. Hall, R. C.; Lindsay, G. A.; Anderson, B.; Kowel, S. T.; Higgins, B. G.; Stroeve, P. In *Nonlinear Optical Properties of Polymers*; Heeger, A. J.; Orenstein, J.; Ulrich, D. R., Eds.; Materials Research Society Symposium Proceedings 109; Materials Research Society: Pittsburgh, PA, 1988; Vol. 109; pp 351–356.
180. Hsiung, H.; Rodriguez-Parada, J.; Bekerbauer, R. *Chem. Phys. Lett.* **1991**, *182*, 88–92.
181. Tillman, N.; Ulman, A.; Schildfraut, J. S.; Penner, T. *J. Am. Chem. Soc.* **1988**, *110*, 6136–6144.
182. Tillman, N.; Ulman, A.; Penner, T. L. *Langmuir* **1989**, *5*, 101–111.
183. Li, D.; Ratner, M. A.; Marks, T. J.; Zhang, C.; Yang, J.; Wong, G. K. *J. Am. Chem. Soc.* **1990**, *112*, 7389–7390.
184. Li, D.; Marks, T. J.; Zhang, T.; Wong, G. K. *Synth. Met.* **1991**, *41–43*, 3157–3162.
185. Katz, H. E.; Scheller, G.; Putvinski, T. M.; Schilling, M. L.; Wilson, W. L.; Chidsey, C. E. D. *Science (Washington, D.C.)* **1991**, *254*, 1485–1487.

RECEIVED for review March 12, 1992. ACCEPTED revised manuscript March 5, 1993.

The Role of Intermolecular Interactions in Molecular Electronics

Computational Design of Architectures with Large Second-Order Optical Nonlinearities

Santo Di Bella,^{1,2} Ignazio L. Fragalá,^{1,2} Mark A. Ratner,¹ and Tobin J. Marks¹

¹ Department of Chemistry and the Materials Research Center,
Northwestern University, Evanston, IL 60208-3113

The role of intermolecular interactions in determining quadratic nonlinear optical macroscopic hyperpolarizabilities is investigated using the intermediate neglect of differential overlap (INDO/S) (ZINDO) sum-over-excited particle-hole-states (SOS) formalism on clusters (dimers and trimers) of archetypical donor-acceptor π -electron chromophores. The calculated aggregate hyperpolarizability strongly depends on relative molecular orientations, exhibiting the largest values in slipped cofacial arrangements, where the donor substituent of one unit is in close proximity to the acceptor substituent of the nearest neighbor. These results argue that cofacial assembly of chromophores having low dipole moments should maximize molecular contributions to the macroscopic susceptibility. The classical "two-level" model is generally a good approximation for estimating hyperpolarizabilities in such systems. The second-order response of model molecular 1:1 and asymmetric 2:1 electron donor-acceptor (EDA) complexes is also investigated using the INDO/S formalism. Intermolecular charge-transfer (CT) transitions in EDA complexes represent a promising approach to achieving sizable second-order optical nonlinearities. Calculated hyperpolarizabilities reflect the strength of the donor-acceptor interaction in the complex, affording for a given acceptor, the largest values in the case of the strongest donors. The large change in dipole moment accompanying intermolecular CT transitions and low-lying

*Corresponding authors.

² Permanent address: Dipartimento di Scienze Chimiche, Università di Catania, 95125 Catania, Italy

0065-2393/94/0240-0223\$08.00/0
© 1994 American Chemical Society

CT excitation frequencies are major sources of the large calculated second-order nonlinearities. The two-level model is again a useful first approximation for predicting the nonlinear response of such complexes.

THE DESIGN OF MOLECULE-BASED MATERIALS exhibiting large second-order nonlinear optical (NLO) responses (1–6) would greatly benefit from accurate and chemically oriented theoretical descriptions of the macroscopic nonlinear susceptibility, $\chi^{(2)}$. To date, however, quantum chemical approaches for calculating NLO properties (7–26) have been largely limited to the study of the molecular nonlinear responses of single chromophore units. Such chromophores are generally conjugated molecules having donor–acceptor substituents and possessing strong intramolecular charge-transfer (CT) excitations. Importantly, the ultimate capability of such theoretical approaches only allows the optimization of the hyperpolarizability of single chromophore molecules (7–26). Although such information is valuable, assembling molecules possessing large microscopic hyperpolarizabilities does not necessarily result in bulk materials having optimum NLO responses, because packing geometries and intermolecular interactions modulate the final NLO characteristics of the material (27–31). In this perspective, it becomes relevant to systematically investigate macroscopic nonlinearities as a function of various packing geometries as well as intermolecular interactions that, of course, must play a major role in determining the macroscopic NLO response (32–34). Regarding the latter topic, cofacial interactions involving substituted aromatic rings of electron donor–acceptor (EDA) complexes (35–37) provide an interesting case study. In EDA complexes, intermolecular CT transitions cause charge redistribution between the electron donor molecule (D) and the electron-acceptor counterpart (A) and thus might represent an alternative approach to achieving significant NLO responses.

In this chapter, we present a theoretical analysis, using the intermediate neglect of differential overlap–sum-over-excited particle-hole-states (INDO–SOS) (ZINDO) formalism (22–24), of the subtle interrelations between effective quadratic hyperpolarizability $\beta(-2\omega; \omega, \omega)$ and the β -determining architectural parameters of molecular clusters (dimers and trimers) containing archetypical chromophore molecules in various relative orientations. The NLO response can be related to various intermolecular interactions, and the possible packing geometries that result in the optimum macroscopic second-order nonlinear susceptibility are explored as well. Finally, the second-order nonlinear responses of 1:1 and asymmetric 2:1 EDA model complexes are studied, to develop new synthetic strategies for efficient NLO materials.

Computational Methods

The SOS formalism (38) has been used in connection with the all-valence INDO/S model (39–41). The details of this computationally efficient ZINDO–SOS-based method for accurately describing second-order molecular optical nonlinearities have been reported elsewhere (22–24). The ZINDO model Hamiltonian is based on a minimum basis set of Slater orbitals, with many matrix elements defined semiempirically. This approach yields rather good agreement with experimental dipole moments and, therefore, it should reliably describe the electrostatic interactions among cluster dimers and trimers. Moreover, the use of Slater orbitals renders the formalism appropriate for treatment of long-range interactions.

The single-determinant, molecular orbital approximate ground state was used, and the monoexcited configuration interaction (MECI) approximation was employed to describe the excited states. In all of the present computations, the 130 lowest energy transitions between self-consistent field (SCF) and MECI electronic configurations were chosen to undergo configuration interaction (CI) mixing and were included in the SOS. This SOS truncation was found to be sufficient for a complete convergence of the second-order response in all the cases considered.

The great advantage of the SOS method can be related to the simplicity of the analysis of β -determining parameters. This simplicity allows both a chemical interpretation of molecular NLO properties as well as the analysis of the role and the nature of intermolecular interactions that modulate the NLO response. In addition, further simplification can be of value when the two-level approximation is applicable (42, 43). In these cases, a single CT transition determines the NLO response (eq 1). Here β_i is the two-level hyperpolarizability term, $\Delta\mu_{ge}$ is the difference between

$$\beta_i(-2\omega; \omega, \omega) = \frac{3e^2}{2} \frac{\hbar\omega_{ge}f\Delta\mu_{ge}}{[(\hbar\omega_{ge})^2 - (\hbar\omega)^2][(\hbar\omega_{ge})^2 - (2\hbar\omega)^2]} \quad (1)$$

excited- and ground-state dipole moments, $\hbar\omega$ is the incident radiation frequency, $\hbar\omega_{ge}$ is the energy, and f is the oscillator strength of the optical transition involved in the two-level process. In the case where the CT transition has a dominant contribution along one-molecular axis (e.g., the z axis), the β_i term should be largely proportional to the β_{zzz} tensor, so that $\beta_i(-2\omega; \omega, \omega) \cong \beta_{i,zzz}$.

Finally, it must be remembered that a number of important theoretical issues (neglect of multicenter exchange repulsion effects, possible role of basis set superposition error, and adequacy of the semiempirical parameterization at long distances) must and ultimately will be addressed further in the context of comparison with extensive *ab initio* studies.

Nevertheless, the results of the present study certainly are of value for understanding the effects of intermolecular interactions on NLO response.

Dimer and Trimer Clusters

We first consider the simplest case represented by two monomeric units of a molecule having donor–acceptor substituents connected by a conjugated pathway such as *p*-nitroaniline (PNA, **1**). The two units are brought together in a cofacial eclipsed conformation (**2**) with dipolar axes aligned parallel to the *z* axis of a reference coordinate system.

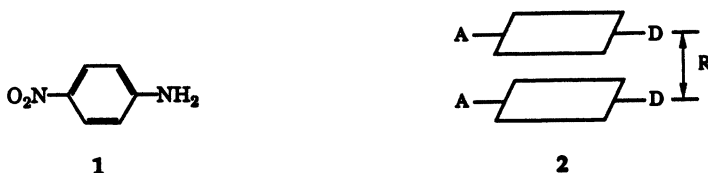
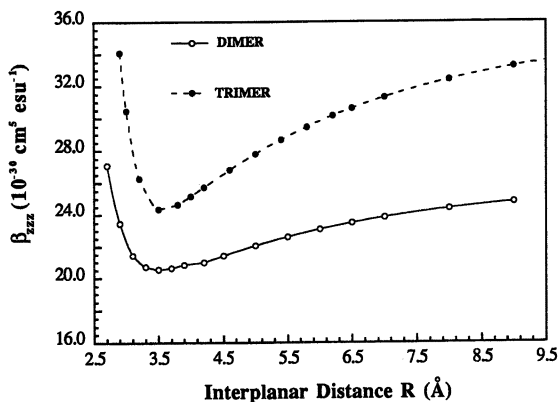


Figure 1A shows the dependence of β_{zzz} (the largest component of the β_{ijk} tensor) upon the interplanar separation (R). At interplanar distances near 3.5 Å (typical mean van der Waals' interaction distances in organic crystals), the curve shows a flat minimum that increases asymptotically to a limiting value at larger distances (>9.0 Å). For distances smaller than 3.0 Å, a sharp increase is observed. For each distance, the estimated two-level $\beta_{i,zzz}$ terms (eq 1) approximate the SOS-derived β_{zzz} values reasonably well (Table I). This means that a single CT transition dominates the perturbation sum. Therefore, the simplified analysis of variables influencing the dependence of β_i is straightforward. In particular, the NLO response at various interplanar distances is largely determined by the position of the lowest energy CT transition. Cofacial interactions occurring at both large and medium distances may be rationalized in terms of exciton theory of interacting monomers. As a matter of fact, the composition of the CI states is rather well described as a linear combination of monomer states, and, therefore, the low-energy β -determining band remains unsplit although slightly shifted to higher energy compared to the monomer (Figures 2A and 2B) by the relative amount of the electrostatic interactions. This shift as well as the gradual decrease of both $\Delta\mu$ and f values, leads to a decrease of β_i as the interplanar spacing is contracted (Table I). In contrast, at distances less than 3.3 Å, the dipole–dipole interactions cause a strong energy splitting of each monomer-related molecular orbital (MO) with a resulting bathochromic shift of the lowest energy CT transition (Table I) and a consequent increase of β_{zzz} values.

The same trend in calculated β -values is observed (Figure 1A) in the case of the analogous PNA trimer having the same conformation

A.



B.

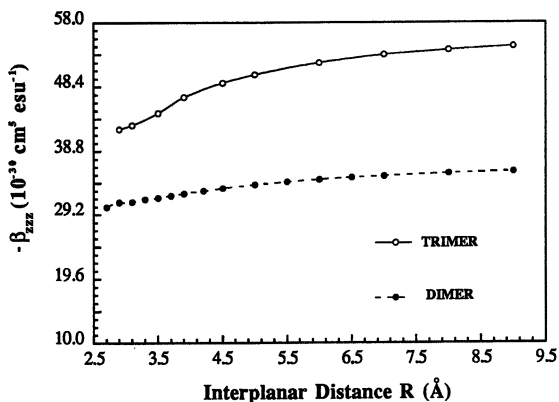


Figure 1. Variation of calculated hyperpolarizability component β_{zzz} ($\hbar\omega = 0.65 \text{ eV}$) with interplanar distance (R) in cofacial eclipsed PNA (A) and POM (B) clusters.

(3), in the same range of interplanar distances. Nevertheless, a more pronounced (than found in the dimer) minimum is observed near the equilibrium interplanar distances. In particular, for $R = 3.5 \text{ \AA}$, on passing from the dimer to the trimer, β_{zzz} values are 16 and 34% smaller than those estimated when considering the simple additivity of monomer β_{zzz} values (Table II). This observation indicates that, at equilibrium interplanar distances, the local field corrections (F) due to intermolecular interactions (27–31) clearly begin to play a role in determining the macroscopic quadratic susceptibility, $\chi^{(2)}$. In contrast, for larger interplanar distances ($>12 \text{ \AA}$), the magnitude of β is an additive quantity.

Table I. Calculated Dipole Moment, Linear Optical Spectroscopic, and Hyperpolarizability Data for PNA and POM Dimers in the Eclipsed Conformation at Various Interplanar Separations

Initial Separation (Å)	μ (debyes)	$\hbar\omega_{ge}^a$ (eV)	f	$\Delta\mu$	β_{tzzz}^b	β_{zzz}
2.7	15.55 (1.80)	3.06 (3.26)	0.34 (0.25)	10.20 (-10.07)	23.72 (-13.78)	27.09 (-30.34)
2.9	15.39 (1.83)	3.46 (3.50)	0.43 (0.29)	11.06 (-10.62)	21.15 (-13.07)	23.49 (-31.09)
3.1	15.33 (1.87)	3.76 (3.68)	0.52 (0.33)	11.42 (-10.25)	20.07 (-12.19)	21.44 (-31.16)
3.3	15.32 (1.92)	3.96 (3.80)	0.63 (0.40)	11.67 (-9.11)	20.82 (-11.60)	20.72 (-31.42)
3.5	15.34 (1.96)	4.08 (3.80)	0.74 (0.54)	11.83 (-7.72)	22.56 (-13.22)	20.54 (-31.77)
3.7	15.36 (1.99)	4.13 (3.82)	0.82 (0.79)	11.93 (-9.22)	24.23 (-22.93)	20.64 (-32.09)
4.2	15.46 (2.05)	4.14 (3.81)	0.91 (1.00)	11.93 (-10.56)	26.53 (-33.68)	21.00 (-32.80)
5.0	15.56 (2.13)	4.10 (3.78)	0.93 (1.07)	11.95 (-10.96)	28.20 (-38.18)	22.06 (-33.74)
6.0	15.73 (2.18)	4.06 (3.76)	0.95 (1.10)	11.97 (-11.11)	29.68 (-40.62)	23.09 (-34.55)
7.0	15.84 (2.23)	4.03 (3.75)	0.96 (1.11)	11.98 (-11.16)	30.74 (-41.96)	23.84 (-35.08)
8.0	15.90 (2.26)	4.01 (3.74)	0.96 (1.12)	11.99 (-11.19)	31.50 (-42.92)	24.39 (-35.48)
9.0	15.93 (2.27)	3.99 (3.73)	0.97 (1.13)	12.00 (-11.18)	32.06 (-43.30)	24.79 (-35.72)
Monomer	8.10 (1.16)	3.90 (3.67)	0.48 (0.56)	11.78 (-10.91)	16.04 (-21.59)	12.29 (-17.23)

NOTES: For definition of parameters *see* text; hyperpolarizability is $\beta(-2\omega, \omega, \omega)(10^{-30} \text{ cm}^5 \text{ esu}^{-1})$, $\hbar\omega = 0.65 \text{ eV}$. 180 states are included in the SOS procedure for PNA and POM dimers. Values for POM dimer are reported in parentheses.

^a Lowest energy CT transition.

^b Calculated using the two-level model of equation 1.

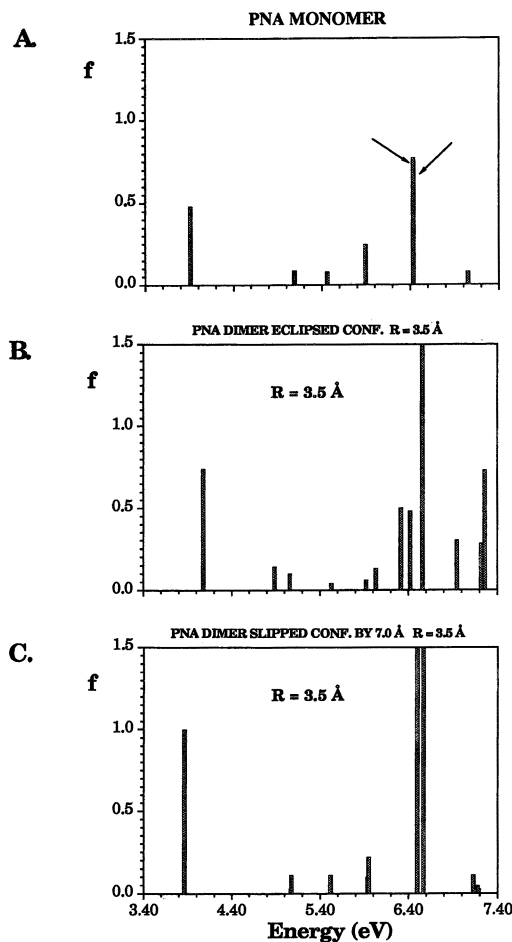
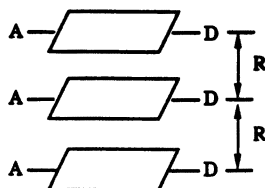


Figure 2. Calculated optical absorption spectra of PNA monomer (A), PNA dimer eclipsed conformation (B), and PNA dimer slipped conformation (C).

Table II. Molecular Hyperpolarizability Values for PNA and POM Monomers and for PNA and Dimers and Trimers in the Eclipsed Conformation

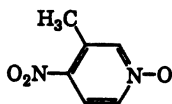
Unit	Monomer	Dimer	Trimer
PNA	12.29	20.54 (24.58)	24.37 (36.87)
POM	-17.23	-31.77 (-34.46)	-43.75 (-51.69)

NOTES: Values in parentheses are calculated by the simple addition of monomer β_{zzz} values; hyperpolarizability is β_{zzz} (10^{-30} cm⁵ esu⁻¹; $\hbar\omega = 0.65$ eV). Interplanar separation is 3.5 Å.



3

Turning now to a cofacial dimer constructed from molecular subunits with nearly vanishing ground-state dipole moments such as 3-methyl-4-nitropyridine-1-oxide (44, 45) (POM, 4), a rather different interplanar spacing-dependent trend in β_{zzz} is observed relative to the PNA dimer (Figure 1B). In this case, the β_{zzz} versus R curve does not show a minimum. On moving to larger distances, the β_{zzz} value increases slightly until ~ 6.0 Å. At this point, the curve becomes nearly flat, reaching twice the calculated β_{zzz} monomer (Table I). The same trend is observed in the analogous POM trimer (Figure 1B), and for distances greater than 6.0 Å, β_{zzz} values are approximately three times the POM monomer values. The NLO response at relatively larger distances may again be rationalized in terms of the two-level approach used for the PNA dimer (Table I), with weaker (than in the PNA dimer) electrostatic interactions and consequent unperturbed ground and excited states (Figures 3A and 3B). For distances less than 3.7 Å, the monomers interact strongly and behave as a supermolecule. In these cases, the CI states cannot be simply described as combinations of monomer states, and the optical spectrum shows new CT bands at lower energies (Figures 3C and 3D). As a consequence, for smaller interplanar distances, the two-level model breaks down (Table I). Furthermore, on passing from the monomer to the dimer and trimer ($R = 3.5$ Å), β_{zzz} values are 8 and 15% smaller, respectively, than those estimated on the basis of the simple additivity of the monomer β_{zzz} values (Table II). Therefore, the deviation from the simple model of molecular β -additivity in determining the hyperpolarizability in POM clusters is smaller than in the PNA analogues.



4

The observed differences in the NLO response of PNA and POM clusters is a consequence of different intermolecular interactions (46, 47). In the PNA clusters, intermolecular interactions are largely electrostatic (dipole–dipole) in nature and dominate the other contributing

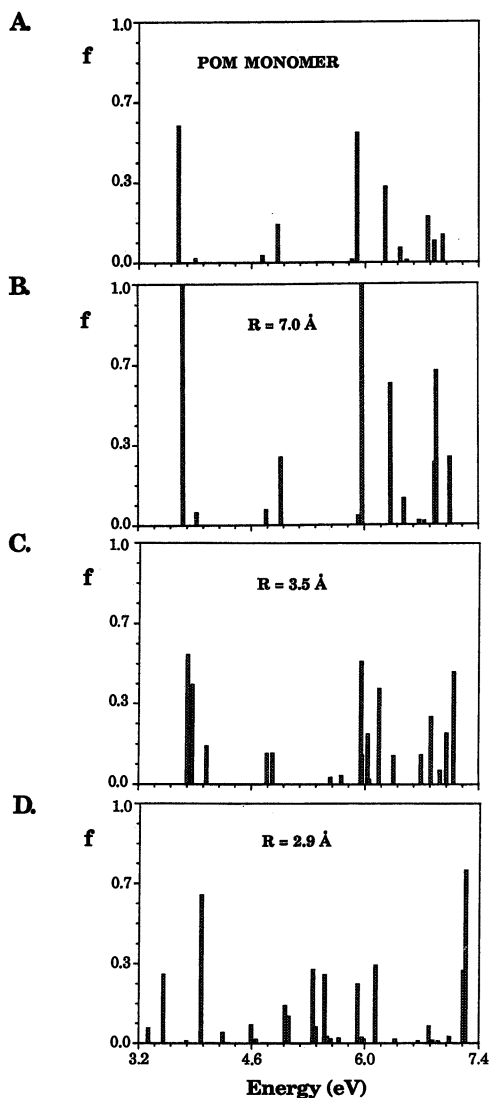


Figure 3. Calculated optical absorption spectra of POM monomer (A) and POM dimer (B–D) in the eclipsed conformation at various interplanar distances (R).

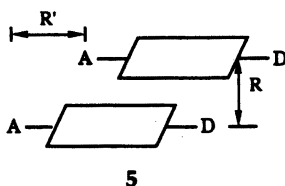
interactions. In contrast, in the POM clusters, delocalization or intermolecular CT interactions operating only at short distances, dominate the intermolecular interactions, whereas for relatively large distances each molecule may be considered to be independent of the surrounding ones, and the aggregate hyperpolarizability is essentially a sum of those of the individual molecular components. That is, local field corrections are relatively unimportant in this regime.

This analysis conveys interesting consequences for the molecular engineering of high-efficiency second-harmonic generation (SHG) thin-film materials (48) such as self-assembled or Langmuir–Blodgett films characterized by relatively low chromophore packing densities (N_s). Using POM-like molecular precursors having small dipole moments, it should in principle be possible to cofacially assemble chromophoric layers having high packing densities without appreciable reduction in molecular susceptibility. In fact, assuming equation 2 for the SHG response, where $\langle T_{ijk} \rangle$ is a transformation

$$\chi_{ijk}^{(2)} = N_s F \langle T_{ijk} \rangle \beta_{zzz} \quad (2)$$

matrix and β_{zzz} is the dominant component of the molecular hyperpolarizability, the $\chi^{(2)}$ value becomes proportional to N_s . Therefore, the optimization of packing density is clearly crucial for obtaining high-efficiency SHG materials.

Among the various possible distortions of idealized molecular arrays, the most interesting case occurs in slipped arrangements (5), generated from the eclipsed conformation ($R = 3.5 \text{ \AA}$) by parallel translations (R')



5

along the z axis. In fact, the increase in slip distances can be correlated with enhanced β -responses (Figure 4). A β -maximum is found when the donor substituent of a PNA unit lies approximately above the acceptor substituent of the other molecule. In this arrangement, all the parameters that give rise to large β -values are optimized (compared to the eclipsed conformation). In particular, the low-energy CT transition is red-shifted, and the oscillator strength is increased in comparison to those of the cofacial dimers (Figures 2B and 2C). This indicates small stabilizing dipole–dipole interactions, with CI states simply characterized as linear combinations of monomer states. It can therefore be concluded that bulk materials having slipped (strongly dipolar) chromophore compo-

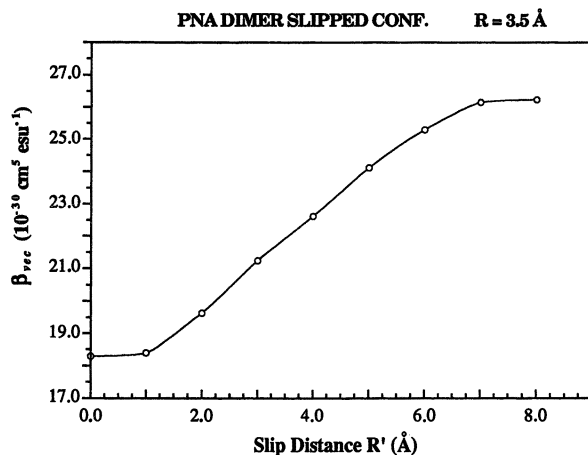


Figure 4. Variation of calculated hyperpolarizability component β_{vvc} ($\hbar\omega = 0.65 \text{ eV}$) with slip distance (R') along the z axis in the PNA dimer.

nents would be expected to exhibit an optimum second-order nonlinearity. As a possible confirmatory example, 3-methyl-4-methoxy-4'-nitrostilbene (NMONS), the crystal structure of which consists of stacked π - π planar molecules in a slipped cofacial donor-acceptor configuration (5), has one of the largest powder SHG efficiencies reported to date (49, 50).

1:1 EDA Complexes

Among the known EDA complexes, those formed by cofacial interaction of substituted aromatic rings seem the most attractive, because they might be readily incorporated into functionalized polymers (51) or into self-assembled architectures. We focus on archetypical π -acceptor molecules such as 7,7,8,8-tetracyanoquinodimethane (TCNQ, 6), tetracyanoethylene (TCNE, 7), and 1,3,5-trinitrobenzene (TNB, 8), interacting with arene molecules having various electron-donating groups (methyl, methoxy, and amine) as substituents. The structures (52, 53) used for calculations on 1:1 EDA complexes are depicted in Scheme I.

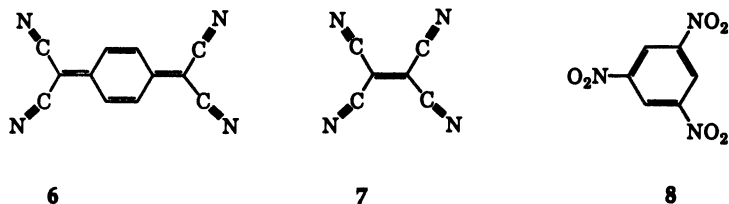
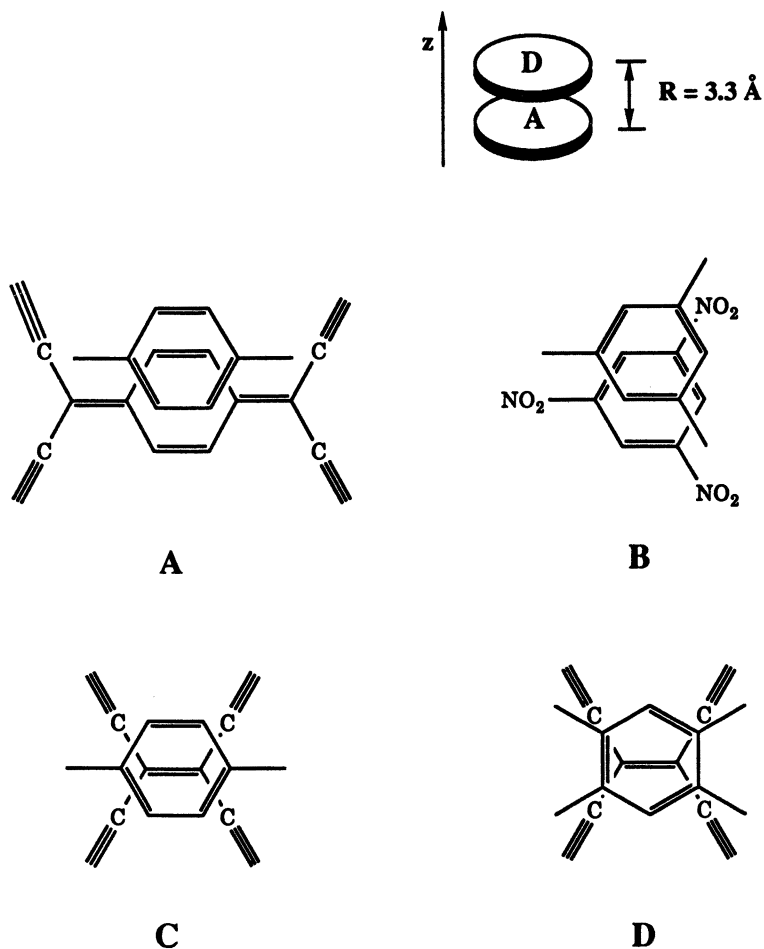


Table III summarizes calculated linear optical, dipole moment, and second-order hyperpolarizability data for selected 1:1 cofacial EDA



Scheme I

complexes. Calculated dipole moments range from 0.5 to 1.5 Debyes, and their magnitude reflects the degree of CT interaction in the ground state, that is, the strength of the EDA complex (35–37). As expected, the dipole moment increases with increasing donor strength and, in each series, is maximum in the case of the aminoarene donor. An analogous trend is observed in the lowest energy CT transition, which becomes stronger (increasing oscillator strength) and is shifted to lower energy as the donor strength increases. Calculated β_{zzz} values (Table III) may be roughly related to the strength of the EDA complexes and may range from $\sim 8 \times 10^{-30} \text{ cm}^5 \text{ esu}^{-1}$ ($\hbar\omega = 0.65 \text{ eV}$), similar to that reported for PNA (Table I), to $\sim 70 \times 10^{-30} \text{ cm}^5 \text{ esu}^{-1}$ ($\hbar\omega = 0.65$

Table III. Calculated Dipole Moment, Linear Optical Spectroscopic, and Molecular Hyperpolarizability Data for Cofacial 1:1 Electron Donor–Acceptor Complexes Involving Various Electron Acceptor Molecules

<i>Donor</i> ^a (<i>D</i>)	μ (<i>debyes</i>) ^b	$\hbar\omega_{ge}$ (<i>eV</i>) ^{b,c}	<i>f</i> ^d	$\Delta\mu_{ge}$ (<i>debyes</i>) ^b	β_{zzz} ^b	β_{zzz} ^d
Acceptor is TCNQ						
TMDP	1.07	2.04	0.14	14.43	68.36	69.96
PD	1.04	2.33	0.14	14.46	39.04	38.50
DMB	0.40	3.02	0.08	14.29	8.39	7.77
PX	0.60	3.27	0.11	13.75	9.08	8.04
HMB	0.68	3.03	0.11	14.04	11.08	10.23
Acceptor is TCNE						
TTAB	1.33	2.04	0.14	14.54	68.51	69.08
PD	0.83	2.45	0.10	14.94	23.22	22.78
DMB	0.54	3.25	0.09	14.98	8.23	7.79
PX	0.62	3.48	0.11	14.95	7.28	6.97
HMB	0.59	3.37	0.12	15.65	9.34	8.95
Acceptor is TNB						
TAB	0.59	2.29	0.06	14.46	21.95	18.97
TRIAZ	0.36	3.00	0.06	15.03	11.18	7.10

NOTES: For definition of parameters *see* text; hyperpolarizability is $\beta(-2\omega, \omega, \omega)(10^{-30} \text{ cm}^5 \text{ esu}^{-1})$; $\hbar\omega = 0.65 \text{ eV}$.

^a TMPD is *N,N,N',N'*-tetramethyl-*p*-phenylenediamine; PD is *p*-phenylenediamine; DMB is 1,4-dimethoxybenzene; PX is *p*-xylene; HMB is hexamethylbenzene; TTAB is 1,2,4,5-tetraaminobenzene; TAB is 1,3,5-triaminobenzene; and TRIAZ is 2,4,6-tris(dimethylamino)-1,3,5-triazine.

^b Calculated using the INDO/S SOS formalism.

^c Lowest energy CT transition.

^d Calculated using the simple two-level model of equation 1.

eV), exceeding those reported for highly efficient second-order NLO chromophores such as (4-*N,N*-dimethylamino-4'-nitrostilbene)stilbene (DANS).

As expected, the NLO response is largely determined by the lowest energy CT transition, so that the two-level model (eq 1) is a suitable guideline for rationalizing the NLO response of EDA complexes (Table III). All of the present EDA complexes are characterized by large, almost constant changes in the dipole moment between the first excited and ground state ($\Delta\mu_{ge}$), so that the β_r -values may be related to $\hbar\omega_{eg}$ and *f*, the optimizations of which are crucial for the design of efficient NLO EDA complexes. For a given acceptor, the energy of the lowest energy CT transition may be simply related to the donor strength, affording

lower $\hbar\omega_{eg}$ values, thus larger hyperpolarizabilities, in the case of amine-substituted donors. The relative orientation of donor-acceptor components is the most important feature, leading to stabilization of the ground state as well as to maximization of the oscillator strength of the lowest energy CT transition (35–37). This requires that the highest occupied molecular orbital (HOMO) (for the donor) and the lowest occupied molecular orbital (LUMO) (for the acceptor) can be mixed by the dipole in the point group of the complex, and f is maximized when these MOs are strongly overlapping. In the case of the TCNQ complexes, the LUMO, independent of the donor molecule, is of b_{2g} symmetry (in the local D_{2h} point group) and the charge distribution is largely localized at the 1, 4, 7, and 8 atomic positions (Figure 5A). Consequently, an aromatic donor molecule having a HOMO of the same symmetry and having two electron-donating substituents in 1 and 4 positions is expected to have an optimum overlap (Figure 5C), thus a large f . In the case of TCNE complexes, the same arguments indicate that overlap maximization may be achieved in the same fashion as the TCNQ complexes or, better, with an arene donor molecule having four substituents in the 1, 2, 4, 5 positions such as the 1, 2, 4, 5-tetraminobenzene (Figures 5B and D). In each case, the trend of calculated f values (Table III) accords well with these qualitative symmetry considerations.

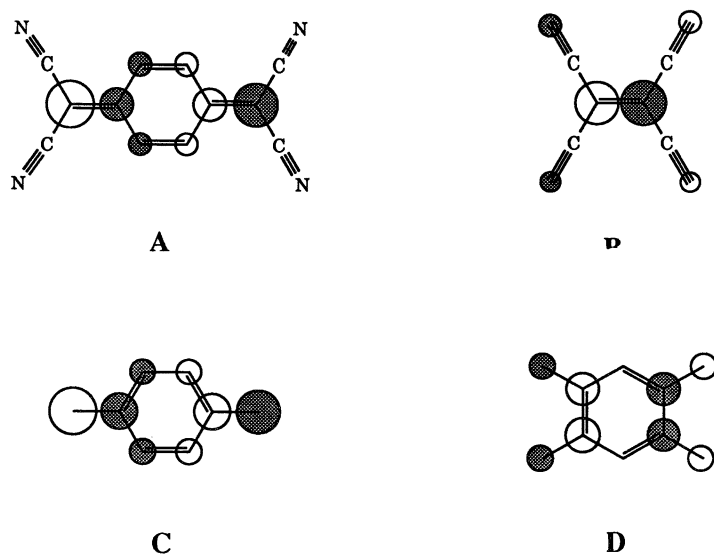
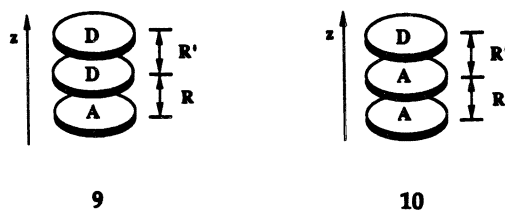


Figure 5. Frontier orbitals of selected EDA complexes: LUMO of TCNQ (A) and TCNE (B) complexes; HOMO of TCNQ-*N,N,N',N'*-tetramethyl-*p*-phenylenediamine (C), and TCNE-1,2,4,5-tetraminobenzene (D) complexes.

Asymmetric 2:1 EDA Complexes

The formation of asymmetric acceptor, donor, donor (ADD)–EDA complexes has been achieved in cyclophane molecules containing rigidly constrained donor–acceptor moieties (54). Formation of ADD or acceptor, acceptor, donor (AAD) complexes has also been reported in functionalized EDA polymeric structures (51). Formation of 2:1 ADD (9) or AAD (10) complexes, the geometries of which are constructed from those of 1:1 analogues ($R = R' = 3.5 \text{ \AA}$), leads to increasing calculated dipole moments (Table IV) that can be related to more extensive CT interactions in the ground state. The lowest energy CT transitions are red-shifted compared to those of the 1:1 analogues, as found experimentally (55–57). In ADD complexes, the lowest energy CT transition in the CI expansion involves, to various extents, a combination of HOMO and second HOMO (SHOMO), both localized in the DD moiety, and the LUMO. The LUMO has essentially the same energy and atomic population found in 1:1 complexes. The red-shift of the CT transition may be simply related to the energy splitting of the HOMO and SHOMO due to the DD interaction. An analogous situation occurs in AAD complexes, where the lowest energy CT transition involves the HOMO and a combination of LUMO and SLUMO.



For the present 2:1 EDA complexes, an increase of β_{zzz} compared with that of the 1:1 analogues is observed (Table IV). The two-level model is still a good approximation in predicting the NLO response. Therefore, the β enhancement in asymmetric 2:1 complexes may be essentially related to the red-shift of the lowest energy CT transition and, to a smaller extent, to the increase of $\Delta\mu_{ge}$.

Conclusions

The present results indicate that intermolecular interactions represent a major factor in determining macroscopic second-order susceptibilities of molecular materials. The NLO response depends critically not only on molecular packing geometries, but also on the characteristics of molecule constituents. At equilibrium intermolecular distances, the NLO response is a strong function of the relative molecular orientations, exhibiting the largest values in slipped cofacial arrangements, that is, in a

Table IV. Calculated Dipole Moment, Linear Optical Spectroscopic, and Molecular Hyperpolarizability Data for Cofacial Asymmetric ADD and AAD Electron Donor-Acceptor Complexes Involving Various Electron Acceptor Molecules

Donor ^a (D)	μ (debyes) ^b	$\hbar\omega_{ge}$ (eV) ^{b,c}	f^b	$\Delta\mu_{ge}$ (debyes) ^b	β_{zzz}^b	$\beta_{t,zzz}^d$
Acceptor is TCNQ						
TMDP	1.42 (1.44)	1.77 (1.77)	0.16 (0.16)	18.29 (17.35)	188.44 (187.92)	199.52 (194.86)
PD	1.25 (1.26)	2.02 (2.05)	0.15 (0.15)	18.63 (17.24)	89.85 (80.68)	95.92 (83.54)
DMB	0.50 (0.47)	2.64 (2.69)	0.08 (0.07)	18.62 (16.27)	16.78 (13.09)	17.38 (11.47)
PX	0.75 (0.67)	2.78 (2.94)	0.11 (0.09)	18.91 (16.03)	20.82 (13.25)	20.80 (11.59)
HMB	0.91 (0.88)	2.58 (2.70)	0.11 (0.09)	19.04 (16.67)	26.29 (17.28)	27.25 (16.37)
Acceptor is TCNE						
TTAB	1.63 (1.63)	1.85 (1.81)	0.16 (0.45)	17.29 (16.91)	148.25 (150.73)	152.75 (157.88)
PD	0.10 (0.96)	2.19 (2.20)	0.11 (0.10)	17.88 (16.84)	49.03 (40.24)	50.17 (41.58)
DMB	0.64 (0.61)	2.99 (2.99)	0.11 (0.09)	16.81 (16.66)	13.75 (11.38)	13.26 (11.30)
PX	0.74 (0.69)	3.01 (3.22)	0.11 (0.10)	19.20 (16.63)	14.76 (9.87)	15.40 (9.86)
HMB	0.80 (0.71)	2.73 (3.13)	0.12 (0.12)	19.74 (15.70)	22.34 (12.16)	23.27 (11.71)
Acceptor is TNB						
TAB	0.71 (0.71)	1.93 (2.05)	0.06 (0.05)	18.57 (15.42)	57.32 (38.50)	45.26 (22.80)

NOTES: Values for AAD complexes are reported in parentheses. For definition of parameters see text; hyperpolarizability is $\beta(-2\omega;\omega,\omega)$; 10^{-30} cm⁵ esu⁻¹; $\hbar\omega = 0.65$ eV.

^a TMPD is N,N,N',N'-tetramethyl-p-phenylenediamine; PD is p-phenylenediamine; DMB is 1,4-dimethoxybenzene; PX is p-xylene; HMB is hexamethylbenzene; TTAB is 1,2,4,5-tetraaminobenzene; and TAB is 1,3,5-triaminobenzene.

^b Calculated using the INDO/S SOS formalism.

^c Lowest energy CT transition.

^d Calculated using the simple two-level model of equation 1.

regime of smaller, stabilizing dipole–dipole interactions. Furthermore, for relatively large intermolecular distances, particularly for component molecules having a small ground-state dipole moment, the aggregate hyperpolarizability is essentially a sum of those of the individual molecular components. That is, the hyperpolarizability at these distances is essentially dominated by weak long-range dipole–dipole interactions.

Finally, these results indicate that intermolecular CT transitions in EDA complexes can, under favorable conditions, lead to sizable second-order NLO responses. Therefore, these results suggest promising alternative approaches to the synthesis of materials having large second-order nonlinearities.

Acknowledgments

This research was supported by the National Science Foundation–Materials Research Laboratory (MRL) program through the Material Research Center of Northwestern University (Grant DMR9120521) and by the Air Force Office of Scientific Research (Contract 93–1–0114). S. Di Bella thanks the Italian Consiglio Nazionale delle Ricerche (CNR, Rome) for a postdoctoral fellowship. We thank D. Kanis for ongoing collaboration.

References

1. Prasad, N. P.; Williams, D. J. *Introduction to Nonlinear Optical Effects in Molecules and Polymers*; Wiley: New York, 1991.
2. *Materials for Nonlinear Optics: Chemical Perspectives*; Marder, S. R.; Sohn, J. E.; Stucky, G. D., Eds.; ACS Symposium Series 455, American Chemical Society: Washington, DC, 1991.
3. *Nonlinear Optical Effects in Organic Polymers*; Messier, J.; Kajar, F.; Prasad, P.; Ulrich, D., Eds.; Kluwer Academic: Dordrecht, The Netherlands, 1989.
4. *Organic Materials for Nonlinear Optics*; Hann, R. A.; Bloor, D., Eds.; Royal Society of Chemistry: London, 1988.
5. *Nonlinear Optical Properties of Organic Molecules and Crystals*; Chemla, D. S.; Zyss, J., Eds.; Academic: Orlando, FL, 1987; Vols. 1, 2.
6. *Nonlinear Optical Properties of Organic and Polymeric Materials*; Williams, D. J., Ed.; ACS Symposium Series 233, American Chemical Society: Washington, DC, 1984.
7. Karna, S. P.; Prasad, P. N.; Dupuis, M. *J. Chem. Phys.* **1991**, *94*, 1171.
8. Meyers, F.; Adant, C.; Bredas, J. L. *J. Am. Chem. Soc.* **1991**, *113*, 3715.
9. Rice, J. E.; Amos, R. D.; Colwell, S. M.; Handy, N. C.; Sanz, J. *J. Chem. Phys.* **1990**, *93*, 8828.
10. Dykstra, C. E.; Jasien, P. G. *Chem. Phys. Lett.* **1984**, *109*, 388.
11. Sekino, H.; Bartlett, R. J. *J. Chem. Phys.* **1986**, *85*, 976; *Int. J. Quant. Chem.* **1992**, *43*, 119.
12. Morley, J. O. *J. Chem. Soc. Faraday Trans.* **1991**, *87*, 3009, 3015.
13. Morley, J. O. *J. Am. Chem. Soc.* **1988**, *110*, 7660.
14. Docherty, V. J.; Pugh, D.; Morley, J. O. *J. Chem. Soc. Faraday Trans. 2*, **1985**, *81*, 1179.

15. Lalama, S. J.; Garito, A. F. *Phys. Rev.* **1979**, *20*, 1179.
16. Morrell, J. A.; Albrecht, A. C. *Chem. Phys. Lett.* **1979**, *64*, 46.
17. Li, D.; Ratner, M. A.; Marks, T. J. *J. Phys. Chem.* **1992**, *96*, 4325.
18. Li, D.; Ratner, M. A.; Marks, T. J. *J. Am. Chem. Soc.* **1988**, *110*, 1707.
19. Li, D.; Marks, T. J.; Ratner, M. A. *Chem. Phys. Lett.* **1986**, *131*, 370.
20. Dirk, C. W.; Twieg, R. J.; Wagniere, G. *J. Am. Chem. Soc.* **1986**, *108*, 5387.
21. Soos, Z.; Ramasesha, S. *J. Chem. Phys.* **1989**, *90*, 1067.
22. Kanis, D. R.; Marks, T. J.; Ratner, M. A. *Int. J. Quantum Chem.* **1992**, *43*, 61.
23. Kanis, D. R.; Ratner, M. A.; Marks, T. J. *Chem. Mater.* **1991**, *3*, 19.
24. Kanis, D. R.; Ratner, M. A.; Marks, T. J. *J. Am. Chem. Soc.* **1990**, *112*, 8203.
25. Parkinson, W. A.; Zerner, M. C. *J. Chem. Phys.* **1991**, *94*, 478.
26. Ulman, A.; Willand, C. S.; Kohler, W.; Robello, D. R.; Williams, D. J.; Handley, L. *J. Am. Chem. Soc.* **1990**, *112*, 7083.
27. Zyss, J.; Chemla, D. S. In *Nonlinear Optical Properties of Organic Molecules and Crystals*; Chemla, D. S.; Zyss, J., Eds.; Academic: Orlando, FL, 1987; Vol. 1, p 23.
28. Shen, Y. R. *Annu. Rev. Phys. Chem.* **1989**, *40*, 327.
29. Hurst, M.; Munn, R. W. *J. Molecular Electron.* **1986**, *2*, 35, 43.
30. Munn, R. W. *J. Mol. Electron.* **1988**, *4*, 31.
31. Singer, K. D.; Kuzyk, M. G.; Sohn, J. E. *J. Opt. Soc. Am. B* **1987**, *4*, 968.
32. Di Bella, S.; Ratner, M. A.; Marks, T. J. *J. Am. Chem. Soc.* **1992**, *114*, 5842.
33. Itch, Y.; Hamada, T.; Kakuta, A.; Mukoh, A. *Soc. Photo Opt. Instrum. Eng. Proc.* **1990**, *1337*, 293.
34. Zyss, J.; Berthier, G. *J. Chem. Phys.* **1982**, *77*, 3635.
35. Mulliken, R. S.; Person, W. B. *Molecular Complexes. A Lecture and Reprint Volume*; Wiley: New York, 1969.
36. Foster, R. *Organic Charge-Transfer Complexes*, Academic: Orlando, FL, 1969.
37. *Molecular Complexes*; Foster, R., Ed.; Elek Science: London, 1973, 1974; Vols. 1, 2.
38. Ward, J. F. *Rev. Mod. Phys.* **1965**, *37*, 1.
39. Anderson, W. P.; Edwards, W. D.; Zerner, M. C. *Inorg. Chem.* **1986**, *25*, 728.
40. Bacon, A. D.; Zerner, M. C. *Theoret. Chim. Acta (Berlin)* **1979**, *53*, 21.
41. Ridley, J.; Zerner, M. C. *Theoret. Chim. Acta (Berlin)* **1973**, *32*, 111.
42. Oudar, J. L. *J. Chem. Phys.* **1977**, *67*, 446.
43. Oudar, J. L.; Chemla, D. S. *J. Chem. Phys.* **1977**, *66*, 2664.
44. Zyss, J.; Chemla, D. S. *J. Chem. Phys.* **1981**, *74*, 4800.
45. Sigelle, M.; Hierle, R. *J. Appl. Phys.* **1981**, *52*, 4199.
46. Rigby, M.; Smith, E. B.; Wakeham, W. A.; Maitland, G. C. *The Forces between Molecules*; Clarendon: Oxford, England, 1986, p 1.
47. Morokuma, K.; Kitaura, K. In *Molecular Interactions*; Ratajczak, H.; Orville-Thomas, W. J.; Radshaw, M., Eds.; Wiley & Sons: New York, 1980; Vol. 1, p 21.
48. Ulman, A. *Ultrathin Organic Films*; Academic: Orlando, FL, 1991.
49. Tam, W.; Guerin, B.; Calabrese, J. C.; Stevenson, S. H. *Chem. Phys. Lett.* **1989**, *154*, 93.
50. Bierlein, J. D.; Cheng, L. K.; Wang, Y.; Tam, W. *Appl. Phys. Lett.* **1990**, *56*, 423.
51. Pearson, J. M.; Turner, S. R. In *Molecular Association, Including Molecular Complexes*; Foster, R., Ed.; Academic: Orlando, FL, 1979; p 79.

52. Mayoh, B.; Prout, C. K. *J. Chem. Soc. Faraday Trans. II* **1972**, *68*, 1072.
53. Herbstein, F. H. In *Perspectives in Structural Chemistry*; Dunitz, J. D.; Ibers, J. A., Eds.; Wiley: New York, 1971; Vol. IV, p 166.
54. Misumi, S. In *Cyclophanes*; Keehn, P. M.; Rosenfeld, S. M., Eds.; Academic: Orlando, FL, 1983; Vol. II, p 573.
55. Merriam, M. J.; Rodriguez, R.; McHale, J. L. *J. Phys. Chem.* **1987**, *91*, 1058.
56. Smith, M. L.; McHale, J. L. *J. Phys. Chem.* **1985**, *89*, 4002.
57. Gribaudo, M. L.; Knorr, F. J.; McHale, J. L. *Spectrochim. Acta Part A* **1985**, *41*, 419.

RECEIVED for review May 22, 1992. ACCEPTED revised manuscript October 21, 1992.

Theoretical Insight into the Design of Organic Molecules for Third-Order Nonlinear Optical Applications

Brian M. Pierce

Hughes Aircraft Company, Radar Systems, Building R02, Mail Stop V518,
P.O. Box 92426, Los Angeles, CA 90009-2426

This chapter examines how semiempirical molecular orbital theory can be used to help design conjugated π -electron organic molecules for third-order nonlinear optical (NLO) applications. First, the materials requirements for the most important third-order NLO application, optical signal processing (optical computing), are reviewed. The second section establishes the relationship between the third-order contribution to the macroscopic polarization ($\chi^{(3)}$) of the bulk material and the third-order polarizabilities (γ) of the molecular units comprising the material. The maximization of $\chi^{(3)}$ for a material composed of weakly coupled molecular units is examined in the third section. The fourth section reviews the calculation of γ , molecular geometry, and molecular electronic structure. The fifth section presents a theoretical analysis of the γ s for linear polyenes and cyanine cations, which represent two distinct classes of quasi-one-dimensional conjugated- π -electron molecules. The final section summarizes guidelines for optimizing the third-order NLO properties of conjugated- π -electron organic molecules.

NONLINEAR OPTICAL PHENOMENA are increasingly being utilized in a variety of photonic applications. The second-order NLO process of second-harmonic generation used to extend the frequency range of a laser (1-3). Electrooptical modulators and switches (e.g., Pockel's cell) operate via the second-order NLO effect of an electric-field induced change in refractive index (3, 4). The third-order NLO phenomenon of an optically induced change in refractive index is fundamental to all optical switching and computing (5, 6), as well as phase-conjugate adaptive optics (7). The efficiencies of these NLO processes are dependent

0065-2393/94/0240-0243\$15.20/0
© 1994 American Chemical Society

upon the material employed to couple the given combination of electrical and/or optical signals.

Most of the NLO materials currently used in the fabrication of passive and active photonic devices are ferroelectric, inorganic crystals. For example, the potassium dideuterium phosphate (KD*P) crystal is widely employed as a laser frequency doubler (2), the lithium-niobate (LiNbO₃) crystal is virtually the exclusive material of choice for electrooptical modulators that operate in the near-IR spectral range (8, 9), and the barium-titanate (BaTiO₃) crystal is being investigated for applications involving phase conjugation (7, 10). Although the crystal-growing technology for these materials is highly developed and their NLO susceptibilities are sufficient for most current photonic applications, they have features that are less than desirable. One such feature is the constraint of working with only single-crystalline materials. Another feature is the large dielectric constant possessed by most ferroelectric, inorganic crystals because of the contribution of ionic polarization, as well as electronic polarization. The very large dielectric constant of BaTiO₃ limits its NLO response time, and hence its optical switching time, to the millisecond range at laser intensities of $\sim 1 \text{ W/cm}^2$ (11). This limitation is not critical in applications involving parallel optical signal processing, but is important for serial processing. In conclusion, new NLO materials are needed to extend the range of photonic applications made possible by the current set of ferroelectric, inorganic crystals.

Organic molecular crystals and polymers are prominent candidates as new NLO materials. They are of interest worldwide because of their relatively low cost, ease of fabrication, custom tailorability, high laser-damage thresholds, low dielectric constants (because electronic polarization tends to dominate over other polarization processes, such as ionic or dipole orientation), fast NLO response times, and nonresonant, NLO susceptibilities comparable to or exceeding those of ferroelectric, inorganic crystals. In principle, it is easier and less expensive to fabricate light waveguides for electrooptic modulators from oriented polymer films than from single-crystalline materials. The research and development of organic molecular crystals and polymers for second-order NLO applications has progressed to the point where polymer-based electrooptic modulators have been demonstrated and are being engineered into products like the polymeric, thin-film, waveguide, electrooptic modulator. For more details on second-order NLO organic materials, the reader is referred to the comprehensive chapter by Gorman et al. Chapter 8 in this book. The research and development of organic materials for third-order NLO applications is still in the early stages. Large third-order NLO susceptibilities ($\sim 10^{-10}$ – 10^{-9} statcoul-cm/statV³) with subpicosecond response times have been measured for the polydiacetylenetoluenesulfonate (PTS) polymer (12–14). These properties

make PTS and related polymers attractive materials for all-optical switching and computing applications. Single-mode optical fibers fabricated from guest–host organic polymers are being developed for all-optical switching applications (15, 16). Organic materials are therefore considered to have great potential as second- and third-order NLO materials (17–22).

Organic molecules with π -electron, conjugated bonding networks, such as polydiacetylene, linear polyenes, merocyanine dyes, cyanine salts, porphyrins, and phthalocyanines are of particular interest because their NLO susceptibilities are exceptionally large in magnitude (17–22). NLO susceptibilities are synonymous here with the electric susceptibility tensors, $\chi^{(n)}$, where $n + 1$ is the rank of the tensor. The term n refers also to the order of the nonlinear effect. It is advantageous to have a $\chi^{(n)}$ to be as large as possible because the larger this susceptibility, the smaller the strengths of the applied electric fields and the shorter the path length needed to achieve the given NLO effect.

The large $|\chi^{(n)}|$ for π -electron organic molecules is principally due to the delocalized nature of π -electron bonding and the consequent ease in which these bonding networks can be polarized by applied electric fields. Therefore, the $\chi^{(n)}$ s for these molecules tend to be dominated by the π -electronic components of $\chi^{(n)}$. In the case where none of the radiation fields involved in the given NLO effect have frequencies near the resonance frequency for an excited molecular electronic state, the dominance of the π -electronic component implies that the NLO response times for π -electron organic molecules should be in the subpicosecond range (see preceding paragraph for PTS). The rapid time scales associated with the contribution of electronic motion to $\chi^{(n)}$ are indicated by the range of resonance frequencies for molecular electronic transitions: $\sim 10^{14} \text{ s}^{-1}$ (near-IR) to $\sim 10^{15} \text{ s}^{-1}$ (UV).

The above emphasis on the electronic contribution to the $\chi^{(n)}$ s should not be taken to imply that the effect of molecular vibrations on these susceptibilities is negligible. In the case of small oligomers of the σ -conjugated *trans*-polysilane polymer, large vibrational effects have been calculated for both the linear and nonlinear polarizabilities (23). These results are consistent with the large vibrational effect on the nonlinear polarizability measured for poly(*n*-octylmethyl)silane (24). The vibrational contributions to $\chi^{(3)}$ for conjugated- π -electron molecules have also been investigated and found to be nonnegligible (25). The cyanine salts investigated in this chapter are calculated to have third-order polarizabilities that are very sensitive to molecular geometry, and hence to vibrationally induced distortions of this geometry.

The NLO susceptibility, or electric susceptibility, for an individual molecule is the molecular polarizability tensor, $\alpha^{(n)}$. The understanding of the relation between the electronic structure of an organic molecule

and its $\alpha^{(n)}$ is important to the development of these molecules as NLO materials. Calculations of $\alpha^{(n)}$ based on quantum mechanical treatments of the interaction of electromagnetic radiation with matter and the distributions of electron density in ground and excited electronic states of molecules can contribute a great deal to the understanding of the relation between $\alpha^{(n)}$ and molecular electronic structure. This understanding can then be employed in the optimization of $\chi^{(n)}$ for the n th order NLO application.

This chapter provides theoretical insight into the design of conjugated- π -electron organic molecules for third-order NLO applications. The first section of the chapter reviews the materials requirements for optical signal processing (optical computing), which is the most important technological application of third-order NLO materials. The second section establishes the relationship between the third-order contribution to the macroscopic polarization induced by applied electric fields in a material, $\chi^{(3)}:E_1E_2E_3$, where $E_{i=1,2,3}$ are the three electric fields mixed by $\chi^{(3)}$ in the material, and the third-order contribution to the dipole moment induced by the applied electric fields in the molecular units comprising the material, $\alpha^{(3)}:E_1E_2E_3$. The maximization of $\chi^{(3)}:E_1E_2E_3$ for a material composed of weakly coupled molecular units is examined in the third section. In the fourth section, the relationship between the third-order molecular polarizability, $\gamma \equiv \alpha^{(3)}$, molecular geometry, and molecular electronic structure is discussed in the context of (1) the sum-over-states (SOS) expression for γ derived using time-dependent perturbation theory, (2) experimental and theoretical determinations of molecular geometries in the condensed phase, and (3) quantum chemical calculations of molecular electronic structure that incorporate the effect of the local environment of the molecule in the condensed phase. The fifth section presents a theoretical analysis of the third-order molecular polarizabilities of linear polyenes and linear cyanine cations, which represent two distinct classes of quasi-one-dimensional conjugated- π -electron molecules. The issues addressed in this section are as follows: (1) the establishment of the validity of the theoretical procedure by comparing calculated and measured third-order polarizabilities; (2) the effect of chain length and conformation on the calculated π -electronic components of γ , γ_π , for the polyenes and cyanines; (3) the identification of the salient ${}^1\pi\pi^*$ states that define γ_π for the two sets of molecules; (4) the identification and analysis of the SOS terms important to γ_π for the molecules, and the derivation of approximations to the complete SOS expression for γ_π that help provide chemical insight into the origin of γ_π for the molecules; and (5) an investigation of the dependence of γ_π , and the π -electronic component of the second-order, electric dipole polarizability, β_π , on (a) the geometric asymmetry of a linear cyanine cation and (b) the deprotonation of the cation. The sixth and final section

summarizes design guidelines for optimizing conjugated- π -electron organic molecules for third-order NLO applications.

This chapter complements a number of recent reviews and papers on the calculation and measurement of the third-order NLO properties of organic molecules. A selection of papers that emphasizes the theoretical analysis of third-order NLO properties of conjugated- π -electron organic molecules is given in references 26–39, while references 40–54 contain a selection regarding experimental studies of third-order NLO properties for this class of molecules. Useful general references on experimental and theoretical studies of both second- and third-order NLO properties of organic molecules and materials are cited in references 17–22.

Materials Requirements for Optical Signal Processing

The high-speed processing of data is fundamental to numerous technologies like computing and telecommunication systems. It is predicted that the future photonic switching office for telecommunications will operate 10,000 channels producing a combined bit-rate of 1 terabit/s or 10^{12} bit/s (55). In contrast, the present electronic switching office handles a combined bit-rate of less than 15×10^9 bit/s (5). All-optical architectures have been designed that are well-suited for the serial and parallel processing of high bit-rate data streams (5, 6, 56, 57). The implementation of all-optical signal processing has been slow because of the lack of materials needed for the components in an optically based signal processor.

The components central to most all-optical signal processors are waveguide devices that switch or control optical beams through phase shifts resulting from light-induced changes in the refractive index of the material comprising the waveguide, for example, the $\frac{1}{2}$ beat-length directional coupler, the 1 beat-length directional coupler, the distributed-feedback grating, the Mach–Zehnder interferometer, the mode sorter, and the prism coupler (56, 57). The phase shift for an optical beam at wavelength λ is related to the light-induced change in refractive index in the following manner:

$$\Delta\varphi(\lambda, I) = 2\pi l\Delta n(\lambda, I)/\lambda \quad (1)$$

where $\Delta\varphi(\lambda, I)$ is the phase shift as a function of the radiation wavelength and light intensity, l is the interaction length, and $\Delta n(\lambda, I)$ is the change in the real part of the refractive index as a function of λ and I . High optical power densities on the order of MW/cm^2 are generally needed to induce $\Delta n(\lambda, I)$ s large enough so that phase shifts close to π -radians can be achieved over interaction lengths on the order of centimeters (56, 57). The extremely low cross-sectional areas of fiber and channel

guided wave structures make it possible to obtain these high power densities using lasers with modest peak power outputs of ≤ 1 W. Candidate materials for these waveguide structures should have (1) high susceptibilities for light-induced changes in refractive index in order that the optical power density can be kept as low as possible, (2) small linear and nonlinear absorption coefficients so that photoinduced heating is minimized and the maximum interaction lengths can be achieved, and (3) subpicosecond lifetimes for the $\Delta n(\lambda, I)$.

Before discussing candidate materials for all-optical signal-processing devices, it is worthwhile to define the light-induced refractive index in greater detail. First, consider the light-induced changes in the real refractive index, $n(\lambda)$, at wavelength λ :

$$n(\lambda) = n_0(\lambda) + \Delta n(\lambda, I) \quad (2)$$

where $n_0(\lambda)$ is the linear real refractive index at λ , and $\Delta n(\lambda, I)$ is the change in real refractive index as a function of λ and the incident light intensity, I . The leading terms in the series expansion for $\Delta n(\lambda, I)$ are $n_2(\lambda)I$ and $n_{th}(\lambda)I$, so that

$$n(\lambda) \cong n_0(\lambda) + [n_2(\lambda) + n_{th}(\lambda)]I \quad (3)$$

The nonlinear refractive index coefficient, $n_2(\lambda)$, expresses the change in refractive index arising from the electric-field-induced polarization of the material, whereas the $n_{th}(\lambda)$ coefficient describes the change in the real part of the refractive index resulting from the light-induced heating of the material (i.e., the thermo-optic effect) (56, 57). Two other processes that can contribute to the nonlinear refractive index are electrostriction and molecular reorientation. These processes are not included here because they occur on much slower time scales than the polarization and thermal contributions. The $n_2(\lambda)$ coefficient is related to the real third-order nonlinear electric susceptibility tensor element, $\chi^{(3)}(\lambda)$, by the following equation (58):

$$n_2(\lambda) = 8\pi^2\chi^{(3)}(\lambda)/[cn_0(\lambda)^2] \quad (4)$$

where c is the speed of light in a vacuum and $n_0(\lambda)$ is the real part of the linear refractive index. The units of all parameters in eq 4 are in centimeter-gram-second system (cgs). This third-order NLO response is also known as the optical Kerr effect or intensity-dependent refractive index.

The $n_{th}(\lambda)$ coefficient for a static medium is related to the linear and nonlinear absorptivities at λ , $\alpha_1(\lambda)$ and $\sum_{n>1}\alpha_n(\lambda)I(\lambda)^{n-1}$, by the following equation (56, 57):

$$n_{th}(\lambda) = (dn_0(\lambda)/dT)[\alpha_1(\lambda) + \sum_{n>1}\alpha_n(\lambda)I(\lambda)^{n-1}]\Phi_{heat}(\lambda)\tau_{th}/(\rho C_p) \quad (5)$$

where $dn_0(\lambda)dT$ is the temperature coefficient for the real part of the linear refractive index, for example, $dn_0(\lambda)/dT = -3.9 \times 10^{-4} \text{ K}^{-1}$ for benzene liquid at room temperature; $\Phi_{\text{heat}}(\lambda)$ is the quantum efficiency for the dissipation of the absorbed photon energy as heat, which is taken to be unity for nonluminescing molecules; τ_{th} is the thermal-relaxation time, which is typically on the order of 10^{-7} – 10^{-6} s; ρ is the density of the material; and C_p is the heat capacity at constant pressure for the material in the illuminated region.

Even at a modest linear absorptivity of 1 cm^{-1} and negligible nonlinear absorption, $|n_{\text{th}}(\lambda)|$ is on the order of $10^{-14} \text{ m}^2/\text{W}$ or $10^{-17} \text{ cm}^2\text{-s/erg}$, which is larger than values of $n_2(\lambda)$ measured for the best-candidate organic NLO materials like the off-resonant $n_2(\lambda)$ measured at ~ 0.8 – $2.0 \mu\text{m}$ for Langmuir–Blodgett films of PTS polydiacetylene is $10^{-19} \text{ cm}^2\text{-s/erg}$ (56, 57). The contribution of $n_{\text{th}}(\lambda)I$ to $\Delta n(\lambda, I)$ can be reduced by using pulsed light with pulsewidths $\Gamma \ll \tau_{\text{th}}$. In this case, $n_{\text{th}}(\lambda)$ is reduced by the ratio Γ/τ_{th} , for example, $n_{\text{th}}(\lambda)$ is on the order of $10^{-23} \text{ cm}^2\text{-s/erg}$ for picosecond pulsewidths. However, the thermal nonlinearity can become significant for a train of pulses, and devices that operate for time periods on the order of τ_{th} . As stressed in references 56 and 57, the careful analysis of thermo-optic effects is very important to signal-processing waveguide devices.

A useful figure of merit that defines the optical switching performance of a third-order NLO material is

$$F(\lambda) = \chi^{(3)}(\lambda)/(\alpha(\lambda)\tau) \quad (6)$$

where $\alpha(\lambda) = \alpha_1(\lambda) + \sum_{n>1} \alpha_n(\lambda)I(\lambda)^{n-1}$, and τ is the lifetime of the third-order NLO response. If one rearranges equation 4 to solve for $\chi^{(3)}(\lambda)$, then equation 6 becomes

$$F(\lambda) = n_2(\lambda)[6cn_0(\lambda)]/[8\pi^2\alpha(\lambda)\tau] \quad (7)$$

Thus, one can conclude from this figure of merit: (1) the larger the magnitudes of $\chi^{(3)}(\lambda)$ or $n_2(\lambda)$, the lower the light intensities required to induce switching; (2) the lower the linear and nonlinear absorptivities at the operational wavelength, the lower probability of thermal effects overwhelming the polarization response; and (3) the shorter the lifetime, the faster the serial processing speed of the switch. In the case of serial all-optical signal processing it is very desirable that τ is subpicosecond.

A comparison of the figures of merit for some of the best candidate third-order NLO materials is instructive. The figure of merit measured at $1.064 \mu\text{m}$ (taken to be off-resonant) for a single crystal of PTS is $\sim 10^{-3} \text{ cm}^4/\text{erg-s}$ (58), which is very close to an off-resonant value measured for GaAs–GaAlAs multiple quantum well structures (59, 60). The respectable figure of merit measured for PTS–polydiacetylene is attrib-

uted to its delocalized, π -electron bonding network, which can be hyperpolarized rapidly to a high degree with a subpicosecond lifetime. The best figure of merit at 1.064 μm measured to date is that for pure silica, with $F = \sim 10^5 \text{ cm}^4/\text{erg}\cdot\text{s}$ (56, 57). The high F for silica is due to its extremely low absorptivity at 1.064 μm and its short τ , which compensate for its low $|\chi^{(3)}|$. Although the figure of merit is a good gauge of the potential for a material to be used in all-optical signal-processing waveguide devices, two other material properties need to be measured: the saturated maximum of $\Delta n(\lambda, I)$, $\Delta n_{\text{sat}}(\lambda, I)$, and the intensity threshold for damage, I_{dam} (56, 57). The off-resonant $\Delta n_{\text{sat}}(\lambda, I)$ s measured for the PTS single crystal and the GaAs–GaAlAs multiple quantum well structures are both $>10^{-3}$, which is four orders of magnitude better than the $\Delta n_{\text{sat}}(\lambda, I)$ for silica at $>10^{-7}$ (56, 57). The damage threshold for silica is, of course, much greater than that for the two other materials.

The requirements for the third-order NLO materials critical to optical signal processing are summarized as follows:

- large nonlinear optical response

$$\begin{aligned} (\chi^{(3)}(\lambda) > 10^{-8} \text{ statcoul}\cdot\text{cm}/\text{statV}^3 \\ \text{or } n_2(\lambda) > 10^{-19} \text{ cm}^2\cdot\text{s}/\text{erg}) \end{aligned}$$

- switching power densities $<1 \text{ MW}/\text{cm}^2$
- fast-switching times $<10^{-12} \text{ s}$
- short response lifetimes $<10^{-12} \text{ s}$
- low linear and nonlinear absorptivities $<1 \text{ cm}^{-1}$
- large saturated changes in refractive index <0.1
- high optical damage threshold
- mechanically tough and formable
- wide operational temperature range
- environmentally resistant
- formable into thin films and coatings

A switching power density of $<1 \text{ MW}/\text{cm}^2$ and a $|n_2(\lambda)| > 10^{-19} \text{ cm}^2\cdot\text{s}/\text{erg}$, or $10^{-6} \text{ cm}^2/\text{MW}$, combine to yield a $\Delta n(\lambda, I) > 10^{-6}$. It is highly desirable that $|n_2(\lambda)|$ can be increased so that the power density needed to achieve a $\Delta n(\lambda, I) > 10^{-6}$ can be reduced. If $|n_2(\lambda)|$ cannot be increased much beyond the value of 10^{-19} electrostatic unit (esu) then greater attention must be given to reducing the linear and nonlinear absorptivities so that longer interaction lengths can be utilized. Recall that the large figure of merit given earlier for silica is principally due to the very low absorptivity. In fact, the first all-optical switches were fabricated from silica glass optical fibers (61). Single-mode optical fibers made from doped organic polymers are being developed with figures of merit potentially larger than that of silica (15, 16). Remember that the linear and

nonlinear absorptivities, $\alpha(\lambda)$, and the nonlinear refractive index, $n_2(\lambda)$, are not independent of each other. Generally, a large $|n_2(\lambda)|$ has a correspondingly large $\alpha(\lambda)$. The optimization of the $|n_2(\lambda)|/\alpha(\lambda)$ ratio at a given λ is one of the major challenges in developing third-order NLO materials. These issues are investigated in greater detail later for π -electron conjugated organic molecules.

Additional insight into the general materials requirements for fast-photon switching can be found in papers by Lines (62) and by Astill (63).

Relation between Macroscopic Susceptibility and Molecular Polarizability

The application of an electric field to a nonconducting, nonmagnetic material of macroscopic dimensions results in the polarization, or separation of positive and negative charges, within the material. The ease at which this material can be polarized is defined by the electric-susceptibility tensors, $\chi^{(n)}$, for the material. The first-order tensor of rank 2, $\chi^{(1)}$, describes the linear-polarization response of the material to a single applied electric field. The second-order tensor of rank 3, $\chi^{(2)}$, describes the second-order nonlinear-polarization response of the material to two different electric fields applied to the material, or to a single electric field inducing a polarization and then interacting with this polarization to first-order (i.e., the first hyperpolarization). The third-order tensor of rank 4, $\chi^{(3)}$, describes the third-order nonlinear-polarization response of the material to three different electric fields applied to the material, or to a single electric field inducing a polarization and then interacting with this polarization to second-order (i.e., the second hyperpolarization). If the applied electric fields are oscillating in time, then the polarization response of the material will also oscillate in time. The time-dependence or frequency of the polarization response depends on the frequencies of the applied electric fields and the propagation relationships between these fields. For example, in the case of second-harmonic generation, two electric fields at the same angular frequency, ω , and propagating in the same direction with respect to a particular axis in a material with a nonzero $|\chi^{(2)}|$ combine to produce a polarization field oscillating at 2ω .

Because a nonconducting, nonmagnetic bulk material can often be seen as composed of molecular units, the macroscopic electric polarization of the material is ultimately determined by the electric-field-induced dipole moment in each molecular unit, and by the electric-field-induced reorientation of the molecular units if they possess permanent electric dipole moments. The ease at which a molecular dipole moment can be induced is defined by the electronic polarizability

tensors, $\alpha^{(n)}$, for the given molecular unit. The first-order tensor of rank 2, $\alpha^{(1)}$, describes the first-order molecular dipole moment induced by a single applied electric field. The second-order tensor of rank 3, $\alpha^{(2)}$, describes the second-order molecular dipole moment induced by two different electric fields applied to the unit, or by a single electric field inducing a dipole moment in the fixed molecular unit and then interacting with this dipole moment to first order (i.e., the first hyperpolarization). The third-order tensor of rank 4, $\alpha^{(3)}$, describes the third-order molecular dipole moment induced by three different electric fields applied to the material, or to a single electric field inducing a dipole moment in the fixed molecular unit and then interacting with this dipole moment to second order (i.e., the second hyperpolarizability). As with the macroscopic polarization response, the induced molecular dipole moments will oscillate in time in response to oscillating electric fields applied to the material. Reoriented permanent electric dipole moments will respond on a slower time scale than the induced electric dipole moments.

The mathematical expression for the polarization of a nonconducting, nonmagnetic medium by an applied external electric field is given by the Taylor-series expansion (1, 3):

$$\begin{aligned}
 P_A(\omega_{pol}) = & \sum_B \chi_{AB}^{(1)} \sum_i E_B(\omega_i) + (1/2!) \sum_B \sum_C \chi_{ABC}^{(2)} \sum_i \sum_j E_B(\omega_i) E_C(\omega_j) \\
 & + (1/3!) \sum_B \sum_C \sum_D \chi_{ABCD}^{(3)} \sum_i \sum_j \sum_k E_B(\omega_i) E_C(\omega_j) E_D(\omega_k) + \dots
 \end{aligned}
 \tag{8}$$

where P_A is the component of the polarization vector along the A-Cartesian-coordinate axis in the laboratory-reference frame; ω_{pol} is the angular frequency of the polarization field, which contains contributions from the linear and nonlinear polarization of the material (e.g., ω_i , $\omega_i + \omega_j$, and $\omega_i + \omega_j + \omega_k$); $\chi_{AB}^{(1)}$, $\chi_{ABC}^{(2)}$, and $\chi_{ABCD}^{(3)}$ are the real components of the electric susceptibility tensors of rank 2, 3, and 4, respectively; and $E_\alpha(\omega_i)$ is the $\alpha = A, B$, or C component of the applied-electric-field vector oscillating at angular frequency ω_i . The electric susceptibility tensors are dependent on frequency, but this dependence is not shown explicitly in equation 8. All terms in equation 8 are in esu units. Furthermore, the $(1/2!)$ and $(1/3!)$ terms in equation 8 will henceforth be incorporated into the definition of $\chi_{ABC}^{(2)}$, and $\chi_{ABCD}^{(3)}$.

Many organic nonlinear optical materials (e.g., organic molecular crystals) are composed of molecular units whose polarizabilities sum to define the macroscopic electric susceptibilities. The electric susceptibility tensors for these media can then be expressed as a function

of the number density of molecular units $[N]$, a term containing the local-electric-field tensor and the direction cosines that relate the molecule fixed coordinate axes to the laboratory coordinate axes $[\mathbf{L}_n(\theta)]$, and the molecular-polarizability tensor of rank $n + 1$ $[\alpha^{(n)}]$:

$$\chi^{(n)} = f [N, \alpha^{(n)}, \mathbf{L}_n(\theta)] \quad (n = 1, 2, 3) \quad (9)$$

The molecular polarizability tensors, $\alpha^{(n)}$ ($n = 1, 2, 3$), are more commonly represented as α (molecular polarizability), β (second-order molecular polarizability), and γ (third-order molecular polarizability), respectively. In the case of organic molecular crystals, the explicit formulation of equation 9 is discussed in detail by Munn and co-workers (64–66).

For weakly coupled molecules randomly oriented in a given medium, $\chi^{(n)}$ can be expressed simply as follows (67–68):

$$\chi^{(n)} = N \cdot \langle \alpha^{(n)} \rangle \cdot L_n \quad (n = 1, 2, 3) \quad (10)$$

where L_n is a scalar local field factor defined by the refractive indices of the medium at the frequencies of the applied electric fields and the polarization field, and $\langle \alpha^{(n)} \rangle$ is the orientationally averaged molecular polarizability tensor. The expression for $\chi^{(n)}$ in equation 10 assumes that the molecular units are far enough apart so that cascading effects do not contribute to the local field tensor. The product, $\langle \alpha^{(1)} \rangle \cdot L_1$, defines the averaged first-order dipole moment induced at the given molecular unit by an applied electric field. In a similar fashion, the products, $\langle \alpha^{(2)} \rangle \cdot L_2$ and $\langle \alpha^{(3)} \rangle \cdot L_3$, define the averaged second- and third-order dipole moments induced at this unit. Note that $\langle \alpha^{(2)} \rangle$ is zero in the case of randomly oriented molecular units. It is emphasized that the local electric field felt by the molecular unit is not the same electric field applied to the material (42).

The combination of eqs 8 and 10 yields an expansion for the macroscopic polarization expressed in terms of the molecular polarizabilities:

$$\begin{aligned} P_A(\omega_{\text{pol}}) = N \sum_{\mathbf{B}} & \langle \alpha^{(1)} \rangle_{\mathbf{AB}} \cdot \sum_{\mathbf{i}} L_1 \mathbf{E}_{\mathbf{B}}(\omega_{\mathbf{i}}) + N \sum_{\mathbf{B}} \sum_{\mathbf{C}} \\ & \langle \alpha^{(2)} \rangle_{\mathbf{ABC}} \cdot \sum_{\mathbf{i}} \sum_{\mathbf{j}} L_2 \mathbf{E}_{\mathbf{B}}(\omega_{\mathbf{i}}) \mathbf{E}_{\mathbf{C}}(\omega_{\mathbf{j}}) + N \sum_{\mathbf{B}} \sum_{\mathbf{C}} \sum_{\mathbf{D}} \\ & \langle \alpha^{(3)} \rangle_{\mathbf{ABCD}} \cdot \sum_{\mathbf{i}} \sum_{\mathbf{j}} \sum_{\mathbf{k}} L_3 \mathbf{E}_{\mathbf{B}}(\omega_{\mathbf{i}}) \mathbf{E}_{\mathbf{C}}(\omega_{\mathbf{j}}) \mathbf{E}_{\mathbf{D}}(\omega_{\mathbf{k}}) + \dots \quad (11a) \end{aligned}$$

or

$$\begin{aligned}
 P_A(\omega_{\text{pol}}) &= N \sum_B \langle \alpha \rangle_{AB} \cdot \sum_i L_1 E_B(\omega_i) + N \sum_B \sum_C \langle \beta \rangle_{ABC} \cdot \sum_i \sum_j L_2 E_B(\omega_i) E_C(\omega_j) + N \sum_B \sum_C \sum_D \langle \gamma \rangle_{ABCD} \cdot \sum_i \sum_j \sum_k L_3 E_B(\omega_i) E_C(\omega_j) E_D(\omega_k) + \dots \quad (11b)
 \end{aligned}$$

where the $(1/2!)$ and $(1/3!)$ factors are now incorporated into the definition of $\langle \beta \rangle$ and $\langle \gamma \rangle$. All terms in eq 11 are in esu units. As with the electric susceptibility tensors in eq 8, the frequency dependence of the polarizability tensors in eqs 11a and 11b is not explicitly shown, as well as the frequency dependence of the local-field tensors. The summations over the laboratory-fixed coordinates for each term in eqs 11a and 11b are nothing but the orientationally averaged molecular dipole moments induced to first-, second-, and third-order by the local electric field at the molecular unit. Thus, the macroscopic polarization can be expressed as an expansion of induced dipole moments:

$$\begin{aligned}
 P_A(\omega_{\text{pol}}) &= N \left[\sum_i \langle \mu \rangle_A^{(1)}(\omega_i) + \sum_i \sum_j \langle \mu \rangle_A^{(2)}(\omega_i + \omega_j) \right. \\
 &\quad \left. + \sum_i \sum_j \sum_k \langle \mu \rangle_A^{(3)}(\omega_i + \omega_j + \omega_k) + \dots \right] \quad (12)
 \end{aligned}$$

where $\langle \mu \rangle_A^{(n)}$ is the component of the n th order induced dipole moment along the A axis of the laboratory reference frame. The natural units of $\langle \alpha \rangle_{AB}$, $\langle \beta \rangle_{ABC}$, and $\langle \gamma \rangle_{ABCD}$ are 10^{-24} , 10^{-30} , and 10^{-36} esu, respectively, and so if one assumes a transient local electric-field strength of $\sim 10^4$ statV/cm corresponding to a peak light intensity of ~ 1 MW/cm², then the magnitudes of $\langle \mu \rangle_A^{(1)}$, $\langle \mu \rangle_A^{(2)}$, and $\langle \mu \rangle_A^{(3)}$ expressed in terms of debyes are 0.01, 0.0001, and 0.000001, respectively. The very small magnitudes of the nonlinear induced dipole moments relative to that of the linear induced dipole moment illustrate the challenge in designing molecular systems with large $|\langle \mu \rangle_A^{(2)}|$ and $|\langle \mu \rangle_A^{(3)}|$.

This chapter is concerned with the third-order NLO properties of π -electron conjugated organic molecules distributed in a given medium, and so the expression in equation 10 relevant to this study is $\chi_{ABCD}^{(3)} = N \cdot \langle \gamma \rangle_{ABCD} \cdot f(\omega_{\text{pol}})f(\omega_i)f(\omega_j)f(\omega_k)$, where $\langle \gamma \rangle_{ABCD} = \langle \alpha^{(3)} \rangle_{ABCD}$, $f(\omega_i)$ are the scalar local field factors for each of the electric fields, and the subscripts A, B, C, and D refer to the directions of the polarization field and the three applied electric fields, respectively, in the laboratory ref-

erence frame. The value of $\langle \gamma \rangle_{ABCD}$ depends on the directions of these fields. Usually $\langle \gamma \rangle_{ZZZZ}$ is measured where all four electric fields have the same polarization, and it is given by

$$\begin{aligned} \gamma = \langle \gamma \rangle_{ZZZZ} = & \left(\frac{1}{5}\right)[\gamma_{xxxx} + \gamma_{yyyy} + \gamma_{zzzz}] \\ & + \left(\frac{1}{15}\right)[\gamma_{xxyy} + \gamma_{xyxy} + \gamma_{xyyx} + \gamma_{yyxx} + \gamma_{yxyx} + \gamma_{yxxy}] \\ & + \left(\frac{1}{15}\right)[\gamma_{xxzz} + \gamma_{xzzx} + \gamma_{zxzx} + \gamma_{zzxx} + \gamma_{zxxz} + \gamma_{zxxx}] \\ & + \left(\frac{1}{15}\right)[\gamma_{yyzz} + \gamma_{yzyz} + \gamma_{yzzy} + \gamma_{zzyy} + \gamma_{zyzy} + \gamma_{zyyz}] \quad (13) \end{aligned}$$

where γ_{abcd} is a component of γ , and a, b, c , and d are the axes in the molecule-fixed coordinate system. This expression for γ is derived from the known nonzero components of γ for the point groups of the molecules of interest (69), and the nonzero orientation averages of direction cosine products like $d_{Zz}d_{Zz}d_{Zz}d_{Zz}$ or $d_{Zx}d_{Zx}d_{Zx}d_{Zx}$ (70, 71).

Due to the symmetry of permuting the three applied electric fields along the molecular coordinate axes, the following set of equalities hold for the dynamic third-order polarizability for third-harmonic generation $[\gamma(-3\omega; \omega, \omega, \omega)]$: $\gamma_{ijij} = \gamma_{ijji} = \gamma_{jiij}$, where $i \neq j \in \{x, y, z\}$. In the case of the dynamic third-order polarizability for electric-field-induced second-harmonic generation $[\gamma(-2\omega; \omega, \omega, \omega, 0)]$, the following relations hold: $\gamma_{ijij} = \gamma_{ijji} \neq \gamma_{jiij}$, where $i \neq j \in \{x, y, z\}$. Equation 13 can therefore be simplified for $\gamma(-3\omega; \omega, \omega, \omega)$ and $\gamma(-2\omega; \omega, \omega, \omega, 0)$:

$$\begin{aligned} \gamma(-3\omega; \omega, \omega, \omega) = & \left(\frac{1}{5}\right)[\gamma_{xxxx} + \gamma_{yyyy} + \gamma_{zzzz} + \gamma_{xxyy} \\ & + \gamma_{yyxx} + \gamma_{xxzz} + \gamma_{zzxx} + \gamma_{yyzz} + \gamma_{zzyy}] \quad (14a) \end{aligned}$$

$$\begin{aligned} \gamma(-2\omega; \omega, \omega, 0) = & \left(\frac{1}{5}\right)[\gamma_{xxxx} + \gamma_{yyyy} + \gamma_{zzzz}] \\ & + \left(\frac{1}{15}\right)[2\gamma_{xxyy} + \gamma_{xyyx} + 2\gamma_{yyxx} + \gamma_{yxxy}] \\ & + \left(\frac{1}{15}\right)[2\gamma_{xxzz} + \gamma_{xzzx} + 2\gamma_{zzxx} + \gamma_{zxxx}] \\ & + \left(\frac{1}{15}\right)[2\gamma_{yyzz} + \gamma_{yzyz} + 2\gamma_{zzyy} + \gamma_{zyyz}] \quad (14b) \end{aligned}$$

Further condensation of equation 14 is possible for the static or direct current (dc) expression of γ $[\gamma(0; 0, 0, 0)]$ because of Kleinman's symmetry rule (72), where $\gamma_{ijij} = \gamma_{jjii} = \gamma_{ijji} = \gamma_{jiij}$ ($i \neq j \in \{x, y, z\}$). The incorporation of these equalities into equation 14 yields the familiar equation (73):

$$\gamma_{DC} = \left(\frac{1}{5}\right)[\gamma_{xxxx} + \gamma_{yyyy} + \gamma_{zzzz} + 2\gamma_{xxyy} + 2\gamma_{xxzz} + 2\gamma_{yyzz}] \quad (15)$$

In the case of the planar molecules emphasized in this chapter, the x molecular axis is along the chain backbone, y is in the molecular plane, and z is perpendicular to this plane. The dominant polarizabilities for these molecules are those defined by virtual electronic transitions within the molecular plane: γ_{xxxx} , γ_{yyxx} , γ_{xxyy} , γ_{yxyx} , and γ_{yyyy} . We assume that

the other polarizabilities involving virtual electronic transitions perpendicular to the molecular plane are very small and can be neglected in the calculation of γ . In the case of π -electron transitions in planar molecules, the third-order polarizabilities with out-of-plane components are exactly zero.

The important second- and third-order nonlinear polarization responses are tabulated in Table I, along with the expressions of $\chi^{(2)}$, β , $\chi^{(3)}$, and γ that represent these responses, and the nonlinear polarization-response frequency of interest. More background on the linear and nonlinear electric polarization of materials and the linear and nonlinear polarizabilities of molecules can be found in the seminal works of Böttcher (74), Bloembergen (1), Ward (75), and Buckingham and Orr (73).

Maximization of the Third-Order Polarization Response

As shown in equation 8, the macroscopic electric polarization of a nonconducting, nonmagnetic material by an external applied electric field is defined by the electric susceptibility tensors characteristic of the material. In the case of a nonconducting, nonmagnetic material composed of isolated molecular units, the preceding section showed that the third-order electric susceptibility can be expressed as

$$\chi^{(3)}(-\omega_{\text{pol}}; \omega_1, \omega_2, \omega_3) = N \cdot \langle \gamma(-\omega_{\text{pol}}; \omega_1, \omega_2, \omega_3) \rangle \cdot L_3(\omega_{\text{pol}}, \omega_1, \omega_2, \omega_3) \quad (16)$$

Table I. Important Second- and Third-Order Nonlinear Optical Responses

<i>Response Description</i>	<i>Macroscopic Susceptibility</i>	<i>Molecular Polarizability</i>	<i>Polarization Frequency</i>
Linear electrooptic, or Pockels effect	$\chi^{(2)}(-\omega; \omega, \Omega)^a$	$\beta(-\omega; \omega, \Omega)^a$	ω
Second-harmonic generation (SHG)	$\chi^{(2)}(-\omega; \omega, \omega)$	$\beta(-2\omega; \omega, \omega)$	2ω
Intensity-dependent refractive index, or Optical Kerr effect	$\chi^{(3)}(-\omega; \omega, -\omega, \omega)$	$\gamma(-\omega; \omega, -\omega, \omega)$	ω
Third-harmonic generation	$\chi^{(3)}(-3\omega; \omega, \omega, \omega)$	$\gamma(-3\omega; \omega, \omega, \omega)$	3ω
DC-electric field-induced SHG	$\chi^{(3)}(-2\omega; \omega, \omega, 0)$	$\gamma(-2\omega; \omega, \omega, 0)$	2ω
DC second hyperpolarization	$\chi^{(3)}(0; 0, 0, 0)$	$\gamma(0; 0, 0, 0)$	0

^a The frequency, Ω , can be zero or much less than the optical frequency ω (e.g., Ω is in the microwave range).

where $\omega_{\text{pol}} = \omega_1 + \omega_2 + \omega_3$ is the angular frequency of the polarization field; ω_1 , ω_2 , and ω_3 are the angular frequencies of the applied electric fields; N is the number density of molecular units; $L_3(\omega_{\text{pol}}, \omega_1, \omega_2, \omega_3)$ is the local-electric-field factor as a function of the angular frequencies of the polarization and applied electric fields; and $\langle \gamma(-\omega_{\text{pol}}; \omega_1, \omega_2, \omega_3) \rangle$ is an averaged third-order polarizability for the molecular unit. As revealed in the section, "Materials Requirements for Optical Signal Processing," an important objective is to increase the magnitude of $\chi^{(3)}(-\omega; \omega, -\omega, \omega)$ without increasing the linear and nonlinear absorptivities, $\alpha(\omega)$, and the third-order polarization-response time, τ . In this section, issues concerning the maximization of $\chi^{(3)}(-\omega_{\text{pol}}; \omega_1, \omega_2, \omega_3)$ are outlined, with emphasis placed on the influence of molecular structure on the molecular third-order polarizability, $\gamma(-\omega_{\text{pol}}; \omega_1, \omega_2, \omega_3)$.

The maximization of $\chi^{(3)}(-\omega_{\text{pol}}; \omega_1, \omega_2, \omega_3)$ can be divided into two parts: a component external to the molecular units and a component internal to the unit. The external component is taken to be the product, $N \cdot L_3(\omega_{\text{pol}}, \omega_1, \omega_2, \omega_3)$, and the orientational averaging of $\gamma(-\omega_{\text{pol}}; \omega_1, \omega_2, \omega_3)$. The most straightforward way to increase $\chi^{(3)}(-\omega_{\text{pol}}; \omega_1, \omega_2, \omega_3)$ is to increase N . The packing of the molecular units in a crystal is the most efficient approach to maximize N . The problem with crystal packing is that it is not easy to control the orientation of the molecular units. It is well-known that molecular orientation is critical to the second-order polarization response of materials, and it is also important to maximizing their third-order polarization response. For example, an ensemble of randomly oriented, linear π -electron conjugated molecules like the linear polyenes has an orientationally averaged $\gamma(-3\omega; \omega, \omega, \omega)$ equal to $\gamma_{xxxx}/5$ (see equation 14a), whereas the ensemble of molecules all oriented along their chain axes has $\gamma(-3\omega; \omega, \omega, \omega)$ equal to γ_{xxxx} . Epitaxial crystal layers, poled polymers, self-assembled structures, Langmuir-Blodgett films, ferroelectric liquid crystals, as well as single crystals, are all structures that can be employed to orient molecular units. More details on the synthesis of ordered structures for NLO materials is covered in Chapter 8 in this book.

The linear optical and NLO properties of molecular units in the condensed phase, as well as their electronic structures and nuclear geometries, can be altered externally by the dielectric nature of their environment defined by the local-electric-field factor (e.g., solvent polarity), the type and concentration of dissolved ions, and pH. In the case of linear optical properties, the λ_{max} for linear merocyanines shifts dramatically to greater values with increasing solvent polarity (76, 77). The origin of this effect lies with the greater contribution of the highly polar π -electronic structure, ${}^+ \text{H}_2\text{N}=\text{CH}-(\text{CH}=\text{CH})_n-\text{O}^-$, to the ground electronic state relative to that of the less-polar π -electronic structure, $\text{H}_2\text{N}-\text{CH}=(\text{CH}-\text{CH})_n=\text{O}$, in polar solvents (76, 77). It is expected that the

NLO properties for the merocyanines can also be tuned by varying the polarity of the solvent (78). Second-harmonic β s, $\beta(-2\omega; \omega, \omega)$, measured at $\omega = 1.06 \mu\text{m}$, for a hemicyanine and a nitrostilbene have been shown to be strongly influenced by the pH of the solvent (79). In summary, experimental studies of the linear optical and NLO properties of a variety of π -electron chromophores strongly suggest that these properties in the condensed phase can be finely tuned in a controlled manner by varying the dielectric nature of their environment. External dielectric tuning can then be considered to be an additional synthetic tool in the effort to maximize $|\gamma(-\omega_{\text{pol}}; \omega_1, \omega_2, \omega_3)|$ for these molecules. The dielectric tuning of the third-order NLO properties of a cyanine cation is analyzed in greater detail in a subsequent section.

The internal component of $\chi^{(3)}(-\omega_{\text{pol}}; \omega_1, \omega_2, \omega_3)$ is $\gamma(-\omega_{\text{pol}}; \omega_1, \omega_2, \omega_3)$. This component is influenced by both electronic and nuclear structural features of the molecular unit: the chemical nature of the bonding network, the dimensionality of the network, the size of the network, the positioning of electron donor and acceptor substituents, the charge and spin of the molecular unit, and the nuclear geometry of the unit. The type of chemical bonding network refers, for example, to the distinction between the more localized electron density in σ -bonds and the more delocalized electron density in π -bonds. The conjugated π -electron bonding networks have generally been shown experimentally and theoretically to be more hyperpolarizable than the σ -electron bonding networks (80), and as a consequence, the rest of the discussion in this chapter focuses solely on conjugated π -electron bonding networks. It is stressed that not all conjugated π -electron bonding networks are alike. For a given number of π -electrons and size of the molecule, the following π -bonding networks can be ranked in descending order of hyperpolarizability: the polymethine network typical of the cyanine dyes > the polyene network > aromatic network. This ranking is explored in greater detail in following sections.

Although this chapter places a great deal of emphasis on π -electron bonding networks, it should be noted that there are σ -electron bonding networks with comparable linear and nonlinear polarizabilities. Namely, the theoretical Hartree–Fock linear polarizability of polysilane (per SiH_2 unit) exceeds that of polydiacetylene (per CH unit) and is on a par with that of polyacetylene (per CH unit) (23). The γ_{xxxx} for polysilane is less than those for polydiacetylene and polyacetylene, but not by orders of magnitude (23).

The dimensionality of the bonding network concerns the distinction between the quasi-one-dimensional π -bonding networks of linear polyenes and polymethines, the two-dimensional networks of planar aromatic molecules, and the quasi-three-dimensional π -bonding networks of the fullerenes. The quasi-one-dimensional networks tend to have the largest

third-order nonlinear optical response for linearly polarized radiation fields (e.g., polyacetylene and polydiacetylene), because the polarization of the molecular unit is constrained along a single axis. The size of the network plays a very important role in determining the magnitude of the third-order response because the physical size of the molecular unit helps to define its linear and nonlinear polarizabilities. Most efforts aimed at maximizing the third-order NLO response have traditionally placed more emphasis on the size of the network, than on the chemical nature of the network and its dimensionality.

The placement of π -electron donor and acceptor substituents at positions along a π -electron bonding network has been used extensively in the maximization of the second-order NLO response of molecules, because of the importance of a donor \rightarrow acceptor charge-transfer (CT) state to this response for linear π -bonding networks. The introduction of π -electron donor and acceptor substituents can be seen as modifying the electric field internal to the molecule. A combination of a strong π -electron donor and acceptor can result in an internal electric field that localizes π -electron density to such an extent that the polarizability of the π -electron bonding network is actually decreased. The interrelationship between donor and acceptor groups and the polarizability of the π -electron bonding network that bridges the two groups is discussed in more detail in Chapter 8 in this book, and in the last section of this chapter.

The charge and spin of the molecular unit influences the third-order NLO response. This influence is exploited in the efforts to synthesize π -electron conducting polymers through their reduction–oxidation and/or protonation–deprotonation. A disadvantage with conducting polymers is that their linear absorptivities are generally high at light wavelengths important to devices.

In the case of conjugated π -electron molecular units, a very important aspect of the nuclear geometry is the planarity of the unit. The introduction of nonplanarity in the network disrupts the delocalization of the π -electron density, with consequent loss in polarizability. It is very desirable to maintain the planarity of the network when seeking to maximize the third-order NLO response for a given unit.

The previous discussion of the electronic features and nuclear structural features of the molecular unit that determine its third-order polarization (NLO) response has assumed that the molecular units are weakly coupled and display no collective or cooperative effects. In the case of the off-resonant response, this assumption appears to be valid (81). However, for resonant NLO phenomena such as two-photon absorption, the assumption of weak coupling is less valid as transition dipole–transition dipole interactions associated with the resonant electronic transition become more important (81). Because the off-res-

onant NLO response is most relevant to device applications, the issue of cooperativity between weakly coupled molecular units will not be discussed in the remainder of this chapter. Of course, in the case of π -electron conjugated polymers with strongly coupled monomer units, cooperative effects are very important. For example, there is the postulated role of soliton–antisoliton configurations in the third-order NLO response of polyacetylene (82). The π -electron–phonon coupling fundamental to these configurations is predicted to substantially increase the magnitude of the third-order NLO response of polyacetylene. Vibrational enhancement of the third-order NLO response for conjugated π -electron molecular systems is also discussed in references 23 and 25.

Although the macroscopic third-order electric susceptibility of a material defines its third-order polarization response, the role of the applied external electric fields and how they can be employed to achieve a particular response must not be forgotten. The frequencies, electric-field strengths, the length of time that the fields are applied, and the polarizations of the applied fields can all be varied. The adjustment of the frequencies is important to tuning the applied fields into or out of resonance with molecular transitions in the material. Tuning into resonance can greatly enhance the third-order polarization response, but it is usually at the expense of introducing photothermal effects and slowing the response time. This tuning is to be avoided as a rule. The electric-field strengths, or radiation intensities, can be increased to compensate for low values of $|\chi^{(3)}(-\omega_{\text{pol}}; \omega_1, \omega_2, \omega_3)|$. This option is limited by the optical damage threshold of the material and the field strength for dielectric breakdown. The optical damage threshold is dependent on the length of time that the fields are applied, or the radiation pulse width. Generally, the shorter the pulse width, the higher the damage threshold and the lower the chance of photothermal effects becoming a concern. The polarization of the applied fields is relevant in the case of materials composed of ordered-molecular units. Finally, new advances being made in the design of ordered-material structures (photonic bandgap materials) for the localization of electromagnetic fields within these structures suggest strategies for increasing the electric fields local to molecular units with significant third-order polarizabilities (83).

Relation between Third-Order Molecular Polarizability, Molecular Geometry, and Molecular Electronic Structure

The preceding section outlined a number of different approaches to maximize the third-order macroscopic polarization of a material. This maximization was seen as consisting of two parts: a component external to the molecular units that comprise the material and a component internal to the molecular unit. The internal component of interest is de-

defined by the third-order molecular polarizability, $\gamma(-\omega_{\text{pol}}; \omega_1, \omega_2, \omega_3)$. The SOS mathematical expression for $\gamma(-\omega_{\text{pol}}; \omega_1, \omega_2, \omega_3)$ is presented in this section and is discussed in terms of the nuclear and electronic structure of the molecular unit. Experimental and theoretical determinations of the geometry of the unit are examined here, as well as quantum chemical calculations of the molecular electronic structure. The importance of treating the effect of the local environment of the molecule in the condensed phase on its nuclear and electronic structure is emphasized.

Third-Order Molecular Polarizability. Three nonresonant, electronic components of the molecular third-order polarizability are of particular interest when comparing calculation and experiment to establish structure–property relationships for the design of molecular systems: static or DC polarizability [$\gamma(0; 0, 0, 0)$], third-harmonic-generation polarizability [$\gamma(-3\omega; \omega, \omega, \omega)$], and DC electric-field-induced second-harmonic-generation polarizability [$\gamma(-2\omega; \omega, \omega, 0)$]. Because only the electrons in a molecule can respond fast enough at the optical frequencies used to measure the third-harmonic-generation polarizability, this polarizability is considered to be completely defined by the electronic component. The nonresonant, electronic component of the molecular third-order polarizability of greatest technological relevance is the intensity-dependent refractive index polarizability [$\gamma(-\omega; \omega, -\omega, \omega)$]. Fortunately, it is not necessary to explicitly calculate all nonresonant, electronic components of γ . Shelton has shown that the dispersion of $\gamma(-\omega_{\text{pol}}; \omega_1, \omega_2, \omega_3)$ at radiation frequencies far off-resonance is accurately represented by a power series in $\omega_L^2 = \omega_{\text{pol}}^2 + \omega_1^2 + \omega_2^2 + \omega_3^2$ (43):

$$\gamma = \gamma_0[1 + A(\omega_L/\Omega)^2 + B(\omega_L/\Omega)^4 + \dots] \quad (17)$$

where γ_0 is $\gamma(0; 0, 0, 0)$, and the value of the frequency dispersion parameter, Ω , is the same for all third-order processes.

We choose to partition the nonresonant γ into a σ -electron component (γ_σ) and a π -electron component (γ_π), so that

$$\gamma \cong \gamma_\sigma + \gamma_\pi \quad (18)$$

This separation is motivated by several reasons: (1) the molecules of interest usually have planar geometries, (2) restricted- π -electron molecular orbital procedures like the Pariser–Parr–Pople method described in Salem’s book (84) have been successful in the calculation of the energies (85) and one- and two-photon absorptivities (86) of excited π -electron states, and second-order NLO properties of π -electron conjugated molecules (87, 88); (3) the π -electrons are expected to dominate the polarization response of these molecules as they increase in

chain length; and (4) measurements of γ for π -electron conjugated molecules have been successfully interpreted in terms of γ_σ and γ_π components (68, 89). It is noted that the approximation of γ given in equation 18 neglects the explicit interaction between π - and σ -electrons, (i.e., no $1_{\sigma\pi}^* \pi^*$ doubly excited configurations were included in the calculation of γ_π).

The Nonresonant γ_σ Component. The nonresonant γ_σ s for unsaturated molecules can be estimated by using the bond-additivity approximation (73) and measured nonresonant values of $\gamma \equiv \langle \gamma \rangle_{zzzz}$ for comparable, saturated molecules (68). In the case of hydrocarbons, the values of γ measured for alkanes are defined completely by σ -electrons, and so these γ s can be used to determine γ_σ s for π -electron conjugated hydrocarbons like the linear polyenes. The bond-additivity approximation makes it possible to express the isotropic γ for an alkane (C_nH_{2n+2}) in terms of third-order polarizabilities for $C_\sigma-C_\sigma$ and $C_\sigma-H_\sigma$ bonds:

$$\gamma = (n - 1)\gamma(C_\sigma-C_\sigma) + (2n + 2)\gamma(C_\sigma-H_\sigma) \quad (19)$$

Levine and Bethea's fit of this equation (68) to values of the nonresonant, electronic component of γ measured for the alkanes, yielded $\gamma(C_\sigma-H_\sigma) \cong +0.12 \times 10^{-36}$ esu and $\gamma(C_\sigma-C_\sigma) \cong +0.11 \times 10^{-36}$ esu. Thus, as an example, the γ_σ estimated for all-*trans*-butadiene with 3 $C_\sigma-C_\sigma$ bonds and 6 $C_\sigma-H_\sigma$ bonds is $\gamma_\sigma \cong 3\gamma(C_\sigma-C_\sigma) + 6\gamma(C_\sigma-H_\sigma) \cong +1.05 \times 10^{-36}$ esu.

The $\gamma_\sigma(0; 0, 0, 0)$, $\gamma_\sigma(-3\omega; \omega, \omega, \omega)$, and $\gamma_\sigma(-2\omega; \omega, \omega, 0)$ are defined to be equivalent in the zero photon frequency limit, as are $\gamma_\pi(0; 0, 0, 0)$, $\gamma_\pi(-3\omega; \omega, \omega, \omega)$, and $\gamma_\pi(-2\omega; \omega, \omega, 0)$ (see the next section). It is assumed that for the π -electron conjugated molecules of interest, we are near the zero photon frequency limit for $\gamma_\sigma(0; 0, 0, 0)$, $\gamma_\sigma(-3\omega; \omega, \omega, \omega)$, and $\gamma_\sigma(-2\omega; \omega, \omega, 0)$ (i.e., the polarization response frequencies and the photon frequencies are far from resonance with σ -electron excited states). The reason is that the π -electron excited states of these molecules are lower in energy than the σ -electron excited states, and so the photon frequencies selected to calculate nonresonant γ_π s will be even more appropriate for nonresonant γ_σ s.

The Nonresonant γ_π Component. The nonresonant $\gamma_\pi(0; 0, 0, 0)$ s, $\gamma_\pi(-3\omega; \omega, \omega, \omega)$ s, and $\gamma_\pi(-2\omega; \omega, \omega, 0)$ s can be calculated using the SOS expression derived by Orr and Ward (90). This expression is particularly useful because it allows the interpretation of γ in terms of three measurable, electronic spectroscopic properties: (1) the transition energies between the ground state and excited states, (2) one-photon transition dipole moments between the ground state and excited states and between excited states, and (3) permanent dipole moments of the ground

and excited states. The expression also calculates both static and dynamic polarizabilities. The major disadvantage with the SOS expression is the summation over an infinite number of excited electronic states. Fortunately, for most molecules of interest, there is a finite number of electronic excited states that dominate the γ_π response (see section A Theoretical Analysis of Linear Cyanines and Polyenes).

The SOS expression for the nonresonant π -electronic component of γ_{abcd} is derived using time-dependent perturbation theory and assuming electric dipole coupling (the molecular dimensions are much less than the radiation wavelength) between the radiation field and the molecule. The zeroth-order Born–Oppenheimer approximation was also employed to separate the electronic and nuclear components of γ . The expression for γ_{abcd} is as follows (90):

$$\gamma_{abcd}(-\omega_{\text{pol}}; \omega_1, \omega_2, \omega_3) = +(2\pi/\hbar)^3 \cdot K(-\omega_{\text{pol}}; \omega_1, \omega_2, \omega_3) \cdot e^4$$

$$\times \frac{\left\{ \sum_P \left[\sum_{i,j,k(\neq 0)} \langle o|r_a|k \rangle \langle k|r_b|j \rangle \langle j|r_c|i \rangle \langle i|r_d|o \rangle \right] \right\}}{(\omega_{ko} - \omega_{\text{pol}})(\omega_{jo} - \omega_1 - \omega_2)(\omega_{io} - \omega_1)}$$

$$- \frac{\sum_P \left[\sum_{j,k(\neq 0)} \langle o|r_a|j \rangle \langle j|r_b|o \rangle \langle o|r_c|k \rangle \langle k|r_d|o \rangle \right]}{(\omega_{jo} - \omega_{\text{pol}})(\omega_{ko} - \omega_1 + \omega_2)} \quad (20)$$

where $\omega_{\text{pol}} = \omega_1 + \omega_2 + \omega_3$ is the polarization response angular frequency; ω_1 , ω_2 , and ω_3 are the angular frequencies of the applied radiation fields; $K(-\omega_{\text{pol}}; \omega_1, \omega_2, \omega_3)$ is a numeric coefficient that makes $\gamma_{abcd}(-\omega_{\text{pol}}; \omega_1, \omega_2, \omega_3)$ equal to $\gamma_{abcd}(0; 0, 0, 0)$ in the zero-frequency limit [$K(0; 0, 0, 0) = 1$, $K(-3\omega; \omega, \omega, \omega) = K(-2\omega; \omega, \omega, 0) = 1/8$]; e is the electron charge; \sum_P indicates summation of the terms obtained by permuting the couplings of the polarization field and the three applied fields with the molecule, that is, permuting the frequencies ω_{pol} , ω_1 , ω_2 , and ω_3 in the denominator of equation 20 and the associated subscripts of r_a in the numerator ($\gamma_{abcd}(-3\omega; \omega, \omega, \omega)$ and $\gamma_{abcd}(-2\omega; \omega, \omega, 0)$ each have 48 terms, and $\gamma_{abcd}(0; 0, 0, 0)$ has 6 terms); i, j , and k are excited π -electronic states, and o is the ground state; r_a is related to the a ($a = x, y, \text{ or } z$) component of the transition length operator and is given by $r_a = r_a - \langle o|r_a|o \rangle$; ω_{io} is the transition frequency between the i and o states. An important difference between equation 20 and equation 43c in reference 90 is that equation 43c averages all terms generated by permuting ω_1 , ω_2 , and ω_3 , while this averaging is not performed in equation 20. Complete expressions of $\gamma_{abcd}(-3\omega; \omega, \omega, \omega)$ and $\gamma_{abcd}(-2\omega; \omega, \omega, 0)$ with all the permutation terms are given in reference 90.

The sign in front of $(2\pi/h)^3$ in equation 20 is positive. This is in contrast to the negative sign in front of the expression for $P^{\omega\sigma}$ in equation 43c of reference 90. The difference between the two equations arises from the fact that in equation 20, we replaced the P and H operators in equation 43c of reference 90 by the operators for the dipole moment and the electrostatic energy of a dipole in a uniform electric field: $e\mathbf{r}$ and $-\mathbf{E}(t) \cdot e\mathbf{r}$, respectively, where e is the electron charge (-4.80298×10^{-10} esu), $\mathbf{E}(t)$ is the time-dependent electric-field vector, and \mathbf{r} is the electron position operator. The convention used to define the electric field is the electric dipole component of the summation:

$$\mathbf{E}(\mathbf{r}, t) = \text{Re} \sum_{\omega, \mathbf{k}} \{ \mathbf{E}(\omega, \mathbf{k}) \exp[i(\omega t - \mathbf{k} \cdot \mathbf{r})] + \text{c.c.} \} / 2 \quad (21a)$$

where \mathbf{k} is the wave vector for the field with angular frequency ω , and c.c. is the complex conjugate of $\mathbf{E}(\omega, \mathbf{k}) \exp[i(\omega t - \mathbf{k} \cdot \mathbf{r})]$. In the case of a given ω and \mathbf{k} ,

$$\mathbf{E}(t) = |\mathbf{E}(\omega, \mathbf{k})| \{ \exp[i\omega t] + \exp[-i\omega t] \} / 2 \quad (21b)$$

In the case of the linear π -electron conjugated molecules discussed in this chapter, γ_π is calculated to converge very quickly with respect to the number of excited π -electron singlet states. Convergence for these molecules was always achieved after summing over at least the 10 lowest energy π -electron excited singlet states. In the case of molecules where convergence is not rapidly achieved, then the SOS method is of considerably less utility, and other methods should be employed to calculate the nonlinear polarizabilities.

Approximations to the complete SOS expression for γ_π that provide chemical insight into the origin of γ_π for a molecular unit can be derived. For molecules with quasilinear or quasi-one-dimensional π -electron bonding networks, the $\gamma_\pi(-\omega_{\text{pol}}; \omega_1, \omega_2, \omega_3)$ tensor is dominated by the single component, γ_{xxxx} , where x is the molecule-fixed axis coincident with the bonding network. Thus, $\gamma_\pi \cong \gamma_{xxxx}/5$ in the case of isotropic orientational averaging (*see eq 13*). This approximation is discussed in greater detail in the following section, where calculations of γ_π for linear polyenes and cyanines are presented and analyzed. Additional analyses concerning approximations to the SOS expression for γ are given in papers by Dirk and Kuzyk (28–30), Garito and co-workers (33, 34), and Pierce (80, 91).

The SOS perturbation method is certainly not the only one available to calculate the nonresonant γ_π in particular, and the nonresonant γ in general. Three other popular approaches are the finite field difference method (92–94), the coupled Hartree–Fock method (36, 95, 96), and the time-dependent Hartree–Fock (TDHF) method (38, 39, 97, 98).

The finite field and coupled Hartree–Fock methods cited here calculate linear and nonlinear molecular polarizabilities by computing derivatives of the molecular electronic energy–TDHF dipole moment of the ground state with respect to static electric fields. The finite field method calculates these derivatives numerically, while the coupled Hartree–Fock method does it analytically. In the case of the Taylor series expansion for the molecular dipole moment, the first derivative is related to the first-order induced dipole moment, or the linear polarizability α ; the second derivative is related to the second-order induced dipole moment, or the second-order nonlinear polarizability β ; and the third derivative is related to the third-order induced dipole moment, or the third-order nonlinear polarizability γ . The static field derivative methods are restricted to calculating the static polarizabilities, whereas the SOS method calculates both static and dynamic polarizabilities. This is not to say that field derivative methods are strictly limited to the calculation of static polarizabilities (*see* reference 99). The field derivative methods are useful in calculating values of the various polarizability tensor elements, but limited in providing insight into the chemical origin of these tensor elements (e.g., relating the tensor elements to such molecular electronic properties as transition energies, transition dipole moments, and permanent dipole moments). As stated previously, the SOS method is very helpful in providing this insight.

The TDHF method is a more general formulation of the coupled Hartree–Fock method that solves the wave function of the ground electronic state in the presence of an oscillating electric field, and thus is a variational method for the calculation of both static and dynamic linear and nonlinear polarizabilities. This approach is in contrast to the SOS perturbation method, where the wave function of the ground electronic state is first solved in the absence of the oscillating electric field, and then this field is introduced as a perturbation to mix the ground electronic state with other excited electronic states via the electric dipole operator. Although the TDHF method yields dynamic linear and nonlinear polarizabilities like the SOS method, it is similar to the field derivative methods in being limited in providing insight into the chemical origin of the various polarizability tensor elements. As a rule, it is easier to incorporate the treatment of electron correlation into the SOS and field derivative methods than the TDHF method. However, the time-dependent multiconfiguration Hartree–Fock method does offer a way to treat electron correlation in the context of the TDHF approach (100, 101). The SOS perturbation method is also more adept than either the TDHF or field derivative methods at handling the effect of vibrationally induced distortions of the molecular geometry (vibronic coupling effects) on the static and dynamic linear and nonlinear polarizabilities. However, vibrational distortion is best treated by the new perturbation method

presented by Bishop and Kirtman (102). In spite of its requirement to sum over a formally infinite number of states, the SOS method has much to offer in terms of both calculating and analyzing linear and nonlinear polarizabilities.

The SOS, static field derivative, and TDHF methods described in the preceding paragraph are useful in calculating γ explicitly in terms of the molecular electronic structure. A very simple physical model of the linear and nonlinear electronic polarization of a molecule is to view the bound electrons in the molecule as anharmonic oscillators (1). The resonant frequencies of these oscillators correspond to electronic transition frequencies. The application of an external oscillating field induces the electrons to oscillate about their equilibrium positions. At low electric-field strengths, this motion is harmonic and gives rise to the linear polarization response. The nonlinear polarization response becomes significant at high electric-field strengths, where the anharmonicity of the electron oscillators must be taken into account. Thus, the linear and nonlinear polarization response of a material consisting of an assembly of molecular units can be reduced to solving the equations of motion for coupled-anharmonic oscillators driven by an electric field. The oscillators corresponding to the monomer units in a conjugated π -electron polymer like polyacetylene are considered very strongly coupled, while the oscillators corresponding to hydrogen-bonded molecules in a molecular crystal are more weakly coupled. This coupling is also influenced by the oscillation frequency of the external electric field; a resonant frequency promotes stronger coupling, and an off-resonant frequency results in weaker coupling.

Two examples of recent theoretical analyses of the NLO properties of molecular materials in terms of the anharmonic-oscillator model are the investigations by Beratan (103) and by Spano and Mukamel (81). The anharmonic-oscillator model may be well-suited for mathematical and physical analysis, but it is presently very limited in providing chemical insight into the origin of the nonlinear polarization response. For example, how does the degree of anharmonicity for an oscillator translate into a molecular structure that optimizes the second- and third-order polarizabilities? The value of the anharmonic-oscillator model could be greatly increased if questions like this one were addressed.

The Resonant γ_{π} Component. The expression for $\gamma_{abcd}(-\omega_{\text{pol}}; \omega_1, \omega_2, \omega_3)$ in equation 20 is applicable only in the case where the frequencies of the applied radiation fields ($\omega_1, \omega_2, \omega_3$) and the frequency of the polarization field (ω_{pol}) are far from being in resonance with transition frequencies between the ground state and the excited electronic state (ω_{io}) (i.e., the denominators in the two parts of equation 21 never approach zero). As shown in equation 43c of reference 90, the calculation

of γ with one, or combinations, of the four radiation fields in resonance with electronic transition frequencies can be performed by adding damping terms to the frequency differences in the denominators in equation 20. These damping terms are complex variables that are proportional to the frequency bandwidth of the n -photon transition to the given electronic state, or equivalently, inversely proportional to the lifetime of this state accessed by the n -photon transition (86, 104). The values selected for these damping terms are generally taken from measurements of the one- and two-photon electronic spectra of the molecular system of interest. The use of equation 20 plus damping terms to calculate the real and imaginary components of the resonant γ -response is applicable only in the case where the populations of the excited electronic states are insignificant with respect to the ground state.

Analogous to the correspondence between one-photon absorption and the resonant, imaginary component of the linear-dynamic polarizability, two-photon absorption via a virtual intermediate state is related to the resonant, imaginary component of the third-order dynamic polarizability for the intensity-dependent refractive index, $\gamma(-\omega; \omega, -\omega, \omega)$. In other words, two-photon absorption via a virtual intermediate state defines an intensity-dependent absorption coefficient. The calculation of molecular two-photon absorptivities can be performed by using an SOS perturbation method and is discussed in detail in references 86 and 105.

Molecular Geometry. The determination of the correct molecular geometry in the ground electronic state is fundamental to calculating an accurate ground state electronic wavefunction, and hence accurate electronic components of the off-resonant linear and nonlinear polarizabilities. The ground-state molecular geometry is most pertinent to the off-resonant polarizabilities because the molecular geometry can be considered to be frozen during the very short off-resonant electronic polarization response times of 10^{-15} – 10^{-14} s (Born–Oppenheimer approximation). Significant differences can exist between the ground-state equilibrium geometries for molecules in the gas phase and the ground-state equilibrium geometries in the condensed phase. For example, the ground-state equilibrium geometry of a conjugated π -electron polyene chain may be linear and planar in the gas phase, but twisted when mixed with an amorphous polymer. Another example is the ground-state equilibrium geometry of the linear merocyanine molecule, $\text{H}_2\text{N}-\text{CH}=(\text{CH}-\text{CH})_n=\text{O}$. The less polar $\text{H}_2\text{N}-\text{CH}=(\text{CH}-\text{CH})_n=\text{O}$ geometry is favored in the gas phase and in nonpolar solvents, whereas the more polar $^+\text{H}_2\text{N}=\text{CH}-(\text{CH}=\text{CH})_n-\text{O}^-$ geometry is dominant in highly polar solvents (76, 77). A hybrid of the two geometries with very little bond length alternation is possible in a solvent of medium polarity (76, 77).

The linear optical and NLO properties associated with the different ground state, condensed-phase geometries of the above π -electron chromophores can vary greatly. Because the condensed phase is most relevant to device applications, calculations of linear and nonlinear polarizabilities must start with the appropriate ground-state molecular geometry for the given condensed-phase environment.

In the case of single-crystalline molecular materials, the ground-state equilibrium geometries of the molecular units can be experimentally determined with X-ray diffraction. Small- and large-angle X-ray scattering, NMR spectroscopy, vibrational spectroscopy, and electronic spectroscopy can all be used to help determine ground-state molecular geometries in amorphous molecular materials. However, these geometries are less definitive than those obtained for single crystals. A number of theoretical approaches have been developed that can be very helpful in the determination of ground-state molecular geometries in both crystalline and amorphous condensed phases, (e.g., atomistic force field methods used in combination with molecular dynamics procedures) (106–110). One convenient theoretical approach to obtaining an idea of the ground-state molecular geometry for a given condensed-phase environment is to perform a quantum chemical calculation of the optimized ground-state molecular geometry for a given condensed-phase environment is to perform a quantum chemical calculation of the optimized ground-state geometry in the presence of charges and dipoles that simulate the electric field of the local environment of the molecule. As an example, the semiempirical, quantum chemical MOPAC software package has a SPARKLES option that makes it possible to perform a ground-state geometry optimization with the molecule surrounded by a distribution of charges and dipoles (111). When employing semiempirical molecular orbital Hamiltonians for ground-state geometry optimization, Hamiltonians parameterized for the treatment of ground-state properties are preferred (e.g., the modified intermediate neglect of differential overlap (MINDO) Hamiltonian instead of the intermediate neglect of differential overlap (INDO/S) Hamiltonian).

Although ground-state molecular geometries are most pertinent for the off-resonant polarizabilities, excited electronic-state equilibrium geometries are also relevant when calculating resonant polarizabilities. Furthermore, both ground- and excited-equilibrium geometries are important when calculating the Franck–Condon factors that define the frequency bandwidths of the one- and two-photon absorption bands of the molecule. These bands are important because they help establish the spectral regions where the molecular material is transparent and therefore suitable for device operation. Finally, the vibrational normal modes of the ground-state equilibrium geometry are needed when calculating the effect of vibrationally induced distortions of the geometry

(vibronic coupling effects) on the static and dynamic linear and nonlinear polarizabilities. The harmonic vibrational normal modes are easy to calculate once the equilibrium geometry and the attendant force-constant matrix (energy second-derivative matrix) have been computed (112).

Molecular Electronic Structure. The molecular electronic structure calculations for ground-state molecular geometries in condensed-phase environments provide the transition energies, transition dipole moments, and permanent dipole moments needed to evaluate the SOS expression for the off-resonant γ_π . Given the large number of theoretical methods that calculate molecular electronic properties, how does one select the method that is best at calculating the properties needed to evaluate the SOS expression for the off-resonant γ_π ? Because these properties are electronic spectroscopic ones, theoretical methods that calculate the one- and two-photon spectroscopic properties of molecules are best suited to calculate nonlinear polarizabilities. In this manner one obtains a consistent treatment of the real (off-resonant) and imaginary (on-resonant) components of the given nonlinear polarizability, and hence electric susceptibility. The theoretical treatment of molecular electronic structure can be divided into two cases: (1) isolated molecules in the gas phase and (2) molecules in the condensed phase modified by their environments.

Molecules in the Gas Phase. A number of quantum chemical methods can be employed in the calculation of isolated molecules in the gas phase. These methods range from the comprehensive but computationally intensive *ab initio* methods (112) to the more tractable density functional and (113) semiempirical (114) methods. Because of computational tractability and success at calculating linear and nonlinear electronic spectroscopic properties of conjugated π -electron molecules, we emphasize here an all-valence-electron, semiempirical self-consistent field (SCF) molecular orbital (MO) procedure combined with at least single- and double-excitation configuration interaction (SDCI). The specific all-valence-electron, semiempirical SCF-MO procedure was an INDO Hamiltonian (114) parameterized to treat electronic spectroscopic properties (i.e., an INDO/S-type Hamiltonian). This formalism in combination with SDCI has been shown to provide a consistent treatment of nonlinear polarizabilities and one- and two-photon spectroscopic properties (80).

The INDO-SCF-MO-SDCI (INDO-SDCI) calculations employed in the theoretical treatment of the electronic structures of the linear polyenes and cyanine cations presented in the following section used the Ohno-Klopman electron repulsion integral (115). This selection was

made because in the treatment of one- and two-photon spectroscopic properties of conjugated π -electron conjugated hydrocarbons, the Ohno–Klopman repulsion integral is best used in combination with SDCI (80). Resonance integrals were calculated using the procedure of Del Bene and Jaffé (116) that distinguishes between σ - and π -electron “mobility.” The important parameters for treating the molecules of interest within this INDO/S formalism are as follows (117): (1) the resonance integral ($\beta_N = 26.0$ eV, $\beta_C = 17.5$ eV, $\beta_H = 12.0$ eV), (2) the average of the ionization potential and electron affinity for the s atomic orbital ($[(I_s + A_s)/2]_N = 20.359$ eV, $[(I_s + A_s)/2]_C = 14.962$ eV, $[(I_s + A_s)/2]_H = 7.171$ eV), (3) the average of the ionization potential and electron affinity for the p atomic orbital ($[(I_p + A_p)/2]_N = 8.114$ eV, $[(I_p + A_p)/2]_C = 5.806$ eV, $[(I_p + A_p)/2]_H = 0.0$ eV), (4) the one-center repulsion integral ($\gamma_{NN} = 11.308$ eV, $\gamma_{CC} = 10.333$ eV, $\gamma_{HH} = 12.848$ eV), and (5) the Slater exponents ($\xi_N = 1.95$, $\xi_C = 1.625$, $\xi_H = 1.2$). β_N and β_C were multiplied by 0.585 for all $2p_\pi$ orbital interactions (116). A minimal atomic orbital basis set was utilized ($1s$ on H, $2s$ and $2p$ on C and N, respectively).

The major advantages of working with an INDO/S-type Hamiltonian are that it (1) has been successful in calculating molecular dipole moments (114) and molecular one- and two-photon spectra (118), (2) can treat all valence electrons, not just the π -electrons, and (3) is computationally tractable, and therefore is applicable to large molecules.

Two sets of configurations defining transitions within the molecular plane can be generated by permuting electrons among the occupied and unoccupied σ - and π -MOs of the closed-shell ground state. One set consists of configurations generated by permuting only the π -electrons among the occupied and unoccupied π -MOs: $^1\pi\pi^*$ singly excited configurations and $^1\pi\pi\pi^*\pi^*$ doubly excited configurations. The second set consists of configurations generated by permuting the σ - and π -electrons among the occupied and unoccupied σ - and π -MOs: $^1\pi\pi^*$ and $^1\sigma\sigma^*$ singly excited configurations, and $^1\pi\pi\pi^*\pi^*$, $^1\sigma\sigma\sigma^*\sigma^*$, and $^1\sigma\pi\sigma^*\pi^*$ doubly excited configurations.

In the present study, we only used the π -electron configurations in our INDO–SDCI ($^1\pi\pi^*$ and $^1\pi\pi\pi^*\pi^*$) calculations of γ_π . The weighting coefficients for each of the configurations in a given state is determined by the diagonalization of the configuration interaction matrix. The eigenvalues of this matrix are the electronic state energies that define the transition energies or frequencies appearing in the SOS expression for γ_π in Equation 20. The eigenvectors of the configuration interaction matrix are the electronic states that define the transition dipole moments and permanent dipole moments appearing in the SOS expression for γ_π in Equation 20. The calculation of these dipole moments is described in reference 84.

Tavan and Schulten (85, 119, 120) have shown that it is not necessary to extend the treatment of electron–electron interactions beyond that of single- and double-excitation configuration interaction (e.g., including triply and quadruply excited π -electron configurations) for the energies of the $^1\pi\pi^*$ states in linear π -electron conjugated molecules shorter than eight atoms. However, for longer linear molecules, the neglect of higher order excitations in the configuration interaction calculation becomes more significant because an inconsistency in the number of singly and doubly excited configurations is generated, which results in an imbalance in the degree to which various electronic states are stabilized by single- and double-excitation configuration interaction (120, 121). This imbalance can be compensated somewhat by calculating the transition energies using the formula (122)

$$\Delta E_{i\leftarrow o} = E_i - (5/N)E_o \quad (22)$$

where E_i is the energy of excited state i , E_o is the ground electronic state energy, and N is the number of conjugated π -molecular orbitals. Equation 22 scales the ground-state energy to compensate for the imbalance in the degree to which the ground state and the $^1\pi\pi^*$ states are stabilized by single- and double-excitation interaction (122). An alternative approach to using equation 22 is to include a number of selected triply excited configurations in the configuration basis set (123).

Although errors in the calculation of γ_π are introduced by limiting the configuration interaction to singly and doubly excited configurations, these errors are relatively insignificant compared to the errors introduced when the calculation is restricted to just single-excitation configuration interaction (SCI). As discussed in detail in reference 80, the INDO–SCI calculations of γ_π for linear polyenes incorrectly yield negative signs for the isotropic γ_π and the wrong magnitudes. In contrast, the INDO–SDCI method correctly calculated positive signs for γ_π and magnitudes within 20% of measured gas-phase values. The INDO–SDCI-calculated values of nonresonant γ s for ethylene, linear polyenes, and benzene are compared with measured values in Table II (80).

Molecules in the Condensed Phase. As is the case for the molecular geometry, the theoretical treatment of molecular electronic structure in the condensed phase is basic to understanding the optical properties of molecular materials relevant to device applications. Steric, nonbonding, and bonding interactions exist in the condensed phase that influence the electronic structures and nuclear geometries of the π -electron molecules, which, in turn, modify their linear and nonlinear polarizabilities. An example of the steric interaction is a crystal-packing geometry that prevents a conjugated π -electron chain from adopting a purely linear

Table II. INDO–SDCI-Calculated and Measured Values of Nonresonant γ s for Ethylene, Linear Polyenes, and Benzene

Molecule ^a	Theory (10^{-36} esu)		Expt (10^{-36} esu) γ
	$\gamma(-3\omega; \omega, \omega, \omega)^b$ $h\omega/2\pi = 0.66$ eV	$\gamma(-2\omega; \omega, \omega, 0)^c$ $h\omega/2\pi = 1.79$ eV	
Ethylene	+0.63	+0.65	+0.758 ± 0.017 ^d
ATB	+2.10	+2.76	+2.30 ± 0.13 ^d
CB	+1.70	+2.14	
ATH	+7.00	+12.10	+7.53 ± 0.7 ^d +9.1 ± 0.4 ^e
CH	+5.88	+9.80	
ATO	+17.90	+36.40	—
CO	+13.50	+25.70	—
Benzene	+2.19	+2.48	+2.06 ± 0.05 ^d +2.4 ± 0.72 ^f

^a ATB, all-*trans* butadiene; CB, *cis*-butadiene; ATH, all-*trans* hexatriene; CH, (3,4)-*cis*-hexatriene, ATO, all-*trans*-octatetraene; CO, (3,4),(5,6)-*dicis* octatetraene.

^b $\gamma(-3\omega; \omega, \omega, \omega) = \gamma\sigma + \gamma\pi(-3\omega; \omega, \omega, \omega)$, $h\omega/2\pi = 0.66$ eV (1.89 μm).

^c $\gamma(-2\omega; \omega, \omega, 0) = \gamma\sigma + \gamma\pi(-2\omega; \omega, \omega, 0)$, $h\omega/2\pi = 1.79$ eV (694.3 nm).

^d $\gamma(-2\omega; \omega, \omega, 0)$, vapor phase, $h\omega/2\pi = 1.79$ eV (694.3 nm) (146).

^e $\gamma(-3\omega; \omega, \omega, \omega)$, liquid phase, $h\omega/2\pi = 0.65$ eV (1.908 μm) (147).

^f $\gamma(-3\omega; \omega, \omega, \omega)$, liquid phase, $h\omega/2\pi = 0.66$ eV (1.89 μm) (148).

and planar geometry. Nonbonding interactions refer to van der Waals forces and local electric fields that act to polarize the molecules and change their electronic structures and nuclear geometries in the ground state and excited electronic state. The covalent attachment of the molecules to a host matrix can result in bonding interactions that strongly alter the molecular structures and properties.

The first step in treating the effect of these steric, nonbonding, and bonding interactions on the electronic structures of conjugated π -electron molecules is to use the methods previously specified for the isolated molecules to calculate the linear and nonlinear polarizabilities for the ground electronic state molecular geometries that have been experimentally and theoretically determined for the given condensed phase. The next step is to incorporate nonbonding interactions in these methods and then to recalculate the properties for the preceding molecular geometries, or geometries obtained with respect to the constraints defined by the nonbonding interactions. Nonbonding interactions can be treated in various degrees of sophistication and computational requirements, for example, (1) allowing uniform electric fields to perturb the diagonal elements of the Fock–Hamiltonian, (2) surrounding the molecule with charges and dipoles that simulate the electric fields associated with the immediate environment of the molecule (e.g., the

SPARKLES option in the MOPAC software mentioned previously), or (3) constructing a supramolecular cluster that includes not only the π -electron molecule, but molecular fragments of the host lattice. The treatment of bonding interactions requires the construction of a supramolecular cluster. In summary, the theoretical analysis of the linear and nonlinear polarizabilities of molecules in the condensed phase is possible when using the methods developed for isolated molecules in the gas phase.

A Theoretical Analysis of Linear Cyanines and Polyenes

Approximations of the SOS expression for γ reveal that candidate molecules for third-order NLO applications should also have large linear polarizabilities, or equivalently through the Kramers–Kronig transform, large one-photon absorptivities (80, 91). Hans Kuhn in his classic 1949 paper (124) grouped the most important organic molecules that absorb visible and near-IR light into three categories: (1) symmetric polymethines, for example, cyanine cations ($\text{H}_2\text{N}-\text{CH}-(\text{CH}-\text{CH})_n^+-\text{NH}_2$) and oxopolyeneolate anions ($\text{O}-\text{CH}-(\text{CH}-\text{CH})_n^--\text{O}$), (2) polyenes and related compounds, for example, merocyanine dyes ($\text{H}_2\text{N}-\text{CH}=(\text{CH}-\text{CH})_n=\text{O}$), and (3) porphyrins and phthalocyanines. The conjugated π -electron bonding networks found in these molecules are the principal reason for their strong absorption of visible and near-IR light. It should therefore not be surprising that the organic molecules with the largest linear and nonlinear electronic polarizabilities measured to date fall into one of the above categories (17–22). In this section, we concentrate on the polymethine and polyene quasi-one-dimensional π -bonding networks exemplified by the linear all-*trans* polyenes and linear cyanine cations.

The symmetric polymethine-like molecules are distinguished by a π -electron bonding network with attenuated alternation of the π -electron bond-orders in the ground electronic state, while the polyene-like molecules have a pronounced π -electron bond-order alternation in the ground electronic state. The attenuated alternation for the symmetric polymethines results from a π -electron ground state that can be described as a resonance hybrid of two equivalent structures, for example, $^+\text{H}_2\text{N}=\text{CH}-(\text{CH}=\text{CH})_n-\text{NH}_2 \leftrightarrow \text{H}_2\text{N}-\text{CH}=(\text{CH}-\text{CH})_n=\text{NH}_2^+$ for the symmetric cyanine cations. The pronounced bond-order alternation in the polyene-like molecules results from a π -electron ground state that is best described by a single structure, for example, the $^+\text{H}_2\text{N}=\text{CH}-(\text{CH}=\text{CH})_n-\text{O}^-$ structure for the merocyanines in a vacuum is not equivalent to the more stable $\text{H}_2\text{N}-\text{CH}=(\text{CH}-\text{CH})_n=\text{O}$ structure.

In free-electron theory, the potential energy of a π -electron in a symmetric polymethine can be represented by a constant value because of the π -electron density delocalization associated with the resonance

hybrid; the potential energy of a π -electron in a polyene-like molecule can be represented by a periodic function with the troughs and crests of the function coinciding with the double and single bonds (124). An important consequence of these different potential energy functions is that the energy difference between the highest occupied molecular orbital (HOMO) and the lowest occupied molecular orbital (LUMO) goes to zero with increasing chain length for symmetric polymethines, but converges to a finite value with increasing length for polyenes. In other words, symmetric cyanines become metallic in the limit of infinite length, whereas, the polyenes resemble semiconductors in this limit (125, 126).

This free-electron-Hueckel theoretical picture is in agreement with experimental and theoretical studies of the linear-optical properties of symmetric polymethines and polyene-like molecules. For example, there is the experimental observation that λ_{\max} for the first one-photon allowed ${}^1\pi\pi^* \leftarrow S_0$ transition increases linearly with chain length for symmetric all-*trans*, polymethine cations with two terminal dimethyl amino groups $[(\text{CH}_3)_2\text{N}=\text{CH}-(\text{CH}=\text{CH})_n^+-\text{N}(\text{CH}_3)_2$ or streptocyanines] (127), but reaches a limiting value in the case of the all-*trans*- α,ω -dialkyl-polyenes (128), and the dimethylamino-merocyanines (127), $(\text{CH}_3)_2\text{N}-\text{CH}=(\text{CH}-\text{CH})_n=\text{O}$. Also, the linear, static electric-dipole polarizabilities of symmetric cyanine cations have been measured (129) and calculated (126, 130, 131) to be larger than those for all-*trans*-linear polyenes of comparable methylation, length, and number of π -electrons.

One would also expect the NLO properties of symmetric polymethines to differ from polyene-like molecules. Third-harmonic generation (THG) measurements of the nonresonant electronic component of the third-order, electric-dipole polarizability $[\gamma_e(-3\omega; \omega, \omega, \omega)]$, with $\omega = 1.91 \mu\text{m}$ for a variety of symmetric cyanine dyes in the condensed phase yielded $\gamma_e(-3\omega; \omega, \omega, \omega)$'s with both negative and positive signs, whereas the measurements for a selection of polyenes yielded only positive $\gamma_e(-3\omega; \omega, \omega, \omega)$ s (129); the magnitudes of the $\gamma_e(-3\omega; \omega, \omega, \omega)$ s measured for streptocyanines met or exceeded those for $\alpha,\alpha,\omega,\omega$ -tetramethyl-polyenes of comparable size and number of π -electrons (129). The THG measurements at $\omega = 1.85\text{--}2.15 \mu\text{m}$ for the polycrystalline powder of a symmetric cyanine dye with terminal quinoline rings determined in $\gamma_e(-3\omega; \omega, \omega, \omega)$ to be greater than that of the well-studied polydiacetylene system, poly-(2,4-hexadiyn-1,6-diol)-bis(*p*-toluene sulfonate), or PTS-PDA (132). Recent studies (28, 133) of the third-order NLO properties for a set of zwitterionic polymethine dyes, the squaryliums, emphasizes the importance of the polymethines as a class of NLO molecules distinct from the polyenes.

The principal subject of this section is the calculation and analysis of the nonresonant, π -electronic components of third-order, electric dipole polarizabilities for a set of linear streptocyanines and unmethylated

streptocyanines (hereafter known simply as cyanines). In contrast to earlier theoretical studies of these polarizabilities for linear cyanines (130, 131), we (1) use a SOS expression to calculate the π -electronic component of the dynamic third-order polarizability for third-harmonic generation, $\gamma_{\pi}(-3\omega; \omega, \omega, \omega)$, as well as the static third-order polarizability, $\gamma_{\pi}(0; 0, 0, 0)$; and (2) treat the π -electronic states using the all-valence-electron, semiempirical INDO-MO procedure combined with SDCI of the singlet π -electron configurations, instead of using original (130) or extended (131) versions of Kuhn's free-electron method (124). Although our theoretical method is more complicated than those based on free-electron theory, it has been shown to provide a consistent treatment of the π -electronic components of the third-order polarizabilities and the linear and nonlinear spectroscopic properties of the $^1\pi\pi^*$ states of linear polyenes and benzene (80). Critical to our consistent calculation of these properties is the treatment of π -electron correlation at least at the level of SDCI (80).

We calculate γ_{π} s for all-*trans*, linear symmetric cyanine and streptocyanine cations with no double-single bond-length alternation, and for cyanine cations with asymmetric geometries resulting from the artificial imposition of double-single bond-length alternation. These γ_{π} s are compared with those previously calculated for all-*trans* linear polyenes with double-single bond-length alternation (80) and for a new set calculated with geometries resulting from the artificial imposition of no double-single bond-length alternation. The structures of the five sets of molecules are shown in Figure 1.

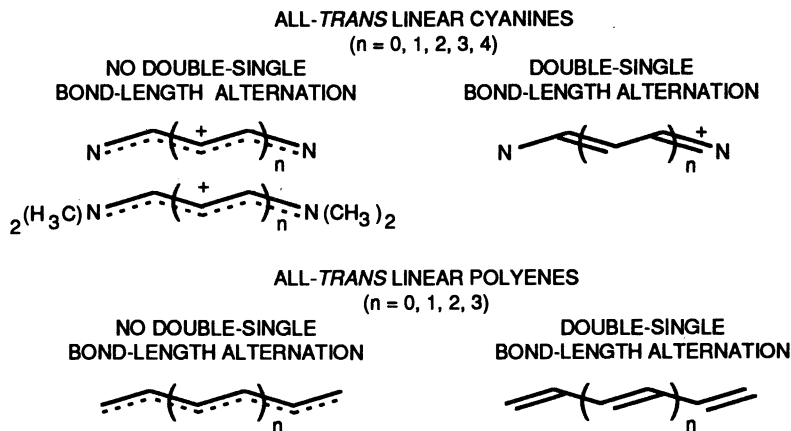



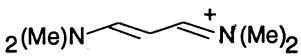

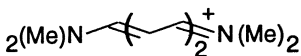

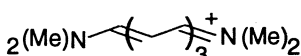
Figure 1. Structures of the linear cyanines and polyenes with and without bond-length alternation. (Reproduced with permission from reference 91. Copyright 1991 The International Society for Optical Engineering.)

Our theoretical analysis of the π -electron, third-order polarizabilities for the molecules shown in Figure 1 consists of five parts: (1) the establishment of the validity of the theoretical procedure by comparing calculated and measured third-order polarizabilities; (2) the effect of chain length and conformation on the calculated π -electronic components of γ , γ_π , for the polyenes and cyanines; (3) the identification of the salient $^1\pi\pi^*$ states that define γ_π for the two sets of molecules; (4) the identification and analysis of the SOS terms important to γ_π for the molecules, and the derivation of approximations to the complete SOS expression for γ_π that help provide chemical insight into the origin of γ_π for the molecules; and (5) an investigation of the dependence of γ_π , and the π -electronic component of the second-order, electric-dipole polarizability, β_π , on (a) the geometric asymmetry of a linear cyanine cation and (b) the deprotonation of the cation.

Molecular Geometries. The π -electron bonding networks in all the molecules in Figure 1 were kept planar. The bond-lengths and bond-angles used for the molecules are as follows: (1) symmetric cyanines with no bond-length alternation: $r(\text{C-N}) = 1.351 \text{ \AA}$ (134), $r(\text{C-C}) = 1.362 \text{ \AA}$ (134), $r(\text{N-H}) = 1.2 \text{ \AA}$ (135), $r(\text{C-H}) = 1.08 \text{ \AA}$ (114), and all bond-angles = 120° (114); (2) symmetric streptocyanines with no bond-length alternation: $r(\text{C-N}) = 1.351 \text{ \AA}$ (134), $r(\text{C-C}) = 1.362 \text{ \AA}$ (134), $r(\text{C-H}) = 1.08 \text{ \AA}$ (114), $r(\text{N-C}_m) = 1.57 \text{ \AA}$ (a standard value taken from ref. 135 + 0.1 \AA), $r(\text{C}_m\text{-H}_m) = 1.09 \text{ \AA}$ (114), $\angle(\text{NC}_m\text{H}_m) = 109.47^\circ$ (114), all other bond angles = 120° (114), and the dihedral angles, $\varphi(\text{CNC}_m\text{H}_m) = 0^\circ, 60^\circ$, and -60° ; (3) asymmetric cyanines with bond-length alternation: $r(\text{C=N}') = 1.306 \text{ \AA}$ (135), $r(\text{C-C}) = 1.46 \text{ \AA}$ (80), $r(\text{C=C}) = 1.35 \text{ \AA}$ (80), $r(\text{C-N}) = 1.4 \text{ \AA}$ (135), $r(\text{N'-H}) = 1.2 \text{ \AA}$ (135), $r(\text{N-H}) = 0.99 \text{ \AA}$ (135), $r(\text{C-H}) = 1.08 \text{ \AA}$ (114), and all bond-angles = 120° (114); (4) linear polyenes with bond-length alternation: $r(\text{C-C}) = 1.46 \text{ \AA}$ (80), $r(\text{C=C}) = 1.35 \text{ \AA}$ (80), $r(\text{C-H}) = 1.08 \text{ \AA}$ (114), and all bond-angles = 120° (114); and (5) linear polyenes with no bond-length alternation: $r(\text{C-C}) = 1.40 \text{ \AA}$ (135), $r(\text{C-H}) = 1.08 \text{ \AA}$ (114), and all bond-angles = 120° (114). It is noted that the π -electron polarizabilities and spectroscopic properties of the molecules are not very sensitive to the lengths of the N-H and C-H bonds. In our investigation of the dependence of γ_π and β_π on the geometry for the pentamethine-cyanine cation, we calculated equilibrium geometries in the presence of a F^- counterion located at different sites along the chain. The cation was constrained to be planar, and the counterion was fixed at a given height above the plane during the geometry optimization. These calculations were performed with the SPARTAN ab initio SCF-MO software package (112, 136) using the minimal STO-3G atomic orbital basis set.

Comparison of the Calculated and Measured Nonresonant γ s for the Linear Polyenes and Streptocyanines. Our theoretical method has been successful in calculating nonresonant $\gamma(-2\omega; \omega, \omega, 0)$ s for ethylene, linear polyenes, and benzene that are in very good agreement with the γ s measured for these molecules in the gas phase (80). The importance of treating electron correlation at least at the level of single- and double-excitation configuration interaction is investigated in detail in reference 80. This comparison is presented in Table II. (The esu units in this table and the other remaining tables and figures are in statcoul cm⁴/statV³.) A similar comparison of calculated and measured γ s is given in Table III for three linear streptocyanine cations of different lengths. This table contains the $\gamma(-3\omega; \omega, \omega, \omega)$ s measured at $\omega = 1.908 \mu\text{m}$ for the three molecules in the liquid phase (129) and the $\gamma(-3\omega; \omega, \omega, \omega)$ s calculated for the streptocyanines with both symmetric and asymmetric geometries. The $\gamma(-3\omega; \omega, \omega, \omega)$ s for the two geometries were calculated because it is unclear which geometry was stabilized by the Cl⁻ counterion and the solvent used in the experimental samples. In this regard, Fabian and Mehlhorn (137) comment that the asymmetric chain geometries seen experimentally (138) in crystals of streptocyanines may be due to a nonsymmetric arrangement of the counterion to the chain in the crystal. The calculated $\gamma(-3\omega; \omega, \omega, \omega)$ s in Table III are separated into σ - and π -electron components. The γ_σ term was estimated by using

Table III. Calculated and Measured γ s for Selected Linear Streptocyanines

Molecule	Theory (10^{-36} esu)			Expt (10^{-36} esu)
	γ_σ	γ_π	γ	
	2.8	-6	-3	$0.5-3 \pm 0.4$
	2.8	-1	2	
	3.3	-80	-80	52 ± 1
	3.3	40	40	
	3.7	-800	-800	-510 ± 50
	3.7	1000	1000	

SOURCE: Reproduced with permission from reference 85. Copyright 1991 The International Society for Optical Engineering.

the bond-additivity approximation described in a preceding section, whereas the γ_π term was that calculated for the unmethylated cyanines.

As shown in Table III, the magnitudes of the measured γ s and those calculated for either the symmetric or asymmetric streptocyanines are in rough agreement. The positive signs of the γ s measured for the two shorter streptocyanines can be explained in terms of the stabilization of the asymmetric geometries by the Cl^- counterion and solvent, whereas the negative sign of the γ measured for the longest streptocyanine can be explained in terms of the stabilization of the symmetric geometry. More measurements are needed to test this hypothesis.

Comparison of Calculated $\gamma_\pi(0; 0, 0, 0)$ s. The $|\gamma_\pi(0; 0, 0, 0)|$ s calculated for the five sets of molecules in Figure 1 are plotted on a logarithmic scale in Figure 2 as functions of the number of π -electrons ($N_{\pi-e}$) in each molecule, which also scales as the length of the molecule. The symmetric, linear streptocyanines with no bond-length alternation are designated LC1 in Figure 2; LC2 is the label for the symmetric, linear cyanines with no bond-length alternation; LC3 represents the asymmetric linear cyanines with bond-length alternation; LP1 designates the linear polyenes with bond-length alternation; and LP2 represents the linear polyenes with no bond-length alternation. A dashed line in

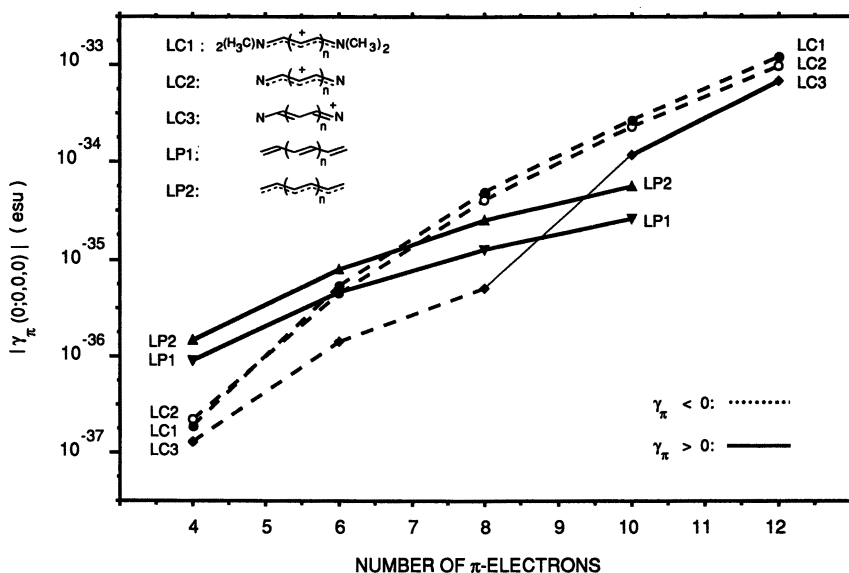


Figure 2. Calculated $|\gamma_\pi(0; 0, 0, 0)|$'s for the five sets of molecules shown in Figure 1. (Reproduced with permission from reference 91. Copyright 1991 The International Society for Optical Engineering.)

Figure 2 indicates a negative $\gamma_\pi(0; 0, 0, 0)$, and a solid line a positive $\gamma_\pi(0; 0, 0, 0)$.

Regarding the sign of $\gamma_\pi(0; 0, 0, 0)$ for the different molecules, the symmetric linear cyanines with and without terminal methyl groups all have negative $\gamma_\pi(0; 0, 0, 0)$ s; the asymmetric cyanines switch from negative to positive signs after $N_{\pi-e} = 8$, or as the chain length increases past five carbon atoms; and both sets of linear polyenes have positive $\gamma_\pi(0; 0, 0, 0)$ s.

In regard to the relative magnitudes of $\gamma_\pi(0; 0, 0, 0)$ for the different molecules, the $|\gamma_\pi(0; 0, 0, 0)|$ s for the symmetric linear cyanines start out less than those for the two sets of linear polyenes, but become much greater than $|\gamma_\pi(\text{LP1})|$ and $|\gamma_\pi(\text{LP2})|$ after $N_{\pi-e} = 6$. This behavior reflects the greater power law dependence of the symmetric cyanines on $N_{\pi-e} < 12$ than that of the linear polyenes (i.e., $|\gamma_\pi(\text{LC1})| \propto N_{\pi-e}^{7.9}$, $|\gamma_\pi(\text{LC2})| \propto N_{\pi-e}^{7.6}$, $|\gamma_\pi(\text{LP1})| \propto N_{\pi-e}^{3.7}$, and $|\gamma_\pi(\text{LC1})| \propto N_{\pi-e}^{4.0}$). Furthermore, the $|\gamma_\pi|$ s for symmetric linear cyanines do not appear to level out with increasing length, while the $|\gamma_\pi|$ s for the linear polyenes appear to level out. This behavior seems to reflect the metallike nature of the delocalized π -electron bonding network in the cyanines and the semiconductorlike nature of the π -electron bonding network in the polyenes. Calculations on longer cyanines and polyenes need to be performed to test this hypothesis.

It is emphasized that the above power law relationships are limited to polyenes and cyanines containing 12 π -electrons or less. It is meaningless to use these relationships in extrapolations of $|\gamma_\pi|$ in the long-chain limit.

Terminal methyl group substitution for the symmetric linear cyanines results in a slight increase in $|\gamma_\pi(0; 0, 0, 0)|$ at each value of $N_{\pi-e}$. Decreasing bond-length alternation for the linear polyenes acts to increase $|\gamma_\pi(0; 0, 0, 0)|$ at each value of $N_{\pi-e}$. This result is reasonable because a lower degree of bond-length alternation will smooth out the potential energy surface of the π -electrons along the polyene chain.

Perhaps the most interesting result shown in Figure 2 is the dramatic effect that molecular geometry has upon the $\gamma_\pi(0; 0, 0, 0)$ s for the linear cyanine cations. Moving between the symmetric geometry with no bond-length alternation and the asymmetric geometry with bond-length alternation can result in large changes in the sign and magnitude of $\gamma_\pi(0; 0, 0, 0)$. This calculated dependence of $\gamma_\pi(0; 0, 0, 0)$ on geometry is discussed further in the following subsections.

Identification of the Important $^1\pi\pi^*$ States That Define $\gamma_\pi(0; 0, 0, 0)$. One way to identify the important $^1\pi\pi^*$ states that define $\gamma_\pi(0; 0, 0, 0)$ is to examine the convergence of the SOS expression for $\gamma_\pi(80)$. Because γ_π for the linear molecules shown in Figure 1 is almost

completely dominated by the tensor component along the chain axis (defined here to be the molecule-fixed x -axis), it is sufficient to examine the dependence of the γ_{xxxx} component on the number of π -electron states. This dependence is shown in Figure 3 for the two types of linear polyenes with $N_{\pi-e} = 6$ and the symmetric and asymmetric cyanines with the same number of π -electrons. The γ_{xxxx} for all four molecules is close to complete convergence after summing over the ground electronic state and the first nine ${}^1\pi\pi^*$ states. The magnitudes of the oscillations in γ_{xxxx} for each molecule in Figure 3 indicate that there is an important low-lying ${}^1\pi\pi^*$ state that provides a negative contribution to γ_{xxxx} , and a higher excited state that provides a positive contribution. The relative magnitudes of these contributions for a given molecule determine the sign and magnitude of γ_{xxxx} , and hence γ_π .

An inspection of the SOS expression for γ_π (28–30, 80, 91, 139, 140), reveals that the ${}^1\pi\pi^*$ states which provide the largest negative contributions to γ_π are those most strongly coupled to the ground state (o) through the application of an external electric field (i.e., the most strongly one-photon allowed ${}^1\pi\pi^*$ [${}^1\pi\pi^*(1)$] states), which have the larg-

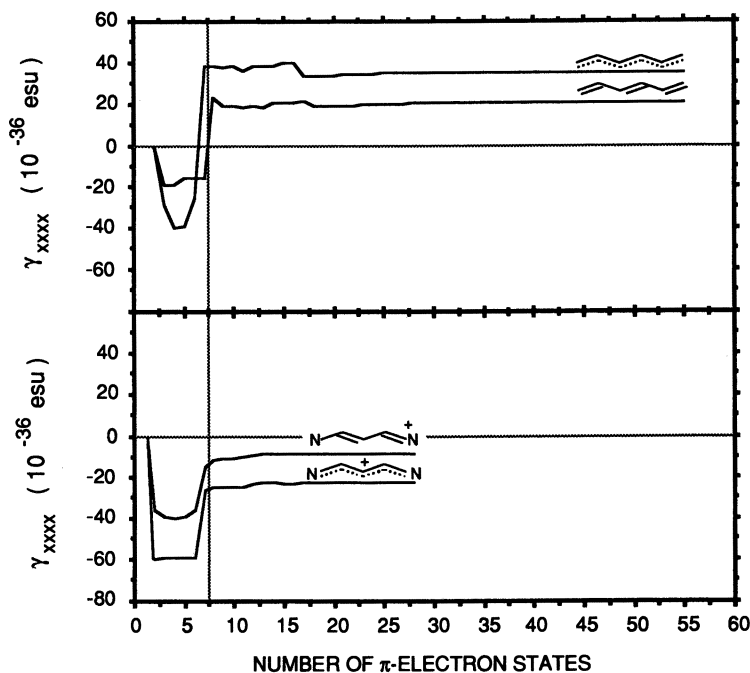


Figure 3. Calculated convergence of the γ_{xxxx} component of $|\gamma_\pi(0; 0, 0, 0)|$ for linear polyenes and cyanines with 6 π -electrons. (Reproduced with permission from reference 91. Copyright 1991 The International Society for Optical Engineering.)

est ${}^1\pi\pi^*(1) \leftrightarrow o$ transition dipole moments. The magnitude of the negative contribution to γ_π by a ${}^1\pi\pi^*(1)$ state can be attenuated in asymmetric molecules that have a change in dipole moment associated with the ${}^1\pi\pi^*(1) \leftrightarrow o$ transition (see the following paragraphs). This attenuation is indicated in Figure 3, where the negative dip in γ_{xxxx} for the asymmetric cyanine is less than that of the symmetric cyanine. The ${}^1\pi\pi^*$ states that provide significant positive contributions to γ_π are those coupled to the dominant ${}^1\pi\pi^*(1)$ states and the ground state via the application of an external electric field (i.e., strongly two-photon allowed ${}^1\pi\pi^*[{}^1\pi\pi^*(2)]$ states), which have large ${}^1\pi\pi^*(2) \leftrightarrow {}^1\pi\pi^*(1) \leftrightarrow o$ transition dipole moments.

The energies of the ${}^1\pi\pi^*(1)$ and ${}^1\pi\pi^*(2)$ states important to the γ_π s for the linear polyenes with bond-length alternation and the symmetric cyanines are presented in Figure 4, along with the ground-state energies and the relevant transition dipole moments between the states; Figure 5 contains the energies of these states and the relevant transition dipole moments for the linear polyenes with no bond-length alternation and the asymmetric cyanines. Figure 5 also presents the changes in dipole

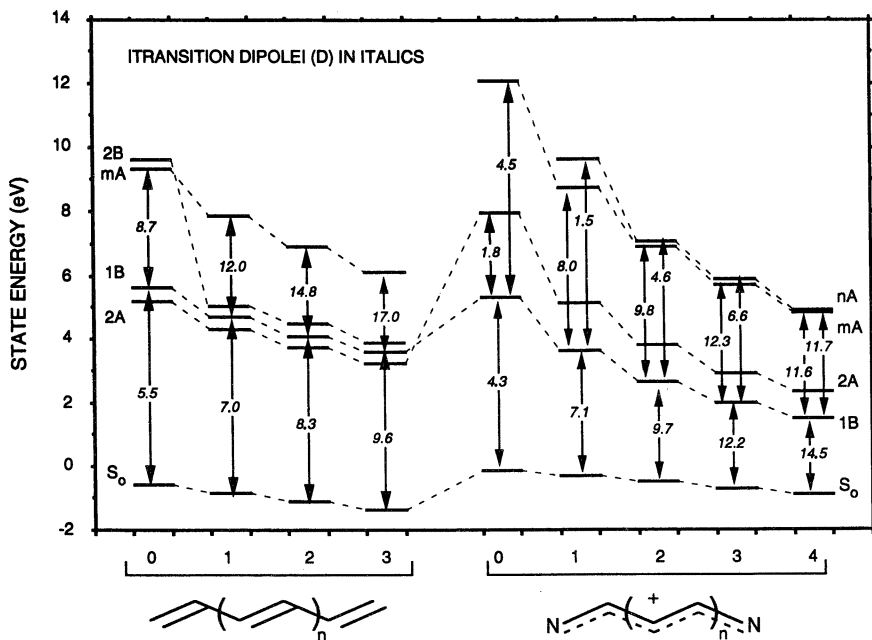


Figure 4. Calculated properties of the ${}^1\pi\pi^*$ states important to γ_π for the linear polyenes with bond-length alternation and the symmetric cyanines. (Reproduced with permission from reference 91. Copyright 1991 The International Society for Optical Engineering.)

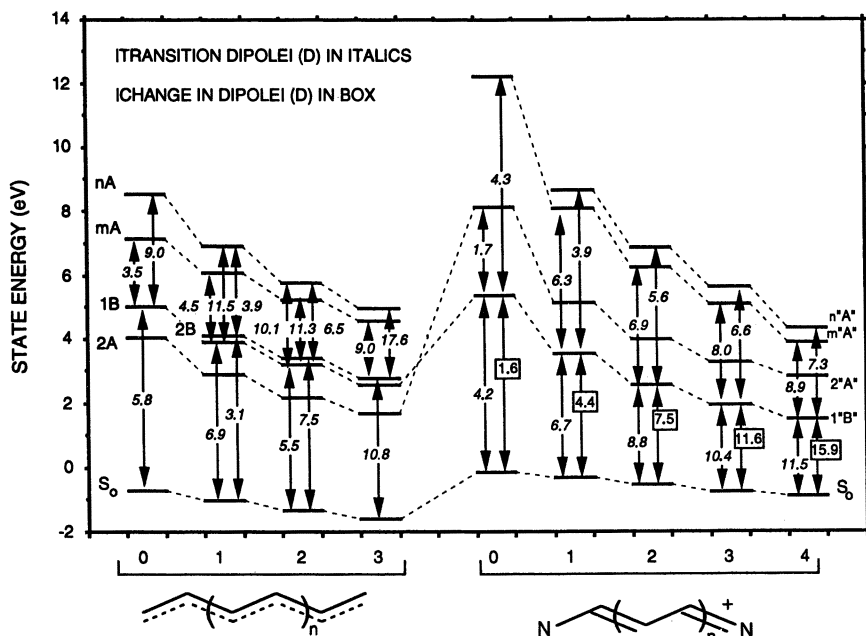


Figure 5. Calculated properties of the ${}^1\pi\pi^*$ states important to γ_π for the linear polyenes with bond-length alternation and the symmetric cyanines. (Reproduced with permission from reference 91. Copyright 1991 The International Society for Optical Engineering.)

moment associated with the important ${}^1\pi\pi^*(1) \leftrightarrow o$ transitions in the asymmetric cyanines. The A and B labels for the states in Figures 4 and 5 refer to the irreducible representations, or symmetries, of the ${}^1\pi\pi^*$ states within the point group for each set of molecules. In the case of the two types of linear polyenes, A and B refer to the A_g and B_u symmetries in the C_{2h} point group; and A and B for the symmetric cyanines refer to the A_1 and B_2 symmetries in the C_{2v} point group. The "A" and "B" labels for the asymmetric cyanines refer to A_g -like ("A_g") and B_u -like ("B_u") symmetries in the C_s point group. The separation of A and B symmetries in the C_s point group is somewhat artificial because both these symmetries technically map to the A' symmetry in this point group. The number or lower case letter directly in front of the labels indicates the energy ordering of the state within a given symmetry (e.g., 1B designates the lowest energy π -electron state with B symmetry).

It is well-known that the most dominant ${}^1\pi\pi^*(1)$ states in symmetric linear, conjugated π -electron molecules belong to the B symmetry class, whereas the most important ${}^1\pi\pi^*(2)$ states possess A symmetry (80, 86, 121). Figures 4 and 5 show that the ${}^1\pi\pi^*(1)$ states important to γ_π for

the linear polyenes and the symmetric cyanines are the low-lying 1B and 2B states, and the salient ${}^1\pi\pi^*(2)$ states are the higher excited mA and nA states. Specifically, 3 π -electron states dominate the γ_π for the linear polyenes with bond-length alternation: S_0 , 1B, and mA; 4 states largely define the γ_π for the symmetric cyanines: S_0 , 1B, mA, and nA; and 5 states dominate the γ_π for the linear polyenes with no bond-length alternation: S_0 , 1B, 2B, mA, and nA. Although the ${}^1\pi\pi^*(1)$ and ${}^1\pi\pi^*(2)$ states in the asymmetric cyanines can possess either "A" or "B" symmetry, the 1 "B" state is still seen to be the most important ${}^1\pi\pi^*(1)$ state, and the m "A" and n "A" states are considered the important ${}^1\pi\pi^*(2)$ states. As shown in Figure 5, four states largely define the γ_π for these molecules: S_0 , 1 "B", m "A", and n "A". Note the large change in dipole moment associated with the 1 "B" $\leftrightarrow S_0$ transition for the asymmetric cyanines.

The 2A and 2B ${}^1\pi\pi^*$ states shown for the linear polyenes deserve more comment. First, although the 2A state is very important to the photophysics and photochemistry of linear polyenes (80, 121, 128), it is calculated to contribute very little to γ_π for these molecules. Instead, a ${}^1\pi\pi^*$ state of A symmetry that is higher in energy than the 1B ${}^1\pi\pi^*$ state is calculated to be the dominant contributor to γ_π . Furthermore, this higher excited A state is calculated to have a nonresonantly enhanced two-photon absorption cross section that is approximately two orders of magnitude greater than that for the 2A state (80). These calculated results are in agreement with a recent two-photon absorption experiment by Etemad, who found a broad two-photon state at an energy considerable higher than the 1B state in poly-4BCMU polydiacetylene (141). More experimental studies are needed to understand the nature of the higher excited A ${}^1\pi\pi^*$ states.

The 2B state is of interest because a recent theoretical analysis by Dixit et al. (142) of the third-order NLO properties of *trans*-polyacetylene and polydiacetylene predicts that the important A ${}^1\pi\pi^*$ state contributing to γ_π for these polymers is bounded in energy by the 1B and 2B ${}^1\pi\pi^*$ states. As shown in Figures 4 and 5 for the two types of linear polyenes, the highly excited A ${}^1\pi\pi^*$ state important to γ_π is outside this bound for all molecules except all-*trans* butadiene. It is difficult to draw any conclusions regarding the existence of this bound from our calculations for small molecules, other than to say that more work should be performed to address this issue.

Identification and Analysis of the SOS Terms Important to $\gamma_\pi(0; 0, 0, 0)$. In the case of the polyenes and cyanines whose ${}^1\pi\pi^*$ states are presented in Figures 4 and 5, the SOS expression for the γ_{xxxx} component of $\gamma_\pi(0; 0, 0, 0)$ can be separated into the three terms shown in Table IV, where $|\mu_{0,1}B^x|$ is the x -component of the transition dipole

Table IV. Important Terms Defining the γ_{xxxx} Component of $\gamma_{\pi}(0;0,0,0)$ for the Molecules of Interest

<i>Term Label</i>	<i>Term</i>
G	$-\frac{ \mu_{o,1B}^x ^4}{\Delta E_{1B}^3}$
X	$\frac{ \mu_{o,1B}^x ^2}{\Delta E_{1B}^2} \sum_{i>1} \frac{ \mu_{1B,iA}^x ^2}{\Delta E_{iA}}$
D	$\frac{ \mu_{o,1B}^x ^2}{\Delta E_{1B}^2} \frac{ \mu_{1B,1B}^x - \mu_{o,o}^x ^2}{\Delta E_{1B}}$

SOURCE: Reproduced with permission from reference 85. Copyright 1991 The International Society for Optical Engineering.

moment between the 1B (or 1“B”) and *o* states, ΔE_{1B} is the transition energy between these states, $|\mu_{1B,iA}^x|$ is the *x*-component of the transition-dipole moment between the 1B (or 1“B”) and *iA* (or *i* “A”) states, ΔE_{iA} is the transition energy between the *iA* (or *i* “A”) and *o* states, and $|\mu_{1B,1B}^x - \mu_{o,o}^x|$ is the change in permanent dipole moment associated with the 1B \leftrightarrow *o* transition. The negative term is labeled G because it is defined solely by π -electronic excitations out of the ground state. It can also be seen that the G term is proportional to $-(\alpha_{\pi o}^2/\Delta E_{1B})$, where $\alpha_{\pi o} \equiv \alpha_{\pi o}(0;0)$ is the static, π -electron polarizability of the ground state (80). The middle positive term is labeled X because it contains couplings between excited electronic states that help to define the π -electron polarizability of the 1B (or “1B”) state. The positive term at the bottom of the table is labeled D because it contains a change in permanent-dipole moment. The D term is nonzero only for molecules with asymmetric π -electron bonding networks.

If the $(|\mu_{o,1B}^x|^2/\Delta E_{1B})$ ratio is factored out of each of the three terms in Table II and sees this ratio as proportional to $\alpha_{\pi o}$ (80), then γ_{xxxx} , and hence $\gamma_{\pi}(0;0,0,0)$, can be interpreted as

$$\gamma_{\pi}(0;0,0,0) \propto \alpha_{\pi o} \left\{ (|\Delta\mu_{1B,o}^x|^2 - |\mu_{o,1B}^x|^2) / \Delta E_{1B}^2 + \sum_{iA} (|\mu_{1B,iA}^x|^2 / \Delta E_{iA} \Delta E_{1B}) \right\} \quad (23)$$

where $\Delta\mu_{1B,o}^x$ is $\mu_{1B,1B}^x - \mu_{o,o}^x$. Thus, $\gamma_{\pi}(0;0,0,0)$, in the case of the molecules shown in Figure 1, can be seen as the product of the linear π -electron polarizability and the nonlinear term in parentheses. This view of $\gamma_{\pi}(0;0,0,0)$ is similar to Stevenson et al.'s (129) expression of

$\gamma_{\pi}(0; 0, 0, 0)$ as the product of the linear polarizability and an “anharmonicity factor.”

As discussed previously and as emphasized in references 18, 91, and 140, the sign and magnitude of $\gamma_{\pi}(0; 0, 0, 0)$ for our molecules is basically determined by the magnitudes of the positive X and D terms relative to that for the negative G term. In the case of the linear polyenes with bond-length alternation and the symmetric cyanines, the D term is zero and $\gamma_{\pi}(0; 0, 0, 0)$ is determined by the balance between the G and X terms. The magnitudes of the G and X terms for these two sets of molecules are plotted in the top half of Figure 6. A negative term is indicated by a dashed line, and a positive term by a solid line. The positive X term is seen to be greater than the negative G term for each of the linear polyenes and therefore $\gamma_{\pi}(0; 0, 0, 0)$ is positive for these molecules. The ordering of the magnitudes of the X and G terms is reversed for the symmetric cyanines, and so $\gamma_{\pi}(0; 0, 0, 0)$ is negative for these molecules. The bottom half of Figure 6 shows how well the G + X approximations for the linear polyenes and the symmetric cyanines match with the complete calculation of γ_{xxxx} , $[=5\langle\gamma_{\pi}(0; 0, 0, 0)\rangle]$.

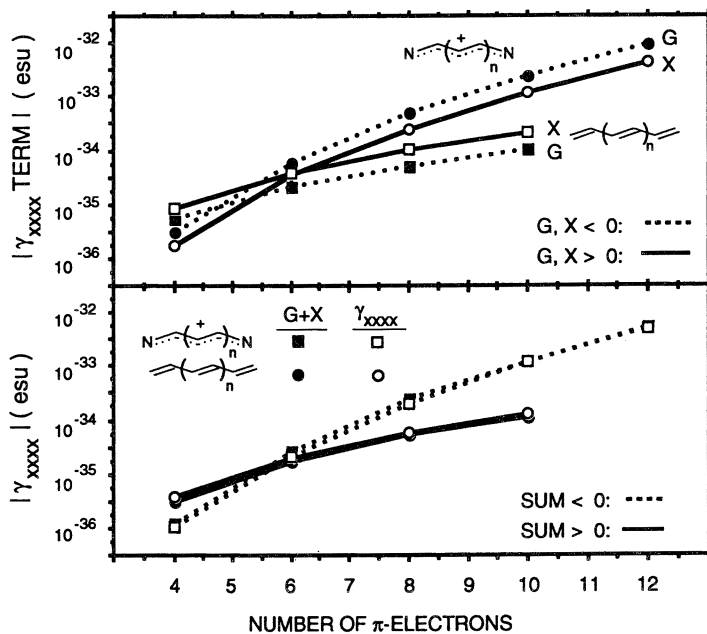


Figure 6. Calculated comparison of the γ_{xxxx} and the G + X approximation of γ_{xxxx} for the linear polyenes with bond-length alternation and the symmetric cyanines. (Reproduced with permission from reference 91. Copyright 1991 The International Society for Optical Engineering.)

It is noted that the power law dependence of $|G|$ and $|X|$ on $N_{\pi-e}$ for either the linear polyenes (LP) or the symmetric cyanines (SC) are very similar to the dependence of $|\gamma_{\pi}(0; 0, 0, 0)|$ for these molecules (i.e., $|G(LP)| \propto N_{\pi-e}^{3.2}$, $|X(LP)| \propto N_{\pi-e}^{3.5}$, and $|\gamma_{\pi}(LP)| \propto N_{\pi-e}^{3.7}$; $|G(SC)| \propto N_{\pi-e}^{7.3}$, $|X(SC)| \propto N_{\pi-e}^{7.1}$, and $|\gamma_{\pi}(SC)| \propto N_{\pi-e}^{7.6}$). The similarity of the calculated dependence of $|G|$, $|X|$, and $|\gamma_{\pi}(0; 0, 0, 0)|$ on $N_{\pi-e}$ within each class of molecules suggests the following two-step approach to investigate the chain-length dependence of $\gamma_{\pi}(0; 0, 0, 0)$ for the above molecules: (1) measure α_o (the ground-state polarizability) and ΔE_{1B} as a function of chain length, (2) recall that $|G| \propto (\alpha_{\pi o}^2 / \Delta E_{1B})$, and plot $|G|$ as a function of chain length.

In the case of the asymmetric cyanines, the D term is nonzero, and so $\gamma_{\pi}(0; 0, 0, 0)$ is determined by the balance between the G, X, and D terms. The magnitudes of the G, X, and D terms are plotted for the asymmetric cyanines in the top half of Figure 7, along with the magnitudes of the G and X terms for the symmetric cyanines. A negative term is indicated by a dashed line, and a positive term by a solid line.

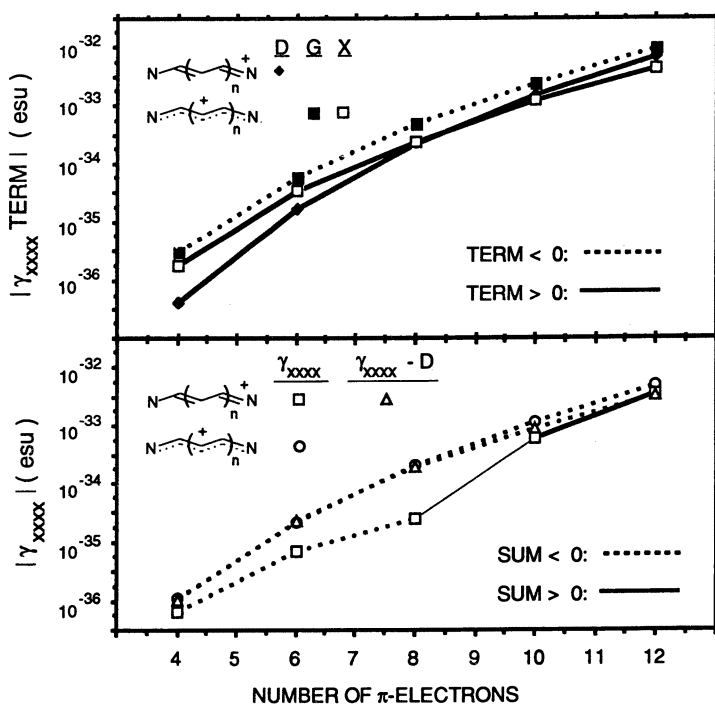


Figure 7. Calculated comparison of γ_{xxxx} and the $G + X + D$ approximation of γ_{xxxx} for the cyanines. (Reproduced with permission from reference 91. Copyright 1991 The International Society for Optical Engineering.)

Since the G and X terms for the symmetric and asymmetric cyanines are virtually identical, it is the D term that distinguishes the $\gamma_\pi(0; 0, 0, 0)$ s of the asymmetric cyanines from those of the symmetric cyanines. This result is also seen in the bottom half of Figure 7, where $\gamma_{xxxx} - D$ for the asymmetric cyanines is nearly equivalent to γ_{xxxx} for the asymmetric cyanines. The calculated change in the sign of $\gamma_\pi(0; 0, 0, 0)$ for the asymmetric cyanines is due to the increasing magnitude of the positive D term with respect to the G and X terms as a function of increasing chain length. The D term is calculated to dominate $\gamma_\pi(0; 0, 0, 0)$ for the longer chain length asymmetric cyanines because its power law dependence is greater than the G and X terms: $|G| \cong |X| \propto N_{\pi-e}^7$ and $|D| \propto N_{\pi-e}^9$.

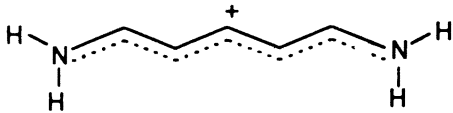
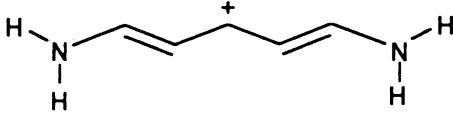
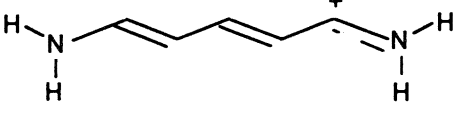
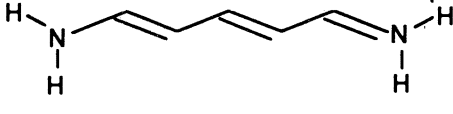
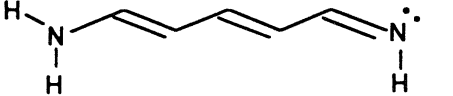
Dependence of $\gamma_\pi(-3\omega; \omega, \omega, \omega)$ and $\beta_\pi(-2\omega; \omega, \omega)$ on Geometry and Protonation for a Linear Cyanine. One of the most interesting results of our calculations is the dramatic effect that molecular geometry has upon the $\gamma_\pi(0; 0, 0, 0)$ s for the linear cyanine cations. Moving between the symmetric geometry with no bond-length alternation and the asymmetric geometry with bond-length alternation can produce large changes in the sign and magnitude of $\gamma_\pi(0; 0, 0, 0)$. This calculated dependence of $\gamma_\pi(0; 0, 0, 0)$ on geometry is further investigated in this section for an all-*trans*-diaminopentamethine cation.

First, we obtained a set of different, consistent geometries that varied in the extent of bond-length alternation. This task was accomplished by calculating optimal geometries for the isolated cation and then in the presence of a negative counterion placed at three different positions along the chain: (1) above the center carbon atom, (2) above the carbon atom next to a terminal nitrogen atom, and (3) above the hydrogen atom attached to a terminal nitrogen atom and *trans* to the carbon chain. The position of the counterion and the planarity of the cyanine were fixed during the optimization process. Additional details on the calculation of the effect of the counterion are given in the preceding subsection on the molecular geometries for the cyanines and polyenes. The following linear optical and NLO properties were then calculated for the four cation geometries with the negative counterion absent: λ_{\max} and the oscillator strength, f , for the $1B^1\pi\pi^* \leftarrow o$ transition; the magnitude of the change in the x -component of the dipole moment associated with this transition, $|\Delta\mu_x|$; the orientationally averaged, π -electronic component of the polarizability tensor, $\langle\alpha_\pi\rangle$; the magnitude of the dot product of the dipole moment vector for the ground state, μ_o , and the π -electronic component of $\beta_{\text{vec}}(-2\omega; \omega, \omega)$, normalized by $|\mu_o|$, $|\beta_{\text{vec}}^\pi\mu_o|/|\mu_o|$; and the orientationally averaged, π -electronic component of $\gamma(-3\omega; \omega, \omega, \omega)$, $\langle\gamma_\pi\rangle$. All polarizabilities were calculated for $\omega = 1.908 \mu\text{m}$.

The calculated linear optical and NLO properties for the different geometries of all-*trans*-diaminopentamethine and for the deprotonated cation are presented in Table V. The linear optical properties of λ_{\max} , f , and $\langle\alpha_x\rangle$ are calculated to change very little as a function of bond-length alternation or geometric asymmetry. However, the second- and third-order nonlinear polarizabilities are very sensitive to the degree of asymmetry. This sensitivity is directly related to the $|\Delta\mu_x|$ that increases with the degree of asymmetry. The fact that $|\omega_{\text{vec}}\pi\mu_o|/|\mu_o|$ is nonzero for the symmetric cyanine geometries reflects the C_{2v} symmetry of these geometries and the existence of an asymmetric polarization along the y -axis in the molecular plane.

Deprotonation of the cyanine cation has a great effect on both its linear optical and NLO properties. While the cyanine cation has two

Table V. Calculated Linear and Nonlinear Optical Properties for Different Geometries of all-*trans*-diaminopentamethine and the Deprotonated Cation

Molecule	λ_{\max} (nm)	f	$ \Delta\mu_x $ (D)	$\langle\alpha_x\rangle$	$ \beta_{\text{vec}}\pi\mu_o / \mu_o $	$\langle\gamma_x\rangle$
	420	1.2	0.0	15	14	-90
	426	1.0	0.0	16	16	-90
	436	1.1	5.4	15	70	-30
	432	0.9	7.2	14	85	+30
	275	0.6	7.1	6	15	+14

NOTE: Units of $\langle\alpha_x\rangle$, $|\beta_{\text{vec}}\pi\mu_o|/|\mu_o|$, and $\langle\gamma_x\rangle$ are 10^{-24} , 10^{-30} , and 10^{-36} esu, respectively.
SOURCE: Reproduced with permission from reference 85. Copyright 1991 The International Society for Optical Engineering.

equivalent, imine-type nitrogen atoms, the deprotonated, neutral cyanine has one imine-type nitrogen atom and one amine-type nitrogen atom. This inequivalence for the deprotonated cyanine leads to a π -electron bonding network, which resembles a polyene network much more than a polymethine network, that is, the $\text{H}_2\text{N}-\text{CH}=(\text{CH}-\text{CH})_2=\text{NH}$ is the more stable electronic structure in a vacuum than the $^+\text{H}_2\text{N}=\text{CH}-(\text{CH}=\text{CH})_2-\text{NH}^-$ structure. As a consequence, the linear optical and NLO properties of the deprotonated cyanine are closer to those of a substituted all-*trans*-hexatriene than to the parent cyanine cation. These theoretical findings are consistent with experimental studies of the effect of pH on the second-order NLO properties of hemicyanine dyes (79).

These calculations suggest (1) that measurements of the NLO polarizabilities of cyanine cations can be used as sensitive probes of their geometries and their environments and (2) a procedure to tune the NLO properties of cyanines by varying the dielectric nature of their environment, and hence their geometries. Clearly, ion placement and pH are calculated to have a large effect on the signs and magnitudes of the second- and third-order polarizabilities for all-*trans*-diaminopentamethine. More work needs to be performed to develop dielectric tuning as a technique for maximizing the second- and third-order polarization responses of materials.

Summary and Conclusions. The π -electron, third-order polarizabilities for a set of polymethines and a set of polyenes were calculated and analyzed in the preceding subsections. The set of polymethines comprised all-*trans*, linear symmetric cyanine and streptocyanine cations with no double-single bond-length alternation, and cyanine cations with asymmetric geometries resulting from the artificial imposition of double-single bond-length alternation. The set of polyenes consisted of all-*trans* linear polyenes with double-single bond-length alternation (80), and all-*trans* linear polyenes with geometries resulting from the artificial imposition of no double-single bond-length alternation. The theoretical analysis consisted of five parts: (1) comparison of the calculated and measured nonresonant γ s for the linear polyenes and streptocyanines; (2) comparison of the calculated $\gamma_\pi(0; 0, 0, 0)$ s for the molecules: effect of terminal methyl group substitution on the γ_π s for the symmetric cyanine cations, effect of bond-length alternation on the signs and magnitudes of the γ_π s, and dependence of $|\gamma_\pi|$ on the number of π -electrons in the molecules and the length of the molecules; (3) identification of the important $^1\pi\pi^*$ states that define $\gamma_\pi(0; 0, 0, 0)$ s for the molecules; (4) identification and analysis of the salient terms contributing to γ_π in the SOS expression for the molecules; and (5) an investigation of the dependence of γ_π , and the π -electronic component of the second-order, electric-dipole polarizability, β_π , on (a) the geometric asymmetry of a

pentamethine cyanine cation, $\text{H}_2\text{N}=\text{CH}=(\text{CH}=\text{CH})_2^+=\text{NH}_2$ and (b) the deprotonation of the cation.

The γ_{π} s of the linear, symmetric, and asymmetric cyanines are calculated to be substantially different from those of the linear polyenes. In regard to the sign of $\gamma_{\pi}(0; 0, 0, 0)$, the symmetric linear cyanines with and without terminal methyl groups all have negative $\gamma_{\pi}(0; 0, 0, 0)$ s; the asymmetric cyanines switch from negative to positive signs as the chain length increases past five carbon atoms; whereas both sets of linear polyenes have positive $\gamma_{\pi}(0; 0, 0, 0)$ s. In regard to the magnitude of $\gamma_{\pi}(0; 0, 0, 0)$, the $|\gamma_{\pi}(0; 0, 0, 0)|$ s for the symmetric linear cyanines start out less than those for the two sets of linear polyenes, but become much greater after the number of π -electrons ($N_{\pi-e}$) exceeds six. This behavior reflects the greater power law dependence of the symmetric cyanines on $N_{\pi-e}$, than that of the linear polyenes, that is, $|\gamma_{\pi}(\text{symmetric cyanines})| \propto N_{\pi-e}^8$, and $|\gamma_{\pi}(\text{linear polyenes})| \propto N_{\pi-e}^{4.0}$. The polymethines in general, and the cyanines in particular, comprise a very interesting class of NLO, π -electron molecules that merit further experimental study.

The origins of the γ_{π} s calculated for cyanines and polyenes can be explained by using a three-term approximation of $\gamma_{xxxx}(0; 0, 0, 0)$, which is the most dominant component of $\gamma_{\pi}(0; 0, 0, 0)$ for the linear molecules. The three terms are G, which is negative and related to the π -electron polarizability of the ground state; X, which is positive and related to the π -electron polarizability of the first strongly one-photon-absorbing π -electron excited state; and D, which is positive and related to the change in dipole between the ground state and the first strongly one-photon-absorbing π -electron excited state. The sign and magnitude of $\gamma_{\pi}(0; 0, 0, 0)$ for the molecules is basically determined by the magnitudes of the positive X and D terms relative to that for the negative G term. In the case of the linear polyenes with bond-length alternation and the symmetric cyanines, the D term is zero and $\gamma_{\pi}(0; 0, 0, 0)$ is determined by the balance between the G and X terms. The positive X term is calculated to be greater than the negative G term for the linear polyenes and so $\gamma_{\pi}(0; 0, 0, 0)$ is positive for these molecules. The ordering of the magnitudes of the X and G terms is reversed for the symmetric cyanines, and so $\gamma_{\pi}(0; 0, 0, 0)$ is negative for these molecules. The ordering of the G and X terms for the linear polyenes can be seen to imply that the π -electron polarizability in the excited state is greater than that in the ground state; whereas the ordering for the symmetric cyanines can be seen to imply that the π -electron polarizability in the ground state is greater than that in the excited state. Although these interpretations are consistent with the delocalized natures of the first strongly one-photon-absorbing π -electron excited state in the linear polyenes (the 1B state) and the ground state in the symmetric cyanines, more work

needs to be done to determine the validity of this interpretation of G and X.

In the case of the asymmetric cyanines, the D term is nonzero, and so $\gamma_{\pi}(0; 0, 0, 0)$ is determined by the balance between the G, X, and D terms. The G and X terms for the symmetric and asymmetric cyanines are calculated to be virtually identical, and thus it is the D term that distinguishes the $\gamma_{\pi}(0; 0, 0, 0)$ s of the asymmetric cyanines from those of the symmetric cyanines. The calculated change in the sign of $\gamma_{\pi}(0; 0, 0, 0)$ for the asymmetric cyanines is due to the increasing magnitude of the positive D term with respect to the G and X terms as a function of increasing chain length. The D term is calculated to dominate $\gamma_{\pi}(0; 0, 0, 0)$ for the longer chain length asymmetric cyanines because its power law dependence on $N_{\pi-e}$ is greater than the G and X terms (i.e., $|G| \cong |X| \propto N_{\pi-e}^{-7}$ and $|D| \propto N_{\pi-e}^{-9}$).

The sign and magnitude of $\gamma_{\pi}(0; 0, 0, 0)$ for a given linear, π -electron molecule is basically determined by the magnitudes of the positive X and D terms relative to that for the negative G term. The optimization of γ_{π} for a π -electron molecule via structural modification should proceed with an awareness of how this modification affects all three terms. For example, the attachment of the strongest π -electron donor and acceptor groups at the ends of a conjugated π -electron bonding network might increase the magnitude of the D term, but might also change the X and G terms such that $|\gamma_{\pi}|$ is diminished. The optimization of γ_{π} is discussed in more detail in the following section.

Perhaps the most interesting result of the calculations is the dramatic effect that molecular geometry has upon the $\gamma_{\pi}(0; 0, 0, 0)$ s for the linear cyanine cations. Moving between the symmetric geometry with no bond-length alternation and the asymmetric geometry with bond-length alternation can produce large changes in the sign and magnitude of $\gamma_{\pi}(0; 0, 0, 0)$. Deprotonation of the cyanine cation has a great effect on both its linear-optical and NLO properties. Calculations of the linear optical and NLO π -electron polarizabilities for a pentamethine cyanine cation in different degrees of geometric asymmetry and protonation suggest (1) that measurements of the NLO polarizabilities of cyanine cations can be used as sensitive probes of their geometries and their environments and (2) a procedure to tune the NLO properties of cyanines by varying the dielectric nature of their environment (e.g., ion type and placement, pH and solvent polarity).

Design of Conjugated π -Electron Molecules for Third-Order NLO Applications

Recall the list of requirements for the third-order NLO materials relevant to optical signal processing that was presented in the second section of

this chapter. Also recall the figure of merit given in equation 6 that defines the optical switching performance of a third-order NLO material. This equation informs us that a combination of (1) a large magnitude for the third-order electric susceptibility tensor, $\chi^{(3)}(\lambda)$; (2) a small linear absorptivity, $\alpha(\lambda)$; and (3) a short lifetime for the third-order polarization response, τ , is desired at the operating light wavelength, λ , for the given device.

As discussed in the preceding sections, materials composed of π -electron conjugated organic molecules are worthy candidates for third-order NLO applications. In the case where λ is not near the resonance wavelength for an electronic transition within these molecules, two of the three objectives relating to the figure of merit are met almost automatically: small $\alpha(\lambda) < 1 \text{ cm}^{-1}$ and small $\tau \sim 10^{-15} - 10^{-14} \text{ s}$. The critical question is whether the magnitude of the real component of $\chi^{(3)}(\lambda)$ is large enough for the given device. The magnitude required for the given device application depends on the optical path length and the light intensity (electric-field strength) within the device. Of course, it is preferred that the optical path length and light intensity be kept as short and low as possible.

Based on the theoretical analysis of the linear cyanines and polyenes presented in the preceding section, a set of design guidelines can be formulated to assist in the optimization of conjugated π -electron organic molecules for third-order NLO applications. These guidelines are derived from two important equations: (1) the relation between the macroscopic third-order polarization, $\chi^{(3)}(-\omega_{\text{pol}}; \omega_1, \omega_2, \omega_3)$ and the product, $N \cdot \langle \gamma(-\omega_{\text{pol}}; \omega_1, \omega_2, \omega_3) \rangle \cdot L_3(\omega_{\text{pol}}, \omega_1, \omega_2, \omega_3)$, in equation 16 and (2) the three-term approximation of $\gamma_{xxxx}(0; 0, 0, 0)$ shown in equation 23 and Table IV, $\gamma_{xxxx}(0; 0, 0, 0) \cong G + X + D$. The maximization of $\chi^{(3)}(-\omega_{\text{pol}}; \omega_1, \omega_2, \omega_3)$ can then be divided into two parts: a component external to the molecular unit given by $N \cdot L_3(\omega_{\text{pol}}, \omega_1, \omega_2, \omega_3)$ and a component internal to the unit represented by $\gamma(-\omega_{\text{pol}}; \omega_1, \omega_2, \omega_3)$.

Guideline 1: Maximize N . The most direct manner to increase $|\chi^{(3)}(-\omega_{\text{pol}}; \omega_1, \omega_2, \omega_3)|$ is to increase the number density of the molecular units. The packing of the molecular units in a crystal is the most efficient approach to maximize N , but there are problems with controlling the orientation of the units. The attachment of side groups like alkyl side chains is to be avoided because it will lower N without contributing much to either the linear or nonlinear polarization response. If the use of side groups cannot be avoided, then these groups should be selected with careful attention given to their third-order polarizabilities.

Guideline 2: Align Molecular Units. The alignment of the molecular units is critical to engineering the second-order NLO properties

of materials, and it is also important to maximizing their third-order NLO properties. The alignment of linear conjugated π -electron organic molecules eliminates the fivefold diminution in $\gamma(-\omega_{\text{pol}}; \omega_1, \omega_2, \omega_3)$ associated with the orientational averaging of the molecular units. The alignment of these units should also preserve their planarity so that the π -electron bonding network is not disrupted. As discussed in Chapter 8 in this book, the ordering of materials at the molecular level is not a trivial task. There are device applications where an isotropic distribution of the molecular units within the material is preferred so that several elements of the γ -tensor can be utilized.

Guideline 3: Select Molecular Units with Large Linear Polarizabilities. A molecule must have a large linear polarizability in the ground electronic state in order to have large nonlinear polarizabilities. This condition is indicated by the three-term approximation of $\gamma_{xxxx}(0; 0, 0, 0)$ shown in equation 23, where the prefactor of the approximation is the π -electron linear polarizability for the ground electronic state. According to the Kramers–Kronig transform, molecules with low-lying, strongly one-photon-absorbing electronic states will have large linear polarizabilities in the ground state. In other words, a molecule with λ_{max} at long wavelengths and a light extinction coefficient very large at λ_{max} (e.g., a dye molecule) will have a large linear polarizability. The challenge in working with these types of molecules is keeping the linear and nonlinear absorption of light low in the wavelength region of interest for device operation.

Guideline 4: Select Molecular Units with Linear Geometries. Molecules with one-dimensional, or quasi-one-dimensional bonding networks tend to have the largest linear optical and NLO responses to linearly polarized radiation fields because the polarization of the molecular unit is constrained along a single axis. For example, as shown in Table II, the third-order polarizability for benzene is less than that for all-*trans* hexatriene with all radiation fields linearly polarized in the same direction. Table II also shows that all-*trans* polyenes have greater $|\gamma|$'s than those with *cis* configurations.

Guideline 5: Consider Linear Molecular Units with Conjugated π -Electron Bonding Networks. The polyene and polymethine conjugated π -electron bonding networks, discussed in the preceding section, as well as thiophene, acetylene, cumulene, and other π -electron conjugated molecular systems, are distinct candidates for third-order NLO applications. The polymethine network in symmetric cyanine cations is calculated to have a greater $|\gamma_{\pi}(0; 0, 0, 0)|$ than the polyene network in linear polyenes of comparable size, number of π -electrons, and amount of methylation. This difference is due to the greater

ionic character (π -electron delocalization) of the cyanine cation ground electronic state with respect to that of the linear polyene ground electronic state. The symmetric linear cyanine cations are therefore preferred over the linear polyenes on the basis of their values of $|\gamma_{\pi}(0; 0, 0, 0)|$ and the greater power law dependence of $|\gamma_{\pi}(0; 0, 0, 0)|$ on chain length.

However, if one also considers chemical stability and transparency at a given wavelength, then the linear polyenes have an advantage. The additional consideration of the electronic absorption bandwidths factors the cyanine cations. Also, the negative sign of $\gamma_{\pi}(0; 0, 0, 0)$ calculated for the symmetric linear cyanine cations is an advantage because a negative sign results in self-defocusing of incident light, thereby increasing the amount of incident light intensity that can be borne by the material before reaching the optical damage threshold. Conversely, the positive sign of $\gamma_{\pi}(0; 0, 0, 0)$ calculated for the linear polyenes results in self-focusing and a decrease in the amount of incident light intensity that can be borne by the material before reaching the optical damage threshold.

Guideline 6: Adjust Electric Fields Internal and External to the Molecular Unit. Electric fields internal and external to the molecular unit polarize the unit and localize electron density. Localization of electron density can be helpful in increasing the contribution of the change in dipole moment associated with the transition from the ground state to a CT state, but at the same time, this localization can decrease the linear polarizability of the ground electronic state, which is the prefactor to $\gamma_{xxxx}(0; 0, 0, 0)$ in equation 23.

Internal electric fields are strongly influenced by the attachment of π -electron donor and acceptor groups to the conjugated π -electron bonding network. Too strong a donor and acceptor can result in too large an internal electric field, which then diminishes the linear polarizability of the ground state. Local external electric fields are largely determined by the dielectric environment of the molecular unit (e.g., solvent polarity or the type, concentration, and placement of ions). The calculated sensitivity of the NLO properties of the symmetric cyanine cations to the position of the negative counterion shown in Table V underscores the importance of adjusting the dielectric environments of these molecules.

The interdependence of the molecular electronic properties that define the two-state approximation to $\beta_{xxx}(0; 0, 0)$ and the three-state approximation to $\gamma_{xxxx}(0; 0, 0, 0)$ is examined here with particular regard to the effect of electric fields. The two-state approximation to $\beta_{xxx} \equiv \beta_{xxx}(0; 0, 0)$ is (143, 144)

$$\beta_{xxx} \propto |\mu_{o,CT}|^2(\mu_{CT} - \mu_o)/\Delta E_{o,CT}^2 \quad (24a)$$

or

$$\beta_{xxx} \propto \alpha_{o\pi}(\mu_{CT} - \mu_o)/\Delta E_{o,CT} \quad (24b)$$

where $\mu_{o,CT}$ is the transition dipole moment between the ground state (o) and the π -electron CT state, $\mu_{CT} - \mu_o$ is the difference in permanent dipole moments between the CT and o states, $\Delta E_{o,CT}$ is the transition energy between these states, and $\alpha_{o\pi}(\propto |\mu_{o,CT}|^2/\Delta E_{o,CT})$ is the π -electron component of the ground-state linear polarizability within the two-state approximation. For a given pair of π -electron donor and acceptor groups, $\mu_{o,CT}$, $\mu_{CT} - \mu_o$, and $1/\Delta E_{o,CT}$, and hence β_{xxx} , increase in magnitude with the increasing length of the conjugated π -electron bonding network that bridges the groups. However, for a π -electron bridge of given length, the peak magnitudes of $\mu_{o,CT}$, $\mu_{CT} - \mu_o$, and $1/\Delta E_{o,CT}$ as functions of π -electron donor-acceptor strength do not coincide (145). Therefore, one must be careful in seeking to maximize $|\beta_{xxx}|$ by single-mindedly maximizing $|\mu_{CT} - \mu_o|$, which is proportional to the π -electron donor-acceptor strength. The ratio, $|\mu_{o,CT}|^2/\Delta E_{o,CT}$, is proportional to the linear π -electron polarizability of the ground state, and as stated above, the maximization of $|\mu_{CT} - \mu_o|$ will localize electron density and thereby reduce $|\mu_{o,CT}|^2/\Delta E_{o,CT}$. Thus, $\mu_{o,CT}$, $\mu_{CT} - \mu_o$, and $\Delta E_{o,CT}$ are strongly coupled and are determined by the nature of the π -electron-bridging network, as well as the π -electron donor and acceptor groups (internal electric fields) and external electric fields. Synthetic strategies seeking to maximize $|\beta_{xxx}|$ should be prepared to manipulate all three of the molecular electronic properties in equation 24.

The coupling between permanent state dipole moments (μ_i), transition dipole moments ($\mu_{i,j}$), and transition energies ($\Delta E_{i,j}$) for π -electron ground and excited states becomes even more significant for $\gamma_{xxxx} \equiv \gamma_{xxxx}(0; 0, 0, 0)$. The reason is that unlike β_{xxx} , the γ_{xxxx} for a polar, conjugated π -electron molecule is generally not approximated well by a single term involving $\mu_{i,j}$'s, μ_i 's and $\Delta E_{i,j}$'s, but by a sum of three terms involving the properties of the ground state and at least two excited states (see equation 23 and Table IV) (28, 91, 140):

$$\gamma_{xxxx} \propto [-|\mu_{o,ex1}|^4/\Delta E_{o,ex1}^3 + (|\mu_{o,ex1}|/\Delta E_{o,ex1})^2(|\mu_{ex1,ex2}|^2/\Delta E_{o,ex2}) + (|\mu_{o,ex1}|/\Delta E_{o,ex1})^2(|\mu_{ex1} - \mu_o|^2/\Delta E_{o,ex1})] \quad (25a)$$

or

$$\gamma_{xxxx} \propto \alpha_{o\pi}[-(|\mu_{o,ex1}|/\Delta E_{o,ex1})^2 + (|\mu_{ex1,ex2}|^2/\Delta E_{o,ex2}\Delta E_{o,ex1}) + (|\mu_{ex1} - \mu_o|/\Delta E_{o,ex1})^2] \quad (25b)$$

where $ex1$ and $ex2$ are the two excited states, $\alpha_{o\pi}(\propto |\mu_{o,ex1}| \propto^2 / \Delta E_{o,ex1})$ is the π -electron component of the ground-state linear polarizability within the three-state approximation, and all other parameters are as defined in equation 24. The right-most term in equation 25 is absent for a non-polar molecule. The sum of the negative (G) term and the positive terms (X + D), combined with the fact that each term contains $\mu_{i,j}$, μ_i , and $1/\Delta E_{i,j}$ raised to high powers, means that γ_{xxxx} can be very sensitive to subtle changes in the π -electron bonding network, the strengths of the π -electron donor and acceptor groups, and external electric fields of the local environment. Synthetic strategies that seek to maximize $|\gamma_{xxxx}|$ should be capable of modifying the electronic and nuclear structure of the candidate molecule in a very controlled manner.

One way to modify the electronic and nuclear structure of a polar molecule is to change the polarity of the solvent in which the molecule is dissolved (i.e., change the dipole moment of the solvent molecules and their associated electric fields). Consider the linear merocyanines. It is known that λ_{max} for the merocyanines shifts dramatically to longer wavelength with increasing solvent polarity (76, 77). The origin of this effect lies with the stabilization of the highly polar π -electronic state, ${}^+H_2N=CH-(CH=CH)_n-O^-$, relative to the less polar π -electronic state, $H_2N-CH=(CH-CH)_n=O$ (76, 77). In other words, the greater the polarity of the solvent, the more the ground electronic state resembles the highly polar π -electronic state. It is assumed that the ground state can be tuned between the two valence bond structures by varying the solvent polarity. This assumption needs to be investigated further, and is discussed in Chapter 8 in this book.

Guideline 7: Adjust pH Where Applicable. The adjustment of pH is relevant only to the symmetric cyanine cations and similar molecules. As shown in Table V for the pentamethine cyanine, the deprotonated neutral cyanine has a calculated $|\langle\gamma_\pi\rangle|$ and $|\beta_{vec}^\pi \mu_o|/|\mu_o|$ less than the protonated symmetric cyanine cation. The cyanine cation has two equivalent, imine-type nitrogen atoms, whereas the deprotonated, neutral cyanine has one imine-type nitrogen atom and one amine-type nitrogen atom. This inequivalence for the deprotonated cyanine leads to a π -electron bonding network that resembles a polyene-bonding network much more than a polymethine network (i.e., the $H_2N-CH=(CH-CH)_2=NH$ form becomes the more stable electronic structure in a vacuum than the ${}^+H_2N=CH-(CH=CH)_2-NH^-$ structure). As a consequence, the linear optical and NLO properties of the deprotonated cyanine are closer to those of a substituted all-*trans*-hexatriene than to the parent cyanine cation. These theoretical findings are consistent with experimental studies of the effect of pH on the second-order NLO properties of hemicyanine dyes (79). In summary, pH and solvent-polarity

tuning are predicted to be two effective approaches to the controlled adjustment of the third-order NLO properties of conjugated π -electron organic molecules.

Outlook for Linear Conjugated π -Electron Organic Molecules. An upper bound on the magnitude of $\chi^{(3)}(0; 0, 0, 0)$ for materials consisting of linear conjugated molecules can be estimated. First, assume the maximum possible number density of 6.023×10^{23} molecules/cm³, with all linear units aligned along the same axis. Second, select an operating wavelength of $1.5 \mu\text{m}$ (~ 0.8 eV) for device application. This wavelength is selected because it is optimal for transmission through silica-based optical fibers. Third, consider the symmetric linear cyanine cations because of their exceptionally large calculated $\gamma_{\pi}(0; 0, 0, 0)$'s. Fourth, assume a $|\gamma_{\pi}(0; 0, 0, 0)|$ of 10^{-32} statcoul cm⁴/statV³ projected for a symmetric cyanine cation with 14 π -electrons (see Figure 2). A cyanine of this size is chosen because it is predicted to be transparent in the condensed phase at $1.5 \mu\text{m}$. Longer cyanines would certainly have larger $|\gamma_{\pi}(0; 0, 0, 0)|$ s, but would also be less transparent at $1.5 \mu\text{m}$. It is also assumed that the 14 π -electron cyanine remains linear and planar at the number density of 6.023×10^{23} molecules/cm³.

The combination of $N = 6.023 \times 10^{23}$ molecules/cm³ and $|\gamma_{\pi}(0; 0, 0, 0)| = 10^{-32}$ statcoul cm⁴/statV³ yields

$$|\chi^{(3)}(0; 0, 0, 0)| \cong 6 \times 10^{-9} \text{ statcoul cm/statV}^3$$

This upper bound on $|\chi^{(3)}(0; 0, 0, 0)|$ is a very generous one assuming an unrealistic-number density of 6.023×10^{23} molecules/cm³ and still it is not enough for device applications that require $|\chi^{(3)}(0; 0, 0, 0)|$ to be at least 10^{-8} statcoul cm/statV³. Thus, trade-offs between $\alpha(\lambda)$, τ and $|\chi^{(3)}(\lambda)|$ will have to be made as the resonance enhancement of $|\chi^{(3)}(\lambda)|$ as well as other approaches are explored. Trade-offs concerning τ are possible because of parallel-processing alternatives to serial processing. In the case of the linear symmetric cyanine cation with 12 π -electrons, the calculated value of $\gamma_{\pi}(-3\omega; \omega, \omega, \omega)$ at $\omega = 1.91 \mu\text{m}$ is $\sim 10^2$ times that of $\gamma_{\pi}(0; 0, 0, 0)$. The utilization of resonance enhancement requires a detailed understanding of the natures of the low-lying excited electronic states of the candidate conjugated π -electron organic molecules. Garito and co-workers have considered the concept of excited-state enhancement both theoretically (149) and experimentally (150). They have investigated the γ response of a dioxane solution of α, ω -diphenylhexatriene molecules pumped into the $2A_g$ and $1B_u$ states. The γ response at 1064 nm was measured to be 10^{-32} esu, which is more than 100 times as large as the response in the ground state (150).

Acknowledgments

I thank Jean-Marie André, Kenn Bates, David Beratan, Robert R. Birge, Jean-Luc Bredas, Chris Bubeck, Joseph Delhalle, T. Kirk Dougherty, Joseph Fripiat, Chris Gorman, Manuel Joffre, Francois Kajzar, Marvin Klein, Christoph Kuhn, Isabel Ledoux, Seth Marder, Joseph Perry, Germain Puccetti, Daniel Rytz, Hideo Sekino, Zhigang Shuai, Richard Wing, and Joseph Zyss for very helpful discussions. Special thanks to Thomas Cooper for his critical reading of the manuscript and to the reviewers for their constructive comments.

References

1. Bloembergen, N. *Nonlinear Optics*; Benjamin: New York, 1965.
2. Zernike, F.; Midwinter, J. E. *Applied Nonlinear Optics*; Wiley: New York, 1973.
3. Shen, Y. R. *The Principles of Nonlinear Optics*; Academic: New York, 1984.
4. Yariv, A.; Yeh, P.; *Optical Waves in Crystals. Propagation and Control of Laser Radiation*; Wiley: New York, 1984.
5. Gibbs, H. M. *Optical Bistability: Controlling Light with Light*; Academic: Orlando, FL, 1985.
6. *Optical Bistability*; Bowden, C. M.; Ciftan, M.; Robl, H. R., Eds.; Plenum: New York, 1981.
7. *Optical Phase Conjugation*; Fisher, R., Ed.; Academic: Orlando, FL, 1983.
8. Weis, R. S.; Gaylord, T. K. *Appl. Phys. A* 1985, 37, 191.
9. Lines, M. E.; Glass, A. M. *Principles and Applications of Ferroelectrics and Related Materials*; Clarendon: Oxford, England, 1977.
10. Klein, M. B.; Dunning, G. J.; Valley, G. C.; Lind, R. C.; O'Meara, T. R. *Opt. Lett.* 1986, 11, 575.
11. Valley, G. C.; Klein, M. B. *Opt. Eng.* 1983, 22, 704.
12. Sauteret, C.; Hermann, J. P.; Frey, R.; Pradere, F.; Ducuing, J.; Chance, R. R.; Baughman, R. H. *Phys. Rev. Lett.* 1976, 36, 956.
13. Kajzar, F.; Messier, J. In *Nonlinear Optical Properties of Organic Molecules and Crystals*, Chemla, D. S.; Zyss, J., Eds.; Academic: Orlando, FL, 1987; Vol. 2, pp. 51–83.
14. Carter, G. M.; Chen, Y. J.; Rubner, M. F.; Sandman, D. J.; Thakur, M. K.; Tripathy, S. K. In *Nonlinear Optical Properties of Organic Molecules and Crystals*; Chemla, D. S.; Zyss, J., Eds.; Academic: Orlando, FL, 1987; Vol. 2, pp. 85–119.
15. Kuzyk, M. G.; Paek, U. C.; Dirk, C. W. *Appl. Phys. Lett.* 1991, 59, 902.
16. Kuzyk, M. G.; Andrews, M. P.; Paek, U. C.; Dirk, C. W. In *Nonlinear Optical Properties of Organic Materials IV*; Singer, K. D., Ed.; SPIE Proceedings 1560, The International Society for Optical Engineering: Bellingham, WA, 1991; pp 44–53.
17. *Nonlinear Optical Properties of Organic Materials IV*, Singer, K. D., Ed.; SPIE Proceedings 1560, The International Society for Optical Engineering: Bellingham, WA, 1991.
18. *Materials for Nonlinear Optics: Chemical Perspectives*, Marder, S. R.; Sohn, J. E.; Stucky, G. D., Eds.; ACS Symposium Series 455; American Chemical Society: Washington, DC, 1991.

19. *Nonlinear Optical Properties of Organic Materials III*; Khanarian, G., Ed.; SPIE Proceedings 1137; The International Society for Optical Engineering: Bellingham, WA, 1991.
20. *Nonlinear Optical Properties of Polymers*; Heeger, A. J.; Orenstein, J.; Ulrich, D. R., Eds.; Materials Research Society Symposium Proceedings 109; Materials Research Society: Pittsburgh, PA, 1988.
21. *Nonlinear Optical and Electroactive Polymers*; Prasad, P. N.; Ulrich, D. R., Eds.; Plenum: New York, 1988.
22. Chemla, D. S.; Zyss, J. *Nonlinear Optical Properties of Organic Molecules and Crystals*; Academic: Orlando, FL, 1987.
23. Kirtman, B.; Hasan, M. J. *Chem. Phys.* **1992**, *96*, 470.
24. McGraw, D. J.; Siegman, A. E.; Wallraff, G. M.; Miller, R. D. *Appl. Phys. Lett.* **1989**, *54*, 1713.
25. Yaron D.; Silbey, R. J. *J. Chem. Phys.* **1991**, *95*, 563.
26. André, J.-M.; Delhalle, J. *Chem. Rev.* **1991**, *91*, 843.
27. Bishop, D. *Rev. Mod. Phys.* **1990**, *62*, 343.
28. Dirk, C. W.; Cheng, L. T.; Kuzyk, M. G. *Int. J. Quantum Chem.* **1992**, *43*, 27.
29. Kuzyk, M. G.; Dirk, C. W. *Phys. Rev. A* **1990**, *41*, 5098.
30. Dirk, C. W.; Kuzyk, M. G. *Phys. Rev. A* **1989**, *39*, 1219.
31. Flytzanis, C. In *Nonlinear Optical Properties of Organic Molecules and Crystals*, Chemla, D. S.; Zyss, J., Eds.; Academic: Orlando, FL, 1987; Vol. 2, pp 121–135.
32. Shuai, Z.; Bredas, J.-L. *Phys. Rev. B* **1991**, *44*, 5962.
33. Heflin, J. R.; Wong, K. Y.; Zamani-Khamiri, O.; Garito, A. F. *Phys. Rev. B* **1988**, *38*, 1573.
34. Garito, A. F.; Heflin, J. R.; Wong, K. Y.; Zamani-Khamiri, O. In *Nonlinear Optical Properties of Polymers*; Heeger, A. J.; Orenstein, J.; Ulrich, D. R., Eds.; Materials Research Society Symposium Proceedings 109, Materials Research Society: Pittsburgh, PA, 1988; pp 91–102.
35. Hurst, G. J. B.; Dupuis, M.; Clementi, E. *J. Chem. Phys.* **1989**, *89*, 385.
36. deMelo, C. P.; Silbey, R. *J. Chem. Phys.* **1988**, *88*, 2567.
37. Beratan, D. N.; Onuchic, J. N.; Perry, J. W. *J. Phys. Chem.* **1987**, *91*, 2696.
38. Karna, S. P.; Talapatra, G. B.; Wijehun, W. M. K. P.; Prasad, P. N. *Phys. Rev. A* **1992**, *45*, 2763.
39. Karna, S. P.; Talapatra, G. B.; Prasad, P. N. *J. Chem. Phys.* **1991**, *95*, 5873.
40. Cheng, L. T.; Tam, W.; Stevenson, S. H.; Meredith, G. R.; Rikken, G.; Marder, S. R. *J. Phys. Chem.* **1991**, *95*, 10631.
41. Cheng, L. T.; Tam, W.; Marder, S. R.; Stiegman, A. E.; Rikken, G.; Spangler, C. W. *J. Phys. Chem.* **1991**, *95*, 10643.
42. Burland, D. M.; Kajzar, F.; Sentein, C.; Walsh, C. *J. Opt. Am. Soc. B* **1991**, *8*, 2269.
43. Shelton, D. P. *J. Am. Opt. Soc. B* **1989**, *6*, 830.
44. Norwood, R. A.; Sounik, J. R. *Appl. Phys. Lett.* **1992**, *60*, 295.
45. Vanheek, J. B.; Kajzar, F.; Albrecht, A. C. *J. Chem. Phys.* **1991**, *95*, 6400.
46. Nunzi, J. N.; Charra, F. *Appl. Phys. Lett.* **1991**, *59*, 13.
47. Neher, D.; Kaltbeitzel, A.; Wolf, A.; Bubeck, C.; Wegner, G. *J. Phys. D* **1991**, *24*, 1193.
48. Aramaki, S.; Torruellas, W.; Zaroni, R.; Stegeman, G. I. *Opt. Commun.* **1991**, *85*, 527.
49. Zhao, M. T.; Cui, Y.; Samoc, M.; Prasad, P. N.; Unroe, M. R.; Reinhardt, B. A. *J. Chem. Phys.* **1991**, *95*, 3991.

50. Pang, Y.; Samoc, M.; Prasad, P. N. *J. Chem. Phys.* **1991**, *94*, 5282.
51. Lupke, G.; Marowsky, G. *Appl. Phys. B* **1991**, *53*, 71.
52. Amano, M.; Kaino, T.; Matsumoto, S. *Chem. Phys. Lett.* **1990**, *170*, 515.
53. Kubodera, K.; Kobayashi, H. *Mol. Crystallog. Liq. Crystallog.* **1990**, *182*, 103.
54. Sakui, T.; Kawabe, Y.; Ikeda, H.; Kawasaki, K. *Appl. Phys. Lett.* **1990**, *56*, 411.
55. Hinton, H. S. *IEEE Spectrum* **1992**, February, 42–45.
56. Stegeman, G. I.; Wright, E. M. *Opt. Quantum Electron.* **1990**, *22*, 95.
57. Stegeman, G. I.; Zanoni, R.; Seaton, C. T. In *Nonlinear Optical Properties of Polymers*; Heeger, A. J.; Orenstein, J.; Ulrich, D. R., Eds.; Materials Research Society Symposium Proceedings 109; Materials Research Society: Pittsburgh, PA, 1988; pp 53–64.
58. Bredas, J. L.; Adant, C.; Tackx, P.; Persoons, A.; Pierce, B. M. *Chem. Rev.* **1994**, *94*, 243.
59. Nunzi, J. M.; Charra, F. In *Organic Molecules for Nonlinear Optics and Photonics*; Messier, J.; Kajzar, F.; Prasad, P., Eds.; NATO ASI Series, Vol. 194; Kluwer: Dordrecht, the Netherlands, 1991; pp 345–357.
60. Friberg, S. R.; Smith, P. W. *IEEE J. Quant. Electr.* **1987**, *23*, 2089.
61. Stolen, R. H.; Lin, C. *Phys. Rev. A* **1978**, *17*, 1448.
62. Lines, M. E. *J. Appl. Phys.* **1991**, *69*, 6876.
63. Astill, A. G. *Thin Solid Films*, **1991**, *204*, 1.
64. Hurst, M.; Munn, R. W. *J. Mol. Electron.* **1986**, *2*, 35.
65. Hurst, M.; Munn, R. W. *J. Mol. Electron.* **1986**, *2*, 43.
66. Hurst, M.; Munn, R. W. *J. Mol. Electron.* **1986**, *2*, 101.
67. Armstrong, J. A.; Bloembergen, N.; Ducuing, J.; Pershan, P. S. *Phys. Rev.* **1962**, *127*, 1918.
68. Levine, B. F.; Bethea, C. G. *J. Chem. Phys.* **1975**, *63*, 2666.
69. Buckingham, A. D.; Stephen, M. J. *Trans. Faraday Soc.* **1957**, *53*, 884.
70. Monson, P. R.; McClain, W. M. *J. Chem. Phys.* **1970**, *53*, 29.
71. Mazely, T. L.; Hetherington, W. M., III *J. Chem. Phys.* **1987**, *87*, 1962.
72. Kleinman, D. A., *Phys. Rev.* **1962**, *126*, 1977.
73. Buckingham, A. D.; Orr, B. J. *Chem. Soc. Quart. Rev. (London)* **1967**, *21*, 195 (1967).
74. Böttcher, C. J. F. *Theory of Electric Polarization*; Elsevier: Amsterdam, the Netherlands, 1952.
75. Ward, J. *Rev. Mod. Phys.* **1965**, *37*, 1.
76. Brooker, L. G. S.; Keyes, G. H.; Sprague, R. H.; VanDyke, R. H.; VanLane, E.; Van Zandt, G.; White, F. L.; Cressman, H. W. J.; Dent, S. G., Jr. *J. Am. Chem. Soc.* **1951**, *73*, 5336.
77. McRae, E. G. *Spectrochim. Acta* **1958**, *12*, 192.
78. Marder, S. R.; Cheng, L. A.; Tiemann, B. G.; Beratan, D. N. In *Nonlinear Optical Organic Materials IV*; SPIE Proceedings 1560; The International Society for Optical Engineering: Bellingham, WA, 1991; pp. 86–97.
79. Xiao, X.; Vogel, U.; Shen, Y. R.; Marowsky, G. *J. Chem. Phys.* **1991**, *94*, 2315.
80. Pierce, B. M. *J. Chem. Phys.* **1989**, *91*, 791.
81. Spano, F. C.; Mukamel, S. *Phys. Rev. Lett.* **1991**, *66*, 1197.
82. Hagler, T. W.; Heeger, A. J. *Chem. Phys. Lett.* **1992**, *189*, 333.
83. Yablonovitch, E.; Leung, K. M. *Nature (London)* **1991**, *351*, 278.
84. Salem, L. *The Molecular Orbital Theory of Conjugated Systems*; Benjamin: New York, 1966.

85. Tavan, P.; Schulten, K. *J. Chem. Phys.* **1986**, *85*, 6602.
86. Birge, R. R.; Pierce, B. M. *J. Chem. Phys.* **1979**, *70*, 185.
87. Li, D.; Ratner, M. A.; Marks, T. J. *J. Am. Chem. Soc.* **1988**, *110*, 1707.
88. Dirk, C. W.; Twieg, R. J.; Wagniere, G. *J. Am. Chem. Soc.* **1986**, *108*, 5387.
89. Hermann, J. P.; Ducuing, J. *J. Appl. Phys.* **1974**, *45*, 5100.
90. Orr, B. J.; Ward, J. F. *Mol. Phys.* **1971**, *20*, 513.
91. Pierce, B. M. In *Nonlinear Optical Properties of Organic Materials IV*; Singer, K. D., Eds.; SPIE Proceedings 1560; The International Society for Optical Engineering: Bellingham, WA, 1991; pp 148–161.
92. Cohen, H. D.; Roothan, C. C. J. *J. Chem. Phys.* **1965**, *43*, S34.
93. Kurtz, H.; Stewart, J.; Dieter, K. *J. Comp. Chem.* **1990**, *11*, 82.
94. Williams, G. J. *Mol. Struct. (Theochem)* **1987**, *151*, 215.
95. Dodds, J. L.; McWeeny, R.; Raynes, W. T.; Riley, J. P. *Mol. Phys.* **1977**, *33*, 611.
96. Papadopoulos, M. G.; Waite, J.; Nicolaidis, C. A. *J. Chem. Phys.* **1982**, *77*, 2527.
97. Sekino, H.; Bartlett, R. J. *J. Chem. Phys.* **1986**, *85*, 976.
98. Langhoff, P. W.; Epstein, S. T.; Karplus, M. *Rev. Mod. Phys.* **1972**, *44*, 602.
99. Rice, J. E.; Handy, N. C. *J. Chem. Phys.* **1991**, *94*, 4959.
100. Albertson, P.; Jorgensen, P.; Yeager, D. L. *Mol. Phys.* **1980**, *41*, 409.
101. Jazunski, M.; McWeeny, R. *Mol. Phys.* **1982**, *46*, 863.
102. Bishop, D. M.; Kirtman, B. *J. Chem. Phys.* **1991**, *95*, 2646.
103. Beratan, D. N. In *Materials for Nonlinear Optics: Chemical Perspectives*; Marder, S. R.; Sohn, J. E.; Stucky, G. D., Eds.; ACS Symposium Series 455; American Chemical Society: Washington, DC, 1991; pp 89–102.
104. Birge, R. R.; Pierce, B. M. *Int. J. Quantum Chem.* **1986**, *29*, 639.
105. Masthay, M. B.; Findsen, L. A.; Pierce, B. M.; Bocian, D. F.; Lindsey, J. S.; Birge, R. R. *J. Chem. Phys.* **1986**, *84*, 3901–3914.
106. Williams, D. E.; Houpt, D. J. *Acta Crystallogr.* **1986**, *B42*, 286.
107. Briggs, J. M.; Matsui, T.; Jorgensen, W. L. *J. Comput. Chem.* **1990**, *11*, 958.
108. Jorgensen, W. L.; Chandrasekhar, J.; Madura, J. D.; Impey, R. W.; Klein, M. L. *J. Chem. Phys.* **1983**, *79*, 926.
109. Straatsma, T. P.; McCammon, J. A. *J. Comput. Chem.* **1990**, *11*, 943.
110. Ryckaert, J. P.; Ciccotti, G.; Berendsen, H. J. C. *J. Comput. Phys.* **1977**, *23*, 327.
111. Stewart, J. J. P. *J. Comput. Aided Mol. Des.* **1990**, *4*, 1.
112. Hehre, W. J.; Radom, L.; Schleyer, P. v. R.; Pople, J. A. *Ab-Initio Molecular Orbital Theory*; Wiley: New York, 1986.
113. Parr, R. G.; Yang, W. *Density-Functional Theory of Atoms and Molecules*; Oxford University: New York, 1989.
114. Pople, J. A.; Beveridge, D. A. *Approximate Molecular Orbital Theory*; McGraw-Hill: New York, 1970.
115. Ohno, K. *Theor. Chim. Acta* **1964**, *2*, 219.
116. Del Bene, J.; Jaffé, H. H. *J. Chem. Phys.* **1968**, *48*, 1807, 4050; **1968**, *49*, 1221.
117. Sichel, J. M.; Whitehead, M. A. *Theor. Chim. Acta* **1967**, *7*, 32.
118. Birge, R. R.; Bennett, J. A.; Hubbard, L. A.; Fang, H. L.; Pierce, B. M.; Kliger, D. S.; Leori, G. E. *J. Am. Chem. Soc.* **1982**, *104*, 2519.
119. Tavan, P.; Schulten, K. *J. Chem. Phys.* **1979**, *70*, 5407.
120. Tavan, P.; Schulten, K. *Phys. Rev. B* **1987**, *36*, 4337.

121. Hudson, B.; Kohler, B. E.; Schulten, K. In *Excited States*; Lim, E. C., Ed.; Academic: Orlando, FL, 1982; Vol. 6, pp 1–52.
122. Schulten, K.; Dinur, U.; Honig, B. J. *Chem. Phys.* **1980**, *73*, 3927.
123. Momicchioli, F.; Baraldi, I.; Ponterini, G.; Berthier, G. *Spectrochim. Acta* **1990**, *46*, 775.
124. Kuhn, H. J. *Chem. Phys.* **1949**, *17*, 1198.
125. André, J. M. Ms.Sc. Thesis, Universitaire Catholique de Louvain, Leuven, Belgium, 1965.
126. Bodar, V. P.; Delhalle, J.; André, J. M. In *Conjugated Polymeric Materials: Opportunities in Electronics, Optoelectronics, and Molecular Electronics*; Bredas, J. L.; Chance, R. R., Eds.; Kluwer: Dordrecht, the Netherlands, 1990; pp. 509–516.
127. Malhotra, S. S.; Whiting, M. C. J. *Chem. Soc.* **1960**, 3812.
128. Kohler, B. E. *J. Chem. Phys.* **1990**, *93*, 5838.
129. Stevenson, S. H.; Donald, D. S.; Meredith, G. R. In *Nonlinear Optical Properties of Polymers*; Heeger, A. J.; Orenstein, J.; Ulrich, D. R., Eds.; Materials Research Society Symposium Proceedings, 109; Materials Research Society: Pittsburgh, PA, 1988; pp 103–198.
130. Rustagi, K. C.; Ducuing, J. *Opt. Comm.* **1974**, *10*, 258.
131. Kuhn, C. *Synth. Met.* **1991**, *41–43*, 3681.
132. Matsumoto, S.; Kubodera, K.; Kurihara, T.; Kaino, T. *Opt. Commun.* **1990**, *76*, 147.
133. Dirk, C. W.; Kuzyk, M. G. *Chem. Mater.* **1990**, *2*, 4.
134. Glier, C.; Dietz, F. J. *Signalaufzeichnungsmaterialien* **1977**, *5*, 285.
135. Birge, R. R.; Hubbard, L. M. *J. Am. Chem. Soc.* **1980**, *102*, 2195.
136. Wavefunction, Inc., Suite 210, 18401 Von Karman Ave., Irvine, CA 92715.
137. Fabian, J.; Mehlhorn, A. *J. Mol. Struct. (Theochem.)* **1984**, *109*, 17.
138. Daehne, D. *Science (Washington, DC)* **1978**, *199*, 1163.
139. Nakano, M.; Okumura, M.; Yamaguchi, K.; Fueno, T. *Mol. Cryst. Liq. Cryst.* **1990**, *182A*, 1.
140. Garito, A. F.; Heflin, J. R.; Wong, K. Y.; Zamiri-Khamiri, O. In *Organic Materials for Nonlinear Optics*; Ando, D. J.; Bloor, D., Eds.; Royal Society of Chemistry: London, 1988.
141. Private communication from S. Etemad to S. N. Dixit reported in ref. 135.
142. Dixit, S. N.; Guo, D.; Mazumdar, S. *Phys. Rev.* **1991**, *43*, 6781.
143. Oudar, J. L. *J. Chem. Phys.* **1977**, *67*, 446.
144. Lalama, S. J.; Garito, A. F. *Phys. Rev. A* **1979**, *20*, 1179.
145. Marder, S. R.; Beratan, D. N.; Cheng, L. T. *Science (Washington, D.C.)* **1991**, *252*, 103.
146. Ward, J. F.; Elliott, D. S. *J. Chem. Phys.* **1978**, *69*, 5438.
147. Stevenson, S. H.; Donald, D. S.; Meredith, G. R. In *Nonlinear Optical Properties of Polymers*; Heeger, A. J.; Orenstein, J.; Ulrich, D. R., Eds.; Materials Research Society Symposium Proceedings 109; Materials Research Society: Pittsburgh, PA, 1988; pp 103–108.
148. Hermann, J. P. *Opt. Commun.* **1973**, *9*, 74.
149. Zhou, Q. L.; Heflin, J. R.; Wong, K. Y.; Zamani-Khamiri, O.; Garito, A. F. *Phys. Rev. A* **1991**, *43*, 1673.
150. Rodenberger, D. C.; Heflin, J. R.; Garito, A. F. *Nature (London)* **1992**, *359*, 309.

RECEIVED for review May 29, 1992. ACCEPTED revised manuscript February 25, 1993.

Molecular Optoelectronics Based on Phthalocyanine

Tatsuo Wada, Masahiro Hosoda, and Hiroyuki Sasabe

Frontier Research Program, RIKEN (The Institute of Physical and Chemical Research), Hirosawa, Wako, Saitama 351-01, Japan

The molecular design and assembly of metallophthalocyanine systems that have the enhanced macroscopic third-order nonlinear susceptibility $\chi^{(3)}_{ijkl}(-\omega_4; \omega_1, \omega_2, \omega_3)$ and show ultrafast responses are described. Enhancement of the third-harmonic susceptibility $\chi^{(3)}_{1111}(-3\omega; \omega, \omega, \omega)$ was observed in vanadylphthalocyanine vacuum-deposited films with the staggered stacking arrangement induced by thermal treatment. A processible polymeric system that was rich in tert-butyl monosubstitutions was developed, and the favorable staggered stacking arrangement was induced in a polymer matrix to enhance $\chi^{(3)}_{1111}(-3\omega; \omega, \omega, \omega)$. Femtosecond time-resolved spectroscopy was performed on vanadylphthalocyanine thin films with different morphological forms to elucidate the exciton dynamics.

ORGANIC PHOTONICS IS THE FRONTIER of optoelectronic applications of organic materials, such as in optical computing, image processing, and communication systems. Fundamentally, the nonlinear optical (NLO) effects of materials are applicable for these purposes, for example, addition or subtraction of optical frequencies for computing, optical bistability for switching and memories, the optical Kerr effect for waveguides, and spatial light modulators. From the materials viewpoint, the intramolecular charge transfer through π -electron conjugation gives large optical nonlinearities on the molecular level, whereas the symmetry of the crystal structure determines the macroscopic second-order nonlinearity $\chi^{(2)}_{ijk}(-\omega_3; \omega_1, \omega_2)$; if the crystal is centrosymmetric, then $\chi^{(2)}$ becomes zero. However, the third-order optical nonlinearity $\chi^{(3)}_{ijkl}(-\omega_4; \omega_1, \omega_2, \omega_3)$ does not depend on the crystal symmetry but on the microscopic third-order susceptibility $\gamma_{ijkl}(-\omega_4, \omega_1, \omega_2, \omega_3)$ of the con-

0065-2393/94/0240-0303\$08.00/0
© 1994 American Chemical Society

stituent molecular unit. Charge-transfer complexes and π -conjugated compounds are the most promising materials for NLO applications, but the systematic investigation of features such as controls of conjugation length, intermolecular interaction, and packing structure is still occurring.

The quantum field theory for low-dimensional systems (1) suggests that in conjugated linear chain structures, such as polyenes and polydiacetylenes, π -electrons are delocalized in their motion only in one dimension along the chain axis. The major contribution to γ_{ijkl} is the dominant chain axis component γ_{xxxx} with all electric fields aligned along the chain axis (x -axis). That is, in the one-dimensional (1D) π -conjugation systems, only one tensor component γ_{xxxx} contributes to the averaged susceptibility $\langle\gamma\rangle$ in isotropic media; $\langle\gamma\rangle$ is equal to $(1/5)\gamma_{xxxx}$. A power law dependence of γ_{ijkl} on the number of carbon atom sites has been found, with exponents of 5.4 for the *trans*-polyene and 4.7 for the *cis*-polyene conformer, and γ_{xxxx} is more sensitive to the physical length of the chain than to the conformation (1). When the dimensionality of the π -electron system is expanded from linear to cyclic chains, the theoretical results on cyclic structures such as cyclooctatetraene show a decrease of γ_{ijkl} due to an actual reduction in the effective length available for the π -electron to respond to an optical electric field (2). In the widely spread two-dimensional (2D) π -conjugation systems, on the contrary, other tensor components also contribute to $\langle\gamma\rangle$, that is,

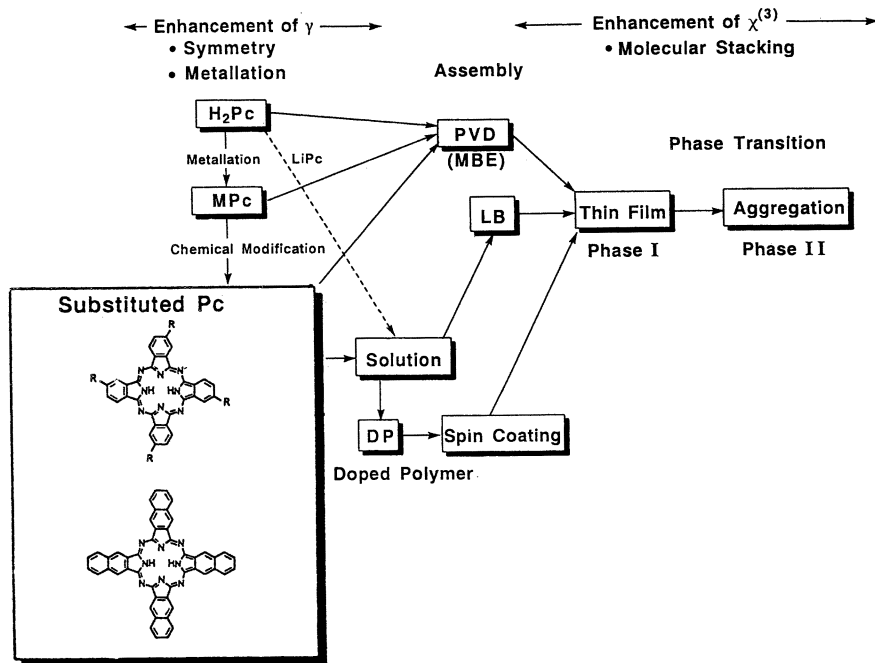
$$\langle\gamma\rangle = 1/5 [\gamma_{xxxx} + \gamma_{yyyy} + 1/3 (\gamma_{xxyy} + \gamma_{xyxy} + \gamma_{xyyx} + \gamma_{yyxx} + \gamma_{yxyx} + \gamma_{yxxy})]$$

The off-resonant third-order optical susceptibility $\chi^{(3)}_{1111}(-3\omega; \omega, \omega, \omega)$ (abbreviated $\chi^{(3)}$ hereafter) for the macrocyclic conjugated structural class of annulenes with an 18–28-membered ring size—tetrahydro-methano-[18]-, -[22]-, -[24]-, and -[28]-annulene—was determined systematically by optical third-harmonic generation (THG) measurements at 1907 nm (3). The $\chi^{(3)}$ value was found to increase with increased size of the macrocyclic conjugated structure in a manner analogous to the behavior of conjugated linear chains. Thus, we focused our research on the development of macrocyclic compounds consisting of 2D conjugated π -electron systems, especially metallophthalocyanine (MPc) derivatives, which exhibit linear and nonlinear optoelectronic responses such as photoconductive, photovoltaic, and photocatalytic behavior. These materials also have attractive physical properties such as large absorption in the visible region, thermal and chemical stability, and thin-film formation. This chapter describes our material research approach (4–8) to developing MPc thin films that enhance the macroscopic nonlinear susceptibility, ultrafast NLO response, and optical waveguide application.

Thin Films of Metallophthalocyanines

Vacuum-Deposited Films. For MPcs, several approaches exist for fabricating a thickness-controlled thin film, as shown in Scheme I. Unsubstituted MPcs show exceptionally high thermal stability. Therefore, vacuum deposition techniques have been widely used to obtain thin films 10 nm to several micrometers thick by controlling the deposition rate and time. In the electronic spectra of MPcs, two characteristic absorption bands are well established, for example, the Soret band (300–400 nm) and the Q-band (the π - π^* transition in 600–800-nm region). The Q-band is sensitive to the environment, such as the orientation and packing of MPc rings. In general, the central metal has little effect on the electronic state of phthalocyanine but a strong influence on the packing arrangement of the phthalocyanine molecules in the condensed state. Therefore, depending on the central metal, features of the Q-band changed remarkably in the condensed state. This Q-band has been widely studied as a probe of the phase transitions induced by thermal or solvent vapor treatment (9).

Our previous studies on THG of MPc vacuum-deposited (VD) films showed that vanadylphthalocyanine (VOPc) has a large $\chi^{(3)}$, of the order



Scheme I. Thin-film fabrication of phthalocyanines.

of 10^{-10} electrostatic units (esu) at a fundamental wavelength of 1907 nm (10). Figure 1 shows typical absorption spectra of VOPc VD thin films. The absorption maximum of an as-prepared VOPc film is located at 740 nm, with a shoulder near 680 nm in the Q-band. Heating the VOPc film at 125 °C in the air produced a new near-IR absorption at 820 nm in the spectrum and decreased the intensities of 740- and 680-nm peaks, as shown in Figure 1. Spectral change ceases after 15 h under these conditions.

A similar absorption change was observed by thermal annealing of TiOPc VD thin films. According to Griffiths et al. (9), the phase with peaks at 680 and 740 nm is attributed to the cofacial packing of VOPc molecules (phase I). The as-prepared film seems to have a cofacially stacked arrangement (phase I); that is, it is aligned linearly along the metal-oxo bond. The packing arrangement that leads to a bathochromic shift in the Q-band is called phase II (9). An X-ray diffraction study showed that the phase II introduced by heating has a triclinic crystal structure with the space group $P\bar{1}$ and is identified as a slipped-stack arrangement, that is, a staggered assembly on adjacent molecules in the thin films (11). Figure 2 shows the molecular packing of phase II of VOPc. In our preliminary X-ray diffraction study, a significant difference in those thin films was observed before and after heating. The peak intensity at $2\theta = 12.7^\circ$ and $2\theta = 25.5^\circ$, corresponding respectively to interplanar distances of 6.96 and 3.48 attributable to the phase II of VOPc, gradually increased with the thermal treatment.

The typical results of rotational THG Maker fringes are shown in Figure 3. Because of the large $\chi^{(3)}$ value of VOPc, the contribution from the fused silica substrate is insignificant. The enhancement of third-

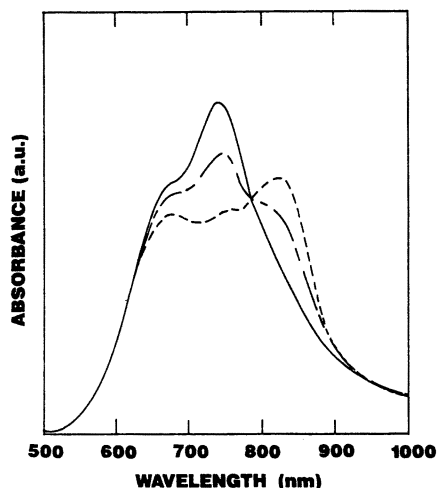
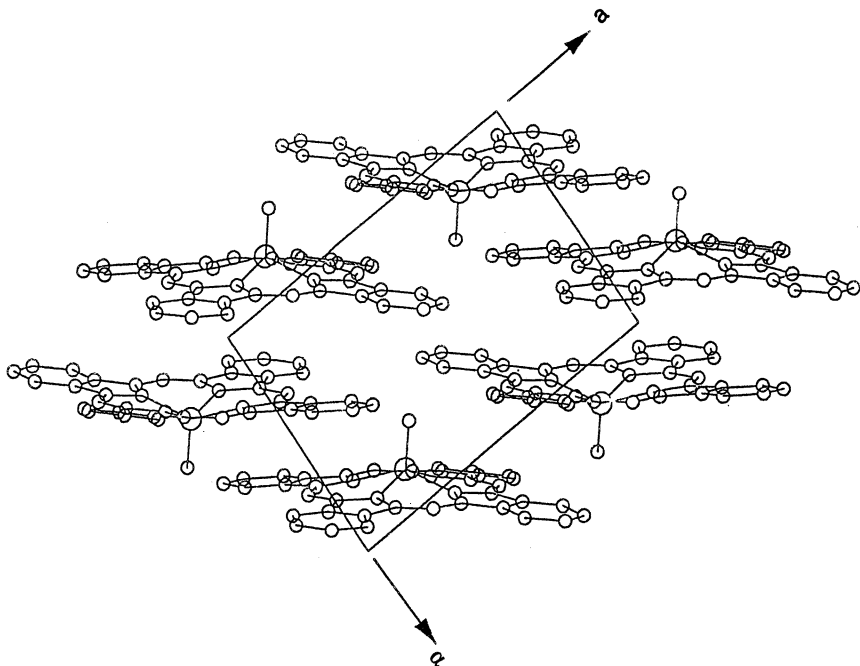


Figure 1. Absorption spectra of VOPc thin films: (solid line) as-prepared film, (line with long dashes) film annealed at 125°C for 1.5 h, and (line with short dashes) film annealed at 125°C for 1.5 h. a.u. (Reproduced with permission from reference 7. Copyright 1991.)



Space group: $P\bar{1}$

$a = 12.027 \text{ \AA}$, $b = 12.571 \text{ \AA}$, $c = 8.690 \text{ \AA}$

$\alpha = 96.04^\circ$, $\beta = 94.80^\circ$, $\gamma = 68.20^\circ$

Figure 2. Projection of molecular packing of phase II of VOPc along the b-axis.

harmonic (TH) intensity is observed in the sample after thermal annealing. The $\chi^{(3)}$ value of fused silica at 1543 nm was calculated from Miller's rule by using $\chi^{(3)}$ at 1907 nm determined by Heflin et al. (12) ($\chi^{(3)} = 1.40 \times 10^{-14}$ esu), as 1.47×10^{-14} esu. The $\chi^{(3)}$ values of the phthalocyanine thin films were estimated with reference to the $\chi^{(3)}$ of fused silica. In a nonabsorbing medium, the TH intensity is given as (13)

$$I_{3\omega} = \frac{256\pi^4}{c^2} \left(\frac{A\chi^{(3)}}{\Delta\epsilon} \right)^2 \sin^2 \left(\frac{\Delta\psi}{2} \right) \quad (1)$$

where c is the velocity of light, $\Delta\epsilon$ the dielectric constant dispersion (and equals $n_\omega^2 - n_{3\omega}^2$, where n is the refractive index), A the factor arising from transmission and boundary conditions, and $\Delta\psi$ the phase mismatch between the fundamental and harmonic frequencies. In an absorbing medium, on the other hand, the TH intensity is given by

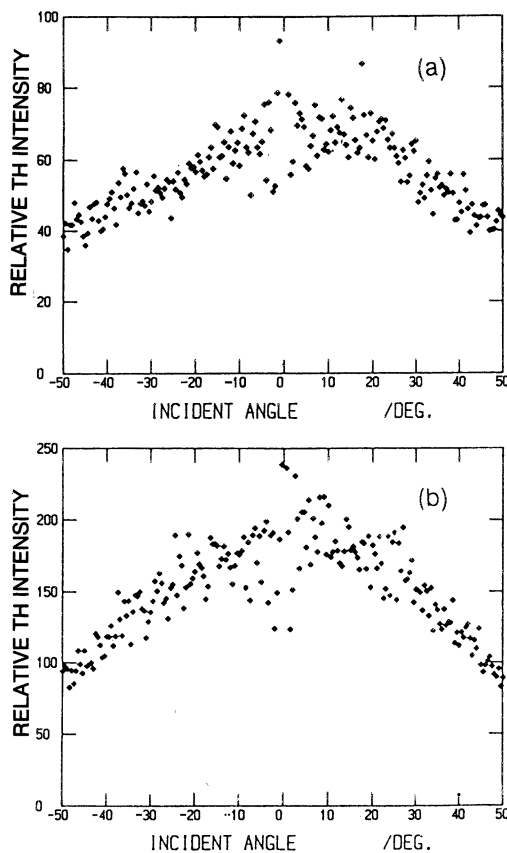


Figure 3. Rotational THG Maker fringe patterns: (a) as-prepared VOPc (thickness 178 nm) on fused silica, and (b) a similar film annealed at 125°C for 15 h. (Reproduced with permission from reference 7. Copyright 1991.)

equation 2 under the condition of l (the sample thickness) $\ll l_c$ (the coherence length) (13),

$$I_{3\omega} = \left(\frac{64\pi^4}{c^2} \right) (AX^{(3)})^2 I_{\omega}^3 f_a \quad (2)$$

where I_{ω} and $I_{3\omega}$ are the light intensity for fundamental and TH frequencies, respectively, and f_a is the absorption-dependent factor,

$$f_a = \frac{[1 - \exp(-\alpha_{3\omega} l/2)]^2 + (\Delta\psi)^2 \exp(\alpha_{3\omega} l/2)}{(n_{3\omega}^2 - n_{\omega}^2 - k_{3\omega}^2)^2 + (2n_{3\omega} k_{3\omega})^2} \quad (3)$$

where n and k are the real and imaginary parts of refractive indices, respectively, and α is the linear absorption coefficient. The results of

THG measurement are summarized in Table I, together with the values of refractive indices of phthalocyanine thin films obtained by Kramers–Kronig analysis. In spite of the small changes in refractive indices at fundamental and TH wavelengths, the macroscopic $\chi^{(3)}$ values in VOPc and TiOPc thin films increased by thermal treatment to about 2–5 times those in untreated films. These results indicate that the macroscopic $\chi^{(3)}$ values are larger in phase II than in the other phase.

Spin-Coated Doped Polymer Films. The major problem encountered with unsubstituted MPc systems is poor processibility, particularly poor solubility in organic solvents. For the waveguide application, the materials should be designed to meet several fabrication requirements. Metallation and chemical modification, such as introduction of functional groups, can be used to improve the physical properties of MPc molecules. For example, several functional groups (e.g., alkyl, alkoxy, trimethylsilyl, and sulfamide groups) introduced into the peripheral position of each of the benzo rings give excellent solubility in common organic solvents (14). A polymer [polystyrene, poly(methyl methacrylate), and so on] doped with tetrakis(*tert*-butyl)-metallophthalocyanines [MPc(*t*-bu)₄s] can be formed easily on various substrates by a conventional spin-coating technique, and these doped polymer (DP) films show excellent optical quality.

Figure 4 shows the absorption spectra of spin-coated pure MPc(*t*-bu)₄ films [M is H₂ (metal free), VO, and Ni). In these MPc(*t*-bu)₄ films, the absorption peaks of the Q-band were observed at 615, 704, and 618 nm, respectively. In comparison with those of corresponding unsubstituted MPcs (15, 16), no remarkable changes of peak position were observed, except for a low-energy peak in VOPc. In poly(methyl methacrylate) (PMMA) doped with the MPc(*t*-bu)₄, the significant peak shift was not observed in the concentration range from 5 to 100 wt%. The relationship between α at each peak wavelength and the weight ratio MPc(*t*-bu)₄:PMMA is linear. Therefore, the dispersed state of MPc(*t*-bu)₄ does not vary under these conditions. The THG measurements show that the $\chi^{(3)}$ value of VOPc(*t*-bu)₄ is smaller by one order of magnitude than that of a VOPc VD film. On the other hand, other MPc(*t*-bu)₄ films with M as Ni or H₂, for example, have the same value of $\chi^{(3)}$ as corresponding unsubstituted MPcs (17).

The differences between VD and spin-coated films can be observed in optical spectra and X-ray diffraction patterns. In the Q-band of pure VOPc(*t*-bu)₄ film prepared by spin-coating or VD, two peaks similar to those of phase I in VOPc VD film were observed. Unlike the VOPc VD film, the VOPc(*t*-bu)₄ spin-coated film showed no evidence of a crystalline structure, even after thermal aging treatment, presumably because of a steric hindrance of the bulky *tert*-butyl groups. Again we realized

Table I. Values of $\chi^{(3)}$ and Refractive Indices in Tetravalent Metallophthalocyanine Thin Films

Film	$\chi^{(3)}(-3\omega; \omega, \omega, \omega)$ at 1543 nm (10^{-12} esu)	$\chi^{(3)}(-3\omega; \omega, \omega, \omega)$ at 1907 nm (10^{-12} esu)	1543 nm		1907 nm	
			n_ω	$n_{3\omega}$	n_ω	$n_{3\omega}$
VOPc						
as-prepared	4.1 ± 0.5	38 ± 5	2.38	1.84	2.17	1.36
annealed	9.0 ± 1.1	81 ± 8	2.52	1.80	2.25	1.34
TiOPc						
as-prepared	2.7 ± 0.4	10 ± 0.6	1.93	1.76	1.81	1.57
annealed	14 ± 2	46 ± 6	1.92	1.74	1.77	1.64

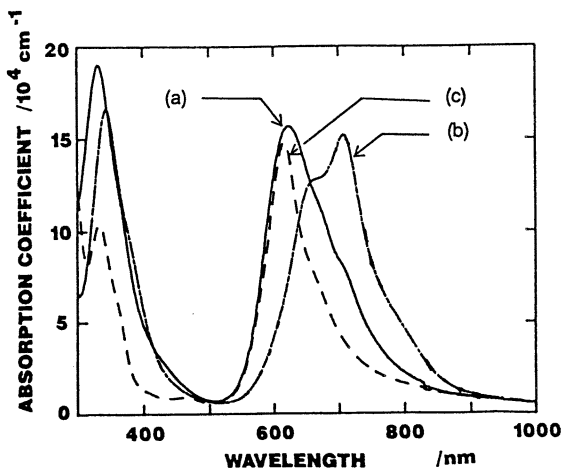


Figure 4. Absorption spectra of the tetrakis(tert-butyl)phthalocyanine films obtained by spin-coating of chloroform solutions: (a) $H_2Pc(t-bu)_4$, (b) $VOPc(t-bu)_4$, and (c) $NiPc(t-bu)_4$. (Reproduced with permission from reference 6. Copyright 1991.)

that the phase II type stacking of VOPc molecules is important to enhance the macroscopic third-order NLO susceptibility. Thus, $VOPc(t-bu)_{1,1}$ was designed to reduce the steric hindrance of bulky substituents.

After dichloroethane vapor treatment, the similar phase transition was observed in both pure and polymer thin films doped with $VOPc(t-bu)_{1,1}$. The $\chi^{(3)}$ values at fundamental wavelengths of 1543 and 1907 nm increased after the crystalline phase transition in various doping concentrations (18). The qualitative evaluation through the deconvolution of electronic spectra indicates that the low-energy band in phase II plays an important role in enhancing both the resonant and off-resonant $\chi^{(3)}$ values (19). Optical quality and mechanical strength of $VOPc(t-bu)_{1,1}$: PMMA are adequate to make a slab optical waveguide by a conventional polymer process. Even after solvent vapor treatment, no significant propagation loss in guided-wave geometry was observed that was due to the scattering from the aggregated particles, and the X-ray diffraction study suggested that the domain size of associated $VOPc(t-bu)_{1,1}$ molecules was on the order of 10 nm.

Molecular Beam Epitaxy Films. Most organic materials crystallize because of weak van der Waals interaction, and hence the crystal structure is governed by several factors, such as hydrogen bonding and steric hindrance. In MPCs, polymorphism was observed, hence the packing structure of the film grown on the substrate can be expected to be easily affected by the interaction with a substrate. Molecular beam

epitaxy (MBE) is a sophisticated vacuum deposition technique in which the lattice matching of deposited molecules to the substrate surface takes place. This technique has been applied to epitaxial growth of MPC films (20).

Tada et al. (21) reported the initial crystal structure of the VOPc thin film grown on alkali halide substrates with the MBE technique by monitoring the reflection high-energy electron diffraction (RHEED) patterns. From the RHEED observation, a square lattice with a fourfold symmetry of VOPc and molecular planes of VOPc parallel to the cleaved (001) face of a KBr substrate were proposed. Compared to VD films, VOPc films grown by MBE show a narrow Q-band with a different peak position. In the condensed state, the broadening in the Q-band was observed as a result of exciton splitting in the Q-band due to transition dipole interactions between adjacent MPC molecules in aggregates. Optical absorption spectra of various VOPc(*t*-bu)_{*n*} (*n* = 0 and 1.1) thin films are summarized in Figure 5. Because of the narrow Q-band in the MBE VOPc film, a highly ordered packing can be expected.

Femtosecond Responses in VOPc(t-bu)_n Thin Films

Another important characteristic of third-order NLO materials is the time response of their nonlinearity. In the resonant region, a resonant enhancement of NLO responses and a relatively slow decay can be expected. In MPC thin films made by various techniques, these compounds can exist in several morphological forms with different stacking arrangements of the disklike phthalocyanine molecules. These structural variations cause a modification of their electronic properties in the condensed state. Neher et al. (22) reported the influence of film

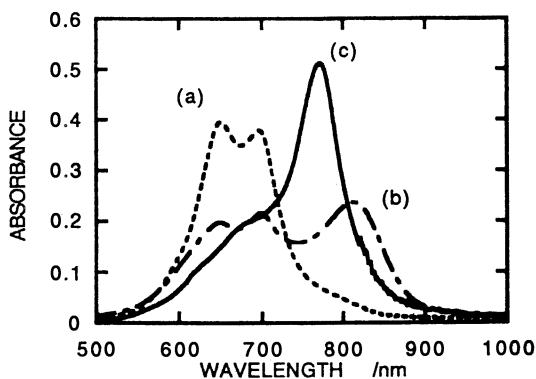


Figure 5. Absorption spectra in polystyrene thin films doped with 10 wt% VOPc(*t*-bu)_{1.1}: (a) phase I rich film, (b) phase II rich film, and (c) VOPc thin film grown by MBE on KBr.

preparation—doped polymer and Langmuir–Blodgett films, for example—on the NLO properties of phthalocyanine films measured by degenerate four-wave mixing. In highly associated $\text{VOPc}(t\text{-bu})_n$, a resonant enhancement of NLO response might be expected without any bottleneck optical process. For this reason, we investigated the exciton decay dynamics in $\text{VOPc}(t\text{-bu})_n$ thin films with femtosecond pump-probe spectroscopy. Ultrashort pulses generated from a colliding-pulse mode-locked (CPM) ring dye laser were amplified up to $2 \mu\text{J}$ per pulse by a multipass amplifier pumped by a copper vapor laser (CVL) operating at 10 kHz. The 620-nm amplified pulses (50–60 fs in duration) were divided into two beams: One was focused onto the sample as a pump with a variable delay time, and the other was focused into an ethylene glycol jet to generate continuum pulses, which were used as a broadband probe. The optical layout and a detailed description of the detection of transmittance changes are described elsewhere (23).

The differential transmission spectra (DTS) of phase II films of $\text{VOPc}(t\text{-bu})_{1,1}$ doped in polystyrene (10 wt%) are shown in Figure 6. The key feature of DTS is that the significant bleaching appears at the lowest energy absorption peak (centered around 810 nm), whereas the

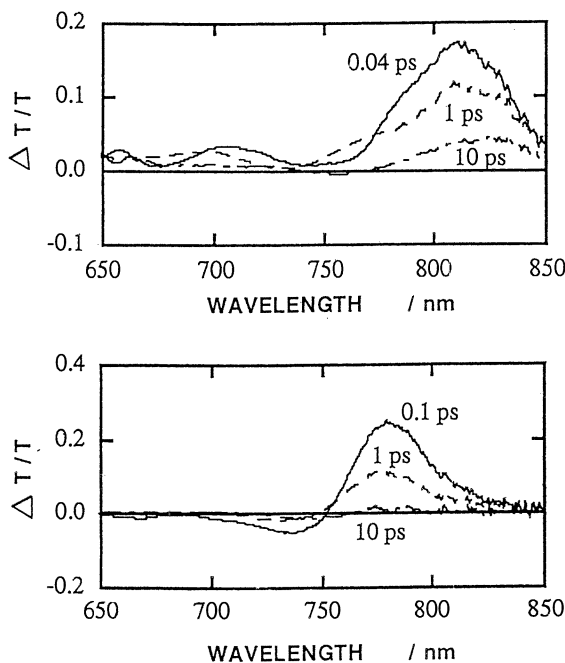


Figure 6. Differential transmission spectra for polystyrene thin films doped with 10 wt% $\text{VOPc}(t\text{-bu})_{1,1}$: (a) phase II rich film and (b) VOPc thin film grown by MBE on KBr.

higher energy absorption peaks bleach only weakly. Thus, either excitons created by the femtosecond pulses at 620 nm undergo very rapid internal conversion to the lowest excited state, or the induced excited-state absorption in this energy region cancels the bleaching signals. In the spectral range 500–600 nm (corresponding to the optical window of ground-state absorption), excited-state induced absorption was observed, which was much weaker than the bleaching signal. The decay curve of the transmittance change consists of three components: a fast (hundreds of femtoseconds), a slower (tens of picoseconds), and a long-lived (longer than hundreds of picoseconds) component. The fast component is interpreted as a bimolecular process, that is, exciton–exciton annihilation, because of its excitation intensity dependence. On the other hand, the slower decay is rather independent of excitation intensity and can be attributed to a unimolecular decay via exciton–phonon coupling. The long-lived component is presumably due to triplet-state formation widely observed in MPCs. To fit the initial decay curve, we employed the exciton–exciton annihilation model with a time-dependent rate of $t^{-1/2}$ based on the long-range dipole–dipole interaction between excitons, or the motion-limited exciton diffusion (24). In this model the exciton density (N) was described by the following equation for a delta-function excitation pulse:

$$\frac{dN}{dt} = -\gamma t^{-1/2} \kappa N^2 - \kappa N \quad (4)$$

where γ and κ are, respectively, bimolecular and unimolecular decay constants. Solving equation 4 gives the following time dependence of the exciton density:

$$\frac{N}{N_0} = \frac{\exp(-\kappa t)}{1 + (2N_0\gamma/\kappa^{1/2})\text{erf}[(\kappa t)^{1/2}]} \quad (5)$$

where N_0 is the initial exciton density at time zero and $\text{erf}(x)$ is the error function. We have added a constant term that phenomenologically accounts for the long-lived component to equation 5. This function can fit the data over a time range up to 100 ps and yields fitting parameters of $N_0\gamma = 9.1 \times 10^5 \text{ s}^{-1/2}$, $\kappa = 2 \times 10^{10} \text{ s}^{-1}$ and a constant term that is ca. 10% of the maximum value of the data. With the assumption of uniform distribution of VOPc(*t*-bu)_{1.1} in polystyrene, γ can be calculated as $8.3 \times 10^{-15} \text{ cm}^3 \text{ s}^{-1/2}$ after estimation of excitation density. Both the pure VOPc(*t*-bu)_{1.1} spin-coated film and the VOPc VD film had a bleaching peak at 810 nm that decayed with almost the same behavior as VOPc(*t*-bu)_{1.1} in polystyrene and were also well described by this model. In these cases, estimated values of parameters κ and γ were $2 \times 10^{10} \text{ s}^{-1}$ and $5.9 \times 10^{-15} \text{ cm}^3 \text{ s}^{-1/2}$ for the VOPc(*t*-bu)_{1.1} spin-coated film and 2

$\times 10^{10} \text{ s}^{-1}$ and $6.0 \times 10^{-15} \text{ cm}^3 \text{ s}^{-1/2}$ for the VOPc VD film, respectively. On the other hand, the MBE VOPc film showed rather fast decay of bleaching compared to the VOPc VD film, presumably because of the different packing arrangements, as shown in Figure 7. The dominant relaxation processes are the formation of a triplet state in the isolated molecules, the exciton–exciton annihilation taking place in the picosecond regime in phase I and phase II with different constants, and the subpicosecond exciton decay in the MBE VOPc film (25). Thus, the long-range order in molecular packing is one of the key issues for developing the resonant-enhanced NLO materials with ultrafast responses.

Implementation of a VOPc(t-bu)_n Optical Waveguide

Intensity-Dependent Refractive Index Change. For optically active devices, the intensity-dependent refractive index change (optical Kerr effect) is essential; the refractive indices n of the material are dependent on the incident light intensity I as

$$n = n_0 + n_2 I \quad (6)$$

$$n_2 = \frac{\chi^{(3)}ijkl(-\omega; \omega, -\omega, \omega)}{n_0^2 \epsilon_0 C} \quad (7)$$

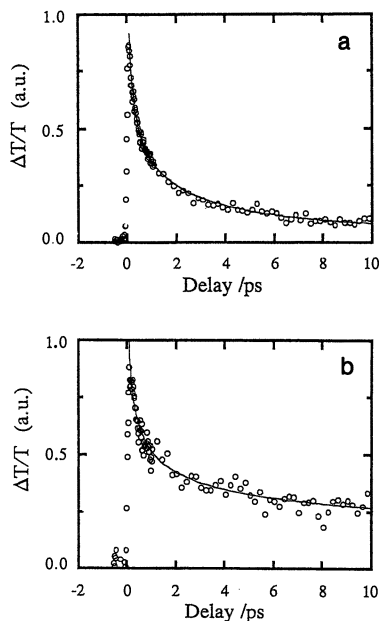


Figure 7. Transmission changes as a function of delay time for (a) VOPc thin film grown by MBE on KBr at 780 nm and (b) VOPc VD film at 810 nm. T is transmission in arbitrary units (a.u.).

where n_0 and n_2 are linear and nonlinear refractive indices, respectively. Therefore, materials with large $\chi^{(3)}$ values are required for this application in addition to transparency. For the direct observation of light propagation in thin films, light should be introduced into the film by prism coupling, grating coupling, or end-fire coupling. In our study the spin-coated doped polymer film on the fused silica substrate was used. The propagating light of a continuous-wave (CW) YAG laser (1064 nm) in the film introduced by means of the prism-coupling technique was monitored by an IR-sensitive charge-coupled device (CCD) camera directly (Figure 8).

We used a slab-type waveguide consisting of quartz substrate as cladding, a glass thin layer as a guiding layer (Corning 7059), and a VOPc VD film as a top layer, which has a gradient of thickness along the y -axis as shown in Figure 9. The laser beam (1064 nm) was coupled and decoupled to a glass layer by a prism-coupling technique, and the output intensities were normalized by the intensity of reflection from the surface of the coupling prism. Figure 9 also shows normalized output intensities of the transverse electric wave (TE_0) mode at a wavelength of 1064 nm as a function of VOPc VD film thickness. The output intensities were almost constant when the thickness of the top layer was zero. With an increase in thickness of the top layer, the output intensity decreased remarkably and then increased gradually at more than the critical thickness (about 100 nm thick in Figure 9b).

The simulation of light propagation shows that the output intensity changes periodically as a function of the top-layer thickness and goes to zero at a critical thickness. This phenomenon can be interpreted as follows: When the field distribution of the propagation mode in region I is similar to that of the guiding layer in region II, the output intensity

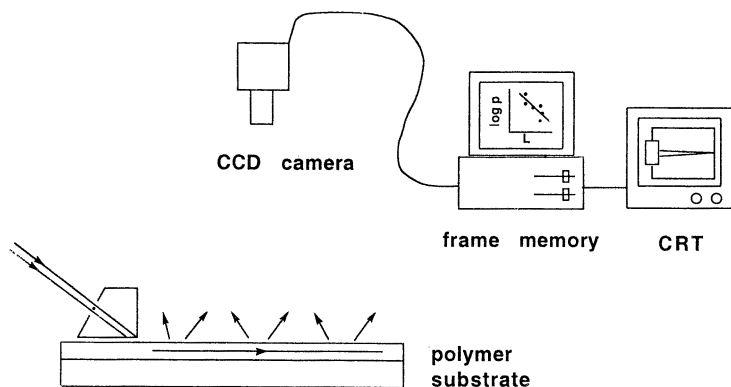


Figure 8. Schematic diagram for the measurement of propagating light in the film.

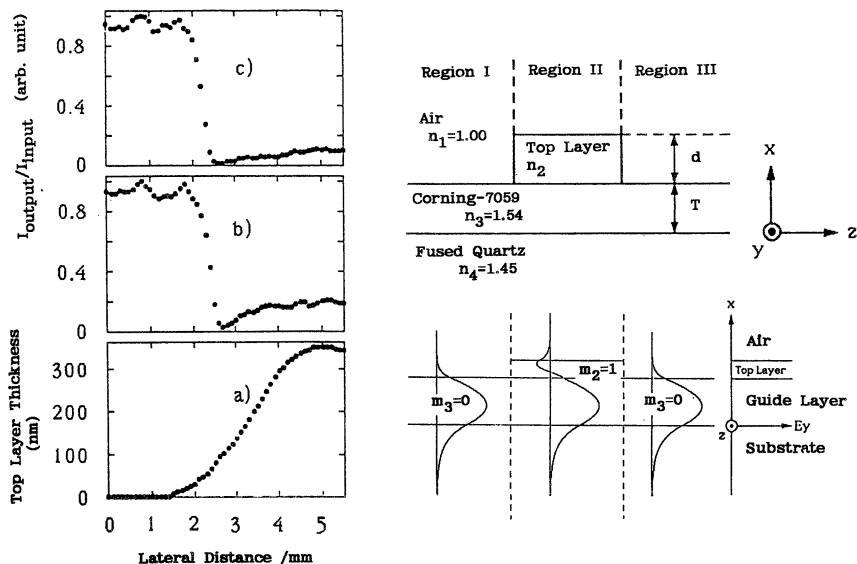


Figure 9. Geometry of a slab waveguide and the normalized output intensity of transmitted light as a function of VOPc top-layer thickness. The VOPc top layer has a gradient of thickness along the y -axis (a). The input light intensity of graph c is 11 times that of graph b.

becomes a maximum, otherwise light cannot propagate well from region I to region II or from region II to region III along the z -axis in Figure 9. When the incident intensity (I_i) was increased by 1 order of magnitude, the minimum intensity point shifted slightly toward a thinner top layer. At this minimum point (about 80 nm thick in Figure 9c), the ratio of output to input power decreased with increasing input power around a high power range.

The glass optical waveguide itself—that is, a film without a VOPc top layer—did not exhibit this nonlinear behavior. The propagation constant changed under high power conditions: The nonlinear refractive indices can be made to appear in a VOPc VD film that has a large $\chi^{(3)}$. This result indicates that n_2 is positive. However, surface plasmon studies on MPc (M is H_2 or VO) showed that the sign of refractive indices change due to thermal effects are negative. Temporal responses in guided-wave geometry are ongoing, as shown by femtosecond optical pulses generated from the mode-locked Ti:sapphire laser system in our laboratory. We also observed a propagation loss due not to absorption but to imperfect energy transport between different regions with a step-indices change, as well as imperfect structure that created a rough surface and boundary.

Mode-Lines Measurement. To check the thin film light guide, the prism–film coupling is an essential technique. The coupling between

the prism (refractive indices of n_p) and the film waveguide (n_f) formed on the substrate (n_s) takes place along the bottom plane of the prism through a thin gap layer (air) of indices n_c , as shown in Figure 10. The propagation constant β of the incident light beam along the waveguide film is given by

$$\beta = n_p K \sin \theta' \quad (8)$$

where $K = 2\pi/\lambda$ and θ' is the incident angle onto the bottom of prism, which is related to the incident angle θ outside the prism through Snell's law as

$$n_c \sin \theta = n_p \sin (\theta_p - \theta') \quad (9)$$

where θ_p denotes the toe angle of prism. If the propagation constant is in a range $n_c < \beta/K < n_f$ (guided mode), the guided wave is excited through the distributed coupling and penetrates as an evanescent wave into the film. In the waveguide film, β is expressed as

$$\beta = K n_{\text{eff}} \quad (10)$$

where $n_{\text{eff}} = n_f \sin \theta''$ and θ'' is the total reflection angle as shown in Figure 10.

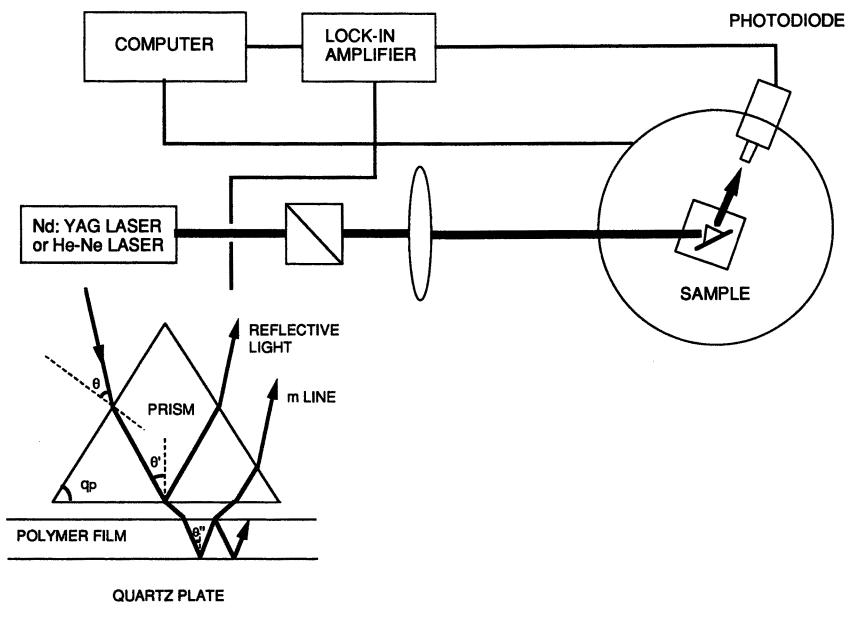


Figure 10. Schematic layout of mode-line measuring system.

From the field equations for the TE mode, the wavenumber in the x direction K_x can be derived in the form of the eigenvalue equation

$$K_x T = m\pi + \tan^{-1} \left(\frac{r_s}{K_x} \right) + \tan^{-1} \left(\frac{r_c}{K_x} \right) \quad (11)$$

where $K_x = K(n_f^2 - n_{\text{eff}}^2)^{1/2}$, $r_s = K(n_{\text{eff}}^2 - n_s^2)^{1/2}$, $r_c = K(n_{\text{eff}}^2 - n_c^2)^{1/2}$, T is the thickness of the waveguide film and m ($= 0, 1, 2, \dots$) denotes the mode number. The incident beam focused on the prism base in a synchronous direction can feed the optical energy into one of the waveguide modes of the film. Because the film scatters the optical energy in the excited mode into other modes, the beam is coupled back to the outside medium by the same prism. This phenomenon gives a series of bright lines on the screen (m -lines). From the positions and the widths of m -lines, the mode spectra, the refractive indices, and the film thickness can be determined. Therefore, when m -lines can be observed by means of a prism-film coupler method, there is good evidence of guided waves.

The refractive indices of a VOPc film, a rutile prism, and a fused silica substrate are 2.00, 2.874, and 1.457, respectively, at 1064 nm (a fundamental wavelength of the YAG laser), and hence it is possible to couple the incident beam of a YAG laser from the prism with a VOPc VD film via the air gap. By rotating the prism-film coupler on the spectrometer, the bright spot on a fundamental m -line ($m = 0$) disappears and then appears on the next line. This occurs periodically; that is, the reflected beam intensity depends on the incident angle. From the angle of zero reflection, the refractive indices of the film can be calculated.

Acknowledgments

We thank A. F. Garito (University of Pennsylvania) for critical discussions and also Y. Matsuoka (HOYA Co.), A. Terasaki, and A. Kaneko for help in experiments.

References

1. Garito, A. F.; Heflin, J. R.; Wong, K. Y.; Zamani-Khamiri, O. In *Nonlinear Optical Properties of Polymers*; Heeger, A. J.; Orenstein, J.; Ulrich, D. R., Eds.; MRS Symposium Proceedings 109; Materials Research Society: Pittsburgh, PA, 1988; pp 91-102.
2. Wu, J. W.; Heflin, J. R.; Norwood, R. A.; Wong, K. Y.; Zamani-Khamiri, O.; Garito, A. F.; Kalyanaraman, P.; Sounik, J. *J. Opt. Soc. Am.* **1989**, *B6*, 707-720.
3. Wada, T.; Ojima, J.; Yamada, A.; Garito, A. F.; Sasabe, H. In *Nonlinear Optical Properties of Organic Materials II*; Khanarian, G., Ed.; SPIE Proceedings 1147; The International Society for Optical Engineering: Bellingham, WA, 1989; pp 286-292.

4. Wada, T.; Yamada, S.; Matsuoka, Y.; Grossman, C. H.; Shigehara, K.; Sasabe, H.; Yamada, A.; Garito, A. F. In *Nonlinear Optics of Organics and Semiconductors*; Kobayashi, K., Ed.; Springer Proceedings in Physics Series 36; Springer-Verlag: Berlin, Germany, 1989; pp 292–301.
5. Sasabe, H.; Wada, T.; Hosoda, M.; Ohkawa, H.; Hara, M.; Yamada, A.; Garito, A. F. In *Nonlinear Optical Properties of Materials III*; Khanarian, G., Ed.; SPIE Proceedings 1337; The International Society for Optical Engineering: Bellingham, WA, 1990; pp 62–72.
6. Hosoda, M.; Wada, T.; Yamada, A.; Garito, A. F.; Sasabe, H. *Jpn. J. Appl. Phys.* **1991**, *30*, 1715–1719.
7. Hosoda, M.; Wada, T.; Yamada, A.; Garito, A. F.; Sasabe, H. *Jpn. J. Appl. Phys.* **1991**, *30*, L1486–1488.
8. Wada, T.; Hosoda, M.; Garito, A. F.; Sasabe, H.; Terasaki, A.; Kobayashi, T.; Tada, H.; Koma, A. In *Nonlinear Optical Properties of Organic Materials IV*; Singer, K., Ed.; SPIE Proceedings 1560; The International Society for Optical Engineering: Bellingham, WA, 1991; pp 162–171.
9. Griffiths, C. H.; Walker, M. S.; Goldstein, P. *Mol. Cryst. Liq. Cryst.* **1976**, *33*, 149–170.
10. Wada, T.; Matsuoka, Y.; Shigehara, K.; Yamada, A.; Garito, A. F.; Sasabe, H. In *Photoresponsive Materials*; Doyama, M.; Somiya, S.; Chang, R. P. H., Eds.; Proceedings MRS International Meeting on Advanced Materials 12; Materials Research Society: Pittsburgh, PA, 1989; pp 75–80.
11. Ziolo, R. F.; Griffiths, C. H.; Troup, J. M. *J. Chem. Soc. Dalton Trans.* **1980**, 2300–2302.
12. Heflin, J. R.; Cai, Y. M.; Garito, A. F. *J. Opt. Soc. Am.* **1991**, *B8*, 2132–2147.
13. Kajzer, F.; Messier, J. *Thin Solid Films* **1985**, *132*, 11–19.
14. Cueller, E. A.; Marks, T. J. *Inorg. Chem.* **1981**, *20*, 3766–3770.
15. Schechtman, B. H.; Spicer, W. E. *J. Mol. Spectrosc.* **1970**, *33*, 28–48.
16. Davidson, A. T. *J. Chem. Phys.* **1982**, *77*, 168–172.
17. Hosoda, M.; Wada, T.; Yamada, A.; Garito, A. F.; Sasabe, H. In *Multifunctional Materials*; Buckley, A.; Daggitt, G. G.; Karasz, F. E.; Ulrich, D. R., Eds.; MRS Symposium Proceedings 175; Materials Research Society: Pittsburgh, PA, 1990; pp 89–94.
18. Hosoda, M.; Wada, T.; Yamada, A.; Garito, A. F.; Sasabe, H. In *Nonlinear Optical Properties of Materials III*; Khanarian, G., Ed.; SPIE Proceedings 1337; The International Society for Optical Engineering: Bellingham, WA, 1990; pp 99–104.
19. Hosoda, M.; Wada, T.; Yamamoto, T.; Kaneko, T.; Garito, A. F.; Sasabe, H. *Jpn. J. Appl. Phys.* **1992**, *31*, 1071–1075.
20. Hara, M.; Sasabe, H.; Garito, A. F. *Jpn. J. Appl. Phys.* **1989**, *30*, L306–308.
21. Tada, H.; Saiki, K.; Koma, A. *Jpn. J. Appl. Phys.* **1991**, *30*, L306–308.
22. Neher, D.; Kaltbeitzel, A.; Wolf, A.; Bubeck, C.; Wegner, G. In *Conjugated Polymeric Materials: Opportunities in Electronics, Optoelectronics, and Molecular Electronics*; Bréedas, J. L.; Chance, R. R., Eds.; Kluwer: Dordrecht, The Netherlands, 1990; pp 387–398.
23. Terasaki, A.; Hosoda, M.; Wada, T.; Yamada, A.; Sasabe, H.; Garito, A. F.; Kobayashi, K. *Nonlinear Optics* **1992**, *3*, 161–168.
24. Powell, R. C.; Soos, Z. G. *J. Lumin.* **1975**, *11*, 1–45.
25. Terasaki, A.; Hosoda, M.; Wada, T.; Tada, H.; Koma, A.; Yamada, A.; Sasabe, H.; Garito, A. F.; Kobayashi, T. *J. Phys. Chem.* **1992**, *96*, 10534–10542.

RECEIVED for review March 12, 1992. ACCEPTED revised manuscript February 22, 1993.

Liquid Crystals as Holographic Recording Media

Jian Zhang and Michael B. Sponsler*

Department of Chemistry and W. M. Keck Center for Molecular Electronics,
Syracuse University, Syracuse, NY 13244-4100

Several properties of liquid crystals, principally their strong birefringence and controllable orientation, make them attractive for use as holographic recording media. A variety of methods from the recent literature that exploit these properties are discussed and compared. The recording methods are complementary in their advantages and disadvantages, offering different combinations of on-off switchability, fast recording, latency, erasability, instant developing, and other features. High efficiency is a common advantage, because all of the methods provide phase holograms with large index modulations. Particular attention is paid to the switching capability of the liquid-crystalline media, because this feature, not offered by any other recording media, is likely to be of great importance in optical processing and molecular electronic applications.

SPECTACULAR THREE-DIMENSIONAL (3D) IMAGES produced through holography are becoming increasingly common. In truth, many current and potential applications of holography fall into this “display” category (1, 2). However, the usefulness of holography does not end with display applications. Other actual and potential uses include nondestructive interferometric testing (3), mechanistic elucidation of photochemical and photophysical processes (4), high-resolution lithography (5), high-density data storage (6), optical signal processing (7, 8), and molecular computing (9). Its intrinsically parallel nature has made holography especially attractive to electrical engineers interested in optical data processing, transfer, and storage. Among this group, however, a fervent need for new holographic recording media is generally expressed. In this chapter,

* Corresponding author

0065-2393/94/0240-0321\$08.00/0
© 1994 American Chemical Society

we will show that liquid-crystalline materials have a great potential to satisfy this need (10).

Holography—The Basics

The simplest holographic experiment will be described first. When two coherent light beams, typically from the same laser, are crossed at a sample, the beams interfere with one another (Figure 1). When plane-wave beams are used, the interference pattern is a sinusoidal grating, with alternating planes of constructive interference (“light” regions) and destructive interference (“dark” regions). If the sample is sensitive to the wavelength of light employed, then a grating of alternating reactant and product regions is obtained. Because the reactant and product regions have different absorbances and refractive indices, the grating thus produced is capable of diffracting light. In fact, if one of the writing beams is blocked, the remaining beam will be partially or completely diffracted so as to reconstruct the blocked beam. This process is termed “reading” the hologram, and the percentage of the reading beam that is diffracted is called the holographic or diffraction efficiency (η).

In display holography, one of the beams is used to illuminate an object (Figure 2). The light reflected from the object (the “object beam”) then interferes at the recording material with the plane-wave “reference beam”. The interference pattern produced is much more complex than a grating, but the reading step is unchanged. When the sample is irradiated with only the reference beam, the object wavefront is recreated, as if the object were still being illuminated. An observer sees a 3D image of the object.

Several apparatuses that allow investigation of the holographic recording processes have been described. Two methods, given the names phase-insensitive holography (PIH) and phase-modulated holography (PMH) by Bräuchle, are representative (11, 12). These methods use crossed laser beams, as described earlier, to create interference fringes that are recorded in the sample through its photochemistry (Figure 1). Simultaneous reading is accomplished in PIH by chopping one beam

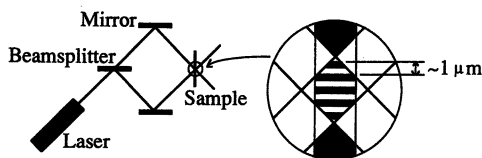


Figure 1. Crossed-beam irradiation generates interference fringes that are recorded in the sample through photochemistry. Photoproduct is formed in the “light” regions, whereas the reactant remains in the “dark” regions. The resulting grating can then diffract one of the beams into the other.

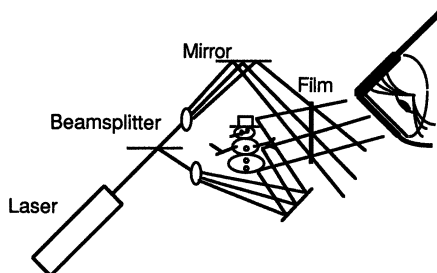


Figure 2. Optical apparatus for recording of holographic images. In the reading step, the object is removed, and the film is illuminated with only the reference beam. The observer will see 3D image of the object, as if the object were still in place. (Adequate eye protection is required!)

and measuring the diffracted intensity with a photodiode. In PMH, one beam is phase modulated and the resulting beat signal is detected in both beams. By using these techniques, the growth of the hologram, reflecting the kinetics of the photoinduced processes, may be followed as well as its decay, reflecting a variety of relaxation processes. The PMH method is much more sensitive than PIH and has the added advantage that diffraction due to refractive-index changes (phase effects) can be separated from diffraction due to changes in absorbance (amplitude effects). A similar phase-modulated apparatus, described as a holographic-relaxation spectrometer by Odear et al., is designed specifically for transient-grating experiments (13). Many researchers have used transient-grating experiments (14).

Of course, analytical holographic techniques such as PIH and PMH are invaluable in the development of new recording media. These techniques allow quantification of efficiency, sensitivity, resolution, and almost every other characteristic that one would like to know about a medium. Furthermore, important insights about the recording mechanism may be gained through analysis of signal growth–decay traces and the dependence of these kinetics upon experimental variables.

Holography and Liquid Crystals Are Synergistic

The combination of holography (a technique) and liquid crystals (a phase of matter) is a synergistic one. Thus, holography may be advantageously used to investigate physical and chemical processes in liquid crystals, and liquid crystals have much to offer as holographic-recording materials, which is the main focus of this chapter. However, the reasons for using holography to study liquid crystals will be addressed first, after a brief introduction to liquid crystals.

Most compounds display solid, liquid, and gaseous phases, but some show additional phases intermediate between the solid and liquid phases.

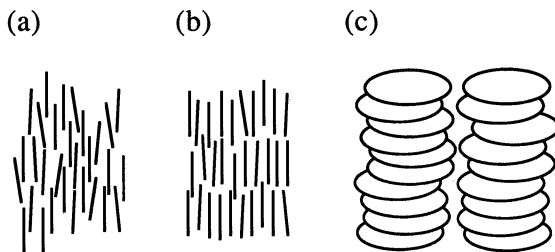


Figure 3. Three different classes of liquid crystals: (a) nematic, (b) smectic, and (c) columnar discotic.

These phases are fluid, yet possess varying amounts of orientational and positional order, and are thus referred to as liquid-crystalline or mesomorphic phases. A compound or mixture may have one or many liquid-crystalline phases. Representations of nematic, smectic, and discotic liquid crystals are shown in Figure 3. Thermotropic liquid crystals, obtained by heating the solid phase, are much more commonly studied than are lyotropic liquid crystals, which are obtained by adding a solvent to the solid.

Liquid crystals, which are anisotropic, lend themselves well to study by holography, an anisotropic technique. The grating formed in plane-wave holography has a well-defined orientation, as shown in Figure 1. The orientation of a liquid-crystalline sample (especially a nematic phase) is easily controlled by treating the surfaces of the sample cell or by applying external electric or magnetic fields. Therefore, samples can be made with the average molecular axis parallel or perpendicular to the interference fringes. By comparing results from the different orientations, the anisotropy of the hologram growth and decay processes may be evaluated.

For example, anisotropic diffusion constants have been obtained by dissolving a photochromic dye in a liquid crystal, creating a grating pattern by using pulsed crossed beams, and measuring the rate of hologram decay (15). Under appropriate conditions, this rate represents the rate of diffusion of the dye from the dark to the light regions, and its isomer in the opposite direction. Holographic measurements of methyl red in *N*-(4-methoxybenzylidene)-4-butylaniline (MBBA) provided a ratio of anisotropic diffusion constants ($D_{\parallel}:D_{\perp}$) of 1.6, in good agreement with previous tracer data.

Why Use Liquid Crystals in Recording Media?

Several factors combine to make liquid crystals attractive as recording materials for holography. The first is their birefringence or refractive-

index anisotropy. Holographic diffraction arises from both absorbance and refractive-index variations, but considerable practical advantages are associated with nonabsorbing media that rely exclusively upon refractive-index changes. "Pure-phase" holograms do not suffer from photochemical degradation in the reading stage, and may theoretically (and also in practice) approach 100% in diffraction efficiency. The theoretical efficiency limit is 7% for a hologram based solely on absorbance (16). The typically high birefringence of liquid crystals, ranging up to 0.3 or higher, suggests that efficient, pure-phase holograms may be obtained through variation of orientation or order between the light and dark regions.

If a clean modulation of liquid-crystalline orientation can be attained by some method, then the refractive-index modulation (Δn) should approach the birefringence ($n_{\parallel} - n_{\perp}$) of the liquid crystal. The Δn values attainable in this way are considerably higher than those obtained with most commercial recording media and are high enough to achieve 100% holographic efficiency with very-thin films. For example, to achieve 100% efficiency with a film 10- μm thick, Δn need only be 0.055, taking a transmission geometry with a wavelength of 633 nm, a recording angle (θ) of 30° from the normal for each beam, and an average refractive index of 1.5 (16).

An alternative approach is to vary the degree of liquid-crystalline order between the light and dark regions. If a modulation involving an ordered state and an isotropic state can be achieved, then Δn should approach $n_{\parallel} - n_{\text{ave}}$ (or $n_{\text{ave}} - n_{\perp}$), or about one-half of the birefringence. The attainable Δn is lower than for modulation of orientation, but is still quite large.

Another feature of liquid crystals that makes them attractive for holography is the easy controllability of orientation. Nematic liquid crystals may be aligned either by using a variety of surface treatments or by applying external electric or magnetic fields. Of course, this property and the high birefringence are exactly the features that allowed the development of the now ubiquitous liquid-crystal display (LCD) and the newer liquid-crystal television (LCTV). For holography, control over orientation at a minimum provides added flexibility in the recording and reading steps and more importantly can allow switching or modulation of diffracted intensity.

The ability to switch a hologram on and off opens many new doors for the field of holography. Potential applications for switchable recording media include holographic spatial-light modulators and beam-steering holographic optical elements. Some preliminary applications work of this type has been reported (17). These and other switchable components might be useful for many types of optical signal processing, including optical computing and associative memories. The media could

also be used to produce frequency-gated holographic signals for applications such as optical-noise reduction. In interferometry, switchable media could allow fine-tuning of the fringe image after recording and without the need for real-time observation. An important feature of switchable holograms is that they remain transparent in the off state, making their function difficult to duplicate with another switching component (e.g., a shutter or spatial-light modulator) combined with a normal hologram. This feature also makes a stacked arrangement of switchable holograms possible, in which individual holograms could be activated as desired.

Early in this section, we stated that pure-phase holograms were generally preferable. This is true, but if the medium does not absorb any of the light, recording is not possible. Each of the recording media subsequently described uses a chromophore of some type for the recording step, which may or may not remain in the reading step. In those cases in which the chromophore remains, a different (nonabsorbed) wavelength was typically used for reading.

The variety of recording schemes reported so far is tremendous. Most of the reports have appeared in the past five years, and the possibilities are far from exhausted. Each method is first discussed briefly and then the various features of all the methods are compared.

Instantaneous Media

The examples in this section illustrate the simplicity that is possible in liquid-crystal recording media, although the examples are only practical for reading during or immediately following the writing step. In the early 1970s Margerum et al. (18) and Poisson (19) reported photoconductor-based media. A nematic liquid crystal was sandwiched between conductive glass plates with a layer of photoconducting material on one of the plates (Figure 4). Under pulsed or continuous crossed-beam irradiation, the photoconductor became conducting in the regions of constructive interference, allowing electric-field alignment of the liquid crystal. This medium showed a fast response (a few milliseconds), high sensitivity, and a steady-state efficiency of 8%. Further refinements of this strategy have been reported (20).

An even simpler medium consists of a nematic liquid crystal with a dissolved dye sandwiched between glass plates (21). Under pulsed holographic irradiation, local warming in the light regions causes a change in refractive index. The result is a phase grating that decays on the microsecond time scale. High-efficiency gratings (25%) were obtained by adjusting the temperature to just below the nematic-isotropic transition, where the refractive index is very sensitive to temperature changes. This medium was successfully used in the demonstration of

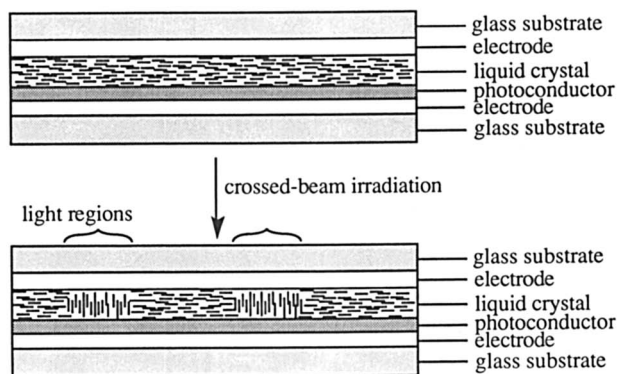


Figure 4. Photoconductor-based instantaneous-recording medium. In the light regions, the photoconductor layer becomes conductive, exposing the nematic liquid crystal to an electric field. The liquid-crystal molecules align with the applied field.

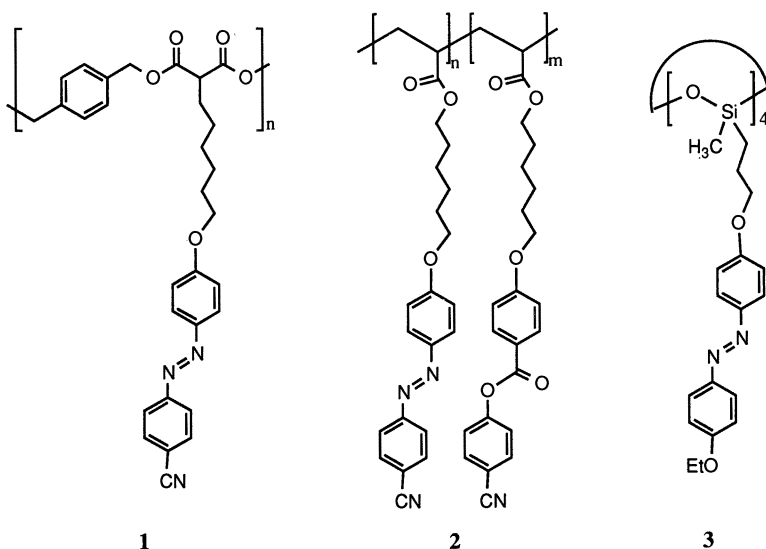
real-time correction of severely aberrated images by degenerate four-wave mixing. Many others (22) have studied the holographic generation of transient thermal and orientation gratings in nematic films. A recent report (23) describes the use of small inorganic particles dispersed in a nematic liquid crystal, allowing bistable, reversible optical recording.

Recording Media Based on Azobenzene Isomerization

Several recording schemes have been based upon the photoisomerization of azobenzene derivatives. These schemes all have the advantage of reversibility, that is, after writing (and reading) a hologram, it may then be erased so that another image can be recorded. In these media, the more stable *trans* isomer of the azobenzene derivative is converted to the *cis* (which may photoisomerize or thermally decay back to the *trans* form), inducing a change in liquid-crystalline order or orientation.

Stable yet reversible hologram storage has been reported in liquid crystals that incorporate the azobenzene structure. Eich and co-workers (24, 25) used polyester 1 and polyacrylate 2 and Ortler et al. (26) used the siloxane 3 all of which have azobenzene units in their side chains. The recording technique is similar to "thermorecording", in which a single laser beam is used to write patterns in a preoriented liquid crystal through local heating of the material into its isotropic phase (27). In the azobenzene materials, absorption of light causes isomerization of the azobenzene chromophore and local disordering of the liquid crystal. As noted in one paper (24), an orientational photoselection effect, described later, is also likely to be important. The recorded image is permanent as long as the film is kept below its glass transition temperature and the

image may be erased by heating. Because the liquid crystal is in its glassy state, switching capability is not expected for these media.



Another azobenzene-containing polyester, similar to 1, has been reported (28) to produce a different holographic effect at higher exposures. The recording of these gratings required not only crossed-beam, 488-nm irradiation, but also irradiation with red light (633 or 670 nm), which could be done either at the same time or several minutes after the 488-nm exposure. Erasure was achieved by heating, and no loss of activity was observed in subsequent recording cycles. The authors postulated that the photoinduced process was a phase transition from isotropic to homeotropic (director normal to the glass plates), apparently caused by a previously unreported photoreaction of the azobenzene chromophore.

Azobenzene chromophores have also been used as a component of a surface layer that can align a nematic liquid crystal (29). When a region of the cell was exposed to polarized light, the liquid crystal near the dye-containing surface was found to reorient with its axis perpendicular to the light polarization. In the reported experiments, only one of the plates contained the azobenzene dye, so a twisted nematic texture was obtained in the illuminated regions (Figure 5). By irradiating with crossed beams, a holographic grating was obtained, and the pattern could be erased or rewritten by changing the polarization of the light. *Cis-trans* isomerization of the surface-bound dye with orientational photo-selection was proposed to account for the effect (30). Recording was also carried out with an empty cell, followed by filling the cell with

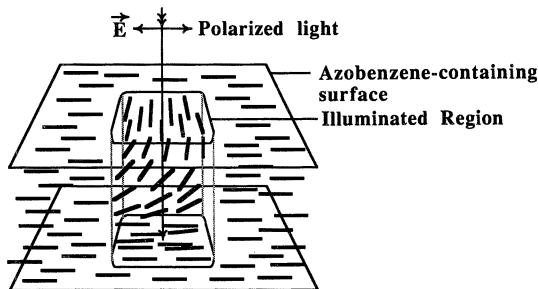


Figure 5. Surface-bound azobenzene recording medium. A nematic liquid crystal is sandwiched between glass plates with aligning surfaces, one of which contains azobenzene chromophores. Illumination with polarized light causes the azobenzene groups to reorient with their long axes perpendicular to the electric-field vector of the light. The liquid-crystal molecules next to this surface also reorient to align with the azobenzene, resulting in a twisted nematic texture in the illuminated regions.

liquid crystal, in a manner similar to the methods discussed in the next section.

The same process of orientational photoselection has more recently been used to write holograms in a nematic liquid crystal doped with 0.5% methyl red, an azobenzene dye (31). Surface interactions still play a major role in the recording mechanism, and with some surface treatments (e.g., polyimide) the holograms persist in the dark (32). If uncoated glass surfaces are used, the holograms may be erased by changing the polarization of the recording beams. With either surface treatment, erasure can be achieved by exposure to 337-nm light (33). We have repeated the experiments employing polyimide coatings and have found that electric-field switching can be used to reversibly enhance the diffraction efficiency by a factor of two.

Postirradiation Filling with Liquid Crystal

Three recording schemes have been reported that introduce the liquid crystal only after the recording stage. In 1987 Sainov et al. (34) reported the liquid-crystal filling of a photoshrinkable material. A layer of dichromated gelatin, which contracts upon photolysis, was coated on a transparent electrode and was exposed to crossed beams, giving a sinusoidal relief grating (Figure 6). The grooves, 1.4 μm deep, were filled with liquid crystal and covered with another electrode. When an electric field was applied across the sample, reorientation of the liquid crystal resulted in a change in Δn , in turn, causing a change in the diffraction efficiency. Under optimum conditions, an efficiency-modulation ratio of nine was obtained.



Figure 6. Liquid-crystal-filled relief grating. When a holographic grating is recorded in dichromated gelatin, a surface relief structure is obtained, because of shrinkage in the exposed regions. By filling the grooves with a nematic liquid crystal and sandwiching between transparent electrodes, a switchable hologram is obtained.

A conceptually similar recording medium (35) is based upon Polaroid's DMP-128 photopolymer (36). This material forms air pockets upon light-induced polymerization, and the unexposed regions can be made light stable by wet processing. If the air pockets are then filled with a nematic liquid crystal, a switchable hologram may be obtained (Figure 7). This polymer-dispersed liquid-crystalline medium has very impressive characteristics with respect to efficiency (close to 100%) and switching time (about 100 μ s).

A considerably more complex medium, which we will describe as "capacitance-coupled," involves a sandwich of three transparent electrodes. The center electrode contains the holographic interference pattern, transferred from the initial hologram recorded in either photoresist or silver halide media (37). The space surrounding the patterned electrode is then filled with liquid crystal. When high frequency voltage is applied between the outer electrodes, the liquid-crystal reorientation follows the pattern of the center electrode, leading to diffraction. When no field is applied, the diffraction efficiency can be very small. These holograms show very short switching times, approximately 100 μ m, and up to 45% efficiency.

Photopolymerization Media

A couple of reports (38) offer a different approach to the formation of a polymer-dispersed liquid crystals similar to those formed in DMP-128 (*see* previous section). In this method, a liquid-crystalline compound is dissolved in a monomer, along with a photoinitiator. Crossed-beam ir-



Figure 7. Liquid-crystal-filled DMP-128 photopolymer. Upon holographic irradiation, Polaroid's DMP-128 forms air pockets in the light regions. When these pockets are filled with a nematic liquid crystal, a switchable hologram results.

radiation causes polymerization of the monomer, leaving droplets of liquid crystal dispersed throughout. The size of the droplets depends on the light intensity. The droplets that form in the light regions are relatively small compared to those that form in the dark regions. The larger liquid-crystal droplets may be aligned with a smaller electric field than that required for the smaller ones, allowing for the desired switching effect.

Photopolymerization of liquid-crystalline monomers is an approach that we have taken (39). A nematic monomer with dissolved photoinitiator is sandwiched between conductive glass plates and then is exposed to the interfering laser beams (Figure 8). This exposure causes polymerization in the light regions preferentially, leaving monomeric dark regions. Upon application of an electric field, the monomeric regions align with the field, whereas the more rigid polymeric regions remain fixed. This switching could theoretically cause Δn to increase from near zero to approximately the birefringence of the monomer, resulting in a sharp increase in diffraction efficiency. At this point the hologram might be switched off again or made permanent by intense single-beam irradiation, causing polymerization of the entire film.

This scheme has been found to work well, with measured efficiencies up to 34%, the theoretical limit for optically thin gratings. We have used the nematic diacrylate 4, and its parent (without the methyl group), reported by Broer et al. (40), because they form cross-linked network polymers that retain the liquid-crystalline order (even upon heating to 300 °C). A typical diffracted response to the polymerization and electric-

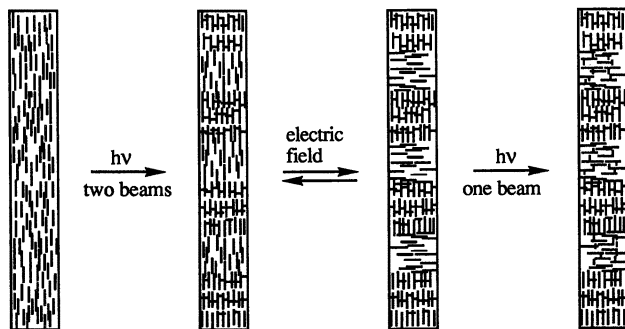
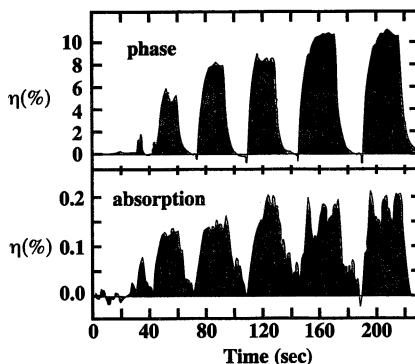
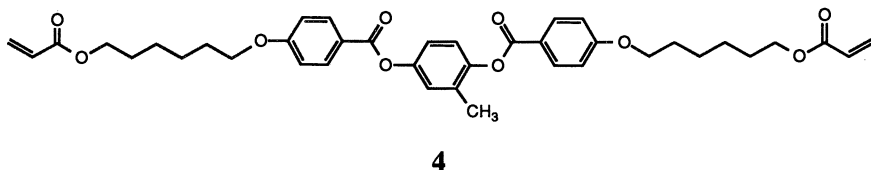


Figure 8. Holographic photopolymerization of a liquid-crystalline monomer. Crossed-beam photolysis causes photopolymerization in the light regions (shading). Upon application of an electric field, the monomeric regions align with the field, whereas the polymeric regions retain the original orientation. Reversible switching is achieved by turning the field on and off. Alternatively, a permanent hologram may be obtained by single-beam exposure, which causes polymerization of the entire film.

Figure 9. Diffraction efficiency modulation observed with electric-field switching from a grating written by photopolymerization of **4** (mixed with 20% 4-cyanophenyl 4-heptylbenzoate and 0.1% photoinitiator) in its nematic phase at 84 °C. Writing was done with 488-nm light (interbeam angle 2.6°, grating spacing 10.8 μm), and reading was done with 633-nm light. The observed ratio $\eta_{\text{on}}/\eta_{\text{off}}$ was 650. Fixing was accomplished through single-beam irradiation, at the arrow.



field switching is shown in Figure 9. The diffraction efficiency due to polymerization is nearly zero, but rises dramatically upon application of the electric field. The intensity is modulated reversibly by a factor that can exceed 10^3 , representing a virtual on-off holographic shutter. The hologram can also be fixed in the “on” state through further exposure, as shown in Figure 9.



Advantages and Disadvantages of the Liquid-Crystalline Media

When a recording material is chosen for a particular holographic application, many characteristics of the media must be taken into account. The efficiency, sensitivity, resolution, shelf life (before and after recording), recording speed, ease of developing and fixing, erasability, multiple-exposure performance, linearity of recording, and latency may all be important. With the recently developed liquid-crystalline media described previously, the opportunity for switching capabilities has arisen, with the added considerations of efficiency-modulation ratio, switching speed, switching durability and voltage. What follows is not an exhaustive analysis of these features, but rather an attempt to identify the most important similarities and differences among the liquid-crystalline media, with comparisons also with commercially available media. Literature data concerning many of these features are lacking for the relatively new liquid-crystalline media.

In principle, high efficiency should be an advantage of the liquid-crystalline media; high Δn and the generally small role of absorbance effects allow this assertion. The available data are supportive. Nearly 100% efficiency was reported for the postirradiation filling of DMP-128, and up to 50% for the liquid-crystalline azobenzene derivatives. High-efficiency holograms were also obtained in the photopolymerization of liquid-crystalline monomers (34% for 6- μm samples).

The very high sensitivity of silver-halide emulsions (photographic films) often makes them the recording media of choice, despite their drawbacks, such as the need for chemical developing. In principle liquid-crystalline media should show good sensitivity, because a single photochemical event may influence the orientation or order of a relatively large region. The photoconductor-based instantaneous media indeed showed sensitivity to exposures of 1 mJ/cm^2 or less, approaching the range of silver-halide media. The capacitance-coupled holograms may be initially recorded in silver halide, taking advantage of its sensitivity. The photopolymerization methods make use of a photoinduced process that is a chain reaction, as well as electric-field-controlled amplification of efficiency (and sensitivity). For the liquid-crystalline monomer media, exposures of 18 mJ/cm^2 were required to achieve 34% efficiency, and significant improvement is expected for samples prepared in the absence of oxygen.

Little has been published about resolution limits in the liquid-crystalline media, although Eich and Wendorff have reported high-resolution capability (3000 lines/mm) for their azobenzene-containing liquid-crystalline polymers (24). Concerning the low-frequency limit, a presumed advantage of liquid-crystalline media may be noted with respect to photopolymerization methods. In most commercial photopolymer media, refractive-index modulation can be attributed to diffusion of monomer into the polymeric regions, resulting in a density modulation. These media have a low-frequency cutoff in the spatial modulation, because it is limited by diffusion. This limitation is removed in the liquid-crystalline media, because they rely on droplet formation or reorientation instead of diffusion.

Ease of development is another strong point for most of the liquid-crystalline media. Except for the postirradiation filling methods, developing is either automatic or requires only irradiation or the application of an electric field. Although some of the methods presumably provide films that are stable to extensive reading, the photopolymerization of liquid-crystalline monomers is the one method that offers a fixing step, an optional postrecording irradiation. Ease of developing and fixing is a general feature of photopolymer media.

Reversibility is a major advantage of the azobenzene media, all of which may be erased and reused. This reversibility may be important

for repetitive applications in which film replacement is impractical. For quick erasability, the surface-bound azobenzene and methyl red-doped media are presumably best, because erasure requires only irradiation and no heating. For applications in which reading need only be carried out immediately after recording, the instantaneous methods offer automatic erasing.

A tremendous advantage of holography as a storage technique is the possibility of recording 100 or more individually addressible images in a single section of film (2). This capability has not yet been reported for liquid-crystalline media. In principle, multiple images should be possible with any of the volume techniques, although this will have to be verified in each case. The surface-based methods, including the surface-bound azobenzene, the capacitance-coupled cell, and the filled dichromated-gelatin methods, are probably suitable for fewer exposures.

Linearity of recording is a measure of how accurately the intensity pattern of the interference fringes are transformed by the recording medium into refractive-index and absorbance patterns. For simplicity, the figures in this chapter show sharp boundaries between light and dark regions, although in reality the recording intensity fluctuations are gradual (sinusoidal). All of the media reviewed are at least theoretically capable of achieving gradual boundaries, but a range of linearities is to be expected. Few data are currently available. In terms of linearity with respect to exposure time and intensity, significant nonlinearities might be expected for the switchable media. For the liquid-crystalline monomers, the switching effect is strongest at low exposure, decreasing rapidly with increasing exposure.

Latency refers to the timing of hologram growth. If a hologram becomes efficient during the recording stage, then significant image distortion may result from the diffracted light. A latent recording medium is one that becomes efficient only after recording, usually in a developing step. Of the liquid-crystalline media discussed here, only five are latent: the filled dichromated gelatin, the surface-bound azobenzene (when used in a postirradiation filling mode), the capacitance-coupled cell, the two-wavelength azobenzene, and the photopolymerized liquid-crystalline monomer. The first three methods are typical of latent techniques, in that to avoid diffraction during the recording step, a postrecording development step is required. In these cases, and in all commercial latent media, the development step involves wet processing. The two-wavelength azobenzene and the liquid-crystalline monomer methods are unusual in that the recording exposure induces very little diffraction (i.e., it is latent), yet the medium can be developed instantly by either exposure to red light or switching on an electric field. With proper index matching, the polymer-dispersed liquid crystals formed by photopolymerization might also have this property.

Comparison of Switching Characteristics

The ability to modulate the intensity of a diffracted beam may be liquid crystals' greatest contribution to the field of holography. The impact of this development on optical processing is too early to judge, but all computers require switches, and tremendous flexibility has been gained with the addition of a holographic switch. Before the new media can find actual applications, however, their switching characteristics must be known.

A likely requirement for many applications is high-contrast, on-off switching. The highest intensity-modulation ratio reported so far exceeds 10^3 , obtained by polymerization of liquid-crystalline monomers. The "off" state is the crucial one in this regard, and it seems likely that any of the methods could achieve high modulation ratios by proper refractive-index matching in the off state. Although switching with the surface-bound azobenzene media was not reported, it might be expected that these holograms could be reversibly switched, with the off state being achieved by the application of an electric field across the sample. This method might provide high-modulation ratios without the need for refractive-index matching.

Switching speed is another crucial feature, especially for computing applications. The filled DMP-128 and capacitance-coupled media currently have the shortest reported switching times, about 100 μs or less. Given the remarkably fast computers of today, 100 μs may seem intolerably slow. However, the enormously parallel nature of holography [exceeding 10^4 bits per image (2)] needs to be considered also. To reduce the switching time in our photopolymerization method, we are currently investigating polymerizable ferroelectric liquid crystals. Ferroelectric liquid crystals are finding applications as optical switches, because of their very fast (microsecond) switching (41).

Switching durability is also a primary concern for any long-term applications. Few prolonged experiments have been reported for any of the switchable media, but the only method with an intrinsic switching-durability problem is the photopolymerization of liquid-crystalline monomers. In this method, the switching medium consists of alternating layers of monomer and polymer. If the same wavelength of light is used for recording and reading, then the monomeric regions will eventually polymerize under prolonged exposure, even if the reading intensity is low. However, when using a nonabsorbed wavelength of light for reading, we observed negligible degradation of signal after 10^5 cycles. An alternative solution may be the use of a two-photon initiator, such as the one developed by Lee and Neckers (42). A colorless benzospiropyran is converted by UV irradiation to a colored merocyanine that thermally reverts quickly to the benzospiropyran, but can initiate polymerization

upon exposure to red light. Thus, recording could be accomplished by using a red laser in the presence of incoherent UV light. However, in the absence of UV light, the sample would be indefinitely stable to the red light used for reading. We are currently investigating this approach.

Striking differences in the voltage required for switching separate the different methods. The polymer-dispersed liquid-crystal methods can require voltages of 100 to 400 V, or as little as 20 V (photopolymerization), depending on the size of the droplets. The photopolymerizable monomers also show a range of values depending on domain size, which, in this case, is the grating spacing. For spacings of about 10 μm , the optimum voltage is only 3 V.

Other Uses for Liquid Crystals in Holography

Aside from their use in recording media, liquid crystals have found a number of other uses in holography. A closely related effort is the use of LCDs and LCTVs in the generation of synthetic holograms. A synthetic hologram is not recorded optically; rather the interference pattern is computed and then somehow generated in a material. Extensive computations are required for anything other than plane-wave diffraction, but that is not the concern here. Generation of synthetic holograms in an LCD (or LCTV) may eventually offer the ultimate switching performance, with no limit to the number of images, because images are stored in the computer and not in the material. However, even in straightforward plane-wave beam-steering experiments, severe limitations exist with this method, mainly due to resolution issues (43).

More promising applications for LCTVs exist in the production of computer-generated and remote-object multiplex holograms (44). In these techniques, a series of images, typically a continuous set of views of an object from different angles, are obtained either by computer generation or by video camera. The images may be sequentially displayed on an LCTV and recorded onto thin vertical sections of the holographic film. The resulting collage or "rainbow" hologram may give a 3D impression, because each eye views a different hologram and "sees" the object from its own angle. These indirect methods allow recording of holograms for objects, such as buildings, that cannot be imaged directly. Before LCTVs, a similar technique was done much more tediously through photography.

A related recent development is the use of an LCTV to "display" holographic interference patterns captured by a video camera (45). The holographic image may then be reconstructed by illumination of the LCTV with an appropriate reference beam.

Mention here of all such uses of LCTV in holography is clearly beyond the scope of this chapter, because the function of the LCTV is

display and not recording. However, the new switchable recording media may be better suited for some such uses. For example, switchable holographic media may be preferable to LCTVs as spatial-light modulators in some applications due to their higher resolution.

Liquid crystals have also found application in acoustic holography. The response of liquid crystals to acoustic waves has been used to convert acoustic signals into optical images (46, 47).

Molecular Electronics

Individually, holography and liquid crystals have desirable features for molecular electronics applications. Holography allows one to optically probe and change submicrometer regions of space without the need for submicrometer-diameter laser beams. Holographic detection is a key part of a recent "molecular-computing" method based on spectral hole-burning (9). Liquid crystals are materials that respond with order or orientation fluctuations to many types of external influence, such as electric and magnetic fields, temperature, pressure (acoustic waves), and surface structure. The response of liquid crystals to these forces may conveniently be monitored optically, by virtue of their large birefringence. Thus, holography and liquid crystals both have features suitable for input and output operations, making their combination a natural one for molecular electronics devices.

Inroads might be made into the difficult problem of small-scale fabrication through the combination of holography and liquid crystals. Performing photochemistry with crossed laser beams allows the creation of submicrometer material gratings with alternating reactant and product layers. The use of liquid-crystalline materials allows static and dynamic control of molecular orientation, including relative orientation between reactant and product regions. More complicated arrays may be fabricated by using multiple exposures or patterned light beams, in combination with liquid-crystal realignment. Such arrays might serve directly as molecular electronics components or as foundations for further elaboration.

Conclusions

For essentially the same reasons that liquid crystals have found applications in other areas of optics (most notably as LCDs and LCTVs), they are also attractive as holographic recording materials. The various liquid-crystalline recording media presented in this chapter offer high efficiency, and some of them offer switching capability, a feature presently unavailable in commercial media. The ability to switch a hologram on and off should significantly extend the usefulness of holography.

Although extensive data are unavailable for the liquid-crystalline media, they seem to offer significant advantages over currently available

media. As with all recording materials, each liquid-crystalline medium has its strengths and weaknesses, and none of them will be suitable for all applications. The recording schemes discussed show a large diversity and hopefully suggest new possibilities to the reader.

Acknowledgment

We thank the donors of the Petroleum Research Fund, administered by the American Chemical Society, the Camille and Henry Dreyfus Foundation New Faculty Award Program, and the W. M. Keck Foundation for partial support of the work carried out at Syracuse University.

References

1. Jeong, T. H. In *Applications of Optical Engineering*; Dubiel, M. K.; Eppinger, H. E.; Gillespie, R. E.; Guzik, R. P.; Pearson, J. E., Eds.; Proceedings of SPIE Vol. 1396; International Society for Optical Engineering: Bellingham, WA, 1991; pp 718–721.
2. Gabor, D. In *Lasers: Theory and Applications*; Thyagarajan, K.; Ghatak, A. K., Eds.; Plenum: New York, 1981; pp 365–402.
3. Ostrovsky, Y. I.; Shchepinov, V. P.; Yakovlev, V. V. *Holographic Interferometry in Experimental Mechanics*; Springer-Verlag: Berlin, Germany, 1991.
4. Bräuchle, C.; Burland, D. M. *Angew. Chem. Int. Ed. Engl.* **1983**, *22*, 582–598.
5. Omar, B. A.; Clube, F.; Hamidi, M.; Struchen, D.; Gray, S. *Solid State Technol.* **1991**, *34*, 89–93.
6. Berra, P. B.; Ghafoor, A.; Guizani, M.; Marcinkowski, S. J.; Mitkas, P. A. *Proc. IEEE* **1989**, *77*, 1797–1815.
7. Psaltis, D.; Brady, D.; Gu, X.-G.; Lin, S. *Nature (London)* **1990**, *343*, 325–330.
8. Soffer, B. H.; Marom, E.; Owechko, Y.; Dunning, G. In *Liquid Crystals and Spatial Light Modulator Materials*; Penn, W. A., Ed.; Proceedings of SPIE Vol. 684; International Society for Optical Engineering Bellingham, WA, 1986; pp 2–6.
9. Wild, U. P.; De Caro, C.; Bernet, S.; Traber, M.; Renn, A. *J. Lumin.* **1991**, *48–49*, 335–339.
10. Birenheide, R.; Wendorff, J. H. *Angew. Makromol. Chem.* **1990**, *183*, 167–195.
11. Pinsl, J.; Gehrtz, M.; Reggel, A.; Bräuchle, C. *J. Am. Chem. Soc.* **1987**, *109*, 6479–6486.
12. Gehrtz, M.; Pinsl, J.; Bräuchle, C. *Appl. Phys. B* **1987**, *43*, 61–77.
13. Odear, R. M.; Park, I. H.; Xia, K.; Johnson, C. S., Jr. *Rev. Sci. Instrum.* **1991**, *62*, 27–32.
14. Eichler, H. J.; Günter, P.; Pohl, D. W. *Laser-Induced Dynamic Gratings*; Springer-Verlag: Berlin, Germany, 1986; Fourkas, J. T.; Fayer, M. D. *Acc. Chem. Res.* **1992**, *25*, 227–233.
15. Hervet, H.; Urbach, W.; Rondelez, F. *J. Chem. Phys.* **1978**, *68*, 2725–2729.
16. Tomlinson, W. J.; Chandross, E. A. *Adv. Photochem.* **1980**, *12*, 201–281.
17. Domash, L.; Schwartz, J.; Nelson, A.; Levin, P. In *Image Storage and Retrieval Systems*, Jamberdino, A., Ed.; Proceedings of SPIE Vol. 1662; International Society for Optical Engineers: Bellingham, WA, 1992; pp 211–217; Do-

- mash, L. H. In *Photonics for Computers, Neural Networks, and Memories*; Miceli, W. J.; Neff, J. A.; Kowel, S. T., Eds.; Proceedings of SPIE Vol. 1773; International Society for Optical Engineers: Bellingham, WA, 1993; pp 372–376.
18. Margerum, J. D.; Beard, T. D.; Bleha, W. P., Jr.; Wong, S.-Y. *Appl. Phys. Lett.* **1971**, *19*, 216–218.
19. Poisson, F. *Opt. Comm.* **1972**, *6*, 43–44.
20. Myl'nikov, V. S.; Ivanov, A. M. *Sov. Phys. Tech. Phys.* **1987**, *32*, 442–445 and references cited therein.
21. Karaguleff, C.; Clark, G. L., Sr. *Opt. Lett.* **1990**, *15*, 820–822.
22. Faulkner, G. E.; Elston, S. J. *Opt. Commun.* **1994**, *105*, 279–284; Yan, P. Y.; Khoo, I.-C. *IEEE J. Quant. Electron.* **1989**, *25*, 520–529 and references cited therein.
23. Kreuzer, M.; Tschudi, T.; Eidenschink, R. *Mol. Cryst. Liq. Cryst. Sci. Technol. Sect. A* **1992**, *223*, 219–227.
24. Eich, M.; Wendorff, J. H. *J. Opt. Soc. Am. B* **1990**, *7*, 1428–1436.
25. Eich, M.; Wendorff, J. H.; Reck, B.; Ringsdorf, H. *Makromol. Chem. Rapid Comm.* **1987**, *8*, 59–63.
26. Ortler, R.; Bräuchle, C.; Miller, A.; Riepl, G. *Makromol. Chem. Rapid Comm.* **1989**, *10*, 189–194.
27. Sasaki, A. *Mol. Cryst. Liq. Cryst.* **1986**, *139*, 103–121.
28. Ramanujam, P. S.; Hvilsted, S.; Andruzzi, F. *Appl. Phys. Lett.* **1993**, *62*, 1041–1043.
29. Gibbons, W. M.; Shannon, P. J.; Sun, S.-T.; Swetlin, B. J. *Nature (London)* **1991**, *351*, 49–50.
30. Jones, C.; Day, S. *Nature (London)* **1991**, *351*, 15.
31. Chen, A. G.; Brady, D. J. *Opt. Lett.* **1992**, *17*, 441–443.
32. Chen, A. G.-S.; Brady, D. J. *Opt. Lett.* **1992**, *17*, 1231–1233.
33. Chen, A. G.; Brady, D. J. *Appl. Phys. Lett.* **1993**, *62*, 2920–2922.
34. Sainov, S.; Mazakova, M.; Pantcheva, M.; Tontchev, D. *Mol. Cryst. Liq. Cryst.* **1987**, *152*, 609–615.
35. Whitney, D. H.; Ingwall, R. T. In *Photopolymer Device Physics, Chemistry, and Applications*; Proceedings of SPIE Vol. 1213; International Society for Optical Engineering: Bellingham, WA, 1990; pp 18–26; Ingwall, R. T.; Adams, T. In *Computer and Optically Generated Holographic Optics*; Cindrich, I.; Lee, S. H., Eds.; Proceedings of SPIE Vol. 1555; International Society for Optical Engineering: Bellingham, WA, 1991; pp 279–290.
36. Ingwall, R. T.; Troll, M. *Opt. Eng.* **1989**, *28*, 586–591.
37. Parker, W. P. In *Practical Holography VII*; Benton, S. A., Ed.; Proceedings of SPIE Vol. 1914; International Society for Optical Engineering: Bellingham, WA, 1993; pp 176–187.
38. Margerum, J. D.; Lackner, A. M.; Ramos, E.; Smith, G. W.; Vaz, N. A.; Kohler, J. L.; Allison, C. R. U.S. Patent 4 938 568, 1990; Sutherland, R. L.; Natarajan, L. V.; Tondiglia, V. P.; Bunning, T. J. *Chem. Mater.* **1993**, *5*, 1533–1538.
39. Zhang, J.; Sponsler, M. B. *J. Am. Chem. Soc.* **1992**, *114*, 1506–1507; Zhang, J.; Carlen, C. R.; Palmer, S. P.; Sponsler, M. B. In *Photopolymers and Applications in Holography, Optical Data Storage, Optical Sensors, and Interconnects*, Lessard, R. A., Ed.; Proceedings of SPIE Vol. 2042; International Society for Optical Engineering: Bellingham, WA, 1994; pp 238–247; Zhang, J.; Carlen, C. R.; Palmer, S.; Sponsler, M. B. *J. Am. Chem. Soc.*, in press.

40. Broer, D. J.; Boven, J.; Mol, G. N.; Challa, G. *Makromol. Chem.* **1989**, *190*, 2255–2268; Broer, D. J.; Hikmet, R. A. M.; Challa, G. *Makromol. Chem.* **1989**, *190*, 3201–3215.
41. Johnson, K. M.; Handschy, M. A.; Pagano-Stauffer, L.-A. *Opt. Eng.* **1987**, *26*, 385–391.
42. Lee, S.-K.; Neckers, D. C. *Chem. Mater.* **1991**, *3*, 858–864.
43. Yamazaki, H.; Yamaguchi, M. *Opt. Lett.* **1991**, *16*, 1415–1417; Yamazaki, H.; Yamaguchi, M.; Fukushima, S. In *Topical Meeting on Photonic Switching*; Goncharenko, A. M.; Hinton, H. S.; Prokhorov, A. M., Eds.; Proceedings of SPIE Vol. 1807; International Society for Optical Engineering: Bellingham, WA, 1993; pp 382–383.
44. Cheng, Y.-S.; Lin, J.-Y. *Appl. Opt.* **1989**, *28*, 829–830.
45. Chen, J.; Hirayama, T.; Lai, G.; Tanji, T.; Ishizuka, K.; Tonomura, A. *Opt. Lett.* **1993**, *18*, 1887–1889.
46. Dion, J. L.; Simard, R.; Jacob, A. D.; Leblanc, A. *Ultrason. Symp. Proc.* **1979**, 56–60.
47. Intlekofer, M. J.; Auth, D. C. *Appl. Phys. Lett.* **1972**, *20*, 151–152.

RECEIVED for review March 12, 1992. ACCEPTED revised manuscript January 29, 1993.

Molecular Devices Using Langmuir–Blodgett Films

O. Albrecht, K. Sakai, K. Takimoto, H. Matsuda, K. Eguchi, and T. Nakagiri

Canon Research Center, 5–1 Morinosato-Wakamiya, Atsugi-shi,
Kanagawa-ken, Japan 243–01

Use of Langmuir–Blodgett (LB) films for the fabrication of devices at the molecular level is investigated. Because these films show control of order and dimensions in one direction only, they are not directly suited for this purpose. However, their properties are so intriguing and in many cases so much superior to other thin-film techniques that it is worthwhile to use them in combination with other technologies. We explored the application of LB films in the fabrication of molecular devices and suggested ways to make the dream come true. Our progress toward this goal is described, along with our attempt to build a memory system that uses an LB film as a storage medium and promises a capacity in the terabit range.

MOLECULAR DEVICES THAT USE LB FILMS as construction elements are still in the visionary stage. This chapter presents a summary of the current difficulties, indications that Langmuir–Blodgett (LB) films are nevertheless useful for fabricating molecular devices, related developments, and our efforts in the field.

The following overview of proposed applications of LB films and alternatives to their use demonstrates the possibilities and inherent problems of LB technology. This overview is followed by proposed uses of LB films in molecular devices, a summary of current problems with the technology, our efforts to solve these problems, and two examples of attempts to use LB films in devices that come close to the molecular limit, at least in one dimension.

Familiarity with the meaning of molecular device, LB films, and insoluble monolayers on aqueous subphases (Langmuir films) is assumed here. Definitions of molecular device are available in other parts of this book. Reference 1 offers a recent summary of LB technology; the best

0065–2393/94/0240–0341\$09.98/0
© 1994 American Chemical Society

presentation of the current state of the art is probably reference 2, the proceedings of the 5th International Conference on LB Films (Paris, 1991).

LB films can be fabricated from molecules that form a monomolecular layer on an aqueous subphase. Most of the molecules that can be used for this process are amphiphiles, consisting of a (small) hydrophilic group and a (larger) hydrophobic group. Some film-forming materials do not fit this model, but nevertheless form monolayers that can be deposited. Deposition of the film requires a surface concentration of molecules within a proper range. A minimum attractive force is needed between the substrate and the film, when either the lower (hydrophilic) side or the upper (hydrophobic) side of the monolayer is brought into close contact. van der Waals forces may provide sufficient attraction, but ionic forces or chemical bonds are more efficient. Often the substrate is already coated with an LB film. If the conditions are right, the film can be deposited simply by dipping the substrate object through the liquid surface, while keeping the surface coverage within a suitable range. In the case of a hydrophobic substrate, the dipping is achieved from above the aqueous surface; if the substrate is hydrophilic it is lifted from below the surface.

Thus the LB technology provides a means to fabricate very thin coatings of organic materials on solid substrates. Repetition of the process generates any desired thickness in multiples of the thickness of individual layers. The film-forming material can be changed in any required sequence. The thickness of individual layers ranges from about 4 to 50 Å. Uniformity of coatings over macroscopic dimensions is excellent, as seen by the clarity of interference colors of even very thick films and as verified by thickness measurements.

Film-forming materials cover the whole spectrum of organic chemistry, from small molecules with a molecular weight of around 200 to polymers with a molecular weight of more than 1,000,000. It is possible to modify the film-forming materials at various stages. They may undergo reactions while still a floating monolayer or after deposition. They can react with themselves, with neighboring films, with reactants in the subphase during fabrication, or with gases and other liquids.

All this looks very attractive. After many decades of slow development, the field was tremendously boosted around the late 1970s and early 1980s because of the promise of timely applications and solutions of problems in many areas of advanced technology.

Traditionally the monolayer and LB field was, and is, used in physics and chemistry to study the properties and interactions of molecules in quasi-two-dimensional systems. Langmuir films show phases and phase transitions analogous to those in three-dimensional systems (like gas, liquid, and solid states in different modifications) as well as many inter-

mediate states that can be described through liquid crystal terminology. Deposition is possible, generally, when the monolayer is in a condensed, solid analog, or liquid crystallike state.

Another source of input into the field comes from the biosciences, where monolayers as well as deposited multilayers are used as models for biological systems. Many membrane-forming materials in living organisms also form monolayers and can be made into LB films. Furthermore, many of the production units (proteins) in living systems can be manipulated by the LB technique in mixtures with lipids (film-forming biomaterials) or sometimes by themselves. These examples of molecular devices are working in an environment so similar to LB films that it seems to be a small step to use the same principles for technological processes.

General advantages of LB technology are:

- Even the thinnest films form continuous coatings, in contrast to vacuum-deposited films (evaporated or sputtered) and spun-on films.
- Very precisely controlled thickness and very good uniformity.
- Coating of curved surfaces with equal uniformity.
- Soft technology; it looks feasible to find materials for practical applications that do not pollute, are not poisonous, and involve small amounts of materials used and waste produced.
- Materials can be synthesized and modified by using the whole range of organic chemistry.
- Temperatures involved are close to room temperature, thus preventing damage to heat-sensitive substrates and molecules.
- The surface of a well-deposited stack of films is generally much smoother than the original surface.
- On suitable substrates, the films can bridge pores up to the micrometer range.

General disadvantages are (or might be, for some applications):

- The coating involves dipping of all objects into an aqueous subphase. (A hydrophobic substrate is coated by a monolayer upon the first immersion.)
- In many cases the coating material of interest has to be modified to render it capable of forming monolayers and

to enhance its adhesion properties. The film is normally composed of functional groups and a percentage (sometimes large) of structural groups that generally reduce the efficiency of the functional groups.

- The process is dependable only on smooth surfaces. Grooves, especially when crosswise to the movement during deposition of the film, prevent smooth coating.
- It is very difficult to find substrates, especially large ones, that have surfaces smooth enough to allow deposition of a monolayer without damage over macroscopic as well as nanoscale dimensions.

Review of Proposed Applications

Applications of these LB films have been proposed in many fields since the initial work was done 60 years ago. However, most applications use these thin films to control bulk properties of the deposited materials rather than individual molecules.

Optical Coatings. The classical application (3, 4) is optical coatings. These films are much more uniform than evaporated films and even coat curved surfaces (e.g., the outside of a cylinder or a ball, except for the poles) with uniform thickness. Thus, they are competitive with existing methods that, at best, would involve additional complicated procedures. However, most organic coatings are mechanically less stable than many conventionally used oxide layers.

A more severe problem is the limit in available refractive indices. One way to extend this range at the lower end was demonstrated by Blodgett herself (4). A film was deposited from a mixture of two species of molecules with very different solubilities in a certain solvent. When the film was exposed to this solvent, the soluble part was removed and the insoluble part was left. Blodgett used a free fatty acid as the soluble species and an ion complex of the same fatty acid as the insoluble species, without destruction of the original order.

Subwavelength voids formed in the film result in a decrease of the refractive index. However, this method of "skeletonizing" a film works dependably for single film applications only, not in the technically more interesting case of stacks of films of different refractive indices. Without using this procedure, a refractive index range from about 1.3 to 1.75 seems possible. This range is somewhat limited, but useful for many purposes. The fabrication of dielectric mirrors and filters is possible without limits for the visible range, and antireflective coatings are feasible for most optical materials. However, very little related work has been published recently, despite the fact that the procedure looks very

rewarding and was one of the first applications proposed by Langmuir and Blodgett.

An especially intriguing aspect of this application is the possibility of choosing two materials with refractive indices at extreme but opposite ends of the available range. Either by simply mixing these materials or by depositing the layers in mixed stacks, any refractive index between the two pure materials is possible. The thickness of the individual layers is much smaller than the wavelength of light, so the light sees only the average index. We plan to demonstrate some of the optical applications in the near future.

Optical and other applications have not been pursued more tenaciously because many publications (5–7) have reported degradation of film properties through a time-dependent reorganization or recrystallization of the film molecules. Nevertheless, many other results would not be possible if this degradation were a general property of LB films. Although this reorganization problem is found in many samples, we are investigating indications that it occurs mainly in poor-quality films, not in well-manufactured samples. The governing factors are still elusive, but published reports indicate ways to inhibit this problem. However, there is a deep-rooted belief in the LB community that the unfavorable results are the usual behavior.

Waveguides. A related goal is the fabrication of waveguides from LB films. For many years publications concluded that the method works in principle, but that the optical losses of the waveguide structure were too high by several orders of magnitude. At the recent LB conference, reports (8) appeared about the fabrication of LB waveguides with optical losses one order of magnitude lower than what is regarded as the technically required minimum for useful thin-film waveguides (9).

Insulation. Another basic application is the use of LB films as insulating layers. Here again, many reports show that these films have pinholes that cause electrical shorts, and very few show the contrary. It has been demonstrated, however, that capacitors can be built with LB films as insulating layers and that field effect transistors (FET) can possibly use an LB film as a gate insulator (10). The leaks are evidently not an intrinsic property, but artifacts. However, measurements on these films show that the electrical behavior is more complicated than anticipated (11).

One major general technical problem presently is to improve the ability to fabricate smaller structures. The common procedure is to use a resist that is deposited on the surface to be patterned. The final resolution depends upon many parameters, including the thickness of the resist layer. The generally used process of “spinning-on” these resist

layers is very difficult to improve beyond the present limit. Here LB films are expected to be helpful, and many reports exist about the feasibility of this approach (12, 13). Resolutions down to tens of Ångströms are reported (14), as well as the fabrication of a 5-inch-square real-life mask, as used for semiconductor processing, with a test pattern (15). The resolution, with a 30-layer LB resist, was better than 0.5 μm . This resist was electron-beam (e-beam) sensitive, and the resolution was the limit of the available e-beam writing equipment.

Surface Modification. Another basic application for LB films is surface modification. These films can be deposited onto almost any pure and homogeneous material. They can be tailored to expose a moiety with almost any chemical or physical character, sometimes after a chemical treatment following deposition. This flexibility provides an opportunity to change the surface properties of substrates very drastically. The most simple and impressive example is the coating of a hydrophilic object, like a glass plate, with one layer of a fatty acid LB film. This treatment changes the surface of the glass from very hydrophilic to very hydrophobic. Applications have been discussed from simple lubrication layers (16, 17) or passivation layers (18) to making the surfaces of medical implants biocompatible (19). One obvious, though often overlooked, application for this surface modification effect is use of a (thin) LB film as an adhesion layer for subsequent deposition of a material that would not coat the original surface.

So far the listed applications are at a very low level of sophistication. The next step is to utilize more specific properties of the film-forming molecules.

Sensors. The first widely investigated application in this context is use of LB films as or in sensors. Many materials react either reversibly or irreversibly with a substance to be detected. The reaction can be detected by a change in electrical or optical properties, by monitoring a weight change, or by several more sophisticated methods. Electrical properties can be measured in a metal-LB-metal configuration by monitoring resistivity or capacity or by measuring the response of a FET where the gate is coated with the LB film. Optical absorption, fluorescence, fluorescence quenching, or reflectivity may be monitored. Configurations that use film-coated fibers are possible. Weight change is usually monitored through the change in frequency of a quartz oscillator coated with the LB film.

Generally the response time of such sensors depends upon the thickness of the sensing layer or upon how far the reactant has to diffuse through the system. The thinness of LB films promises to yield very quick response times. However, in practice, the response time is often

much slower than expected because the high order in good-quality films hinders fast diffusion. Thus, the sensors work well only when the film quality is poor. This means the LB films have no advantage over less time-consuming methods like dip-coating or spinning-on of the material.

Few materials are selective enough to allow the identification of a chemical compound in a real-life system (e.g., blood or sewage water) with certainty. This general sensor problem (not limited to LB sensors) can be solved by developing materials that are selective enough. This is probably the way to go for sensing large molecules, but it requires quite some effort. Another way is to use several different sensors and to deduce the truth by comparing the various responses via microprocessor. Degradation of the sensor can also be a problem that is enhanced due to the very small amounts of material in an LB film.

Membrane Separation. Specific reactions between a substrate and a reactant also lead to diffusion rate differences for different reactant molecules. In the simplest case the specific interaction is the exclusion of large molecules by small pores. This process is used in many technical applications like reverse osmosis, ultrafiltration, and other membrane-separation processes. Even alcohol-free beer and wine are made this way. With very thin LB films as membranes, the throughput is expected to grow when the thickness decreases. After many failed attempts to fabricate defect-free LB membranes, the results with good-quality films indicate that the diffusion coefficients are much lower than expected (20) because of the high molecular order in good films. The films could probably be used as a carrier for molecules that show the desired selective transport properties (copying nature). The problem in this case is that individual layers are clearly not strong enough mechanically and the deposition of multilayers does not lead to pores through the whole stack. In biological systems sometimes pores can form in a double layer when two pore formers, each in its own monolayer, diffuse until they are aligned. However, in a biological system the films are in a liquid analog state. LB films generally form only while the materials are in a solid analog state, and the order is destroyed when the finished films are heated.

Nonlinear Optics. Another application in this context is the use of LB films for nonlinear optics and (because the molecules are often the same) as heat sensors or piezo electric elements. Many organic molecules show promising properties when studied individually, but when used in bulk the effects of individual molecules cancel out and no net effect is measurable. LB films offer the possibility of forcing the molecules into a structure that enables them to enhance each other's properties, thus resulting in large effects. Reports exist (21) about engineered ma-

terials that perform equally well or better than conventional “natural” materials. Applications in this field are missing, in spite of promising research results.

Industrial Applications. The only known industrial or practical applications, as opposed to an abundance of applications in research, are the following:

- General Electric, the company where Langmuir and Blodgett performed their studies, sold thickness gauges made of an X-ray shield glass plate coated with a step pattern of a fatty acid LB film. The (optical) thickness of any other thin film can be estimated by comparing the interference colors.
- Cadmium–stearate or cadmium–arachidate LB films are used in several laboratories for calibration of X-ray diffraction equipment. However, we know of no commercial source for these standards.
- A company in Japan (Shimadzu, Kyoto) fabricates soft X-ray mirrors from cadmium–fatty acid films.
- A company in England (Hughes Whitlock Ltd., Malvern) sells (or sold) radiation standards fabricated by LB deposition of a thin film of radioactively marked molecules. The self-absorption of the thin film is negligible, and no other technique is available to fabricate such thin and homogeneous coatings.

Alternative Methods

Because LB films are rarely used in industry—whereas optical coatings, insulating thin films, resists, and surface-modification methods are used widely—alternatives to LB films are obviously available. It depends, however, on how close the limits are drawn. If the question is whether we can fabricate thin films by other means, many options are open. Evaporation, sputtering, spin coating, oxidation, electrolytic oxidation, and self-assembled monolayers (SA layers), which will be described in more detail, come to mind immediately. If the question is whether we can fabricate 20-Å continuous layers or stacks of optical layers with sharp defined interfaces and a very small thickness variation, both within Ångstrom dimensions, the field gets very narrow. Even LB films do not always show these properties in practice because of the low level of most of the equipment used and procedures applied. Another question limits the choices drastically: Can we deposit thin films of heat-sensitive materials, containing chemical functions of almost any simple or complex

nature, onto materials that range from metals, ceramics, glasses, and water-insoluble salts to hard and flexible plastic materials? This is easily done by the LB process.

The only serious competition seems to come from the field of the SA layers. For this process molecules are tailored to carry one group that reacts with the surface to be coated chemically, and usually selectively. This reaction is done in a suitable solvent and allows monolayers to build up on a limited number of surfaces (22). There are several advantages and several drawbacks to this process. The advantages are that no special equipment is required; surface irregularities do not hinder the formation and adhesion of the film in the vicinity of that defect; objects of any shape can be coated, even the inside of tubes or hollow objects; and the adsorption of the film can be limited to certain areas by pre patterning the surface. This modification is effective because in the SA process the molecules usually stick to one kind of surface only (e.g., a clean gold surface). Disadvantages are that the surface density is always less than that of comparable LB films, although obviously homogeneous; the number of available molecules is very limited; the types of surfaces onto which SA films can be built-up are very limited, and a specific match is necessary for each surface-material system; the buildup of multilayers is possible, but limited to the low tens of layers. So far the quality degrades quickly with the number of layers.

The right place for this technology is probably not as a competitor to the LB field; the two processes can supplement each other or can even be combined. For LB films, the final durability depends upon the strength of the bonds between the layers. A weak point is the interface between the substrate and first layer. SA layers could be used as adhesion layers, or the SA molecules themselves could be deposited by using the LB process to increase the surface coverage.

Something similar to SA layers is already used regularly to fabricate samples of LB films. The substrates are often coated with a layer of silane, from solvent or from the gas phase. One of the standard materials, HMDS (hexamethyldisilazane), can be used to render oxide surfaces strongly hydrophobic. This process is borrowed from the semiconductor industry, where it is used to homogenize an otherwise heterogeneous surface and to act as an adhesion layer (e.g., for resist films). However, it does not necessarily provide a surface coated with an ordered layer or a monolayer of material.

Molecular LB Devices

None of these applications could be associated with molecular devices. In all these cases a large number of molecules contributes collectively to produce the desired effect. Molecular devices, in contrast, are indi-

vidual functional units consisting of one molecule only and functioning alone, as an individual. However, existing molecular devices used by nature in abundance to make life possible do not necessarily show that units cannot be working in parallel. This configuration is probably a necessity for all applications of molecular devices, because it is very unlikely that each fabricated molecule will be free of defects. Using several in parallel will ensure reliability as well as providing a larger output signal that is easily detected.

The simplest application for this is an LB sensor fabricated from a film that contains very specific binding sites (*see, e.g., 23*) each of which can selectively bind a specific molecule from a real-life mixture, like blood. One attached molecule cannot be detected, but a monolayer (or at least a substantial percentage of a monolayer) of these molecules bound to the surface is easily detected. If the supporting film is deposited on a reflective substrate and is of a thickness that results in an interference color, a slight shift in color can be detected with a spectrometer or even by eye.

Communication. The first problem in using LB films to fabricate molecular devices is that any molecular device incorporated in the film needs to talk to the outside world in some way. The conventional way is to use conductors, waveguides, or (light) waves for communication. The most simple example for the last case was shown in the last paragraph, where a shift in the reflected spectrum is used to read the response. A severe limit for conductors and waveguides is the possible number of connections, which is limited by the size of the smallest possible structures. The present limit for this is around $0.5 \mu\text{m}$. Clearly, the present technology is so coarse that addressing individual molecules in this way does not make much sense. The use of light limits the addressable unit to the dimensions of the wavelength. The size of the transmitter and receiver itself, however, does not have that limit. This type of communication with individual units would require that each unit within the smallest addressable field reacts to a certain code only and answers either with a code attached or only after being asked to answer (while all other units are silent).

Another effect that also could be used for communication between units and the outside world is electron emission from the surface of a metal-LB film-(thin) metal structure (*24*), which has been found in our LB laboratory. Because the wavelength of electrons is smaller than that of light, electrons can be directed by electric and magnetic fields, and they do not need a special transducer at the receiving end, electron emission could be the method of choice to connect subassemblies. One immediate application could be used in displays, where the chromophore is directly deposited onto the surface of the device. The chromophore

also could be one of the recently developed luminescent Si structures (25, 26). The structure of such an electron-emitting device is as simple as the structure of an LED (light-emitting diode) and also requires low voltages only. The drawback for efficient use, however, is again the lack of ability to form very small structures.

Order within Film. The second problem is that LB films show well-defined order in one dimension only, perpendicular to the plane of the film. Within the plane of a layer the position of individual molecules is random for long distances, although it may show a short distance correlation. The direction of preferred axes in some cases is correlated to the direction of movement during deposition. However, all films that show this movement also show domain structures of various dimensions. Films without domain structures are amorphous, like some mixed films or most simple polymer LB films. This movement makes it very difficult to address and identify individual units of molecular dimensions. There are successful attempts reported (27) to improve on this. By fabricating an LB film with binding sites at the exposed surface for a large molecule of interest and then exposing this film to a solution of the molecules, a dense crystalline layer of the molecules can be obtained when the spaces between the binding sites are small enough.

Other attempts use the fact that domains can be made to grow in the floating monolayer to macroscopic dimensions. However, it is difficult to deposit these ordered films without disrupting the order. Attempts to overcome these limits are at least very cumbersome and slow, as opposed to the simplicity of the basic LB process (28, 29).

Another obstacle to getting order at the molecular level in organic films over macroscopic dimensions is the relatively low purity of the available materials. If only every 1000th molecule is defective or completely different (this would be a very high purity for large organic molecules) macroscopic crystalline order is clearly impossible. To overcome this difficulty, large molecules might be designed that define the position and distance of the next neighbor by shape or short-range forces. In such a system it is feasible that individual defects are kept local and do not destroy the long-range order. This possibility is illustrated in Figure 1.

Sometimes the direction of preferred axes in LB films is correlated with the direction of movement during fabrication. This situation is intuitively understandable because the flow during deposition can cause this orientation. We will elaborate about this phenomenon later. For the moment it is sufficient to note that this flow orientation can be used to orient polymer chains parallel, to a large degree, to the dipping direction. We will use this fact at the end of this section to show how the structure of a high-density molecular device might be constructed.

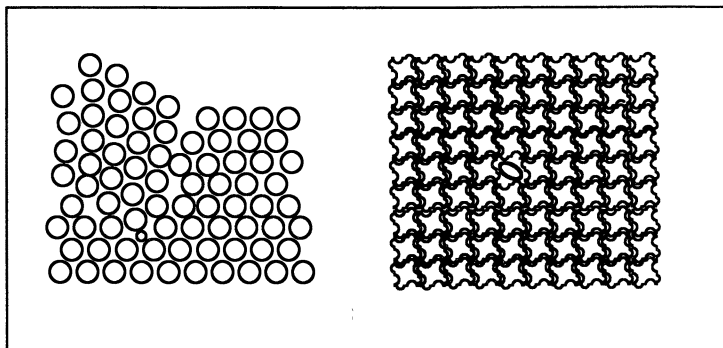


Figure 1. Inhibition of long-range order, caused by a different molecule in a typical LB film (left). Molecules on the right are shown with a shape that resists perturbation by impurities of the long-range order.

Use of LB Films. There are more ways to utilize LB films in constructing molecular devices. So far we were concerned only about using the films or molecules mixed into the films as active material. However, building molecular devices requires not only active components, but also passive components—similar to a television set that requires not only transistors, silicon chips, capacitors, resistors, luminescent dyes, and switches, but also many simple structural materials like sheet metal, printed boards, wires, and glass. Even an individual transistor or a packaged chip requires a variety of additional materials and related specialized techniques to function.

One way to utilize LB films is without doubt as a means to provide some of these things. The surface of an LB film that is several tens of layers thick is generally much smoother at a molecular level than the surface of any substrate. It is expected to rival mica or HOPG (highly oriented pyrolytic graphite) surfaces, but can be fabricated in any size. These smooth surfaces might be useful as substrates for devices, because they can be mass-produced easily and cheaply. Future molecular devices will require methods for fabricating very fine structures. LB resists might be useful in this respect, as well as for insulating layers between units or passivating layers on top of finished assemblies. For communication between subunits, the waveguiding properties might be useful. Even conductive LB films (30, 31) could be used as shielding planes or, after patterning, as electrical connectors.

Structure of a Molecular Device. Now we will show how the structure of a molecular device could be constructed, using the present technology and an LB film as active layer. This idea is very similar to ideas described in reference 32, which we will illustrate later. The dif-

ference is that this system would be a real molecular device and use LB films with all their shortcomings. In addition, the structure is very simple.

One of the problems is the limited number of electrical connections that can be fabricated, due to the restrictions in minimum feature size. A memory device, for example, will require a large number of connections in order to be of practical use. Nevertheless, we want to construct a memory device. The problem of the limited number of available outside connections will be addressed by using units that work like shift registers. We use a polymer that is made of individual memory units that can exist in two distinct states and that can transfer their state to the neighboring unit upon an external signal (e.g., a flash of light). The direction of information travel is given by an electric field. Other problems that need to be addressed are that the position of individual units is not well-defined and individual molecules or even polymer chains of molecules cannot be connected. How can we fabricate a useful device?

Figure 2 shows a schematic drawing of a section of the device. We deposit a layer of our memory chain polymer onto a suitable substrate under conditions in which the chains are in more or less parallel alignment. A suitable substrate could be a glass plate that allows light to reach the LB film. We pattern the film in small strips, crosswise to the alignment. We deposit onto that structure first an insulator and metal strips that are connected to one end of the film strips, then place crosswise another similar structure in which the metal strips are connected to the other end of the LB film stripes. We can now select one specific area of film for each pair of crossed conductors.

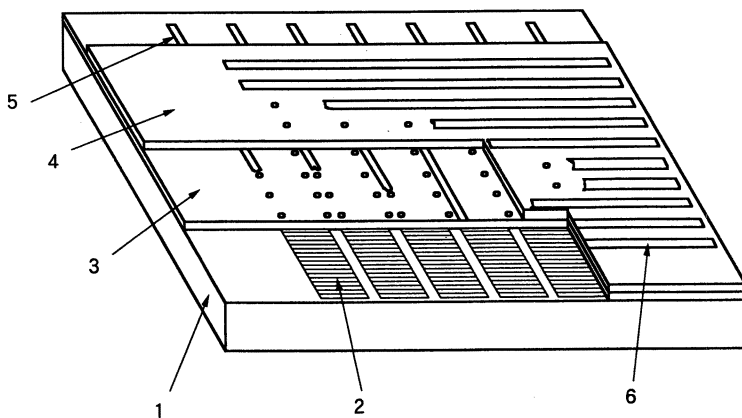


Figure 2. Structure of a molecular LB device. (1), substrate; (2), patterned LB film of a long-chain polymer; (3), insulator with contacting holes for metal strips 5 and 6; (4), insulator with contacting holes for metal strips; (6); see text for explanation.

Movement of Information. If we apply a voltage between these conductors and choose the right timing for the light flashes, we can move information along the strands of memory polymer. The information for the first storage unit has to be generated by some additional mechanism (like light-induced photon emission, using a second wavelength) or by choosing different voltages, the lower of which is not enough to allow electrons to tunnel to the first unit.

Now the problem is that the many strands connecting each pair of electrodes have different lengths and the information reaches the other end after a different number of cycles. This problem can be solved by reading and writing at the same end of the strands. If we write and read at the same end, the information in parallel strands always arrives at the same time during reading, but our polymer has to have some way to reverse the direction of information travel. One prerequisite for the functioning of this unit is that defective units do not supply any signal upon reading. If they supply the wrong answer or statistical noise, the output signal degrades with increasing number of such defects.

Fabricating the Device. However, this system would satisfy many requirements. There are many information units operated in parallel to give the required redundancy. The order of the polymer does not have to be very high. Only a small percentage of the polymer chains is required to work. If we assume that we can fabricate units that require about $10 \mu\text{m}^2$ and that we can write 100 bits into one cable of information polymer, we already reach a density of 1 Gbyte/cm². This system is not thought to be a real-world model, but it shows that even with all the limitations that have been enumerated, it is not impossible to build such devices. The structure itself is very simple and does not require very sophisticated processing, if we assume that a memory polymer with the required properties is available. The device could be built, in reverse orientation from the one described, on top of a chip that contains the circuitry that uses the information that is stored (e.g., a microprocessor), thus eliminating the need for many messy outside connections.

Fabricating the memory polymer itself is a different problem. It is, however, very simple compared to what is expected to be possible in the future. It is certainly more realistic, within a limited time scale, than the self-assembling computer (33). A polymer that works as required could be a copolymer of conductive strands with photoconductive short units. Another possibility would be chains of units that trap a charge, but release it upon irradiation with light. In the last paragraph we will briefly describe ideas on how to fabricate a device that performs similarly, but does not use molecular storage units.

The essential point about this model, in any case, is the redundancy that is built into the system in a natural way, with no additional logic

required to check or verify results. Similar ideas can be used for molecules that provide the result of mathematical functions or the results of pieces of microcode when fed with appropriate inputs.

Problems with Applications

For many years technical applications of LB films have been predicted to be feasible in the not too distant future (34). However, nothing significant has emerged so far. What are the obstacles on the way to applications?

The main problem seems to be that researchers are not interested in equipment that is useful for production of devices, with respect to throughput and quality, and that people from the applied field are not willing to invest in a technology that has problems in repeating results in different laboratories and on different days. However, the development of a biomolecular device cannot depend upon a technology that is in the development stage itself. A biochemist who has designed a new molecule does not want to test it with a technology that is very difficult to control.

The problems might be similar to the problems of the early semiconductor industry. The idea of a FET, as solid-state analog for the vacuum valves, was the driving force for working in that field. The basic idea is very simple and does not look very difficult to achieve. However, many things had to be investigated and engineered before that idea was successfully implemented and FETs could be manufactured in large quantities at a low cost. The actual cost dropped from dollars per transistor to cents per transistor; it is now better described by a figure that gives transistors per cent. The substrate material had to be of a much higher purity than had been dreamed of before, the material initially used was not appropriate, the production technology had to be developed, and clean rooms had to be invented. Many uses for this technology had been found before the initial idea was successful. Indeed, the semiconductor industry was flourishing before the first FET was working.

Many ideas for LB films can be borrowed from the semiconductor industry. Examples are the clean room technology, water purification systems, substrate cleaning and handling procedures, liquid filtering and handling procedures, and even silicon wafers that can be used as inexpensive, high-quality substrates for LB fabrication. However, LB films are different; the requirements are certainly not the same and are very likely much more stringent.

Clean Rooms. Very few LB laboratories exist in which these necessary technologies are used. In many cases the common practice is opposed to what can be learned from the clean room–semiconductor

area. For example, it is still common practice to leave the subphase, on which the films initially float, in the trough for hours or even days. Semiconductor experience has shown that stagnant water will be contaminated within a very short time. Nobody in the semiconductor field uses water that has been stagnant for more than a few minutes.

Furthermore, no commercial LB equipment is available that is built to clean-room specifications or that considers any production requirements, like the possibility of coating large objects or many samples within a reasonable time. In some cases this procedure would be necessary or very helpful, even for basic research.

Contemporary clean rooms eliminate particles down to a size on the order of magnitude of $0.1\ \mu\text{m}$. This is sufficient for today's semiconductors and micromechanical devices because the features are several times larger and the resist layers used are so thick that a particle of that size never penetrates the film. In contrast, an LB film, even when the final layer is of the same thickness as in semiconductors, is much more sensitive. A $0.1\text{-}\mu\text{m}$ particle is about 50 times larger than an individual layer and thus leads to irregular deposition around it, causing a defect that is generally much larger than the dust particle and might penetrate the whole stack of layers.

Chemical Contamination. There are indications that current clean-room technology is not sufficient in another respect, because to a large extent it controls only mechanical contamination. Chemical contamination caused by organic vapors is not controlled. This control is rarely essential, although for epitaxy and wafer bonding it is becoming more and more a concern in semiconductor processing. Chemical contamination, in the sense used here, means molecules adsorbed from the air, like solvent vapors, water, even inorganic vapors and fumes that can modify the surface. Why the requirements are more stringent for LB films than for other technologies is easily explained by using the resist example once more. When a conventional resist is spun on, it is dissolved in a solvent. This solvent wets the surface to be coated first and can, to some extent, help to remove impurities on the surface. Some of these impurities are removed with the excess resist solution. Then the solvent evaporates and leaves the remaining impurities dispersed in the polymer resist matrix, where they might not do too much harm. In the LB case there is no solvent involved. Whatever is on the surface while the film is deposited is coated over and can lead to a problem with adhesion. This problem might not necessarily become visible during deposition of the next layer, but might cause visible defects when the finished resist is developed or the patterned resist is used as an etch mask.

In view of the chemical contamination problem, it is surprising that the process works at all. From ultrahigh vacuum investigations like LEED

(low-energy electron diffraction) or AES (auger electron spectroscopy) it is known that a clean metal surface at a pressure of 10^{-9} torr is usable (i.e., clean) for about 10 min. Extrapolated from this to ordinary pressure and "smelly" clean-room air, the time between cleaning and coating should be smaller than fractions of nanoseconds. Problems with chemical contamination have been noticed in other laboratories. In one LB lab charcoal filters have been installed in the clean-room air inlet (C. Brown, IBM, personal communication). The use of a closed system has been recommended for then the amount of air involved is small and thus better controllable (35), like installing the deposition equipment in a vacuum-tight glove box.

Speed of the Procedure. One very stringent problem for applications of LB films is the speed at which the coating process can be performed. The basic work in the 1950s that was, at least in part, responsible for raising the interest in LB films in the past decade used speeds on the order of magnitude of millimeters per second (36). The quality of these films, though often questioned, was probably better than most of what is produced today, generally at speeds of millimeters per minute or even slower (10), on equipment that is, supposedly, much more refined.

One who actually did some of this work (H. Kuhn, personal communication) wondered about these slow speeds. According to his experience, it is not possible to get good-quality films in this way. There are 9-year-old reports (37) about the upper limits of the deposition speed; centimeters per second are possible, even for the coating of large objects (38). However, these reports have not yet had any impact on the field, maybe because commercial equipment does not allow the use of such high speeds. It is not easy to control the state of the film during fast deposition, and many films are too stiff to allow such fast transfer. In the latter case the problem of low deposition speeds often may be solved in the hands of a chemist (*see, e.g.,* 39) by slightly modifying the material or by finding an additive for easier processing.

Another problem impeding applications is the availability of equipment that provides films in large quantity and good quality. The batch process is still state of the art, in spite of publications (40, 41) more than 10 years ago about ways to produce films on a continuous basis (42). There was surprisingly little interest in this field, even after recent reports about success in this respect (15, 38), despite its many obvious advantages.

Ways To Improve the Technology

The first problem delaying work with LB films at the production level is the commercially available equipment. Unfortunately, it is mandatory

to produce equipment in-house when serious attempts are undertaken to prove (or disprove) that the LB film technology can be brought up to industry standards. Meeting these standards is a prerequisite for large-scale application of these films in devices on either the molecular level or a less sophisticated level.

Film Lift System. For this reason we are currently developing three major pieces of equipment. The first is a lift system. Film lift is the term for the moving mechanism that controls the movement of the substrate during coating. This device is built to handle objects of up to 20-cm dimensions and up to the kilogram weight range. Available speeds for each stroke range from the usual low speeds of fractions of millimeters per minute to 20 mm/sec. Almost any sequence of layers can be deposited automatically, like a regular step pattern, or some parts of a sample can be coated with a thin film while others are coated with thicker films (43). The controlling computer communicates with the film balance that provides the films and can ask for different materials. It can suspend dipping until the new material is spread or, more importantly, until a new film is ready for transfer when the previous one is either used up or too old.

The mechanical part of this lift is completely enclosed except for a small slit in front for the arm to which the samples are attached. The housing is connected to vacuum so that any particles that might be produced by the mechanism are removed immediately and do not reach the environment. The sample holder is connected to the dip arm with a magnet that is completely enclosed in plastic. This allows the operator to attach and detach samples in a way that minimizes the production of particles that might fall onto the monolayer film prior to deposition and minimizes the time for manipulation above the film balance surface.

Conventional Film Balance. The second part is a conventional large film balance. The surface is 80×40 cm. This system is also run completely automatically. This does not mean, as it is used sometimes in the literature, that a motor moves the barrier that confines the film-covered area and that the surface pressure, as a measure for the surface coverage, is plotted on an x - y recorder, as opposed to manual data collection. We mean that the film balance keeps itself clean by changing the water subphase regularly while not in use, the water level is kept constant automatically, the temperature can be controlled by the computer, any residual dirt film or a leftover film after an experiment can be aspirated off automatically, and new films of several materials can be spread under computer control. It also is able to communicate with the film lift. This machine will provide more than 0.25 m^2 of film in one batch. This means the productivity might be up to $1 \text{ m}^2/\text{h}$ for films that

can be deposited fast and do not need to be aged before the process begins.

Some technical problems remain to be solved, such as how the left-over films can be removed automatically. Films are normally removed with a fine aspirator tip that touches the water surface. However, many films are so stiff that the film does not flow to the tip, at least not within any reasonable time. For manually cleaning the surface, the aspirator tip is usually moved across the water surface, and the barriers are opened and closed several times. We solved this problem by blowing a stream of nitrogen onto the surface in a way that transports the film and any other trace impurities to the aspirator tip. It is a good idea to spread a small amount of the new film material and remove it before the film actually used is spread. This procedure is very frustrating for human operators, but computers are designed to do that type of work.

Continuous Film Balance. The third piece of equipment will be a film balance that produces the films continuously. The productivity will be on the order of magnitude of 5–10 m² of monolayer film per hour. It communicates with the same type of lift and can also select automatically between different materials. The construction of this machine is based on ideas that can be found in the very scarce publications about continuous LB film production (15, 40, 42).

The most useful feature of a continuous machine, as compared to a conventional one, is the ability to control the age of the film. There are several reports in the literature that the properties of an LB film change with time (15, 44), a process that is sometimes referred to as aging. If a film is deposited from a conventional trough, the age changes with subsequent layers. Thus, the film is composed of layers with different properties. On a continuously producing machine this age can be controlled by continuously removing excess film. After an induction period, the age of the film is determined by the area of the film-covered surface and the removal rate (which is the same as the spreading rate). A means has to be installed to remove film at a controllable rate (15, 40). An additional benefit of this removal mechanism is that the equipment is continuously cleaned because the monolayer is always moving, taking with it impurities that bind to the film molecules.

It is a matter of course that these machines will be installed in a clean room equipped with semiconductor processing equipment for sample preparation and cleaning. Unfortunately, we do not at present have the means to control the chemical environment. However, one of the machines is designed in such a way that the housing can be upgraded. It forms a separate totally enclosed chamber that can be conditioned independently.

Dual Trough. Experts in the field will notice that our developments do not include a trough for deposition of alternating layers (dual trough). We think that it is more important at the moment to learn more about the basic deposition mechanisms. It should be no problem to fabricate alternating structures well when the requirements for standard deposition are met. Furthermore, our film balances are fully automatic and can spread several different materials. This equipment gives the opportunity to build up alternating layers, although it is a slow process, by changing the film after each stroke of the sample. We do not expect, however, that this will result in very good films. Because of the long time involved (at least several minutes per layer), the risk of picking impurities is very high.

Automation. Why do we think that automatic equipment is essential? For some functions this is easily seen; it saves operator time and avoids contamination attributable to the absence of the operator and mistakes caused by the inability of humans to repeat processes many times without error. However, the most important point is that automation is the only way to keep the equipment sufficiently clean. The requirements for cleanliness in a film balance are similar to those in a vacuum system, except that the vacuum is filled with H₂O molecules and perhaps a residual gas pressure of some added ions or other chemicals. A vacuum system can be kept clean only by continuously pumping; similarly, a film balance can be kept clean only by continuously removing contaminants. The analogy can be extended to the “baking out” of a vacuum machine. Repeatedly heating a film balance to higher temperatures, while it is filled with clean, pure water also helps to remove impurities (*see, e.g., 45*).

Realistically, these procedures are possible only under computer control. The computer changes the water regularly, raises the temperature as needed to increase the diffusion rate of contaminants, cleans airborne and film-forming contaminants off the water surface with aspirator tips, keeps track of the history, and checks safe operation 24 h/day, including weekends. Constant checking is essential because of the damage that can be caused by water in a clean room or, even worse, by a water heater that runs dry.

Materials and the Deposition Process

Many basic and essential facts about materials and what happens during deposition are not known. Even the best researched and most commonly used material for LB films, fatty acid films, were shown to exhibit many more phases and phase transitions than had been known previously (46). This “had been known” is relative because some earlier publications

showed the facts (47, 48). However, these publications had been ignored by most researchers because the features were very similar to features caused by experimental problems, such as impurities in the materials and equipment. Since that rediscovery, several puzzling facts about the deposition of fatty acids can be understood. For instance, discrepancies were found in the deposition behavior of supposedly corresponding phases of the homologous series. Now it is clear that the phases are not the same, which explains why the deposition is different. More surprises like this are probably coming in the future.

Changing Properties. It is intuitively clear that films on the water surface change their properties because of both age and the dipping process itself. The flow in the film will change the order in the film with time. Generally the film, as spread at low density and then compressed to the proper density for deposition, has random orientation or a very weak orientation due to the change in geometry during compression. When the film is deposited, the flow toward the sample induces a preferred orientation parallel to the flow (i.e., in the fabricated film, parallel to the dipping direction). Many publications mention this phenomenon (49–51), but so far only one recognizes that this effect not only changes the monolayer, but it also causes inhomogeneity in the deposited film. The first layers are deposited from a less ordered film, and the following ones from a more ordered film (43).

To produce homogeneous films, the film should be subjected to flow before the first layer is deposited. The sample dimensions and film balance should be such that a steady state for the flow is established. If this is not done, any subsequent measurement of the orientation of deposited films will be ambiguous. The question will remain whether the orientation of the first layers or of the following layers is measured.

Fortunately, the fatty acids exhibit epitaxial growth. The visible structure of the first layer is preserved during the deposition of subsequent layers, and in thick layers the structure can be made visible under a microscope. Thus, this effect is easily investigated. In contrast to conclusions of previous investigations, we think that the effect we see is not dependent upon deposition speed, but is due solely to the geometrical flow of the film. Our conditions, however, differ from the deposition conditions of other investigations. The main difference is that we generally use much higher speeds.

Defect Control. A very important problem in using LB films for applications like building up molecular devices is the control of defects. There are many different types of defects at various levels and many different methods to make them visible.

The first requirement for obtaining reasonable defect levels is the use of smooth, defect-free substrates. Some requirements concern the

macroscopic structure, as already mentioned. Steps perpendicular to the deposition direction or spikes sticking out of the surface tend to prevent the film from contacting the surface smoothly, thus trapping water between subsequent layers (on the way up) or forming air pockets (on the way down). The surface may be wavy or curved, but the minimum radius of that curvature has to be large, comparable to the radius of the meniscus that forms during deposition. This minimum radius is different for the directions parallel and perpendicular to the deposition direction. It follows that small holes are not permitted, because they are bridged by the film and left filled with air or water. However, this effect could be used intentionally to form such structures.

At the microscopic level, the substrates have to be smooth to a degree that allows the films to conform completely to the surface without disruption of the film structure. This requires a perfect, low-index single-crystal plane that can be obtained at the present state of technology only in very special cases. Even high-grade Si wafers show high-index crystal planes. As a result, the cut along a crystal plane is never absolutely parallel to one of the crystal axes, but slightly tilted. Even when the cut is on an average parallel, some steps develop locally. This formation can be seen graphically in recent scanning tunnelling microscope (STM) (52) studies. The known best surfaces for these studies are materials like HOPG, mica, or similar cleavable materials. However, their number is limited and they are generally not available in the quality and quantity needed for industrial fabrication.

One way to overcome this problem could be to process the substrates in such a way that the remaining steps in the surfaces are more or less regular and then to use them to induce order in the deposited films. Only one publication (53) so far gives evidence that such a plausible effect exists. We found that in fatty acid films, under certain ill-defined conditions, such an effect can be observed as a sudden change in the domain orientation along steps or cracks. This influence of a step, formed by a previously deposited amorphous LB film, extends only a very short distance (micrometers). However, this influence is larger than the mean spacing of the structures under consideration and thus looks useful.

One more possibility for the fabrication of the required substrates should be mentioned. LB films generally tend to coat small irregularities in the substrates and to eliminate the influence of them after several layers have been deposited. Why not use LB films as substrates or as replicas for fabricating substrates? This trick is used in research on a regular basis. Many LB samples are deposited onto a substrate that has been precoated with several layers of a fatty acid salt for which the conditions for good deposition of the first layer are established.

Defect Identification. There are many different methods to investigate the defects that still exist, even if a perfect substrate would

be possible. The methods range from simply monitoring the amount of material that is deposited (transfer ratio) to optical and electron microscopic techniques, and from spectroscopic techniques to STM and atomic force microscopy (AFM). STM is useful in specific cases only, because it depends on a tunnelling current that flows over a small gap. Insulating layers, like most LB films, act as a tunnelling gap and are generally too thick to allow that current to flow before they are destroyed. We think that this generally holds despite some reports that claim success in visualizing regular LB film structures in an STM (54).

Another problem is that STM requires a conductive, very smooth substrate. The available materials, like HOPG, unfortunately do not allow easy deposition of regular LB films. We found that fatty acids deposited onto HOPG and MoS₂ form structures in which the molecules are attached flat onto the substrate. This configuration differs from the normal LB film structure, in which the molecules are expected to be aligned in a close packing perpendicular to the substrate (55). We are continuing to investigate these structures with AFM, which is a better choice (56). With this method the sample or substrate that carries the sample does not have to be conductive; this difference allows us to use mica, which has better properties for LB deposition.

Another of our studies investigated the dependence of the number and topology of defects upon substrate and film-forming materials (57). The substrates in this study were glass plates, silanized and then coated with vacuum-deposited gold; the defects were visualized by electrodepositing copper (58). This method shows conductive defects only, which are of prime importance for many device applications. The result is that single or double layers of LB films are always very leaky, and tens of layers of standard monomeric materials are required to eliminate conductive defects. However, polymer materials can exhibit useful defect densities in stacks of less than 10 layers.

Defect Visibility. Our laboratory recently developed a new method for making defects in LB films visible (59) in the range between optically observable and STM–AFM resolvable defects. A typical conventional method is the copper decoration method. This method is limited to conductive defects, conductive substrates without oxide coating. It requires some skill to establish the proper conditions for the actual copper deposition. Otherwise the film could be destroyed electrochemically or chemically during electroplating. The new method uses a standard light microscope with an additional inexpensive fiber-optic illuminator, works on any substrate and any film (even conductive films), and shows not only conductive defects. Furthermore, it requires no preparation of the sample and is nondestructive. Thus, it can be used

on-line for quality testing or as an immediate feedback value for adjusting fabrication conditions.

Small particles and defects scatter light, the intensity of which depends upon size in a smooth function. Particles also scatter when they are smaller than the wavelength of the light. This phenomenon, known as Tyndall effect, is used for routine inspection of wafers in the semiconductor industry, but normally only in a crude visual observation. To use this effect we illuminated a film sample on the microscope stage with a bright light source under a low angle, so that no direct or reflected light entered the microscope lens, only scattered light. Particles and defects showed up as small light spots, whose intensity depended upon the size of the defect. As expected, we saw the same features as in the previous copper deposition experiments. Because the illumination of the microscope is easily changed between low-angle illumination and normal illumination, the features in both modes can be correlated. The location of defects can easily be compared to the location of optical grain boundaries.

Attempts To Use LB Films for Molecular Devices

We do not know of any molecular devices that have been fabricated utilizing LB films, unless the definition of a molecular device is taken very loosely. Therefore, this section describes two ideas or technologies that are a step in the direction of using LB films to fabricate molecular devices, although several more steps are necessary.

Inchworm Memory. The first idea (32) is a way to construct a memory system to solve the present problem with the limited smallest size of features. The ideas presented earlier in this chapter were strongly influenced by this work. All necessary building blocks are readily available, so the problems with this approach seem to be only how to actually manufacture it. A device of that type was called inchworm memory by the inventors (60). Because the feature size on a substrate cannot be diminished to get higher packing density, they decided to leave the two dimensions of a plane and build structures in three dimensions. Access into that third dimension is achieved through a shift-register structure, which can be built with LB films.

The structure for accessing the memory consists of a bottom plane of metal filaments and a top plane of metal filaments where the direction has been rotated by 90°. Thus, each pair of metal strips defines one location on the device, the dimensions of which are defined by the best lateral resolution that can be achieved. Between these two connecting planes, a stack of LB layers is deposited. The stack consists of alternating layers of conductive and nonconductive material that result in an elec-

tronic structure, as shown in Figure 3. This stacking can be done in different ways, and the boundaries between conductive and nonconductive material can be within a layer or between layers. The entire stack of layers is patterned into squares so that each square is accessed by two corresponding wires in the connecting planes. This structure looks very simple. The problem seems to be to deposit such a stack of layers with a low enough defect density and high number of layers.

When a small voltage is applied, charges in the deep wells are bound and any charges in the shallow wells tunnel into the deep wells. When the voltage is increased, the tunnelling probability into the shallow wells becomes higher, as is demonstrated in Figure 3. The memory device is supposed to work in the following way: A small voltage is applied permanently across the stack of layers. We assume that some of the conductive layers carry charges. All of these charges are forced against the

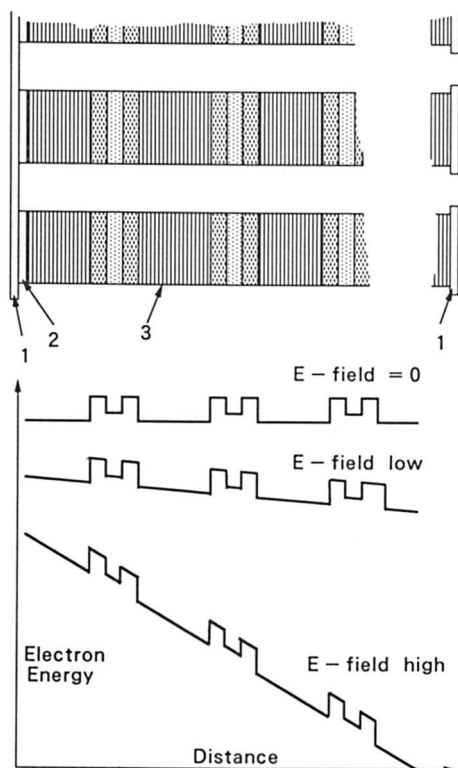


Figure 3. Principle of the "Inchworm" memory. Top: Mechanical assembly (not to scale); 1, electrodes; 2, charge injecting layer; 3, LB film assembly. Bottom: Electron energy in the assembly structure at three different voltages between the two electrodes (32, 60).

next tunnelling barrier, by the applied field. If a short high-voltage pulse is applied, the charges can migrate to the next conductive layer, where they again are trapped by the next barrier, provided the voltage is reduced in a timely fashion. To allow for proper timing, the inventors of this device inserted a number of additional tunnelling barriers into the deep wells. This allows them to tailor the travelling speed of the charges. The presence or absence of a charge can be read when it reaches the second electrode. To write information into the system, a charge-injecting mechanism is built into the first electrode.

Structures like this are, in principle, easily fabricated from LB films (other techniques are also being tried). The intriguing idea is that it should be possible some day to reduce the area per memory stack to the lowest possible feature size, even down to molecular dimensions. At the present level the increase in storage capacity, as compared to standard devices, would be very large, proportional to the number of shift register units in one stack. This could be on the order of hundreds or even thousands.

Terabit Memory. A still-novel method of manipulating molecules and even atoms has been made possible by developments in STM and AFM technology. The scientific literature (61–63) contains several reports about the manipulation of individual atoms. In some cases the effect is reversible and repeatable, so that a memory structure could be built. We will now describe how the use of this idea in conjunction with a memory effect in LB films can be used to design a memory device with a huge capacity. Our in-house name for this device is terabit memory.

In our laboratory, several years ago, a switching effect was found in metal–LB–metal structures (64). The basic behavior is seen in Figure 4 (65). If a low voltage is applied to a device in the nonconductive zero state, the current through the device is very low. If the voltage is increased beyond a critical level, the current suddenly increases and the resistivity stays low, even when the voltage is lowered again. The voltage can even be removed completely, for at least 1 year, and the highly conducting state is still found upon reactivation of the circuit. So far this memory can be programmed once only. However, a high enough voltage, positive or negative, establishes the nonconducting state once more. The device can be cycled through this procedure hundreds of times, at least. No damage is visible to the structure of the device, in contrast to other reports about similar effects (e.g., 66).

Materials that show this effect are LB films made of molecules that incorporate conjugated bonds (e.g., polyimide can be used for this purpose). Polyimides are especially interesting because they show a high thermal stability (67).

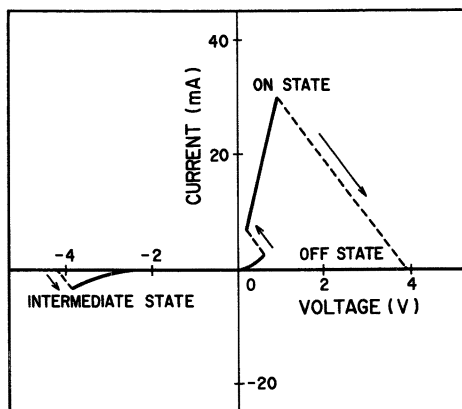


Figure 4. Electrical characteristics of metal A-LB-metal B memory device. (Reproduced with permission from reference 65. Copyright 1988 American Institute of Physics.)

There is not much advantage over the present memory technology in using this device as it is. The maximum density is still limited by the limits for fabricating small structures and large numbers of connections.

However, the effect also works when the second, top, electrode is replaced by the tip of an STM, as shown schematically in Figure 5. The tip current is monitored to read the state of the film at a certain location, and pulses of short duration are applied to switch the bit written into that location. The obvious advantage of this system is that the theoretical resolution is limited by the resolution of the STM. This resolution has

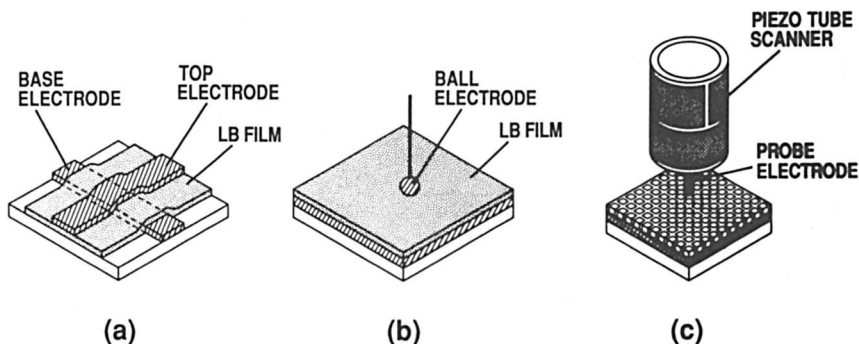


Figure 5. Illustration of the principle of the terabit memory. (a), an individual metal-LB-metal memory device; (b), the top electrode is replaced by a temporary removable electrode; (c), the top electrode is formed by the tip of a scanning tunneling microscope. (Reproduced with permission from reference 64. Copyright 1989 Elsevier Sequoia.)

been demonstrated in the recent past to be better than the size of an atom. This means that the STM is certainly capable of addressing individual molecules or any cluster of molecules that exhibits a desired response.

In between the read and write cycles, the STM drive system is used in the imaging mode to track the location and do housekeeping tasks, like the system of a disk drive. It replaces defective areas with working ones and keeps a directory that minimizes the access time to data records that are possibly not always in consecutive locations.

LB films certainly do not show enough order to allow random access to individual molecules. Furthermore, individual molecules are not always fixed to their initial position. That is why we attempted to use an amorphous film of a polymer that exhibits the memory effect and to switch domains that contain many functional units. However, even with this limit, we expect to obtain a density of 1 terabit/cm².

Unfortunately, any technical implementation of the idea is far removed from this simple description. One of the problems is how to package all the necessary hardware and software into a reasonably small package, which may be comparable to today's large-chip packages. Another problem with a memory system of such a capacity becomes obvious when estimating the time for testing the system. If we assume that the testing can be done at a rate of one megabit/s, the test can be finished in slightly less than 12 days. Last, but not least, it is certainly a big task to fabricate an LB film of a useful quality, which includes the fabrication of a useful substrate.

In any case, development of such a device will open the door for utilizing and manipulating very small entities, with access to individual molecules or atoms in a reproducible and reliable way as the final goal.

More effects are presently under investigation that use LB films to enable molecular devices. We just want to mention the efforts to build organic diodes (68) or transistors (69, 70), which are still very far from competing with silicon-based technology. However, the first transistor was also far from being a serious threat to the vacuum valve.

Conclusion

Although nothing exists that could be called a "molecular device, using LB films," the idea of fabricating such devices is not pure fantasy. There have been attempts to go in that direction. LB films are not only of interest as active materials for such a technology; they could also be useful to provide some of the auxiliary structures and technologies, in spite of the limitations of these films. Other methods that could provide a similar functionality look even more complicated to use. The alternative, to go directly to three-dimensional structures, is tempting. It is

still only a futuristic dream that might come true not by jumping, but by going ahead small steps at a time.

References

1. *Langmuir-Blodgett Films*; Roberts, G. G., Ed.; Plenum: New York, 1990.
2. *Langmuir-Blodgett Films 5, Proceedings of the 5th International Conference on Langmuir-Blodgett Films*; Barraud, A.; Palacin, S., Eds.; Elsevier: Amsterdam, The Netherlands, 1992; *Thin Solid Films* **1992**, *210-211*.
3. Blodgett, K. B. U.S. Patent 2 220 860, 1940.
4. Blodgett, K. B.; Langmuir, I. *Phys. Rev.* **1937**, *51*, 964-982.
5. Kopp, F.; Fringeli, U. P.; Mühlethaler, K.; Günthard, Hs. H. *Z. Naturforsch.* **1975**, *30C*, 711.
6. Braun, H. G.; Fuchs, H.; Schrepp, W. *Thin Solid Films* **1983**, *159*, 301.
7. Naito, K. J. *Colloid Interface Sci.* **1989**, *131*, 35-42.
8. Hickel, W.; Appel, G.; Lupo, D.; Praß, W.; Scheunemann, U. *Thin Solid Films* **1992**, *210-211*, 182-184.
9. Tredgold, R. H.; Young, M. C.; Hodge, P.; Khoshdel, E. *Thin Solid Films* **1987**, *151*, 441-449.
10. Larkins, G. L., Jr.; Fung, C. D.; Rickert, S. E. *Thin Solid Films* **1989**, *180*, 217-225.
11. Geddes, N. J.; Sambles, J. R.; Couch, N. R.; Parker, W. G.; Jarvis, D. J. *Thin Solid Films* **1989**, *179*, 143-153.
12. Uekita, M.; Awaji, H.; Murata, M.; Mizunuma, S. *Thin Solid Films* **1989**, *180*, 271-276.
13. McAlear, J. H.; Wehrung, I. M. *Molecular Electronic Devices*; Dekker, New York, 1982.
14. Barraud, A.; Rosilio, C.; Ruadel-Teixier, A. *Solid State Technol.* **1979**, *8*, 1120-1124.
15. Albrecht, O.; Ginnai, T.; Harrington, A.; Marr-Leisy, D.; Rodov, V. In *Molecular Electronics, Biosensors and Biocomputers*; Hong, F.-T., Ed.; Plenum Press, New York, 1990.
16. Ginnai, T.; Harrington, A.; Rodov, V.; Matsuno, M.; Saito, K. *Thin Solid Films* **1989**, *180*, 277-286.
17. Seto, J.; Nagai, T.; Ishimoto, C.; Watanabe, H. *Thin Solid Films* **1985**, *134*, 101-108.
18. Harkins, W. D. *The Physical Chemistry of Surface Films*; Reinhold, New York, 1952.
19. Albrecht, O.; Johnston, D. S.; Villaverde, C.; Chapman, D. *Biochem. Biophys. Acta* **1982**, *687*, 165.
20. Cackovic, H.; Schwengers, H. P.; Springer, J.; Laschewsky, A.; Ringsdorf, H. *J. Membr. Sci.* **1986**, *26*, 63.
21. Petty, M. C. *Thin Solid Films* **1992**, *211*, 417-426.
22. Pomerantz, M.; Seegmüller, A.; Netzer, L.; Sagiv, J. *Thin Solid Films* **1985**, *132*, 153-162.
23. Ringsdorf, H.; Schlarb, B.; Venzmer, J. *Angew. Chem. Int. Ed. Engl.* **1988**, *27*, 113.
24. Takimoto, K.; Kawade, H.; Sakai, K.; Yanagisawa, Y.; Eguchi, K.; Nakagiri, T. In *Polymers for Microelectronics—Science and Technology*; Kodansha: Tokyo, Japan, 1990; pp 761-767.
25. Takagi, H.; Ogawa, H.; Yamazaki, Y.; Ishizaki, A.; Nakagiri, T. *Appl. Phys. Lett.* **1990**, *56*, 2379.

26. Brus, L. *Nature (London)* **1991**, *353*, 301–302.
27. Ahlers, M.; Blankenburg, R.; Grainger, D. W.; Meller, P.; Ringsdorf, H.; Saless, C. *Thin Solid Films* **1989**, *180*, 93–99.
28. Von Tscharn, V.; McConnell, H. M. *Biophys. J.* **1981**, *36*, 421–427.
29. Kumehara, H.; Kasuga, T.; Watanabe, T.; Mijata, S. *Thin Solid Films* **1989**, *178*, 175–182.
30. Kawabata, Y. In *Molecular Electronics: Biosensors and Biocomputers*; Hong, F. T., Ed.; Plenum Press, New York, 1989; pp. 25–31.
31. Akatsuka, T.; Tanaka, H.; Toyama, J.; Nakamura, T.; Kawabata, Y. *Chem. Lett.* **1990**, *6*, 975–978.
32. Burrows, P. E.; Donovan, K. J.; Wilson, E. G. *Thin Solid Films* **1989**, *179*, 129–136.
33. Carter, F. L. *Physica* **1984**, *10D*, 175–194.
34. Vincett, P. S.; Roberts, G. G. *Thin Solid Films* **1980**, *68*, 135–171.
35. Tredgold, R. H.; Young, M. C.; Hodge, P.; Khoshdel, E. *Thin Solid Films* **1987**, *151*, 441–449.
36. Kuhn, H.; Möbius, D.; Bücher, H. In *Physical Methods of Chemistry*; Weissberger, A.; Rossiter, B., Eds.; John Wiley: New York, 1972; Vol. 1, p 577.
37. Peterson, I. R.; Russel, G. J.; Roberts, G. G. *Thin Solid Films* **1983**, *109*, 371–388.
38. Albrecht, O.; Ginnai, T.; Harrington, A.; Marr-Leisy, D. *Thin Solid Films* **1989**, *178*, 171–174.
39. Peng, J. B.; Barnes, G. T.; Schuster, A.; Ringsdorf, A. *Thin Solid Films* **1992**, *210–211*, 16–18.
40. Barraud, A.; Vandevyver, M. *Thin Solid Films* **1983**, *99*, 221–225.
41. Barraud, A.; Gras, R.; Vandevyver, M. U.S. Patent 4 093 757, 1978.
42. Nitsch, W.; Kurthen, C. *Thin Solid Films* **1989**, *178*, 145–155.
43. Albrecht, O.; Matsuda, H.; Eguchi, K.; Nakagiri, T. *Thin Solid Films* **1992**, *221*, 276–280.
44. Peterson, I. R.; Russel, G. J.; Roberts, G. G. *Thin Solid Films* **1983**, *109*, 371–378.
45. Albrecht, O. *Thin Solid Films* **1983**, *99*, 227–234.
46. Bibo, A. M.; Peterson, I. R. *Adv. Mater.* **1990**, *2*, 309–311.
47. Ställberg-Stenhagen, S.; Stenhagen, E. *Nature (London)* **1945**, *156*, 239.
48. Lundquist, M. *Chem. Scripta* **1971**, *1*, 5.
49. Malcolm, B. R. *Thin Solid Films* **1989**, *178*, 17–25.
50. Daniel, M. F.; Hart, J. T. T. *J. Mol. Electron.* **1985**, *1*, 97–104.
51. Sugi, M.; Minari, N.; Ikegami, K.; Kuroda, S.; Saito, K.; Saito, M. *Thin Solid Films* **1989**, *178*, 157.
52. Mo, Y. W.; Kariotis, R.; Swartzentruber, B. S.; Webb, M. B.; Lagally, M. G. *J. Vac. Sci. Technol.* **1990**, *B8*, 232–236.
53. Vogel, V.; Wöll, Ch. *Thin Solid Films* **1988**, *159*, 429–434.
54. Smith, D. P. E.; Bryant, A.; Quate, C. F.; Rabe, J. P.; Gerber, Ch.; Swalen, J. D. *Proc. Natl. Acad. Sci. U.S.A.* **1987**, *84*, 969.
55. Matsuda, H.; Kishi, E.; Kuroda, R.; Albrecht, O.; Eguchi, K.; Hatanaka, K.; Nakagiri, T. *Thin Solid Films* **1993**, *224*, 248–252.
56. Meyer, E.; Howald, L.; Overhey, R. M.; Heinzelmann, H.; Frommer, J.; Güntherodt, H.-J.; Wagner, T.; Schier, H.; Roth, S. *Nature (London)* **1991**, *349*, 398–400.
57. Matsuda, H.; Kawada, H.; Takimoto, K.; Morikawa, Y.; Eguchi, K.; Nakagiri, T. *Thin Solid Films* **1989**, *178*, 505.
58. Peterson, I. R. *J. Mol. Electron.* **1986**, *2*, 95.

59. Albrecht, O.; Matsuda, H.; Eguchi, K.; Nakagiri, T. Poster presentation at the 5th International Conference on LB Films, Paris, 1991; poster AP7.
60. Burrows, P. E.; Wilson, E. G. *J. Mol. Electron.* **1990**, *6*, 209–220.
61. Eigler, D. M.; Lutz, C. P.; Rudge, E. E. *Nature (London)* **1991**, *352*, 600–603.
62. Eigler, D. M.; Schweizer, E. K. *Nature* **1990**, *344*, 524–526.
63. Mamin, H. J.; Guethner, P. H.; Ruger, D. *Phys. Rev. Lett.* **1990**, *65*, 2418–2421.
64. Sakai, K.; Kawada, H.; Takamatsu, O.; Matsuda, H.; Eguchi, K.; Nakagiri, T. *Thin Solid Films* **1989**, *179*, 137–142.
65. Sakai, K.; Matsuda, H.; Kawada, H.; Eguchi, K.; Nakagiri, T. *Appl. Phys. Lett.* **1988**, *53*, 14.
66. Ottenbacher, D.; Schierbaum, K. D.; Göpel, W. *J. Mol. Electr.* **1991**, *7*, 79–84.
67. Suzuki, M.; Kakimoto, M.; Konishi, T.; Imai, Y.; Iwamoto, B.; Hino, T. *Chem. Lett.* **1986**, 395.
68. Aviram, A.; Joachim, C.; Pomerantz, M. *Chem. Phys. Lett.* **1988**, *146*, 490–495.
69. Garnier, F.; Horowitz, G.; Peng, X.; Fichou, D. *Adv. Mater.* **1990**, *2*, 592–594.
70. Paloheimo, J.; Kuvalainen, P.; Stubb, H.; Vuorimaa, E.; Yli-Lahti, P. *Appl. Phys. Lett.* **1990**, *56*, 1157–1159.

RECEIVED for review March 12, 1992. ACCEPTED revised manuscript December 29, 1992.

Photoinduced Electron Transfer and Energy Transfer in Langmuir–Blodgett Films

Masamichi Fujihira

Department of Biomolecular Engineering, Tokyo Institute of Technology,
4259 Nagatsuta, Midori-ku, Yokohama 227, Japan

Photoinduced electron transfer and energy transfer in Langmuir–Blodgett films, which have been studied recently in this laboratory in relation to the simulation of the primary process in photosynthesis, are reviewed. In photosynthesis, solar energy harvested by antenna pigments is funneled to special electron–hole pairs by highly efficient energy migration and energy transfer in a photosynthetic reaction center; there multistep electron-transfer reactions proceed successively to electron–hole pairs widely separated in the lipid bilayer thylakoid membrane. The well-organized molecular arrangement in the antenna systems and the reaction centers plays an important role in this unidirectional energy transfer and charge separation. In a series of studies, light harvesting and the succeeding charge-separation processes with Langmuir–Blodgett films were simulated.

IN BIOSYSTEMS, MOLECULES ORGANIZE THEMSELVES into complex functional entities with cooperating components of molecular dimensions. For example, well-organized molecular assemblies in thylakoid membranes play an important role in photosynthetic processes of plants and bacteria (1). In 1984, the atomic structure of the reaction center (RC), that is, the basic machinery for the beginning events of photosynthesis, of purple bacterium *R. viridis* was determined with X-ray diffraction (2, 3). All RCs are complexes containing protein subunits and donor–acceptor molecules. These RCs span an inner membrane in the plant or bacterial cell, and their donor–acceptor complexes perform charge separation that creates a potential gradient across the membrane. Before

0065–2393/94/0240–0373\$08.36/0
© 1994 American Chemical Society

the charge separation can take place at any RC, solar energy must be harvested by light-absorbing antenna pigments and transmitted to the RC. The number of pigment molecules per RC is large; 100 to 200 in green plants, and 50–100 in photosynthetic bacteria.

Two types of antenna complexes are known (4): the core antenna and the peripheral antenna. The core antenna is tightly coupled with the RC complex in the membranes and is a direct energy donor to the RC. The peripheral antenna is an additional system that facilitates transfer to the core system: It is often localized in the membranes; however, extramembranous antenna systems are also known, such as phycobiosome in cyanobacteria and chlorosome in green bacteria. In these antenna systems, the adsorbed light energy is transferred sequentially among photosynthetic pigments and finally to the RC. The energy flow is quite unidirectional, and the correct structure of the antenna systems is a prerequisite for the transfer process.

To design artificial photosynthetic molecular systems (5–9) for solar energy conversion, one method is to mimic the elaborate molecular machinery for the light harvesting and the charge separation. The correct structure and function of the antenna systems and the RC, that is, the unidirectional spatial arrangement of the energy (or electron) donors and acceptors in the light-harvesting and in the charge-separation unit for the unidirectional energy (or electron) flow, is essential. The Langmuir–Blodgett (LB) film is one of the most appropriate artificial materials with which the spatial arrangement of the various functional moieties across a film can be constructed readily at atomic dimensions. In a series of studies, we have attempted to simulate the elemental processes of photosynthesis by taking advantage of LB monolayer assemblies. In this chapter, recent developments in the studies of the photoinduced electron transfer and energy transfer in LB films from our group are reviewed.

Molecular Photodiodes

Heterogeneous A/S/D Langmuir–Blodgett Films. The first molecular photodiode was fabricated with a molecularly ordered film on a gold optically transparent electrode (AuOTE) prepared by the LB method (10) as shown in Figure 1a, where hydrophilic and hydrophobic units are indicated by gray circles and white squares, respectively. With their amphiphilic properties, three functional compounds tend to orient regularly in the heterogeneous LB films. Another interesting and fascinating application of LB films is their use as controlled-thickness spacers or “distance keepers”. Therefore, the distances between the three functional moieties, that is, A, S, and D, can be closely controlled at known values. The electron-transfer process in such molecular assem-

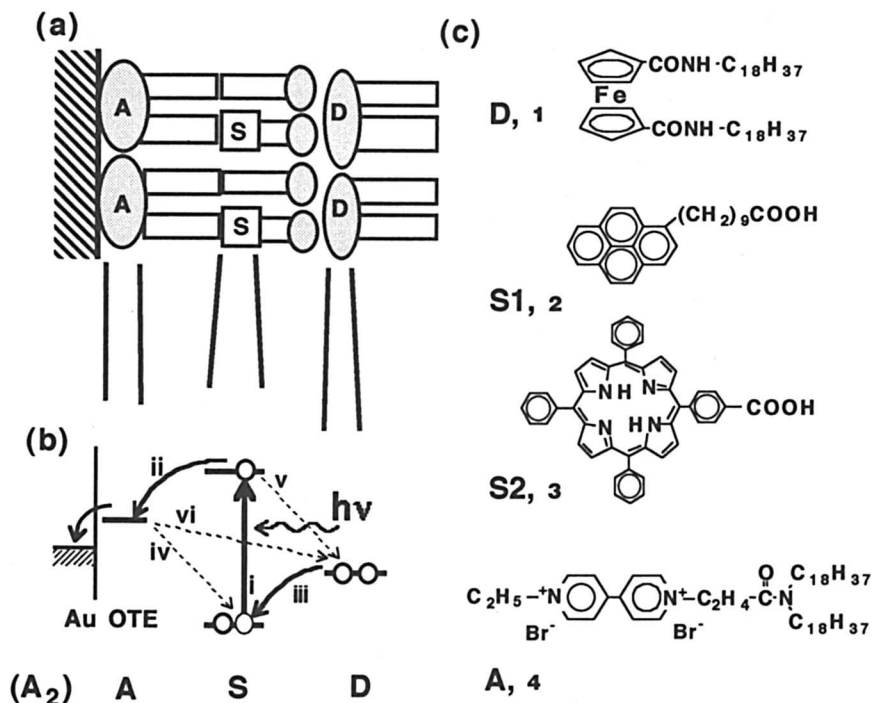


Figure 1. Molecular photodiode with heterogeneous A/S/D LB film on AuOTE: (a) structure, (b) energy diagram, and (c) structural formulae of A, S and D.

blies is free from any complication due to diffusion. Kuhn (5, 6) and Möbius (7, 8) studied the distance dependence of the rate of photoinduced electron transfer in LB films. Their proposed dependence agrees with the experimental (5–17) and theoretical (18) results for nonadiabatic electron transfers at fixed distance r , which are described by the rate constant (18)

$$k = \frac{2\pi}{h} H_{AB}^2 F \quad (1)$$

where h is Planck's constant, H_{AB} is the electronic matrix element describing the electronic coupling of the reactants' electronic state with the products, and the quantity F is the Franck–Condon factor, which is a sum of products of overlap integrals of the vibrational and solvational wave functions of the reactants with those of the products suitably weighted by Boltzmann factors. The quantity H_{AB}^2 decreases exponen-

tially with separation distance for many systems, so the first-order rate constant can be rewritten as

$$k = k(r) \exp\left(\frac{-\Delta G^*}{RT}\right) \quad (2)$$

$$k(r) = k_0 \exp[\beta(r - r_0)] \quad (3)$$

where ΔG^* is the free energy barrier for the reaction, R is the gas constant, and T is temperature. In addition to the described distance dependence, the effect of the standard free energy difference ΔG° for the electron transfer is another important factor in determining the rate of electron transfer. Equation 4 was first introduced by Marcus (19); ΔG^* in equation 2 was given in terms of the reorganization energy λ :

$$\Delta G^* = \frac{\lambda}{4(1 + \Delta G^\circ/\lambda)^2} \quad (4)$$

The changes in bond lengths of the reactants and the changes in solvent orientation coordinates in the electron transfer are related to λ (18). In Marcus's original theory, the motion of the nuclei was treated classically. There have been several attempts to treat the nuclear coordinates quantum mechanically by calculating the quantity F in equation 1 and to modify the equation for the energy gap ΔG° (18, 20, 21). In connection with the design of the proper energy diagram for the molecular photodiode, the inverted region, where the rate decreases with an increase in a large excess of $-\Delta G^\circ$, predicted by equation 4 is most important (22). The presence of the inverted region has been confirmed experimentally by the use of internal electron-transfer systems with rigid spacers (23).

Keeping the distance and the ΔG° dependence in mind, we considered how to design a better molecular photodiode (10, 22). In Figure 1b, the energy diagram of the A/S/D molecular photodiode is depicted as a function of distance across the LB film. If the forward processes (solid lines) are accelerated and the backward processes (dashed lines) are retarded by setting the distances and the energy levels appropriately, the photoinduced vectorial flow of electrons can be achieved. Namely, the acceleration that results from setting $-\Delta G^\circ$ equal to λ is assumed for the forward electron-transfer processes ii and iii, whereas the retardation, as a consequence of the inverted region, is assumed for the reverse electron-transfer processes iv and v.

For the evaluation of H_{AB} , it is better to regard the backward processes iv and v as hole-transfer processes rather than electron-transfer processes, because the highest occupied molecular orbitals of the in-

tervening alkyl chains may play a more important role than the lowest unoccupied ones in the superexchange model (18, 24) for an indirect electron-exchange interaction between the reactant and product. Once an electron-hole pair is separated successfully, the recombination of the pair across the large separation by the LB film (process vi) is hindered in terms of the distance dependence.

The three kinds of functional amphiphilic derivatives used for the first A/S/D type molecular photodiode (10) are shown in Figure 1c together with porphyrin sensitizer, 3, used later (25). By depositing these three amphiphiles on AuOTE, as shown in Figure 1a, and by using the resulting electrode as a working electrode in a photoelectrochemical cell (11–13), the photoinitiated vectorial flow of electrons was achieved and detected as photocurrents. The AuOTE is a metal electrode and hence does not by itself possess a rectifying ability as does a semiconductor electrode (11–13). In spite of the inability of the substrate electrode to rectify, the photocurrent flowed in opposing directions, depending on the spatial arrangement of A/S/D or D/S/A. The direction was in accordance with the energy profile across LB films in Figure 1b.

Much higher photocurrents were observed for stacks of multilayers of each component, for example, in the form of A,A,A/S,S,S/S/D,D,D and D,D,D/S,S,S/A,A,A (10, 25). The direction of the photocurrent also agreed with what was expected for these multilayered systems. An amphiphilic porphyrin derivative, 3, was also used as a sensitizer (25).

In such heterogeneous LB films, the long alkyl chains intervened between the A and S and between the S and D moieties. As a result, part of the excited sensitizers was deactivated by the emission of photons without quenching by electron transfer. To cope with this problem, polyimide LB films consisting of A, S, and D units were used for constructing more efficient molecular photodiodes in collaboration with Kakimoto, Imai, and co-workers (26). They had reported the preparation and properties of polyimide LB films (27–29). Because polyimide LB films have no long alkyl spacer between the layers (monolayer thickness 0.4–0.6 nm), electrons should be more readily transferred. For example, photocurrents on the order of sub-microamperes were observed for AuOTEs that were coated with six layers of A, two layers of S, and six layers of D. These magnitudes are ca. 10 times those for photodiodes with conventional LB films. The efficiency was further improved by the use of a polyimide that had triphenylamine units as the electron donor layers (30). The triphenylamine units are known to be good hole carriers among organic photoconductors (31).

Folded-Type S–A–D and Linear-Type A–S–D Triads. Another approach to shortening the distances between the functional moieties is the use of unidirectionally oriented amphiphilic triad monolayers

(9, 10, 32). Each triad contained an A, S, and D moiety as its functional subunits. Other groups also studied the two-step photodriven charge separation and reverse electron-transfer reactions of triad molecules of the S-A1-A2 (33, 34) or A-S-D (35-37) types. They succeeded in retarding charge recombination in homogeneous solution, but did not attempt to orient these triad molecules in one direction and thus to conduct a direct photoelectric conversion. In our first amphiphilic triad **5** (Figure 2) (10), A, S, and D corresponded to viologen, pyrene, and ferrocene moieties, respectively. The viologen moiety is hydrophilic, whereas the pyrene and ferrocene moieties are hydrophobic. Subunits A and S were linked together with a C₆ alkyl chain, and subunit D was linked to subunit A with a longer C₁₁ alkyl chain. Later, a modified triad, **6** (Figure 2), was synthesized (32) to improve the balance of the two distances between A and S and between S and D. Figure 2 also shows the structures of "linear"-type A-S-D triads and their reference compounds, A-S-, S-D, and -S-.

Because of their amphiphilic properties, the A, S, and D moieties were considered to be arranged spatially in this order, owing to the

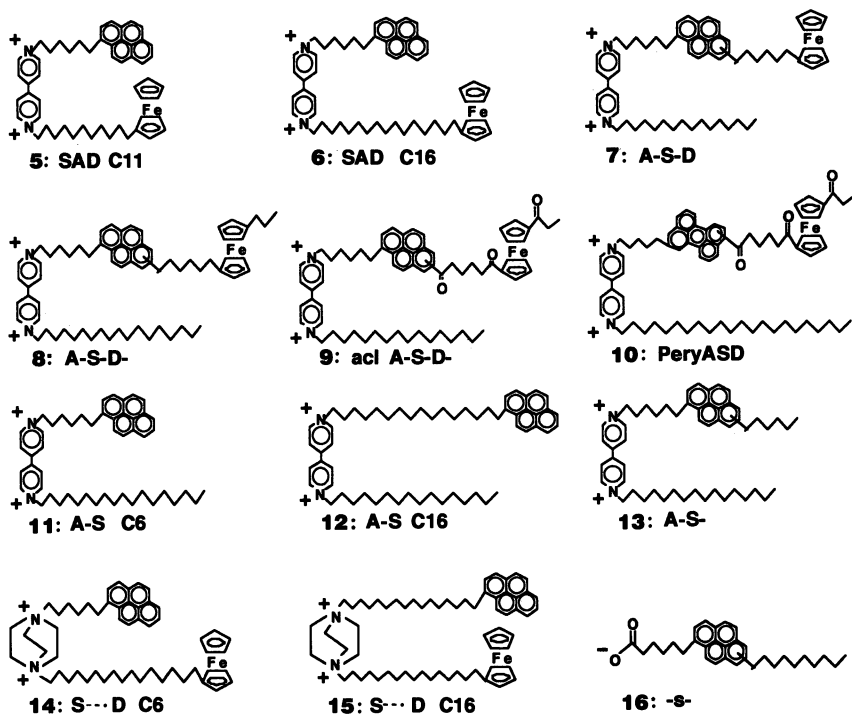


Figure 2. Structural formulae of folded-type S-A-D and linear-type A-S-D triads and their reference A-S-, S-D, and -S- compounds.

difference in length of two alkyl chains, from the electrode to the electrolyte solution perpendicularly as visualized in Figure 3b. This arrangement was confirmed by observing anodic photocurrents, the direction of which was in accordance with the photoinduced vectorial flow of electrons expected from the energy diagram of the oriented triad, as depicted in Figure 3d. From the shape illustrated in Figure 3b, S–A–D is called “folded”-type triad. The photodiode function of these folded-type S–A–D triads was studied in detail (32) in terms of (1) the wavelength of the incident photons, (2) the surface pressure applied for monolayer deposition, (3) the applied electrode potentials, (4) the distances between A and S and between S and D, and (5) the role of the D moiety.

The photocurrent spectra in terms of the formal quantum efficiency (11–13) were recorded for the mixed monolayers [triad 5 and arachidic acid (AA) (1:2)] that were deposited on AuOTEs at the two different surface pressures indicated by P and Q in Figure 3a. The most important and interesting point was that the photocurrent increased by a factor of ca. 20 when the surface pressure for film deposition was only changed from 15 (at Q) to 35 mN m^{-1} (at P). The increase in the surface concentration by compression from Q to P was insufficient to explain such a dramatic increase in the photocurrent. Rather, the nonoriented structure of triad 5 and the unfavorable relative location of the A, S, and D moieties (Figure 3c) in the monolayer at the low surface pressure (Q) might be responsible for the small photocurrent. By contrast, the much larger photocurrents observed at the high surface pressure (P) support

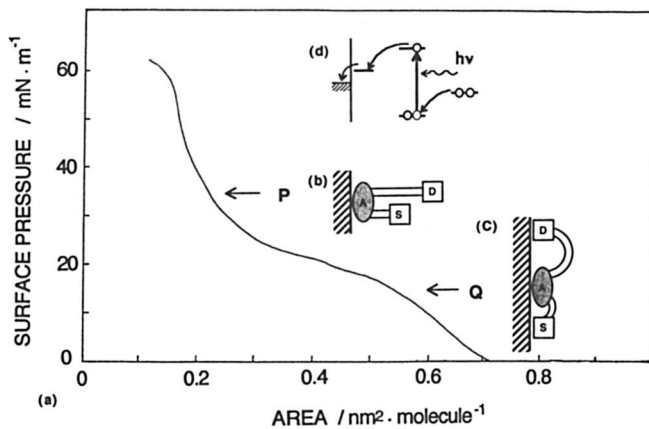


Figure 3. Surface pressure versus area isotherm (a) of a mixed monolayer of triad 5 with AA and a schematic representation of oriented (b) and non-oriented (c) triad 5, with the corresponding energy diagram (d).

the more favorable orientation of the folded-type S–A–D triad molecule postulated in Figure 3b.

A higher efficiency of triad 6 compared to that of triad 5 was also observed, which might be attributed to a better matching in concurrent electron-transfer reactions between A and S and between S and D owing to an improved balance between the A–S and S–D distances. Another amphiphilic compound (11) without the D moiety (Figure 2) confirmed a positive contribution of the D moieties in triads 5 and 6.

To improve the orientation of triad molecules in the monolayer, the linear-type A–S–D triads in Figure 2 were synthesized (38). The mixed monolayer of one of the linear-type A–S–D triads (7) with behenic acid (BA) exhibited a much higher photocurrent than did that of the folded-type S–A–D triads. Thus, a better spatial arrangement of the A, S, and D moieties was attained for the linear triad molecules in the mixed monolayer.

Kinetics of Photoinduced Electron Transfer and the Effect of an Electrical Double Layer

As described in the section “Heterogeneous A/S/D Langmuir–Blodgett Films”, the kinetics of photoinduced multistep electron transfer plays a crucial role in the efficiencies of the molecular photodiodes. To clarify the energy gap and the distance dependence of the photoinduced electron transfer in heterogeneous LB films or triad monolayers, nanosecond and picosecond laser photolyses were carried out.

As a reference in photoinduced multistep electron transfer in the A/S/D and D/S/A LB films, the luminescence decay curves were recorded for sensitizers such as pyrene and $\text{Ru}(\text{bpy})_3^{2+}$ (bpy is bipyridine) derivatives confined as one monolayer in LB films. These films also contained other monolayers of acceptor or donor amphiphiles that were deposited apart from the sensitizer monolayer by a fixed distance, as shown in Figure 4. The structures of the sensitizers and those of amphiphilic acceptors and donors are shown in Figures 1c and 5. In addition to the difference of 1.0 V in the oxidation potentials between the excited pyrene (2) and the $\text{Ru}(\text{bpy})_3^{2+}$ (17) derivatives, the redox potentials of four acceptors, 4 and 18–20, ranged widely up to 1.8 V. Thus, we were able to examine the energy gap ΔG° dependence of the photoinduced electron-transfer rate of the A/S LB films (22). It was concluded from the results that the possibility of a Marcus-type inverted region exists at highly negative ΔG° , although this conclusion is not definite yet because of the limited data.

To examine the energy gap law for S/D LB films, four kinds of amphiphilic ferrocene derivatives (21–24) as electron donors with different standard redox potentials E° and with the same alkyl chain spacer were

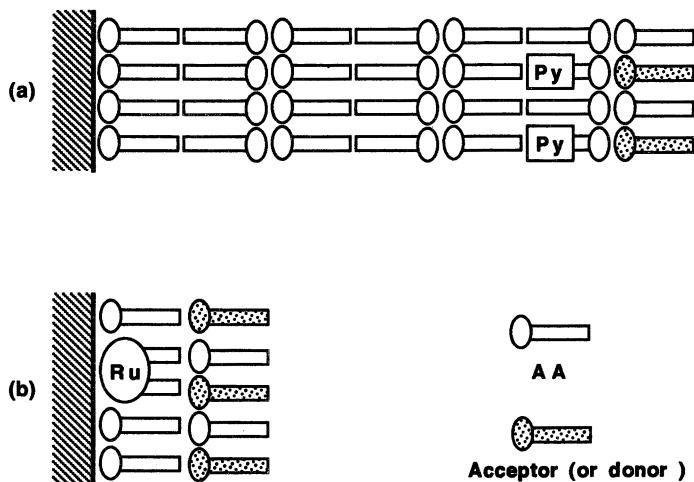


Figure 4. Heterogeneous LB films used for kinetic study of photoinduced electron transfer: (a) pyrene-decanoic acid (2) and A (or D), (b) Ru C19 (21) and A (or D).

synthesized (39, 40). The comparison of the ΔG° dependence of the reductive quenching of the $\text{Ru}(\text{bpy})_3^{2+}$ derivative 17 with the ferrocene derivatives for three different systems—that is, the LB films, the micellar systems (41, 42), and the solution systems—implies that the electrical potential difference between the hydrophilic head groups in LB films has to be taken into account when estimating the effective energy gap ΔG° . Namely, an efficient photoinduced electron-transfer quenching happens, even in an S/D LB film in which the reaction was expected to be uphill ($\Delta G^\circ > 0$) on the basis of half-wave potentials and thus too slow to be detected. The result also contradicted that of the corresponding solution system.

The effect of the inner potential difference in the electrical double layer was further studied by using three kinds of amphiphilic ferrocene derivatives, 21, 25, and 26, with an anionic, a cationic, and a nonionic head group, respectively (43, 44) (Figure 5). All of the redox potentials of the three ferrocene derivatives were ca. 0.9 V versus the standard calomel electrode (SCE) and more positive than the reduction potential of excited $\text{Ru}(\text{bpy})_3^{2+}$ of 0.6 V versus SCE. The luminescence decay curves for 17 in three types of S/D systems were recorded together with that in a reference LB film in which the pure monolayer of AA was deposited in place of the ferrocene donor layer. Only the decay curve for 17/21 showed a fast decay component, whereas the other two curves are very similar to that for the reference LB film and showed almost a single exponential decay without appreciable quenching. However, the

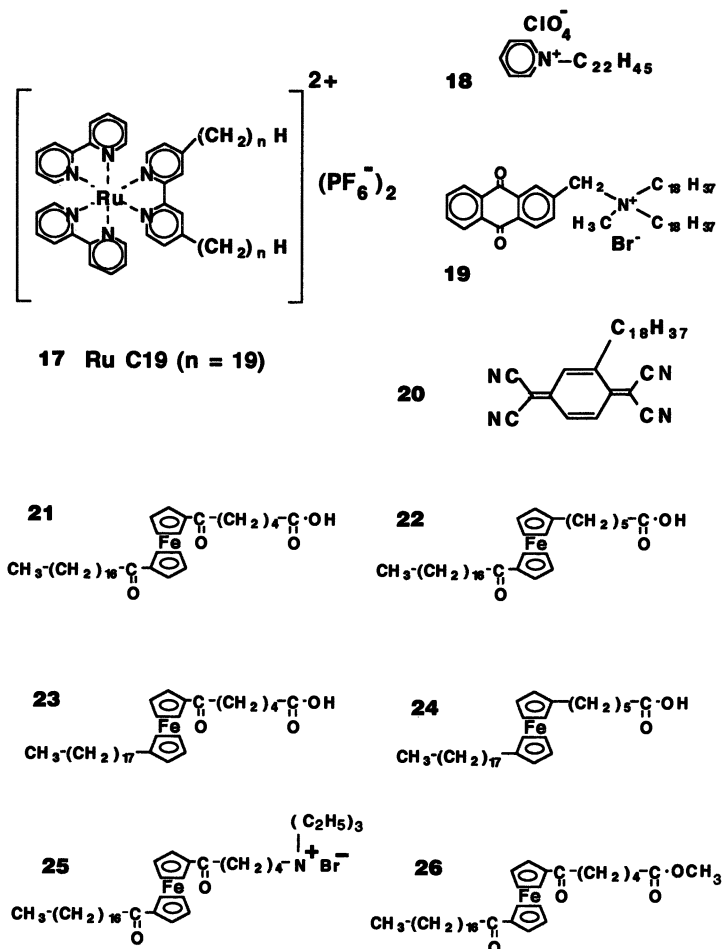


Figure 5. Structural formulae of amphiphilic $\text{Ru}(\text{bpy})_3^{2+}$ sensitizer and electron acceptor and donor amphiphilic derivatives used in the kinetic study.

fast decay component in the luminescence decay curves of $\text{Ru}(\text{bpy})_3^{2+}$ LB films without intentionally added quenchers was observed frequently.

To clarify the origins of the fast decay component, we studied how the decay curves were affected by the conditions used for preparation of LB films and for luminescence lifetime measurements (dilution ratios, measuring atmosphere, laser power, and irradiation time) and succeeded in finding the conditions with which the luminescence decay curves were fitted by a single exponential function (39, 40, 45).

The change in sign of the head-group charge was expected to vary signs of the electrical double layer and thus the effective energy gap

ΔG° . The potential difference will readily become a few hundreds millivolts, as observed for monolayers at the air–water interface (46–48) and for micellar surfaces (49, 50). If this potential difference is taken into account, appreciable electron-transfer quenching, observed specifically in the $\text{Ru}(\text{bpy})_3^{2+}$ /anionic ferrocene derivative system, is rationalized. It is noteworthy that the electrostatic potential effect was proposed to explain why the photochemical reaction follows the L pathway in the reaction center with almost C_2 symmetry (51).

To increase the response time and efficiency of the molecular photodiode consisting of folded-type S–A–D triad molecules, it is important to know the distance and orientation dependence of the electron-transfer quenching in A–S and S–D monolayers. For this purpose, A–S and folded-type S–D amphiphiles with alkyl chain spacers of different carbon numbers (Figures 6a and 6b, respectively) were prepared. The luminescence decay of these LB films was measured with picosecond laser photolysis (52). The linear decrease in $\log k_q$ (rate constant of quenching) with an increase in carbon number was observed for the A–S monolayers (Figure 6c), but the regular dependence of $\log k_q$ on the alkyl chain lengths could not be obtained for folded-type S–D systems.

Thus, the alkyl chains in the A–S dyad molecules are extended in their monolayers and therefore the distance between A and S can be controlled by changing the carbon number, whereas this is not the case for the folded-type S–D dyads as visualized in Figure 6d. Therefore,

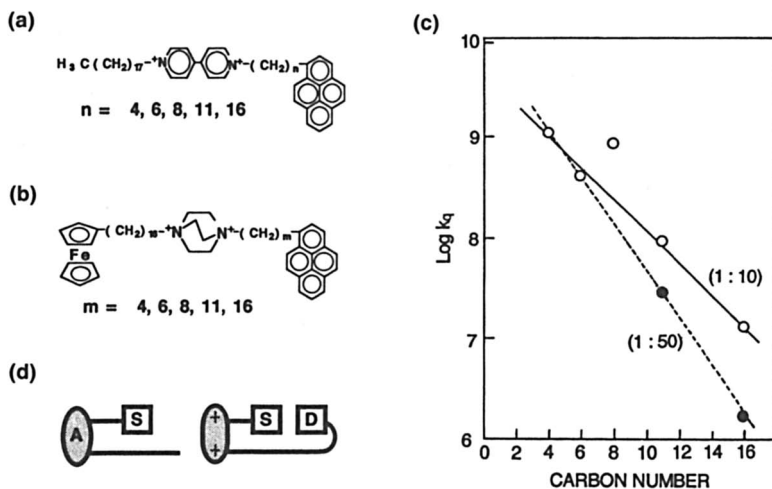


Figure 6. Structural formulae of (a) A–S and (b) S–D compounds used to study the effect of alkyl chain lengths on kinetics of electron-transfer quenching in mixed monolayers of A–S (or S–D) with AA, (c) the measured electron-transfer quenching rate constant, k_q , as a function of carbon number for A–S, and (d) schematic representations of oriented dyads in LB films.

the linear-type S–D dyads were synthesized and the luminescence decay measurements of their LB films were carried out.

Simulation of the Primary Process in the Photosynthetic Reaction Center with a Mixed Monolayer with Triad and Antenna Molecules

In the next step, we simulated the light-harvesting and succeeding charge separation processes by a monolayer assembly consisting of synthetic antenna pigments and triad molecules, as illustrated in Figure 7 (9, 53, 54). For the light-harvesting (H) antenna pigments, an amphiphilic pyrene derivative was used (55). For the amphiphilic linear triad molecule, an acylated perylene moiety, as the S unit, and viologen and ferrocene

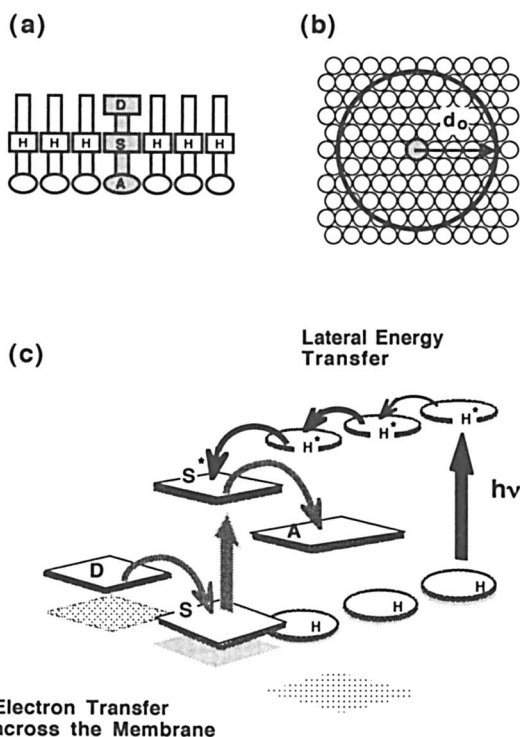


Figure 7. Schematic representation of the artificial photosynthetic reaction center by a monolayer assembly of Pery A–S–D triad 10 and antenna –S–16 molecules for light harvesting (H), energy migration and transfer, and charge separation via multistep electron transfer: (a) side view of monolayer assembly, (b) top view of a triad surrounded by antenna molecules, and (c) energy diagram for photoelectric conversion in a monolayer assembly.

moieties, as the A and the D units, respectively, were used. The structures of the antenna (16) and the triad (10) molecule are also shown in Figure 2. Because of the overlap of the emission spectrum of the antenna pyrene and the absorption spectrum of the sensitizer acylated perylene moiety of the triad (Figure 8a), light energy harvested by the antenna molecules were efficiently transferred to the sensitizer moiety of the triad. Thus, the excitation energy of the perylene moiety should be converted to electrical energy via multistep electron transfer across the monolayer as described earlier.

Figure 8b shows the photocurrent spectrum of the mixed monolayer of the triad and the antenna with a molar ratio of 1:4. Maxima of anodic photocurrents at ca. 350 and 470 nm are found. These correspond to the adsorption maxima of pyrene and acylated perylene. The anodic direction of the photocurrent agrees with the energy diagram and the orientation of the triad shown in Figure 7. In contrast, negligible photoresponse was obtained with the pure antenna monolayer. Thus, charge separation in the triad molecules was initiated by light absorption both with perylene sensitizer itself and with the pyrene antennas followed by energy transfer.

Special attention has also been paid recently to dynamics of the Förster-type excitation energy transfer in molecular assemblies of restricted molecular geometries in LB films (56) and photosynthetic light-harvesting antenna pigment systems (57). Photochromic LB films as an optical switching device were also proposed by Yamazaki and co-workers (58, 59).

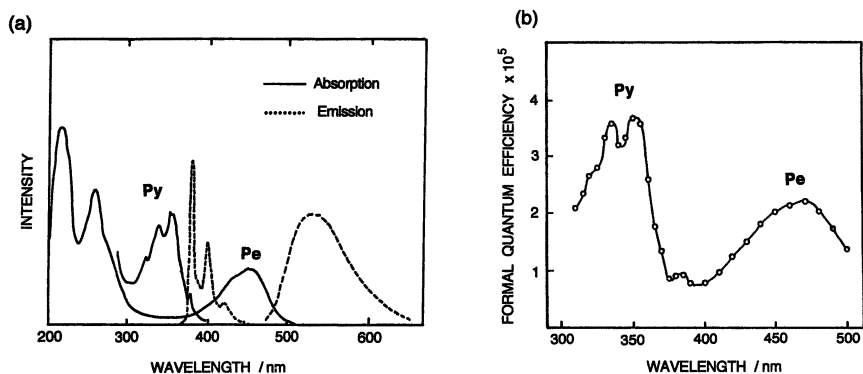


Figure 8. UV and visible absorption and emission spectra (a) of antenna pyrene 16 and perylene triad 10 derivatives in ethanol and photocurrent spectrum (b) of the mixed monolayer of 10 and 16 (1:4) deposited on AuOTE. (Reproduced with permission from reference 54. Copyright 1989 Elsevier Sequoia.)

Energy-Transfer Quenching of Pyrene-Substituted Fatty Acid by Its Photooxidized Product

Description. In studying characterization of LB films containing pyrene-substituted fatty acid (2) (60) by fluorescence microscopy (61) and Penning ionization spectroscopy (62), we discovered the drastic decrease in the fluorescence intensity with time under UV illumination for fluorescence microscopy, especially under an atmosphere containing oxygen. A clear contrast in the excimer intensity between the virgin area and the area that had previously experienced UV exposure can be seen in a fluorescence micrograph shown in Figure 3A in reference 61. To clarify the mechanism of this fluorescence quenching, the photochemical reaction of mixed LB films of PDA (2) with arachidic acid (AA) in the presence of oxygen was studied (63).

In addition to the decrease in the excimer fluorescence intensity, the much slower decrease in UV-visible absorbance due to the pyrene moieties was observed with an increase in the UV irradiation time. The UV-irradiated LB films revealed a new visible broad band in the wavelength region longer than 365 nm and new infrared absorption peaks, which are attributed to introduction of carbonyl groups. The much higher rate in the decrease in the fluorescence intensity than that in the UV-visible absorbance due to pyrene moieties can be ascribed to the energy-transfer quenching of the photoexcited pyrene moieties by the described photooxidative products. The energy-transfer quenching of the Förster type was confirmed by examining dependence of the fluorescence quenching on the spacer thickness between the monolayers of the pyrene moieties and the photoproducts in the heterogeneous LB films shown in Figure 9. The heterogeneous LB films were prepared as follows: A mixed monolayer of PDA-AA was first UV irradiated for 160 min, then covered with another fresh mixed monolayer with an appropriate number of spacer layers of AA in between.

The highly efficient—in terms of energy transfer—lateral quenching by the photoproduct is schematically illustrated in Figure 10a. One photooxidative product can quench a large number of excited pyrene moieties inside a circle with a radius of the critical length of energy transfer, r_0 , in the monolayer (inside a sphere with a radius of r_0 for LB films thicker than $2r_0$). This quenching can be regarded as one of the chemical amplification reactions and can be applied to a very sensitive photoresponsive memory. In other words, in the fluorescence intensity reading mode, the sensitivity increases by the number of quenched PDA molecules within the circle (N_q) per photooxidized PDA molecule (PDA_{po}), that is, $N_q/\text{PDA}_{\text{po}}$. If the same monolayer assembly is used as an optical memory based on photochromic behavior, the signal will be the change in absorbance of PDA or the product by the photooxidation,

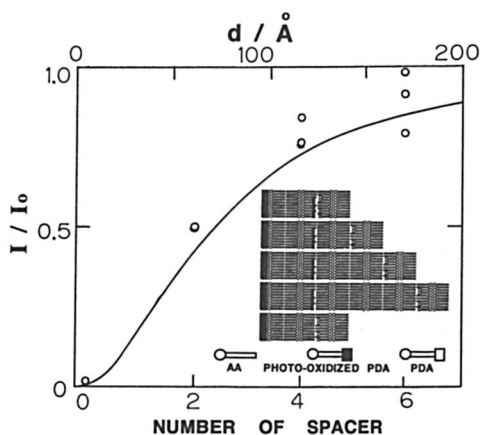


Figure 9. Change in the fluorescence intensity of the schematically illustrated LB films as a function of the number of spacer layers. The solid line was calculated on the assumption of the Förster mechanism (5) for energy transfer from PDA to photooxidized PDA in the built-up multilayers.

and its intensity will be proportional to the change in the number of PDA molecules or the product (n) from the Beer-Lambert law.

In contrast, surrounding unreacted PDA molecules around one PDA_{po} molecule inside the circle can be quenched, and thus n molecules of PDA_{po} can quench nN_q molecules of unreacted PDA under weak irradiation. The decrease in the fluorescence intensity should be proportional to N_q times of n under the initial weak irradiation, that is, the amplification will be N_q .

Optical Memory Applications. This result prompted us to develop a new monolayer assembly that consists of a fluorescent dye without a photoinactive fatty acid stabilizing the monolayer, such as AA. The sensitivity will increase as much as the increased number of quenched fluorescer (inside the circle in Figure 10b), and the increase in the contrast of the fluorescence image between the virgin area and the area that experienced UV exposure will be proportional to the square of the concentration of the fluorescent dye. PDA, however, could not be used by itself as an amphiphile for the pure monolayer because it was crystallized readily in monolayers in high concentrations (60, 61).

To stabilize monolayers consisting of pyrene-substituted fatty acids, we synthesized a new type of pyrene derivatives that have a pyrene moiety in the middle of the alkyl chain of the fatty acids, that is, $\text{C}_n\text{H}_{2n+1}\text{Py}(\text{CH}_2)_{m-1}\text{COOH}$ (HPDA, $n = 6$, $m = 10$; and DPDA ($-S-$ 16 in Figure 2), $n = 10$, $m = 6$) (55). These compounds were synthesized by twice repeating a Friedel-Crafts acylation followed by reducing the

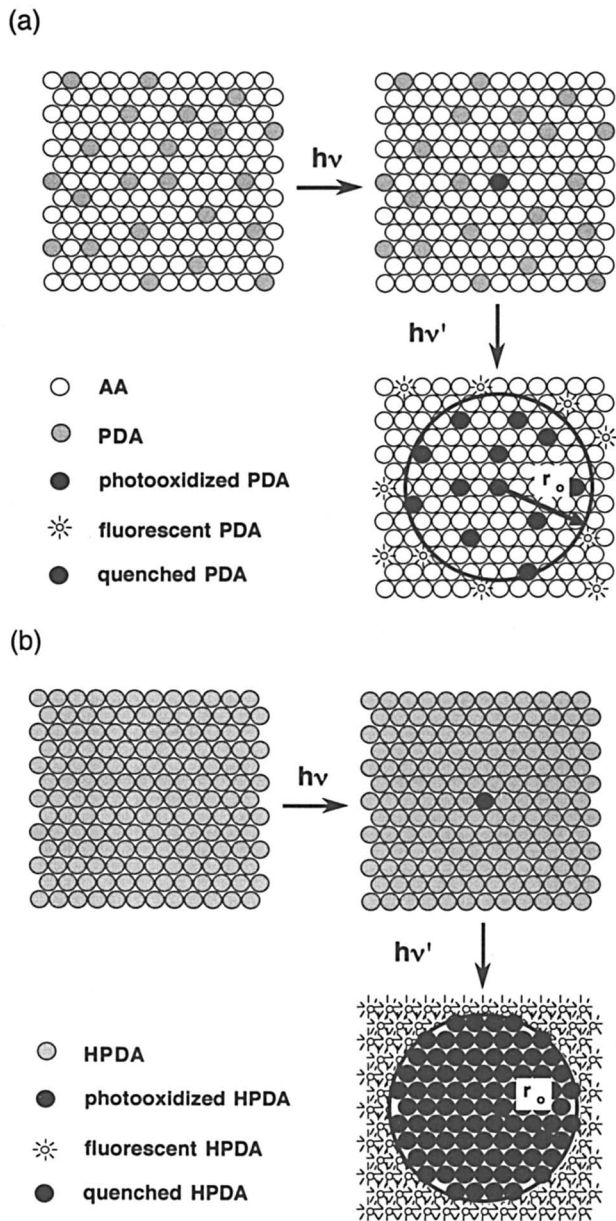


Figure 10. Schematic representation of the photochemical amplification mechanism of optical memory in the fluorescence intensity reading mode showing highly efficient lateral energy-transfer quenching by photooxidized pyrene-substituted fatty acids for (a) a mixed monolayer of PDA-AA and (b) a pure monolayer of HPDA. (Reproduced with permission from reference 67. Copyright 1992 Materials Research Society.)

resulting carbonyl intermediates (64, 65). The compounds were expected to be obtained as the mixtures of position isomers of dialkylated pyrenes, that is, 1,3-, 1,6-, and 1,8-position isomers, and HPDA and DPHA had lower melting points, 50–60 and 85–93°C, respectively (66), than that of PDA, 113–114°C (65).

The presence of three position isomers was confirmed very recently by 500-MHz NMR spectroscopy of the dialkylated product (67). Lowering of the melting points due to the mixture of the position isomers resulted in difficulty in crystal formation and thus an increase in the stability of the monolayers without fatty acids. By the use of polyion complexation with polyallylamine (PAA), the stability of the LB films of HPDA or DPHA was further improved (55, 66).

Figure 11 shows a fluorescence micrograph of the polyion-complexed HPDA/PAA LB film (22 layers) irradiated by N₂ laser through a standard photomask (66). High homogeneity in the LB film plane and

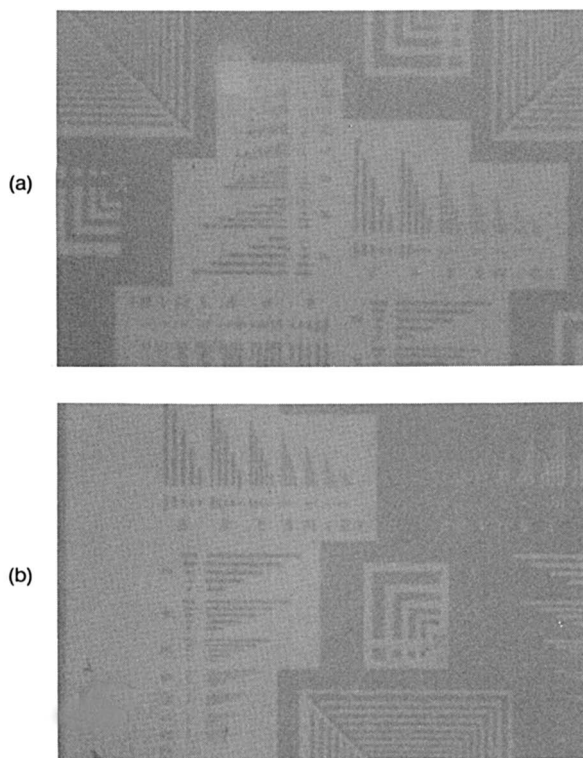


Figure 11. Fluorescence micrographs of the polyion-complexed LB film of HPDA with PAA (22 layers) irradiated by a N₂ laser through a standard photomask under air (a) and under N₂ (b) with a fluorescence micrograph used previously (61).

high resolution of the photooxidatively quenched pattern were clearly seen under N_2 . The homogeneity and high sensitivity of the LB film may allow us to record with a light source with dimensions less than the wavelength through the use of a near-field optical probe (68–70). The writing and the reading by the probe are now under investigation. In these cases, however, the photooxidation of the pyrene moieties is irreversible, and therefore the recording can be done in the presence of oxygen, and the resulting memory has to be read repeatedly under an inert atmosphere. If a mixed film of reversible photochromic (71) and fluorescence compound is used and the colored form of the photochromic molecule can quench the excited state of the fluorescence molecule, a read–write optical memory can be prepared. Such a read–write and highly sensitive optical memory is illustrated in Figure 12.

Photoinduced Proton Transfer in LB Films as a Simple Model of a Proton Pump in Bacteriorhodopsin

Some kinds of halophilic bacteria have a unique solar energy conversion process (1). The polypeptide unit, bacteriorhodopsin, pumps a proton as a result of photoisomerization of retinal and subsequent proton-hopping reactions between residues of the polypeptide. This molecular process suggests a novel molecular device for solar energy conversion that differs from the described molecular photodiode based on photoinduced electron transfer. To simulate such a direction-controlled proton-hopping reaction, we assembled LB films containing proton donors and acceptors (72). To our knowledge, this is the first attempt to control the direction of intermolecular proton transfer in artificial aggregates.

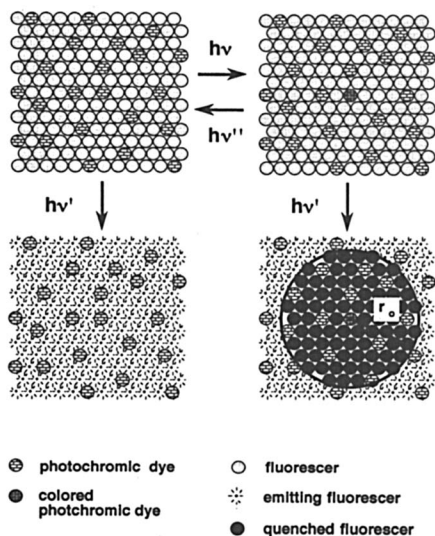


Figure 12. Schematic representation of read–write, highly sensitive optical memory in the fluorescence intensity reading mode. A mixed monolayer of reversible photochromic dye with fluorescence dye is used to cause amplified quenching of the excited state of fluorescer by the colored form of the photochromic dye. (Reproduced with permission from reference 67. Copyright 1992 Material Research Society.)

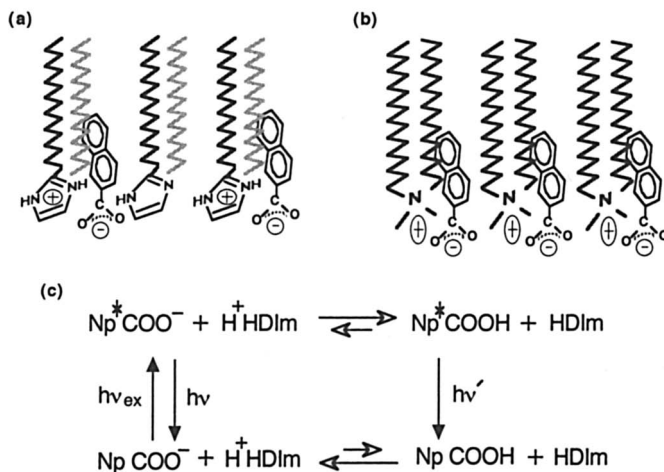


Figure 13. Schematic view of the LB films (a) HDIm-OD, and (b) DODA⁺ and the reaction mechanism of photoinduced proton transfer (c). (Reproduced with permission from reference 72. Copyright 1992 Elsevier Sequoia.)

Figure 13a represents a film in which photoinduced proton transfer is expected. The reaction scheme is shown in Figure 13c. The film consists of 2-heptadecylimidazol (HDIm) and octadecane (OD) (HDIm:OD, 1:1). Depending on the pH of the subphase, the π -A isotherm shows that HDIm is partially protonated (H⁺HDIm) and an equal amount of 2-naphthoate (NpCOO⁻) is adsorbed in the film as the counter ion. H⁺HDIm is a proton-donating amphiphile, NpCOO⁻ is a proton acceptor, and OD is a space-filling molecule stabilizing the film. A photoexcited 2-naphthoate (Np*COO⁻) can pull a proton away from a H⁺HDIm cation with its stronger proton affinity (73–75) compared with that in the ground state (Figure 13c).

Diocadecylammonium cation (DODA⁺), which has no proton-donating ability, was also deposited together with NpCOO⁻ as a reference LB film. The schematic view of the reference film (DODA⁺ film) is shown in Figure 13b. With Fourier transform infrared spectroscopy, UV-visible absorption, and fluorescence spectroscopic data, it was confirmed that photoinduced intermolecular proton transfer proceeded in the HDIm-OD film (72).

Acknowledgments

I thank all my colleagues who collaborated in this research. This research was supported by a Grant-in-Aid for Scientific Research (61470076) and Grants-in-Aid on Priority Areas (63604534 and 63612506) from

the Ministry of Education, Science, and Culture and by a grant from the Nissan Science Foundation.

References

1. Stryer, L. *Biochemistry*, 3rd ed.; Freeman: New York, 1988.
2. Deisenhofer, J.; Epp, O.; Miki, K.; Huber, R.; Michel, H. *J. Mol. Biol.* **1984**, *180*, 385.
3. Deisenhofer, J.; Epp, O.; Miki, K.; Huber, R.; Michel, H. *Nature (London)* **1985**, *318*, 618.
4. Mimuro, M. *Bot. Mag.* **1990**, *103*, 233.
5. Kuhn, H. *J. Photochemistry* **1979**, *10*, 111.
6. Kuhn, H. *Thin Solid Films* **1983**, *99*, 1.
7. Möbius, D. *Ber. Bunsen Ges. Phys. Chem.* **1978**, *82*, 848.
8. Möbius, D. *Acc. Chem. Res.* **1981**, *14*, 63.
9. Fujihira, M. *Mol. Cryst. Liq. Cryst.* **1990**, *183*, 59.
10. Fujihira, M.; Nishiyama, K.; Yamada, H. *Thin Solid Films* **1985**, *132*, 77.
11. Osa, T.; Fujihira, M. *Nature* **1976**, *264*, 349.
12. Fujihira, M.; Ohishi, N.; Osa, T. *Nature (London)* **1977**, *268*, 226.
13. Fujihira, M.; Kubota, T.; Osa, T. *J. Electroanal. Chem.* **1981**, *119*, 379.
14. Verhoeven, J. W. *Pure Appl. Chem.* **1986**, *58*, 1285.
15. Miller, J. R.; Beitz, J. V.; Huddleston, R. K. *J. Am. Chem. Soc.* **1984**, *106*, 5057.
16. Miller, J. R. *Nouv. J. Chim.* **1987**, *11*, 83.
17. Mooney, W. F.; Whitten, D. G. *J. Am. Chem. Soc.* **1986**, *108*, 5712.
18. Marcus, R. A.; Sutin, N. *Biochim. Biophys. Acta* **1985**, *811*, 265.
19. Marcus, R. A. *J. Chem. Phys.* **1965**, *43*, 2654.
20. Ulstrup, J.; Jortner, J. *J. Chem. Phys.* **1975**, *63*, 4358.
21. Siders, P.; Marcus, R. A. *J. Am. Chem. Soc.* **1981**, *103*, 748.
22. Fujihira, M.; Nishiyama, K.; Aoki, K. *Thin Solid Films* **1988**, *160*, 317.
23. Miller, J. R.; Calcaterra, L. T.; Closs, G. L. *J. Am. Chem. Soc.* **1984**, *106*, 3047.
24. Beratan, D. N.; Onuchic, J. N.; Hopfield, J. J. *J. Chem. Phys.* **1987**, *86*, 4488.
25. Fujihira, M.; Nishiyama, K.; Yoneyama, H. *J. Chem. Soc. Jpn.* **1987**, 2119.
26. Nishikata, Y.; Morikawa, A.; Kakimoto, M.; Imai, Y.; Hirata, Y.; Nishiyama, K.; Fujihira, M. *J. Chem. Soc. Chem. Commun.* **1989**, 1772.
27. Suzuki, M.; Kakimoto, M.; Konishi, T.; Imai, Y.; Iwamoto, M.; Hino, T. *Chem. Lett.* **1986**, 395.
28. Kakimoto, M.; Suzuki, M.; Konishi, T.; Imai, Y.; Iwamoto, M.; Hino, T. *Chem. Lett.* **1986**, 823.
29. Nishikata, Y.; Kakimoto, M.; Morikawa, A.; Kobayashi, I.; Imai, Y.; Hirata, Y.; Nishiyama, K.; Fujihira, M. *Chem. Lett.* **1989**, 861.
30. Nishikata, Y.; Fukui, S.; Kakimoto, M.; Imai, Y.; Nishiyama, K.; Fujihira, M. *Mol. Cryst. Liq. Cryst.* **1993**, *224*, 95.
31. Mort, J.; Pfister, G. In *Electronic Properties of Polymers*; Mort, J.; Pfister, G., Eds.; John Wiley and Sons: New York, 1982.
32. Fujihira, M.; Yamada, H. *Thin Solid Films* **1988**, *160*, 125.
33. Nishitani, S.; Kurata, N.; Sakata, Y.; Misumi, S.; Karen, A.; Okada, T.; Mataga, N. *J. Am. Chem. Soc.* **1983**, *105*, 7771.
34. Mataga, N.; Karen, A.; Okada, T.; Nishitani, S.; Kurata, N.; Sakata, Y.; Misumi, S. *J. Phys. Chem.* **1984**, *88*, 5138.

35. Moore, T. A.; Gust, D.; Mathis, P.; Mialoeq, J. C.; Chachaty, C.; Bensasson, R. V.; Land, E. J.; Doizi, J. C.; Liddel, P. A.; Lehman, W. R.; Nemeth, G. A.; Moore, A. L. *Nature (London)* **1984**, *307*, 630.
36. Wasielewski, M. R.; Niemczyk, M. P.; Svec, W. A.; Pewitt, E. B. *J. Am. Chem. Soc.* **1985**, *107*, 5562.
37. Maruyama, K.; Osuka, A. *Pure Appl. Chem.* **1990**, *62*, 1511.
38. Fujihira, M.; Sakomura, M. *Thin Solid Films* **1989**, *179*, 471.
39. Kondo, T.; Yamada, H.; Nishiyama, K.; Suga, K.; Fujihira, M. *Thin Solid Films* **1989**, *179*, 463.
40. Kondo, T.; Fujihira, M. *Kobunshi Ronbunshu* **1990**, *47*, 921.
41. Suga, K.; Fujita, S.; Yamada, H.; Fujihira, M. *Bull. Chem. Soc. Jpn.* **1990**, *63*, 3369.
42. Ohsawa, Y.; Shimazaki, Y.; Aoyagui, S. *J. Electroanal. Chem.* **1980**, *114*, 235.
43. Kondo, T.; Fujihira, M. *Chem. Lett.* **1991**, 191.
44. Kondo, T.; Yanagisawa, M.; Fujihira, M. *Electrochim. Acta* **1991**, *36*, 1793.
45. Fujihira, M.; Yanagisawa, M.; Kondo, T.; Suga, K. *Thin Solid Films* **1992**, *210/211*, 265.
46. Vogel, V.; Möbius, D. *Thin Solid Films* **1985**, *132*, 205.
47. Vogel, V.; Möbius, D. *Thin Solid Films* **1988**, *159*, 73.
48. Vogel, V.; Möbius, D. *J. Colloid Interface Sci.* **1988**, *126*, 408.
49. Wolff, C.; Grtzel, M. *Chem. Phys. Lett.* **1977**, *52*, 542.
50. Grtzel, M. *Heterogeneous Photochemical Electron Transfer*; CRC Press: Boca Raton, FL, 1989.
51. Norris, J. R.; Schiffer, M. *C&EN News* **1990**, *July 30*, 22.
52. Fujihira, M. In *Photochemical Processes in Organized Molecular Systems*; Honda, K., Ed.; Elsevier: New York, 1991.
53. Fujihira, M. In *2nd International Symposium on Bioelectronic and Molecular Electronic Devices R&D Association for Future Electron Devices*; 1988; p 35.
54. Fujihira, M.; Sakomura, M.; Kamei, T. *Thin Solid Films* **1989**, *180*, 43.
55. Fujihira, M.; Kamei, T.; Sakomura, M.; Tatsu, Y.; Kato, Y. *Thin Solid Films* **1989**, *179*, 485.
56. Yamazaki, I.; Tamai, N.; Yamazaki, T. *J. Phys. Chem.* **1990**, *94*, 516.
57. Mimuro, M.; Yamazaki, I.; Tamai, N.; Katoh, T. *Biochim. Biophys. Acta* **1989**, *973*, 153.
58. Minami, T.; Tamai, N.; Yamazaki, T.; Yamazaki, I. *J. Phys. Chem.* **1991**, *95*, 3988.
59. Yamazaki, I.; Tamai, N.; Yamazaki, T. In *Photochemical Processes in Organized Molecular Systems*; Honda, K., Ed.; Elsevier: New York, 1991.
60. Fujihira, M.; Nishiyama, K.; Hamaguchi, Y. *J. Chem. Soc. Chem. Commun.* **1986**, 823.
61. Fujihira, M.; Nishiyama, M.; Hamaguchi, Y.; Tatsu, Y. *Chem. Lett.* **1987**, 253.
62. Ozaki, H.; Harada, Y.; Nishiyama, K.; Fujihira, M. *J. Am. Chem. Soc.* **1987**, *109*, 950.
63. Fujihira, M.; Tatsu, Y. *Fuji LB Post-Conference*; 1988; p 31.
64. Galla, J. H.; Thielen, U.; Hartman, W. *Chem. Phys. Lipid* **1979**, *23*, 239.
65. Sunamoto, J.; Kondo, H.; Nomura, T.; Okamoto, H. *J. Am. Chem. Soc.* **1980**, *102*, 1146.
66. Fujihira, M.; Kamei, T. In *3rd International Symposium on Bioelectronic and Molecular Electronic Devices R&D Association for Future Electron Devices*; 1990; p 43.

67. Fujihira, M. In *Material Research Society Symposium Proceedings Vol. 277*; Jenekhe, S. M., Ed.; Material Research Society: Pittsburgh, PA, 1992.
68. Betzig, E.; Trautman, J. K.; Harris, T. D.; Weiner, J. S.; Kostelak, R. L. *Science (Washington, D.C.)* **1991**, *251*, 1468.
69. Lieberman, K.; Harush, S.; Lewis, A.; Kopelman, R. *Science (Washington, D.C.)* **1989**, *247*, 59.
70. Lewis, A.; Lieberman, K. *Nature (London)* **1991**, *354*, 214.
71. Irie, M. *Jpn. J. Appl. Phys.* **1989**, *28*, 215.
72. Fujihira, M.; Niidome, Y. *Thin Solid Films* **1992**, *210/211*, 378.
73. Kovi, P. J.; Dchulman, S. G. *Anal. Chim. Acta* **1973**, *39*, 63.
74. Donckt, E. V.; Poter, G. *Trans. Faraday Soc.* **1978**, *3215*, 64.
75. Ireland, J. F.; Wyatt, P. A. H. In *Advances in Physical Organic Chemistry*; Gold, V.; Bethell, X., Eds.; Academic: Orlando, FL, 1976; Vol. 12, p 131.

RECEIVED for review March 12, 1992. ACCEPTED revised manuscript March 16, 1993.

Intelligent Biomaterials Based on Langmuir–Blodgett Monolayer Films

Biotinylated Polymers–Streptavidin and Biotinylated Lipid–Streptavidin Recognition Incorporating Photodynamic Proteins

K. A. Marx¹, L. A. Samuelson², M. Kamath¹, J. O. Lim¹, S. Sengupta³,
D. Kaplan², J. Kumar⁴, and S. K. Tripathy¹

¹ Department of Chemistry, University of Massachusetts at Lowell,
Lowell, MA 01854

² Biotechnology Division, U.S. Army Natick Research, Development,
and Engineering Center, Natick, MA 01760

³ Molecular Technologies Inc., 145 Moore Street, Lowell, MA 01854

⁴ Department of Physics, University of Massachusetts at Lowell,
Lowell, MA 01854

Our aim is to use Langmuir–Blodgett (LB) trough technology in novel ways incorporating biological components to create new types of monolayer and multilayer materials possessing interesting electronic and optical properties. In a major focus of our research we have demonstrated an LB trough cassette approach to create ordered systems by using either a biotinylated lipid or a biotinylated polymer that first binds streptavidin protein. In a second step streptavidin binds added biotinylated phycoerythrin, a fluorescent antenna protein. For signal transduction possibilities, conducting polymers may be mixed with the biotinylated lipid in the LB monolayer film in this system. This cassette approach would allow the attachment and ordering of any biotinylated species. These techniques can yield ordered monolayer films possessing unusual optical and electronic properties for potential device applications.

THE CREATION OF A CLASS OF INTELLIGENT BIOMATERIALS with sensory, adaptation, or response capabilities comprised of ordered monolayer

0065–2393/94/0240–0395\$08.00/0
© 1994 American Chemical Society

films for sensing applications is our intent. These systems share the LB trough technology as a basis for organizing them into thin-film layered structures. The thin film can be subsequently transferred onto desired substrates for further investigation and integration of their optical and electronic properties. We discuss here the systems we have been investigating that involve using biotinylated lipids or biotinylated polymer, in some cases mixed with conducting polymers, to create ordered monolayer films. This approach involves the utilization of bridging streptavidin or avidin proteins, both possessing four biotin binding sites. After binding to the film, unoccupied biotin binding sites are available in the subphase for further interaction. Other biotinylated biological macromolecules can then interact with the remaining sites on the bound streptavidin or on avidin protein. The result is an ordered monolayer in which the biochemical properties of the biomolecular component can be integrated with the LB monolayer optoelectronic signal transduction properties.

We use the inherently high specificity of the biotin–streptavidin interaction ($K_a = 10^{15}$) (which forms the basis of many assays in the field of biomedical research (1, 2) and has been demonstrated to function in an LB trough experiment) to bind biotinylated macromolecules with high specificity (3–6). The system of biotinylated lipid or polymer monolayers binding avidin or streptavidin, which then can bind and order other biotinylated components in a hierarchical structure forms a general “cassette system” for creating monolayer or multilayer sensing devices.

Biological macromolecules as materials possess superior “intelligent material” properties that have evolved over evolutionary time to function efficiently in integrated macromolecular arrays in cells in response to their environment. Another intelligent material is the ordered two-dimensional LB monolayer, in our approach comprised of mixed biotinylated lipids and electroactive and electrically conducting polymeric lipid materials (such as polyalkylpyrrole and polyalkylthiophene), and biotinylated polyalkylthiophene copolymer system. These systems possess interesting optical and electronic properties (7) that can be exploited for signal-transduction purposes.

A number of different classes of photodynamic proteins have been considered for this work, including algal phycobiliproteins and bacteriorhodopsin. We will focus on our work with the phycobiliprotein phycoerythrin as illustrative of the approaches possible. Phycobiliproteins are components of supraassemblies located on the thylakoid membranes of marine algal cells that function as light receptors to funnel ambient light into the photoreactive center to drive photosynthesis (8). The light receptor chromophores of these proteins are open-chain tetrapyrroles coupled to the protein residues through thioether linkages. The phycobiliproteins (phycoerythrin, phycocyanin, and allophycocyanin in se-

quence) are arrayed *in vivo* in an antenna-like structure called the phycobilisome, each with a region of maximum and relatively narrow wavelength of absorption in the visible spectrum. Light energy is transferred by a Forster-type mechanism with over 90% efficiency.

Some of these proteins are used commercially as biochemical and biotechnological probes (9). Additional interest centers on the regulatory control of these proteins' synthesis, because these systems are an example of light-regulated transcription, in that the amounts and types of the specific phycobiliproteins present in the phycobilisome *in vivo* appear to be regulated at the transcriptional level by the spectral features of the available light energy (10).

Methods

Conducting Polymers Synthesis and Characterization. In recent years, conducting polymers have constituted a growing field of science and engineering. One such class of compounds are polymers that have aromatic rings as repeat constituent units. Polythiophene, polypyrrole, and their derivatives are included in this group. These polymers exhibit excellent thermal and temporal stability and may be produced in many chemically modified forms. Although the pristine materials are insoluble because of their stiff macromolecular chains with strong interchain interactions, the materials can be made soluble by attaching long alkyl chains as the side groups of these conducting polymers. Appropriate molecular design can also make them amenable for manipulation on the LB trough. The poly(3-alkylthiophenes) with long alkyl side groups are readily soluble in common organic solvents and can subsequently be processed into uniform mixed monolayer films from their solutions.

Poly(3-hexylthiophene) can be synthesized by dehydrogenation condensation of 3-hexylthiophene by using FeCl_3 in an appropriate medium such as chloroform solution (Figure 1). In a similar manner, other poly(3-alkylthiophene)s have been synthesized from the corresponding monomers. For poly(3-hexylthiophene) the reaction proceeds as follows (11). In a three-necked round-bottomed flask anhydrous FeCl_3 (4.866 g, 0.06 mol) was put under dry nitrogen atmosphere. The reaction vessel was then connected to a vacuum line and evacuated at 100 °C prior to the reaction. Dry nitrogen was then reintroduced into the reaction vessel and dry distilled chloroform (100 mL) was added into the flask under dry nitrogen flow. 3-Hexylthiophene (1.164 g, 0.02 mol) was added dropwise to the metal-halogenide solution under vigorous agitation with a magnetic stirrer. After all the thiophene monomer was added, the reaction mixture was stirred for another 2 days at room temperature to ensure the completion of the reaction. The solution turned blue im-

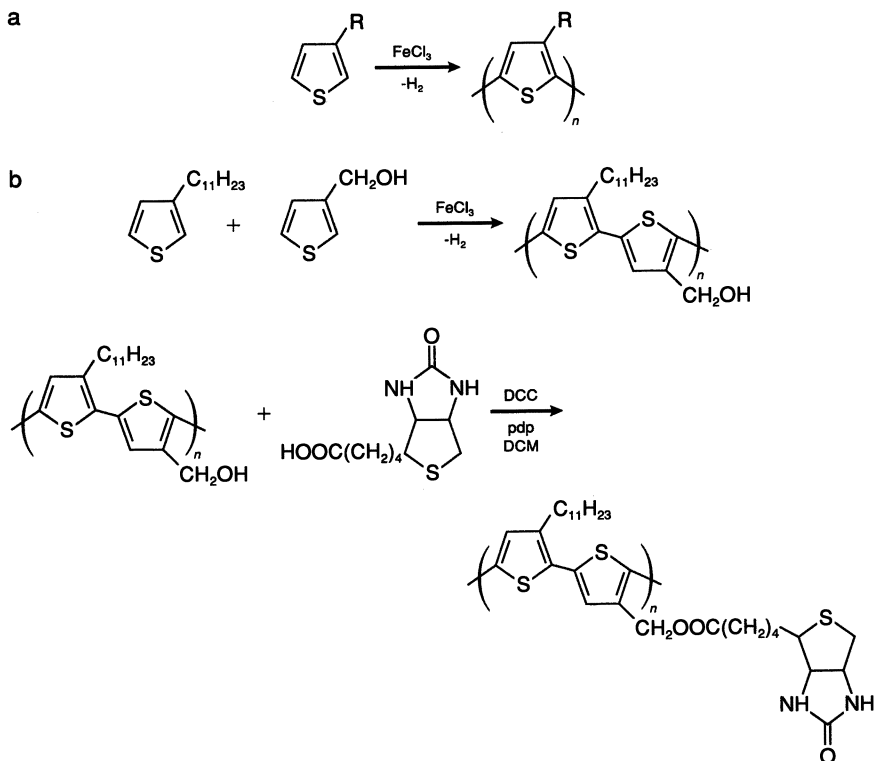


Figure 1. Synthetic schemes of (a) poly(3-alkylthiophene) and (b) B-PMUT.

mediately after addition of the thiophene monomer and took on a deeper color with time (oxidized form).

After completion of reaction, the reaction mixture was precipitated into methanol (500 mL). The resulting blue-black precipitate was collected by filtration. The precipitate turned dark red (neutral form) after being washed alternately with a large amount of methanol and water and was cleaned successively with methanol in a Soxhlet extractor for 20 h. It was further purified through reprecipitation into methanol (poor solvent) from an appropriate solution of good solvent such as 2-methyltetrahydrofuran.

Copolymers of 3-substituted thiophenes, such as poly(3-undecylthiophene-co-3-methanolthiophene) (PMUT), have been synthesized and subsequently biotinylated. Copolymer, PMUT, can be synthesized as follows. Synthetic grade anhydrous ferric chloride (Aldrich), 0.09 mol, was dried under vacuum at 100 °C prior to reaction. Then nitrogen was introduced along with 100 mL of dry chloroform (Aldrich). Next, 0.02 mol of 3-undecylthiophene (TCI America) and 0.01 mol of 3-metha-

nolthiophene (Aldrich) in 10 mL of chloroform was added dropwise with vigorous stirring. The reaction mixture was allowed to stir for 2 days until the reaction was complete. The reactant solution was precipitated into 500 mL methanol (Aldrich). The product was then purified with methanol in a Soxhlet extractor for 2 days.

Attachment of biotin to the PMUT copolymer, resulting in B-PMUT, can be accomplished by the following methods. A solution of 0.01 mol biotin (Biomed), 0.011 mol *N,N*-dicyclo-hexylcarbodiimide (Aldrich), 0.011 mol PMUT and 0.001 mol 4-pyrrolidinopyridine (Aldrich) in 50 mL dichloromethane (Aldrich) was stirred at room temperature until esterification was complete. The *N,N*-dicycloundecyl urea was filtered, and the filtrate was washed with water (3×50 mL), 5% acetic acid solution (3×50 mL), again with water (3×50 mL), dried (MgSO_4) and the solvent evaporated in a rotary evaporator under reduced pressure to give the biotinylated copolymer.

The UV-visible spectra of poly(3-hexylthiophene), PMUT, and B-PMUT thin film on a glass slide are shown in Figure 2.

An absorption maximum for poly(3-hexylthiophene) is located at 505 nm and two shoulders are noticeable around 550 and 600 nm. Both the copolymers showed an absorption maximum around 400 nm with absorption starting from 600 nm, indicating the presence of extended π -conjugation along the polymer backbone. B-PMUT exhibited a blue shift due to the breakage of π -conjugation by the introduction of biotin.

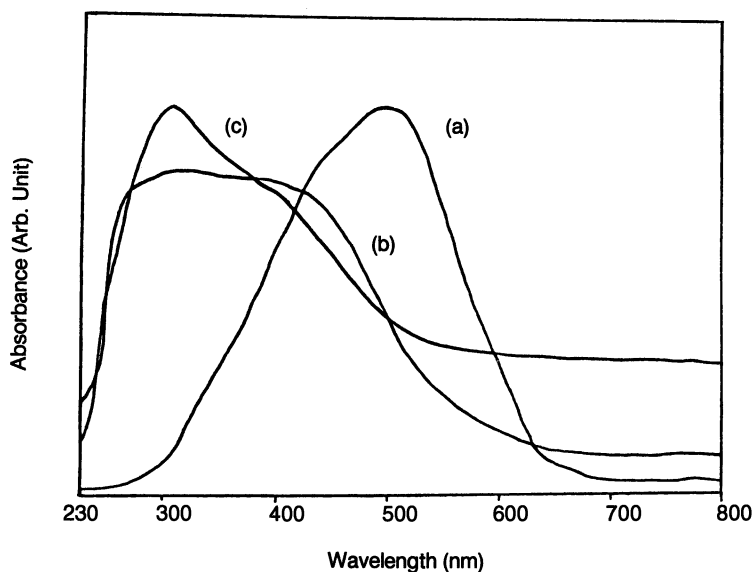


Figure 2. The UV-visible spectra of (a) poly(3-hexylthiophene), (b) PMUT, and (c) B-PMUT.

The Fourier-transform infrared (FTIR) spectrum of solution cast thin films of poly(3-hexylthiophene) showed a distinct peak around 845 cm^{-1} due to the C–H out-of-plane vibration of the 2,3,5-trisubstituted thiophene. FTIR measurements of both PMUT and B–PMUT showed a principal absorption peak at 780 cm^{-1} due to the C–H out-of-plane vibration of the 2,5-disubstituted thiophene, and a distinct peak around 810 cm^{-1} due to the C–H out-of-plane vibration of the 2,3,5-trisubstituted thiophene. B–PMUT exhibited new characteristic peaks at 1678 cm^{-1} due to the ester linkage, and a sharp peak at 3400 cm^{-1} from N–H stretching. Meanwhile, the broad O–H absorption peak at 3400 cm^{-1} shown in PMUT disappeared in B–PMUT (12).

The number average MW of poly(3-hexylthiophene) and B–PMUT were found to be 5×10^3 and 2.5×10^3 g/mol, respectively, through gel permeation chromatography.

3-Hexadecylpyrrole monomer was prepared at Brookhaven National Laboratory, and the synthetic procedure is described in an earlier publication (13).

LB Film Formation and Characterization. The biotinylated phospholipid, *N*-(biotinoyl)dipalmitoyl-*L*- α -phosphatidylethanolamine, triethylammonium salt, (B–DPPE), was purchased from Molecular Probes (Eugene, OR) and used as received. *L*- α -Dipalmitoyl phosphatidylethanolamine (DPPE) was purchased from Avanti Polar Lipids (Pelham, AL) and was used as received. The unconjugated phycoerythrin (PE), biotinylated phycoerythrin (B–PE), and avidin- and streptavidin-conjugated R-phycoerythrin proteins used in our work were purchased from Biomeda Corporation (Foster City, CA) or from Molecular Probes.

Monolayer studies were carried out on Lauda MGW Filmwaage troughs with a surface area of approximately 930 cm^2 . The subphase was composed of an aqueous solution of 0.1 mM sodium phosphate and 0.1 M NaCl, pH 6.8. In the case of pressure-area isotherms, the lipid and the polymer were spread from a 0.5 mM chloroform solution, and 0.1 mg of the protein in 5 mL of the buffered subphase was injected under the spread film and left to incubate for 2 h at $30\text{ }^\circ\text{C}$. Compression was then carried out at a speed of approximately $2\text{ mm}^2/\text{min}$, until collapse of the film was observed. For transfer studies, the lipid and the polymer were spread, followed by protein introduction and incubation in the expanded state for 2 h, and then were compressed to an annealing surface pressure of approximately 15 mN/m , for deposition. Monolayer films were then transferred onto glass solid supports for fluorescence spectroscopy.

Results

LB Trough. Our aim in this area is to create different lipid and polymer monolayers that are ordered and to provide a diverse array of

functional groups both to bind biological macromolecules (by biotin) in ordered arrays and subsequently to use the intelligent properties of the biological systems through signal-transduction mechanisms in the monolayer.

The LB technique has recently been used to prepare such oriented and spatially organized protein-molecular assemblies (3–6, 14). The LB technique is the method of choice because it allows direct manipulation of the molecular components that comprise the assembly. Furthermore, following monolayer formation, the ultrathin monolayer films may subsequently be transferred, a single monolayer at a time, for characterization and ultimately for device fabrication. In addition, judicious selection of the specific lipids incorporated in the monolayer should provide unique biomimetic environments to fully elicit the desired characteristics of the biological component. The initial approach involved the highly specific recognition of biotin on the LB trough subphase surface of biotinylated LB lipid monolayers by streptavidin-conjugated phycoerythrin (Str-PE) and avidin-conjugated phycoerythrin (Av-PE).

LB Trough Formation of Biotin Lipid-Str-PE Monolayers. The biotinylated lipid B-DPPE forms a well-behaved LB isotherm. This is shown in Figure 3 along with the isotherms of B-DPPE from three experiments, where the following proteins were injected into the trough subphase: PE, Str-PE, and Av-PE. In all cases the isotherms displayed a relatively steep slope after a pressure of 15 mN/M, which corresponds to an area per molecule of approximately 100 \AA^2 . However, the biotin binding Str-PE and Av-PE protein monolayers, but not the PE control, exhibited much different behavior in the expanded state. A significant increase in surface pressure was observed with these monolayers at larger areas per molecule. This behavior suggests that the conjugated protein systems are in some way incorporating themselves into the B-DPPE monolayer in the expanded state. As compression is continued, the protein-injected monolayers reach a stage where they actually overlap the pure B-DPPE isotherm. This behavior differs from that observed in a previous study where fluorescein-labeled streptavidin was injected under the subphase of a biotinylated lipid monolayer using somewhat similar preparative conditions, but a significantly higher subphase ionic strength and without any phosphate buffer (3).

In the present case the large isotherm shift with binding Str-PE and Av-PE may be rationalized by the bulkiness of these conjugates. Phycoerythrin by itself is known to be disc-shaped, having dimensions of approximately $60 \times 120 \text{ \AA}$ and a 240-kD MW (8). In the schematic presented in Figure 4, we indicate the effect of the large Str-PE conjugate on the expanded state pressure. When the Str-PE conjugates bind to biotin in the expanded state, a significantly greater pressure

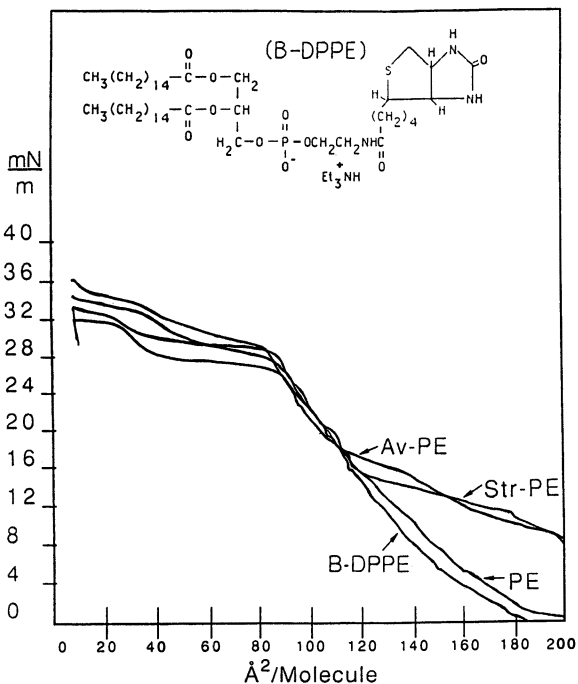


Figure 3. Structure of the biotinylated phospholipid (B-DPPE) and pressure-area isotherms of B-DPPE and B-DPPE with protein PE, Av-PE, and Str-PE injected into the subphase. (Reproduced with permission from reference 15. Copyright 1992.)

develops from protein-protein steric interactions than in the case of the small streptavidin (60 kD) by itself.

The overlapping of the isotherms for Str-PE and Av-PE with the others also fit this model because the bulky conjugates will swing down into the subphase to reorient as a monolayer as the barrier pressure is increased. The control experiment of PE protein only injected into the B-DPPE monolayer exhibits the same isotherm as B-DPPE, supporting the idea that biotin binding to the streptavidin and avidin binding sites are solely responsible for the monolayer isotherm film effects seen.

Formation of Polymer-Streptavidin-Biotinylated Protein Monolayers. We next demonstrated that the fluorescent PE protein could be attached to form a fluorescent monolayer film in a sequential fashion by using a modular or "cassette" approach, involving the streptavidin-biotinylated copolymer interaction. In this case, streptavidin is injected under the subphase of an expanded B-PMUT film. Then, in a subsequent step, biotinylated PE was injected under the film and allowed

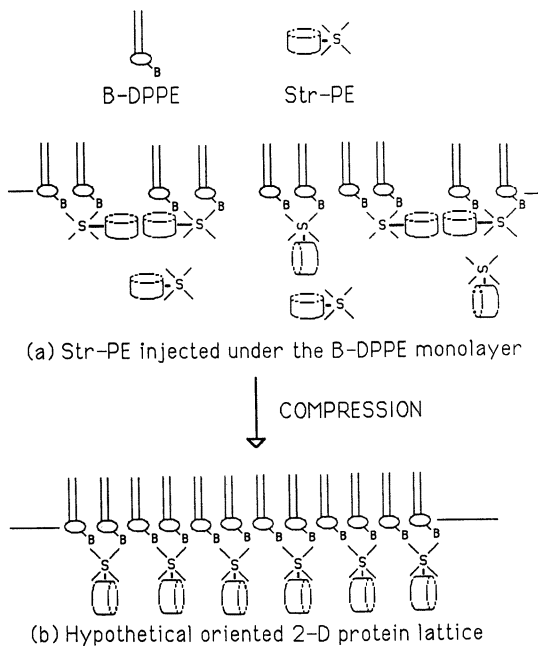


Figure 4. Idealized schematic of the binding and two-dimensional ordering of Streptavidin-derivatized protein monolayers onto a biotinylated lipid LB film. (Reproduced with permission from reference 15. Copyright 1992.)

to bind to the other available biotin binding sites on the bound streptavidin. The cassette approach is shown in schematic form in Figure 5. The isotherms for this sequence of experiments are displayed in Figure 6. Clearly, a different behavior is noted from our previous isotherm. In this case an increase in area throughout the entire compression cycle occurs not only in the expanded phase but also for the monolayer when B-PE was injected. This continuous expansion suggests that the streptavidin and B-PE are interacting with the monolayer film, but do not reorient upon compression in the same manner as the Str-PE system.

As already discussed, this difference may be due to the sizes of the protein systems interacting with the B-DPPE or B-PMUT. The relatively small streptavidin does not obviously create any significant pressure in the expanded state, as evidenced by its isotherm. However, the streptavidin followed by B-PE, a bulky system attached to the expanded film, does create a significant additional pressure noticeable in the isotherm. These results seem to compare well with the initial observations of Blankenburg et al. (3), and to suggest that the bulkiness of the protein initially interacting with the monolayer plays a significant role in the monolayer formation.

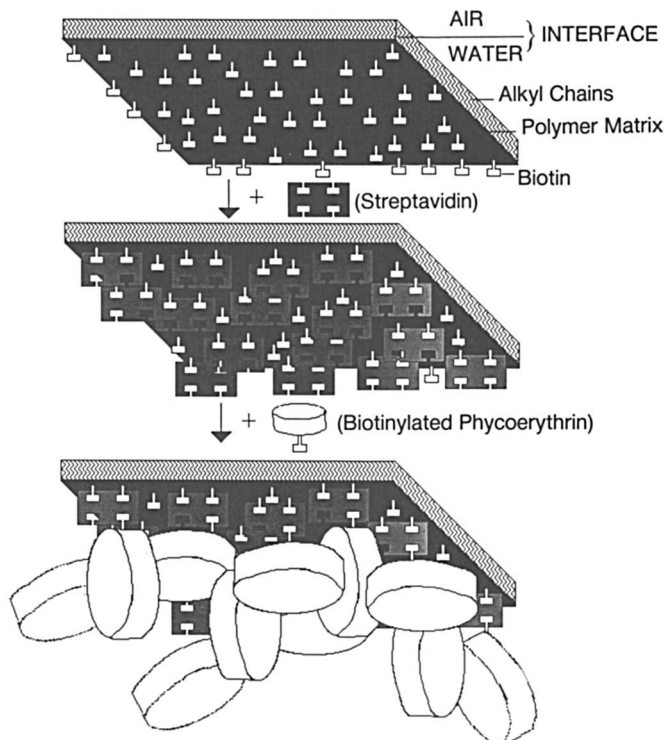


Figure 5. Schematic of the experimental sequence and hierarchical ordering of the protein on the subphase surface of the B-PMUT monolayer in the "cassette" approach.

Using the LB trough technique, we have shown that the mixed-monomer system of either substituted polyalkylthiophenes or polyalkylpyrroles and B-DPPE are capable of forming good monolayers as seen in their isotherms in Figure 7. Both B-DPPE and poly(hexadecylpyrrole) form good characteristic isotherms and their 1:1 mixture has an isotherm of intermediate character. Poly(octylthiophene) mixed with B-DPPE possesses a modified B-DPPE isotherm as shown in Figure 8. These film-forming abilities are important because our intention is to use the optical and electronic properties of the conducting polymers like alkylpolythiophenes, in signal transduction roles in the monolayers of systems such as those described previously. Bulk conductivity measurement of the poly(3-hexylthiophene) has been carried out by the four-point probe method and gives a value of 0.012 S/cm (16). LB films of these electroactive systems containing biomolecules have been successfully prepared, and the electrical measurements are currently under investigation.

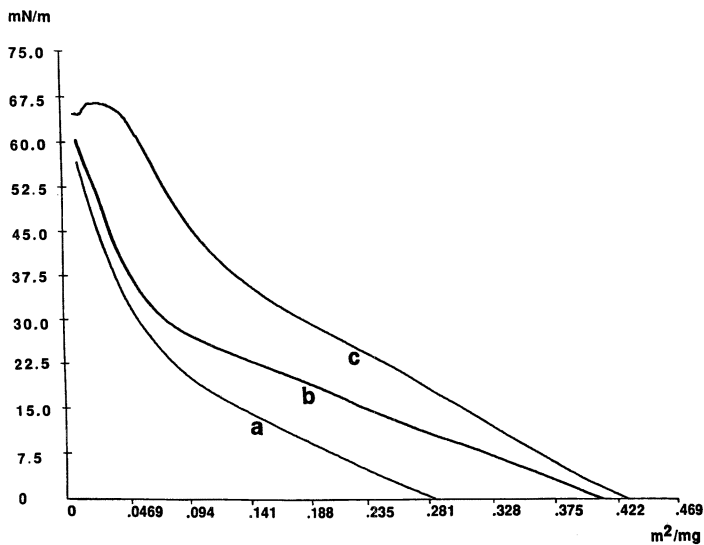


Figure 6. Pressure–area isotherms of (a) B–PMUT, (b) B–PMUT + streptavidin-injected, and (c) B–PMUT + streptavidin + B–PE injected, “cassette” system.

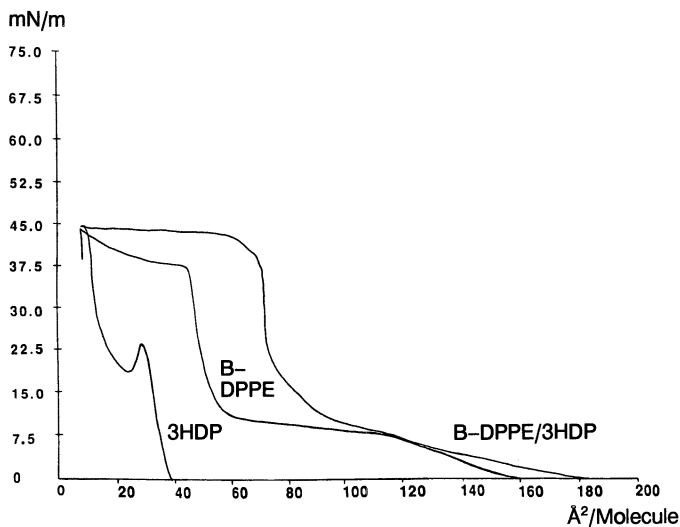


Figure 7. Pressure–area isotherms of B–DPPE, 3-hexadecylpyrrole and a 1:1 mixture of B–DPPE and 3-hexadecylpyrrole.

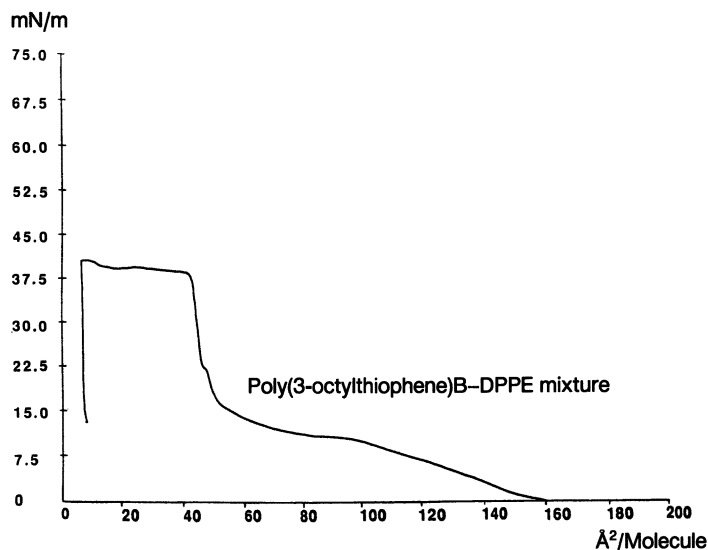


Figure 8. Pressure–area isotherm of a mixture of B-DPPE and poly(3-octylthiophene).

Fluorescence Spectroscopy. Following formation of the films, presented in the isotherms of Figures 3 and 6, we transferred the monolayer films for further characterization. For this transfer the film was compressed to an annealing surface pressure of approximately 15 mN/m. Monolayer films were then vertically transferred onto hydrophilic glass solid supports, with transfer ratios ranging from 100 to 150%. Vertical deposition results in transfer ratios ranging from 100 to 150% on the upstroke. This high value may be explained by possible disruption of this now very rigid film during transfer, which results in either a slight collapse of the film or reorganization of the molecules upon passage of the substrate through the film.

Transferred monolayer protein films were characterized by fluorescence spectroscopy. The measurement system is shown schematically in Figure 9. The pump light source was an argon ion laser, with 10-mW laser power. The excitation wavelength used for PE was 496.5 nm, which is close to the absorption peak of the native PE. The laser beam was collimated with a cylindrical lens and the illuminated area of the sample was imaged, with 1:1 ratio, onto the entrance slit of the monochromator. A 500- μm slit width of the monochromator provided a 6- \AA spectral resolution. Emission was scanned from 500 to 700 nm and the signal was detected with a photomultiplier tube (PMT) cooled to $-20\text{ }^{\circ}\text{C}$ and then sent to a photon counter with an integration time of 1 s. Background correction for the glass solid support was performed. The photon counter

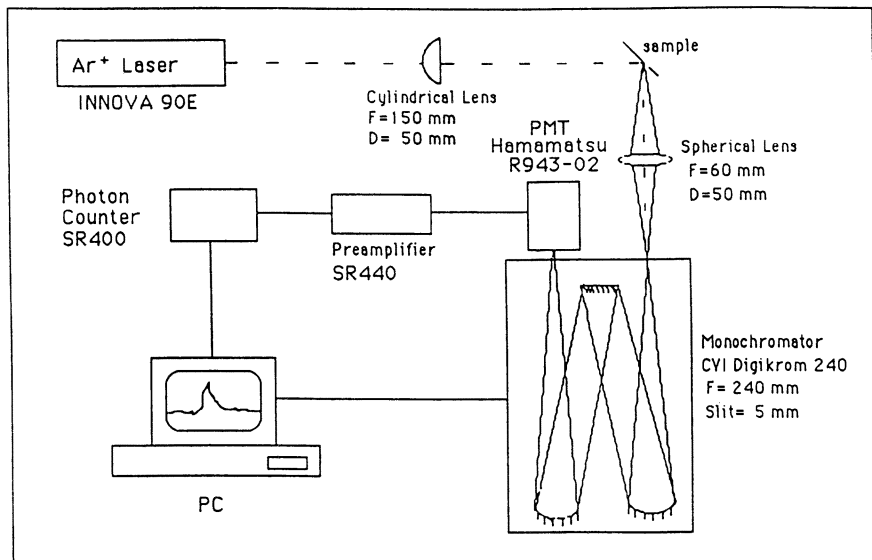


Figure 9. Schematic diagram of the fluorescence set-up. (Reproduced with permission from reference 17. Copyright 1992 Plenum.)

and monochromator were both interfaced to a personal computer. As the monochromator was scanned at 10-Å increments, the computer recorded the counts from the photon counter in the set range.

Because of the intense fluorescence signals from the high quantum efficiency multiple chromophores of the phycobiliproteins, fluorescence spectroscopy provides a very sensitive probe for the monolayer protein film samples. Figure 10 displays the emission spectra for the films described in the Figure 3 isotherms. The native emission spectra for PE can be seen in the Str-PE-injected sample, which is bound to B-DPPE. However, no native fluorescence can be seen for the PE-injected B-DPPE film, or when Str-PE was injected under a DPPE lipid film, which lacks the biotin functionality. These controls establish that the highly specific biotin-streptavidin interaction is responsible for the protein binding to films observed here.

In Figure 11 a similar result can be seen with Av-PE injected under the subphase, resulting in binding and a native PE-emission spectrum. Two further negative controls were performed, as shown, to support the conclusion that the biotin-streptavidin interaction is responsible for the binding of PE in these monolayer films. Furthermore, the visual fluorescence from these films was continuous at the light microscope level of resolution. These data are not shown, because the low-fluorescence intensity observation could not be photographically imaged.

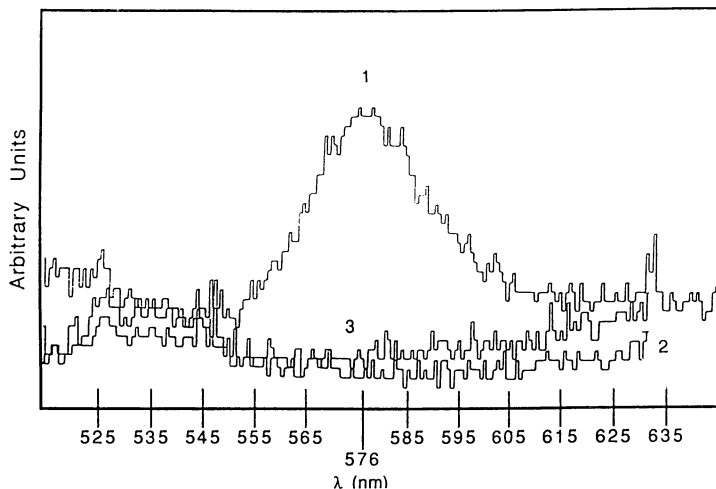


Figure 10. Fluorescence spectra of protein-adsorbed LB films. Subphase: 0.1 mM Na phosphate buffer, pH 6.8, and 0.1 M NaCl. 1. B-DPPE + Str-PE-injected, 2. B-DPPE + PE-injected (control) (2), and 3. DPPE + Str-PE-injected. (Reproduced with permission from reference 15. Copyright 1992.)

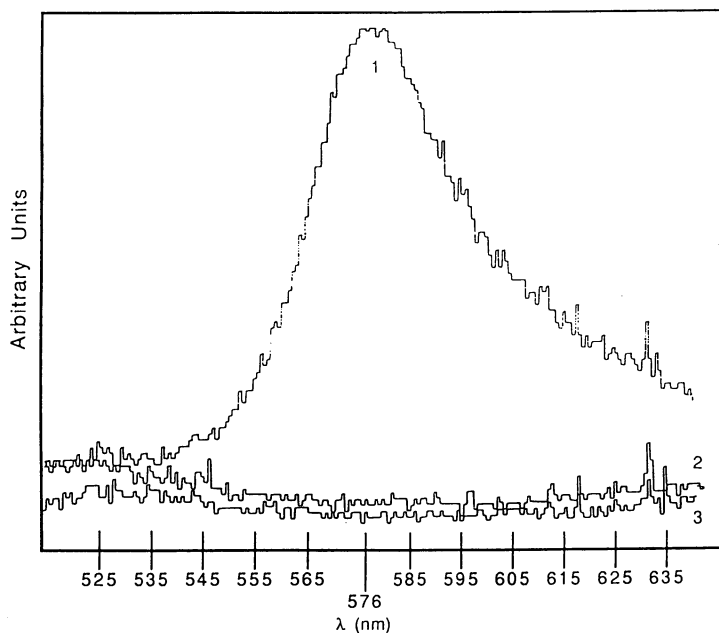


Figure 11. Fluorescence spectra of protein adsorbed LB films. Subphase: 0.1 mM Na phosphate buffer, pH 6.8, and 0.1 M NaCl. 1. B-DPPE + Av-PE-injected, 2. control (monolayer cleaned off the subphase) (2), and 3. control (slide down in subphase only).

Finally, in Figure 12 we demonstrate that monolayer films containing B-PMUT formed by the second LB method, using the cassette approach, also result in native PE emission spectra. These results argue that we are measuring a native protein chromophore environment for the tetrapyrrole moiety in PE. Thus, at least for this protein, the LB methodology yields an undistorted native structure bound to the LB monolayer. This may be an important point, because the significant advantage for the use of this technique in creating intelligent biomaterials would be its ability to stably incorporate labile biological components. This apparent stability may have to do with both the anchoring by biotin bound to its streptavidin binding site, as well as the potential for close protein packing known to occur for streptavidin in these monolayers (3).

Photoconductivity. Photocurrent from layered-photodynamic-protein systems with different chromophores may be used as a probe for sensing the incident radiation. Prior to measurements on multilayered structures, photoconductivity measurements were carried out on dried films of PE. About 20 μL of an aqueous solution of PE (concentration 1 mg/mL) was deposited on an interdigitated gold electrode and allowed to dry at room temperature. Contact was made to the electrode system through silver-plated copper wires attached with silver paint, and the photoconductivity as a function of direct current (dc) bias voltage was measured at a given laser-power level. The arrangement of the apparatus for these measurements is shown in Figure 13. The light source was

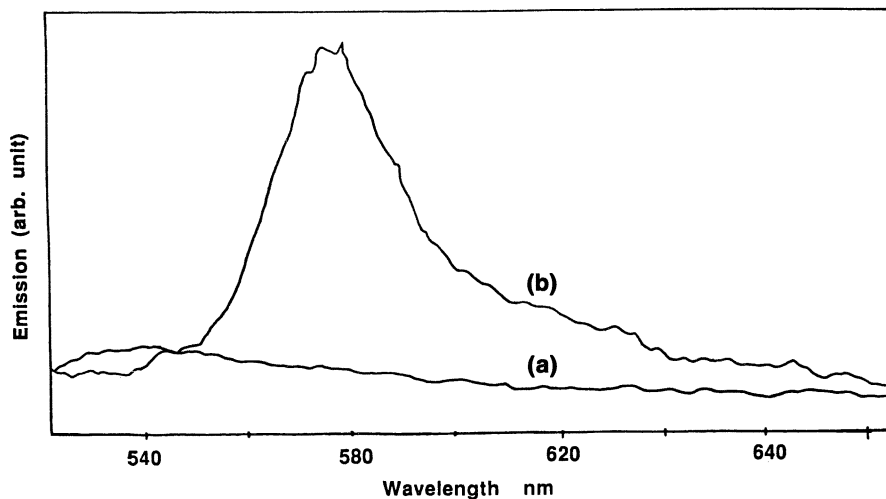


Figure 12. Fluorescence spectra of (a) B-PMUT (b) B-PMUT+.Str.+B-PE monolayers on glass substrates Subphase: 0.1 mM Na phosphate buffer, pH 6.8, and 0.1 M NaCl.

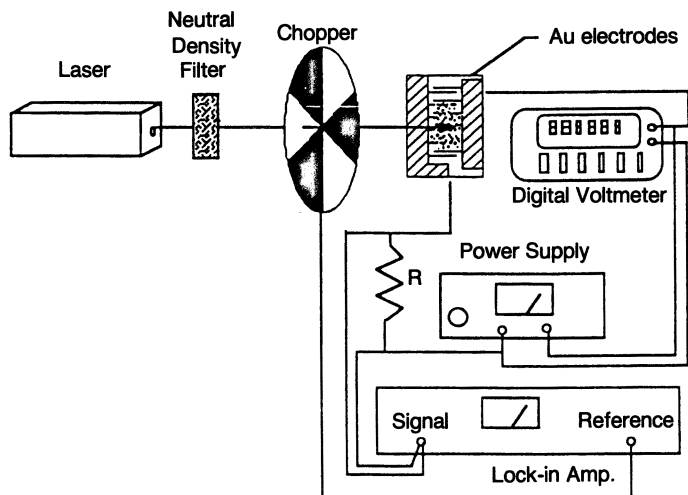


Figure 13. Schematic arrangement for the photoconductivity measurement experiment.

selected lines from an Ar⁺-ion laser (Coherent Innova 90), operating at a 10-mW level, further attenuated through a variable neutral density filter to the indicated value. The laser radiation was chopped, and the photocurrent was measured across a 1-M Ω resistor with a lock-in amplifier. The dc bias voltage was supplied by standard laboratory power supplies.

A typical measurement run at 496 nm is shown in Figure 14. The photocurrent saturates at higher bias voltages. The slight downward drop after saturation could be due to time-dependent effects, such as photodegradation of the protein, or polarization, and other electrochemical reactions at the electrodes, which would be both time- and voltage-dependent. The detailed conduction mechanism needs to be established, but involves charge generation at the chromophore, and transport assisted by the high external dc field applied (the interelectrode separation is only 15 mm, so the fields involved are quite large).

Measurements carried out on buffer sample blanks showed very small photocurrents, so that the photocurrent can be definitely assigned to the photodynamic protein system. Large amounts of electrolytes (as in buffers) interfere with the measurements, by forming solid layers on the electrodes and by creating excessive electrical noise, due to large electrolytic currents.

Discussion

Thin films of biologically derived materials have already been shown to possess interesting optical and electronic properties with potential future

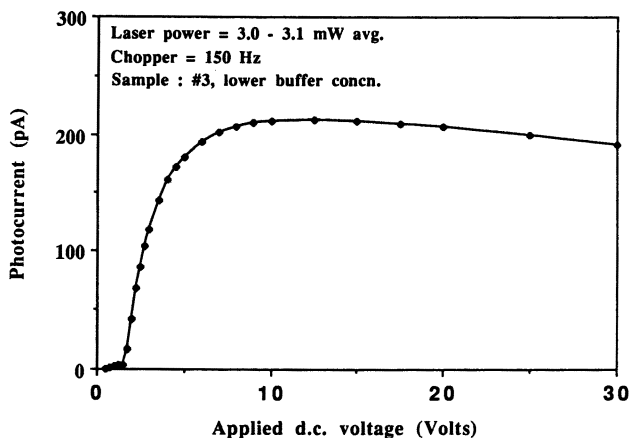


Figure 14. Photocurrent as a function of applied dc voltage in films of PE.

applications. LB assemblies of the kind described in this chapter further expand the role of biomaterials. Synthetic materials may be incorporated into the monolayers to tailor their properties for specific applications. Signal transduction in these materials may result in monitoring of fluorescence, chemiluminescence, photoconduction, absorption, or surface plasmon resonance signals.

Through combinations of photodynamic proteins, organized monolayers, and conducting polymers, a variety of materials and assemblies with intelligent properties can be designed and assembled. These systems would have the ability to respond in a highly specific fashion to optical and electronic inputs and to produce characteristic optical or electronic outputs. In addition, the systems should be stable, sensitive over a broad photodynamic range, and should provide opportunities to create conformal coatings. Most significantly, these approaches to assembling the individual components in the system are generic. Thus the cassette approach described allows for the incorporation of virtually any protein that can be derivatized with avidin, streptavidin, or biotin in virtually any hierarchical array desired based on the multiplicity of binding sites. Aside from the photodynamic proteins themselves, enzymes, antibodies, and nucleic acid probes could be incorporated into specific device designs based on the cassette technology and measurement methodologies described.

Acknowledgments

We acknowledge the support of Grant DAAL03-91-G-0064 from the Army Research Office.

References

1. Green, N. M. *Adv. Protein Chem.* **1975**, *29*, 85–95.
2. Wilchek, M.; Bayer, E. A. *Trends Biochem. Sci.* **1989**, *14*, 408–412.
3. Blankenburg, R.; Meller, P.; Ringsdorf, H.; Salesse, C. *Biochemistry* **1989**, *28*, 8214–8221.
4. Samuelson, L. A.; Miller, P.; Galotti, D.; Marx, K. A.; Kumar, J.; Tripathy, S. K.; Kaplan, D. L. *Proteins—Structure, Dynamics and Design*; Renugopalakrishnan, V.; Carey, P. R.; Smith, I. C. P.; Huang, S. G.; Storer, A. C., Eds.; ESCOM: Leiden, The Netherlands, 1991; 160–164.
5. Samuelson, L. A.; Miller, P. P.; Galotti, D.; Marx, K. A.; Kumar, J.; Tripathy, S. K.; Kaplan, D. L. *Langmuir* **1992**, *8*, 604.
6. Samuelson, L. A.; Yang, Y.; Marx, K. A.; Kumar, J.; Tripathy, S. K.; Kaplan, D. L. *Biomimetics* **1992**, *1*, 51.
7. Yang, X. Q.; Chen, J.; Hale, P. D.; Inagaki, T.; Skotheim, T. A.; Fischer, D. A.; Okamoto, Y.; Samuelson, L.; Tripathy, S.; Hong, K.; Watanabe, I.; Rubner, M. F. *Langmuir* **1989**, *5*, 1288.
8. Glazer, A. N. *Annu. Rev. Biophys. Biophys. Chem.* **1985**, *14*, 47–77.
9. Ol, V. T.; Glazer, A. N.; Stryer, L. *J. Cell Biol.* **1982**, *93*, 981–986.
10. Federspiel, N. A.; Grossman, A. R. *J. Bacteriol.* **1990**, *172*, 4072–4081.
11. Hotta, S.; Soga, M.; Sonoda, N. *Synth. Met.* **1988**, *26*, 267.
12. Hotta, S.; Shimotsuma, W.; Taketani, M.; Kohiki, S. *Synth. Met.* **1985**, *11*, 139.
13. Inagaki, T.; Yang, X. Q.; Skothen, T. A.; Okamoto, Y. *Synth. Met.* **1989**, *28*, C245.
14. Haas, H.; Mohwald, H. *Thin Solid Films* **1989**, *180*, 101.
15. Samuelson, L.; Miller, P.; Galotti, D.; Marx, K. A.; Kumar, J.; Tripathy, S.; Kaplan, D. *Thin Solid Films*, **1992**, *210/211*, 796.
16. Streetman, B. G. *Solid State Electronic Devices*, 2nd ed.; Prentice-Hall: Englewood Cliffs, NJ, 1980; p 352.
17. Samuelson, L. A.; Yang, Y.; Marx, K. A.; Kumar, J.; Tripathy, S. K.; Kaplan, D. L. *Biomimetics* **1992**, *1(1)*, 51.

RECEIVED for review March 12, 1992. ACCEPTED revised manuscript March 12, 1993.

Colloid Chemical Approach to Band-Gap Engineering and Quantum-Tailored Devices

Janos H. Fendler

Department of Chemistry, Syracuse University, Syracuse, NY 13244-4100

Silver-magnetic and semiconductor particulate films have been generated in situ at monolayer- and bilayer-lipid-membrane interfaces. The chemical method of preparation involved the attachment of one of the precursors to the membrane and the infusion of the other precursor across the membrane from the opposite side. Silver particulate films have also been generated by the electrochemical reduction of silver ions at monolayer interfaces. Evolution of the particulate film involved the initial formation of well-separated, 20–30-Å diameter and 5–6-Å high nanoclusters that grew in height to longer and more densely packed conical particles, which ultimately formed the interconnected arrays of the porous particulate film. Preparation, characterization, and potential applications of these systems are discussed.

RECENT ADVANCES IN MOLECULAR-BEAM EPITAXY have permitted the atom-by-atom generation of heterostructures. Such band-gap engineering has led to the formation of quantum-confined semiconductor particulates and particulate films that have enormous potential applications in memory storage and optical switching devices. This type of molecular-beam epitaxy requires ultrahigh-vacuum technologies, ultrapure facilities, and unique and expensive instrumentation. The approach has been limited to very few selected semiconductors, predominantly involving the GaAs–AlAs system. Furthermore, the approach primarily involved physicists. Realizing the opportunities of semiconductors we initiated a colloid- and surface-chemical approach to advanced materials in our laboratories. The approach was inspired by the organizational capability of the biological membrane, and the approach utilized monomolecular-

0065-2393/94/0240-0413\$09.08/0
© 1994 American Chemical Society

and bimolecular-layer surfactants as active matrices for the generation of metallic, magnetic, and semiconductor particulate films. The relative ease of preparation has permitted the detailed characterization of this system, both in situ and ex situ. Our initial results on the generation, characterization, and utilization of silver, magnetic, and semiconductor particulate films are discussed in this chapter.

Generation of Metallic, Magnetic, and Semiconductor Particulate Films at Bilayer Lipid Membranes

Bimolecular, thick, bilayer or black lipid membranes (BLMs) provide the thinnest human-made semipermeable barrier that separates two compartments containing aqueous solutions (1, 2). Advantage has been taken of BLMs to model the functioning of the biological membrane by incorporating synthetic and natural ion carriers (3, 4). Sensitive electrical measurements, voltage clamping, and single-channel recording have formed the bases of our current understanding of biological-transport mechanisms (4, 5). BLMs have been used in our laboratories as matrices for the in situ generation of metallic (6), magnetic (7), and semiconducting particulate films (8–11). BLMs were made by “painting” the BLM-forming solution across a 0.80-mm-diameter Teflon hole separating two compartments that contained 0.10 M aqueous KCl. Thinning of the films to 50 ± 5 -Å-thick BLMs was monitored by observation of the reflected light and by capacitance measurements (9).

Silver particles were prepared in situ from AgNO_3 on BLM surfaces (6). Aqueous AgNO_3 was injected into one side of the BLM and was thoroughly stirred. Silver ions, attracted to the BLM surface, were reduced either by photolysis (illuminating one side of the BLM) or by the addition of 5 μL of 50% aqueous hydrazine to the opposite side of the BLM. A few seconds after the hydrazine injection, small greenish-yellow dots became visible, through the microscope, on the BLM surface. With time, these dots grew in number and size. Merging of the islands resulted in the appearance of a nonuniform silver film. No continuous smooth silver mirror could be formed on the BLM surface. Some control of silver deposition could be accomplished by the prompt exchange of the aqueous solution surrounding the BLM. This also resulted in the removal of all excess ions and particles that were not attached to the BLM.

Preformed, positively stabilized, ultrasmall (70-Å mean diameter) magnetic particles could be attached to the negatively charged BLM surface (6). Semiconductor particulate films were formed on the BLM by introducing freshly prepared stock solutions (0.10 M) of CdCl_2 , ZnCl_2 , CuCl_2 , or InCl_3 (typically 10–15 μL) to the cis side of the BLM (containing 1.0 mL solution of buffered KCl). Subsequent to 10- to 15-min incubation, H_2S gas (20–25 μL) was injected into the trans side of

the BLM. Sizes of microcrystalline semiconductors formed on the cis side of the BLM depended on the rate and amount of H₂S injection.

Generation of Metallic and Semiconductor Particulate Films at Monolayers

Chemical Generation. Semiconductor particles were generated in situ at the monolayer headgroup–aqueous subphase interface (12–20). An aqueous metal-ion solution (1.0×10^{-3} M CdCl₂, ZnCl₂, or CuSO₄) constituted the subphase. Either a commercial Lauda model P Langmuir film balance or a simple circular trough was used for monolayer formation and the subsequent generation of semiconductor particles (15). The Lauda film balance was enclosed in a Plexiglass hood and placed on a Micro-g optical-isolation table. The water surface was cleaned several times by sweeping with a Teflon barrier prior to monolayer formation. The subphase was deemed to be clean when the surface-pressure increase was less than 0.2 dyn/cm upon compression to one-twentieth of the original area and when this surface-pressure increase remained the same subsequent to aging for several hours. An appropriate amount of chloroform solution of the chosen surfactant (8×10^{17} molecules per mL) was carefully injected onto the clean, thermostated (25.0 °C), aqueous surface. The surfactants were compressed at a rate of $2\text{--}5 \times 10^{-3}$ Å² per molecule per second. Subsequent to 5–15 min of incubation at the desired surface pressure [25 mN/m for arachidic acid (AA) and 50 mN/m for bovine-brain phosphatidylserine (PS)], dioctadecyldimethylammonium bromide (DODAB), *n*-hexadecyl-11-(vinylbenzamide)undecyl hydrogen phosphate (1), and bis(2-*n*-hexadecanoyloxyethyl)methyl(*p*-vinylbenzyl)ammonium chloride (2)], 200–250 μL H₂S was slowly injected into the nitrogen-filled Plexiglass hood covering the film balance. The semiconductor particulates were transferred onto solid support where their composition and crystal structure were determined by X-ray and electron-diffraction measurements (16).

The schematics of the circular, 4.0 cm deep, Pyrex trough (7.0 cm² surface area) used for in situ semiconductor particle generation are shown in Figure 1 (15). The trough was placed on a clean (chromic acid and copious amounts of water) flat glass plate and covered by a circular (7.5-cm high and 14.5-cm diameter) glass jar whose flat frosted bottom provided a gas-tight contact. The water surface was cleaned by sweeping it through a water aspirator. An appropriate amount of the spreading solution (1.5×10^{-3} M surfactant in CHCl₃) was carefully injected onto the clean subphase to give a coverage of 20 Å² per molecule of AA and 40 Å² per molecule of PS, DODAB, 1 and 2. Subsequent to 20 min of incubation, a Hamilton syringe containing 200–500-μL H₂S was intro-

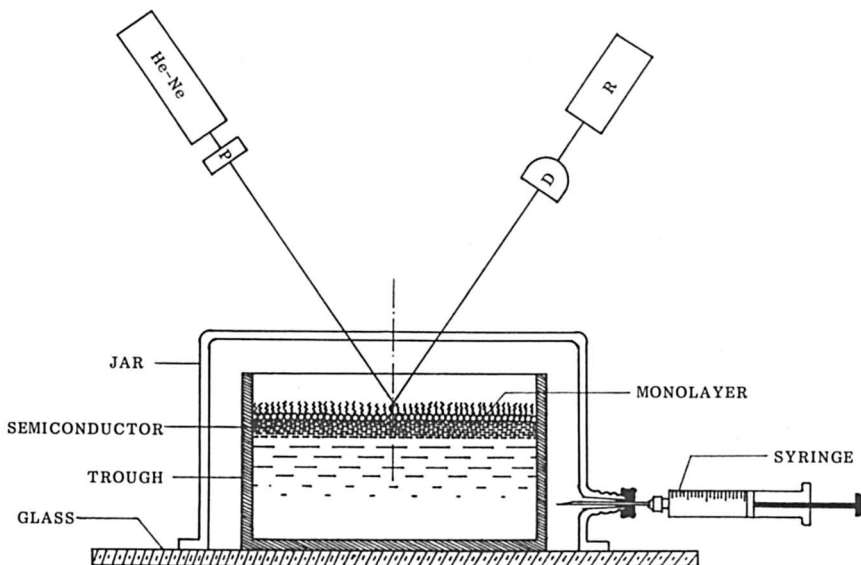


Figure 1. Schematics of the experimental arrangements (not drawn to scale) used for the generation of semiconductor particles at the negatively charged, surfactant headgroup–aqueous (1.0×10^{-3} M MCl_2) subphase interface and that used for the *in situ* monitoring of reflectivities. P is polarizer, D is detector, and R is chart recorder.

duced into the atmosphere covering the monolayer via a rubber septum (Figure 1). The barrel of the syringe was kept at the same position. This ensured the extremely slow (several hours) diffusion of H_2S into the chamber and, hence, into the monolayer–water interface. Formation of semiconductor particulate films formed were transferred onto solid substrates by horizontal lifting for subsequent characterization (16).

Silver particles were formed analogously at negatively charged monolayers floating on aqueous $AgNO_3$ upon exposure to formaldehyde (see Figure 2) (21).

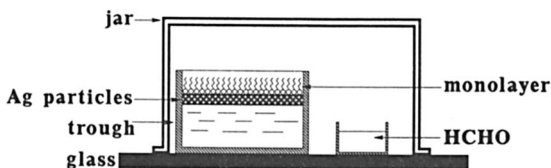


Figure 2. Schematics (not drawn to scale) illustrating the chemical generation of silver particles.

Electrochemical Generation. Electrochemical reduction of silver ions at the interfaces of monolayers prepared from positively charged surfactants resulted in the two-dimensional (2D) formation of uniform films that consisted of interconnecting, roughened silver particles (22). The schematics of the experimental setup are shown in Figure 3. A 1.0-mm diameter, 3-cm-long silver electrode was immersed into the sub-phase. Electrical connection was made through a 20- μm -diameter platinum electrode that was floated (subsequent to monolayer formation) on the water surface at the middle of the trough. The surface of the aqueous 1.0×10^{-3} M AgNO_3 solution was cleaned with a water aspirator just prior to monolayer spreading. An appropriate amount of the spreading solution (1.0×10^{-3} M surfactant in CHCl_3) was carefully injected into the cleaned aqueous surface to form 20 \AA^2 molecular monolayers from negatively charged surfactants. Ten to 20 min subsequent to monolayer formation, a potential of 1.8–1.9 V was applied across the electrodes (keeping Pt to be negative) by means of a direct current (dc) power supply.

The silver-particulate films formed at the surfactant–water interface were transferred to solid substrates by horizontal lifting (22). With time, silver particles grew concentrically, forming larger and larger circles at the monolayer–water interface. The rate of this 2D growth was 1–2 cm^2/h . Importantly, no silver particles could be observed upon applying the same potential to the water surface in the absence of surfactants or to monolayers prepared from positively charged surfactants. Negatively charged monolayers are essential for the electrochemical generation of silver particles. These monolayers provide binding sites for silver ions that are reduced at the cathodic surface. The initially formed silver particles extend the cathode and continue to reduce silver counterions at the monolayer surface. The absorption spectrum of silver particles on quartz is unique in that it shows an interband transition at 321 nm, in addition to an absorption maximum at 387 nm (Figure 4). Interband transitions characteristically appear in the reflection spectrum of rough surfaces (23–25).

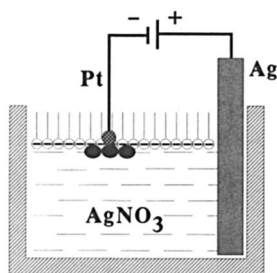


Figure 3. Schematics of the circular trough (not drawn to scale) used for the electrochemical generation of silver particulate films at monolayer interfaces.

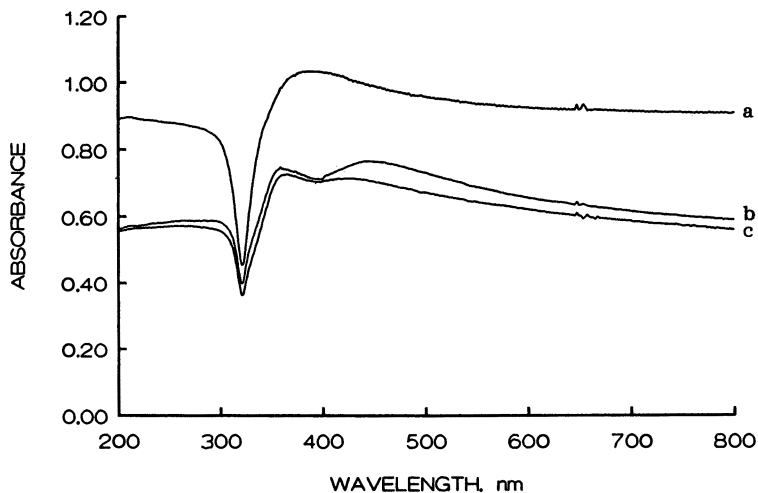


Figure 4. Absorption spectrum of a silver particulate film prior, *a*, and subsequent to 5 min, *b* and 15 min, *c* annealing at 300 °C. The silver-particulate film was formed electrochemically at the interface of a monolayer prepared from a dialkyl-polymerizable phosphate surfactant. The subphase contained 1.0×10^{-3} M AgNO_3 .

Characterization of Particulate Films

Growth of particles at BLM and monolayer surfaces was monitored by reflectivity measurements (15). A typical behavior of the reflected-light intensity as a function of Fe_3O_4 particle deposition onto the glyceryl monooleate (GMO)-BLM is illustrated in Figure 5 (7). The perpendicularly polarized 6328-Å laser line was allowed to impinge upon the middle of the cis side of the BLM at an incident angle of 45° during the introduction of the magnetic Fe_3O_4 particles into the trans side of the bathing solution. Point A in Figure 5 represents the introduction of ca. 0.5 mL of 4.0×10^{-3} M solution of stabilized Fe_3O_4 into the bottom of the BLM bathing solution by a Teflon syringe. Parallel with the development of a brown color in the bathing solution, a thin gray layer appeared on the BLM. With time, the intensity of the reflected light increased exponentially to a plateau value. At this point (point B in Figure 5), the aqueous bathing solution, surrounding both sides of the BLM, was carefully exchanged with dust-free pure water by pumping. Water exchange continued until no measurable absorbance ($A < 10^{-4}$ at 300 nm in a 1.00-cm cell) was detected in the bathing solution. Subsequent to this water exchange, all of the colloidal Fe_3O_4 particles remained firmly attached to the very much stabilized BLM, where they formed a particulate thin film. This particulate thin magnetic film could not be pulled away from the BLM by a magnet even as strong as 400 Oersted.

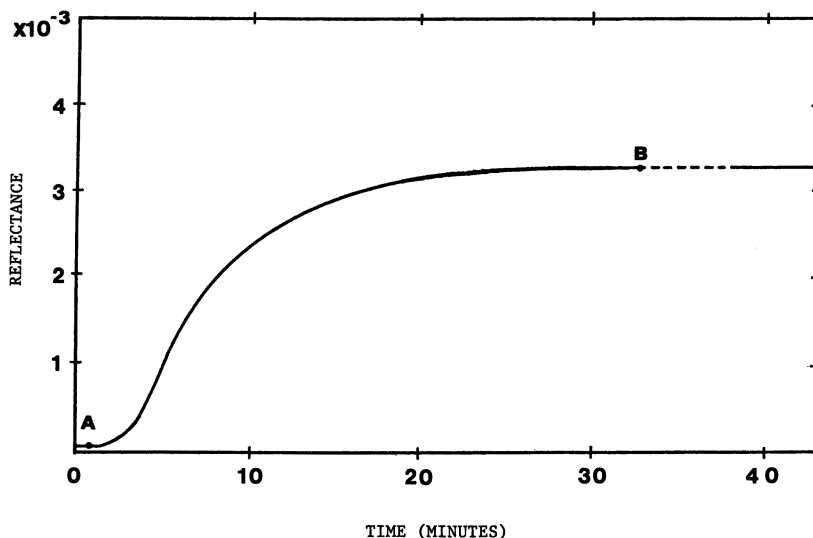


Figure 5. Intensity of the light reflected from the middle of the cis side of a GMO BLM as a function of time prior and subsequent to the deposition of Fe_3O_4 particles into the trans side. The perpendicularly polarized 6328-Å laser line was allowed to impinge upon the cis side at a 45° incident angle. Point A represents the introduction of the magnetic particles. Point B represents the interchange of the solution bathing the BLM.

Apparently, strong forces maintain the magnetic particles in the matrix of the BLM. These Fe_3O_4 -particle-coated BLMs remained stable for several days. The steady value obtained for the reflected-light intensity was found to be independent of the concentration of the Fe_3O_4 particles injected but depended somewhat on their deposition rate. Similar results were obtained on introducing the ferromagnetic particles into both sides of the BLMs.

Reflectivity and capacitance measurements have provided the basis for constructing a model for the GMO-BLM-deposited thin particulate magnetic film (7). Prior to the deposition of magnetic particles, the optical thickness of the GMO-BLM, d_b , was determined to be 62 ± 2 Å. This value is the sum of the thicknesses of the hydrocarbon bilayer ($d_h = 48$ Å), and the polar headgroups ($d_p = 6-8$ Å) and agree well with that reported in the literature (26).

Capacitances measured across the GMO-BLM were found to change less than 1% during the entire course of formation of thin Fe_3O_4 films. This small percentage of change is interpreted to imply that the magnetic particulate thin film does not penetrate beyond the headgroup region into the BLM. The density of the magnetic particles per unit area in the GMO-BLM was assessed, therefore, by the effective medium theory,

fruitfully employed previously in treating island films and other composite structures (27). A model of the thin magnetic Fe_3O_4 film on the GMO-BLM, and the parameters used in the films assessment are shown in Figure 6. The calculated diameter of the magnetic particle on the BLM is smaller than that measured for the isolated particles, but it agrees well with that determined by transmission electron microscopy for a similarly deposited particulate Fe_3O_4 layer on a phospholipid monolayer ($59 \pm 2 \text{ \AA}$) (28).

Introduction of the magnetic particles into the bathing solution results in their attraction to the surface of the GMO-BLM. This attraction is strong enough to overcome electrostatic repulsions between neighboring particles, and it permits the coverage of the BLM to the extent that it is tantamount to the formation of a monolayer of particulate film. Figure 7 represents the artist's impression of such an Fe_3O_4 particulate film. Electrostatic forces provide a long-term stability. The integrity of the individual, tightly packed particles remain intact for extended periods on the BLM. The observed optical data are not compatible with the presence of a smooth-surfaced, solid-state thin film (29). Conversely, the data are compatible with rough surfaces (30). Once the BLM is coated by a monoparticulate layer of magnetite, the forces of the membrane are insufficient to allow the deposition of a second layer of Fe_3O_4 particles.

Reflectivity and Brewster-angle microscopy (31, 32) provide the most convenient methods for characterizing semiconductor particulate films

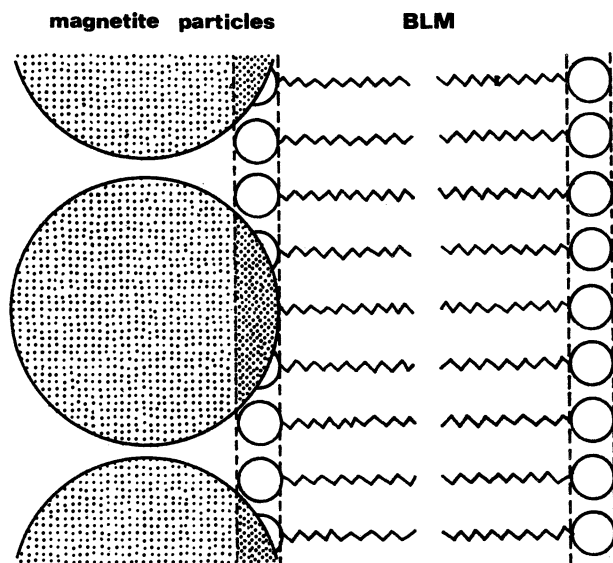


Figure 6. Schematics of the particulate thin Fe_3O_4 film on one side of the GMO-BLM.

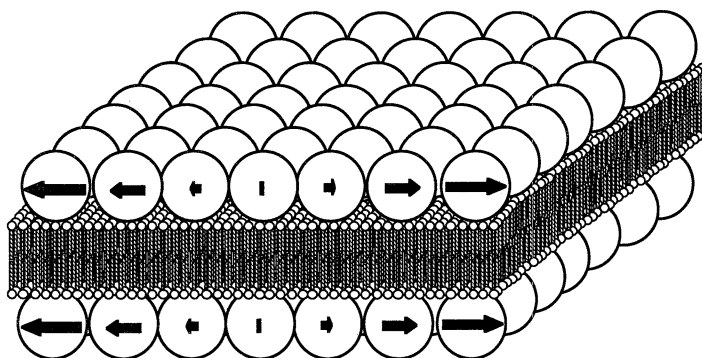


Figure 7. Artist's rendering of the GMO-BLM coated on both sides by monoparticulate Fe_3O_4 thin films. The arrows represent magnetization vectors in a section of the assumed 400-Å Néel wall and indicate the in-plane rotation. The transmembrane wall-to-wall interaction is purely speculative.

both at monolayer interfaces and in the solid state. The effective refraction indices, n_s , and volume fractions, F , of arachidate-monolayer-supported semiconductor particulate films are collected in Table I.

The semiconductor particulate films subsequent to their transfer onto substrates can be characterized by a myriad of different techniques. Absorption spectroscopy has proven to be the most convenient method for estimating the sizes of the semiconductor particles in semiconductor particulate films (16). Typical absorption spectra of in situ-generated semiconductor particulate films at different stages of their growth are shown in Figure 8.

The absorption spectra of semiconductor particulate films thicker than 30–40 Å showed long tails near their absorption edges. These long tails could be due to defect states, indirect transitions, and particle size

Table I. Effective Refractive Indices and Volume Fractions of Semiconductor Particulate Films at Monolayers and on Solid Supports

	<i>Monolayer-Supported</i>		<i>Solid-Supported</i>		<i>Bulk Semiconductor</i> n_b
	n_s	F (%)	n'_s	F' (%)	
CdS	2.14	75.5	2.25	79.5	2.50
ZnS	1.84	55.4	1.88	58.3	2.37

NOTES: n_s is the effective refractive index of the monolayer-supported semiconductor-particulate film; n'_s is the effective refractive index of the substrate-supported semiconductor-particulate film; F , is the volume fraction of the monolayer-supported semiconductor-particulate film; and F' is the volume fraction of the substrate-supported semiconductor-particulate film.

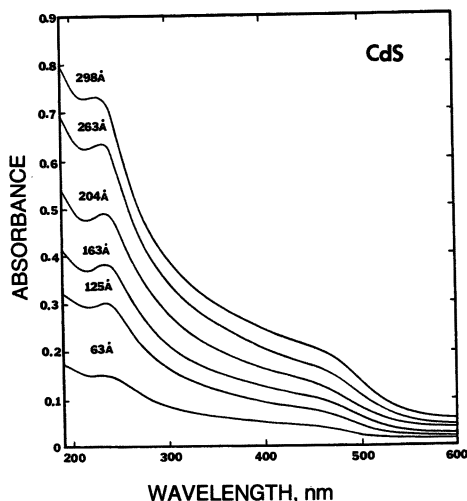


Figure 8. Absorption spectra of 8, 35, 218, 298, and 328 Å thick (indicated on the curves) CdS-particulate films on quartz supports. The arrow indicates the absorption spectrum of a 328 Å thick, quartz-supported CdS-particulate film after it was heated at 400 °C for 20 min. Particulate films were prepared by the infusion of H₂S onto a cadmium-arachidate monolayer.

distribution. Theoretical calculations for semiconductor crystallites established that the square-of-absorption coefficients times energy, $(\sigma h\omega)^2$, increases gradually above the band gap (E_0 transition) with increasing energy (33). This increase can be approximated by

$$(\sigma h\omega)^2 = (h\omega - E_g)c \quad (1)$$

where $h\omega$ is the photon energy, E_g is the direct band gap, and c is a constant. Reflectivity measurements provided values for the thickness (d_s') of the semiconductor particulate films, which permitted the calculation of σ ($\sigma = A/d_s'$, where A is the measured absorbance) and, upon substitution into equation 1, led to the plot of $(\sigma h\omega)^2$ against $h\omega$. Thus, absorption spectra provided band-gap values for semiconductor particulate films.

Evolution of semiconductor particulate films from their earliest stages of growth can be convincingly seen in scanning tunneling microscopic (STM) images (12). The initially formed (typically 2–6 min of H₂S exposure), well-separated, 20–30-Å diameter, and 5–6-Å-high nanoclusters grew quickly in height to longer and more densely packed, conical particles. Longer exposure (>20 min) to H₂S resulted in increased lateral growth of the nanocrystallites and their clumping into intercon-

nected arrays. Quite often, individual nanocrystallites of chained or disk-shaped semiconductor particulate assemblies are visible in the STM images. Large clusters were also demonstrated to be composed of much smaller (15–40-Å diameter) nanoparticles by STM. Prolonged exposure (>30 min) ultimately lead to the formation of a “first layer” of particulate semiconductor film. Inspection of STM images at this stage revealed the presence of 30–40-Å thick, 30–80-Å diameter, disk-shaped semiconductor particles.

Transmission electron microscopy has been used to confirm the sizes and size distributions of semiconductor particulate films. Electrical and photoelectrical measurements were carried out on semiconductor particulate films deposited on glass substrates or on Teflon sheets. The resistivity (ρ) of a semiconductor particulate film, measured between two parallel copper electrodes, is given by

$$\rho = R \frac{Ld_s'}{a} \quad (2)$$

where R is the measured resistivity in Ω , L is the length of the copper electrodes, a is the distance between them, and d_s' is the thickness of the semiconductor particulate film. For example, resistivities of 200–300-Å thick, CdS particulate films were $3\text{--}6 \times 10^7 \Omega \text{ cm}$. This range represents measurements of 10 samples of different thicknesses and is caused partly by the presence of different amounts of water in the films. The ρ values determined for CdS particulate films are some six orders of magnitude higher than those observed for materials having intrinsic conductivity.

The dark resistance of CdS particulate films decreases with increasing temperature exponentially. Illumination decreased the resistivity (i.e., increased the conductivity) of CdS particulate films by some two orders of magnitude and matched the absorption spectrum of the corresponding CdS particulate film nicely. Photoconductivity originates, therefore, in the production of conduction-band electrons, e_{CB}^- , and valence-band holes, h_{VB}^+ , in band-gap irradiation of CdS:



Electrochemistry and photoelectrochemistry on semiconductor particulate films have also been carried out at nanometer resolution by STM. The structures of semiconductor particulate films have been elucidated by X-ray and electron diffractometry.

Demonstration of size quantization in semiconductor particulate films is the most significant result of our work. Confinement of the elec-

tron and the hole in a particle that is smaller than the exciton diameter (i.e., the DeBroglie wavelength) of the bulk semiconductor results in the quantization of the energy levels (33–38). This behavior is in contrast to a bulk semiconductor in which the conduction bands constitute virtual continua. The length of the exciton diameter depends on the extent of electron delocalization and on the effective mass of the charge carrier. In the crystal lattice of semiconductors (e.g., CdS, ZnS, and GaAs), the effective mass of the charge carrier is substantially smaller than that in free space and, hence, the exciton diameter can be quite long (e.g., 60–80 Å for CdS) (38). Consequently, size quantization becomes observable in CdS particles whose diameters are equal to or smaller than 60–80 Å. It manifests in the transformation of the continuous bands of the bulk semiconductor into a series of discrete-energy levels and in the shifting of the lowest allowed absorptions to higher energy.

Electronic Behavior of Particulate Films

Electron Transfer (ET) and Junctions. In the absence of additives or adventitious impurities, the BLM is an electrical insulator. Current flow, on the order of only 10^{-9} A, was detected in the range of -0.10 to $+0.10$ V (Figure 9a). The determined resistance and capacitance of a 1.00-mm diameter GMO-BLM bathed in 0.10 M KCl, $3-5 \times 10^8 \Omega$ and 2.0–2.2 nF, agreed well with those reported previously ($3 \times 10^8 \Omega$, $0.380 \mu\text{F}/\text{mm}^2$) (9, 39). In situ semiconductor formation on the BLM surface resulted in marked changes in the electrical response. Depending on the system, the current flow was found to increase asymmetrically and the BLM became very much more stable and longer lived. ET across biological membranes and their artificial analogs have been rationalized in terms of three different mechanisms (40). The first model is the electronic conductance by direct electron tunneling. In the second model, ET is considered to occur by electron hopping via impurity states. This is sometimes referred to as resonance tunneling. It is assumed in the third model that charge is carried by chemical species (i.e., the conductance is electrolytic).

Three different systems have been investigated (Figure 10). A single composition of particulate semiconductor deposited only on one side of the BLM constituted system A. Two different compositions of particulate semiconductors sequentially deposited on the same side of the BLM represent system B. Finally, two different compositions of particulate semiconductors deposited on the opposite sides of the BLM made up system C.

Single-composition microcrystalline-semiconductor particles incorporated onto only one side of the BLM represent the most straightforward system, already investigated in some detail by other methods (8–

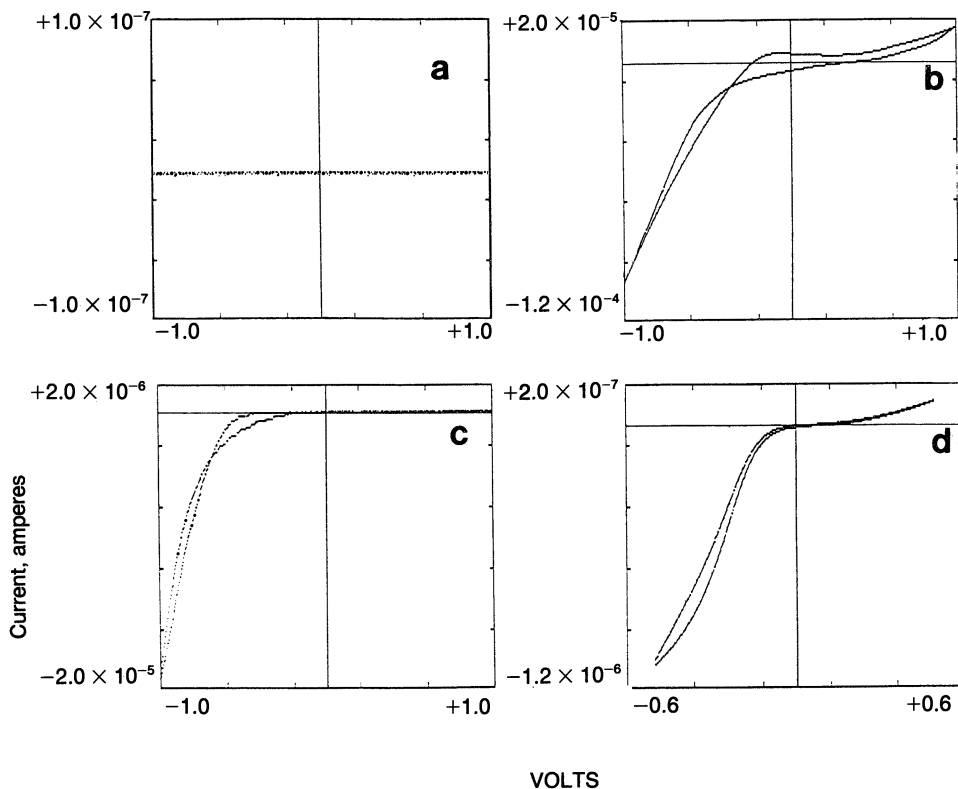


Figure 9. Cyclic voltammograms of a GMO-BLM in the absence, a, and in the presence of ZnS, b, CdS, c, and In_2S_3 , d, particles on its surface (system A). Scan rate, 100 mV/s.

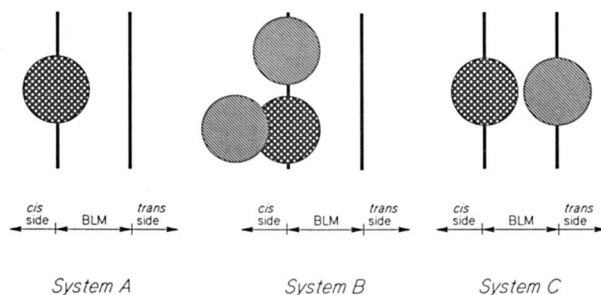
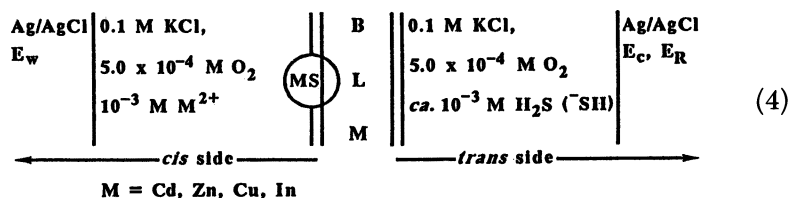
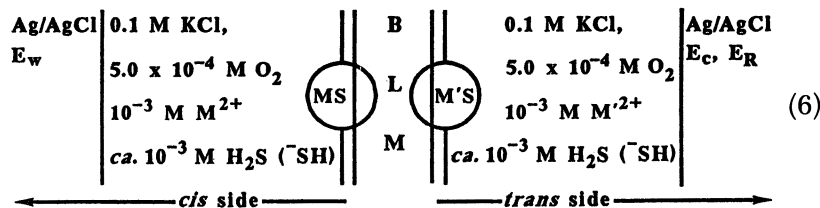
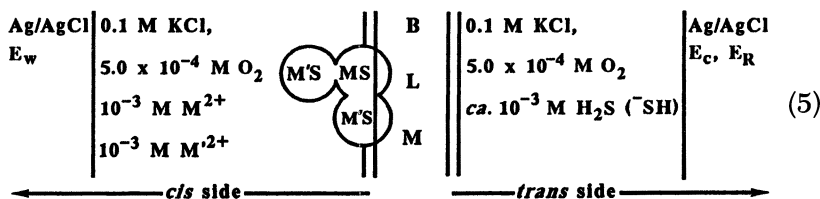


Figure 10. Schematic representation of the different semiconductor-coated BLMs. A single composition of particulate semiconductor deposited only on one side of the BLM constituted system A. Two different compositions of particulate semiconductors sequentially deposited on the same side of the BLM represent system B. Finally, two different compositions of particulates deposited on the opposite sides of the BLM made up system C.

10). The composition of the electrochemical cell used in investigating system A is explicitly shown in equation 4:



where E_w , E_c , and E_R indicate the working, the counter, and the reference electrodes, respectively. Presumably, systems B and C are also porous structures, explicitly shown respectively in equations 5 and 6.



Equations 4, 5, and 6, as well as Figure 10, are gross oversimplifications and should in no way be considered to convey any structural information beyond the location of the semiconductor particles and their penetration into the BLM.

Typical current–voltage (I – V) curves of ZnS, CdS, In₂S₃, and Cu_{2–(x+y)}S are illustrated in Figures 9 and 11, respectively. The shapes and characteristics of the I – V curves remained essentially independent of the rate of scanning from 10 to 10⁶ mV/s. Independence of cyclic voltammetric behavior on the frequency of scanning is used as a criterion to support electronic (as opposed to electrolytic) charge-transfer mechanisms (41–43). Uncertainties in and nonlinearities of the resistances of BLM-incorporated semiconductor systems do not allow an unambiguous use of this criterion. Different semiconductor particles penetrate to different extents into the BLM. Although the membrane remained intact (as seen by the blackness of the reflected light), formation of microscopic defects cannot be excluded. Such pinholes would facilitate electrolytic

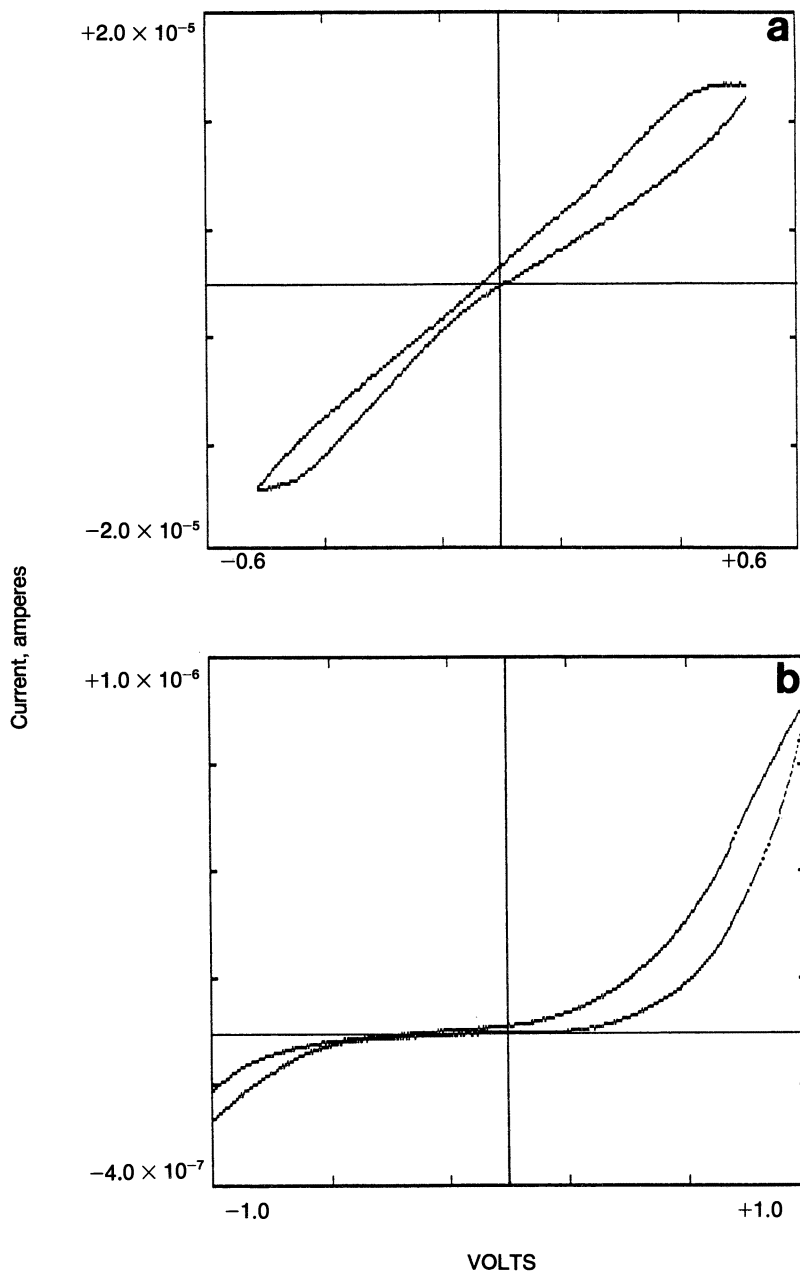


Figure 11. Cyclic voltammograms of the initial formation of semimetallic Cu_{2-x}S , a, and its subsequent reduction to $\text{Cu}_{2-(x+y)}\text{S}$, b, on the cis surface of a GMO-BLM (system A). Scan rate is 100 mV/s from +1.0 to -1.0 V.

charge transport. Similarly, presence of adventitious and deliberately added (H_2S , O_2) dopants in the BLM matrix may well mediate resonance electron tunneling. Accordingly, electron transfer across a semiconductor-containing BLM may be governed either by electronic or by electrolytic conductance or indeed by some combination of both of these mechanisms. Regardless of the mechanism involved, the role of the semiconductor particles is crucial. Different semiconductor particles have elicited substantially different I - V behavior (see Figures 9 and 11) and the observed photovoltage action spectra corresponded to the absorption spectra of semiconductor particles deposited on the BLMs (9). Pigmented (44) and protein-containing BLMs (42, 43, 45-47) behaved analogously. Their electrochemical responses also depended on the given pigment (or protein) incorporated into the BLM and on the potential of the redox species surrounding it.

To a first approximation, the BLM can be considered to behave like a parallel-plate capacitor immersed in a conducting electrolyte solution (44, 48). The equivalent circuit describing the working (E_w), the reference (E_R), and the counter (E_c) electrodes; the resistance (R_m) and the capacitance (C_m) of the BLM; the resistance (R_H) and capacitance (C_H) of the Helmholtz electrical double layer surrounding the BLM; as well as the resistance of the electrolyte solution (R_{sol}) are shown in Figure 12a.

Deposition of a particulate semiconductor on the cis side of the BLM (system A) alters the equivalent circuit to that shown in Figure 12b, where R_f and C_f are the resistance and capacitance due to the particulate semiconductor film; R_m' and C_m' are the resistance and capacitance of the parts of the BLM that remained unaltered by the incorporation of the semiconductor particles; R_{sc} and C_{sc} are the space-charge resistance and capacitance at the semiconductor particle-BLM interface; and R_{ss} and C_{ss} are the resistance and capacitance due to surface state on the semiconductor particles in the BLM. Electrolytes short circuit the porous semiconductor particles ($R_f = R_{\text{sol}} = 1.4 \text{ k}\Omega$) and their contribution, along with that due to the Helmholtz layer, can be neglected. This allows the simplification of the equivalent circuit to that shown in Figure 12c. As seen, the working electrode is connected (via ions) to the semiconductor particulate film.

Band models (49, 50) of n - and p -type semiconductor-containing BLM-ES junctions (system A) are drawn in Figure 13. Charge injection into the conduction band of the n -type semiconductor by a sufficiently active surface donor or by an applied voltage (making the trans side positive relative to the cis side) results in the accumulation of the majority carriers at the space-charge region (cis) surface of the semiconductor particles (Figure 13a). The variation of potential with distance accom-

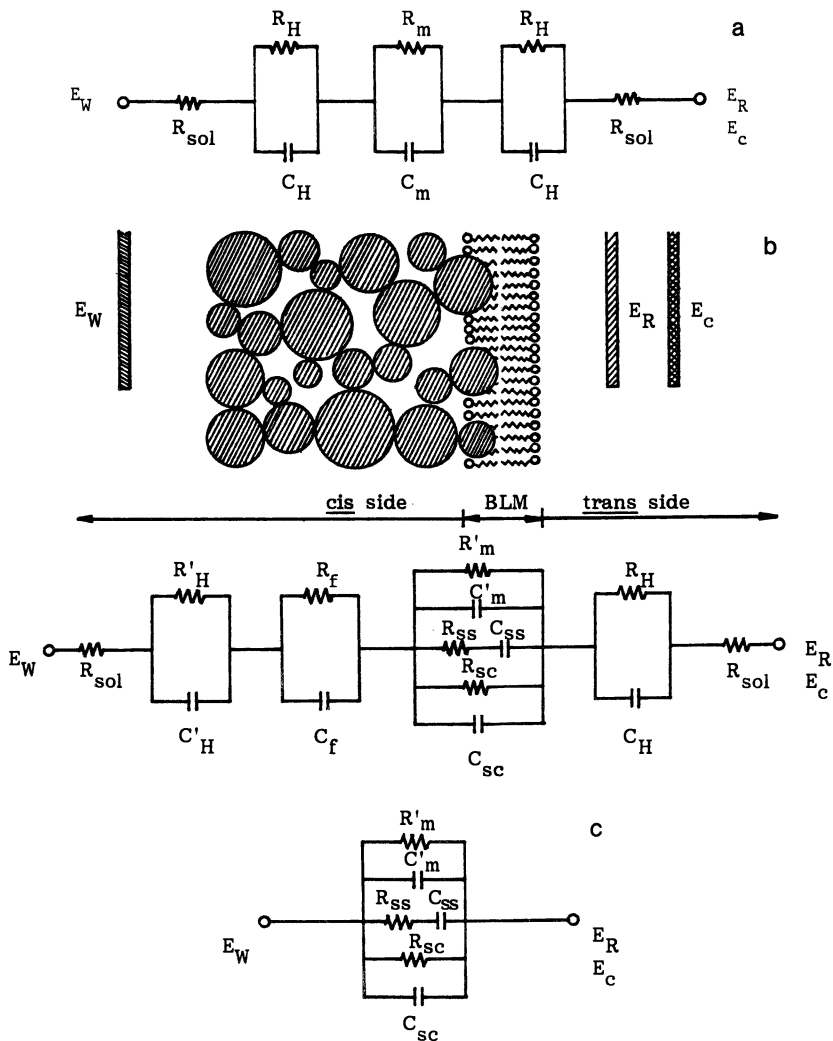


Figure 12. Proposed equivalent circuits for an "empty", a, and a semiconductor-particle-coated, b, BLM. Porous structure of the semiconductor particles allowed the simplification of the equivalent circuit to that shown in c. R_m , R_H , and R_{sol} are resistances due to the membrane, to the Helmholtz electrical double layer, and to the electrolyte solutions, while C_m and C_H are the corresponding capacitances; R_f and C_f are the resistance and capacitance due to the particulate semiconductor film; R'_m and C'_m are the resistance and capacitance of the parts of the BLM that remained unaltered by the incorporation of the semiconductor particles; R_{sc} and C_{sc} are the space charge resistance and capacitance at the semiconductor particle-BLM interface; and R_{ss} and C_{ss} are the resistance and capacitance due to surface state on the semiconductor particles in the BLM.

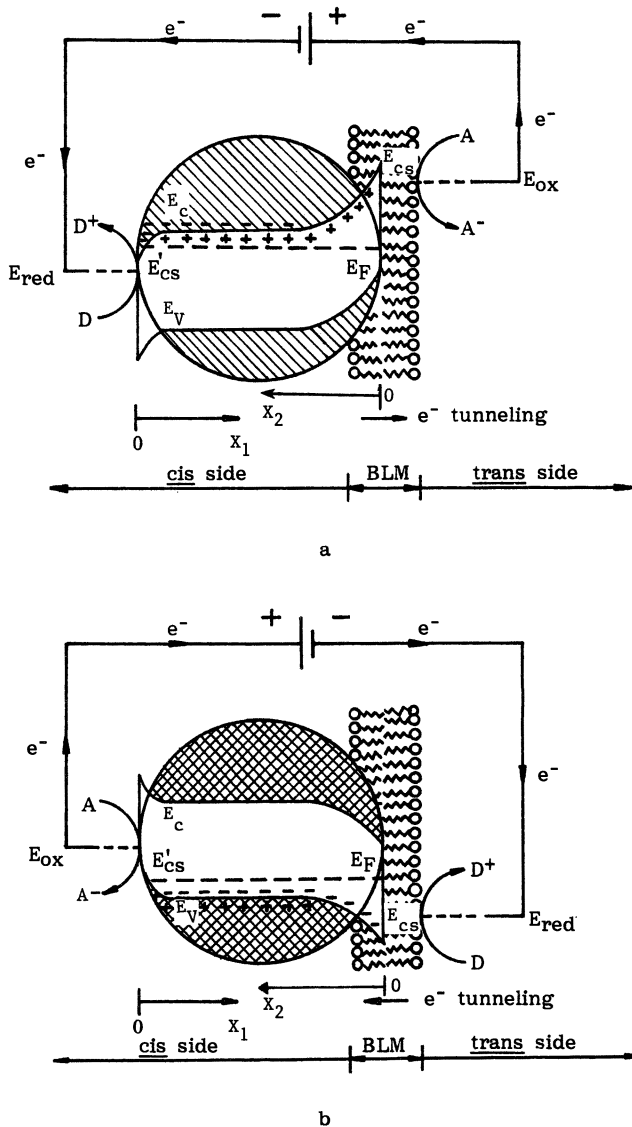


Figure 13. Band models for an n-type (a) and a p-type, (b) semiconductor-containing BLM-ES junction (system A). E_{cs} and E'_{cs} represent the conduction-band edge at the semiconductor-BLM interface and at the semiconductor cis surface. E_F is the Fermi energy level and E_{red} and E_{ox} are energy levels of the reducing and oxidizing agents, respectively. A and D stand for an electron acceptor and an electron donor, respectively.

panying the accumulation of the majority carrier in the space-charge region (cis surface) is given by Poisson's relations as follows:

$$\frac{d^2V}{dX_1^2} = \left(-\frac{n_B e}{\epsilon_s \epsilon_o} \right) [\exp(-eV/kT) - 1] \quad (7)$$

where $V(X_1) = \psi_b - \psi(X_1)$, ψ_b is the potential in the bulk of the semiconductor, n_B is the bulk density of the majority carrier, X_1 is the distance from the semiconductor cis surface (as shown in Figure 13a), e is the electronic charge, ϵ_s is the dielectric constant of the semiconductor, k is Boltzmann's constant, T is the absolute temperature, and V is the applied potential. The first and second terms in the right side of equation 7 represent the contribution of electrons and immobile positive charges, respectively. Simple integration of equation 7 results in

$$\left(\frac{dV}{dX_1} \right)^2 = \left(\frac{2n_B e}{\epsilon_s \epsilon_o} \right) \left\{ \left[\left(\frac{kT}{e} \right) \exp\left(\frac{-eV}{kT} \right) - 1 \right] + V \right\} \quad (8)$$

Downward bending of the conduction-band energy (E_{cs}) provides for a favorable overlap with the energy level of the reducing agent (E_{red}) at the cis-electrolyte surface and the semiconductor particle provides an ohmic contact with the cis electrolyte. A depletion layer is formed at the particle surface, which is immersed in the BLM, and Poisson's equation becomes

$$\frac{d^2V}{dX_2^2} = \frac{eN_{sc}}{\epsilon_o \epsilon_s} \quad (9)$$

where N_{sc} , for an n -type semiconductor, is the density of the immobile positive charge in the space-charge layer and X_2 is the distance of the semiconductor-BLM interface (see Figure 13a). Integrating twice equation 9 results in

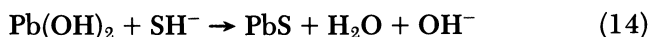
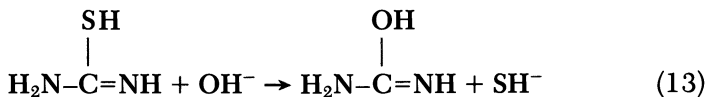
$$V = \frac{eN_{sc}}{2\epsilon_o \epsilon_s} (X_2 - W)^2 \quad (10)$$

where W is the depletion layer. At the surface $X_2 = 0$, the surface barrier, V_s , is given by

$$V_s = \frac{eN_{sc} W^2}{2\epsilon_o \epsilon_s} = \frac{E_{cs} - E_c}{e} \quad (11)$$

Hence, the conduction-band energy, E_c , is upwardly bent to the energy of the conduction-band edge at the surface, E_{cs} . Current flow is observed under cathodic (trans-side positive with respect to the cis side) potential because E_{red} is located in the band-gap region. Electrons are assumed to tunnel through the modified, very-thin BLM (or to be transported by electrolytes) to the overlapping unoccupied energy levels of the oxidizing agent (E_{ox}). The exponential increase of cathodic current with applied voltage is the expected consequence of decreased band bending and increased surface-electron densities. Behavior of the p -type semiconductor can be analogously rationalized.

Preparation-Dependent Rectification Behavior of Semiconductor Particulate Films. Lead-sulfide semiconductor particulate films have been shown to have preparation-dependent rectification behavior (20). PbS-semiconductor particulate films were generated with two different methods. Method 1, the introduction of NH_3 into lead nitrate and thiourea subphase through the arachidic-acid monolayer, is governed by equations 12–14:



Absorption spectra, taken at the earliest times (1–5 s), corresponded to those of $Pb(OH)_2$ whereas those taken at longer exposure times indicated the presence of nanocrystalline PbS. Bright-field TEM examination of the semiconductor particulate film subsequent to three minutes of NH_3 exposure showed the presence of small (15–25-Å diameter) PbS particles on the surfaces of the rod-shaped $Pb(OH)_2$. With continuous infusion of NH_3 , the growth of the semiconductor particulate films was accompanied by an observable change from a whitish-grey color to a mirrorlike black surface. This transition manifested in a gradual shift of the absorption edges to longer wavelengths. Apparently the $Pb(OH)_2$ initially formed under the AA monolayer is gradually replaced by PbS.

In method 2, PbS was generated by the established procedure (15) of infusing H_2S into the AA-coated $Pb(NO_3)_2$ solution (subphase A). The electronic behavior of PbS-particulate films, prepared by the two different methods have been characterized by scanning tunneling spectroscopy (STS). I - V curves, recorded at the surfaces of indium-film-coated copper-foil-supported PbS-particulate films at different tunneling air caps indicate typical Schottky behavior (Figure 14). Importantly, n -

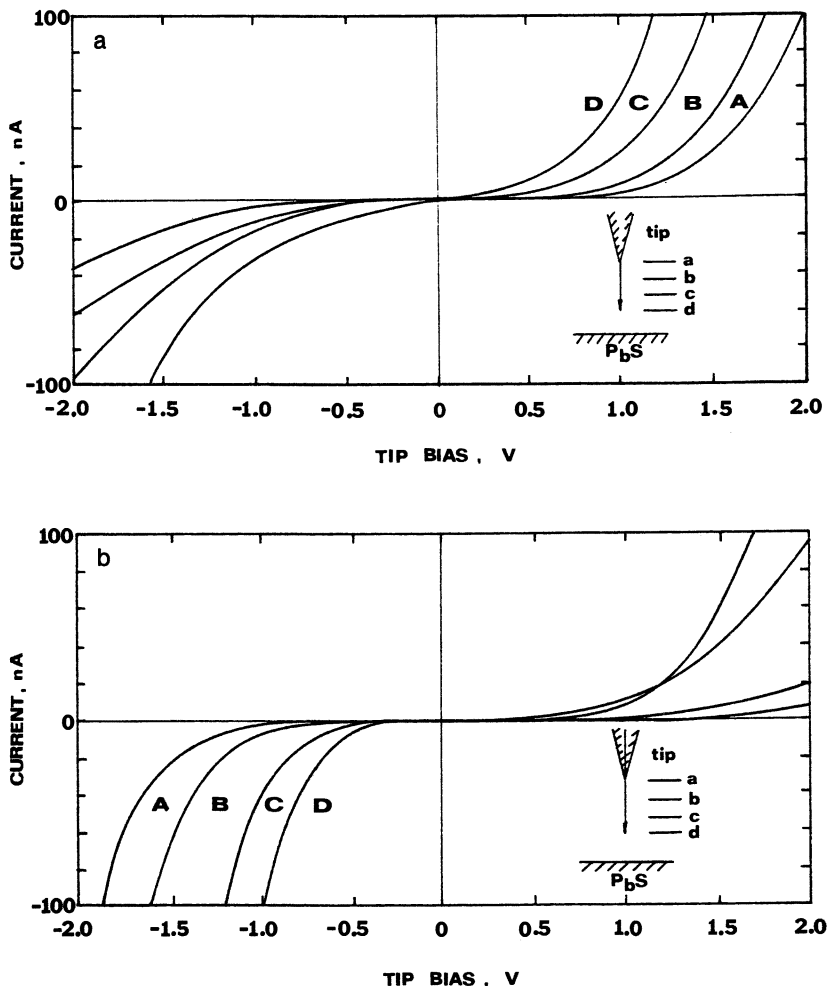


Figure 14. C-V spectra of PbS-particulate films prepared by methods 2 (a) and 1, (b). In method 2, the PbS-particulate film was formed by a 10-min infusion of H_2S to an AA-coated 1.0×10^{-3} M aqueous $Pb(NO_3)_2$ solution (subphase A). In method 1, the PbS-particulate film was formed by the introduction of NH_3 to AA monolayers floating on a mixture of 1.0×10^{-3} M aqueous $Pb(NO_3)_2$ and 2.0×10^{-2} M $CS(NH_2)_2$ for 10 min. The samples were transferred to indium-film-coated Cu foils, dried for 24 h in a desiccator, and the surfactant monolayer was then removed by gentle rinsing with chloroform and acetone. The tip-to-sample distance decreased in the order $A > B > C > D$.

type rectifications for PbS are prepared by H₂S infusion (Figure 14a; method 2), whereas *p*-type rectifications for samples are prepared by NH₃ infusion (Figure 14b; method 1).

Magnetic Domains. The magneto-optical Kerr effect is particularly useful for domain imaging. The reflected light undergoes Kerr rotation at the plane of polarization, which permits the visualization of domain structures by polarized microscopy. However, the domain contrast tends to be weak, particularly for films with rough surfaces, because the magneto-optical signal is superimposed on a large amount of background light. We have overcome these difficulties by using an intense argon-ion laser as the light source and sensitive video-enhanced microscopy (Figure 15). The analyzer was set to the original extinction direction to attenuate the background reflected from the film surface thus allowing the Kerr signal to be detected by the video camera. Contrast was optimized on the video image by adjusting the polarizer and analyzer.

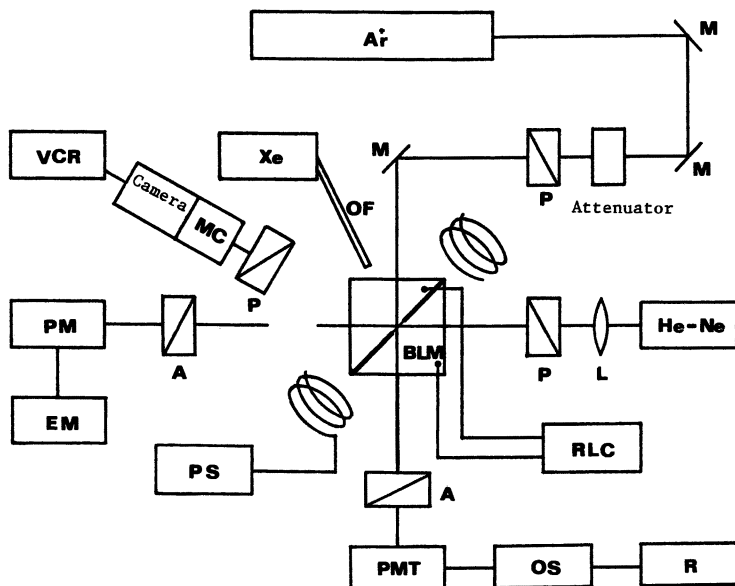


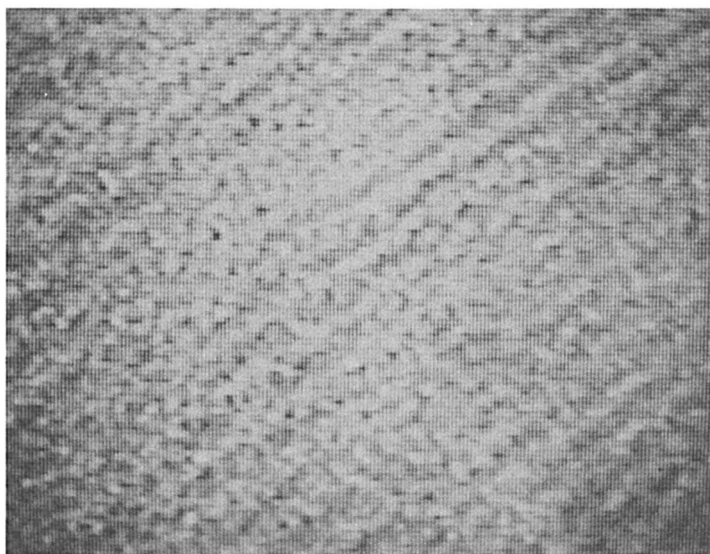
Figure 15. Experimental setup for magneto-optical measurements: Ar⁺ is Spectra Physics model 2020 argon-ion laser, He-Ne is 10-mW helium-neon laser, M is mirror, P is polarizer, VCR is videorecorder, Xe is 150-W xenon lamp, OF is optical fiber, MC is Olympus model PM-10-M microscope, A is analyzer, EM is Keithley model 602 electrometer, PM is Spectra Physics model 404 silicon-photocell power meter, RLC is Genrad Corp. model 1689 digibridge, PMT is Hamamatsu R-928 photomultiplier, PS is power supply, OS is oscilloscope, R is recorder, and L is lens.

The magnetooptically characterized, monoparticulate thin film was uniform when looked at with the Kerr microscope. The resolution of this microscope ($1\ \mu\text{m}$) did not allow the observation of domains smaller than $1\ \mu\text{m}$. Domains on the BLM could, in principle, be smaller than $1\ \mu\text{m}$ or, alternatively, so large as to cover the entire surface of the GMO-BLM. This latter case is, however, highly unlikely.

Domains were observed upon disturbing the uniformity of the film by vigorous shaking of the BLM and rotating the direction of the applied 800-Oersted magnetic field (Figure 16). The dimension of the particulates demands the assumption of the presence of Néel domain walls. In Néel walls, rotation of the magnetization M can occur only in the plane but not out of it. Magnetization distribution of Néel domains are sometimes referred to as "one-dimensional" (51). The speculative nature of the model shown in Figure 7 is emphasized; transmembrane wall-to-wall interactions, particle thicknesses of $D_m = 57\ \text{\AA}$, membrane thicknesses of $d_b = 62\ \text{\AA}$, and wall sizes of $400\ \text{\AA}$ were assumed.

Conclusion

The method described in this chapter permits convenient thickness, morphology, and dimensionality controls in the in situ formation of me-



40 mm



Figure 16. Maze-domain pattern of the particulate Fe_3O_4 film deposited on one side of a GMO-BLM.

tallic, magnetic, and semiconductor particulate films. Manipulation of the surfactant organization and the chemistries at the monolayer and bilayer interfaces and the subphase will provide a much better control of semiconductor particulate film formation and will permit the colloid-chemical generation of periodically and spatially modulated superlattices. Most importantly, substrate-supported, metallic, magnetic, and semiconductor particulate films can be fully characterized by solid-state methodologies and can be exploited as novel electronic devices. Our studies, described here, are in accord with and are related to the investigations of metallic and semiconductor particles in organized assemblies being carried out by the research groups of Bard (52), Henglein (35, 53, 54), Kamat (55), Meisel (56), Pileni (57, 58), and Wang (38).

Acknowledgments

Support of this work by a grant from the National Science Foundation is gratefully acknowledged. I thank my co-workers, whose names appear in joint publications, for their creative, skillful, and dedicated work.

References

1. Fendler, J. H. *Membrane Mimetic Chemistry*; Wiley-Interscience: New York, 1982.
2. Tien, H. T. *Bilayer Lipid Membranes (BLM) Theory and Practice*; Marcel Dekker: New York, 1974.
3. Miller, C. *Ion Channel Reconstitution*; Plenum: New York, 1986.
4. Hille, B. *Ionic Channels of Excitable Membranes*; Sinauer Associates: Sunderland, MA, 1984.
5. Sakmann, B.; Neher, E. *Single-Channel Recording*; Plenum: New York, 1983.
6. Zhao, X. K.; Fendler, J. H. *J. Phys. Chem.* **1988**, *92*, 3350.
7. Zhao, X. K.; Xu, S.; Herve, P. J.; Fendler, J. H. *J. Phys. Chem.* **1989**, *93*, 908.
8. Baral, S.; Zhao, X. K.; Rolandi, R.; Fendler, J. H. *J. Phys. Chem.* **1987**, *91*, 2701.
9. Zhao, X. K.; Baral, S.; Rolandi, R.; Fendler, J. H. *J. Am. Chem. Soc.* **1988**, *110*, 1012.
10. Baral, S.; Fendler, J. H. *J. Am. Chem. Soc.* **1989**, *111*, 1604.
11. Zhao, X. K.; Baral, S.; Fendler, J. H. *J. Phys. Chem.* **1990**, *94*, 2043.
12. Zhao, X. K.; Yuan, Y.; Fendler, J. H. *J. Chem. Soc. Chem. Commun.* **1990**, 1248.
13. Yuan, Y.; Cabasso, I.; Fendler, J. H. *Chem. Mater.* **1990**, *2*, 226.
14. Yi, K. C.; Fendler, J. H. *Langmuir* **1990**, *6*, 1519.
15. Zhao, X. K.; Xu, S.; Fendler, J. H. *Langmuir* **1991**, *7*, 520.

16. Zhao, X. K.; Fendler, J. H. *Chem. Mater.* **1991**, *3*, 168.
17. Zhao, X. K.; Fendler, J. H. *J. Phys. Chem.* **1991**, *95*, 3716.
18. Zhao, X. K.; McCormick, L. D.; Fendler, J. H. *Langmuir* **1991**, *7*, 1255.
19. Zhao, X. K.; McCormick, L. D.; Fendler, J. H. *Chem. Mater.* **1991**, *3*, 922.
20. Zhao, X. K.; McCormick, L. D.; Fendler, J. H. *Adv. Mater.* **1992**, *4*, 93.
21. Yi, K.; Fendler, J. H. PhD Dissertation, Syracuse University, 1993.
22. Zhao, X. K.; Fendler, J. H. *J. Phys. Chem.* **1990**, *94*, 3384.
23. Beaglehole, D.; Hunderi, O. *Phys. Rev. B* **1970**, *2*, 309.
24. Hunderi, O.; Beaglehole, D. *Phys. Rev. B* **1970**, *2*, 321.
25. Hunderi, O. *J. Phys. (Fr.) Colloq. (Suppl.)* **1977**, *11*, C5.
26. Cherry, R. J.; Chapman, D. *J. Mol. Biol.* **1969**, *40*, 19.
27. Garnett, M. J. C. *Philos. Trans. R. Soc. (London)* **1904**, *203*, 385.
28. Zhao, X. K.; Fendler, J. H., Syracuse University, unpublished results.
29. Borrelli, N. F.; Murphy, J. A. *J. Appl. Phys.* **1971**, *42*, 1120.
30. Fenstermaker, C. A.; McCrackin, F. L. *Surf. Sci.* **1969**, *16*, 85.
31. Hénon, S.; Meunier, J. *Rev. Sci. Instrum.* **1991**, *62*, 936.
32. Hönig, D.; Möbius, D. *J. Phys. Chem.* **1991**, *95*, 4590.
33. Brus, L. A. *J. Phys. Chem.* **1986**, *90*, 2555.
34. Wang, Y.; Suna, A.; Mahler, W.; Kasowski, R. *J. Chem. Phys.* **1987**, *87*, 7315.
35. Henglein, A. *Topics Curr. Chem.* **1988**, *143*, 113.
36. Steigerwald, M. L.; Brus, L. E. *Acc. Chem. Res.* **1990**, *23*, 183.
37. Fendler, J. H. *Chem. Rev.* **1987**, *87*, 877.
38. Wang, Y. *Acc. Chem. Res.* **1991**, *24*, 133.
39. Fettiplace, R. *Biochim. Biophys. Acta* **1978**, *513*, 1.
40. Kahn, S. U. M. *J. Phys. Chem.* **1988**, *92*, 2541.
41. Bard, A. J.; Faulkner, L. R. *Electrochemical Methods*; Wiley: New York, 1980.
42. *Photoinduced Electron Transfer. Part A. Conceptual Basis*; Fox, M. A., Chanon, M., Eds.; Elsevier: Amsterdam, Holland, 1988.
43. Habib, M. S.; Bockris, J. O'M. *J. Bioelectr.* **1982**, *1*, 289.
44. Krysinski, P.; Tien, H. T. *Prog. Surf. Sci.* **1986**, *23*, 317.
45. Habib, M. A.; Bockris, J. O'M. *J. Bioelectr.* **1984**, *3*, 247.
46. Michel, A. R.; Habib, M. A.; Bockris, J. O'M. In *Electric Double Layer in Biology*; Blank, M., Ed.; Plenum: New York, 1986; p 167.
47. Habib, M. A.; Bockris, J. O'M. *J. Biophys.* **1986**, *14*, 31.
48. Hong, F. T. *Photochem. Photobiol.* **1976**, *24*, 155.
49. Morrison, S. R. *Electrochemistry at Semiconductor and Oxidized Metal Electrodes*; Plenum: New York, 1980.
50. Hodes, G.; Grätzel, M. *Nouv. J. Chim.* **1984**, *8*, 509.
51. Cohen, M. S. *Ferromagnetic Properties of Films*; McGraw-Hill: New York, 1970; p 17.1.
52. Smotkin, E. S.; Brown R. M., Jr.; Rabenberg, L. K.; Salomon, K.; Bard, A. J.; Campion, A.; Fox, M. A.; Mallouk, T. E.; Webber, S. E.; White, J. M. *J. Phys. Chem.* **1990**, *94*, 7543.
53. Henglein, A. *Israel J. Chem.* **1993**, *33*, 77.
54. Henglein, A.; Fojtik, A.; Weller, H. *Ber. Bunsenges. Phys. Chem.* **1987**, *91*, 441.
55. Kamat, P. V. *Chem. Rev.* **1993**, *93*, 267.
56. Jain, T. K.; Billoudet, F.; Motte, L.; Lisiecki, I.; Pileni, M. P. *Colloid Polym. Sci.* **1992**, *89*, 106.

57. Pileni, M. P. *J. Phys. Chem.* **1993**, *97*, 6961.
58. Wang, Y.; Harmer, M.; Herron, N. *Israel J. Chem.* **1993**, *33*, 31.

More recent work in the field is amply summarized in the book, *Membrane-Mimetic Approach to Advanced Materials*; Fendler, J. H., Ed.; Springer-Verlag: Berlin, Germany, 1994.

RECEIVED for review March 12, 1992. ACCEPTED revised manuscript December 10, 1993.

Self-Assembling Bilayer Lipid Membranes on Solid Support

Building Blocks of Future Biosensors and Molecular Devices

A. Ottova-Leitmannova,¹ T. Martynski,² A. Wardak,³ and H. T. Tien*

Membrane Biophysics Laboratory (Giltner Hall), Department of Physiology, Michigan State University, East Lansing, MI 48824

Planar bilayer lipid membranes (BLMs) have been widely used as a model for biomembranes. We first summarize certain BLM experiments with biosensors and molecular devices, after describing the conventional BLM system. These discussions will be followed by a description of a new BLM system based on self-assembling process of amphiphilic molecules. In recent years advances in microelectronics coupled with sustained interest in thin organic films have prompted a number of investigators to exploit the conventional BLM system as a basis for molecular devices as well as for the development of electrochemical sensors. The new supported BLMs (s-BLMs) have the requisite mechanical stability, besides possessing desired dynamic properties. Thus, the s-BLM system offers opportunities for basic studies as well as for technological applications.

THE CONCEPT OF THE LIPID BILAYER as the basic structure of biological membranes became generally known only in the late 1950s (1, 2). Realizing the importance of the lipid bilayer, Rudin and his associates (3) and Tien (4) succeeded in 1960 in reconstituting a bimolecular or bilayer lipid membrane (BLM) between two aqueous solutions. Experimental BLMs (planar BLMs and the spherical liposomes that were developed shortly afterward by Bangham and co-workers, *see* reference 5), have

¹ Current address: Slovak Technical University, Bratislava, Czechoslovakia/Slovakia

² Current address: Institute of Physics, Poznan Technical University, Poznan, Poland

³ Current address: Department of Physics, Technical University of Lublin, Lublin, Poland

* Corresponding author.

0065-2393/94/0240-0439\$08.00/0
© 1994 American Chemical Society

been extensively used as models of all sorts of biomembranes (4–11). It is now recognized that this universal bilayer structure exists because of the unique properties of lipid molecules. At one end of a lipid molecule is a hydrophobic fluid–hydrocarbon chain, and at the other end is a hydrophilic polar group. When lipid molecules are in aqueous media, this arrangement causes them to assemble spontaneously into a bilayer configuration (1, 4, 10, 12).

Unmodified BLMs, like the closely related liposomes, are dynamic structures that can be easily modified by incorporating a variety of compounds that will endow them with functional characteristics. The resulting modified BLMs have proven since the 1960s to be ideal for investigating electrical, mechanical, immunological, photoelectrical, and a host of other properties associated with the lipid bilayer of biomembranes (10–15). Further, as evidenced by publications from a number of laboratories (10, 11, 15–20), the BLM system is of interest in solar energy transduction, biosensor development, and molecular electronic devices fabrication.

BLMs formed in the conventional manner (i.e., by spreading a lipid solution across a small hole in a hydrophobic partition separating two aqueous compartments) are not very stable. These BLMs rarely last more than a few hours. For practical applications and for long-term studies, a durable BLM (lipid bilayer) is a prerequisite. In this chapter we describe a simple mechanical procedure for the self-assembly of lipid bilayers on solid supports (12, 21). These supported lipid bilayers have a long life, thereby offering opportunities for the preparation of a variety of probes with diverse applications in membrane biophysics, biochemistry, physiology, and biotechnology (22, 23). An overview of potentially BLM-based biosensor technology is given in Table I.

Experimental Details

Materials. The BLMs on solid substrates described in this study were formed from various lipid solutions, for example, different concentrations of phosphatidylcholine (PC) in *n*-octane; 5% lecithin, PC (Walgreen Laboratories, Inc.) in *n*-decane (Aldrich Chemical Company); 50% PC in *n*-decane; 1% glycerol monooleate (GMO) (K & K Laboratories, Inc., Rochester, NY), in squalene (Eastman Kodak Co., Rochester, NY); oxidized cholesterol in *n*-octane; and glycerol dioleate (GDO) (K & K Laboratories, Inc., Rochester, NY), in squalene. Supported BLMs were also formed from a GDO solution saturated with zinc phthalocyanine (Zn PLC) (Strem Chemical Company) or from 4-*n*-octyl-4'-cyanobiphenyl (8-CB) (BDH Chemicals, Ltd.) dissolved in squalene (1:5 or 1:10 v/v) and saturated with 7,7,8,8-tetracyano-*p*-quinodimethane (TCNQ) (Aldrich Chemical Company). The bathing solution was 0.1 M KCl. All chemical compounds (KCl, NaCl, AlCl₃, MgSO₄, ascorbic acid, K₃Fe(CN)₆, K₄Fe(CN)₆, and Pb(NO₃)₂) were obtained commercially and were used without further purification. In some experiments

Table I. An Overview of the s-BLM-Based Biosensor Technology

<i>Type of Measurement</i>	<i>Type of Transducer</i>
Electrochemical:	Oxygen electrode
Potentiometry	Ion-selective electrode
Amperometry	Modified metal electrode
Conductimetry	Field effect transistor
Impedimetry	Conductimeter
Photometric	Spectrophotometry
	Laser light scattering
	Optical fibers combined with absorption and fluorescence
	Surface plasmon resonance
Thermometric	Thermistors
Acoustic	Piezoelectric crystal
	Surface acoustic wave device

NOTE: To be developed as a future technology.

SOURCE: Adapted from references 22 and 23.

the following buffer solutions were used: phthalate buffer (pH 4.0), phosphate buffer (pH 7.0), and carbonate buffer (pH 10.0) (all were obtained from Altex, CA). Double distilled water in the preparation of all solutions was used (24–27).

For solid substrates, metallic wires of Pt, Ag, and stainless steel (ss), of consisted of different concentrations of PC in *n*-octane or of 1% GMO, or 1% GDO in squalene. In some experiments the lipid solutions were modified with chlorophylls, TCNQ, and other modifiers promoting redox reactions of redox couples such as ferro- and ferricyanide, KI, and ascorbate.

The aim of these experiments was to demonstrate two points: (1) formation of a structure with the electrical parameters of a BLM on a solid support and (2) modification of this structure so that it is sensitive to the bathing solution (0.1 M KCl). The membrane-forming solutions wet the ss wire and SnO₂ surfaces better than the electrolyte solution does. Although no direct measurements of thickness was performed, the similarities of the electrical parameters—resistance (R) and capacitance (C)—to those for lipid bilayers suggest that a bilayer arrangement was probably formed in the present system. To show some possibilities for modification of the supported BLM, we used several modifiers that promote redox reactions. The current–voltage relationship for SnO₂–GDO in squalene, chlorophyll–ferricyanide, and KCl–SnO₂ in a two-electrode system (SnO₂-covered glass as a reference electrode) is not symmetrical. The system is sensitive for 1- μ M ferricyanide. The same system modified with TCNQ was less sensitive. Further studies were done for the changes in the current–voltage relationship in the presence of 1-mM K₃Fe(CN)₆ for the same system as described previously but with TCNQ as the modifier (SnO₂–GDO in squalene, TCNQ–ferricyanide, and KCl–SnO₂). Also in this case, the current–voltage curve is not symmetrical. For more details see reference 26. As stated there, the purpose of the redox-reaction experiments was to demonstrate the potential of this system. No attempt was carried out to investigate the electrochemistry of the occurring reactions. The significance of these experiments is that the s-

BLM can be modified to achieve a particular function. This seems to be very important for the successful development of s-BLM-based biosensors diameters ranging from 0.02 to 0.2 mm, with and without Teflon coating (0.075 mm), were obtained from Medwire Corp., Mount Vernon, NY. In some experiments pure platinum wires (Pt, 99.95%) (AESAR Johnson Matthey, Inc., Ward Hill, MA), 0.5-mm diameter, were used as metallic solid surfaces. Tubes made of Teflon (TEF, Berghof/America, Inc., Rochester, NY) were used as sleeves to coat Pt wires for the modified version of the original method of solid s-BLM formation. The inner and outer diameters were 0.52 and 1.2 mm, respectively.

The use of BLMs supported on solid substrates like silver wires coated with Teflon and SnO₂ on glass for analysis of sensor-development problems, with relevance to a possible novel type of biomolecular device is also described in our work.

Methods. Electrical properties of supported BLMs were measured at room temperature (21 ± 1 °C) using the setup that consisted of a high-impedance electrometer (model 610 BR, Keithley Instruments Company, Taunton, MA), a picoammeter (model 417, Keithley Instruments Company, Taunton, MA), a low-level capacitance meter (model I-6, IC Electronics, Taunton, MA). We also used an IBM (model EC/225) voltammetric analyzer in conjunction with a strip-chart recorder. In some experiments, namely in the case of the modified version of solid s-BLM formation also Potentiostat/Galvanostat (model 173) with interface model 276 (EG&G, Princeton Applied Research, Princeton, NJ) connected to an IBM PC/XT computer with Headstart software (EG&G, Princeton Applied Research, Princeton, NJ) was used (24–27).

In all of the experiments described here the s-BLM was used as a working electrode in a three-electrode setup in which a coil of Pt wire was used as the counter electrode. A calomel electrode with a salt-bridge served as a reference electrode. The bathing solution was usually 0.1 M KCl. The only exception was the case of s-BLM on solid substrates like silver wires that were coated with Teflon and of SnO₂ on glass for analysis of biosensor development problems. In this case s-BLM was used as a working electrode in a two-electrode system. Ag–AgCl, saturated calomel electrode (SCE), or SnO₂-covered glass were used as reference electrodes (24–27).

Techniques for Spontaneous Assembly of an s-BLM. An s-BLM (or lipid bilayer) as described here is formed by two consecutive self-assembling steps: (1) placing lipid molecules in contact with a freshly fractured metal surface and (2) immersing the lipid layer that becomes adsorbed onto the metal surface in an aqueous solution. In this chapter we present a brief summary of the procedure described in detail elsewhere (24–27).

Figure 1 portrays the most essential steps of our experimental procedure. In Figure 1 (left), the tip of a Teflon-coated wire (platinum, silver, or ss) has been cut with a sharp knife under a lipid solution, for example, a 1% glycerol dioleate in squalene. When the nascent metal surface is exposed in a lipid solution, a monolayer of lipid molecules is irreversibly bound onto its surface, as shown in Figure 1 (left). The adsorbed lipid monolayer with unattached hydrocarbon chains interacts with the hydrophobic chains of other lipid molecules. When the lipid-coated wire is immersed in an aqueous solution (e.g., 0.1 M KCl), as illustrated in Figure 1 (right), this immersion leads eventually (under favorable conditions) to the spontaneous formation

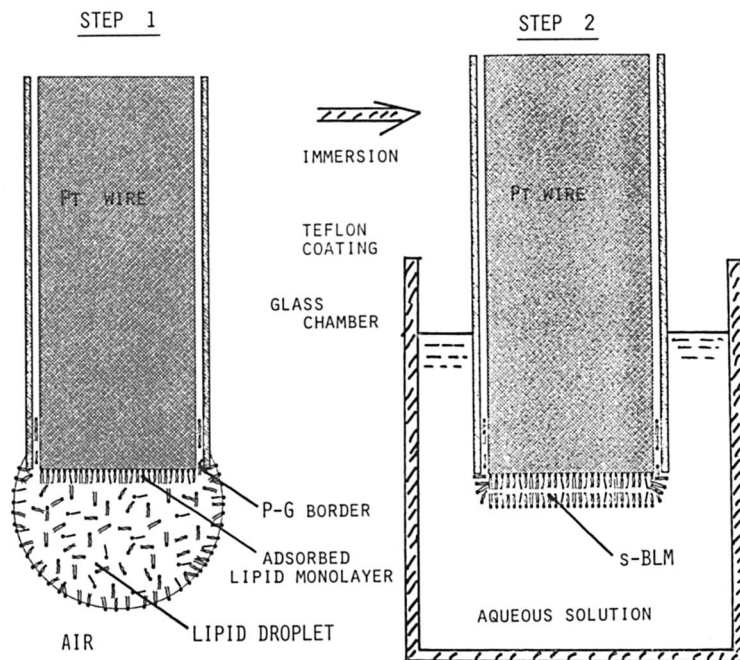


Figure 1. Self-assembling of *s*-BLMs in two steps (12, 21, 24).

of an exceptionally stable, self-assembled lipid bilayer, as shown in Figure 1 (right).

The precise arrangement and degree of ordering of the lipid molecules in the final structure shown in Figure 1 (right) is not known for certain. But it is highly probable that the bilayer nature of the assembly is a consequence of the thermodynamics of free-energy changes at the metal–lipid surface and at the lipid–aqueous solution interface (12). Our measurements of the electrical properties of *s*-BLMs are consistent with those of conventional BLMs and closely related systems (4, 28): In the series of our experiments, we have found that *s*-BLMs not only have desired electrochemical and optical properties but also have some areas of practical applications as well (21–23). All of these results have demonstrated a simple and useful method of solid *s*-BLMs.

For further improving both the reproducibility of obtaining BLM systems with similar electrochemical properties and of getting even longer lifetime of such *s*-BLMs, a modified version of the original method of *s*-BLM formation is presented. More details are given in reference 27. For the best cutting of Pt wire, we constructed a miniature guillotine where the sharp knife is moved vertically onto the wire placed on the flat base. The wire is then cut while immersed in a drop of lipid solution so that the initial contact of the newly exposed wire surface is with the lipid solution. The newly cut surface is almost perpendicular to the length of wire. This lipid-coated wire is then inserted into a small piece of Teflon tubing (TEF, 10 mm) that has been filled with lipid solution. This assembled Teflon-covered Pt wire is trans-

ferred into an aqueous bathing solution. We then let the system stand for a few minutes or hours. Supplied by diffusion within the lipid solution, the nascent platinum support surface will attract the polar groups of lipid molecules. To promote the process of self-assembling of BLM, one of the following two methods has been used: (1) by removing GDO solution from TEF sleeve simply with capillary forces or (2) by using a piston system (27). The final step is self-adjusting thinning and formation of the Plateau–Gibbs (P–G) border. During the time of self-adjusting process, the change in capacitance of a layer was monitored. After 5–10 min the capacitance reaches a constant value and the bilayer structure has been formed. With these methods we are able to control both the rate of the BLM formation process and the ratio of BLM to the P–G border. These simple steps allow us to produce stable and very similar s-BLMs.

Results and Discussion

In our experiments we showed that the time change of resistance in a s-BLM on platinum is very similar to that observed with a conventional single BLM (4, 12). This change means that the resistance decreases during the thinning process until it reaches a constant value on the order of 10^6 to $10^7 \Omega \text{ cm}^2$, for a variety of unmodified BLMs. The value for a platinum-supported 8-CB + TCNQ bilayer's resistance drops to $10^5 \Omega \text{ cm}^2$. The capacitance of a BLM, along with optical reflectance, is a well-established parameter for estimating the thickness of lipid bilayers (4, 10). Therefore, the capacitance measurements were used to monitor the BLM formation process and to estimate the thickness of the lipid bilayer. The capacitances were measured as a function of time. The thinning process was fairly rapid; the capacitance value reached a plateau in about 2 min, indicating corresponding thicknesses of 4.0 and 4.5 nm, respectively, for the supported BLMs formed from GDO and lecithin lipids. Characteristic values of the capacitance for s-BLMs are in the range of 0.2- to $0.5 \mu\text{F cm}^{-2}$, which are fairly consistent with those of conventional BLMs. Other electrical measurements were made after completion of the thinning process. We measured a number of typical electrical parameters such as cyclic voltammograms (CV), potential (V), and capacitance (C). The CV curves for the s-BLMs are strongly asymmetrical. Especially in the negative part of the curve, the current depends on the type of ions in the bathing solution. To reduce this negativity, current influence of several ions has been tested: KCl, NaCl, MgSO_4 , AlCl_3 in different concentrations from 0.001 to 0.1 M. The best shape of CV curves and the longest lifetime of the system were obtained for a 0.1 M AlCl_3 bathing solution. After a few CV measured between -100 and $+700 \text{ mV}$ at sweep rate of 100 mV s^{-1} , the CV curves became wider. Further, saturation of bathing solution with argon decreased the cathodic current even more, and the bilayer systems became even more stable.

Further experiments were performed on s-BLMs with well-known redox compounds in the bathing solution (25). The CV for ascorbic acid shows two anodic peaks: one in the forward and one in the reverse potential scan (Figure 2). The peak in the forward potential scan, appearing for both a membrane-modified and a bare Pt electrode, is characteristic for the oxidation of ascorbic acid. The position of this peak, for the electrode modified with a lipid bilayer, was shifted toward more-positive potentials, as compared to the bare electrode. The peak on the reverse scan was recorded for the modified electrode only. The observed dependence of the positions of both peaks on the concentration of ascorbic acid is related to pH changes. In buffered solutions no dependence on the concentration of ascorbic acid was found, but a strong dependence on pH is observed. The peak current for the forward scan is linearly dependent on the concentration of ascorbic acid. The dependence for the reverse scan peak is linear only for lower concentrations. At higher concentrations of ascorbic acid, the dependence is sublinear

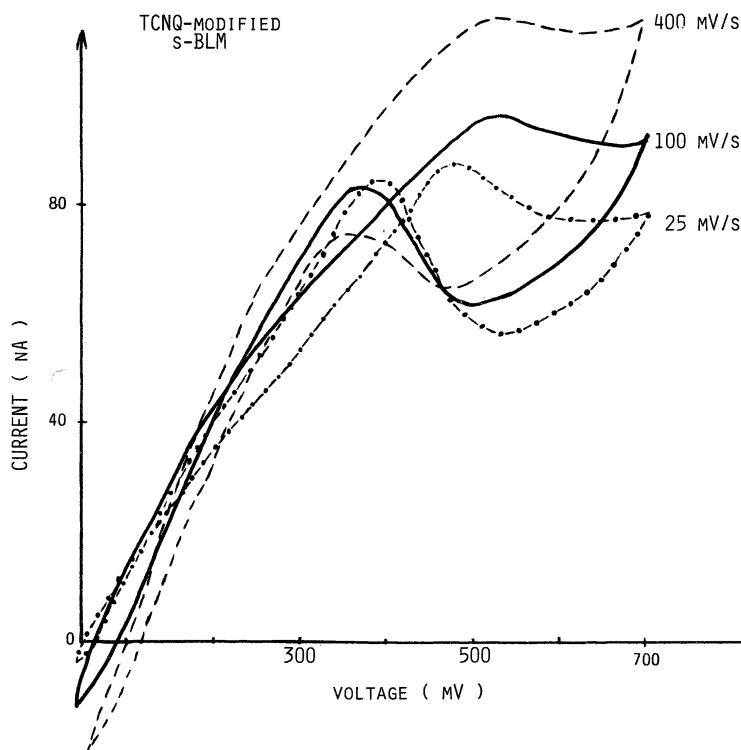


Figure 2. Dependence of the cyclic voltammograms on scan rate for a s-BLM in 0.5 M KCl containing 1-mM ascorbic acid. (Reproduced with permission from reference 25. Copyright 1990 Elsevier Sequoia.)

and the peak is usually weakly pronounced. Both, the peak potentials and the peak currents are dependent on the scan rate (Figure 2). At high scan rates, the forward scan peak current increases while the reverse scan peak current decreases, and the peak is weakly pronounced. At low scan rates, the peak in the forward scan is shifted to lower potentials, and the peak in the reverse scan is shifted to higher potentials. For more details *see* reference 25.

Also in ferri- and ferrocyanide solutions, oxidation and reduction peaks were recorded. The CV currents were dependent on the scan rate and on the concentration of $K_3Fe(CN)_6$ and $K_4Fe(CN)_6$. No peaks were observed below 2 mM. The currents at 500 mV, that is, over the peak levels, were compared for bilayer electrodes and for bare electrodes. For the bilayer-covered electrodes, the currents were lower (Table II). At the same time, the positions of the peaks were changed and the peak-to-peak separation increased (Table II). For TCNQ-modified membranes the peaks were more pronounced than for unmodified membranes, and the peaks were recorded even at a concentration of 0.2 mM. Modification of *s*-BLMs increases the currents and decreases the peak-to-peak separation (Table II).

The experiments described in the preceding paragraphs show that an electrode modified by supporting a lipid bilayer on it has some new features when compared with a bare electrode. Compared to conventional BLMs, BLMs supported on an electrode are much more stable. Their high stability is a feature that makes them very useful in analytical studies. The modified Pt electrode can presumably be used to study redox species to which the lipid membrane is highly sensitive. The appearance of characteristic peaks in CV and the linear dependence of peak currents on concentration make both qualitative and quantitative studies possible. Suitable modification of the membranes can make them even more sensitive. CV studies of a lipid bilayer supported (*i.e.*, *s*-BLM) on the working electrode can probably also provide some information about the transfer of species through the solution–lipid interface and through the bilayer interior, as well as about redox reactions at and in the membrane.

Table II. Properties of *s*-BLMs with and without Modification

<i>Kind of s</i> -BLM	<i>No. of Expts.</i>	<i>Peak Separation (mV)</i>	<i>I/I₀^a</i>
Bare wire	9	89 ± 4	1
No modification	11	365 ± 30	0.029
With TCNQ	11	279 ± 40	0.054

^a The ratio between the current of an electrode covered with lipid membrane and the current of a bare electrode.

SOURCE: Adapted from reference 25.

A typical CV for a Pt-supported (8-CB + TCNQ) bilayer in 0.1-M KCl bathing solution at a sweep rate of 100 mV sec⁻¹ exhibits three oxidation peaks, occurring at -650, -90, and +450 mV. The presence of more than two oxidation peaks indicates that a charge-transfer (CT) complex (8-CB⁺TCNQ⁻) is formed, as indicated by a new peak. Taking into account previous CV results with TCNQ in different solvent, it can be assumed that the two peaks that occur at -650 and -90 mV are probably caused by the oxidation of TCNQ²⁻ (TCNQ²⁻ → TCNQ⁻ + e) and TCNQ⁻ (TCNQ⁻ → TCNQ + e), respectively, whereas the third peak at +450 mV is a result of the CT complex (8-CB⁺TCNQ⁻) oxidation (8-CB⁺TCNQ⁻ → 8-CB⁺ + TCNQ + e).

The CV of the system with 100 and 300 μM of Pb(NO₃)₂ in the bathing solution displays a reduction (at -608 mV) and oxidation peak (at -448 mV). A large separation potential between peaks indicates that the system is irreversible. The height of the oxidation peak increases sharply with an increasing concentration of lead ions. The peak height's dependence on concentration is linear over a micromolar range of lead-ion concentration, with the lowest detectable ion level around 100 μM.

Although bare Pt wire of the same size, coated with Teflon but without a BLM deposited on its surface, shows a much more reversible CV signal (voltage separation between peaks is 60–80 mV), the lowest concentration of Pb ions detected by such a system is three orders of magnitude lower [100 mM of Pb(NO₃)₂] in the bathing solution. Thus, it is evident that the presence of a (8-CB + TCNQ) bilayer on the surface of a Pt wire modifies a platinum electrode's behavior with respect to Pb²⁺ ions, significantly increasing its sensitivity to them and changing peak heights, peak potentials, and peak shapes, as well.

When compared to results with a bare electrode, the increased sensitivity (by three orders of magnitude) of a platinum electrode covered with a (8-CB + TCNQ) bilayer seems to be a most significant finding. The observed increase in sensitivity indicates that (1) the interaction between the TCNQ present in a bilayer system and lead molecules is strong enough to keep a higher concentration of lead at the surface of a Pt-supported bilayer system than in the bulk solution, and (2) an energetic barrier for an electron exchange between an (8-CB + TCNQ) system, and lead is probably lower than that between a bare Pt electrode and lead.

To demonstrate further our novel method for self-organizing BLM formation on a solid substrate, a pigmented BLM from a GDO solution saturated with Zn PLC, according to the new procedure was formed. The properties of this organometallic complex containing BLM were characterized simultaneously by electrical and spectroscopic techniques. As it has been shown (24), the spectral sensitivity of a photocurrent corresponds well to the absorption spectrum of the Zn PCL in the BLM-

forming solution, and the magnitude of the photoresponse is linear to the light intensity used (at low light intensities). For details *see* Figure 3. A similar correspondence was found between the electrical properties of the supported BLM and those of BLM formed in the traditional manner. Thus, the findings provide clear evidence that the photoactive compound was incorporated into a supported BLM and that the photocurrent is a result of the Zn PLC photoexcitation.

Our method for self-assembly of BLMs on solid supports complements the conventional BLM technique that has been used extensively in membrane reconstitution and in basic studies (21–28). The s-BLMs, owing to their stability and ease of formation, offer an approach especially useful in the research and development of lipid bilayer-based sensors and molecular devices (29–36). For example, to develop optical devices based on s-BLMs, we have incorporated semiconductor materials into BLMs (35), which not only displayed nonlinear electrical properties

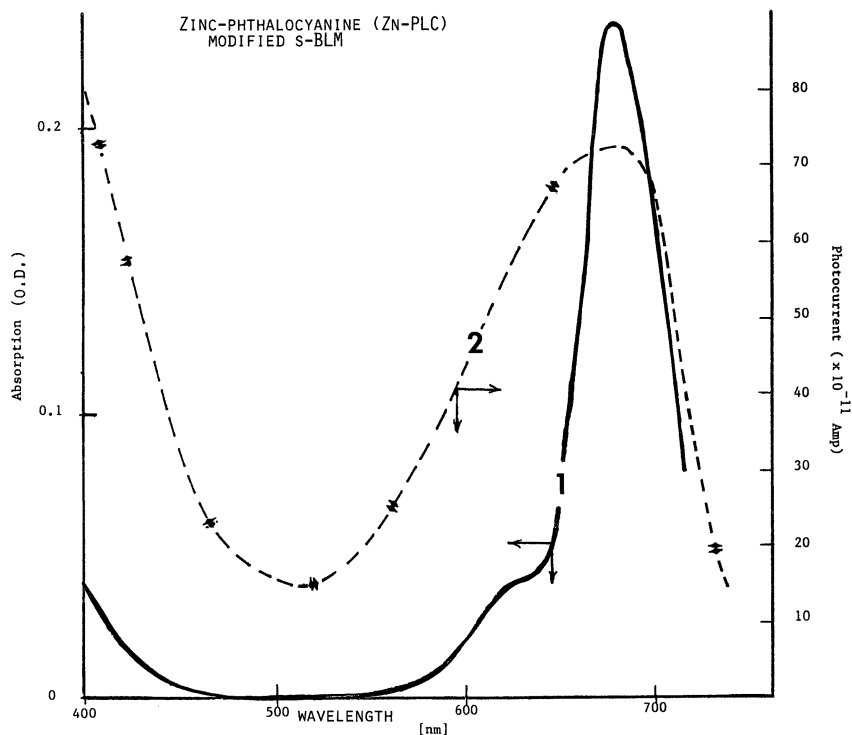


Figure 3. Photoelectric effect of a s-BLM containing Zn PLC. The photocurrent action spectrum (2) corresponds well with the absorption spectrum (1) of the lipid solution from which the s-BLM has been formed. (Reproduced with permission from reference 24. Copyright 1989 Elsevier Sequoia.)

but also displayed photoactive properties in the presence and absence of dyes (35). These features seem promising for their technical applications.

In one of our experiments we compared the peak current as a function of H_2O_2 concentration in 0.1 M KCl for the following systems: bare ss wire, ss wire cut under PC + cholesterol lipid solution, ss-wire cut under lipid solution with TCNQ, and ss-wire cut under lipid solution containing molecular iodine. In all these experiments the forward as well as backward peak currents (Figures 4 and 5) showed a sigmoid-shaped curve in dependence of H_2O_2 concentration. The analyses of results show a strong closeness of bare-wire experiments with those of wire cut under lipids with I_2 (Figure 6). The lipid conductivity exhibits similarity with those of s-BLM system containing I_2 .

To facilitate our delineation, we define "biosensors" as sensors that incorporate biomolecules as their principal sensing components. However, the word "biomolecule" is meant to include those compounds that exist in nature as well as in human-made analogues. It seems evident that, first of all, the key to the successful fabrication of supported BLM-based biosensors is the ability to incorporate active biomolecules (receptors) into the lipid bilayer, so that they are anchored with their activity and specificity intact (Figure 7). However, the process of incorporation that takes place in natural receptors is not easy to imitate, requiring expert knowledge and experience of scientists of diverse backgrounds. This and other technological challenges in biosensor- and

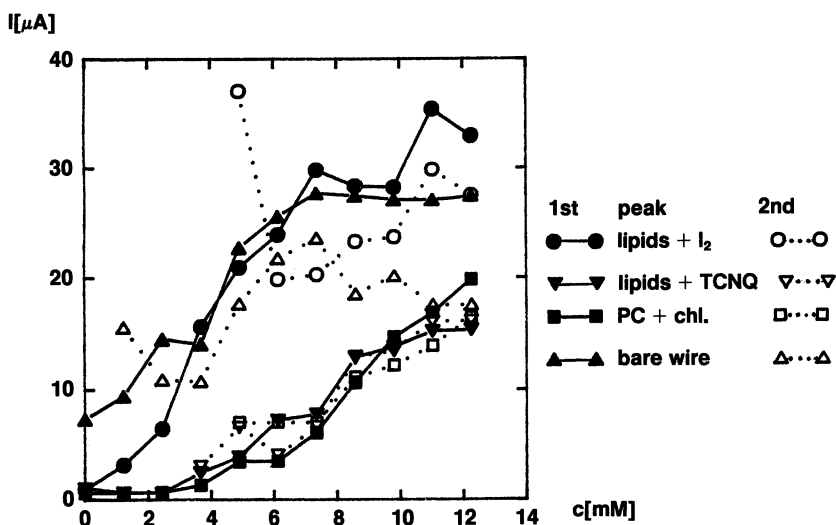


Figure 4. Peak current (forward direction) as a function of H_2O_2 concentration in 0.1-M KCl for different s-BLMs and for bare electrode (ss-wire).

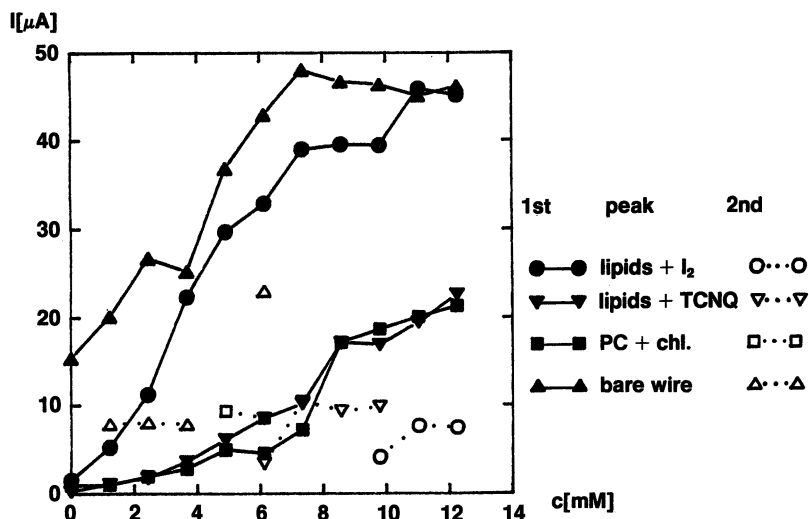


Figure 5. Peak current (backward direction) a function of H_2O_2 concentration in 0.1-M KCl for different s-BLMs and for bare ss-wire.

molecular-device development will be met eventually, since the basic design common to all such probes, based on a supported lipid bilayer, is now available for experimentation (21, 23, 28).

In our experiments concerning these questions, we worked with s-BLMs on metallic (silver wires coated with Teflon) and metal oxide (SnO_2 on glass) surfaces (26). The significance of these experiments is that the supported BLM (s-BLM) can be modified to achieve a particular function. This seems to be very important for the successful development of s-BLM-based biosensors in the near future.

Conclusions

The BLM system has been extensively investigated as a model of biological membranes since the early 1960s. However, until recently, relatively few attempts have been made to exploit their potential in practical applications such as sensors and molecular devices. From the viewpoint of membrane biophysics and physiology, biological membranes are essentially the basic structure of nature's sensors and devices. For example, the thylakoid membrane of green plants functions as an energy transducer, converting sunlight into electrical and chemical energy; in visual perception, the photoreceptor membrane of a rod's outer segment detects photons; and the plasma membranes of cells and organelles possess the ability to sense ions (e.g., differentiating Na^+ and K^+ with great specificity). Furthermore, the plasma membrane provides sites for a

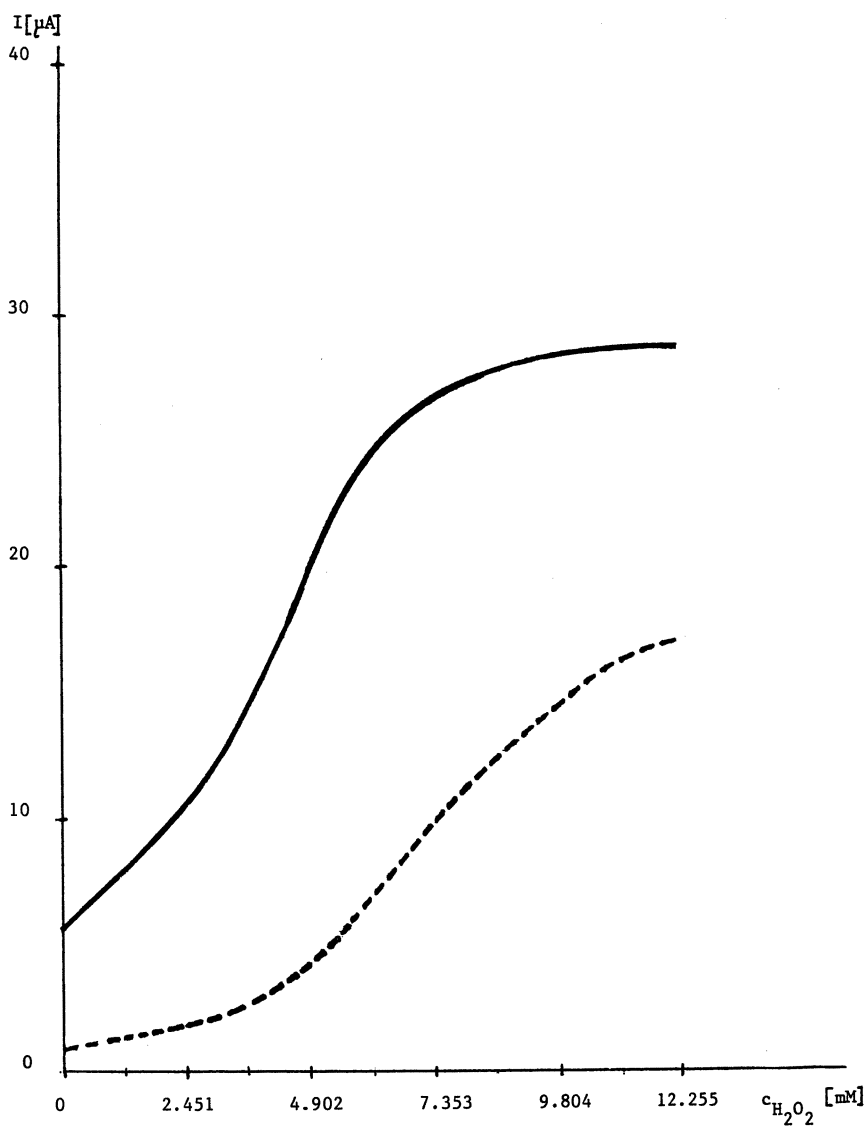


Figure 6. Typical sigmoid-shaped curves for the bare ss-wire electrode and for s-BLM containing I_2 (solid line) and for s-BLMs containing TCNQ (dashed line).

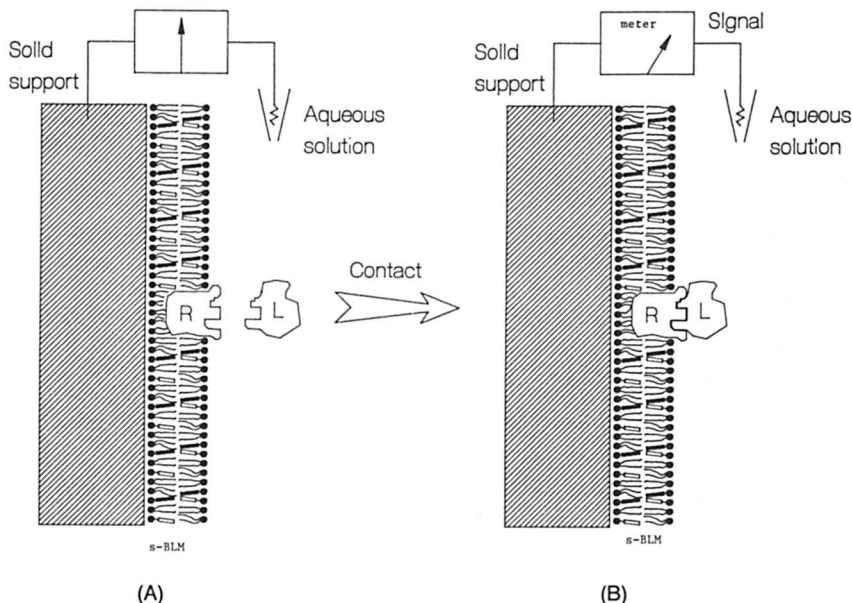


Figure 7. A general scheme illustrating ligand (L) and receptor (R) contact interaction in a s-BLM formed in accordance to the procedure given in Figure 1. Conformational changes of imbedded species (e.g., biomolecules and redox compounds) may lead to alterations in the electrical parameters of s-BLM, that can then be detected, amplified, transduced, and displayed by appropriate state-of-the-art microelectronics technology. (Reproduced with permission from reference 21. Copyright 1990.)

host of ligand–receptor contact interactions such as antigen–antibody formation. In view of the fact that these and numerous other vital functions are associated with cell membranes, it is not surprising that the past two decades or so have witnessed an enormous research effort directed toward membranes. Reconstituted planar BLMs and spherical liposomes have played a primary role in this research. In our work a new BLM system is described—a s-BLM system, which, with its ease of formation, its stability, and its long life, offers new possibilities for applications in biosensors and molecular electronics.

Acknowledgments

This work was supported by USARO Grant No. DAALO3–91–G–0062. We thank Robert Birge for organizing the Third International Symposium on Molecular Electronics and Biocomputing, held in New York City in 1991 in conjunction with the American Chemical Society Meeting.

References

1. *Chemistry of Biosurfaces Surface*; Hair, M. L., Ed.; Marcel Dekker: New York, 1971; Vol. 1, pp 234–348.
2. *Electrical Double Layers in Biology*; Blank, M., Ed.; Plenum: New York, 1986; pp 149–166.
3. Mueller, P.; Rudin, D. O.; Tien, H. T.; Wescott, W. C. *J. Phys. Chem.* **1963**, *67*, 534.
4. Tien, H. T. *Bilayer Lipid Membranes (BLM): Theory and Practice*; Marcel Dekker: New York, 1974.
5. Bangham, A. D. In *Progress in Biophysics and Molecular Biology*; Butler, J. A. V.; Noble, D., Eds.; Pergamon: New York, 1968; Vol. 18, pp 29–95.
6. Antonov, V. F.; Rovin, Y. G.; Trofimov, L. T. *A Bibliography of Bilayer Lipid Membranes*; All Union Institute for Scientific Information: Moscow, Russia, 1976.
7. Antolini, R.; Gliozzi, A.; Gorio, A. *Transport in Membranes: Models Systems and Reconstitution*; Raven: New York, 1982; p 57.
8. Fendler, J. H. *Membrane Mimetic Chemistry*; Wiley: New York, 1982.
9. Koryta, J. *Ions, Electrodes and Membranes*; Wiley: New York, 1982; p 197.
10. *Thin Liquid Films*; Ivanov, I. B., Ed.; Marcel Dekker: New York, 1988; p 927.
11. *Progress Surface Science*; Davison, S. G., Ed.; Pergamon: New York, 1989; Vol. 30, p 1.
12. *Surfactants in Solution*; Mittal, K. L., Ed.; Plenum: New York, 1989; Vol. 8, p 133.
13. Robinson, J. N.; Cole-Hamilton, D. J. *Chem. Soc. Rev.* **1991**, *20*, 49.
14. Dryhurst, G.; Niki, K. *Redox Chemistry and Interfacial Behavior of Biological Molecules*; Plenum: New York, 1988.
15. Mauzerall, D. In *Light-Induced Charge Separation in Biology and Chemistry*; Gerischer, H.; Katz, J. J., Eds.; Springer-Verlag: Berlin, Germany, 1979; p 241.
16. Gerischer, H. In *Topics in Applied Physics*; Seraphin, B. O., Ed.; Springer-Verlag: Berlin, Germany, 1979; pp 115–172.
17. Thompson, M.; Krull, V. J.; Bendell, L. I. In *Proceedings of the International Meeting on Chemical Sensors*; Seiyama, T.; Fueki, K.; Shiokawa, J.; Suzuki, S., Eds.; Elsevier-Kodansha: New York, 1983; p 576.
18. Janata, J. In *Proceedings of the Symposium on Chemical Sensors*; Turner, A. P. F., Ed.; The Electrochemical Society, Inc.: Pennington, NY, 1987; p 258; *J. Anal. Chem.* **1990**, *62*, 33R.
19. Ringsdorf, H.; Schlarb, B.; Venzmer, H. *J. Angew. Chem. Int. Ed. Engl.* **1988**, *27*, 113–158.
20. Krull, U. J. *Anal. Chim. Acta* **1987**, *197*, 203.
21. Tien, H. T. *Adv. Mater.* **1990**, *2*, 316.
22. Tien, H. T.; Salamon, Z.; Kochev, V.; Ottova, A.; Zviman, M. *Symposium on Molecular Electronics: Biosensors and Biocomputers*; Hong, F. T., Ed.; Plenum: New York, 1989; p 259.
23. Tien, H. T. *J. Surf. Sci. Technol.* **1988**, *4*, 1–21; *J. Clin. Lab. Anal.* **1988**, *2*, 256–264.
24. Tien, H. T.; Salamon, Z. *Bioelectrochem. Bioenerg.* **1989**, *22*, 211–218.
25. Wardak, A.; Tien, H. T. *Bioelectrochem. Bioenerg.* **1990**, *24*, 1–11.
26. Zviman, M.; Tien, H. T. *Biosens. Bioelectron.* **1991**, *6*, 37–42.
27. Martynski, T.; Tien, H. T. *Bioelectrochem. Bioenerg.* **1991**, *25*, 317–324.

28. Tien, H. T.; Salamon, Z.; Kutnik, J.; Krysinski, P.; Kotowski, J.; Ledermann, D.; Janas, T. J. *Mol. Electron.* **1988**, *4*, S1.
29. *Molecular Electronic Devices: Proceedings of the Third International Symposium*; Carter, F. L.; Siatkowski, R. E.; Wohltjen, H., Eds.; North-Holland: Amsterdam, The Netherlands, 1988; pp 209–225.
30. Reichert, W. M.; Bruckner, J.; Joseph, J. *Thin Solid Films* **1987**, *152*, 345.
31. Cherny, V. V.; Mirsky, V. M.; Sokolov, V. S.; Markin, V. S. *Bioelectrochem. Bioenerg.* **1989**, *21*, 373.
32. Mountz, J. M.; Tien, H. T. *Photochem. Photobiol.* **1978**, *28*, 395.
33. Yoshikawa, K.; Hayashi, H.; Shimooka, T.; Terada, H.; Ishii, T. *Biochem. Biophys. Res. Commun.* **1987**, *145*, 1092.
34. Fare, T. L.; Rusin, K. M.; Bey, P. P. *Sens. Actuators* **1991**, *3*, 51.
35. Kutnik, J.; Tien, H. T. *Photochem. Photobiol.* **1987**, *46*, 413.
36. Schuhmann, W.; Heyn, S.-P.; Gaub, H. E. *Adv. Mater.* **1991**, *3*, 388.

RECEIVED for review March 12, 1992. ACCEPTED revised manuscript March 3, 1993.

Self-Assembling Tubules from Phospholipids

R. Shashidhar and J. M. Schnur*

Center for Bio/Molecular Science and Engineering, Code 6900,
Naval Research Laboratory, Washington, DC 20375

We present a state-of-the-art review on the fundamental aspects and potential applications of tubules formed from phospholipid molecules. Tubules constitute a unique form of self-assembling microstructures. An understanding of their formation is important to enhance our current understanding of the thermodynamics and intermolecular forces responsible for the self-assembly of amphiphiles into nonspherical structures. Tubules also enable us to explore the potential of developing different types of advanced materials using self-assembling microstructures.

PHOSPHOLIPIDS ARE IMPORTANT COMPONENTS of biological membranes. They are amphiphilic and can self-assemble into a variety of molecular aggregates or microstructures in aqueous solutions. These microstructures are, in general, topologically spherical in shape. The fundamentals of the self-assembly of spherical microstructures formed by amphiphilic molecules have been discussed in terms of intermolecular forces in several recent books and review articles (1–3). Self-assembly of lipid molecules into nonspherical structures is less common. The first observation of helical self-assembled structures was by Nakashima et al. (4). Earlier studies by Kunitake and co-workers (5–7) on some amino acid-derived amphiphiles gave an indication of superstructures with remarkably high circular dichroism. Following-up on this, Nakashima et al. (4) made a direct optical observation of helical superstructures in aqueous dispersions of several double-chain ammonium amphiphiles. This was followed by Kunitake and Yamadas' observation (8) of similar helical structures in single-chain amphiphiles.

* Corresponding author

0065-2393/94/0240-0455\$08.00/0
© 1994 American Chemical Society

Independent of these observations of Kunitake and his group, Ihara and co-workers (9) also found the existence of helical self-assembled aggregates in a series of double-chain alkyl amphiphiles with polyamino head groups. Similar aggregates were observed also from poly(L-aspartic acid) derivatives (10–11) and from single- and double-chain phosphate amphiphiles (12). At about the same time as the first observation of helical structures by Nakashima et al. (4), Yager and Schoen observed (13) another type of nonspherical structure: a hollow cylindrical structure called “tubules”, while studying the phase behavior of a synthetic diacetylenic phospholipid, 1,2-bis(10,12-tricosadinyoyl)-*sn*-glycero-3-phosphocholine, hereafter abbreviated as DC_{8,9}PC. A tubule is morphologically similar to a soda straw (Figure 1). Typically, the diameter is of the order of 0.5 μm whereas the lengths can range from a few micrometers to a few hundred micrometers. The thickness can vary from one bilayer ($\approx 60 \text{ \AA}$) to several bilayers. Quite often, the tubules appear to consist of helically wrapped bilayers with the edges of the bilayer being packed together. However, in some cases, this helical wrapping is not seen.

Since the observation of Yager and Schoen, tubules have formed the subject matter of a large number of studies (14, 15). This interest is essentially due to two reasons. First, tubules constitute a unique form of self-assembly and a fundamental understanding of their structure and formation is expected to enhance our current understanding of the thermodynamics and intermolecular forces responsible for the self-assembly of amphiphiles into nonspherical structures. Also, the recently

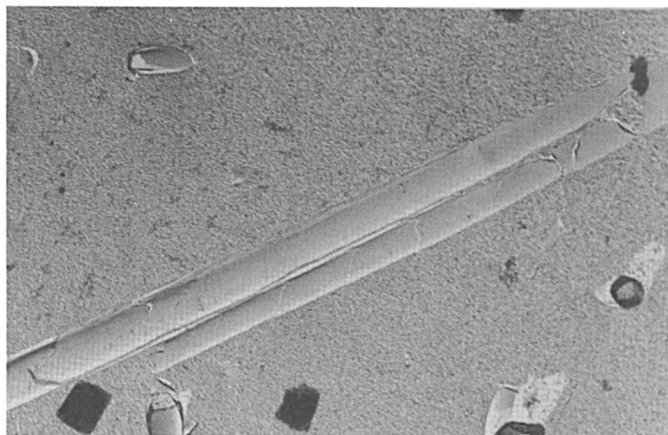


Figure 1. Electron micrograph of a “tubule”, a hollow cylinder formed from DC_{8,9}PC. The diameter of the tubules in this picture is $\approx 0.5 \mu\text{m}$ whereas the length is $\approx 12 \mu\text{m}$. The wall of the tubule is made up of helically wrapped bilayers.

observed single-bilayer thick tubules (16) constitute finite-size quasi-two-dimensional (2D) systems and therefore serve as models to elucidate the statistical mechanics of 2D and quasi-2D systems. The second reason for the considerable current interest in tubules arises from their potential use in many areas of technological applications. For example, they can be coated with different materials (metals as well as alloys) oriented and then cast into a composite. Such a composite will, in turn, have many unique material properties of relevance to different areas of applications. Also, because tubules are hollow, they can be used for controlled-release applications. The proof of the principle for many of these applications has already been demonstrated. In this chapter, we briefly review the current state-of-the-art findings regarding tubule formation with emphasis on the most recent results and then discuss, in some detail, the application aspects.

Tubule Formation

Tubules are known to form from diacetylenic phosphocholine lipids ($DC_{m,n}PC$) with the general chemical formula shown in Figure 2 (14, 15, 17). The lipid molecule contains the phosphocholine head group, that is, glycerol backbone and two diacetylene ($-C\equiv C-C\equiv C-$) moieties in the two identical hydrocarbon chains. The variables m and n refer to the number of methylene groups between the head group and the diacetylene moiety and between the diacetylene moiety and the terminal methyl group, respectively. Essentially, tubules are formed by two methods: thermal method (18–20) and precipitation (21, 22). In the case of the thermal method, the lipid is dissolved in a solvent system such as water or alcohol and water, heated to a temperature above the chain melting temperature (T_m), and then cooled. Tubules are formed when the solution is cooled below T_m . In the case of the second method, the lipid is dissolved in the alcohol and then a second solvent, usually water, is added so that the tubules precipitate out of the solution. The thermal method of tubule formation has been studied in some detail by calorimetric techniques. It has been demonstrated that when water is used

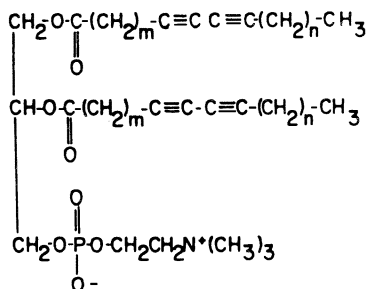


Figure 2. General chemical formula of $DC_{8,9}PC$.

as the solvent, the formation of tubules is dependent on the size of the vesicles in the L_α or liquid-crystalline phase. When the vesicles are large (the multilamellar vesicles), tubule formation is seen as a phase transition on cooling from the L_α phase below T_m (22). However, when the vesicles are sonicated into small unilamellar vesicles (SUVs) and then cooled below T_m , no tubules formation is seen. Instead, a stacked bilayer structure (referred to as “sheet”) has been observed (19) to form at 2 °C. Heating and cooling of this sheetlike structure then yields tubules. The reasons for this dependence of tubules formation on the thermal history and morphology of the sample are not yet clear.

On the other hand, when an ethanol and water system is used as the solvent, tubule formation is seen reproducibly as a phase transition without any dependence on sample history. It also has been shown (23) that tubule formation is strongly dependent on the volume fraction of the ethanol in the solvent as well as on the lipid concentration. In fact, a “window” of ethanol fraction (60–80%) exists in which tubule formation is seen. At lower fractions, the solution transforms on cooling to a nontubular solid form, whereas for higher fractions, the lipid is fully dissolved in the solvent at room temperature. A similar window of tubule formation has been observed (16) for methanol–water and propanol–water solvents as well. The window systematically shifts to a higher volume fraction of the solvent with decreasing length of the alcohol chain. Also, the efficiency of tubule formation is seen to increase with decreasing lipids concentrations for all alcohol–water systems.

All these methods of tubule formation involve water as the solvent or as one of the constituents of the solvent systems. Also a report has been made (24) on the formation of cylindrical microstructures from DC_{8,9}PC when acetonitrile is used as the solvent. Although high-resolution electron-microscopic studies are needed to establish if these cylindrical structures are similar to tubules, this observation is nevertheless very important: It shows that lipid molecules can self-assemble without the presence of bulk water. It would be of interest to study the role played by bound water in the self-assembly.

Dependence of Tubule Formation on Intrinsic (Molecular) Parameters

Tubule formation has been studied for a series of DC_{*m,n*}PC lipids (19) varying both *m* and *n*, keeping *m* and *n* in the range of 15–23. In all these cases, tubules of approximately the same diameter were observed, showing that the location of the diacetylenic unit in the chain is not crucial for the formation of the tubules. However, the presence of this moiety is very important; lipids without a diacetylenic unit in both of the chains have not been observed to form tubules. Also, a lyso lipid

(i.e., a lipid with only a single chain) does not promote tubule formation. Some recent studies (25) on the effect of the head group modification have been made. These studies indicate that the size and shape of the head group affects the tubule diameter considerably. Another relevant molecular parameter is the nature of the chirality. The D and L forms of DC_{8,9}PC as well as the racemate form tubules (26). Electron micrographs show that tubules formed from the racemate have both right and left helically wrapped structures, which is likely to be due to molecular-level phase separation of the D and L forms of the lipid, indicates that the macroscopic chirality of the tubule is probably dictated by the molecular chirality. However, the observation of somewhat similar cylindrical morphologies in a nonchiral surfactant, namely, di(hexa cosa-12,14-diyne)dimethyl ammonium bromide (27), raises the question whether molecular chirality is essential for tubule formation. Because all of the above-mentioned tubule-forming molecules do contain the diacetylenic moiety in their chains, it is likely that this is an important factor. We shall discuss this aspect in subsequent sections.

Structure of Tubules. Tubules consist of bilayers that are helically wrapped into the form of hollow cylinders (14, 15). The diameter of the tubule formed from DC_{8,9}PC does not appear to be dependent upon the processing conditions. Typically, tubules grown from DC_{8,9}PC have diameters of about 0.5 μm regardless of the solvent system used and the method of preparation. The thickness can show small variations depending upon the number of bilayers that constitute the wall. Recently, it has been shown by Ratna et al. (16) that tubules grown from methanol-water are one bilayer thick, whereas those obtained from ethanol-water or water have multiple bilayers as walls. The methanol-grown tubule is therefore a very special instance of a self-assembled finite-size 2D system. High-resolution studies on these single-walled tubules are expected to enhance our understanding of melting and phase transitions in finite-size systems.

Several investigations to elucidate the structure of tubules have been conducted. Infrared studies (28, 29) on tubules have shown that tubules have highly ordered acyl chains. Raman studies (28, 30, 31) have led to the observation of the longitudinal-acoustic modes indicating that the chains are fully ordered and are in an all-trans configuration. Also, the infrared spectra of tubules, the stacked bilayer sheets obtained on cooling the sonicated unilamellar residues (32), and of nontubular solids (22) are found to be similar. Although these studies do indicate that the chains of the tubule are as highly ordered as in a nontubular solid, this cannot be taken as proof of the existence of true long-range crystalline order in the tubule. This aspect will be discussed in detail in a subsequent section.

The first X-ray diffraction studies on tubules are attributed to Rhodes et al. (32). A multilayer stack of flattened “dry” tubules were obtained by centrifugation and were then mounted on a curved glass surface. Low-angle X-ray diffraction data collected on such samples shows 16 orders-of-diffraction maxima in the equatorial direction, the layer spacing being in the range of 68 to 61 Å depending upon the temperature and relative humidity. The observation of so many higher harmonics clearly shows that the lamellar or bilayer order is extremely high in the tubules. These data also revealed a very small unit-cell size. The corresponding one-dimensional (1D) electron-density profile yielded a chain tilt of 28° with respect to layer normal. A partial-chain interdigitation was also suggested by this profile. However, subsequent data as well as more refined computations by Blechner et al. (33) show that this is not the case. Blechner et al. have also carried out low-angle X-ray diffraction studies on DC_{8,13}PC and DC_{9,12}PC. Their data indicate that the acyl chains in DC_{9,12}PC are more disordered than in DC_{8,9}PC.

Caffrey et al. (34) carried out X-ray studies on hydrated tubules as well as on sheets formed from SUVs (the lipid being DC_{8,9}PC). The X-ray diffractograms of tubules (Figure 3) show 15 orders-of-diffraction maxima. These data, which have about the same resolution (4 Å) as Rhodes et al. (32), are consistent with a 32° tilt of the chain, minimal-chain interdigitation, and fully extended all-*trans* methylene segments (Figure 4). The sample conditions of Caffrey et al. (34) are different from those of Rhodes et al. (32), who have studied hydrated tubules, whereas Caffrey et al. studied dry tubules. Despite this difference, the results are essentially the same. Caffrey et al. also have assigned the thermodynamic phase of tubules as L_c or a lamellar-crystalline phase with a lamellar spacing of 66.4 Å. Upon heating L_c , it is found to transform into the liquid-crystalline L_α phase with $d = 72.5$ Å and with a

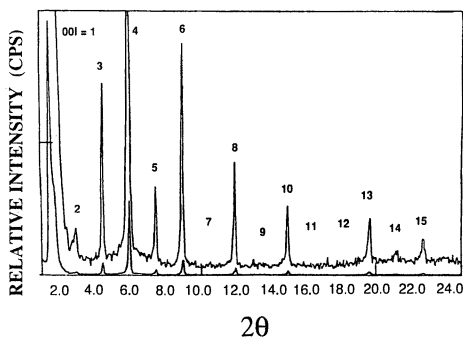


Figure 3. Θ - 2Θ diffraction scans of DC_{8,9}PC tubules. Fifteen orders of diffraction maxima are seen that show the high degree of lamellar order. (Reproduced from reference 30. Published 1987 Gordon & Breach.)

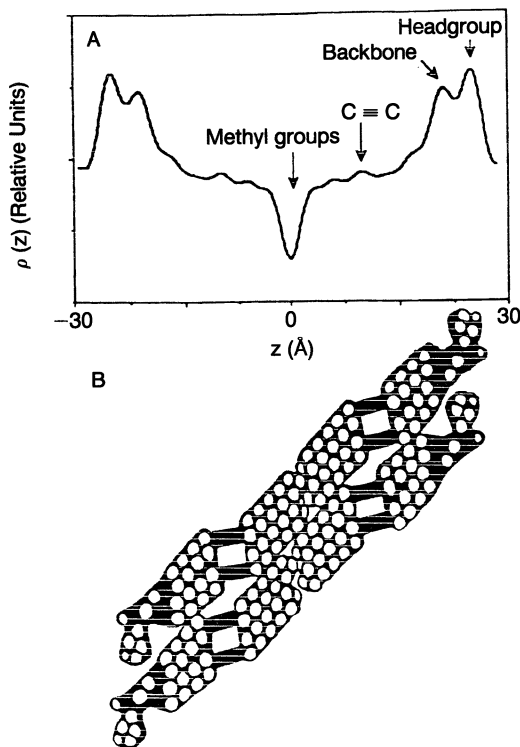


Figure 4. One-dimensional electron-density profile of $DC_{8,9}PC$ in tubule morphology at 57% RH and 22 °C (A). The origin of the various peaks and valleys in the profile is indicated above the profile and is referenced to the proposed molecular conformation of the lipid in the tubule morphology as shown in B. The lamellar repeat distance is 59 Å and the tilt of the long axis is 32°. (Reproduced from reference 34. Published 1991 American Chemical Society.)

diffuse scattering around 4.5 Å due to the fluidlike packing of the hydrocarbon chains. Reversing the temperature retrieves the L_c phase with the same periodicity, showing that the transition to the L_c phase (tubules) from L_α is reversible. The diffraction patterns of the hydrated tubules are identical to those of sheets (obtained by cooling SUVs) showing that the sheets and the tubules should be structurally similar. This result is consistent with the Fourier transform infrared studies (29).

There has also been an electron-diffraction study (35) on dry tubules formed from $DC_{8,9}PC$. The diffraction spots have been indexed as belonging to a monoclinic unit cell. It has also been found that a six-layer Langmuir–Blodgett film of the same materials also has the same unit cell. The question may be asked whether tubules have a true long-range

crystalline order. None of the experiments carried out so far have sufficient resolution to probe the extent of the correlation length. The observation of a large number of higher harmonics of the (001) spacing only indicates that the lamellar order is extremely well-defined, but does not necessarily prove the crystalline nature of the tubules. [For instance, the liquid-crystal L_α phase, which has fluidlike in-plane order, is known to show several orders of diffraction maxima (36)]. Also, no data are available on tubules in both their dry and hydrated states.

Some of these questions have been addressed in the recent experiments by Thomas et al. (37). These experiments have been carried out on dry tubules as well as on tubules hydrated in the ethanol–water solvent system. The diffraction pattern for the dry tubule consists of a large number of peaks including combination reflections. The data have been indexed as belonging to a monoclinic unit cell, in conformity with the electron-diffraction results of Lando and Sudiwala (35). On the other hand, the tubules hydrated in ethanol–water have a much smaller number of diffraction peaks and, more significantly, the combination reflections are absent. This, in turn, shows that interlayer correlations, which exist in dry tubules, are definitely absent in the hydrated tubules. The in-plane structure of the hydrated tubules has also been studied. These results indicate that the in-plane order for the hydrated tubules is finite, but is much greater than that expected for a fluid. Thus, we can infer that the hydrated tubule is either a 2D crystal with a finite correlation length or a hexatic structure of the kind seen in both thermotropic and lyotropic liquid crystals (38, 39). Further studies are needed to clarify the situation.

Effect of Electric and Magnetic Fields on Tubules. Rosenblatt and co-workers (40–42) studied the effects of both electric and magnetic fields on tubules. They measured the magnetic birefringence of dilute sample of tubules of DC_{8,9}PC in magnetic fields of up to 4 T (40). The tubules were found to orient with their long axes parallel to the field direction. The order parameter $S > 0.95$ for fields $H > 2$ T. Here $S \equiv \langle P_2(\cos \Theta) \rangle$, P_2 being the second Legendre polynomial given by $\frac{1}{2}(3 \cos^2 \Theta - 1)$ and Θ being the angle between the tubule axes and the magnetic field. From known distributions of lengths and the number of bilayers in the walls, Rosenblatt and co-workers calculated the diamagnetic anisotropy ($\Delta\chi_m$) of tubules to be -7×10^{-9} erg cm⁻³ G⁻². This value of $\Delta\chi_m$ is of the same order of magnitude as values obtained for vesicles of egg lecithin and dimyristoyl lecithin. This value is, however, smaller than the value of -9.6×10^{-9} for dimyristoyl phosphatidylcholine (DMPC). This is not surprising because in DC_{8,9}PC the tails consist of both double and triple carbon–carbon bonds, whose susceptibility anisotropies are of opposite sign compared to that of a single bond. Also,

because tubules exhibit different magnetic susceptibilities perpendicular and parallel to the tubules axis, an applied field imparts a torque on the tubule to minimize the total magnetostatic enthalpy. By effectively inducing complete or nearly complete orientational order, it should be possible to extract the volume magnetic susceptibility $\Delta\chi_m$. Rosenblatt et al. (40) found that the $\Delta\chi_m$ evaluated in this manner was simply an orientational average of the individual molecular susceptibility anisotropies. Thus, it can be concluded that the alignment of the macroscopic tubules arises from a "cooperative effect" of the intrinsic diamagnetic anisotropy of the individual DC_{8,9}PC molecules.

Li et al. (41) performed light-scattering measurements on tubules subjected to an electric field. When using alternating current (ac) fields, it was found that tubules exhibited considerable orientational order for fields as small as 30 V/cm; at higher fields turbulence precluded the increase of orientational order. By fitting the data for fields less than 30 V/cm, Li et al. evaluated the volume electric susceptibility anisotropy $\Delta\chi_E$. It was found that $\Delta\chi_E$ was nearly three orders of magnitude larger than what would be expected if the volume susceptibility was merely the sum of the molecular anisotropies. It has been suggested that this increase arises from an orientational anisotropy of the total electrostatic enthalpy for a dielectric tubule in an electric field. The effective value of $\Delta\chi_E$ has also been determined by Wood et al. (42) from birefringence measurements on the tubule under electric fields. This value agrees with that obtained from the light scattering data of Li et al. (41). Thus, the magnetic- and electric-field orientations of the tubules are shown to rely on two vastly different mechanisms.

Mechanism of Formation of Helical Structures and Tubules. Several theoretical approaches have attempted to explain the mechanism of formation of helical bilayer structures as well as of tubules. These approaches are summarized in this section.

The first theoretical attempt to explain formation of helical bilayer structures is due to Helfrich (43). The basic idea behind his approach is that the edges of a single solid bilayer consisting of chiral molecules may prefer a state of torsion similar to that of certain polymers (44) and to the spontaneous twist of cholesteric liquid crystals (45). In this approach two elastic moduli, the bending rigidity of the frozen bilayer and the torsion coefficient of the bilayer edge, dictate the helical geometry. The theory predicts that for the helical structure to be in equilibrium, the gradient angle of the helix (Φ) should be 45° and the pitch (P) is $2\pi a$, where a is the radius of the helix (Figure 5). The bending rigidity of the frozen bilayer is supported by experiments: Φ is found to be 45° for helical structures and even for a tubule consisting of fully wound helical strips. The second prediction on the relation between P

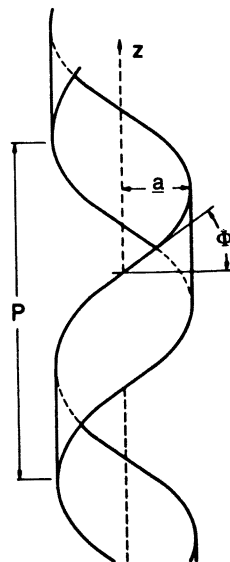


Figure 5. Schematic of a helically wound strip. Φ is the gradient angle of the helix, P is the pitch, and a is the radius of the helix. (Reproduced from reference 43. Published 1986 American Institute of Physics.)

and a has not been quantitatively established experimentally. It should also be pointed out that the theory is for a single solid bilayer strip and has to be modified to be applicable to several bilayer thick strips.

More recently, Helfrich and Prost (46) proposed an improved theory that explains the formation of helical ribbons by fluid membranes as well as by crystalline membranes. Helfrich and Prost introduce a linear term linked to molecular chirality in the bending energy of membranes with C_2 or D_2 symmetry. This symmetry is analogous to the linear term in the elastic energy of smectic liquid crystals previously introduced by deGennes (45). The introduction of the linear term allows cylindrical curvatures for the membranes. Helfrich and Prost find that this term alternates in sign, depending on the direction of a cylindrical curvature. The consequences of this alternation on anisotropic solid membranes and on tilted fluid bilayers have been considered. According to their model, both crystalline (solid) and fluid membranes are capable of forming helical ribbons and tubules, depending upon the width of the bilayer ribbon.

In more recent theoretical treatments (47, 48) the tilt and surface shape-equilibrium equations for tilted chiral bilayers have been derived in analogy with cholesteric liquid crystals. On a cylindrical surface, the field-of-tilt directions of the molecules forms a right helix with 45° gradient angle for $k_2 > 0$ or a left helix with -45° for $k_2 < 0$, where k_2 is the cholesteric chiral-curvature modulus. In addition, the theory explains the formation of another type of helical structure, which was not considered by any of the previous treatments, twisted strips or helicoids.

By including additional terms in the elastic free energy, Ou-Yang and Liu made predictions on the sizes of tubules as well as of helical structures that appear to be in reasonable agreement with experiments.

Chappell and Yager (49) recently proposed a model for crystalline order within helical and tubular structures of chiral bilayers. In this model, the packing interactions transverse to the helical chains is very important for the stability of a crystalline-cylindrical bilayer. Theoretical approaches (47, 48, 50) consider the formation of a cylindrical tubule from a spherical surface. Because of the cooperative tilt of the molecules in the bilayer, a closed-spherical surface constituted by such a tilted bilayer will have two singular points. In the presence of sufficiently strong long-range positional order, these defects cost too much energy and the structure opens spontaneously to form a hollow cylinder. Ou-Yang and Liu have also discussed (47, 48) the transitions from a spherical surface to helical structures and then to tubules.

In all these approaches, the anisotropic packing within the bilayer plays an important role in stabilizing the cylindrical curvature. However, a completely different theoretical approach has been adopted by deGennes (51) to explain tubules formation. Recognizing that the bilayers forming the tubule have the same symmetry as that of the ferroelectric-smectic C* phase, deGennes has suggested electrooptic buckling as the mechanism by which tubules form. The curvature in this case is expected to arise from an electrostatic attraction of the edges of a bilayer. This approach predicts that the addition of salt should suppress tubule formation. However, recent experiments (52) using zwitterionic head-groups do not seem to support this prediction. It is possible that deGennes' predictions might be perturbed by the zwitterionic charges. Therefore, similar experiments on tubules from phospholipids with a charged head group would be of interest.

Thus, the different theoretical approaches are successful in explaining several aspects of geometry of tubules and their formation. However, none of these explains all the experimental observations. Some key questions, for example, what are the factors that determine the width of the bilayer constituting the tubules, are yet to be addressed quantitatively. Also, none of the theoretical models predict precisely the molecular aspects that may be responsible for tubule formation.

Potential Applications of Tubules. Tubules have many unique features associated with their geometry. First, they are hollow cylindrical microstructures with micrometer diameters and a wide range of aspect ratios, leading to a large degree of shape anisotropy. Second, the dimensions of tubules can be controlled by manipulating either the molecular structure of the lipid or the processing conditions under which the tubules form, enabling us to "tune" the shape anisotropy. Third, a

tubule, due to its cylindrical symmetry and a small hollow core, is essentially a “microvial” in which a solid or liquid can be encapsulated. As already mentioned, tubules can be coated with a variety of metals, and therefore become “templates” for fabricating anisotropically shaped metallic particles of different sizes.

A combination of all these features makes tubules extremely attractive from the point of view for many technological applications. In particular, the tubules become building blocks for fabricating novel materials with unique anisotropic electromagnetic properties. Tubules can also be used to fabricate special types of devices. In addition, tubules can be used for many controlled-release applications. The proof of principle regarding many of the areas of potential applications of tubules have already been demonstrated. We briefly discuss some of these areas.

Materials with Anisotropic Electric and Magnetic Properties. Several types of novel materials with highly anisotropic electric and magnetic properties can be fabricated with tubules coated with a suitable metal (53). The metalized tubules (Figure 6) are usually dispersed in an epoxy and aligned with a small magnetic field, the tubules orienting in the field direction. This alignment is then locked-in by curing the epoxy. The resultant composite can be sectioned parallel or perpendicular to the long axis of the tubule.

Tubules coated with nickel and cast into a composite as discussed previously exhibit extremely interesting dielectric properties. Both the real and imaginary part of the dielectric permittivity have been measured (54) for giga Hertz frequencies up to a weight fraction of 0–4% tubules in the composite (Figure 7). The real part (ϵ_R), measured at 9.5 GHz,

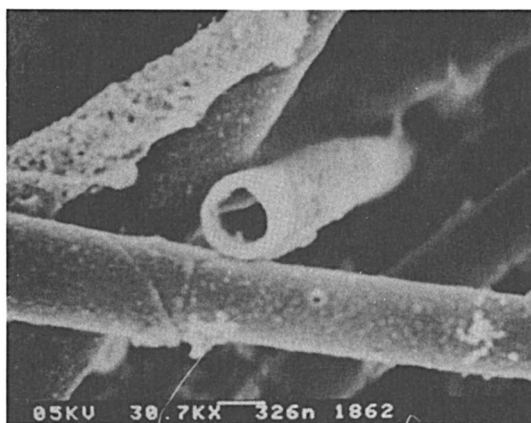


Figure 6. Scanning electron-microscope photograph of nickel-coated lipid tubules.

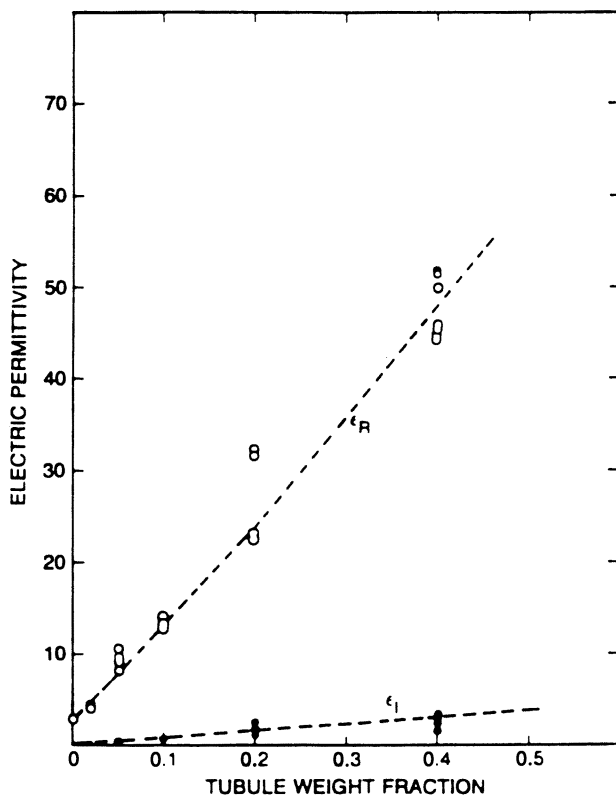


Figure 7. Real and imaginary parts of the dielectric permittivity of a composite consisting of aligned nickel-coated tubules plotted against the weight fraction of the tubules in the composite. The measuring field is parallel to the axis of the tubules. (Reproduced from reference 54. Published 1990 American Institute of Physics.)

shows that a strong increase with increasing weight fraction, from about 2 for the pure epoxy (without tubules) to about 55 at 0.3 weight% loading of metalized tubules. For the same loading fraction, the imaginary part of the dielectric permittivity (ϵ_i) also increases considerably (Figure 7). The essentially linear dependence of both ϵ_R and ϵ_i on the loading fraction is in good agreement with the curves evaluated from a simple theoretical treatment of the interaction of electromagnetic radiation with a dilute dielectric medium consisting of noninteracting metalized tubules. Such a dielectric medium with very low losses and large anisotropic dielectric constant has great promise in many areas of technological applications, such as development of microwave capacities and waveguides.

It is also possible to achieve anisotropic magnetic properties for a tubule-based composite by using tubules coated with a ferromagnetic material such as nickel and permalloy (an iron–nickel alloy) (55). Hysteresis curves measured for field directions parallel and perpendicular to the long axis of the tubules show pronounced differences (56). The values of permeability evaluated from the initial slopes of the B–H curve are found to be highly anisotropic with $\mu_{\parallel} \approx 50$ and $\mu_{\perp} \approx 5$. Another interesting feature was the small coercivity (width of the hysteresis curve at zero field) for both parallel and perpendicular directions. Also, the magnetization direction for a bulk-sample, sectioned perpendicular to the tubule axis, lies normal to the surface of the sample (along the tubule direction). These properties are usually typical of thin magnetic films. It is unique that a bulk composite of magnetic tubules exhibits magnetic properties that are characteristic of thin magnetic films.

Yet another attractive feature associated with tubules with regards to their magnetic properties exists because tubules can have different aspect ratios (length-to-diameter ratio), it is possible to control the shape anisotropy of the medium. In addition, it is possible to metalize tubules in the presence of large magnetic fields. Consequently, it should be possible to control the crystalline anisotropy when the tubules are coated with materials such as cobalt with a large inherent anisotropy. Thus, tubules provide the unique opportunity to manipulate both the shape anisotropy and the crystalline anisotropy of a medium. A combination of all these features makes a tubule-based magnetic composite attractive for many areas of applications such as magnetic recording, electromagnetic induction shielding, mode filters, and high-density packaging applications.

Devices and Systems Using Metalized Tubules. As discussed previously, metalized tubules have several features: They have small diameters (0–5 μm), their aspect ratios can be varied from about 20 to over 200, and they are ferromagnetic and electrically conducting. In addition, tubules can be oriented in an epoxy matrix and can be cured in this aligned state to form an uniaxially conducting composite. These features can be used to fabricate a variety of tubule-based devices and systems that will be used in many technological areas. In this section, a specific type of device, namely a microcathode fabricated from metalized tubules, is discussed. Many technological areas like high-energy particle accelerators, laser-pumping systems, and microwave devices use electron-beam sources. Presently available electron sources can be categorized into three types: typical thermally excited cathodes (vacuum electronics), laser-activated photo-emitters, and field emitters. Two types of field emitters, exploding field emitters (or plasma cathodes) and vacuum field emitters, exist. The generation of macroscopic electron-beam

currents through vacuum-field emission from a large number of emission sites requires a surface with a complex microstructure. Fabrication of surfaces suitable for vacuum-field emission is usually done using microlithographic techniques. Recently, a novel way of fabricating a microcathode array using metalized tubules has been demonstrated (57, 58). The structure essentially consists of hollow metallic tubules protruding by uniform distance from the base electrode (Figure 8). Because the edges of the tubules are thin and sharp, a very-large local electric-field enhancement results allowing for the vacuum-field emission of significant current densities. It has also been demonstrated (57, 58) that the observed continuous field emission is in accordance with the process of quantum-field emission described by the Fowler–Nordheim expression (59) (Figure 9). It is remarkable that an array of microcathodes, fabricated with self-assembled tubule structures as templates, offers an interesting alternative to the microlithographic techniques. Similar possibilities are likely in many other areas like cross talk reduction in multichip modules and high-density interconnects for pyroelectric detectors.

Tubules for Controlled Release Applications. As previously noted, the tubules formed from phospholipids become mechanically rugged and solvent-resistant when coated with metals like gold, copper, and nickel. Freeze-drying these metalized tubules leads to a dispersible powder of hollow metallic cylinders that are “microcapillary” tubes; these microcapillaries can capture and retain a chemical encapsulant or colloidal suspension. The encapsulated material is released at a controlled rate over periods of time extending from hours to several years. Recently,

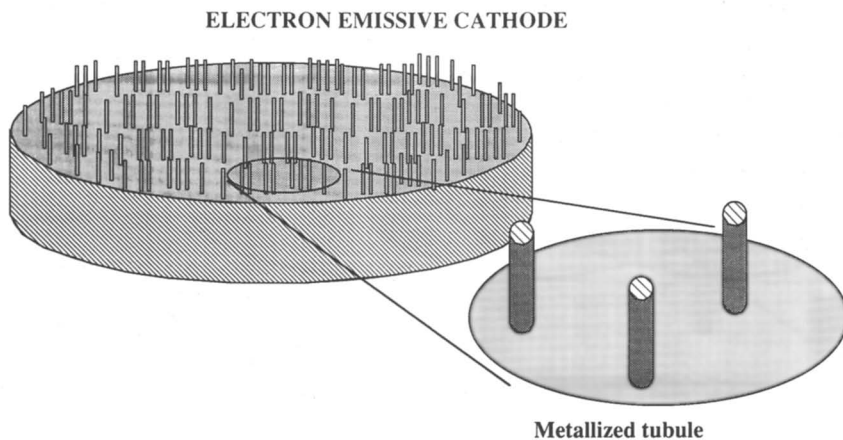


Figure 8. Schematic diagram of a field-emission cathode fabricated from tubules. (Reproduced from reference 57. Published 1991 The Institute of Electrical and Electronics Engineers, Inc.)

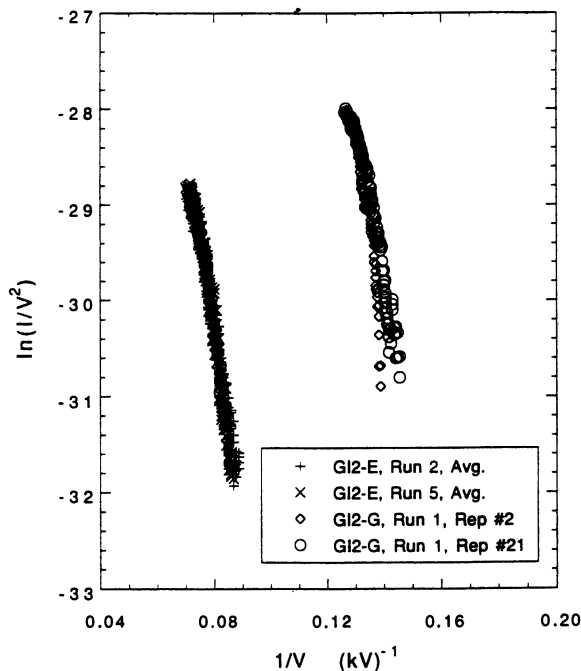


Figure 9. Fowler-Nordheim plot of the cathode performance for the cathodes fabricated from tubules. (Reproduced from reference 57. Published 1991 The Institute of Electrical and Electronics Engineers, Inc.)

Price and Patchan (60) demonstrated the encapsulation of a mixture of tetracycline, epoxy monomers polymers inside metal-coated tubules. The in vitro release kinetics of the tetracycline were studied in both static and dynamic environments. A more or less linear-release rate was observed over a period of 30 days. It has also been shown (61) that when employed in paint coatings, tubules can deliver the encapsulated tetracycline over a long period extending to over 26 months. Controlled release over a long period has also been confirmed (61) by the observations on metal structures coated with a tubule-based paint and immersed in the sea. These structures have not shown any evidence of barnacle growth for over a year. It is clear that the tubules, because of their length, can indeed serve as controlled-release systems for many other areas of engineering and biomedical applications.

Summary

Tubules constitute a unique form of self-assembling microstructures. Understanding their structure and formation is of considerable funda-

mental interest. Tubules also have considerable potential in many areas of technological applications such as high-dielectric materials, magnetic materials for recording and shielding, high-density packaging, interconnect technology, microcathodes, and controlled-release applications. Another interesting and important aspect of tubules is that they demonstrate how the principle of self-assembly of molecules into well-defined structures can be harnessed to develop a variety of advanced materials. This field is indeed fertile, and work on tubules is an important step in this direction.

Acknowledgments

The financial assistance of Defense Advanced Research Projects Agency (DARPA), the Office of Naval Technology, and the Naval Research Laboratory is gratefully acknowledged.

References

1. Israelachvili, J. N. *Intermolecular Forces and Surface Forces*; Academic: London, 1985.
2. *Physics of Amphiphiles: Micelles, Vesicles and Microemulsions*; Degiorgio, V.; Corti, M., Eds.; Proceedings of the International School of Physics, Enrico Fermi; North Holland: Amsterdam, The Netherlands, 1985.
3. Cevc, G.; Marsh, D. *Phospholipid Bilayers*, John Wiley & Sons: New York, 1987.
4. Nakashima, N.; Asakuma, S.; Kunitake, T. *J. Am. Chem. Soc.* **1985**, *107*, 509–510.
5. Kunitake, T.; Nakashima, N.; Shimomura, M.; Okahata, Y.; Kano, K.; Ogawa, T. *J. Am. Chem. Soc.* **1980**, *102*, 6642–6644.
6. Kunitake, T.; Nakashima, N.; Morimitsu, K. *Chem. Lett.* **1980**, 1347–1350.
7. Nakashima, N.; Fukushima, H.; Kunitake, T. *Chem. Lett.* **1981**, 1207–1210.
8. Kunitake, T.; Yamada, N. *J. Chem. Soc. Chem. Commun.* **1986**, 655–656.
9. Yamada, K.; Ihara, H.; Fukumoto, T.; Hirayama, C. *Chem. Lett.* **1984**, 1713–1716.
10. Ihara, H.; Fukumoto, T.; Hirayama, C.; Yamada, K. *Polym. Commun.* **1986**, *27*, 282–285.
11. Ihara, H.; Fukumoto, T.; Hirayama, C. *Nippon Kagaku Kaishi* **1987**, 543–545.
12. Kunitake, T. In *Supramolecular Assemblies: New Developments in Biofunctional Chemistry*; Murakami, Y., Ed.; Mita: Tokyo, Japan, 1990; pp 17–24.
13. Yager, P.; Schoen, P. *Mol. Cryst. Liq. Cryst.* **1984**, *106*, 371–381.
14. Schnur, J. M.; Price, R.; Schoen, P.; Yager, P.; Calvert, J. M.; Georger, J.; Singh, A. *Thin Solid Films* **1987**, *152*, 181–206.
15. Rudolph, A. S.; Calvert, J. M.; Schoen, P. E.; Schnur, J. M. In *Biotechnological Applications of Lipid Microstructures*; Gaber, B. P.; Schnur, J. M.; Chapman, D., Eds.; Plenum: New York, 1988, pp 325–320.
16. Ratna, B. R.; Baral-Tosch, S.; Kahn, B.; Rudolph, A. S.; Schnur, J. M. *Chem. Phys. Lipids* **1992**, *63*, 47–53.
17. Chapman, D. Eur. Patent 32622, 1981.

18. Yager, P.; Schoen, P. E.; Davis, C.; Price, R.; Singh, A. *Biophys. J.* **1985**, *48*, 899–906.
19. Burke, T. G.; Rudolph, A. S.; Price, R.; Sheridan, J. P.; Dalziel, A. W.; Singh, A.; Schoen, P. E. *Chem. Phys. Lipids* **1988**, *48*, 21–230.
20. Rudolph, A. S.; Singh, B. P.; Singh, A.; Burke, T. G. *Biochim. Biophys. Acta* **1988**, *943*, 454–462.
21. Lando, J. B.; Hansen, J. E. *Thin Solid Films*, **1989**, *180*, 141–152.
22. Georger, J. H.; Singh, A.; Price, R.; Schnur, J. M.; Yager, P.; Scheon, P. J. *Am. Chem. Soc.* **1987**, *109*, 6169–6175.
23. Rudolph, A. S.; Testoff, M. A.; Shashidhar, R. *Biochim. Biophys. Acta* **1992**, *1127*, 186–190.
24. Rudolph, A. S.; Calvert, J. M.; Ayers, M. E.; Schnur, J. M. *J. Am. Chem. Soc.* **1989**, *111*, 8516–8517.
25. Markowitz, M.; Singh, A. *Langmuir* **1991**, *7*, 16–18.
26. Singh, A.; Burke, T. G.; Calvert, J. M.; Georger, J. H.; Herendeen, B.; Price, R.; Schoen, P. E.; Yager, P. *Chem. Phys. Lipids* **1988**, *47*, 135–148.
27. Singh, A.; Schoen, P. E.; Schnur, J. M. *J. Chem. Soc. Chem. Commun.* **1988**, 1222–1223.
28. Schoen, P. E.; Yager, P. *J. Polym. Sci. Polym. Phys.* **1985**, *23*, 2203–2216.
29. Rudolph, A. S.; Burke, T. G. *Biochim. Biophys. Acta* **1907**, *902*, 349–359.
30. Schoen, P. E.; Yager, P.; Sheridan, J. P.; Price, R.; Schnur, J. M.; Singh, A.; Rhodes, D. G.; Blechner, S. L. *Mol. Cryst. Liq. Cryst.* **1987**, *153*, 357–366.
31. Sheridan, J. P. *NRL Memorandum Report* **1988**; pp 5975.
32. Rhodes, D. G.; Blechner, S. L.; Yager, P.; Schoen, P. *Chem. Phys. Lipids* **1988**, *49*, 39–47.
33. Blechner, S. L.; Morris, W.; Schoen, P. E.; Yager, P.; Rhodes, D. G. *Chem. Phys. Lipids*, **1991**, *58*, 41–54.
34. Caffrey, M.; Hogan, J.; Rudolph, A. S. *Biochemistry* **1991**, *30*, 2134–2146.
35. Lando, J.; Sudiwala, R. V. *Chem. Mater.* **1990**, *2*, 596–599.
36. Safinya, C. R.; Roux, D.; Smith, G. S.; Sinha, S. K.; Dimon, P.; Clark, N. A.; Bellocq, A. M. *Phys. Rev. Lett.* **1986**, *57*, 2718–2721.
37. Thomas, B.; Safinya, C. R.; Plano, R. J.; Clark, N. A.; Ratna, B. R.; Shashidhar, R. *MRS Proceedings on Complex Fluids*; Materials Research Society: Pittsburgh, PA, **1992**; Vol. 248, pp 83–86.
38. Pindak, R.; Moncton, D.; Davey, S. C.; Goodby, J. W. *Phys. Rev. Lett.* **1981**, *46*, 1135–1138.
39. Sirota, E. B.; Smith, G. S.; Safinya, C. R.; Plano, R. J.; Clark, N. A. *Science (Washington, D.C.)* **1988**, *242*, 1406–1409.
40. Rosenblatt, C.; Yager, P.; Schoen, P. E. *Biophys. J.* **1987**, *52*, 295–301.
41. Li, Z.; Rosenblatt, C.; Yager, P.; Schoen, P. E. *Biophys. J.* **1988**, *54*, 289–294.
42. Wood, D. M.; Li, Z.; Rosenblatt, C.; Yager, P.; Schoen, P. E. *Mol. Cryst. Liq. Cryst.* **1989**, *167*, 1–6.
43. Helfrich, W. *J. Chem. Phys.* **1986**, *85*, 1085–1087.
44. Bugl, P.; Fujita, S. *J. Chem. Phys.* **1969**, *50*, 3137–3142.
45. deGennes, P. G. *Physics of Liquid Crystals*; Clarendon: Oxford, England, **1985**.
46. Helfrich, W.; Prost, J. *Phys. Rev. A* **1988**, *38*, 3065–3068.
47. Ou-Yang, Z.-c.; Liu, J.-x. *Phys. Rev. Lett.* **1990**, *65*, 1679–1682.
48. Ou-Yang, Z.-c.; Liu, J.-x. *Phys. Rev. A* **1991**, *43*, 6826–6836.
49. Chappell, J. S.; Yager, P. *Chem. Phys. Lipids* **1991**, *58*, 253–258.
50. Lubensky, T. C.; Prost, J. *J. de Physique II* **1992**, *2*, 371–382.

51. deGennes, P. G. *C. R. Acad. Sci. (Paris)* 1987, 304, 259–263.
52. Chappel, J. S.; Yager, P. *Biophys. J.* 1991, 60, 952–965.
53. Schnur, J. M.; Schoen, P. E.; Yager, P.; Calvert, J. M.; Georger, J.; Price, R. U.S. Patent 4 911 981, March 27, 1990.
54. Behroozi, F.; Orman, M.; Reese, R.; Stockton, W.; Calvert, J.; Rachford, F.; Schoen, P. *J. Appl. Phys.* 1990, 68, 3688–3693.
55. Krebbs, J.; Rubinstein, M.; Lubitz, P.; Harford, M. Z.; Baral, S.; Shashidhar, R.; Ho, Y. S.; Chow, G. M.; Qadri, S. *J. Appl. Phys.* 1991, 70, 6404–6406.
56. Shashidhar, R.; Baral, S.; Ho, Y. S.; Chow, G. M.; Ratna, B. R.; Chien, C. L., submitted to *J. Appl. Phys.*
57. Kirkpatrick, D. A.; Schoen, P. E.; Stockton, W. B.; Price, R.; Baral, S.; Kahn, B. E.; Schnur, J. M.; Levinson, M.; Ditchek, B. M. *IEEE Trans. Plasma Science* 1991, 19, 749–756.
58. Kirkpatrick, D. A.; Bergeron, G. C.; Czarnaski, M. A.; Hickman, J. J.; Chow, G. M.; Price, R.; Ratna, B. R.; Schoen, P. E.; Stockton, W. B.; Baral, S.; Ting, A. C.; Schnur, J. *J. Appl. Phys. Lett.* 1992, 60, 1556–1558.
59. Fowler, R. H.; Nordheim, L. *Proc. R. Soc. London A* 1928, 119, 173–178.
60. Price, R.; Patchan, M.; Clare, A.; Rittschof, D.; Bonaventura, J. *Bionfonling* 1992, 6, 207–210.
61. Price, R.; Patchan, M. *J. Microencapsulation* 1991, 8, 301–306.

RECEIVED for review March 12, 1992. ACCEPTED revised manuscript April 2, 1993.

Engineering Proteins for Electrooptical Biomaterials

Patrick S. Stayton, Jill M. Olinger, Susan T. Wollman, Paul W. Bohn,* and Stephen G. Sligar*

The Beckman Institute for Advanced Science and Technology, University of Illinois at Urbana-Champaign, 405 North Mathews, Urbana, IL 61801

Protein engineering techniques have been used to manipulate the optical and electron transfer (ET) properties of heme proteins in ways that apply to the construction of biomolecular electronic devices. Two important aspects have been directly addressed. First, genetic engineering techniques have been used in conjunction with silane-based self-assembly systems to construct close-packed protein monolayers on optical substrates. The resulting structures have been characterized with immunological and surface-enhanced resonance Raman spectroscopy techniques. Recombinant DNA techniques have also been used to study the role of electrostatic forces in protein-protein interactions and may be used to gain control over the assembly of multicomponent protein thin films. In addition to these assembly considerations, protein engineering techniques can be used for a second purpose: the manipulation of optical and ET properties of heme proteins. Control over the heme absorption transition energies, redox potentials, and redox center composition can be realized through a combination of genetic engineering and protein chemistry techniques. These experiments are aimed at producing multifunctional protein components with designed assembly and functional properties.

THE USE OF BIOLOGICAL MACROMOLECULES AS BUILDING BLOCKS in the construction of molecular devices has recently generated much enthusiasm. The exquisite selectivity in the recognition of small molecules has made proteins a natural choice for sensor design. Additionally, many protein systems are electrooptically active, and even express degrees

* Corresponding authors.

0065-2393/94/0240-0475\$08.00/0
© 1994 American Chemical Society

of state-dependent switching (termed allostery by the protein chemist). Although several systems such as bacteriorhodopsin and the photosynthetic reaction center are receiving close attention as candidates for molecular devices (1), the proteins that nature has provided do not often have the exact physical and chemical properties required for use as molecular building blocks. For this reason, recombinant DNA technology is a useful collaborative technique, providing the essential synthetic control over protein structure–function relationships. Because the synthetic goals for protein-based materials naturally parallel many of the ultimate aims in nonbiological molecular device construction, we endeavor here to review concomitantly both the general features that make heme-containing proteins particularly interesting as potential electronic device components and to point out how protein engineering and chemistry techniques provide the means to manipulate and optimize key features in biomolecular assemblies.

The optical and electron conducting properties associated with heme proteins make them attractive candidates for biomolecular electronic device fabrication. These inherent optical and electrical properties can be manipulated through the site-specific alteration of protein structure by using recombinant DNA techniques. Intertwined with the functional aspects, and indeed a strong determinant of certain properties, is the element of macromolecular assembly structure. The generation of highly ordered structures requires an understanding of the forces and potentials that control the specificity of protein–protein and protein–surface interactions and that could be manipulated to control in-plane ordering and poling. As a first step in the development of ordered protein assemblies, a genetically engineered heme protein system has been used to yield oriented protein arrays through judiciously positioned and unique reactive surface sites. Control over the molecular orientation of protein components in thin film assemblies should lead to a myriad of applications in the biomaterial field.

A central player in our attempts to develop an understanding of the physical, chemical, and biological principles governing the assembly of supramolecular protein assemblies has been cytochrome b_5 . This macromolecule is a bis-imidazole-ligated heme protein, for which high-resolution crystal and NMR structures of the water soluble domain are available (2, 3) (Figure 1). A bacterial over-expression system, based on an easily manipulated synthetic gene construction, has been developed (4). This system permits the production of large quantities of recombinant protein in both the membrane-bound or water-soluble form (4). Cytochrome b_5 exhibits good overall stability and has a fairly symmetric globular structure that should lead to efficient packing at planar surfaces. In functional terms, cytochrome b_5 is also quite versatile, forming stable and active electron transfer (ET) complexes with a variety of proteins

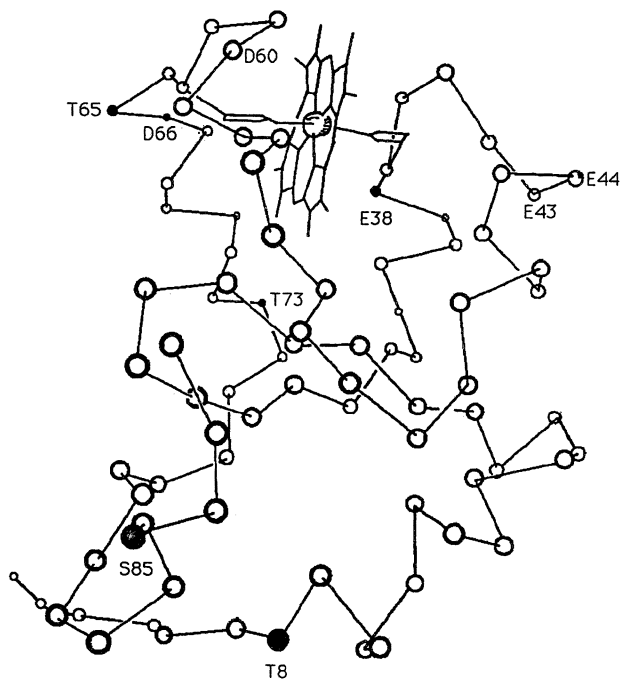


Figure 1. Schematic 3D cytochrome b_5 structure. The positions of cysteines introduced through site-directed mutagenesis techniques and the conserved carboxylate binding contacts are noted.

including cytochrome c, myoglobin, hemoglobin, and cytochrome P450 (5–8). These properties make cytochrome b_5 a particularly attractive candidate for biomaterial studies.

Assembly of Protein Thin Films

Single-Component Monolayers. We are interested in developing the means to control the structure of organized assemblies of biological macromolecules in both two and three dimensions. Figure 2 presents a schematic outline for controlling two-dimensional (2D) crystallization events. The first step involves the tethering of a macromolecule to a surface in a nonrandom orientation. The scheme for accomplishing the orientation of a biological macromolecule involves the introduction of a unique amino acid reactive side-chain at a specific site on the water-accessible surface of the protein (9). In particular, because cytochrome b_5 lacks any sulfur-containing amino acids, site-directed mutagenesis techniques were used to produce four mutants in which a single highly reactive and specific thiol functional group was introduced

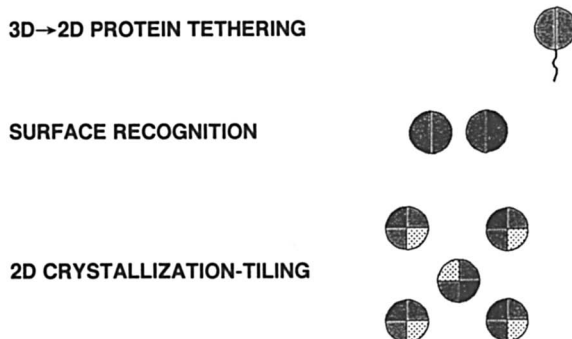


Figure 2. Macromolecular assembly of heterogeneous protein thin films. Shading patterns represent complementary interaction surfaces.

at four independent points on the protein surface. These cysteine residues replaced threonine 8 (mutant T8C), threonine 65 (T65C), threonine 73 (T73C), and serine 85 (S85C) (Figure 1). In addition, two double mutants T65C,T8C and D66C,E38C, which present binary thiol reactivity, have been made. Substitution of cysteine residues, with their nucleophilic thiolate functionality, allows for anchoring to a solid substrate derivatized with a complementary electrophilic reactant, typically a silyl ether terminated with an alkyl halide (for the formation of a thioether surface linkage). These reaction schemes are outlined in Figure 3.

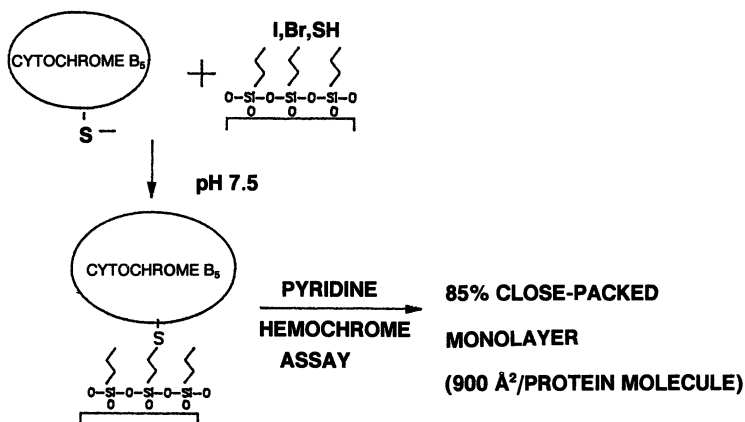


Figure 3. Protein derivatization and surface coverage. Cytochrome b₅ is reacted with alkylhalide- or alkylthiol-derivatized glass substrates in 50 mM KPi, pH 7.5, and dried under nitrogen. The degree of surface coverage is then determined by measuring the heme content of the protein assemblies through the use of a pyridine hemochrome assay.

Glass substrates were prepared by treatment with a silane coupling agent, either 3-iodo- or 3-bromopropyltrimethoxy silane. A thiopropyl analogue of these silanes was used to estimate surface coverage through a spectrophotometric titration using dithionitrobenzoate (DTNB). This method yields a quantitation of the surface thiols, for which a coverage area of ca. $65 \text{ \AA}^2/\text{molecule}$ was measured. Molecular models show that the size of an individual alkylsilane should be dominated by the cross-sectional area of the alkyl chain, which in the all-trans configuration is ca. 25 \AA^2 . Assuming that the alkyl-halide linkers exhibit similar reactivities, the surface coverage is estimated to be around 40%. The protein is subsequently incubated with the derivatized substrates at pH 7.5–8.0. The slides are then washed in nanopure water and dried under nitrogen. Very little physisorbed cytochrome b_5 is ever observed under these conditions, presumably because the protein has a very hydrophilic surface and a large net anionic charge inhibiting hydrophobic and electrostatic interactions with the covered or bare substrate (control experiments with wild-type protein also demonstrate the requirement for the surface thiol). To assess the coverage of the protein monolayer, we have relied on quantitation of the heme prosthetic group concentration. The pyridine–heme chromagen assay (10), which uses spectrophotometric measurement of the well-characterized pyridine–heme adduct, yields a coverage of ca. $750\text{--}900 \text{ \AA}^2/\text{molecule}$. Because the crystallographic dimensions of cytochrome b_5 are $25 \times 25 \times 30 \text{ \AA}$, the surface coverage ranges between 85–100%. Because of the large size of the macromolecule relative to the linker, protein coverages approaching 1.0 can be obtained from surfaces on which the linker molecules are present at significantly lower coverages.

Low-resolution characterization of the surface-bound protein was conducted by monitoring antigenic activity (Figure 4). A thiopropyl-derivatized surface was reacted with the genetically engineered T8C mutant, and the resulting substrates were exposed to polyclonal antibodies directed against cytochrome b_5 . Cross-reactivity was followed with ^{125}I -labeled protein A, which yields a radiometric signal proportional to the primary anti-cytochrome b_5 antibody concentration. The inset to Figure 4 tabulates the results of controlled experiments that clearly demonstrate the presence of cytochrome b_5 in these assemblies. The use of polyclonal antibodies precludes any high-resolution conclusion about structure retention, but does confirm that chemisorbed (not removed by buffer washes) protein is present along with the heme prosthetic group monitored by the pyridine–heme chromagen assay.

Significantly more structural detail has been obtained through the use of surface Raman spectroscopy. As background to the current work, two aspects of surface Raman scattering at dielectric interfaces have been extensively studied (11, 12). The first aspect is the construction of

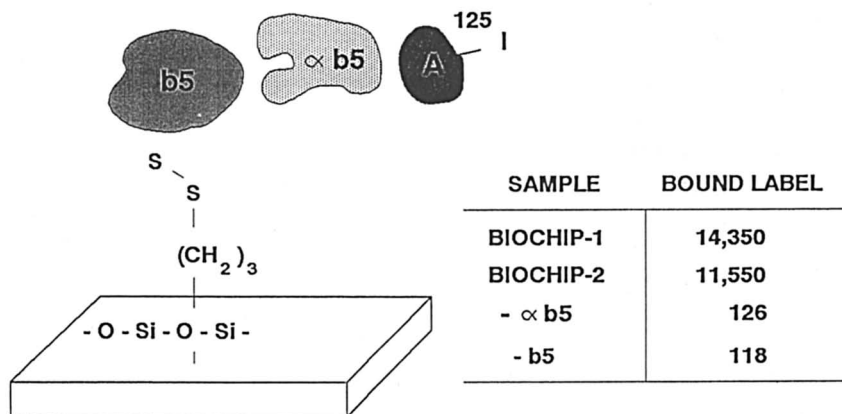


Figure 4. Immunological assay for cytochrome b_5 . Protein monolayers were treated with an α -cytochrome b_5 polyclonal antibody preparation and subsequently with ^{125}I -labeled protein A to detect surface-bound antibody. Control measurements demonstrate the presence of chemisorbed cytochrome b_5 on the optical substrates.

structures that permit the surface chemistry required for linker derivatization, while still retaining the necessary enhancement of Raman signals associated with the chemisorbed molecules. In addition, analyses to extract molecular-orientation information from polarize-scattering measurements have been developed. Structures consisting of initial Ag or Au islands (ca. 50 Å) deposited over masked SiO_2 substrates are subsequently overlaid with 50–100 Å of SiO_2 spacer. Adsorbates are probed with excitation radiation coupled into the structure just above the critical angle for total internal reflection (calculated for the metal-free interface) as shown in Figure 5. Detailed experiments, including measurements of chemical resistance, Auger spatial mapping and depth profiling, coverage dependences of Raman signals, and studies of the signal intensity versus spacer layer thickness, demonstrate that the majority of the Raman signals are located at the SiO_2 surface and not in defect channels to the metal surface. These defects are not a crucial consideration for the protein assemblies because of the large size of the molecules relative to all but the largest defects. Our primary interest was in characterizing the state of the heme prosthetic group. The heme oxidation state is characterized by transitions in the region 1340–1370 cm^{-1} , the spin state by bands in the region 1480–1510 cm^{-1} , and the core size, reflecting doming or nonplanarity, in the region ca. 1550–1600 cm^{-1} (13). These marker bands are summarized in the frequency correlation diagram shown in Figure 6, and the spectra for chemisorbed monolayers of T8C and T65C are shown in Figure 7. Both proteins exhibit very similar marker band energies. If we assume that the positions of the marker

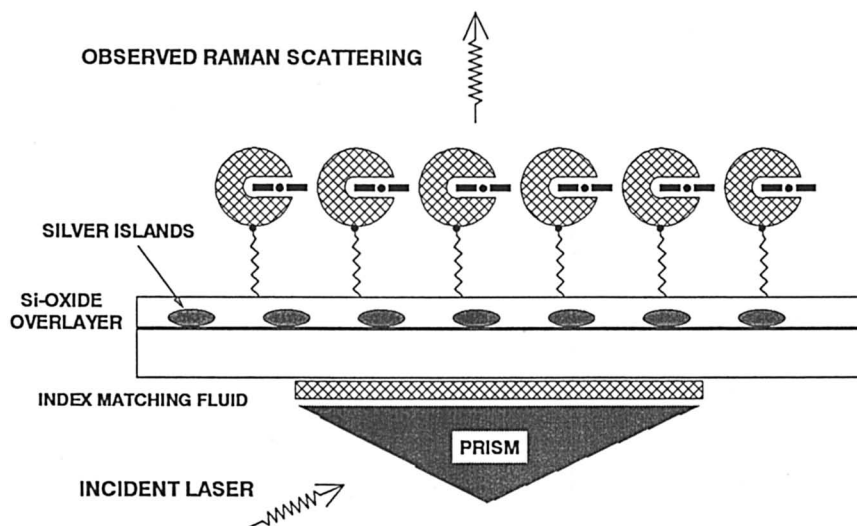


Figure 5. Schematic of the surface structures used for total internal reflection Raman scattering experiments.

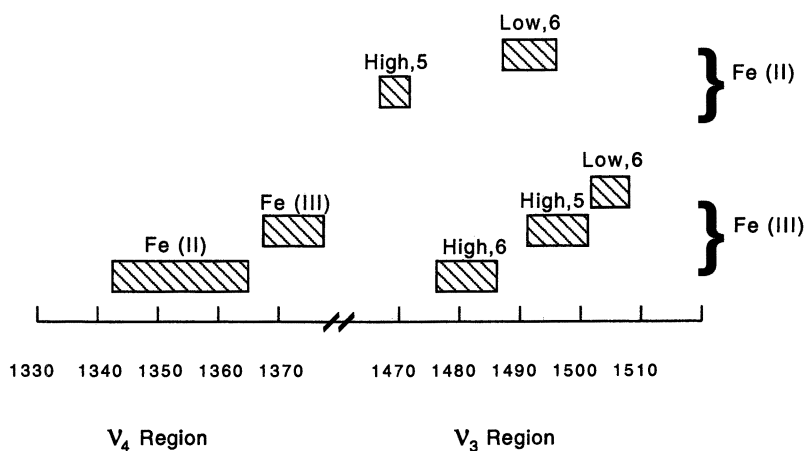


Figure 6. Heme protein marker band positions. Solution-derived resonance Raman band frequencies associated with the chemical and electronic states of the heme-prosthetic group. ▨ represent the range of Raman shifts observed for the given heme state in a number of heme-protein systems (13). These markers can be used to assign the spectra of Figure 7.

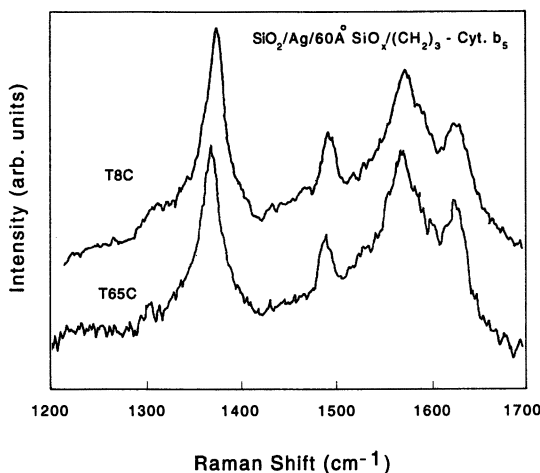


Figure 7. Surface-enhanced resonance Raman spectra for T8C and T65C cytochrome b_5 assemblies. The structure configurations shown in Figure 5 were used to obtain the fingerprint region spectra with laser excitation at 457.9 nm.

bands are unaffected by binding to the substrate, then the following observations about the state of the heme proteins can be made (by comparison to the solution spectra). The oxidation state marker band is characteristic of the expected oxidized ferric heme, although the reduced species can be generated through a photoreduction process under sufficiently strong laser fluences. The spin state marker positions are most consistent with assignment as six-coordinate, high-spin heme, where the cytochrome b_5 prosthetic group is present in solution as six-coordinate, low-spin heme. We are currently undertaking a more detailed study of the surface Raman spectra to more definitively assign the spin-spin state. Several phenomena could explain these observations, including a slight alteration in the heme pocket bonding interactions, a distribution of high-spin, 5-coordinate and low-spin, 6-coordinate species (argued against by the width of the observed bands), or simply a slightly shifted band position for the spin state marker in the surface environment.

Multicomponent Assemblies. As previously mentioned, cytochrome b_5 is particularly attractive as a component in heterogeneous macromolecular assemblies due to its ability to specifically recognize a number or to partner heme proteins. Control over the assembly of a multicomponent protein thin film ultimately depends on control over the general process of protein-protein molecular recognition. Thus, we are interested in defining and manipulating the protein surfaces involved

in the packing of two proteins during complex formation, and subsequently in tiling schemes to propagate order radially (Figure 2). Protein surfaces can be readily manipulated by using genetic engineering techniques to control electrostatic properties and the distribution of hydrophilic and hydrophobic surface side chains. Of particular importance to surface design is the need to separate the contributions of electrostatics and nonpolar interactions and to develop the computational methodology to predict native and altered electrostatic potential surfaces. Again, site-directed mutagenesis has been invaluable in this endeavor. To map the electrostatic potential surface around cytochrome b_5 , we have used a series of 15 surface point mutations that change the number and polarity of surface charged amino acid side chains (14, 15). These mutations together with the change in the charge number relative to wild-type protein are shown in Table I. Although detailed self-consistent field theories are needed to describe accurately the electrostatic fields around a biological macromolecule at all points in space and for all solvent and protein conditions, it turns out that to manipulate protein-protein recognition events, a two-continuum dielectric-based calculation can provide an excellent picture of electrostatic surfaces (16, 17). To check the accuracy of this model of macroscopic electrostatics, we use the heme as a reporter group and calculate the effect of each surface charge mutation on the redox potential of the heme prosthetic group (18). Figure 8 shows the excellent agreement between experiment and theory and gives confidence that modeling can lead experiment in the de novo generation of docked potential surfaces to control assembly in planar arrays.

Table I. Surface Point Mutations

<i>Cytochrome b_5 Mutants</i>	Δ Charge	E_o' (mV vs. NHE)
Q13E	-1	-9
S64D	-1	-13
D66S	+1	+1
E11Q	+1	-7
E37Q	+1	-5
E56Q	+1	-3
E44Q	+1	-1
E48Q	+1	+1
D66S	+1	+1
D60N	+1	+3
E44Q, E48Q	+2	+5
E43Q, E44Q	+2	+7
D66K	+2	+5
E44K	+2	+1
E44Q, E48Q, D60N	+3	+13

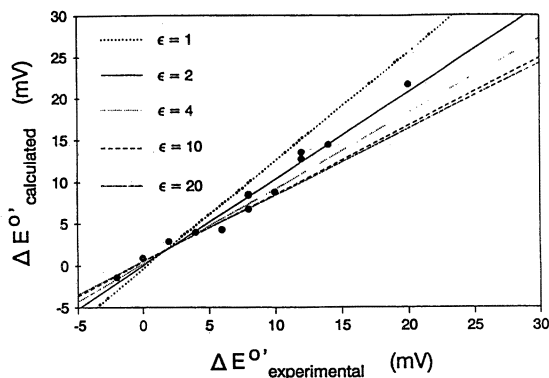


Figure 8. Comparison between theoretical and experimental redox potential changes with surface charge mutations. Plots of redox potential shifts as calculated using DELPHI (Biosym Technologies) versus electrochemically measured experimental changes. The straight lines represent the calculated fits at the dielectric strength for the protein interior as noted (16, 17).

Manipulation of Electrical Properties

The primary physiological duty of cytochrome b_5 is to transfer electrons to partner proteins. Biological ET is a complex process that is dependent on a number of factors, including driving force, orientation factors, and nuclear reorganization energies (19). Control of these factors by the protein structural environment gives biological systems a high degree of regulatory power. Thus, although biological ET rates are not generally superior to more conventional materials, the specificity associated with ET is indeed notable and often state-dependent (e.g., regulation by small molecule binding). We have been interested in developing a system of closely related macromolecules whose ET properties exhibit a gradient of regulated activity. A combination of genetic engineering and protein chemistry techniques have been used to generate cytochrome b_5 and myoglobin variants with altered redox-center properties, but which still retain the native three-dimensional (3D) structure and assembly properties. In this way, for example, a monolayer of homogeneous 3D architecture can be constructed, but which contains a heterogeneous collection of redox centers.

Redox Potentials. Driving force is an important determinant for ET reactions, and thus an important goal is to control the heme center redox potentials. A wide spectrum of heme potentials can be found in nature, demonstrating the control over this equilibrium wielded by the protein environment. Therefore, it is possible to generate an altered heme redox potential through genetically engineering the local struc-

ture. As previously noted, one particularly striking method for doing this takes advantage of the relationship between redox potential and electrostatic forces. The cytochrome b_5 redox potential is sensitive to alterations in the nearby surface electrostatic potential field, and this has provided a means for generating charge mutants that exhibit a gradient of redox potentials (18). These surface charge mutants follow straightforward theoretical predictions making designed variants possible. Much larger effects are expected with side-chain alterations in the low dielectric interior. This has indeed been observed with myoglobin, where the placement of negatively charged side chains in the ligand binding pocket close to the heme prosthetic group leads to dramatic changes in measured redox potential. Shifts of up to -200 mV in E^0 have been observed with both sperm whale and human myoglobin site-directed mutants (20, 21). These results are in the direction expected for electrostatic point charge effects, with stabilization of the ferric state (net charge +1) arising through favorable interactions with a negatively charged side chain. Thus, site-directed mutagenesis techniques can be used to produce protein molecules with altered redox properties that retain the native 3D structure.

Redox Center Reconstitution. Another means for generating ET variants within a given protein is the substitution of a modified porphyrin for the native heme-prosthetic group. Cytochrome b_5 has been reconstituted with various chlorin derivatives (22), which differ from the b-type heme porphyrin in having a saturated pyrrole ring, successfully leading to altered electronic properties, but still retaining ET activity with cytochrome c. Myoglobin has also been reconstituted with chlorin derivatives and the resulting proteins have been characterized in detail (23, 24). The five-coordinate heme proteins are ideal for reconstitution with luminescent metalloporphyrins that for structural reasons prefer not to have a second axial ligand. For example, myoglobin and hemoglobin tightly bind the luminescent Zn porphyrin derivative (25, 26), which is a particularly interesting ET center. The heme group can be removed with careful organic extraction techniques, followed by the addition of the modified porphyrin and subsequent renaturation. ET is photoinitiated through excitation of the Zn porphyrin to the strongly reducing triplet state. The intermediate species, driving forces, and kinetic parameters associated with these redox center cycles have been well-characterized (27, 28). The Zn porphyrin moiety is thus responsible for two primary characteristics: a large driving force (strong reducing center) and a photoinitiated, reversible redox cycle with partner macromolecules. These centers therefore provide an electron source for transfer over long distances (on the molecular scale) and for ET to the native heme prosthetic group of unsubstituted protein molecules.

A related technique for initiating ET to heme centers relies on the addition of redox centers to specific surface side chains. Photoactivated ruthenium(II) complexes bonded to imidazole functionalities have been used to study ET from the surface to the buried heme prosthetic group in myoglobin (29, 30). The placement of unique thiol functionalities at defined loci on the cytochrome b_5 surface has also been used to add a second protein-bound redox center (31). A sulfhydryl specific ruthenium complex has been attached to the T65C mutant. The ruthenium complex provides a photoinitiated source of electrons for the fast reduction of the cytochrome b_5 heme center. The reduced cytochrome b_5 can then transfer electrons to cytochrome c, demonstrating the utility of using a second redox center as an electron source. Genetic engineering techniques allow for the proper choice of the attachment site, maintaining a short distance and fast electron pumping for ruthenium to cytochrome b_5 heme reduction, while avoiding inhibition of the most favorable complex formation geometry. These considerations and abilities are of importance in the assembly of protein thin films where control over ET pathways are the important functional goal.

Manipulation of Optical Properties

Heme Pocket Alterations. The optical properties of heme proteins are similarly controlled by the local protein environment. This control makes it possible to manipulate these properties through judicious site-directed mutation of side chains near the heme prosthetic group. Two general classes of these mutants can be distinguished on the basis of whether the introduced side chain alters the optical spectrum through directly bonded ligand field effects (becomes an axial ligand) or through changing the polarity of the local environment leading to a redistribution of transition energies. A good example of the first class is a myoglobin mutant substituting tyrosine for the distal pocket histidine (32). This variant has been characterized in detail with UV-vis optical, electron paramagnetic resonance (EPR), and resonance Raman spectroscopies (Figure 9). The EPR spectrum and resonance Raman spectra clearly demonstrate that the ferric protein is a six-coordinate, high-spin species. The resonance Raman marker bands at ca. 590 cm^{-1} ($\nu_{\text{Fe-O}}$) and at ca. 1300 and 1500 cm^{-1} (internal modes) of this mutant are very similar to iron-tyrosinate heme proteins, indicating that the tyrosine provides axial ligation in the ferric state. Optically the tyrosine mutant exhibits new ligand-to-metal charge-transfer absorption transitions at ca. 485 and 600 nm . In layman terms this means that the reddish-brown myoglobin has been turned green while retaining an identical 3D structure.

The second class of mutations perturbing the optical features do not rely on direct ligation of the iron porphyrin. A number of sperm whale

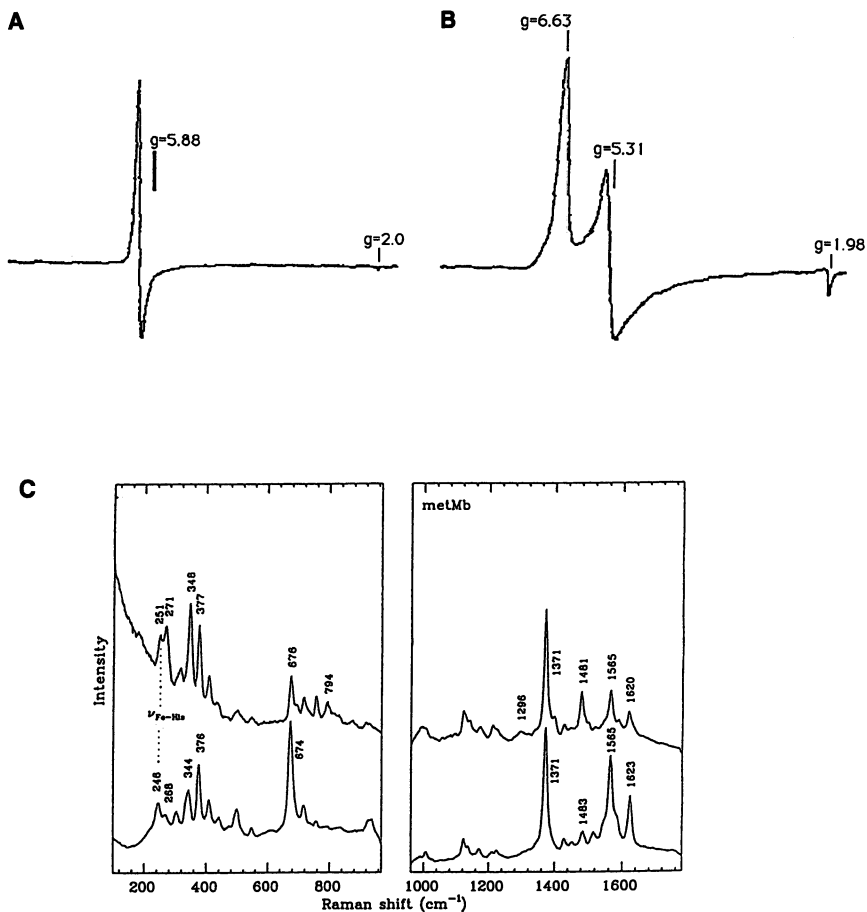


Figure 9. Alteration of myoglobin axial ligation by site-directed mutagenesis. EPR spectra of wild-type myoglobin (A) versus His(E7)Tyr myoglobin (B) and the mutant's resonance Raman spectra (C). The EPR spectra demonstrate a rhombic splitting of the high-spin protein consistent with tyrosine ligation. Definitive assignment of tyrosine axial ligation is provided by the similarity of the mutant resonance Raman spectrum to iron-tyrosinate proteins.

myoglobin mutants, which exhibit altered visible spectra, have been constructed. These mutant sites reside in the myoglobin distal pocket adjacent to the site where small molecules such as O_2 and CO are bound at the heme iron. By changing the polarity of the heme environment, they change the ET energies and yield altered optical properties. For example, substituting the distal histidine (E7) with leucine leads to a shift in the Soret transition peak of over 10 nm. Although these results

clearly demonstrate the efficacy of altering the heme based π - π^* transitions in sperm whale myoglobin, different results have been noted in human myoglobin (24). With this protein little perturbation of the pure heme-based transitions (Soret, α , β) and small charge-transfer band alterations with the introduction of pocket mutations occurs. Substitution of chlorophyll derivatives for the heme group in this study yielded similar results and were interpreted as evidence against a theoretical study (33) suggesting that buried point charges can have a substantial effect on the spectral properties of bound chromophores. Our results with sperm whale myoglobin, where both introduced point charges and mutations substituting nonpolar residues in the binding pocket lead to altered heme transitions (primarily for the met-ligand state), suggest that the local protein environment can indeed substantially effect the π - π^* transition energies.

Reconstitution with New Optical Centers. We have previously noted that reconstitution of heme proteins with porphyrin derivatives can be used to introduce new centers exhibiting desirable redox features. The same process can be used to derive desirable optical variants. For example, cytochrome b_5 reconstituted with chlorin derivatives is visibly changed from red to green because of the presence of a visible ligand-to-metal charge-transfer band at 600 nm (22). Similarly, extensive work with chlorophyll derivatives in myoglobin has described the well-characterized optical properties arising from these substitutions (23, 24). In addition to altering the absorption spectra associated with these proteins, reconstitution can also give rise to new polarization properties. The heme-based transitions are generally x,y (defined in the heme plane) degenerate and localized roughly in the tetrapyrrole ring system. Many of the chlorophyll derivatives, however, have well-defined, nondegenerate x - and y -directed transitions. Thus, these derivatives represent wavelength-dependent absorption polarities that may be taken advantage of with polarized optical probes. Finally, reconstitution can provide new optical characteristics, such as fluorescence and phosphorescence, not available with the native heme prosthetic group. We have, for example, reconstituted the T8C mutant with protoporphyrin IX and observed the porphyrin-based visible fluorescence signal in chemisorbed monolayer assemblies. Substitution of the luminescent Zn porphyrins can also provide novel and potentially useful fluorescent properties and signals.

Conclusions

As with any potential new material, the usefulness of protein-based biomaterials will be dependent upon the ability to control structure–func-

tion relationships. This chapter has focused on the ways in which genetic engineering and protein chemistry techniques can be used to create versatile hybrid macromolecules with combined properties directing assembly and electrooptical function. The key to accomplishing these aims is a standard synthetic goal: change one property while retaining others. Because genetic engineering techniques allow the site-directed alteration of single amino acid side chains, this ability provides the basis for creating protein components in such a fashion. Current knowledge of protein structure–function relationships is still largely evolving and is far from the state at which small molecule chemistry is understood. Rather than looking at this fact as detrimental to biomaterial science, we believe that the goal of producing biomolecular-based devices will lead to many exciting and novel advances in our understanding of how both isolated and assembled proteins accomplish their multifaceted functions.

Acknowledgments

This work was supported by Grant Nos. GM–31756 and –33775 from the National Institutes of Health (S. G. Sligar), the National Science Foundation (NSF) support of the Illinois Materials Research Laboratory, NSF Grant No. CHE 9120066 (P. W. Bohn), the Biotechnology Research and Development Corporation, and The Beckman Institute.

References

1. Lawrence, A. F.; Birge, R. R. Chapter 6 in this volume.
2. Mathews, F. S.; Levine, M.; Argos, P. *J. Mol. Biol.* **1972**, *64*, 449–464.
3. Pochapsky, T. C.; Sligar, S. G.; McLachlan, S. J.; La Mar, G. N. *J. Am. Chem. Soc.* **1990**, *112*, 5258–5263.
4. von Bodman, S. B.; Schuler, M. A.; Jollie, D. R.; Sligar, S. G. *Proc. Natl. Acad. Sci. U.S.A.* **1986**, *83*, 9443–9447.
5. Mauk, M. R.; Reid, L. S.; Mauk, A. G. *Biochemistry* **1982**, *21*, 1843–1846.
6. McLendon, G.; Miller, J. R. *J. Am. Chem. Soc.* **1985**, *107*, 7811–7816.
7. Stayton, P. S.; Fisher, M. T.; Sligar, S. G. *J. Biol. Chem.* **1988**, *263*, 13544–13548.
8. Mauk, M. R.; Mauk, A. G. *Biochemistry* **1982**, *21*, 4730–4734.
9. Stayton, P. S.; Olinger, J.; Bohn, P. W.; Sligar, S. G. *J. Am. Chem. Soc.* **1992**, *114*, 9298–9299.
10. Berry, E. A.; Trumpower, B. L. *Anal. Biochem.* **1987**, *161*, 1–15.
11. Walls, D. J.; Bohn, P. W. *J. Phys. Chem.* **1990**, *94*, 2039–2042.
12. Walls, D. J.; Bohn, P. W. *J. Chem. Phys.* **1989**, *93*, 2976–2982.
13. *Biological Applications of Raman Spectroscopy: Resonance Raman Spectra of Heme and Metalloproteins*; Spiro, T. G., Ed.; John Wiley & Sons: New York, 1988.
14. Rodgers, K. K.; Pochapsky, T. C.; Sligar, S. G. *Science (Washington, D.C.)* **1988**, *240*, 1657–1659.
15. Rodgers, K. K.; Sligar, S. G. *J. Mol. Biol.* **1991**, *221*, 1453–1460.

16. Sharp, K. A.; Honig, B. *Annu. Rev. Biophys. Biophys. Chem.* **1990**, *19*, 301–322.
17. Gilson, M.; Sharp, K.; Honig, B. *J. Comput. Chem.* **1987**, *9*, 327–335.
18. Rodgers, K. K.; Sligar, S. G. *J. Am. Chem. Soc.* **1991**, *113*, 9419–9421.
19. Marcus, R. A.; Sutin, N. *Biochim Biophys. Acta* **1985**, *811*, 265–322.
20. Varadarajan, R.; Zewert, T. E.; Gray, H. B.; Boxer, S. G. *Science (Washington, D.C.)* **1989**, *243*, 69–72.
21. Sligar, S. G., Bechman Institute, University of Illinois, unpublished results.
22. Martinis, S. A.; Sotiriou, C.; Chang, C. K.; Sligar, S. G. *Biochemistry* **1989**, *28*, 879–884.
23. Wright, K. A.; Boxer, S. G. *Biochemistry* **1981**, *20*, 7546–7556.
24. Varadarajan, R.; Lambright, D. G.; Boxer, S. G. *Biochemistry* **1989**, *28*, 3771–3781.
25. Blough, N. V.; Zemel, H.; Hoffman, B. M.; Lee, T. C. K.; Gibson, Q. H. *J. Am. Chem. Soc.* **1980**, *102*, 5683–5685.
26. McGourty, J. L.; Peterson-Kennedy, S. E.; Ruo, W. Y.; Hoffman, B. M. *Biochemistry* **1987**, *26*, 8302–8312.
27. Natan, M. J.; Hoffman, B. M. *J. Am. Chem. Soc.* **1989**, *111*, 6468–6470.
28. Liang, N.; Mauk, A. G.; Pielak, G. J.; Johnson, J. A.; Smith, M.; Hoffman, B. M. *Science (Washington, D.C.)* **1988**, *240*, 311–313.
29. Nocera, D. G.; Winkler, J. R.; Yocom, K. M.; Bordignon, E.; Gray, H. B. *J. Am. Chem. Soc.* **1984**, *106*, 5145–5150.
30. Crutchley, R. J.; Ellis, W. R.; Gray, H. B. *J. Am. Chem. Soc.* **1985**, *107*, 5002–5004.
31. Willie, A.; Stayton, P. S.; Sligar, S. G.; Durham, B.; Millett, F. *Biochemistry* **1992**, *31*, 7237–7242.
32. Egeberg, K. D.; Springer, B. A.; Martinis, S. A.; Sligar, S. G.; Morikis, D.; Champion, P. M. *Biochemistry* **1990**, *29*, 9783–9791.
33. Eccles, J.; Honig, B. *Proc. Natl. Acad. Sci. U.S.A.* **1988**, *80*, 4959–4962.

RECEIVED for review March 12, 1992. ACCEPTED revised manuscript March 9, 1993.

The Photochemical Reaction Cycle of Bacteriorhodopsin

Janos K. Lanyi

Department of Physiology and Biophysics, University of California,
Irvine, CA 92717

The complex spectroscopic transformations during the reaction cycle of the light-driven proton pump, bacteriorhodopsin, are satisfactorily explained with a single-photoreaction scheme, which contains reversible reactions. The proposed model, derived by fitting time-resolved difference spectra, is $BR \xrightarrow{h\nu} K \leftrightarrow L \leftrightarrow M_1 \rightarrow M_2 \leftrightarrow N \leftrightarrow O \rightarrow BR$. Some of these reactions are correlated with retinal bond motions, others with proton transfers internal and external to the protein. Thermodynamic analysis indicates that mechanistic coupling to proton potential is at the $M_1 \rightarrow M_2$ step, which also functions as the switch that confers direction to the net proton translocation.

BACTERIORHODOPSIN IS A SMALL INTEGRAL MEMBRANE PROTEIN, located in two-dimensional hexagonal arrays of approximately 0.5- μm diameter ("purple membrane") on the surface of halobacteria (for reviews cf. references 1–9). The polypeptide chain consists of seven closely packed α -helical segments looped across the lipid bilayer (10). The interhelical space enclosed by the helices contains an all-*trans*-retinal whose carbon skeleton lies about 21° inclined from the plane of the membrane. The retinal is linked to lys-216 on helix G as a protonated Schiff base. The light-induced *trans*-to-*cis* isomerization of the C₁₃–C₁₄ bond, and possibly other bond torsions, set off a cyclic reaction in which protons are transferred between the Schiff base and the aspartate residues internal to the protein. This series of proton transfer reactions results in the net electrogenic transfer of a proton from one side of the protein (and the membrane) to the other (11). The overall turn-over time for the cycle is about 10 ms, which allows use of light even at high intensities. Thus,

0065-2393/94/0240-0491\$08.00/0
© 1994 American Chemical Society

bacteriorhodopsin is an effective light-driven proton pump and a transmembrane current generator (5, 6).

The thermal reactions that follow the appearance of the first stable intermediate in the cyclic reaction sequence have been studied in the visible and the Fourier transform infrared (FTIR and resonance Raman) domains with a large number of different ways (reviewed recently in reference 9): measurement of transient flash-dependent absorption changes at single wavelengths (12–16), phase-modulation spectroscopy (17–20), measurement of photostationary states and their thermal transitions at low (e.g., liquid nitrogen) temperatures (21–25), gated optical multichannel spectroscopy (26–32), and stroboscopic methods (33–35). Individually, many of these methods are deficient in some way; the sensitivity, the time and wavelength resolution, and the unambiguous interpretation of the results have presented problems.

Nevertheless, it has been evident for some time that the bacteriorhodopsin reaction cycle, or “photocycle”, is described by six spectroscopically distinct intermediates that occur in a roughly linear sequence. The intermediates are labeled J, K, L, M, N, and O, sometimes including their wavelength maxima in the visible as subscripts. The time scale on which these species arise and decay ranges from femtoseconds to milliseconds. Vibrational spectroscopy has indicated that K represents a strained 13-*cis* retinal configuration (36–38), which relaxes in the L state. In the L to M reaction the Schiff-base proton passes to asp85 (39–43), and an unknown residue is triggered to release a proton to the extracellular side of the membrane (44–48). The Schiff base is reprotonated from asp96 in the M to N reaction (33, 40, 49–52), followed by reprotonation of asp96 itself from the cytoplasmic surface (51–54) and reisomerization of the C₁₃–C₁₄ bond to *trans* (55) in the N to O reaction. The final O to BR (bacteriorhodopsin) reaction recovers the initial chromophore via loss of proton from asp85 (35).

A more exact description of these and possibly other reactions, which might take place, has been hindered by lack of a methodology to determine the rate constants from the measurable spectroscopic changes during the photocycle (56–58). Also missing, and for the same reasons, was a description of the energetics of the reactions and how free energy is passed from the chromophore to the transported proton during the photocycle so as to create an electrochemical proton gradient across the membrane.

Strategies toward Solving the Kinetics

The solution of kinetics that generate complex multicomponent spectral mixtures, as in the case of bacteriorhodopsin, is very difficult, if not impossible, when the component spectra are not known. In the nano-

second to millisecond time domain, the bacteriorhodopsin photocycle contains at least five spectrally distinguishable species. Because the fractional sum of their concentrations adds up to 1 but the amount of bacteriorhodopsin that enters the photocycle is usually unknown, the problem is $5 \times 4 + 1$ (i.e., 21-dimensional). Faced with a problem of this magnitude, most investigators have not attempted to find mathematically exact solutions. Instead, the time courses of the observable reactions were determined at various wavelengths in the visible and infrared domains (and with photoelectric measurements), and their phenomenological descriptions were examined for consistency with various plausible models.

From these measurements (summarized in reference 59), it is evident that the kinetics are described by at least six relaxation times, depending to some extent on the noise in the data and the method of fitting. Nevertheless, the numbers obtained are approximately the same regardless of the means of measurement. The numbers are generally agreed to be 1–2, 30–70, and 200–300 μs and 1–1.5, 3–5, and 10–20 ms. These time constants are often associated with specific interconversions of the photocycle, but in reality they are related to elementary rate constants in a complex and model-dependent (i.e., unknown) way. The fact that the absorption spectra associated with these relaxation times are clearly mixtures rather than spectra of individual components rules out a single sequence with unidirectional reactions (30, 60).

Most measurements in the past were on the M state, which has a maximum well removed from that of bacteriorhodopsin, whereas those of the others overlap it and each other considerably. The observed kinetics of the rise and decay of M have been also inconsistent with a single sequence of unidirectional reactions. Both rise and decay occur with several time constants, and in a pH-dependent manner. These complications have led to suggestions of multiple interconvertible bacteriorhodopsin subpopulations, each with a photocycle and reactions of different time constants (61–64), as well as branched (65) or multiphoton (53) photocycles. The common thread in these models is that the multiexponential kinetics are attributed to parallel reactions that overlap in time, and each pathway has its own time constants that are observed as components of apparent multiexponential processes. The amplitudes in these models are directly related to the fraction of bacteriorhodopsin that participates in the parallel reaction pathways or branches. Thus, the time constants and the amplitudes are entirely independent of one another. Another kind of model attributes the multiexponential kinetics to a single pathway but one which contains reversible reactions (31–33, 51, 52, 66–68). These reactions are described by sums of exponentials also, but the amplitudes and time constants are both functions of the same elementary rate constants and therefore are not independent of

one another. The single pathway kind of model is easier to examine than the multiple pathway kind of model, because changing the conditions that will change the elementary rate constants, such as temperature, pH, humidity of bacteriorhodopsin films, and so on, constitutes a rigorous test of the model. The fact that models with reverse reactions have survived such testing (27, 32, 52, 68, 69) argues, to some degree, in their favor.

A more common, intuitive approach to solving this kind of a kinetic problem is to decide among the possible models by designing specific experimental conditions that test their predictions. Such thinking has been applied to explore single isolated questions concerning photocyclic steps. For example, perturbation of the O decay reaction with a temperature jump (66) was used to test the idea that this intermediate might be in equilibrium with the state preceding it (i.e., N). Resumption of normal O decay after temperature reequilibration indeed argued for a temperature-dependent $N \leftrightarrow O$ equilibrium. Similarly, varying the pH tested the model in which the $N \rightarrow O$ step, but not the postulated $M \leftrightarrow N$ internal reaction, represents protonation directly from the external medium (51, 52, 54).

Optical Multichannel Spectroscopy

A global solution of the photocycle requires measurements of absorption changes at several wavelengths, so as to include all states in the measured kinetics. In principle the number of wavelengths at which the changes are followed need not be more than the number of intermediates (58). Nevertheless, increasing the wavelength resolution will add redundant information, a consideration well worth taking into account when the measurements have low signal-to-noise ratio. Analyses that depend on the shape of the derived component spectra (cf. the next section) require good wavelength resolution in any case. Gated optical multichannel spectroscopy produces excellent resolution in the wavelength domain, although less so in the time domain. In our adaptation of this measurement (70) it is with a Princeton Instruments Corporation Optical Spectroscopic Multichannel Analyzer (OSMA) sketched in Figure 1A. The sample is placed usually in a 4×10 mm thermostatted cuvette (the shorter pathlength in the direction of the probe beam). In most cases the bacteriorhodopsin is encased in a fully hydrated polyacrylamide gel, which improves the optical properties and ensures good repeatability. Alternatively, the protein is deposited on the diagonal inside wall of a triangular cuvette, and the hydration of the film is controlled with a strip of filter paper soaked in a salt solution of the appropriate concentration (27). When the measurements are much below ambient temperature, condensation of moisture is prevented with a stream of dry

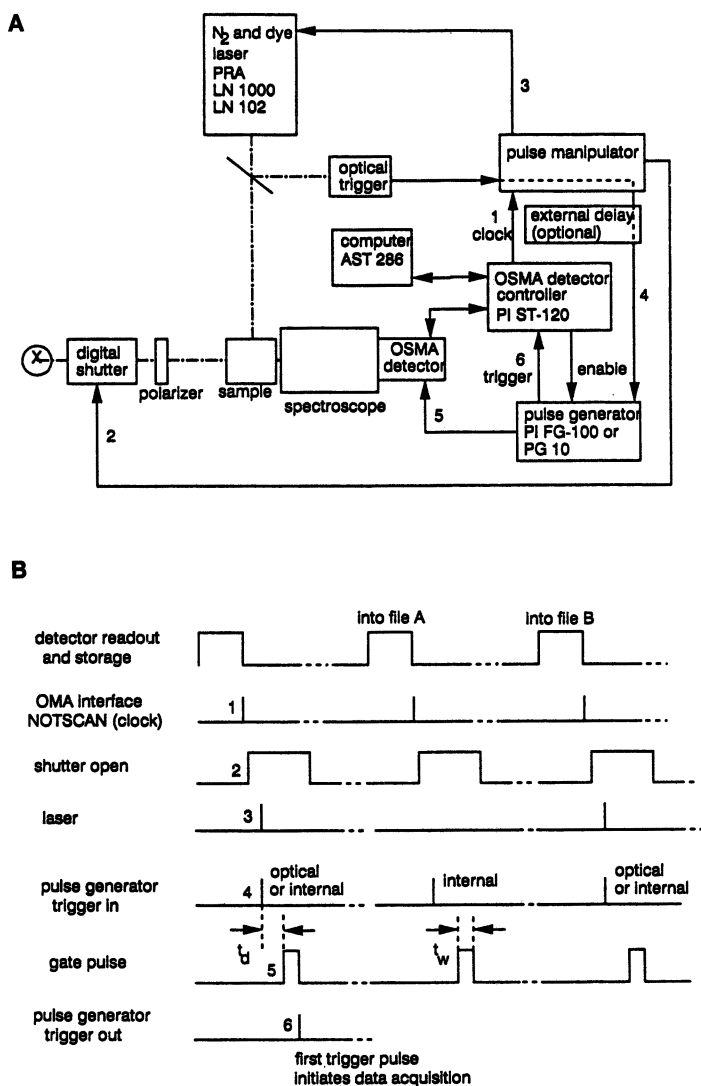


Figure 1. Schematic description of an optical multichannel analyzer (A) and its triggering (B). The numbers 1–6 refer to timing signals, as explained in the text. (Reproduced from reference 70. Copyright 1989 American Chemical Society.)

nitrogen over the cuvette faces. The pump beam (laser flash) is at a right angle to the measuring light. The measuring light is polarized at the "magic angle", taking into account the polarization ratio of the laser (15), to eliminate possible interference of rotation of the protein and the chromophore with the measured kinetics. The probe beam (a white continuum) is provided by a 250 W tungsten-halogen lamp, and the incident intensity is reduced by a 1.5-mm diameter diaphragm placed immediately in front of the lamp to avoid actinic and heating effects. For the same reasons, the probe beam is chopped with a digital shutter. The source of the actinic light is a nitrogen laser pumped dye laser, of 600-ps pulse duration (Photochemical Research Associates, models LN 1000 and LN 102). The wavelength maximum of the dye is usually 580 nm. After the sample the probe beam is focussed on the entrance slit of a Jarrell–Ash Monospec 27 spectroscopy, equipped with a 150 groove per mm grating. The spectrum is projected onto a Princeton Instruments IRY-700 gated intensified diode array detector, connected to a Princeton Instruments ST-120 detector controller. Gating of the detector is with Princeton Instruments FG-100 and PG-10 gate pulse generators, in the 50- to 250-ns and the 250-ns to 7-ms delay ranges, respectively. Longer delays are generated externally. The lengths of the gating pulses are varied from 20 ns to several microseconds, in order to provide optimal signal-to-noise ratios while keeping the pulses short relative to the delay times. The delay times (given, for example, in Figure 2) are the time intervals between the flash and the center of the gating pulse width. The control of data acquisition and analysis is with an AST 286 desktop computer, using software provided by Princeton Instruments Corporation, as well as Lotus 123 spreadsheets, the SPSEV program, and various programs written in compiled BASIC. The timing of the experiments is set with a home-built transistor–transistor logic (TTL)-pulse manipulator.

The timing of trigger signals is shown in Figure 1B. The ST-120 detector controller runs freely at several Hz, adjusted by software, providing an exposure time of several hundred ms. The NOTSCAN output (as provided by the manufacturer) of the controller (1) is used as primary clock pulse source. The pulse manipulator provides trigger pulses for the digital shutter (2), the laser (3), and the gate pulse generators (4). After the arrival of each NOTSCAN signal, the shutter is opened for 20 ms (or 20–100 ms when longer delay times are selected). Five ms after every second shutter opening, the laser is fired and the signal from an optical trigger is used to trigger the gate pulse generators. For every other shutter opening, when the laser is absent, a trigger pulse internally generated by the pulse manipulator is sent to the gate pulse generators. The gate pulse generators provide gating pulses of the desired delay and width (5), and the detector accumulates signals proportional to the

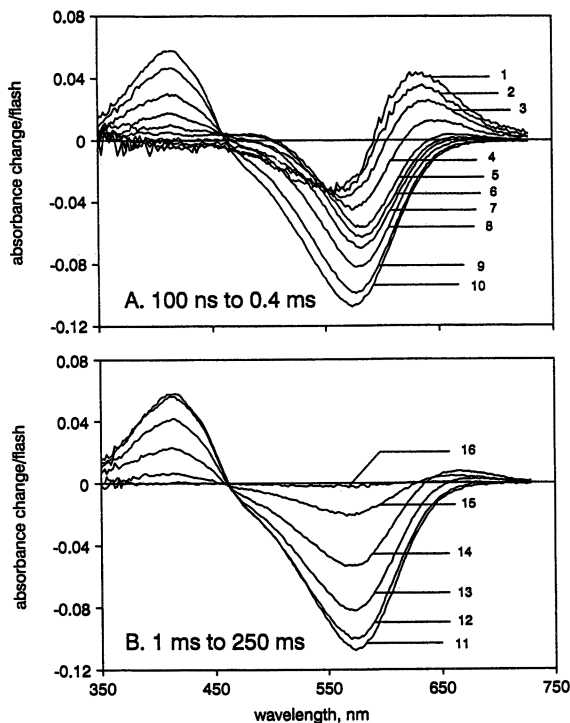


Figure 2. Time-resolved difference spectra from a bacteriorhodopsin sample. Delay times after photoexcitation for the curves, designated with 1 through 16, were 100, 250, and 600 ns; 1.5, 4, 10, 25, 60, and 150 μ s; and 0.4, 1, 2.5, 6, 15, 40, and 250 ms, respectively. Conditions: 40 nmol/ml bacteriorhodopsin in 100 mM NaCl and 50 mM phosphate, pH 7.0, 20°C. (Reproduced from reference 31. Copyright 1991 American Chemical Society.)

light intensity at 700 out of the 1024 diodes during the gating, resolving the wavelength range of 350–725 nm. Readout and storage of the data follows each exposure period before the next acquisition cycle. The first trigger-out signal from the gate pulse generators (6) initiates the data acquisition sequence; then these trigger-out signals are disregarded by the detector controller. For each particular gating pulse delay up to 1000 scans are averaged alternately into each of two separate files, one with and another without the laser. In this way, the initial state absorption and the absorption of the intermediates are measured in parallel, eliminating the effect of slow changes in either lamp intensity or sample absorbance and scattering. As a result, the difference spectra calculated from the two files are virtually free of baseline distortions. The same cuvette with the corresponding buffer solution is used to re-

cord the incident light intensity, and using this, the absolute spectrum of the sample is calculated for each difference spectrum. When necessary, the difference spectra are normalized according to the absolute spectra to eliminate effects of any changes in the sample absorbance over many measurements. A mathematically constructed light-scattering spectrum is subtracted from some of the absolute spectra, with the criterion that the resulting absorbance spectra closely resemble the absorbance of octylglucoside-solubilized bacteriorhodopsin sample.

Grid-Search

Figure 2 shows typical time-resolved difference spectra at various delay times after photoexcitation. A spectrally oriented analysis of such spectra (31, 32) regards the data set as a collection of difference spectra made up of different linear combinations of component spectra. Instead of extracting the time dependencies of the reactions from the data, the task here is to derive the component spectra from considerations of their likely properties (shapes, bandwidths, relative amplitudes, etc.) in a model-independent way. All spectra allowed by the data are generated, and those inconsistent with the carefully chosen criteria are rejected. The validity of this approach depends on how much is known or predicted about these spectra, and if there is a strong global minimum (i.e., if all solutions allowed by the criteria cluster close together on grid points in multidimensional parameter space).

It is essential to know how many spectral species are present. Sometimes this information is apparent from the way the difference spectra develop in time, and from their isosbestic points. If clearcut, the number of basis spectra in SVD analysis (29, 30) will be a basis for deciding how many components make up the data. For the bacteriorhodopsin photocycle it is generally agreed that in the nanosecond to millisecond time range five spectrally distinct intermediate states are found: K, L, M, N, and O. Typically, from the set of 30–40 measured difference spectra, spaced evenly on a logarithmic time scale between 10^{-7} and 10^{-1} s, we choose five subsets in which one of each putative component is represented with a larger amplitude than the others. These subsets are the difference base spectra, and they are evaluated after adding the spectrum of bacteriorhodopsin with an amplitude corresponding to the amount of chromophore entering the photocycle (71). The amount of chromophore is not known from the measurement, but can be estimated either from successive approximations or by a less subjective method, as described later. Because the base spectra $\epsilon_i(\lambda)$ are linear sums of the component spectra and the spectra of the intermediates K, L, M, and so on, are $\epsilon_K(\lambda)$, $\epsilon_L(\lambda)$, $\epsilon_M(\lambda)$, and so on,

$$\epsilon_i(\lambda) = a_{i1} \cdot \epsilon_K(\lambda) + a_{i2} \cdot \epsilon_L(\lambda) + a_{i3} \cdot \epsilon_M(\lambda) + \dots \quad (1)$$

where a_{ij} are the (unknown) amplitudes of the component spectra. The base spectra are used to generate candidates for the component spectra in the following way. For five intermediates, the matrix A contains 5 times 5 elements

$$A = \begin{pmatrix} a_{11} & a_{12} & a_{13} & \cdots \\ a_{21} & a_{22} & a_{23} & \cdots \\ a_{31} & a_{32} & a_{33} & \cdots \\ \cdots & & & \\ \cdots & & & \end{pmatrix} \quad (2)$$

but because the spectra can be scaled so that for each i

$$\sum_{j=1}^j a_{ij} = 1 \quad (3)$$

A has only 20 independent elements. A is determined therefore by a 20-dimensional array whose axes assume values from 0 to 1, forming a 20-dimensional grid of N points. Each of these points is thus determined by 20 coordinate values, and gives a spectrum for K , L , and M , as follows:

$$\epsilon_K(\lambda) = \frac{\begin{vmatrix} \epsilon_1(\lambda) & a_{12} & a_{13} \\ \epsilon_2(\lambda) & a_{22} & a_{23} \\ \epsilon_3(\lambda) & a_{32} & a_{33} \\ \cdots & & \\ \cdots & & \end{vmatrix}}{\det A} \quad (4)$$

$$\epsilon_L(\lambda) = \frac{\begin{vmatrix} a_{11} & \epsilon_1(\lambda) & a_{13} & \cdots \\ a_{21} & \epsilon_2(\lambda) & a_{23} & \cdots \\ a_{31} & \epsilon_3(\lambda) & a_{33} & \cdots \\ \cdots & & & \\ \cdots & & & \end{vmatrix}}{\det A} \quad (5)$$

and similarly for the other intermediates.

In the search through array A the calculated component spectra are subjected to various restricting criteria (71). Some of these criteria are rigorous, such as requiring that the spectra have no negative amplitudes at any wavelength; others are less certain but defensible to various degrees based on what is known about polyene excited states and measured rhodopsin spectra in general.

A 20-dimensional array cannot be fully explored with available computing power, but a smaller array that corresponded to the simpler photocycle of the recombinant asp96asn protein was recently thoroughly described (71) at a grid resolution of 1:50 (i.e., with increments of 0.02 along each of the axes). In this system the reprotonation of the Schiff base (i.e., the M \rightarrow N reaction) is considerably slowed by the lack of an internal proton donor and neither N nor O accumulate. The spectral mixtures contain therefore only K, L, and M, and the array A is six-dimensional. Three filters were used: (1) negative absorption and more than one absorption band for M were disallowed, (2) amplitudes for K and L near 400 nm different from the absorption of bacteriorhodopsin were disallowed, and (3) amplitudes greater than the absorption maximum of bacteriorhodopsin and spectral half-widths greater than usually observed for rhodopsins were disallowed. Two surprising results emerged from this analysis. First, the number of solutions show a narrow distribution around the photocycling bacteriorhodopsin fraction. This distribution fixes the scaling amplitude for the bacteriorhodopsin spectrum in the conversion of difference base spectra into absolute base spectra (cf. the preceding paragraph). Second, the averages of the six matrix elements remain within one standard deviation (SD) from their initial value after the first filter as the solution space is narrowed down, progressively with the two subsequent filters, to a few hundred array points. The results indicated that the solution lies within a dense cluster of valid array points, and the filtering process eliminates preferentially those points that are farthest away from this point. All of this suggest that in such a spectrally oriented analysis the solution converges toward a strong and unequivocal global minimum.

Attempts were made to find the global minimum for five intermediates by dividing the photocycle into two halves and by searching the two arrays intuitively with an interactive program (31, 32). Although no a priori assurance that this method leads to the single and best solution exists, the results with the simpler asp96asn photocycle (31) suggest that it does. Indeed, the spectra for K, L, and M are quite similar from the simplified and the complete photocycle, and the spectra for K, L, and M provided also the spectra for N and O as well. An independent way of deciding if the spectra are correct is provided from earlier low-temperature studies of bacteriorhodopsin photoequilibria (24, 72), and from the ethylenic stretch frequencies of the intermediates that are linearly related to the wavelengths of the absorption maxima in the visible domain (73). The derived spectra, shown in Figure 3, are consistent with these.

Kinetic Models

If the component spectra derived from the base spectra are valid for each of the individual measured spectra, the individual measured spectra

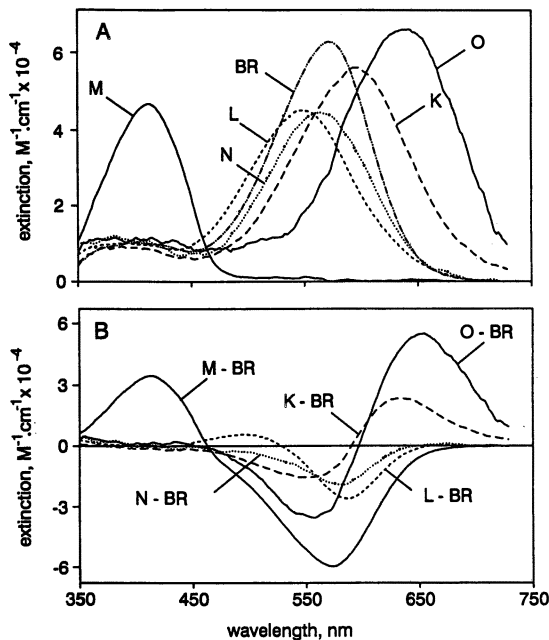


Figure 3. Derived absolute absorption spectra (A) and difference spectra (B) for the photocycle intermediates. (Reproduced from reference 31. Copyright 1991 American Chemical Society.)

can be fitted with the weighted combination of the component spectra and the sums of the weights will be constant until the initial state begins to repopulate. This repopulation is an important criterion of the validity of the spectra (27), as is the fact that in most single photocyclic models, regardless of their complexity earlier in the reaction cycle, the recovery of the initial bacteriorhodopsin state is described by a single exponential. The weights of the components are, of course, the time dependent concentrations that are to be fitted with various alternative models. For a process that includes six to seven orders of magnitude of time, as the bacteriorhodopsin photocycle, the concentrations are best represented on a logarithmic time scale, as in Figure 4. The predictions of various kinetic models and their rate constants are generated with numerical integration.

Important conclusions about the kinetics can be drawn already from the simplified kinetics of the asp96asn protein, or the first half of the photocycle of the wild-type protein. Three time constants are seen, which are all shared by the decays of K and L and the rise of M. This fact makes simple schemes with parallel photocycle very unlikely and argues instead in favor of the $K \leftrightarrow L \leftrightarrow M$ scheme. This scheme is sup-

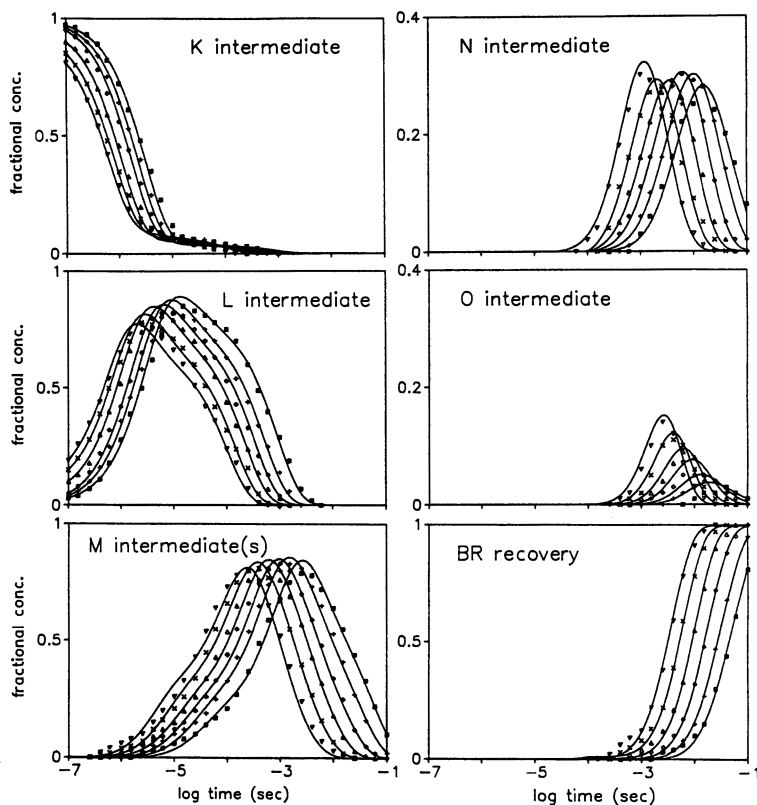


Figure 4. Calculated time-dependent concentrations of the photocycle intermediates at 5, 10, 15, 20, and 25 °C, and the best fit of the single photocycle model in the text (lines). Key: ■, 5 °C; +, 10 °C; ◆, 15 °C; ▲, 20 °C; ×, 25 °C; and ▼, 30 °C. (Reproduced from reference 32. Copyright 1991 American Chemical Society.)

ported by the consistency of the time constants with the amplitudes, a requirement for the reversible reactions. The consistency remains remarkably good at different temperatures where the elementary rate constants change and to different extents. The second half of the photocycle is not as easily analyzed because N and O do not accumulate in large enough amounts to calculate their spectra with great certainty. Nevertheless, there is enough independent supporting evidence to accept, for the time being, the scheme $M \leftrightarrow N \leftrightarrow O \rightarrow BR$. Interestingly, the data indicate that in bacteriorhodopsin immobilized in the purple membrane lattice, and particularly at higher pH, there is an additional shunt reaction, $N \rightarrow BR$ (32, 74).

The combined scheme for the two halves of the photocycle, $K \leftrightarrow L \leftrightarrow M \leftrightarrow N \leftrightarrow O \rightarrow BR$ (plus $N \rightarrow BR$) does not fit the data, however,

without an additional feature. In such a model the kinetics of each intermediate will contain, by necessity, components with the time constants of all the intermediates that follow. However, the intermediates K and L, in particular, decay to zero concentration whereas M is at maximal concentration (Figure 4). This fact is not as easily established with wild-type bacteriorhodopsin because the spectra of L and N are not different enough to calculate their exact concentrations if and when they coexist, as they do just at this time in the photocycle (31, 68). However, under properly chosen conditions N does not accumulate in the asp96asn protein and the kinetics of L can be followed with confidence. In this system the concentration of L was <1% of M (i.e., below measurement error) near the time of the maximum concentration of M (31).

The simplest way to solve this paradox was to introduce two M substates that are connected by a unidirectional reaction: $M_1 \rightarrow M_2$ (31, 32, 67). In this modification of the model, K first equilibrates with L, then both equilibrate with M_1 , and finally the mixture containing constant proportions of K, L, and M_1 decays with the rate of the $M_1 \rightarrow M_2$ reaction. Initially, therefore, the idea of M substates was a kinetic concept. In monomeric bacteriorhodopsin, however, a splitting of the M spectra into two is seen, separated by a 4-nm shift in their maxima, and the interconversion of these spectroscopic substates has the same time course as the predicted $M_1 \rightarrow M_2$ reaction from the kinetics (31). The shift in the spectrum of M is confirmed in other reports (30, 75). For reasons that are not yet clear, in the monomeric recombinant protein asp115asn the shift is as large as 15 nm (76). These observations provide independent support for the proposed M substates.

The photocycle scheme with the single reaction sequence, thus derived, $BR \xrightarrow{h\nu} K \leftrightarrow L \leftrightarrow M_1 \rightarrow M_2 \leftrightarrow N \leftrightarrow O \rightarrow BR$ (32) greatly simplifies the conceptual framework for studying the mechanism of proton transport in this system and has led to insights to the exchange of free energy between the chromophore and the transported proton.

The Photocycle in Bacteriorhodopsin Films

Thin films formed by deposition of purple membranes onto a glass surface are optically superior to suspensions, and light-induced absorption changes in such a system have been determined with better signal-to-noise ratio. These films also afforded the opportunity to study the effects of withdrawing water from the protein (27) because greater dehydration was possible than when using osmotically active solutes in aqueous solutions (52).

It has been known for some time that the photocycle is affected by the amount of water associated with bacteriorhodopsin. The O inter-

mediate was not observable in films at humidities below 90% (77). As humidity was further decreased, both the M rise and the M decay deviated increasingly from single exponentials; the M rise was accelerated, whereas the M decay was slowed down (77, 78). The photoelectric signals attributed to these spectroscopic transitions indicated that with decreasing humidity less and less net transfer of protons occurred across the protein (77, 79). Instead, the $M \rightarrow BR$ pathway seemed to consist of the intramolecular return of the charge (proton) to the Schiff base without the additional movement necessary to breach the full length of the dielectric barrier. These effects were beginning to dominate at about 60% humidity. At still lower water activities, other phenomena, such as changes in the thermal *cis-trans* isomerization equilibrium (80), spectral shifts (81), and the disappearance of the M intermediate (79, 82), were also reported.

The results with optical multichannel spectroscopy (27) confirmed, by and large, expectations from the earlier studies. At 100% hydration the photocycle kinetics of the films were similar, although not quite identical to what was observed for membrane suspensions. The main effects of dehydration at about 65% relative humidity were: (1) The normal course of the decay of M_2 through N was blocked, and the recovery of BR was thereby greatly lengthened, and (2) Recovery of BR was increasingly through a direct pathway from M_2 and even M_1 . Recent results with asp96asn bacteriorhodopsin (52) make it very likely that the latter pathways do not involve reprotonation of the Schiff base from asp96 because lesser internal hydration of the protein near asp96 increases the free energy of the aspartate-proton ion pair, which constitutes the transition state of this reaction.

Transport Mechanism and Thermodynamics

The model $K \leftrightarrow L \leftrightarrow M_1 \rightarrow M_2 \leftrightarrow N \leftrightarrow O \rightarrow BR$, and the elementary rate constants calculated from it, provides a framework for evaluating a large amount of other available information. From the perspective of this model the molecular explanation of the photoreactions can be summarized as follows. The light-induced bond distortions of the retinal in K relax, in a reaction equilibrium lying about 10:1 in the forward direction, to a more stable 13-*cis* retinal configuration in L. The proton transfer from the Schiff base to asp85 is a reaction at about a 1:1 equilibrium (i.e., between two groups of the same pK) (32). The unidirectional $M_1 \rightarrow M_2$ reaction serves as the much discussed (9, 10, 83–85) switch that enables reprotonation of the Schiff base from a residue other than its proton acceptor (i.e., asp96). Since asp85 is on the extracellular side of the protein relative to the Schiff base, whereas asp96 is on the cytoplasmic side, the switch confers directionality on the overall

proton transfer pathway. Reprotonation of asp96 in the $N \rightarrow O$ reaction is indeed from the cytoplasmic surface (54). The reprotonation of the Schiff base from asp96 is again in an equilibrium not far from unity [i.e., the proton transfer is again between two groups of the same negative logarithm of equilibrium constant (pK)] (32). Because the pK of asp85 in the initial bacteriorhodopsin state is about 3, whereas that of asp96 is about 10, the driving force for the internal proton transfers must be retinal isomerization-dependent pK shifts, more likely in the Schiff base than in the asp residues (cf. the following paragraphs). Reisomerization of the retinal to all-*trans* appears to depend, and in an unknown way, on the reprotonation of asp96, because at pH >8 the $N \rightarrow O$ reaction, which encompasses both, is linearly dependent on the proton concentration on the protein surface (49, 51–53, 67).

Because the internal proton transfers take place nearly isoenergetically, the question naturally arises: How is the excess free energy in the chromophore conferred onto the transported proton, so that it will be eventually conserved in the form of an increased electrochemical gradient of protons (protonmotive force) across the membrane. The flow of energy through this system, and the forms it takes during the photocycle is a question that naturally follows the kinetic description of the reaction sequence.

The excess enthalpy of the K intermediate was determined by calorimetry (86); a recent recalculation of the data gave a value of about 50 kJ/mol (87). This is almost certainly the magnitude of the excess free energy as well, because the retinal does not have a large enough number of degrees of motional freedom for a large entropy term, and large-scale conformational changes in the protein cannot take place on the nano-second time scale. A ΔG of this size would lower the Schiff-base pK to about 3 in L, a realistic value because this value is about equal to the pK of asp85. Hence by L most or all the excess free energy might reside in the lowered proton affinity of the Schiff base. An approximation of the free energy cycle of bacteriorhodopsin in purple membrane suspensions, shown in Figure 5C, can be obtained from the calculated rate constants of the model, and the consideration that in this open system neither the $M_2 \rightarrow M_1$ nor the $BR \rightarrow O$ back reactions can be faster than 0.005–0.01 times the rate of the forward reactions (31, 32). Thus, these data show that ΔG is lost only at these two reactions, whereas all others take place near zero ΔG . It is these two unidirectional reactions that drive the photocycle in the direction in which the transported proton gains free energy; because in a closed system, such as intact cells or cell envelope vesicles, protonmotive force accumulates M (88, 89) rather than O, the direct coupling to the protons must be to the $M_1 \rightarrow M_2$ reaction. The decrease of free energy at the $O \rightarrow BR$ reaction must serve, therefore, to reset the system to its initial state.

More detailed information about the forms the free energy takes as it passes through the system is available from the enthalpy and entropy cycles. The enthalpy cycle is defined by the measured enthalpy gain of the K intermediate, the activation enthalpies calculated from the temperature dependencies of the rate constants (which for the reversible reactions give also the enthalpy levels), and the earlier reported large enthalpy decrease near the middle of the photocycle (90, 91), which must be attributed in the present model to the $M_1 \rightarrow M_2$ reaction. The results, given in Figure 5A, indicate that the enthalpy level remains roughly constant until the switch reaction, and following the drop of ca. 80 kJ/mol below the enthalpy of the initial state at this step, it recovers via a series of endothermic reactions, M_2 to BR via N and O. The entropy cycle, shown in Figure 5B, is similar: The entropy is roughly constant until the $M_1 \rightarrow M_2$ reaction, where it sharply decreases. This decrease is so great (about 300 J/mol·K) that it must be attributed to a large-

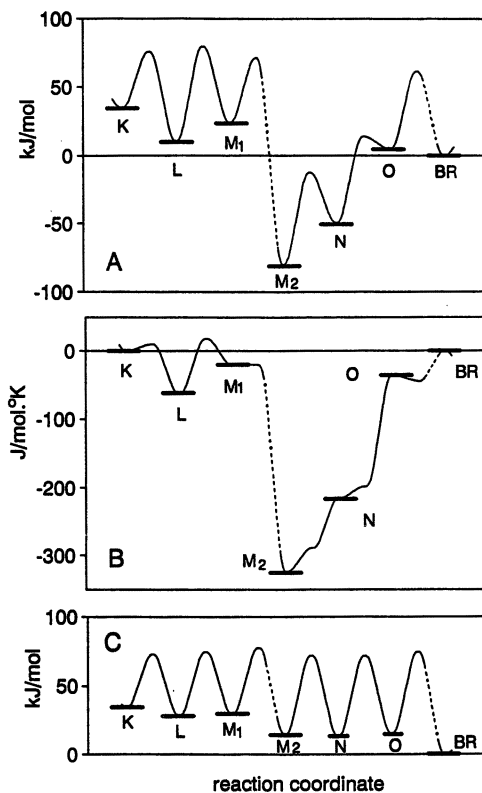


Figure 5. Enthalpy (A), entropy (B), and free energy (C) levels of the photocycle intermediates, and their transition states. For the sake of clarity, the $N \rightarrow BR$ shunt is left out (32).

scale protein conformational change. Part of this conformational change might serve the mechanistic function of reorienting the Schiff base from asp85 to asp96. The principal rationale for the striking enthalpy–entropy conversion at the $M_1 \rightarrow M_2$ reaction lies probably elsewhere; however, at this step part of the excess free energy is transferred to the transported proton, and the rest to the protein so that the Schiff-base pK will rise to its initial level above 10 and reprotonation from asp96 can take place. The free energy is stored as $T \cdot \Delta S$ by the protein conformational change drives the recovery of the initial bacteriorhodopsin state.

A variety of observations indicate that protein conformational changes do indeed occur in the photocycle and that they take place during and after the decay of M. The most interesting of these changes are those in the structure factors from time-resolved X-ray diffraction (92), which are associated, as are the entropy changes (32), with the $N \rightarrow O$ reaction.

Acknowledgment

The author is supported by grants from the National Institutes of Health (Grant No. GM 29498), Department of Energy, Office of Basic Energy Sciences (Grant No. DE-FGOER 13525), and the National Aeronautics and Space Administration (Grant No. NAGW-212).

References

1. Lanyi, J. K. In *Comparative Biochemistry: Bioenergetics*; Ernster, L., Ed.; Elsevier: Amsterdam, The Netherlands, 1984; pp 315–350.
2. Ovchinnikov, Yu. A. *Photochem. Photobiol.* **1987**, *45*, 909–914.
3. Oesterhelt, D.; Tittor, J. *Trends Biochem. Sci.* **1989**, *14*, 57–61.
4. Khorana, H. G. *J. Biol. Chem.* **1988**, *263*, 7439–7442.
5. Keszthelyi, L.; Ormos, P. *J. Membr. Biol.* **1989**, *109*, 193–200.
6. Trissl, H. W. *Photochem. Photobiol.* **1990**, *51*, 793–818.
7. Birge, R. R. *Biochim. Biophys. Acta Bioenerg.* **1990**, *1016*, 293–327.
8. Kouyama, T.; Kinosita, K.; Ikegami, A. *Adv. Biophys.* **1988**, *24*, 123–175.
9. Mathies, R. A.; Lin, S. W.; Ames, J. B.; Pollard, W. T. *Annu. Rev. Biophys. Biophys. Chem.* **1991**, *20*, 491–518.
10. Henderson, R.; Baldwin, J. M.; Ceska, T. A.; Zemlin, F.; Beckmann, E.; Downing, K. H. *J. Mol. Biol.* **1990**, *213*, 899–929.
11. Lozier, R. H.; Niederberger, W.; Bogomolni, R. A.; Hwang, S.; Stoeckenius, W. *Biochim. Biophys. Acta* **1976**, *440*, 545–556.
12. Dencher, N. A.; Wilms, M. *Biophys. Struct. Mech.* **1975**, *1*, 259–271.
13. Engelhard, M.; Gerwert, K.; Hess, B.; Kreutz, W.; Siebert, F. *Biochemistry* **1985**, *24*, 400–407.
14. Lozier, R. H.; Niederberger, W.; Ottolenghi, M.; Sivorinovsky, G.; Stoeckenius, W. In *Energetics and Structure of Halophilic Microorganisms*; Caplan, S. R.; Ginzburg, M., Eds.; Elsevier: Amsterdam, The Netherlands, 1978; pp 123–139.
15. Lozier, R. H. *Methods Enzymol.* **1982**, *88*, 133–162.

16. Chronister, E. L.; Corcoran, T. C.; Song, L.; El-Sayed, M. A. *Proc. Natl. Acad. Sci. U.S.A.* **1986**, *83*, 8580–8584.
17. Sherman, W. V.; Korenstein, R.; Caplan, S. R. *Biochim. Biophys. Acta* **1976**, *430*, 454–458.
18. Sherman, W. V.; Slifkin, M. A.; Caplan, S. R. *Biochim. Biophys. Acta* **1976**, *423*, 238–248.
19. Sinton, M. H.; Dewey, T. G. *Biophys. J.* **1988**, *53*, 153–162.
20. Hasselbacher, C. A.; Dewey, T. G. *Biochemistry* **1986**, *25*, 6236–6243.
21. Tokunaga, F.; Iwasa, T.; Yoshizawa, T. *FEBS Lett.* **1976**, *72*, 33–38.
22. Shichida, Y.; Matuoka, S.; Hidaka, Y.; Yoshizawa, T. *Biochim. Biophys. Acta* **1983**, *723*, 240–246.
23. Lozier, R. H.; Niederberger, W. *Fed. Proc.* **1977**, *36*, 1805–1809.
24. Becher, B.; Tokunaga, F.; Ebrey, T. G. *Biochemistry* **1978**, *17*, 2293–2300.
25. Ormos, P. *Proc. Natl. Acad. Sci. U.S.A.* **1991**, *88*, 473–477.
26. Milder, S. J.; Kliger, D. S. *Biophys. J.* **1988**, *53*, 465–468.
27. Váró, G.; Lanyi, J. K. *Biophys. J.* **1991**, *59*, 313–322.
28. Duñach, M.; Berkowitz, S.; Marti, T.; He, Y.-W.; Subramaniam, S.; Khorana, H. G.; Rothschild, K. J. *J. Biol. Chem.* **1990**, *265*, 16978–16984.
29. Hofrichter, J.; Henry, E. R.; Lozier, R. H. *Biophys. J.* **1989**, *56*, 693–706.
30. Milder, S. J.; Thorgeirsson, T. E.; Miercke, L. J. W.; Stroud, R. M.; Kliger, D. S. *Biochemistry* **1991**, *30*, 1751–1761.
31. Váró, G.; Lanyi, J. K. *Biochemistry* **1991**, *30*, 5008–5015.
32. Váró, G.; Lanyi, J. K. *Biochemistry* **1991**, *30*, 5016–5022.
33. Gerwert, K.; Souvignier, G.; Hess, B. *Proc. Natl. Acad. Sci. U.S.A.* **1990**, *87*, 9774–9778.
34. Braiman, M. S.; Ahl, P. L.; Rothschild, K. J. *Proc. Natl. Acad. Sci. U.S.A.* **1987**, *84*, 5221–5225.
35. Braiman, M. S.; Bousché, O.; Rothschild, K. J. *Proc. Natl. Acad. Sci. U.S.A.* **1991**, *88*, 2388–2392.
36. Braiman, M. S.; Mathies, R. A. *Biochemistry* **1980**, *19*, 5421–5428.
37. Rothschild, K. J.; Roepe, P.; Ahl, P. L.; Earnest, T. N.; Bogomolni, R. A.; Das Gupta, S. K.; Mulliken, C. M.; Herzfeld, J. *Proc. Natl. Acad. Sci. U.S.A.* **1986**, *83*, 347–351.
38. Siebert, F.; Mantele, W. *Eur. J. Biochem.* **1983**, *130*, 565–573.
39. Braiman, M. S.; Mogi, T.; Marti, T.; Stern, L. J.; Khorana, H. G.; Rothschild, K. J. *Biochemistry* **1988**, *27*, 8516–8520.
40. Butt, H.-J.; Fendler, K.; Bamberg, E.; Tittor, J.; Oesterhelt, D. *EMBO J.* **1989**, *8*, 1657–1663.
41. Otto, H.; Marti, T.; Holz, M.; Mogi, T.; Stern, L. J.; Engel, F.; Khorana, H. G.; Heyn, M. P. *Proc. Natl. Acad. Sci. U.S.A.* **1990**, *87*, 1018–1022.
42. Marti, T.; Rösselet, S. J.; Otto, H.; Heyn, M. P.; Khorana, H. G. *J. Biol. Chem.* **1991**, *266*, 18674–18683.
43. Stern, L. J.; Ahl, P. L.; Marti, T.; Mogi, T.; Duñach, M.; Berkowitz, S.; Rothschild, K. J.; Khorana, H. G. *Biochemistry* **1989**, *28*, 10035–10042.
44. Grzesiek, S.; Dencher, N. A. *FEBS Lett.* **1986**, *208*, 337–342.
45. Heberle, J.; Dencher, N. A. *FEBS Lett.* **1990**, *277*, 277–280.
46. Drachev, L. A.; Kaulen, A. D.; Skulachev, V. P. *FEBS Lett.* **1984**, *178*, 331–335.
47. Váró, G.; Lanyi, J. K. *Biochemistry* **1990**, *29*, 6858–6865.
48. Liu, S. Y. *Biophys. J.* **1990**, *57*, 943–950.
49. Tittor, J.; Soell, C.; Oesterhelt, D.; Butt, H.-J.; Bamberg, E. *EMBO J.* **1989**, *8*, 3477–3482.

50. Gerwert, K.; Hess, B.; Soppa, J.; Oesterhelt, D. *Proc. Natl. Acad. Sci. U.S.A.* **1989**, *86*, 4943–4947.
51. Otto, H.; Marti, T.; Holz, M.; Mogi, T.; Lindau, M.; Khorana, H. G.; Heyn, M. P. *Proc. Natl. Acad. Sci. U.S.A.* **1989**, *86*, 9228–9232.
52. Cao, Y.; Váró, G.; Chang, M.; Ni, B.; Needleman, R.; Lanyi, J. K. *Biochemistry* **1991**, *30*, 10972–10979.
53. Kouyama, T.; Nasuda-Kouyama, A.; Ikegami, A.; Mathew, M. K.; Stoeckenius, W. *Biochemistry* **1988**, *27*, 5855–5863.
54. Kouyama, T.; Nasuda-Kouyama, A. *Biochemistry* **1989**, *28*, 5963–5970.
55. Smith, S. O.; Pardo, J. A.; Mulder, P. P. J.; Curry, B.; Lugtenburg, J.; Mathies, R. A. *Biochemistry* **1983**, *22*, 6141–6148.
56. Parodi, L. A.; Lozier, R. H.; Bhattacharjee, S. M.; Nagle, J. F. *Photochem. Photobiol.* **1984**, *40*, 501–506.
57. Nagle, J. F.; Parodi, L. A.; Lozier, R. H. *Biophys. J.* **1982**, *38*, 161–174.
58. Nagle, J. F. *Biophys. J.* **1991**, *59*, 476–487.
59. Müller, K.-H.; Butt, H. J.; Bamberg, E.; Fendler, K.; Hess, B.; Siebert, F.; Engelhard, M. *Eur. Biophys. J.* **1991**, *19*, 241–251.
60. Xie, A. H.; Nagle, J. F.; Lozier, R. H. *Biophys. J.* **1987**, *51*, 627–635.
61. Hanamoto, J. H.; Dupuis, P.; El-Sayed, M. A. *Proc. Natl. Acad. Sci. U.S.A.* **1984**, *81*, 7083–7087.
62. Dancsházy, Z.; Govindjee, R.; Ebrey, T. G. *Proc. Natl. Acad. Sci. U.S.A.* **1988**, *85*, 6358–6361.
63. Diller, R.; Stockburger, M. *Biochemistry* **1988**, *27*, 7641–7651.
64. Bitting, H. C.; Jang, D.-J.; El-Sayed, M. A. *Photochem. Photobiol.* **1990**, *51*, 593–598.
65. Butt, H.-J.; Fendler, K.; Dér, A.; Bamberg, E. *Biophys. J.* **1989**, *56*, 851–859.
66. Chernavskii, D. S.; Chizhov, I. V.; Lozier, R. H.; Murina, T. M.; Prokhorov, A. M.; Zubov, B. V. *Photochem. Photobiol.* **1989**, *49*, 649–653.
67. Váró, G.; Lanyi, J. K. *Biochemistry* **1990**, *29*, 2241–2250.
68. Ames, J. B.; Mathies, R. A. *Biochemistry* **1990**, *29*, 7181–7190.
69. Váró, G.; Lanyi, J. K. *Biochemistry* **1991**, *30*, 7165–7171.
70. Zimányi, L.; Keszthelyi, L.; Lanyi, J. K. *Biochemistry* **1989**, *28*, 5165–5172.
71. Zimányi, L.; Lanyi, J. K. *Biophys. J.* **1993**, *64*, 240–251.
72. Lozier, R. H.; Bogomolni, R. A.; Stoeckenius, W. *Biophys. J.* **1975**, *15*, 955–963.
73. Aton, B.; Doukas, A. G.; Callender, R. H.; Becher, B.; Ebrey, T. G. *Biochemistry* **1977**, *16*, 2995–2999.
74. Váró, G.; Duschl, A.; Lanyi, J. K. *Biochemistry* **1990**, *29*, 3798–3804.
75. Subramaniam, S.; Greenhalgh, D. A.; Rath, P.; Rothschild, K. J.; Khorana, H. G. *Proc. Natl. Acad. Sci. U.S.A.* **1991**, *88*, 6873–6877.
76. Váró, G.; Zimányi, L.; Chang, M.; Ni, B.; Needleman, R.; Lanyi, J. K. *Biophys. J.* **1992**, *61*, 820–826.
77. Váró, G.; Keszthelyi, L. *Biophys. J.* **1983**, *43*, 47–51.
78. Korenstein, R.; Hess, B. *Nature (London)* **1977**, *270*, 184–186.
79. Kovács, I.; Váró, G. *J. Photochem. Photobiol. B.* **1988**, *1*, 469–474.
80. Korenstein, R.; Hess, B. *FEBS Lett.* **1977**, *82*, 7–11.
81. Lazarev, Y. A.; Terpigov, E. L. *Biochim. Biophys. Acta* **1980**, *590*, 324–338.
82. Hildebrandt, P.; Stockburger, M. *Biochemistry* **1984**, *23*, 5539–5548.
83. Nagle, J. F.; Mille, M. J. *Chem. Phys.* **1981**, *74*, 1367–1372.

84. Schulten, K.; Schulten, Z.; Tavan, P. In *Information and Energy Transduction in Biological Membranes*; Bolis, A.; Helmreich, H.; Passow, H.; Eds.; Alan R. Liss: New York, 1984; pp 113–131.
85. Gerwert, K.; Siebert, F. *EMBO J.* 1986, 5, 805–811.
86. Birge, R. R.; Cooper, T. M. *Biophys. J.* 1983, 42, 61–69.
87. Birge, R. R.; Cooper, T. M.; Lawrence, A. F.; Masthay, M. B.; Zhang, C.-F.; Zidovetzki, R. *J. Am. Chem. Soc.* 1991, 113, 4327–4328.
88. Groma, G. I.; Helgerson, S. L.; Wolber, P. K.; Beece, D.; Dancsházy, Z.; Keszthelyi, L.; Stoeckenius, W. *Biophys. J.* 1984, 45, 985–992.
89. Helgerson, S. L.; Mathew, M. K.; Bivin, D. B.; Wolber, P. K.; Heinz, E.; Stoeckenius, W. *Biophys. J.* 1985, 48, 709–719.
90. Ort, D. R.; Parson, W. W. *Biophys. J.* 1979, 25, 355–364.
91. Garty, H.; Caplan, S. R.; Cahen, D. *Biophys. J.* 1982, 37, 405–415.
92. Koch, M. H. J.; Dencher, N. A.; Oesterhelt, D.; Plöhn, H.-J.; Rapp, G.; Büldt, G. *EMBO J.* 1991, 10, 521–526.

RECEIVED for review March 12, 1992. ACCEPTED revised manuscript December 10, 1992.

Bacteriorhodopsin Variants for Holographic Pattern Recognition

Norbert Hampp¹, Ralph Thoma¹, Dieter Zeisel¹, Christoph Bröchle¹, and Dieter Oesterhelt²

¹ Institute for Physical Chemistry, University of Munich, Munich, Germany

² Max-Planck Institute of Biochemistry, Martinsried, Germany

Because of optimization in the course of evolution, biological photochromes have photophysical properties attractive for optical applications. These materials have not yet, however, reached a state in which their use in recording media for optical information recording and processing is realistic. To implement a biological component into a technical setup, not only favorable properties and easy accessibility but also modification and adaptation to specific requirements are necessary—these needs constitute a major problem. Bacteriorhodopsin (BR) seems to be an exception, because these criteria are met and tools for its engineering and thereby controlled modification are available. An adaptation of its optical properties to the specific physical demands of a particular application therefore seems feasible. An example is the optical and holographic properties of BR films containing wild-type BR BR_{D96N} (Asp96 → Asn96). Their application in dynamic holographic pattern recognition is presented, and the advantages of BR films containing mutated BRs are described.

THE HALOBACTERIAL RETINAL PROTEIN BACTERIORHODOPSIN (BR), which is related to the human visual pigment, is contained in the purple membrane (PM) domains of the cell membrane in *Halobacterium salinarum* as a two-dimensional crystalline lattice. It was discovered about 20 years ago (1) and is now one of the best-investigated membrane proteins (for reviews, see references 2–5). In the halobacterial cell BR acts as a light-driven proton pump. In light it generates a proton gradient over the cell membrane that is utilized by a membrane-bound ATP-synthase for adenosine triphosphate (ATP) regeneration from adenosine diphosphate (ADP). The attractive biochemical and photophysical

0065-2393/94/0240-0511\$08.00/0
© 1994 American Chemical Society

properties of this retinal protein (*see* Table I), in particular its stability against chemical, thermal, and photochemical degradation, are not affected by the isolation of PMs from the halobacterial cell. Rather soon after its discovery, different technical applications of BR in PM form were proposed (for review, *see* for example reference 6). Attempts were made to use the proton-pumping and photoelectric properties of BR for the desalination of sea water (7, 8), for the conversion of sunlight into electricity (9, 10), and for the development of so-called "biochips", with BR as a molecular switch (11, 12) or as an indicator element (13, 14). The optical properties of BR—high quantum yield, excellent photochemical stability, and photoconversions on the picosecond time scale (15)—attracted the interest of many scientists. On the basis of its photochromic properties (i.e., the light-induced reversible color changes of the BR molecule), its use in optical data storage (16, 17), in the construction of optical neural networks (18, 19), in image processing (20, 21), and in holographic applications (22–27) [in particular, in holographic pattern recognition (28)] were suggested.

Table I. Biochemical and Photophysical Properties of BR

<i>Property</i>	<i>Value</i>
Biochemical properties	
Molecular weight	26,000 daltons
Structure	
primary	248 amino acids
secondary	7 α -helical domains
tertiary	cage with proton pore
quarternary	trimers, 2D crystalline, unidirectionally oriented
Lipid bilayer	transmembrane-embedded BR, 10 lipid molecules per BR
Chromophoric group	retinal, attached via Lys216
Biological function	light-driven proton pump
Stability	constant illumination, oxygen and light, temperatures > 80 °C, pH 3–10, most proteases
Photophysical properties	
Initial absorption	$\epsilon_{570} = 63,000 \text{ L mol}^{-1} \text{ cm}^{-1}$
Quantum efficiency	$\phi \geq 64\%$ (for the primary step)
Angle of retinal to membrane plane	20°
Photoactive intermediates	at least 4
Photochromism	trans–cis isomerization, change of the protonation state of the Schiff base
Refractory period after relaxation	none
Instabilities	UV light, organic solvents

Photochemical and Photophysical Properties of BR

The light-driven proton transport through the halobacterial cell membrane is intimately connected to the photochemical conversion of the chromophore in BR (29) (Figure 1). The retinal is covalently bound to the protein moiety via a Schiff base linkage with the amino acid residue Lys216 (30). In the dark, a mixture of the so-called B-state (all-trans and 15-anti) and D-state (13-cis and 15-syn) exists (31–33). Continuous, but weak, illumination leads to exclusive formation of the B-state. From here, the photointermediate J is formed within less than a picosecond after absorption of a photon, and the all-trans configuration of retinal is changed to 13-cis (34–39). Then BR relaxes through a sequence of thermal reactions within about 50 μ s to the M^I state, and aspartic acid 85 (D85) is protonated while another proton leaves the protein to the extracellular side (40–42). The M^I to M^{II} transition is an essentially irreversible step (43–45). In both M states, which are blue-shifted about 160 nm compared to the B-state, the Schiff base of the retinal chromophore is deprotonated. During the M^{II} \rightarrow N transition, the Schiff base is reprotonated by the internal proton donor aspartic acid 96 (D96) (46–48). The reprotonation of Asp96 occurs presumably before the retinal chromophore is reisomerized from 13-cis to all-trans during the N \rightarrow O transition.

Wild-type BR (BR_{WT}) requires approximately 10 ms in aqueous suspension of pH 7 to thermally reach the B-state from the M^{II} state. BR variants exist for which the lifetime of the M intermediate is prolonged by several orders of magnitude, for example, by lack of the proton donor D96 (49). A fast photochemical conversion from M to B is known (50, 51), and therefore a purely photo-controlled switching of BR between the B and M state by yellow (B \rightarrow M) and blue (M \rightarrow B) light can be achieved. Because of the excellent stability of PMs toward photochemical degradation, the B \rightarrow M and M \rightarrow B transitions can be performed reversibly a million times without noticeable degradation (52).

The high specific absorption of the B state (ϵ_B at 570 nm is 63,000 L mol⁻¹ cm⁻¹) and the high quantum efficiency ($\phi \geq 0.64$) (53) of the

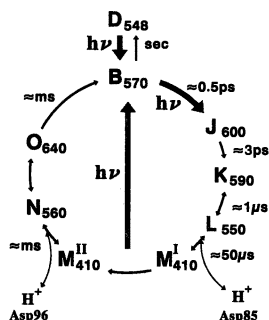


Figure 1. Photochemical and thermal conversions of BR.

primary photoreaction $B \rightarrow J$ is the cause of an intrinsically high light sensitivity. The apparent light sensitivity is determined by the ratio of the rates for photochemical depopulation and thermal (or photochemical) repopulation of the B state, that is, by the lifetime of the respective photointermediates and the radiation applied. A strong intensity dependence of the light-induced changes of the absorption and, connected to it, of the refractive index of BR films results.

Modification of the Photophysical Properties of BR

The photophysical properties of BR can be modified by altering the extramolecular environment of BR in the sample preparations or by altering BR itself by modification of the chromophoric group or functionally important amino acids. The main extrinsic parameter is the proton availability. It can be reduced by the removal of water, the addition of chemicals, or the change of pH (54–57). Modified BRs have been generated through replacement of the retinylidene group by retinal analogue compounds (58–62) and mutation of the bacterio-opsin gene (63–67). Some of these BR variants proved to have superior optical properties for holographic applications compared to BR_{WT}. The most prominent among these modifications is the mutant BR_{D96N}. It contains an asparagine residue in position 96 instead of aspartic acid. As already mentioned, in the wild-type this residue catalyzes the reprotonation of the Schiff base during the photocycle (49, 68) and therefore determines the lifetime of M. The loss of this internal proton donor capability shifts the control of the M decay to the bulk pH. Thus, proton availability (and mobility) in the film regulates the photochemical transitions.

Holographic Properties of BR Films

BR films can be obtained by embedding purple membranes in inert matrices like poly(vinyl alcohol) or poly(acrylamide). These films can be used as reversible holographic recording media. For hologram formation and erasure, both photochemical conversions $B \rightarrow M$ (“B-type” holograms) and $M \rightarrow B$ (“M-type” holograms) can be employed (27). As a response to the incident holographic intensity pattern, a spatially modulated population distribution between B state and M state is induced. In B-type recording, the information is written with a wavelength inside the absorption band of the B state (e.g., 568 nm); in M-type recording, blue light (e.g., 413 nm) is used. In addition, a pumping beam that initiates the $B \rightarrow M$ reaction to achieve a high population of the M state is needed for M-type recording. The pumping beam can be used simultaneously as a readout beam and is not destructive but constructive for the hologram formation (27).

For holographic applications, the absolute values of, and the relation between, the light-induced changes of the absorption Δa and the refractive index Δn , as well as the initial optical density a_0 , are important (69), because these parameters affect the holographic diffraction efficiency η of the BR films. This relation,

$$\eta = (\sin^2 P + \sinh^2 A) \cdot \exp(-2D) \quad (1)$$

where

$$P = \frac{\pi n_1(\lambda, I)d}{\lambda \cos \theta}$$

$$A = \frac{\alpha_1(\lambda, I)d}{2 \cos \theta}$$

$$D = \frac{\alpha_0(\lambda, I)d}{\cos \theta}$$

was analytically derived by Kogelnik (70) for the case of mixed amplitude and phase gratings, where $\alpha_1 = \Delta a/2$ and $n_1 = \Delta n/2$ represent the modulation amplitudes, $\alpha_0 = a_0 - a/2$ denotes the average absorption, I is the local intensity in the interference pattern, and λ and θ are the wavelength and the angle of incidence of the reading beam.

A modified Michelson interferometer operating in “pump-probe” mode was used to characterize the basic photochemical properties of BR films—in particular, to measure the light-induced changes of the refractive index and the absorption coefficient simultaneously (71). The spectral relation of these changes, induced by actinic light of wavelength 568 nm and with an intensity of 20 mW/cm², in a BR_{D96N} film of an initial optical density of 4.0 at 570 nm and thickness 25 μm at pH 8 is shown in Figure 2. Changes of the optical density of $\Delta a_{\max}(\lambda, I) = 1.5$ lead to refractive index changes of $n(\lambda, I) = 0.004$ at the wavelength 633 nm. The relation of light-induced absorption and refractive index changes closely follows the Kramers–Kronig relation. Thus, the retinal-containing chromophore system in BR, which consists of the retinylidene group linked to Lys216 and an inner shell of amino acids (72) can be regarded as an almost undisturbed chromophoric group with respect to its photorefractive properties. It is encased in the protein and shielded from the outer matrix. No major contributions from the charge separation due to the proton pumping, from the dense packing of the PM patches in the films, or from other “long-distance” forces are observed.

The bleaching rate $\Delta a/a_0$, where a_0 is the initial optical density of the BR film, is a specific parameter for a particular BR material. On the basis of the verified spectral $\Delta a(\lambda, I)/\Delta n(\lambda, I)$ relation (*see* Figure 2), the

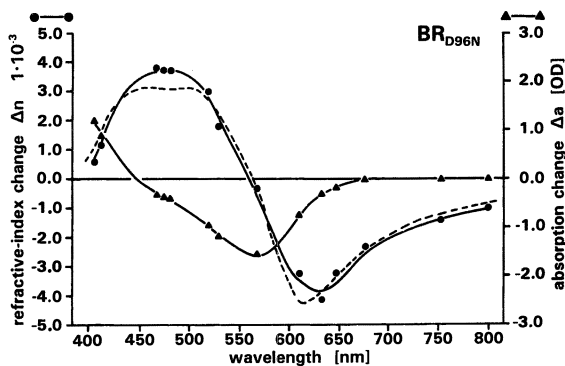


Figure 2. Light-induced changes of the absorption and the refractive index in a BR_{D96N} film and comparison with the Kramers-Kronig relation (\bullet , refractive index changes; \blacktriangle , absorption changes; and ---, refractive index changes derived from the absorption changes by the Kramers-Kronig relation).

wavelength dependence of achievable diffraction efficiencies for BR films with varying a_0 values but a fixed $\Delta a/a_0$ ratio can be numerically derived by Kogelnik's formula. The spectral dependence of the diffraction efficiency on the initial optical density a_0 is plotted in Figure 3. The dependence of the diffraction efficiency on the initial optical density is indicated as bold lines for the wavelengths 600 and 630 nm. The position of the experimentally confirmed wavelength dependence of the diffraction efficiency of the BR film (data from Figure 2) is also marked in bold (71). In the spectral region where the amplitude hologram dominates (400–600 nm), the diffraction efficiency passes through a maximum with increasing initial optical density. At wavelengths around 650–700 nm, a steady increase of the diffraction efficiency with the initial optical

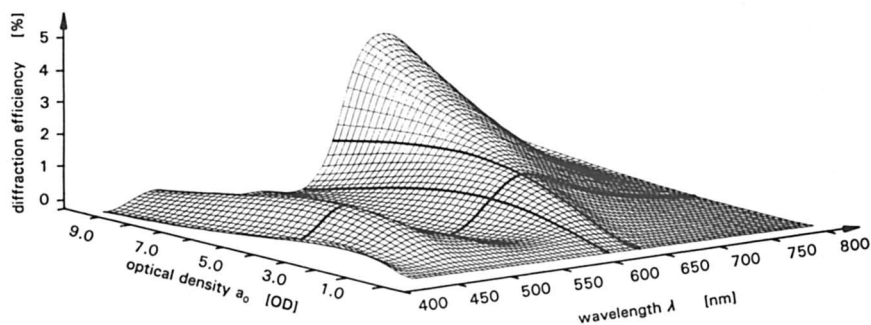


Figure 3. Numerical simulation of the wavelength dependence of the diffraction efficiency in relation to the initial optical density of the BR films.

density a_0 is derived. In this wavelength regime, an almost pure phase grating occurs.

A systematic experimental investigation of the dependence of diffraction efficiency of BR films containing BR_{WT} , BR_{D85E} , and BR_{D96N} on intensity, pH, and temperature revealed that a balanced choice of several interfering parameters must be considered in the selection of BR films for different holographic applications (73).

In relation to the M lifetime in BR_{D96N} films, a recording sensitivity ranging from 1 to 80 mJ/cm² is observed. The twofold higher diffraction efficiency of BR_{D96N} films compared to BR_{WT} films is related to the accumulation of intermediates, for example, the O state and the resulting lower modulation amplitude (73). The spatial resolution of BR films is $>5000 \text{ mm}^{-1}$ and independent of the BR variant. The holographic properties of the BR_{WT} and BR_{D96N} films that are available are summarized in Table II.

Fourier Polarization Holograms in BR Films

Polarization holograms can be efficiently recorded in BR films because of their photoinducible anisotropy (74, 75). In Figure 4, an optical setup for Fourier polarization holography is shown schematically. The beam emitted by laser 1 is split into two coherent beams by a polarizing beam-splitter (PBS). The beam in the upper arm is expanded by a lens (BE), spatially filtered (SF), and then projected onto the BR film by the Fourier transform lens (FTL). In this arrangement a post-lens Fourier transformation of the object, which is placed directly behind the FTL, is obtained

Table II. Holographic Properties of BR_{WT} and BR_{D96N} Films

<i>Parameter</i>	<i>Value</i>
Spectral range	
recording	400–700 nm
readout	400–800 nm
Resolution	≥ 5000 lines per millimeter
Recording sensitivity	
B-type (BR_{D96N})	1–80 mJ/cm ²
M-type	30 mJ/cm ²
Diffraction efficiency	0.1–7%
Reversibility	$>10^6$ WRE ^a cycles
Polarization recording	possible
Relaxation to the initial B state	
thermal	10 ms–100 s
photochemical	$\leq 50 \mu\text{s}$
Thickness	10–400 μm

^a WRE means write, read, erase.

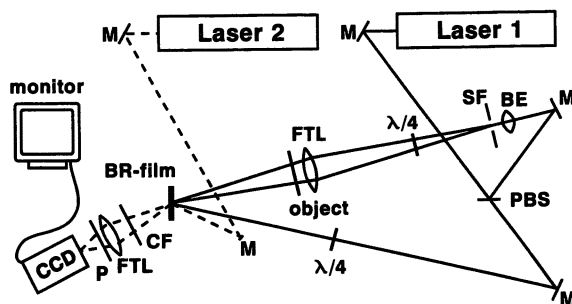


Figure 4. Drawing of a setup for holographic polarization recording with BR films.

in the plane of the BR film (76). The Fourier pattern of the object is superimposed with the reference beam from the lower arm. The holographic grating formed is recorded in the BR film and read by a second beam (from laser 2) that has a different wavelength. The wave diffracted by the hologram and the transmitted recording beams are separated by means of a color filter (CF), and the hologram wave is retransformed (FTL) onto a charge-coupled device (CCD) detector array.

In Figure 5 the relations among the state of polarization of the two writing beams (PW1 and PW2), the reading beam (PR), the diffracted holographic wave (PH), and the scattered light (SL) are shown. The last column gives the relative diffraction efficiency (RDE) of each configuration normalized to that in line 1. In particular, the configurations in lines 3 and 4 are important in practice. For oppositely circular polarized writing beams, a hologram wave results that is almost linearly polarized and is perpendicular to the polarization of the scattered light (SL). Therefore, with a linear polarizer the scattered light can be suppressed effectively without weakening the hologram signal significantly (28). The components used to establish the necessary polarization relations are shown in Figure 4. The $\lambda/4$ plates are used to obtain circular polarization of the writing beams, and the polarizer P in the readout arm is employed for the suppression of the scattered light. It is turned 90° versus the polarization of the readout laser light.

PW1	PW2	PR	PH	SL	RDE
↑	↑	↑	↑	↑	100%
↑	→	↑	→	↑	30%
○	○	↑	⊖	↑	90%
○	○	→	⊖	→	90%
○	○	↑	↑	↑	80%
○	○	→	→	→	80%

Figure 5. Relations of the polarization states of the holographic waves for B-type and M-type polarization recording in BR films.

Figure 6A shows the reconstructed hologram of a U.S. Air Force test pattern, which was photographed directly from the television monitor connected to the CCD detector without any further electronic or optical processing. As a means of comparison, Figure 6B shows a photograph of the same hologram without polarization filtering. Thus, the polarization recording capabilities of BR films allow a substantial improvement of the signal-to-noise (S/N) ratio in holography.

Holographic Pattern Recognition

One of the most promising applications of BR films is their use as a recording medium for dynamic holographic pattern recognition; the fast rise and decay times of M-type holograms and the S/N ratio improvements due to the polarization recording properties of BR films are combined. The experimental implementation is based on a so-called dual-axis joint Fourier transform correlator (77). In the following sections a short mathematical description of the system and an example for its operation are given.

Mathematical Description of the Dual-Axis Joint Fourier Transform Correlator. The amplitudes of the two input functions are given by $g(x_1, y_1)$ and $h(x_1', y_1')$ where x_1, y_1 and x_1', y_1' are the coordinates in the respective planes, which are the planes of the input spatial light modulators (SLMs) in the experiment. Both functions are Fourier transformed and overlapped in the correlation plane at an angle

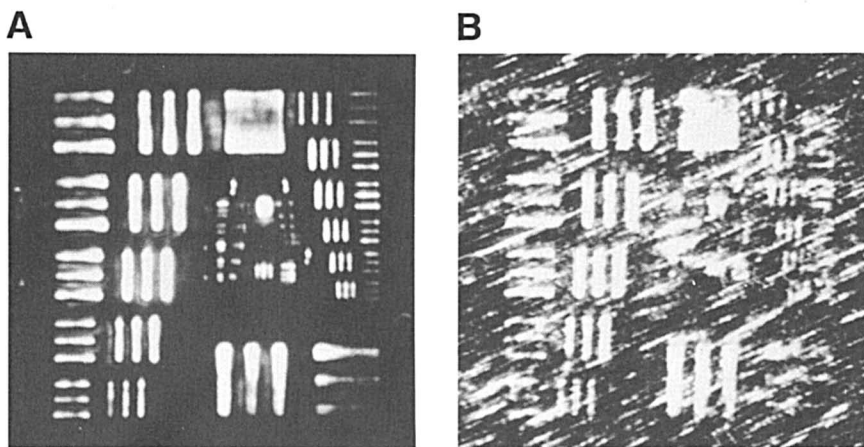


Figure 6. Screen photograph of a U.S. Air Force test pattern recorded as a Fourier hologram in a BR film with (A) and without (B) polarization filtering.

of $2\theta_1$. The resulting amplitude distribution A_{in} in the Fourier plane (x_2, y_2) can be written as

$$A_{in} = G' + H' \quad (2a)$$

$$G' = \frac{1}{\lambda_1 f} G\left(\frac{x_2}{\lambda_1 f}, \frac{y_2}{\lambda_1 f}\right) \exp\left(\frac{2\pi i x_2 \sin \theta_1}{\lambda_1}\right) \quad (2b)$$

$$H' = \frac{1}{\lambda_1 f} H\left(\frac{x_2}{\lambda_1 f}, \frac{y_2}{\lambda_1 f}\right) \exp\left(\frac{-2\pi i x_2 \sin \theta_1}{\lambda_1}\right) \quad (2c)$$

with $G = \mathfrak{F}(g)$ and $H = \mathfrak{F}(h)$, where \mathfrak{F} denotes the Fourier transform; f is the focal length of the Fourier transform lens, and λ_1 the wavelength of the recording beams.

The resulting intensity distribution $I(x_2, y_2)$ in the Fourier plane is

$$I(x_2, y_2) = A_{in}^2 = |G' + H'|^2 \quad (3a)$$

$$I(x_2, y_2) = G'G'^* + H'H'^* + G'H'^* + G'^*H' \quad (3b)$$

where the asterisk denotes the complex conjugate. This gives

$$\begin{aligned} I(x_2, y_2) &= \frac{1}{\lambda_1^2 f^2} GG^* + \frac{1}{\lambda_1^2 f^2} HH^* \\ &+ \frac{1}{\lambda_1^2 f^2} GH^* \exp\left(\frac{4\pi i x_2 \sin \theta_1}{\lambda_1}\right) \\ &+ \frac{1}{\lambda_1^2 f^2} G^*H \exp\left(\frac{4\pi i x_2 \sin \theta_1}{\lambda_1}\right) \end{aligned} \quad (4)$$

In a first-order approximation it is assumed that the local amplitude transmission $T(x_2, y_2)$ is proportional to the incident local intensity.

$$T(x_2, y_2) \propto I(x_2, y_2) \quad (5)$$

If this hologram is read by a plane wave of unity amplitude and wavelength λ_2 at an angle θ_2 obeying the Bragg condition $\sin \theta_1 \lambda_2 = \sin \theta_2 \lambda_1$, the amplitude distribution directly behind the film can be written as

$$A_{trans} \propto T(x_2, y_2) \exp\left(\frac{2\pi i x_2 \sin \theta_2}{\lambda_2}\right) \quad (6)$$

To yield the amplitude distribution A_{out} in the output plane, A_{trans} is again Fourier transformed:

$$A_{\text{out}} \propto \mathfrak{F} \left[T(x_2, y_2) \exp \left(\frac{2\pi i x_2 \sin \theta_2}{\lambda_2} \right) \right] \quad (7a)$$

$$A_{\text{out}} = \frac{1}{\lambda_2 f} [t \otimes \delta(x_3 + f \sin \theta_2, y_3)] \quad (7b)$$

A convolution is denoted by \otimes , and t is defined by

$$t = \lambda_2 f \mathfrak{F} [T(x_2, y_2)] \quad (8)$$

Thus, the Fourier transform of the film transmission can be found in the output plane centered around an axis tilted by an angle θ_2 against the optical axis in the writing plane. This Fourier transform in the plane (x_3, y_3) can be written as

$$\begin{aligned} \mathfrak{F} [T(x_2, y_2)] &= \frac{1}{\lambda_1^2 \lambda_2 f^3} [g \otimes g^*] \\ &+ \frac{1}{\lambda_1^2 \lambda_2 f^3} [h \otimes h^*] \\ &+ \frac{1}{\lambda_1^2 \lambda_2 f^3} [g \otimes h^* \otimes \delta(x_3 + 2f \sin \theta_2, y_3)] \\ &+ \frac{1}{\lambda_1^2 \lambda_2 f^3} [g^* \otimes h \otimes \delta(x_3 - 2f \sin \theta_2, y_3)] \quad (9) \end{aligned}$$

The first two terms are separated on the x -axis from the third and the fourth by the δ functions. The first two terms represent the autocorrelation of g and h , respectively. The third and the fourth term represent the convolution between one of the input amplitude distributions and the complex conjugate of the other and thus give a coordinate-dependent measure of the similarity of the two functions. As long as $g(x_1, y_1)$ and $h(x_1', y_1')$ are pure amplitude modulations, these so-called cross-correlation terms differ only in the sign of the convolution. In this arrangement, for example, term four is observed at the angle $-\theta_2$ in the output, that is, in the detector plane.

Experimental Implementation of a BR-Based Real-Time Holographic Correlator. For holographic pattern recognition with BR films, a modified dual-axis joint Fourier transform (DAJFT) correlator (Figure 7) is used (77); it combines the elements of the DAJFT correlator and the polarization recording setup shown in Figure 4. As input spatial

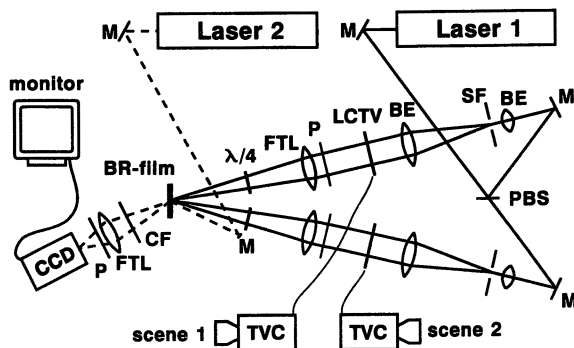


Figure 7. Setup for dynamic holographic pattern recognition with BR films.

light modulators, two liquid crystal television (LCTV) screens are used. The patterns fed from two television cameras (TVCs) to the LCTVs in the two arms of the correlator are both Fourier-transformed by the FTL lenses and are superimposed in the plane of the BR film. The interference pattern of the two coherent Fourier spectra is recorded. In the described experiments, M-type holograms were used with a read-pump beam of 530 nm (dashed) and writing beams of 413 nm (solid). The diffracted wave is retransformed onto a CCD detector array, and the correlation signal is monitored on a screen. From the first camera a constant picture of a sailing boat is transmitted to one of the SLMs. The other TVC captures the moving boat and displays it on the second SLM in the other arm of the correlator.

If the two input functions in equation 1 are identical, as is the case here, the correlation term $g^* \otimes h$ reduces to a delta function, that is, a bright spot in the Fourier plane. A coordinate shift applied to one of the functions leads to a proportional shift of the correlation function due to the linear properties of the convolution operation. Thus, the movement of the correlation spot tracks the movement of the sailing boat. The correlation signal was recorded on videotape. The photograph in Figure 8 was taken at an exposure time of 4 s from a replay of the videotape to a monitor. The line in the photograph is the superposition of the visible correlation spots. Stopping the boat leads to a brighter spot in the photograph because of the longer exposure time. The thickness of the line is thus related to the speed of the boat.

Conclusions

During the past few years, the use of BR films for dynamic holographic pattern recognition has been studied in detail (20, 28, 78), and optimized film compositions have been developed (71, 73). For holographic pattern

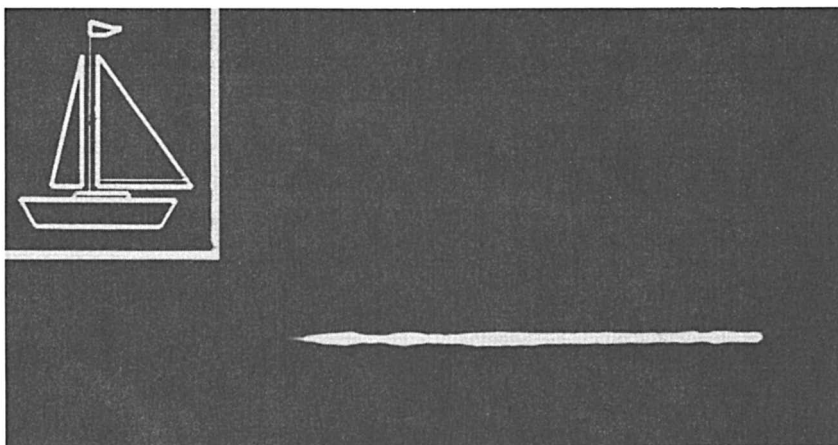


Figure 8. The sailing boat in the upper left corner was tracked during its passage through the viewing range of the television camera.

recognition, the attainable signal-to-noise ratio is the most important parameter, because this is an analog optical computing method. Because of the polarization recording properties of BR, the suppression of scattered light can be effectively realized, and an excellent *S/N* ratio is obtained (78). Because of the fast response of the BR films, the video frame rate of the correlator presently limits the data throughput.

The BR_{D96N} variant shows improved holographic properties and the same high reversibility compared to the BR_{WT}. Thus, small modifications of the bacterio-opsin sequence do not affect the excellent photophysical and thermodynamic stability of BR, but allow the modification of its photophysical properties over a wide range.

The increasing knowledge of the molecular properties of BR and the advanced possibilities to modify this retinal protein by genetic engineering are the basis of a future “custom” design of BR variants with specifically optimized optical properties. In particular, for holographic pattern recognition a spectral range that allows the use of cheap and compact diode lasers would be desirable.

Acknowledgments

This work was supported by the Bundesministerium für Forschung und Technologie (FKZ 0319231 B).

References

1. Oesterhelt, D.; Stoeckenius, W. *Nature (London) New Biol.* **1971**, *233*, 149–152.

2. Kouyama, T.; Kinoshita, K. J.; Ikegami, A. *Adv. Biophys.* 1988, 24, 123–175.
3. Lanyi, J. K. *Bacteria* 1990, 12, 55–86.
4. Mathies, R. A.; Lin, S. W.; Ames, J. B.; Pollard, W. T. *Annu. Rev. Biophys. Biophys. Chem.* 1991, 20, 491–518.
5. Tittor J. *Curr. Opin. Struct. Biol.* 1991, 1, 534–538.
6. Oesterhelt D.; Braüchle, C.; Hampp, N. *Q. Rev. Biophys.* 1991, 24, 425–478.
7. Oesterhelt D. *FEBS Lett.* 1976, 64, 20–22.
8. Hind G.; Mills, J. D. In *Proceedings of the International Symposium on Biological Applications of Solar Energy*; Gnanam, A.; Krishnaswamy, S.; Kahn, Joseph S., Eds.; Macmillan: New York, 1978; p 175.
9. Sieh, P. K. *Neng Yuan Chi K'an* 1978, 8, 7–16.
10. Singh, K.; Korenstein, R.; Lebedeva, H.; Caplan, S. R. *Biophys. J.* 1980, 31, 393–401.
11. Hong, F. T. *BioSystems* 1986, 19, 223–236.
12. Watanabe, T. *Jpn. Kokai Tokkyo Koho* 1990, A2.
13. Trissl, H. W. *Optoelektron. Mag.* 1987, 3, 105–107.
14. Miyasaka, T.; Koyama, K.; Itoh, I. *Science* 1992, 255, 342–344.
15. Nuss, M. C.; Zinth, W.; Kaiser, W.; Koelling, E.; Oesterhelt, D. *Chem. Phys. Lett.* 1985, 117, 1–7.
16. Birge, R. R.; Fleitz, A.; Gross, R. B.; Izgi, J. C.; Lawrence, A. F.; Stuart, J. A.; Tallent, J. R. *Ann. Int. Conf. IEEE Eng. Med. Biol. Soc.* 1990, 12, 1788–1789.
17. Birge, R. R. *Bull. Am. Phys. Soc.* 1989, 34, 483.
18. Takei, H.; Lewis, A.; Chen, Z.; Nebenzahl, I. *Appl. Opt.* 1991, 30, 500–509.
19. Haronian, D.; Lewis, A. *Appl. Opt.* 1991, 30, 597–608.
20. Thoma, R.; Hampp, N.; Braüchle, C.; Oesterhelt, D. *Opt. Lett.* 1991, 16, 651–653.
21. Braüchle, C.; Hampp, N.; Oesterhelt, D. *Adv. Mater.* 1991, 3, 420–428.
22. Werner, O.; Fischer, B.; Lewis, A.; Nebenzahl, I. *Opt. Lett.* 1990, 15, 1117–1119.
23. Burykin, N. M.; Korchemskaya, E. Y.; Soskin, M. S.; Taranenko, V. B.; Dukova, T. V.; Vsevolodov, N. N. *Opt. Commun.* 1985, 54, 68–70.
24. Vsevolodov, N. N.; Ivanitskii, G. R.; Soskin, M. S.; Taranenko, V. B. *Avtometriya* 1986, 41–48.
25. Korchemskaya, E. Y.; Soskin, M. S.; Taranenko, V. B. *Kvantovaya Elektron. (Moscow)* 1987, 14, 714–721.
26. Bunkin, F. V.; Vsevolodov, N. N.; Druzhko, A. B.; Mitsner, B. I.; Prokhorov, A. M.; Savranskii, V. V.; Tkachenko, N.V.; Schevchenko, T. B. *Sov. Tech. Phys. Lett. (Engl. Transl.)* 1981, 7, 630–631.
27. Hampp, N.; Braüchle, C.; Oesterhelt, D. *Biophys. J.* 1990, 58, 83–93.
28. Hampp, N.; Thoma, R.; Braüchle, C.; Oesterhelt, D. *Appl. Opt.* 1992, 31, 1834–1841.
29. Varo, G.; Lanyi, J. K. *Biochemistry* 1990, 29, 2241–2250.
30. Lemke, H. D.; Oesterhelt, D. *FEBS Lett.* 1981, 128, 255–260.
31. Oesterhelt, D.; Meentzen, M.; Schuhmann, L. *Eur. J. Biochem.* 1973, 40, 453–463.
32. Sperling, W.; Carl, P.; Rafferty, C. N.; Dencher, N. A. *Biophys. Struct. Mech.* 1977, 3, 79–94.
33. Harbison, G. S.; Smith, S. O.; Pardoan, J. A.; Winkel, C.; Lugtenburg, J.; Herzfeld, J.; Mathies, R.; Griffin, R. G. *Proc. Natl. Acad. Sci. U.S.A.* 1984, 81, 1706–1709.

34. Ebrey, T. G. *Biological Events Probed Ultrafast Laser Spektroscopy*; Alfano, R. R., Ed.; Academic: Orlando, FL, 1982; p 271.
35. Sharkov, A. V.; Pakulev, A. V.; Chekalin, S. V.; Matveets, Y. A. *Biochim. Biophys. Acta* **1985**, *808*, 94–102.
36. Zinth, W.; Dobler, J.; Kaiser, W. *Springer Ser. Chem. Phys.* **1986**, *46*, 379–383.
37. Ottolenghi, M.; Sheves, M. *Springer Proc. Phys.* **1987**, *20*, 144–153.
38. Petrich, J. W.; Breton, J.; Martin, J. L. *Springer Proc. Phys.* **1987**, *20*, 52–60.
39. Birge, R. R. *Biochim. Biophys. Acta* **1990**, *1016*, 293–327.
40. Needleman, R.; Chang, M.; Ni, B.; Varo, G.; Fornes, J.; White, S. H.; Lanyi, J. K. *J. Biol. Chem.* **1991**, *266*, 11478–11484.
41. Thorgeirsson, T. E.; Milder, S. J.; Miercke, L. J. W.; Betlach, M. C.; Shand, R. F.; Stroud, R. M.; Kliger, D. S. *Biochemistry* **1991**, *30*, 9133–9142.
42. Butt, H. J.; Fendler, K.; Bamberg, E.; Tittor, J.; Oesterhelt, D. *EMBO J.* **1989**, *8*, 1657–1663.
43. Kriebel, A. N.; Gillbro, T.; Wild, U. P. *Biochim. Biophys. Acta* **1979**, *546*, 106–120.
44. Varo, G.; Lanyi, J. K. *Biochemistry* **1991**, *30*, 5008–5015.
45. Varo, G.; Lanyi, J. K. *Biochemistry* **1991**, *30*, 5016–5022.
46. Holz, M.; Drachev, L. A.; Mogi, T.; Otto, H.; Kaulen, A. D.; Heyn, M. P.; Skulachev, V. P.; Khorana, H. G. *Proc. Natl. Acad. Sci. U.S.A.* **1989**, *86*, 2167–2171.
47. Gerwert, K.; Hess, B.; Soppa, J.; Oesterhelt, D. *Proc. Natl. Acad. Sci. U.S.A.* **1989**, *86*, 4943–4937.
48. Otto, H.; Marti, T.; Holz, M.; Mogi, T.; Lindau, M.; Khorana, H. G.; Heyn, M. P. *Proc. Natl. Acad. Sci. U.S.A.* **1989**, *86*, 9228–9232.
49. Miller, A.; Oesterhelt, D. *Biochim. Biophys. Acta* **1990**, *1020*, 57–64.
50. Ohno, K.; Govindjee, R.; Ebrey, T. G. *Biophys. J.* **1983**, *43*, 251–254.
51. Zimanyi, L.; Tokaji, Z.; Dollinger, G. *Biophys. J.* **1987**, *51*, 145–148.
52. Hampp, N.; Bräuchle, C. In *Photochromism (Molecules and Systems)*; Dürr, H.; Bouas-Laurent, H., Eds.; Studies in Organic Chemistry; Elsevier: Amsterdam, Netherlands, 1990, Vol. 40, pp 954–975.
53. Tittor, J.; Oesterhelt, D. *FEBS Lett.* **1990**, *263*, 269–273.
54. Hildebrandt, P.; Hagemeyer, A.; Stockburger, M. *Springer Proc. Phys.* **1985**, *4*, 246–249.
55. Varo, G.; Lanyi, J. K. *Biophys. J.* **1991**, *59*, 313–322.
56. Dyukova, T. V.; Vsevolodov, N. N.; Chekulayeva, L. N. *Biophysics* **1985**, *30*, 668–672.
57. Nakasako, M.; Kataoka, M.; Tokunaga, F. *FEBS Lett.* **1989**, *254*, 211–214.
58. Tokunaga, F.; Govindjee, R.; Ebrey, T. G.; Crouch, R. *Biophys. J.* **1977**, *19*, 191–198.
59. Balogh-Nair, V.; Nakanishi, K. *Methods Enzymol.* **1982**, *88*, 496–506.
60. Crouch, R. K.; Or, Y. S.; Ghent, S.; Chang, C. H.; Govindjee, R.; Ebrey, T. G.; Callender, R. H.; Pande, A. *J. Am. Chem. Soc.* **1984**, *106*, 8325–8327.
61. Koelling, E.; Gaertner, W.; Oesterhelt, D.; Ernst, L. *Angew. Chem.* **1984**, *96*, 76–78.
62. Mitsner, B. I.; Khodonov, A. A.; Zvonkova, E. N.; Evstigneeva, R. P. *Bioorg. Khim.* **1986**, *12*, 5–53.
63. Soppa, J.; Otomo, J.; Straub, J.; Tittor, J.; Meessen, S.; Oesterhelt, D. *J. Biol. Chem.* **1989**, *264*, 13049–13056.

64. Ni, B. F.; Chang, M.; Duschl, A.; Lanyi, J.; Needleman, R. *Gene* **1990**, *90*, 169–172.
65. Lam, W. L.; Doolittle, W. F. *Proc. Natl. Acad. Sci. U.S.A.* **1989**, *86*, 5478–5482.
66. Shand, R. F.; Miercke, L. J.; Mitra, A. K.; Fong, S. K.; Stroud, R. M.; Betlach, M. C. *Biochemistry* **1991**, *30*, 3082–3088.
67. Krebs, M. P.; Hauss, T.; Heyn, M. P.; Rajbhandary, U. L.; Khorana, H. G. *Proc. Natl. Acad. Sci. U.S.A.* **1991**, *88*, 859–863.
68. Braiman, M. S.; Mogi, T.; Marti, T.; Stern, L. J.; Khorana, H. G.; Rothschild, K. J. *Biochemistry* **1988**, *27*, 8516–8520.
69. Birge R. R.; Izgi, K. C.; Sturat, J. A.; Tallent, J. R. *Proc. Mater. Res. Soc.* **1991**, *218*, 131–140.
70. Kogelnik, H. *Bell. Sys. Tech. J.* **1969**, *48*, 2902–2947.
71. Zeisel, D.; Hampp, N. *J. Phys. Chem.* **1992**, *96*, 7788–7792.
72. Fischer, U.; Oesterhelt, D. *Biophys. J.* **1979**, *28*, 211–230.
73. Hampp, N.; Popp, A.; Braüchle, C.; Oesterhelt, D. *J. Phys. Chem.* **1992**, *96*, 4679–4685.
74. Kakichashvili S. D. *Opt. Spectrosc.* **1972**, *33*, 171; *Opt. Spektrosk.* **1972**, *33*, 324.
75. Todorov T.; Nikolova, L.; Tomova, N. *Appl. Opt.* **1984**, *23*, 4588–4591.
76. Goodman, J. W. *Introduction to Fourier Optics*; McGraw-Hill: New York, 1968.
77. Lee, T. C.; Rebholz, J.; Tamura, P. *Opt. Lett.* **1979**, *4*, 121–123.
78. Thoma, R.; Hampp, N. *Opt. Lett.* **1992**, *17*, 1158–1160.

RECEIVED for review June 1, 1992. ACCEPTED revised manuscript March 2, 1993.

Retinal Proteins in Photovoltaic Devices

Felix T. Hong

Department of Physiology, Wayne State University School of Medicine,
Detroit, MI 48201

Retinal proteins are a class of membrane pigments that contain covalently bound retinal (vitamin A aldehyde) as the chromophore. Bacteriorhodopsin (BR), which is the most extensively investigated member of the class, is chemically stable and possesses remarkable photonic and photovoltaic properties. Both properties have been exploited for molecular-device construction. This chapter reviews the basic mechanism of the generation of photoelectric signals, as applied to retinal protein-containing membranes. The physiological significance of these electric signals is discussed, and useful tips for the design of molecular electronics are presented. Prototype devices based on the fast photoelectric effect are reviewed.

THE ASTONISHING DEVELOPMENT OF MICROELECTRONIC TECHNOLOGY in the past few decades allows for more circuit elements to be packaged into a small integrated circuit. It is a valid observation that the size of memory in a memory chip increases exponentially with the passage of time. Will this trend continue until the device dimensions eventually approach atomic scale? The general consensus is that this will not happen with conventional inorganic-electronic materials because the thermal effect and quantum interference will make the devices unreliable.

The perceived limit imposed by fundamental physical laws on conventional devices prompted scientists and engineers to evaluate the alternative use of organic molecular materials as building blocks. The success in using synthetic molecules for this purpose is best illustrated by the development of a new field of materials science called synthetic metals or conducting polymers. Biological molecules are traditionally perceived as being mechanically fragile and chemically unstable. Bacteriorhodopsin (BR) is a notable exception (1-4). It can withstand extreme conditions, such as temperatures as high as 140 °C (5), dehydra-

0065-2393/94/0240-0527\$10.34/0
© 1994 American Chemical Society

tion (6, 7), and extreme pH near 0 (8), at least for a limited duration. For these reasons, BR as a building block is the choice for a number of experimental prototypes.

In the 1980s, Vsevolodov's group in Pushchino, Russia, developed a "Biochrom" film made of modified BR embedded in a polymeric matrix (9). The synthetic retinal analog used in the substitution of the natural chromophore slowed down the decay of the M412 state so that the Biochrom film could be used as a two-state photochromic material that is capable of storing images for minutes. By "fixing" an exposed film with hydroxylamine, Vsevolodov et al. (10) obtained instead a high-quality microfilm. By using a genetic variant of BR in which the aspartate residue at position 96 is replaced by asparagine, Hampp and co-workers (11, 12) successfully developed a holographic film. Birge's group (13, 14), by exploiting earlier photochemical events of BR, is currently developing experimental prototypes of holographic spatial light modulators, and high-speed 3-dimensional (3D) random access memory.

Another property of BR that finds applications in molecular-device development is the rapid charge separation process initiated by light. Because BR is oriented in the purple membrane of *Halobacterium halobium*, a macroscopic photovoltaic effect can be detected; the rise time of the photovoltaic signal was estimated to be faster than 5 ps (15, 16). A similar fast photoelectric signal was first detected in monkey retina in 1964 (17). This photosignal, known as the early receptor potential (ERP), differs from many bioelectric signals such as the action potential, in the molecular mechanism of generation. This class of electric signals, which is known collectively as displacement currents, is not generated by diffusion of ions through water-filled membrane channels, but rather, is generated by rapid charge displacement (18, 19). While bioelectric signals generated by diffusion are usually taking place in the millisecond time range, the displacement photocurrent is much faster and has been proposed for applications in the development of a molecular switch or a high-speed photosensor (20, 21). Recently, Haronian and Lewis (22) developed a cellular automaton using the displacement photocurrent for signal processing. Miyasaka et al. (23) developed a multipixel photosensor by exploiting the same property for detecting movement of images. The fast photoelectric effect also has been exploited for the design of a high-speed high-density 3D optical memory (14).

The photoelectric properties of BR have been extensively investigated and reported in the literature (for reviews, see references 24–31). But the basic mechanisms of photosignal generation are not generally understood, and the molecular interpretation of displacement photocurrents remains controversial. For example, conventional wisdom indicates that the early receptor potential is generated by light-induced intramolecular charge displacement and the concurrent formation of a

transient electric dipole array inside the membrane. Yet in a model-membrane system, Hong and Mauzerall (32, 33) have shown that a light-induced interfacial electron transfer between a membrane-bound pigment magnesium porphyrin and an aqueous-soluble electron acceptor can also generate a photoelectric signal that possesses all major characteristics of a displacement photocurrent.

Thus, in principle, the early receptor potential and the ERP-like signal in BR membranes can both be generated by the interfacial charge-transfer mechanism, because both BR and rhodopsin bind aqueous protons upon light stimulation. However, the ERP and the corresponding signal in BR membranes do not show any significant dependence on the pH or on the ionic strength of the aqueous medium. As a consequence, the interfacial proton transfer mechanism has never been taken seriously by most investigators. However, Hong and Montal (34) demonstrated a significant pH dependence of the ERP-like signal in a BR thin film under a near-short-circuit condition, whereas the same system exhibits no significant pH dependence under open-circuit conditions.

In this chapter, we present a systematic analysis of displacement photocurrents, starting with the two molecular mechanisms mentioned above. An equivalent circuit scheme will be derived from an electrochemical and electrophysiological analysis by using only accepted physical principles. The equivalent circuit scheme so derived is therefore system-independent. The applicability of the analysis to retinal-protein membranes or thin films must then be based on its consistency with experimental data.

In the analysis to be described, we found that remarkable consistency can be maintained if the scheme of signal decomposition used in the literature of the early receptor potential is followed. This consistency probably occurs because the resulting signal components correspond directly to individual molecular processes. The ERP has a faster temperature-insensitive component (R1) and a slower temperature-sensitive component R2 (R2 can be reversibly inhibited by low temperature). The corresponding components in the ERP-like signal in BR membranes will be named B1 and B2, and those in halorhodopsin membranes will be named H1 and H2.

In contrast, most investigators decomposed the ERP-like signal from BR membranes in terms of observed exponential components. However, the reported relaxation times differ among various laboratories. Furthermore, the individual signal components so obtained do not correspond to a distinct chemical reaction, because it is the general consensus that the fast photoelectric signal is a capacitive signal. Therefore, a discrete component of displacement photocurrent should have a zero time-integral (35). But this condition cannot be satisfied by a current

pulse with a single exponential decay (*see* reference 31 for further details).

All the above-mentioned difficulties vanish upon adoption of our combined electrochemical and electrophysiological analysis. In addition, the analysis permits investigators to take control of the fast photoelectric signals for design purposes (36). The unifying scheme also allows us to investigate Nature's design principles for the visual photoreceptors and the photosynthetic apparatus (37).

Photovoltaic Effect and the Molecular Mechanisms of Signal Generation

Many pigments and organic dyes, in the presence of an oxidizing agent, respond to visible-light stimulation by a rapid charge separation. However, if there is no self-shading and the illuminating light is spatially uniform, no macroscopic photovoltaic effect can be detected in a solution phase where the light-absorbing molecules are randomly oriented. Biological pigments that exhibit photovoltaic effects are usually membrane-bound. In addition, an asymmetry either in the orientation of the membrane-bound pigment or in the aqueous phase is required for the direct observation of a macroscopic photovoltaic signal. A biological prototype of the photovoltaic effect is given by the bacterial reaction center of *Rhodospseudomonas viridis* (38). The reaction center is primarily a light-driven electron pump (Figure 1).

The primary electron donor is a dimer of bacteriochlorophyll (the "special pair"). In addition, a pair of monomer bacteriochlorophyll molecules and a pair of bacteriopheophytin molecules, and a pair of quinones (one tightly bound, Q_A , and one loosely bound, Q_B) exist. Absorption of a visible photon by the "special pair" leads to ejection of an electron to Q_A within 200 ps and then to Q_B . This process of charge separation manifests itself as a macroscopic photovoltaic signal in the direction perpendicular to the membrane from the cytoplasmic side to the periplasmic side. The charges separate further as an electron from the secondary donor, cytochrome, moves to fill the "hole" created by photooxidation of the "special pair". Because of the involvement of quinone, the inward electron movement is converted to an equivalent proton movement in the opposite direction at the two membrane-water interfaces. If a pair of reversible electrodes is placed across the membrane, a dc photovoltage or a dc photocurrent will be detected with its positive polarity on the periplasmic side. This process represents a net transfer of protons from the cytoplasmic to the extracellular side.

It is well-known that the photosynthetic electron transfer (ET) reactions are accompanied by reverse reactions that are also referred to as charge recombination. This charge recombination process represents

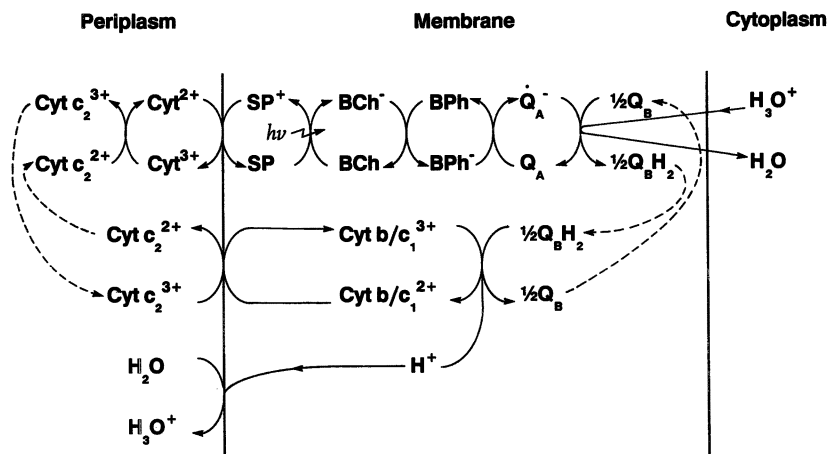


Figure 1. Coupled consecutive ET reactions with reverse electron-proton cotransport in the photosynthetic reaction center of Rhodospseudomonas viridis. SP, "special pair"; BChl, monomer bacteriochlorophyll; BPh, bacteriopheophytin; Q_A , the tightly bound quinone; and Q_B , the loosely bound quinone. The ET reactions in the cytochrome $b-c_1$ complex are simplified to become a single step; so are those in the four bound cytochromes on the periplasmic surface. Cyt c_2 is the peripheral protein cytochrome c_2 . The dotted arrows indicate the diffusion of Q_B and Cyt c_2 . The reverse reactions are not shown in the schematic.

a nonproductive process from the energetic point of view because the photocurrent so generated is an ac photocurrent. Under physiological conditions, both dc and ac photocurrents can be measured, and the time integral of the photocurrent represents the net amount of charges being transported across the membrane. A pure ac photocurrent component would give rise to a zero time integral because there is no net charge transfer.

Energetically, BR performs essentially the same task as the entire reaction center. However, other than the initial excitation of the chromophore, no direct involvement of electron movement occurs. Most investigators believe that the driving force for proton pumping is the light-induced decrease of pK_a (or increase of pK_b , where K_b is the base dissociation constant, whereas K_a is the corresponding acid dissociation constant) of the Schiff's base proton-binding site. This event sets off movement of protons along a partially known pathway leading from the cytoplasmic surface to the extracellular surface (39, 40). The simplest model is shown in Figure 2, which depicts the movement of protons as hopping from one binding site to an adjacent binding site (41). This process is similar to what electrons do in the bacterial reaction center. Essentially, both schemes can be considered light-driven coupled charge-

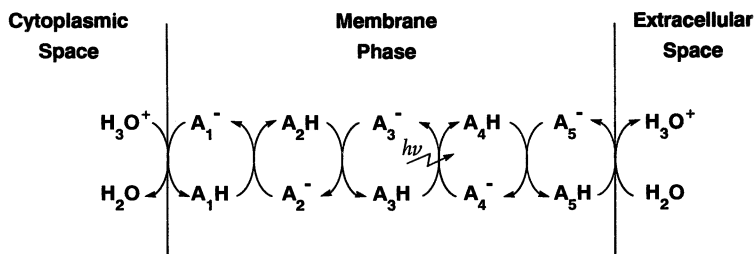


Figure 2. Coupled consecutive proton-transfer reactions across the purple membrane of Halobacterium halobium. The actual number of binding sites are not known. For simplicity, only five binding sites (A_1 – A_5) are shown. Site A_3 is the proton-binding site at the Schiff's base linkage. Its two adjacent sites, A_2 and A_4 , are the residue 96 aspartate and the residue 85 aspartate, respectively. It is possible that additional sites exist between site A_1 and site A_2 , as well as between site A_4 and A_5 . It is understood that the Schiff's base is neutral when unprotonated and is positively charged when protonated. The reverse reactions are not shown. (Reproduced with permission from reference 41. Copyright 1990 National Taiwan University College of Medicine.)

transfer reactions, in the sense that products of a preceding reaction become the reactants of the subsequent reaction. Simple kinetic consideration reveals that the minimum requirement for such a proton pump to work is to have at least one light-driven forward reaction. Thus, photoexcitation caused the pK_a of site A_3 to decrease, resulting in a shift of equilibrium favoring site A_4 to be occupied by the hopping protons. Reequilibration will eventually push protons into the extracellular aqueous phase via deprotonation of site A_5 . Deprotonation of site A_3 creates a “negative hole”. Again the shift of equilibrium will favor deprotonation of site A_2 and protonation of site A_3 . This process is similar to the refilling of the hole in the “special pair”; an electron is transferred from a cytochrome on the periplasmic surface. Back propagation of equilibration will eventually reach the cytoplasmic surface, resulting in the filling of the empty site A_1 via binding of an aqueous proton from the cytosol. This simple model is consistent with models proposed by Nagel and Morrowitz (42) and by Honig (43).

During the light-induced proton translocation across the purple membrane, the dc photovoltaic effect is represented by net proton movement from the cytosol to the extracellular space. A fraction of charges that move forward recombine via the reverse reaction. This fraction of charge movement is represented as the ac photovoltaic effect. In principle, every step of forward and reverse reaction can be manifest as an ac photocurrent. In practice, it is convenient to differentiate between two types of ac photocurrents.

Considering the protonation and deprotonation of the Schiff's base proton-binding site A_1 , as well as the ET from the "special pair" to pheophytin, for example, the forward reaction in either case generates a transient array of electric dipoles as shown in Figure 3. Notice that for simplicity the separated charge pairs are shown to span the membrane. The dipole array vanishes upon charge recombination. This pro-

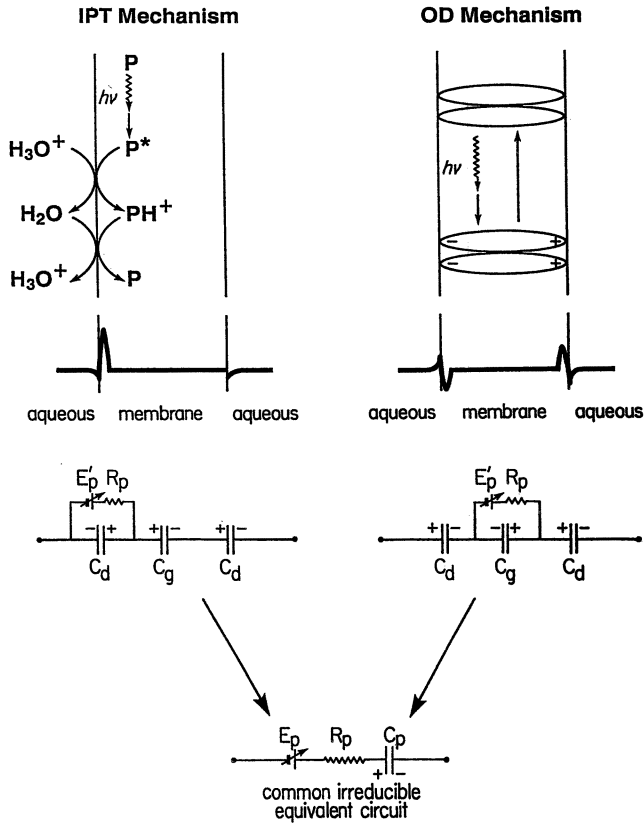


Figure 3. Two different molecular mechanisms of charge separation for the generation of a displacement photocurrent in the purple membrane. The OD mechanism describes the light-induced generation of a transient array of electric dipoles, and the IPT mechanism describes the transfer of a proton from the adjacent aqueous phase to the membrane phase, while leaving the counterion behind in the aqueous phase. A mechanistically equivalent event occurs at the opposite surface when a proton is released from BR to the aqueous phase. The charge distribution profile is also shown together with two slightly different equivalent circuits. These two circuits can be further reduced to a common irreducible one as shown at the bottom of the diagram. See text for further explanation. (Reproduced with permission from reference 44. Copyright 1982 Elsevier Sequoia.)

cess is tantamount to charging and discharging of a capacitance and is the oriented dipole (OD) mechanism that was accepted in the literature of the early receptor potential. However, the process inherent in the OD mechanism is not the only kind of charge separation–recombination encountered in Figures 1 and 2.

The proton-binding process at the cytoplasmic surface is a bimolecular reaction, as is the proton-releasing process at the extracellular surface. Proton transfer from the aqueous donor H_3O^+ to the membrane-bound BR (A_1) results in a state of charge separation because the counterion must then be left behind in the diffuse double layer of the cytoplasmic side. This process is depicted as the interfacial proton transfer (IPT) mechanism in Figure 3. The reverse reaction in which the bound proton at site A_1 is released back to the cytosol constitutes the subsequent charge recombination.

Is the capacitance encountered in the oriented dipole mechanism and in the interfacial proton transfer mechanism the same membrane capacitance that is being charged when an external voltage or current source is applied to change the membrane potential? Our analysis indicates that all three capacitances are physically distinct (26). The distinction is most readily visualized by applying the Gouy–Chapman theory to the two models shown in Figure 3 (44). The analysis allows us to deduce the potential profile and the charge-distribution profile across the membrane (for details, *see* references 31, 33, or 44). These profiles can then be used to derive specific equivalent circuits, which are also shown in Figure 3. These two equivalent circuits can be further reduced to a common irreducible equivalent circuit as shown in Figure 3 (bottom). The distinct feature in the irreducible circuit is the capacitance C_p that is connected in series with the photovoltaic source (E_p). This capacitance is named chemical capacitance (32, 33) to emphasize its physical distinction from an ordinary membrane capacitance (C_m).

The complete equivalent circuit, including both the dc and the ac photovoltaic effects, is shown in Figure 4A. The photoelectromotive force (photoemf), E_p , drives dc photocurrent through R_s but drives ac photocurrent through C_p , R_p being the internal resistance of the photovoltaic cell. From the equivalent circuit, it is readily deduced how the relaxation time course is affected by changes of some of the circuit parameters (45). Figure 4B shows the relaxation time course of a fast photoelectric signal in response to the illumination of a brief light pulse or a long rectangular light pulse. The following important conclusions can be drawn.

First, the model is derived for a single relaxation process that is either first order (as applied to the OD mechanism) or pseudo-first order (as applied to the IPT mechanism). Under these circumstances, all input parameters for the computation of the photocurrent can be experimen-

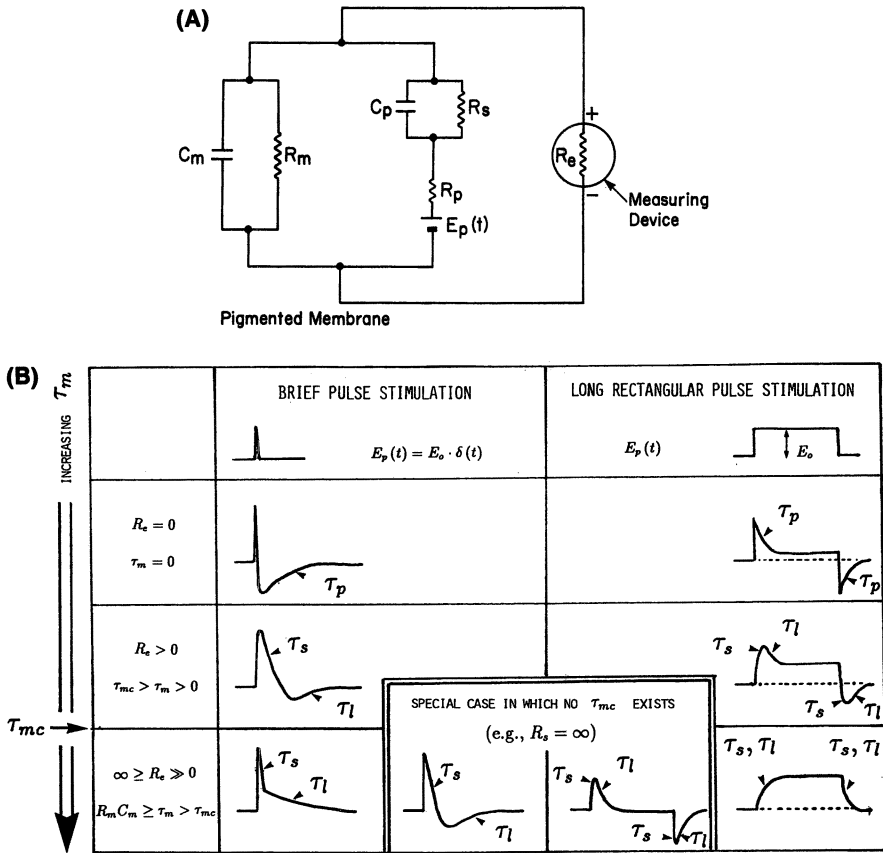


Figure 4. A universal equivalent circuit for the dc and the ac photoelectric effect (A) and its prediction on the photosignal relaxation time course (B). (A) The photochemical event is represented by an RC network including the photoemf, $E_p(t)$, the internal resistance, R_p , of the photocurrent source, the chemical capacitance, C_p , and the transmembrane resistance, R_s . With the exception of a strictly short-circuit measurement, the time course of the photocurrent so generated is further shaped via interaction with the RC network formed by the membrane resistance, R_m , and the membrane capacitance, C_m , as well as the access resistance, R_e . The access resistance (impedance) includes the input impedance of the amplifier, the electrode impedance, and the impedance of the intervening electrolyte solution. (B) The photosignal relaxation time courses are deduced from the equivalent circuit shown in A. Two types of illumination are considered: brief δ -functionlike light pulse and long rectangular light pulse. Notice that the relaxation time course changes with the change of the discharging time constant, τ_m , as defined by: $1/\tau_m = 1/R_e C_m + 1/R_m C_m$. Under open-circuit conditions (i.e., $R_e = \infty$), the photosignal relaxes in two exponential time constants, of which the longer one approaches the membrane RC relaxation time constant, $R_m C_m$. Under short-circuit or near-short-circuit conditions, the photosignal generated by a long rectangular light pulse exhibits an “on-overshoot” spike and “off-undershoot” spike, as expected for a linear high-pass RC filter. This characteristic waveform may disappear if τ_m exceeds a critical value, τ_{mc} . (Reproduced from reference 45. Copyright 1980 American Chemical Society.)

tally determined. No freely adjustable parameter exists. The existence and uniqueness proof of these parameters has been published (33). Prior to its application to retinal-protein-containing membranes, this model has been field-tested in a lipid-bilayer model system in which an ac photovoltaic signal is generated by a light-induced interfacial electron transfer reaction under a pseudo-first order regime of relaxation (33). Since the ERP and the ERP-like signals in BP membranes consists of at least two molecular components, decomposition of the signal is a prerequisite for testing the equivalent circuit model.

Second, the experimentally observed photoelectric signal either as a photovoltage or as a photocurrent depends on the interaction of the photochemical event and the passive event of membrane resistive–capacitive (RC) relaxation. The apparent relaxation time course can be varied over a wide range via the change of the access impedance, R_e (Figure 5A). In addition, it is possible to vary the apparent relaxation time course by manipulating the passive RC elements that constitute the inert supporting structures in a membrane or thin-film configuration (Figures 5B and 6). This effect is the basis of discrepancies among relaxation data reported by various laboratories. When the measurement is performed under near-short-circuit conditions, the relaxation tends to be fast. When the measurement is performed under open-circuit conditions, the relaxation tends to be slow, and it consists mainly of the passive RC relaxation (Figure 4B). This behavior is part of the reason why the ERP was found to be independent of pH in the physiological range. Further detail for reconciling these discrepancies can be found in references 26 and 46. The tuning effect of varying the loading conditions (changing R_e) or trimming the inert supporting structure is particularly relevant for molecular electronics, because many prototypes are configured as a membrane or a thin film supported on a solid substrate. Our observations recently have been confirmed by Ikonen et al. (47).

Third, the distinction between an OD process and an IPT process can be made on the basis of chemical-kinetic analysis. For example, in the model system of interfacial ET mentioned above, the photocurrent relaxation can be modulated by changing the pseudo-first order relaxation time via manipulation of the electron-acceptor concentration in the adjacent aqueous phase. Such an analysis can be used to extract the second order rate constant of the reverse ET (*see* Figure 22 in reference 33). The true-first order relaxation encountered in an OD process is less likely to be influenced by a change of the aqueous composition. Thus, in a molecular device based on interfacial charge transfer, the photovoltaic signal can be modulated chemically by manipulating the adjacent aqueous phase. This feature is absent in a conventional device that does not undergo chemical reactions during its operation.

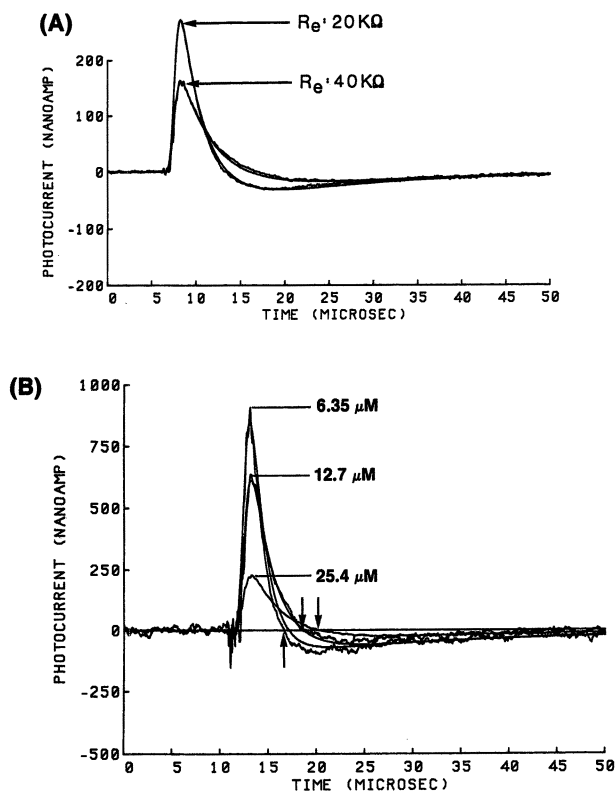


Figure 5. (A) The effect of varying the access impedance on the time course of the B1 component. The photosignals were obtained from the same multilayered dry film at two different values of access impedance (20 and 40 k Ω). The light source is a pulsed dye laser (output 590 nm; duration about 1 μ s). Equivalent circuit analysis of the data measured at 20 k Ω generated a complete set of circuit parameters, which were then used to compute the theoretical time course for 40 k Ω . Notice that even the amplitude changes are predictable by the equivalent circuit analysis (determined peak $E_p = 122$ mV; computed peak $E_p = 120$ mV). Similarly, the theoretical curve fitting the data at 20 k Ω was obtained by using circuit parameters derived from measurements at 40 k Ω . (Reproduced with permission from reference 35. Copyright 1967 American Association for the Advancement of Science.) (B) The effect of varying the thickness of the supporting Teflon film on the time course of the B1 component. The photosignals were obtained from three separate multilayered dry films of purple membranes on a substrate of Teflon sheet with a thickness of 6.35, 12.7, and 25.4 μ m, respectively. The input parameters for computed curves were obtained by deconvolution of the experimental data of the preparation with 6.35 μ m Teflon. The intrinsic relaxation time obtained by deconvolution is 12.3 ± 0.7 μ s ($n = 8$) for 6.35 μ m, and is 12.9 ± 0.6 μ s ($n = 6$) for 12.7 μ m. These two numbers are not statistically different at the level of 5%. (Reproduced with permission from reference 20. Copyright 1986 Elsevier Ireland.)

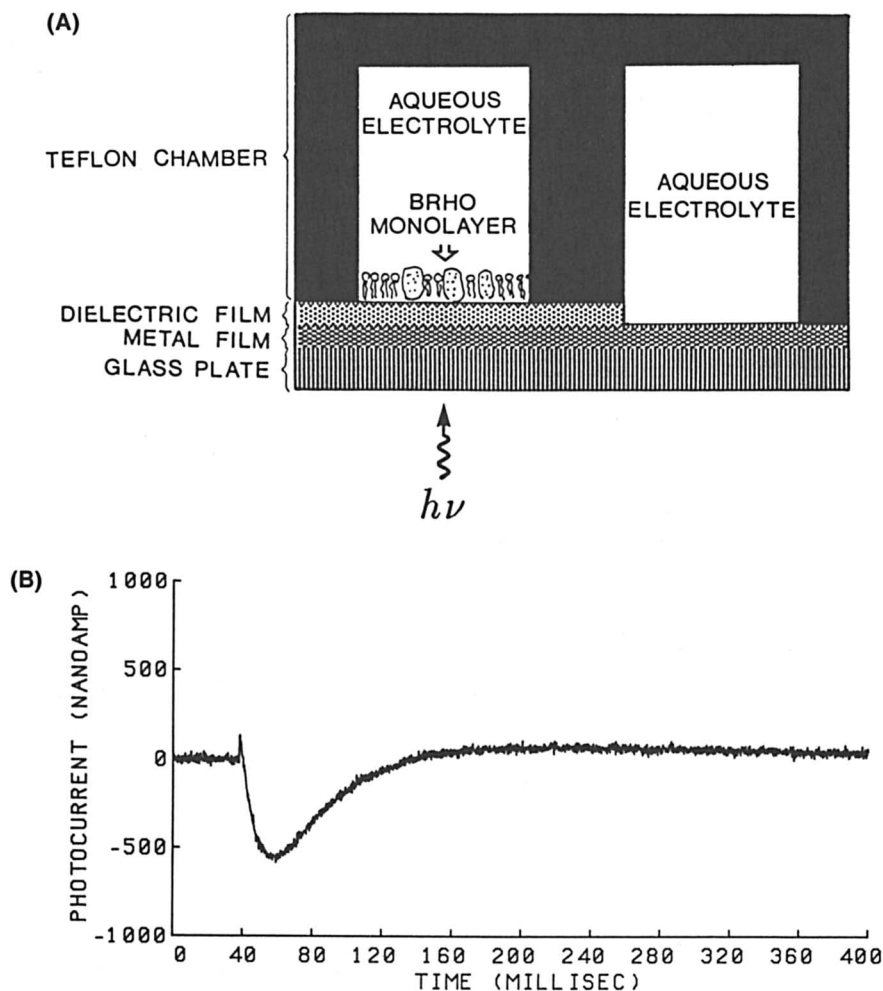


Figure 6. An ac photocurrent generated from a purple membrane thin-film assembly supported on a solid glass substrate. (A) The substrate is a glass coated with a transparent metal electrode, which is partially overlaid with a thin layer of dielectric (approximately 800 Å in thickness). (B) The photocurrent was measured with an access impedance of 80 Ω. The temperature was 26 °C. The aqueous solution contained 3 M KCl and 0.05 M L-histidine buffered at pH 3. Notice the relaxation is stretched into the range of about one-half a second by manipulating the RC time constant of the inert supporting structure. (Reproduced with permission from reference 20. Copyright 1986)

Fourth, the chemical capacitance acts like a built-in high-pass filter that makes the source impedance frequency-dependent. Thus, a photovoltaic signal measured in the high-frequency range (e.g., MHz range) tends to show a more prominent ac component than dc component. In fact, the faster the kinetics, the more prominent the amplitude. In the megahertz time scale, the dc component is usually buried in the noise. By ignoring the small dc component, the equivalent circuit automatically satisfies the zero time-integral condition mentioned above. Thus, although each step of charge separation–recombination is expected to contribute an ac component, only the faster ones will show up in the microsecond time scale. In the case of BR membranes, fast charge separation and recombination is expected in the process associated with photoisomerization of the chromophore, as well as interfacial proton transfers at the two membrane surfaces. The distinction between the two signals thus hinges upon the elusive pH dependence of at least one of the signal components.

Using a reconstitution system originally developed by Trissl and Montal (48), we found that the composite photovoltaic signal is sensitive to both temperature and aqueous pH (Figure 7A). That is, qualitatively,

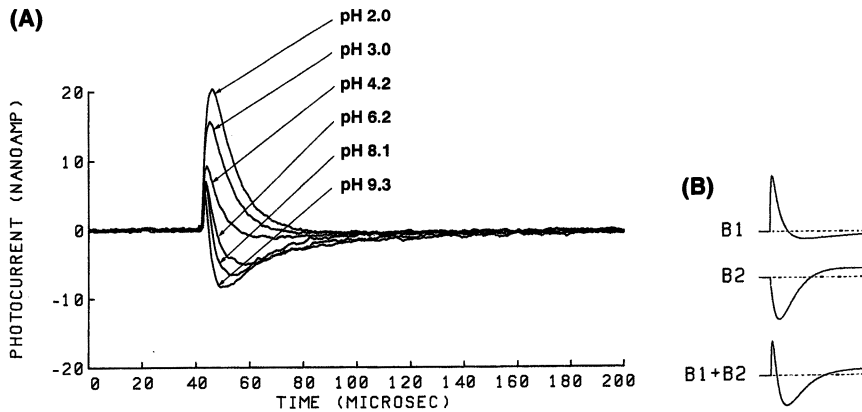


Figure 7. (A) pH dependence of the pulsed light-induced photosignal from a Trissl–Montal film containing BR. The signal contains both B1 and the B2 component. (Reproduced with permission from reference 56. Copyright 1992 American Institute of Physics.) (B) Schematic showing the correct way of decomposition of the composite signal containing two components of opposite polarities, B1 and B2, as shown in A. Each component decays in two exponential terms as dictated by the equivalent circuit when the access impedance is not negligible compared with the source impedance. Each component satisfies the zero time-integral condition. Notice that the inhibition of the B2 component alone results in a decrease of the negative peak but an increase of the positive peak. The exclusive inhibition of B2 could be misinterpreted as a concurrent enhancement of B1. (Reproduced with permission from reference 34. Copyright 1979 Rockefeller University.)

the B2 component can be inhibited reversibly by low temperature and low pH. The reason that the pH dependence could be observed is because the photovoltaic signal was measured under a near-short-circuit condition. Whether the B1 component is independent of temperature and pH requires a quantitative analysis in which the B1 component can be isolated from any B2 contribution. This issue is important because the R1 component of the ERP was perceived as temperature-insensitive and also because the B2 component does indeed vanish at low pH, whereas the B1 component increases its amplitude instead.

Component Analysis of the Fast Photovoltaic Signal from BR Membranes

The Trissl–Montal method of BR membrane reconstitution allows purple-membrane sheets to be attached to a thin Teflon film (thickness 6.35 μm). The predominant orientation of the purple-membrane sheets is such that the extracellular side is attached to the Teflon surface. Thus, both the dc component and the possible contribution from proton release at the extracellular surface are conveniently excluded. We have initially characterized the photosignal as a linear combination of a B1 and a B2 component primarily on the basis of the similarity to the ERP's temperature dependence.

Because the equivalent circuit shown in Figure 4A was derived to describe the photosignal that consists of a single step of either first order or pseudo-first order relaxation process, the first step toward a quantitative verification of the equivalent circuit requires the separation of the photosignal into a pure B1 component and a pure B2 component. For example, if the B2 component can be completely eliminated by a chemical modification of BR, the remaining B1 component can then be compared with the prediction of the equivalent circuit. Because neither component has an a priori definition to begin with and because we object to the conventional approach of exponential analysis, we have adopted an alternative approach.

Instead, we searched for methods that would “trim” the photosignal in such a way that the remaining part of the photosignal will consistently agree with the equivalent circuit analysis. In other words, we treat the agreement as the end point of our search and then justify the validity of our signal-decomposition protocol by the contrasting behaviors of the two different components. One treatment that fulfills this requirement is a modified reconstitution method called the rehydrated multiple-layered thin-film method (46). We define the photosignal so obtained as the pure B1 component. Experimentally, we found the relaxation time course of this component to be completely insensitive to the change

of the pH in the adjacent aqueous phase (from pH 0 to 11). Therefore, the B1 component can also be defined as the pH-insensitive portion of the photosignal. We further found B1 to be insensitive to the kinetic-isotope effect following a replacement of water with D₂O (46, 49). In contrast, the remaining signal, which we refer to as the B2 component, is sensitive to these changes.

In agreement with our earlier semiquantitative analysis (34), the B1 component persists in low temperature. Surprisingly, this component does have a slight temperature dependence (activation energy 2.5 kcal/mol) (46). The behavior of the B1 component is consistent with the OD mechanism, most likely a process related to the *trans-cis* photoisomerization of the chromophore (*see* the next section).

The agreement between photosignals generated in a multilayered thin film helps identify the pure B1 component but does not explain why the method works. The fact that the amplitude of a B1 signal obtained by means of the multilayered method is almost 10 times greater than that obtained by means of the Trissl–Montal method suggests that the multiple layers are by and large oriented the same way as the relatively few layers (possibly one layer) of purple-membrane sheets in a Trissl–Montal film. Thus, in principle, a multilayered film can be converted into a Trissl–Montal film if the multiple layers, except for the bottom layer immediately adjacent to the Teflon film, can be stripped. The stripping can be readily done by using a cotton swab to wipe the surface of the thin-film preparation (50, 51). The resulting preparation exhibits a photosignal that is considerably smaller but can still be superimposed, after normalization, with the signal (B1) before stripping; the relaxation time courses of both signals are totally insensitive to pH changes. However, this description is accurate only if the multilayered thin film has been dried for more than a few days before rehydration. For those multilayered thin films that have been dried for less than 2 days, the pH dependence persists. This pH dependence in the freshly prepared multilayered film is less pronounced than in a Trissl–Montal film. Stripping such a film converts the photosignal back to one that is almost indistinguishable from the signal of a Trissl–Montal film. That is, the pH dependence can be enhanced by stripping the multilayered film with a cotton swab.

The simplest interpretation is as follows. The B1 signal is generated from within the hydrophobic region of BR and is therefore magnified by the number of oriented layers. In contrast, the B2 component is generated at the exposed hydrophilic domain by interfacial proton transfer and can only be generated from the outermost layer of the multilayered thin film. This accounts for the diminished pH dependence in a fresh multilayered film as compared with a Trissl–Montal film and for the subsequent restoration after stripping with a cotton swab. Fur-

thermore, prolonged drying leads to denaturation of the exposed hydrophilic domain of BR but not to its hydrophobic domain, resulting in permanent impairment of the B2 mechanism but preservation of the B1-generating mechanism. This interpretation is further supported by the effect of chemical modification with fluorescamine. Fluorescamine binds to primary amine groups of a protein but hydrolyzes rapidly in water. Thus, it can be used as a nonpenetrating reagent to modify a sample of BR suspension in an electrolyte solution. This treatment almost completely abolishes the pH dependence and, therefore, the B2 component but it does not affect the B1 signal (49, 52).

Thus, the pH dependence of the photosignal observed in a Trissl–Montal film can be completely attributed to the B2 component. Superficial examination of such a signal gives the impression that there is a reciprocal effect of pH on the two components: low pH decreases the B2 peak but increases the B1 peak. This apparent effect is again expected from our equivalent circuit (Figure 7B). Our component analysis is capable of making a definite assignment of the pH dependence exclusively to the B2 component because two different reconstitution methods are used to separate the two components unequivocally.

The analysis associated with the interfacial proton transfer mechanism suggests that proton release at the extracellular surface could, in principle, generate a B2-like signal, which will be named the hypothetical B2' component. Our analysis predicts that this B2' component will have the same polarity as that of the B2 component and that it may also be pH-dependent. If so, the differentiation between the B2 and the B2' component may be problematic. However, a simple kinetic analysis suggests that the B2 and the B2' process may not be rate-limiting in the proton transport. A slow process may intervene between the Schiff's base proton-binding site and the proton-binding sites at both surfaces of the membrane. If so, the B2 and the B2' processes will be kinetically decoupled in the millisecond time scale. As a consequence, the B2 signal will not be sensitive to pH changes at the extracellular surface. Likewise, the hypothetical B2' component will not be sensitive to the cytoplasmic pH, although it may be sensitive to the extracellular pH. This reasoning is summarized as a concept of local reaction conditions (53), and it also suggests an experimental design to differentiate between the B2 and the B2' component.

BR is reconstituted in a modified lipid bilayer membrane, originally developed by Drachev et al. (54), and the pH of the two aqueous phases are independently varied. As shown in Figure 8, acidification of the cytosol reversibly inhibits the B2 component as expected from analysis of a Trissl–Montal film. However, acidification of both the extracellular phase and the cytoplasmic phase reveals a new component with the same polarity as that of the B2 component but with a faster decay and

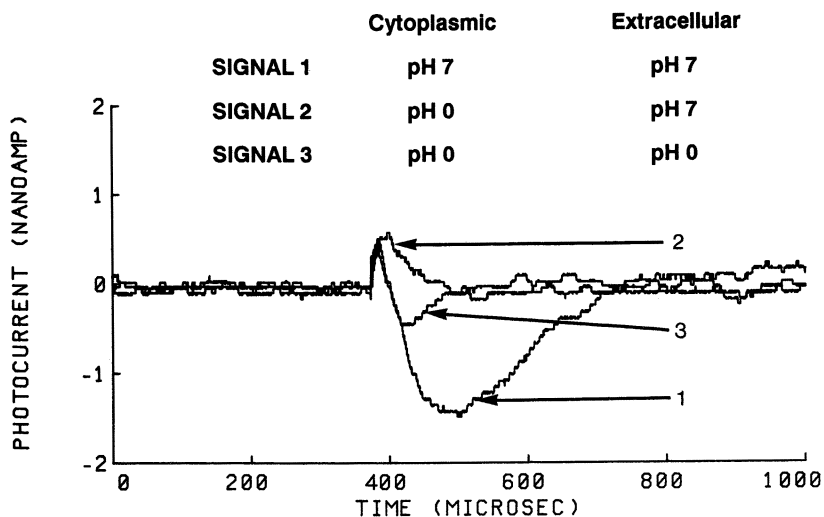


Figure 8. The “differential experiment” showing the existence of two components of photosignals due to proton uptake and release, respectively, at the two membrane–water interfaces. See text for explanation. (Reproduced with permission from reference 49. Copyright 1987 University of Illinois.)

an opposite pH dependence. The behavior of this new component is consistent with what is expected of the hypothetical B2' component. Unequivocal demonstration of the B2' component requires the use of a modified Trissl–Montal film with the attached purple-membrane sheets oriented in the opposite direction so that the extracellular surface is now exposed to the aqueous phase.

Effect of Point Mutation on the Photoelectric Signal

Because the three components of the composite ac photosignal are associated with three spatially separated domains, they may serve as reporter signals if the variation of these signals is correlated with structural changes caused by chemical modifications or site-directed mutagenesis (55). From the point of view of device construction, the photosignals can be manipulated through structural changes of BR.

The pattern of pH dependence of the composite signals from Trissl–Montal films reconstituted from four mutant BRs shows that each mutant BR is distinct (56). In particular the mutant D212N, in which the aspartate residue at location 212 is replaced by asparagine, exhibits no pH dependence in the pH range from 6 to 10 (Figure 9). This replacement abolishes the B2 component. In fact, the photosignals measured at pH 5.4, 6.0, 7.7, 9.4, and 9.9 superimpose after normalization (inset).

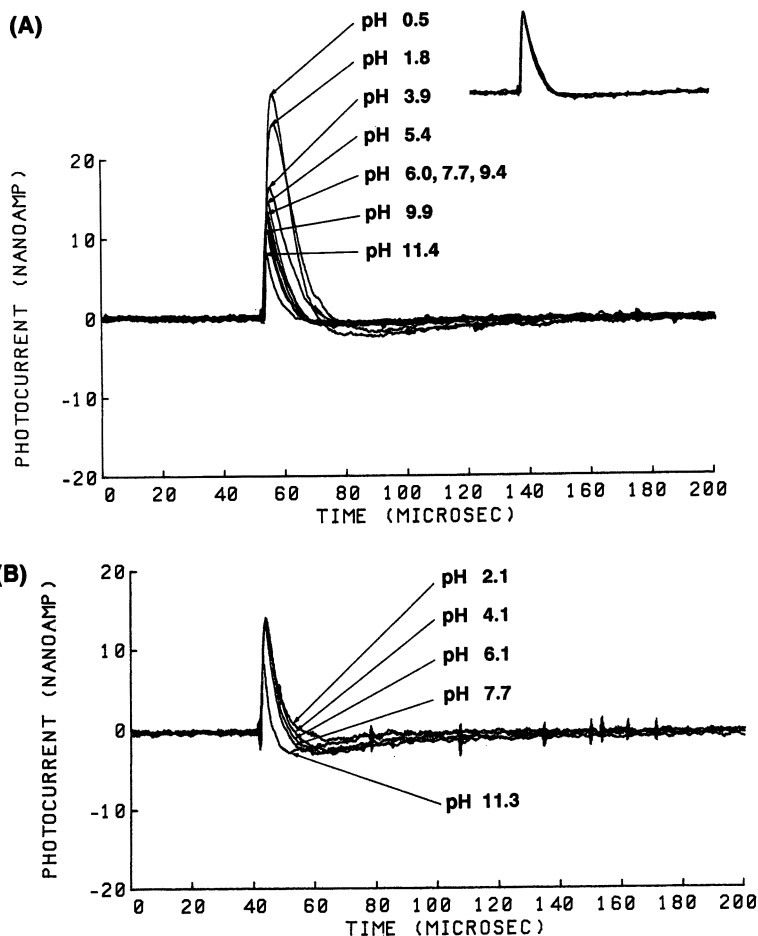


Figure 9. pH dependence of photocurrents from mutant bacteriorhodopsin D212N (aspartate-to-asparagine mutation at residue 212) (A); D115N (B); D85N (C); and D96N (D). The inset in A shows superposition of records at pH 5.4, 6.0, 7.7, 9.4, and 9.9, after normalization of the peak amplitudes. (Reproduced with permission from reference 56. Copyright 1992 American Institute of Physics.)

As expected from the above analysis, these signals also superimpose with the photosignal from a multilayered thin film reconstituted from D212N BR after normalization (57). The structure–function relation as revealed by mutation at residue 212 is not clear. An examination of the 3D structure reported by Henderson et al. (40) indicates that the residue 212 is actually farther away from the cytoplasmic surface (where presumably the B2 signal is generated) than from the extracellular surface. The effect of this structural modification, which seems rather indirect

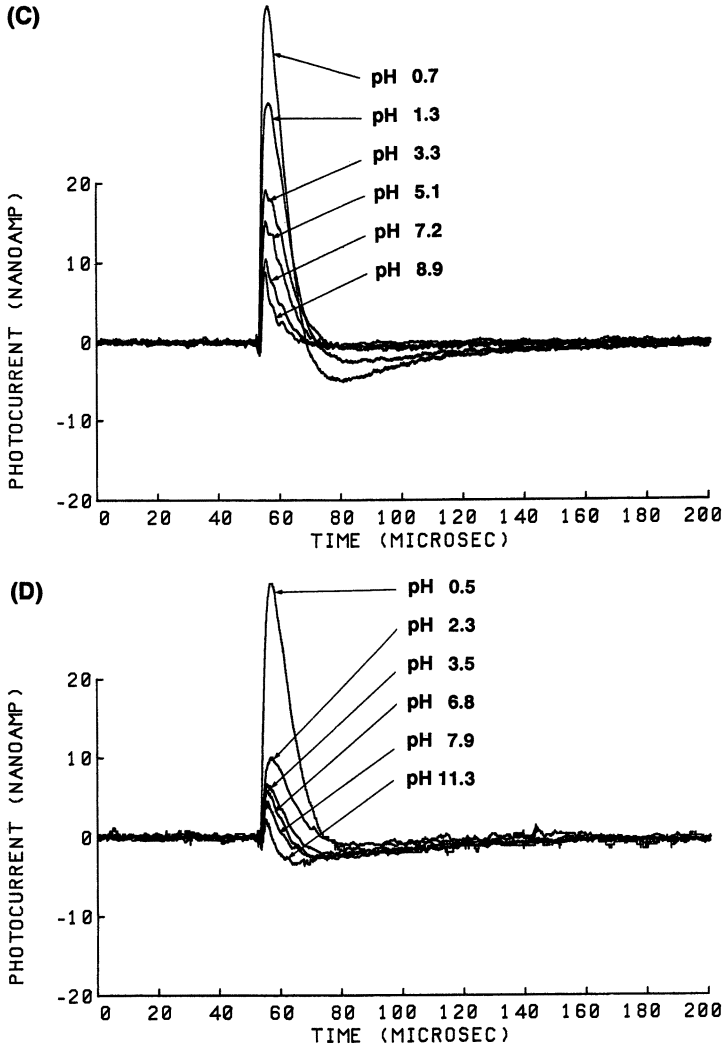


Figure 9.—Continued.

on the B2 process, needs to be further investigated. The significance here is that it is possible to isolate the pure B1 component by a single point mutation, and the observation reinforces our conviction that the B1 component is indeed a natural entity.

The photoelectric behavior of the D212N BR at low pH is more complicated (57). The photosignal at low pH does not superimpose on the B1 signal after normalization, suggesting the existence of an additional component. Thus, the B2 component as defined above may reflect

processes other than interfacial proton binding. The additional component that appears at low pH has a polarity opposite to the B2 signal at mid-to-high pH and is significantly more prominent in 4 M NaCl than in 0.1 M NaCl. This salt-enhancement effect, however, is not due primarily to increased ionic strength or charge screening. This additional component is absent in a chloride-ion-free medium such as (0.1 M Na₂SO₄ buffered with phosphate) even at pH 0.5. The signal appears as soon as 0.01 mM of NaCl is added, which does not affect either the ionic strength or the ability to screen charges. The molecular basis of this additional signal contained in the B2 component needs to be further investigated.

The B1 component persists in all four mutants shown in Figure 9. The B1 component has been attributed to deprotonation of the Schiff's-base proton-binding site. However, our data do not support this interpretation. We found that the B1 component is not affected by overnight exchange with D₂O (46). Furthermore, the B1 component persists in D85N in which the proton-binding site of the residue 85 is eliminated. Because the carboxylate group is considered to be the primary acceptor of the Schiff's-base proton, B1 is probably not generated by the deprotonation at the Schiff's-base proton-binding site. Molecular-dynamics calculations performed by Birge's group (13, 14) further indicate that deprotonation of the Schiff's-base proton is probably not fast enough to account for the B1 signal. Instead, Birge attributed the B1 component to charge shifting in conjunction with photoisomerization of BR.

Photovoltaic Effect in Visual Photoreceptor Membranes

The visual membrane and the photosynthetic membrane represent two classes of naturally occurring photovoltaic devices. Both types of membranes respond to pulsed-light illumination with the generation of displacement photocurrents and the appearance of transient transmembrane photovoltages. However, the functions of these two types of membranes are different, and the significance of their displacement currents is also different. Light-induced charge separation is a primary event in photosynthetic membranes. In addition, a proton-binding site exists at the cytosolic surface and a protein-release site exists at the opposite surface. It is expected that both B1- and B2-like displacement photocurrents can be observed. The purple-membrane system, which resembles the photosynthetic membrane in its function but resembles the visual membrane in its photochemistry and photoelectric behavior, may serve as a conceptual link between vision and photosynthesis.

A comparison of BR and rhodopsin is shown in List I. The similarity in the photochemistry apparently is a consequence of similar chemical structures. However, little homology exists between the amino acid se-

List I. Comparison of Bacteriorhodopsin and Rhodopsin

Common Features

1. transmembrane protein (7 transmembrane α -helices)
2. chromophore (retinal) bound to a lysine residue via a Schiff's-base linkage
3. C-terminus located on the cytoplasmic surface
4. similar photochemical intermediates
5. primary event—chromophore photoisomerization and rapid charge separation
6. major conformational changes during the M1 to M2 transition and during the metarhodopsin I to metarhodopsin II transition, respectively
7. similar displacement photocurrent signals (ERP)
8. binds protons on the cytoplasmic surface

Differences

Bacteriorhodopsin	Rhodopsin
photon-energy converter	photon-signal transducer
photocyclic reactions	photobleaching reactions
transports protons	does not transport protons
conducting polymer	nonconducting polymer

quences of these two retinal proteins. It is somewhat surprising that the photoelectric signals that reflect charge separation also carry such a striking resemblance: Both B1 and R1 are temperature-insensitive, whereas both B2 and R2 are temperature-sensitive. B1 and R1 are most likely generated by the internal charge separation that accompanies the photoisomerization of the chromophore. A significant amount of light energy, which is subsequently used to drive the conformational changes that lead to proton pumping in the purple membrane and visual transduction in the visual membrane, is stored in this step of charge separation (58, 59). The major conformational change in rhodopsin occurs during the metarhodopsin I to metarhodopsin II transition (60), and the conformational change in BR occurs during the M1 to M2 transition (61). Both of these conformational changes are important steps in the function of the respective proteins. However, the functional requirements of these later processes are completely different. Whereas energy-conversion efficiency is important in proton pumping and in photosynthesis in general, it is not of primary concern in vision. This difference occurs because the preformed sodium-ion gradient across the plasma membrane stores the energy required to carry out visual transduction; photon energy acts merely as a trigger to unleash this energy. In this context, it is intriguing to notice that both the R2 signal in the visual membrane and the B2 signal in the purple membrane are a manifestation of interfacial proton binding by the membrane-bound pigment during the respective major conformational changes. Proton binding is an obligatory

process in proton pumping but its role in vision is not obvious. In fact, the early receptor potential of which the R2 is one of the two components has long been dismissed as an epiphenomenon—an evolutionary vestige that serves no physiological purpose.

Is the early receptor potential really an epiphenomenon or is there an undiscovered physiological role of the early receptor potential in vision? Such a role was dismissed for two reasons. First, the ERP is small in amplitude (a few μV in extracellular measurements). Second, ERP-like signals are ubiquitous and can be found in diverse biological structures such as chloroplasts and pigment epithelium of the eyes. In my opinion these reasons are not sufficiently compelling and can be refuted readily by the following arguments. The ubiquity of ERP-like signals can be understood by the fact that light-induced charge separation, which is the primary process in photobiological membranes, is also shared by many pigments and organic dyes. The ERP-like signals are small in amplitude mainly because they are generated by a current source that resides either at the membrane–water interface or inside the membrane and thus are shielded from outside observation by the diffuse electrical double layer (charge screening effect).

Proton binding by rhodopsin will result in a positive surface potential. The electric potential must decline from its finite value at the membrane surface to nearly zero within the order of the Debye length, which is no more than 1 Å in a physiological solution. This steep slope of the potential profile is manifest as an intense electric field in the vicinity of the membrane surface, but is insignificant beyond the double layer (for details, *see* reference 29). Furthermore, a suddenly increased surface potential at one of the two membrane surfaces is also manifest as a sudden increase of the electric field within the membrane phase. Thus, the small amplitude of the ERP as measured extracellularly is more expected than surprising. This speculated surface potential has actually been observed by Cafiso and Hubbell (62).

From a heuristic point of view, the light-induced surface potential change at one side of the visual membrane is an ideal mechanism for triggering visual transduction because it has a fast rise time and because it is highly localized (63). The highly localized feature sits well with the fact that the pretransductional process is a local event; however, the posttransductional process is a global event involving the entire photoreceptor cell. Thus, it is not inconceivable that the positive surface potential associated with the R2 signal may be the trigger for visual phototransduction. But is it compatible with the present understanding of the biochemical process of visual phototransduction?

It is known that a major conformational change of rhodopsin takes

place during the metarhodopsin I to metarhodopsin II transition and that a proton is bound to rhodopsin at the same time (60). The spectral change signifying the transition is time-correlated with the R2 component of the ERP (18). Thus, in analogy to the B2 signal, the R2 component may be generated by the proton uptake. A direct assay with visual-membrane vesicles using a pH indicator dye shows that a proton is taken up from the cytoplasmic side (64, 65). Furthermore, the polarity of the R2 signal is consistent with proton uptake at the cytoplasmic side (65, 66). Thus, the appearance of metarhodopsin II coincides with the appearance of a positive surface potential at the cytoplasmic surface. The biochemical process of visual transduction begins with binding of transducin (a G protein) to metarhodopsin II at the cytoplasmic surface (67). Thus, the R2-related surface potential change occurs at the right place and at the right time to serve as a trigger mechanism for transducin binding and activation. By the same token, the appearance of a negative surface potential at the cytoplasmic surface during the deactivation of transducin or the activation of arrestin may serve as the trigger to switch off the visual transduction process. This negative surface potential, although not yet directly observed, is expected from the known fact of photophosphorylation of nine residues of threonine and serine at the cytoplasmic surface (68). Such a massive phosphorylation process at the cytoplasmic hydrophilic domain is absent in BR, probably because it is not needed from an evolutionary point of view. Likewise, the proton release and the expected surface potential change at the extracellular surface of BR has no counterpart in rhodopsin.

All these observations may be circumstantial when taken individually but could press a strong case for the possibility that the visual photoreceptor membrane may operate like a phototransistor with the photoregulated surface potential being the control for switching the photocurrent known as the late receptor potential. Whereas the final verdict awaits experimental verification, it is interesting to consider the question of whether the above-outlined mechanism can serve as a trigger mechanism. Such a question seems to find an affirmative answer in the experiment reported by Drain et al. (69, 70) (Figure 10).

Drain et al. studied the voltage-driven transmembrane transport of a lipophilic ion, tetraphenylboride, which carries a negative charge, across an artificial lipid bilayer membrane. At the same time, they configured the lipid bilayer such that light illumination will generate a symmetric positive surface potential on both surfaces of the membrane. These surface potentials are generated by a light-induced ET from the membrane-bound magnesium octaethylporphyrin molecule to an aqueous electron acceptor with equal concentrations in the two aqueous phases (Figure 10A). No macroscopic photovoltaic signal can be detected because the

photocurrents generated by interfacial ETs at both surfaces are equal in magnitude but opposite in polarity. Nevertheless, the positive surface potential induced by light at the two membrane surfaces increases the surface concentration of tetraphenylboride ions with a fast rise time (Figure 10B). Correspondingly, a sudden increase of ionic current carried by tetraphenylboride ions is detected. As expected, if tetraphenylboride ions are replaced by tetraphenylphosphonium ions, each of which carries a positive charge, light illumination would cause a sudden decrease of the ionic current (Figure 10C). This surface potential-in-

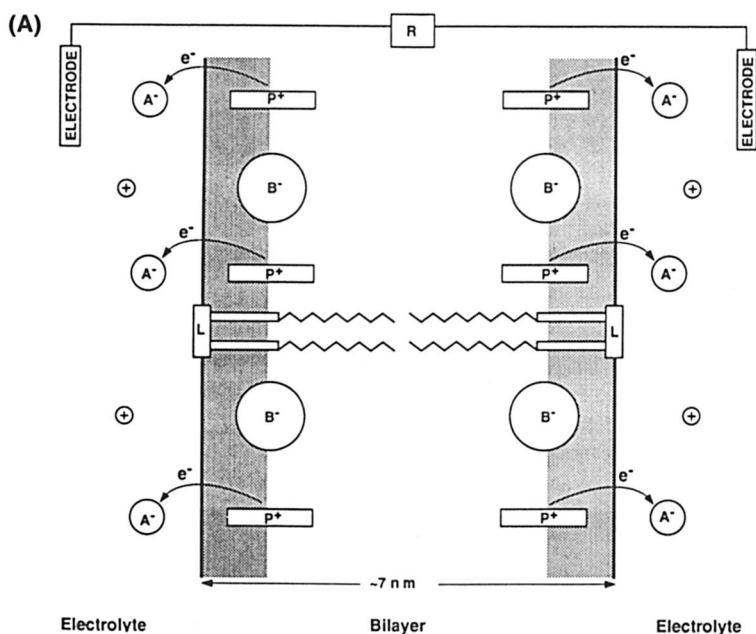


Figure 10. An experimental prototype showing switching of ionic currents based on light-induced surface potentials. (A) The lipid bilayer contains magnesium octaethylporphyrin that is lipid soluble (3.6 mM). The aqueous phases contain the electron acceptor methyl viologen in equal concentrations on both sides (20 mM). Tetraphenylboride ions, B^- , are partitioned into the membrane at the region of polar head groups of lipid, the so-called boundary region. Photoactivation of magnesium octaethylporphyrin generates two symmetrical positive surface potentials (or rather, boundary potentials), which increase the surface concentration of B^- . (B) The ionic current of 1 μM tetraphenylboride ions increases 50% upon illumination with a 1- μs laser pulse. (C) The ionic current of 5 mM of tetraphenylphosphonium ions decreases 25% upon illumination. In both B and C, the spike on the left is the capacitive transient upon imposition of an applied potential of +50 mV. Light pulses are indicated by arrows. (Reproduced with permission from reference 69. Copyright 1989 National Academy of Science.)

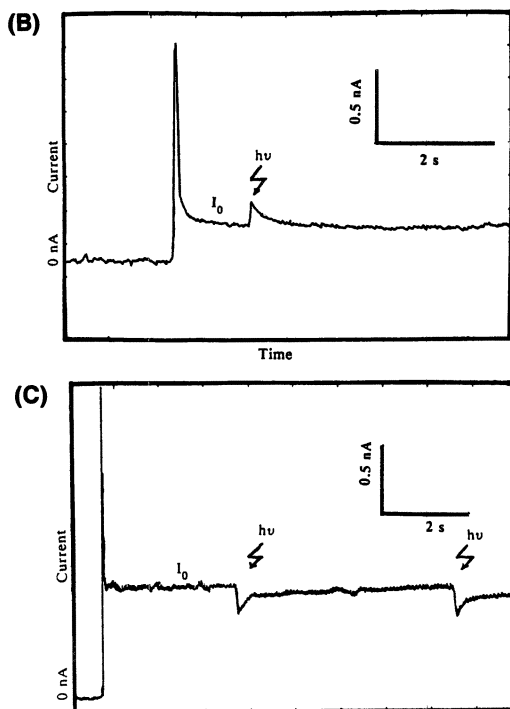


Figure 10.—Continued.

duced change of ionic concentration would have been even more pronounced if the ionic species being transported were multivalent.

Photovoltaic Effect in Other Reconstituted Photobiological Membranes

The generation mechanisms of displacement photocurrents outlined in Figure 3 can be modified to describe processes other than proton displacement. The theoretical framework was originally developed to explain the observation of displacement photocurrents in an artificial model membrane where the prominent process is an ET from a membrane-bound pigment, magnesium porphyrin, to an aqueous-bound electron acceptor via an interfacial ET mechanism (33). The oriented dipole mechanism outlined above may also describe the intramembrane charge separation process that accompanies the electron-hole pair production when electrons are transferred from the “special pair” to its primary or secondary acceptor in the bacterial reaction center. An examination of the waveform of the pulsed light-induced photoelectric signal reported by Hara et al. (71) reveals that it is similar to the isolated B1

signal from BR and that it fulfills the condition of a zero-time integral, indicating that it is indeed a capacitative current.

Further evidence of the generality of our electrochemical analysis is provided by the experimental observation of displacement photocurrents in a reconstituted halorhodopsin membrane (72). Halorhodopsin is the second-most abundant pigment in the red-membrane fraction of *Halobacterium halobium*. Halorhodopsin is a light-driven chloride-ion pump; chloride ions are pumped from the extracellular space to the intracellular space (73). The equivalent circuit would remain the same if the interfacial proton mechanism is modified to accommodate the fact that it is now chloride ions instead of protons that are transferred across the membrane-water interface (interfacial chloride-ion transfer mechanism). By analogy, a photoelectric signal corresponding to such a process is expected to be Cl^- -dependent rather than pH-dependent. This expectation agrees with experimental results. An H1 component and an H2 component were observed. The H2 component can be reversibly altered by an increase or a decrease of aqueous Cl^- concentration.

Molecular Devices Based on Photovoltaic Effect

The mechanism of displacement photocurrents differs from that of many commonly known bioelectric signals such as action potentials, synaptic potentials, and so on. The latter class of bioelectric signals tends to have a slow rise time because diffusion of ions is the primary process. Thus, BR membranes or thin films can be the basis of constructing a high-speed photosensor. Although the dc photoelectric effect is important in the function of BR because it represents the net proton transport across the purple membrane, the effect is less suitable for molecular-device construction. BR-based molecular devices are commonly configured as oriented BR thin films on the support of a transparent electrode. Without the use of a reversible electrode, a proton current such as the dc current in a BR film cannot be converted to an electron current without the help of auxiliary redox compounds such as quinone (discussed in greater detail in reference 63). On the other hand, ac photocurrents (such as B1 and B2) can be detected with a pair of transparent electrodes. That is, the BR sensor so constructed is sensitive only to the onset and to the cessation of illumination. In other words, the BR sensor is sensitive to a sudden increase or to a sudden decrease of illumination. A BR-based artificial photoreceptor has recently been realized by Miyasaka et al. (23). The waveform of such a photocurrent (Figure 11) is typical of the output of a high-pass filter. An examination of the irreducible common equivalent circuit shown in Figure 3 indicated that the series connection between the chemical capacitance and the photoemf (photocurrent source) fulfills the requirement for the construction of a high-pass filter (see also Figure 4B).

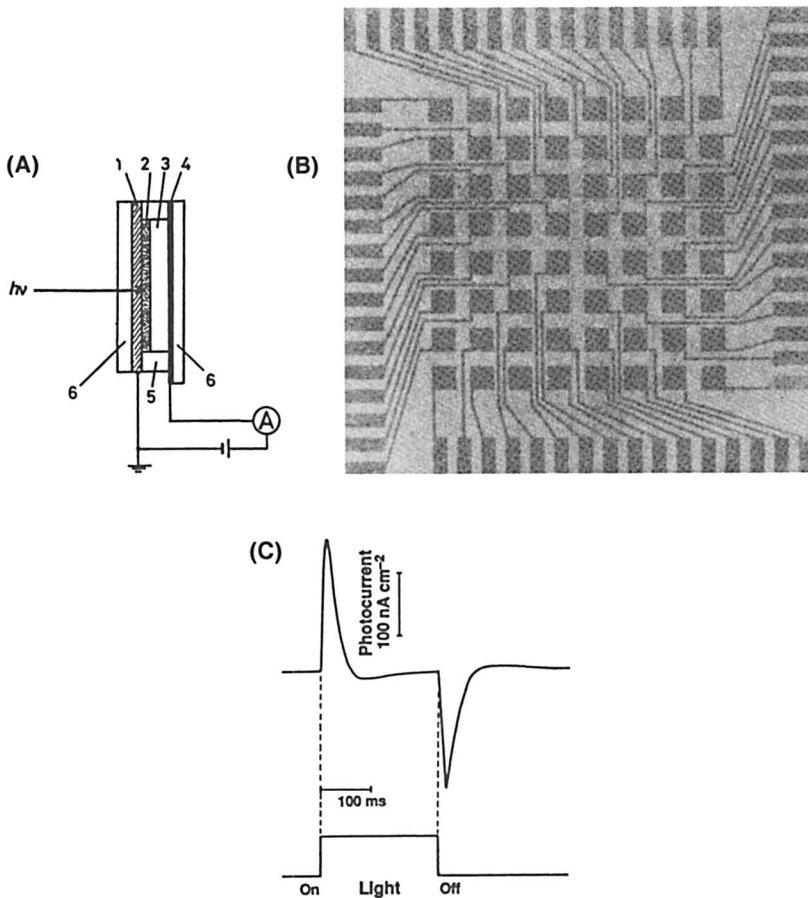


Figure 11. A motion-sensitive sensor array based on the ac photovoltaic effect of BR. (A) Cross-section of a photocell, formed by immobilizing BR on a transparent electrode; 1, SnO₂ transparent conductive layer; 2, purple membrane LB film (typically 6–10 layers); 3, aqueous electrolyte-gel layer (200-μm thick); 4, Au layer (<1,000 Å) as counter-electrode; 5, Teflon ring spacer; 6, glass substrate. (B) Indium tin oxide (ITO) electrode patterned with 64 pixels used for image-sensing. Pixels of ITO (2.5 by 2.5 mm, 1000 Å thick transparent layer) are two dimensionally arrayed on a glass plate; each pixel has a separate wire leading to the four edge terminals along the sides for interfacing with an amplifier circuit. (C) The photocurrent generated in each pixel by a square light pulse of about 200-ms duration. The positive spike of the “on” response and the negative spike of the “off” response are characteristic of a response of a high-pass filter to a long rectangular pulse of applied current (see also Figure 4B). The high-pass filter is formed by the irreducible equivalent circuit shown in Figure 3. (Reproduced with permission from reference 20. Copyright 1986 Elsevier Ireland.)

Applications of the photovoltaic effect are not limited to photodetectors. Birge's group (14) developed a scheme to design a 3D memory from BR. The memory operates on the basis of the fast photovoltaic effect discussed above and on a related phenomenon known as the photoreversal potential, which was first discovered in retina (74). If a retina preparation is first illuminated with a green light, which converts most rhodopsin molecules to metarhodopsins, then the photoreversal potential can be elicited in response to a subsequent blue-light pulse. This potential has a time course similar to that of the early receptor potential except that its polarity is opposite. Concurrently, the metarhodopsins are regenerated back to rhodopsin. Presumably, the forward and reverse charge movements are reversed in the photoregeneration process.

Conclusions and Perspectives

The photovoltaic effect is the predominant physical event in several major photobiological membranes with diverse functions. All these membranes contain integral protein pigments that maintain a fixed orientation with respect to the membranes. Because of the asymmetric orientation of the photopigments, illumination causes vectorial charge movement with prominent components pointing in the direction perpendicular to the membrane. Such charge movement can be detected macroscopically if a pair of electrodes can be placed across the membrane. Two types of photovoltaic effect need to be differentiated. The dc photovoltaic effect represents net charge transport across the membrane, whereas the ac photovoltaic effect represents transient charge displacement with no net charge transport across the membrane or the membrane-water interface. Whereas the ac photovoltaic effect is non-productive from the bioenergetic point of view, it is a fact of life because it represents the ever-present reverse charge combination following the light-induced charge separation. Although the ac photocurrent signal tends to have considerably greater amplitude than the concurrent dc photocurrent, the short duration of the ac signal ensures that the amount of charges being transferred back and forth counts for much less weight as compared with the net (dc) charge transfer than is apparent from the dramatically different amplitudes of the types of photosignals.

The interpretation of displacement photocurrents (ac photovoltaic effect) has been a controversial subject and several apparent paradoxes about the underlying molecular processes have appeared in the literature (discussed in reference 26) since the discovery of the early receptor potential in the monkey retina. The advent of the technique of making artificial lipid bilayer membranes has spurred an increase in the activity of reconstituting membranes with both natural and artificial pigments. In many of these investigations, almost invariably an ad hoc model has

to be proposed to account for the behavior of each study. Furthermore, it is not uncommon that various laboratories working on the same subject do not agree with each other.

Our systematic investigation of the ac photovoltaic effect started with an artificial lipid bilayer model system that contains a membrane-bound magnesium porphyrin and a redox gradient in the aqueous phase. We found that it is necessary to combine electrochemical analysis with electrophysiological analysis. We have developed an analytical framework centered around the concept of chemical capacitance and a tunable voltage-clamp method of electrical measurement (75) that takes into account the interaction between the photochemical event with the passive event of RC relaxation of a capacitor-resistor network. We have demonstrated that such an approach is universally applicable to almost all types of photobiological membranes as well as to many experimental-artificial pigmented-membrane systems that respond to pulsed light with a vectorial charge separation in the direction perpendicular to the membrane (45). The required modifications often involve merely substituting protons, or other charge carriers, for electrons. Despite the fundamental physical differences between ET and proton transfer, the mesoscopic event (i.e., the mechanistic event occurring on the scale between macroscopic and microscopic) in either case seems to be mechanistically equivalent.

The behavior of the fast photoelectric signal under different loading conditions and the interaction between photoactive events and passive relaxation of the inert supporting structures are indeed expected in conventional microelectronics. It can thus be concluded that no fundamental difference between the photovoltaic effect in organic thin films and in conventional microelectronic circuitry exists. However, further consideration reveals one major difference. Whereas conventional microelectronic devices mostly use the bulk physical effect and interfacial physical effect (e.g., at a pn junction in a semiconductor device), the naturally occurring bioelectronic devices also include the effect of chemical reactions between the constituent components. As a result, the mesoscopic effect dominates the picture.

It is especially remarkable for a medium-sized membrane-bound protein, such as BR to possess several domains, both hydrophilic and hydrophobic. The decomposition of the displacement photocurrent in BR into three major components demonstrates that these individual components have a local origin as far as the molecular mechanism is concerned and yet that these components may be strongly coupled "allosterically" because the generating mechanisms all reside on the same molecule. The overall photosignal thus represents integration of electric signals originating from various parts of the molecule. Such a peculiar nature is almost certainly going to add to the colorful repertoire of phys-

ical and chemical events that can be exploited for technological applications. Maybe this is why Nature chose to construct living organisms with predominantly organic materials to carry out many vital functions, and leave inorganic materials for uses primarily as structural materials (e.g., shells and bones). Incidentally, metals are used in major redox components and in catalysis (trace amounts). Proton-transfer reactions seem to be more widespread than ET reactions in the living world. This factor explains why maintenance of an optimal pH in the blood is of vital importance whereas maintenance of optimal redox potentials is important only in the redox centers, which are often buried deeply inside the membrane or a protein molecule.

Attempts to analyze various photobiological membranes mechanistically further reveal that these microstructures and their constituent molecules are optimized for their function via billions of years of evolution. In other words, the structures perform their intended function at a level that far exceeds the minimum requirement of the task. The sophistication in the molecular and supramolecular design can be summed up in the concept of intelligent materials (75–78). However, the intelligence of molecules and molecular assemblies must be evaluated with reference to their intended function. Because Nature may not have our technological applications in mind, the intelligence acquired by biomolecules via evolution may be unsuitable for construction of molecular devices. Fortunately, the advent of modern recombinant-DNA technology makes it possible to conduct artificial breeding of modified biomolecules by forcibly providing the assembly codes to bacteria and thus greatly shortening the time span required for perfection of the molecular design.

Acknowledgments

This research was supported by a contract from the Office of Naval Research (Grant No. N00014–87–K–0047) and by a contract from Naval Surface Warfare Center (Grant No. N60921–91–M–G761). The author acknowledges the contribution of his collaborators: Janos Lanyi, Lowell McCoy, Mauricio Montal, and Richard Needleman. The cited experimental work of Man Chang, Albert Duschl, Filbert Hong, Sherie Mi-chaille, Baofu Ni, and Ting Okajima are also acknowledged.

References

1. Stoeckenius, W. *Sci. Am.* **1976**, *234*(6), 38–46.
2. Stoeckenius, W.; Bogomolni, R. A. *Annu. Rev. Biochem.* **1982**, *51*, 587–616.
3. Mathies, R. A.; Lin, S. W.; Ames, J. B.; Pollard, W. T. *Annu. Rev. Biophys. Chem.* **1991**, *20*, 491–518.
4. Lanyi, J. K. *J. Biochim. Biophys. Acta* **1993**, *1183*, 241–261.

5. Shen, Y.; Safinya, C. R.; Liang, K. S.; Ruppert, A. F.; Rothschild, K. J. *Nature (London)* **1993**, *366*, 48–50.
6. Váró, G.; Keszthelyi, L. *Biophys. J.* **1983**, *43*, 47–51.
7. Draheim, J. E.; Gibson, N. J.; Cassim, J. Y. *Biophys. J.* **1988**, *54*, 931–944.
8. Hong, F. H.; Chang, M.; Ni, B.; Needleman, R. B.; Hong, F. T. In *Biomolecular Material by Design*; Bayley, H.; Kaplan, D.; Navia, M., Eds.; Material Research Symposium Proceedings 230; Materials Research Society: Pittsburgh, PA, in press.
9. Vsevolodov, N. N.; Druzhenko, A. B.; Djukova, T. V. In *Molecular Electronics: Biosensors and Biocomputers*; Hong, F. T., Ed.; Plenum: New York, 1989; pp 381–384.
10. Vsevolodov, N. N.; Druzhenko, A. B.; Djukova, T. V. In *Proceedings of the 11th Annual International Conference of the IEEE Engineering in Medicine and Biology Society*; Kim, Y.; Spelman, F. A., Eds.; The Institute of Electrical and Electronics Engineers, Inc.: New York, 1989; p 1327.
11. Hampp, N.; Bräuschle, C.; Oesterhelt, D. *Biophys. J.* **1990**, *58*, 83–93.
12. Oesterhelt, D.; Bräuschle, C.; Hampp, N. *Quart. Rev. Biophys.* **1991**, *24*, 423–478.
13. Birge, R. R. *Annu. Rev. Phys. Chem.* **1990**, *41*, 683–733.
14. Birge, R. R. *Computer* **1992**, *25(11)*, 56–67.
15. Groma, G. I.; Ráski, F.; Szabó, G.; Váró, G. *Biophys. J.* **1988**, *54*, 77–80.
16. Simmeth, R.; Rayfield, G. W. *Biophys. J.* **1990**, *57*, 1099–1101.
17. Brown, K. T.; Murakami, M. *Nature (London)* **1964**, *201*, 626–628.
18. Cone, R. A.; Pak, W. L. In *Handbook of Sensory Physiology, Principles of Receptor Physiology*; Loewenstein, W. R., Ed.; Springer: Berlin, Germany, 1971; Vol. 1, pp 345–356.
19. Hong, F. T. In *Handbook of Organic Photochemistry and Photobiology*; Horspool, W.; Song, P.-S., Eds.; CRC Press: Boca Raton, FL, in press.
20. Hong, F. T. *BioSystems* **1986**, *19*, 223–236.
21. Rayfield, G. W. In *Molecular Electronics: Biosensors and Biocomputers*; Hong, F. T., Ed.; Plenum: New York, 1989; pp 361–368.
22. Haronian, D.; Lewis, A. *Appl. Opt.* **1991**, *30*, 597–608.
23. Miyasaka, T.; Koyama, K.; Itoh, I. *Science (Washington, D.C.)* **1992**, *255*, 342–344.
24. Skulachev, V. P. *Methods Enzymol.* **1982**, *88*, 35–45.
25. Keszthelyi, L. In *Information and Energy Transduction in Biological Membranes*; Bolis, C. L.; Helmreich, E. J. M.; Passow, H., Eds.; Alan R. Liss: New York, 1984; pp 51–71.
26. Hong, F. T.; Okajima, T. L. In *Electrical Double Layers in Biology*; Blank, M., Ed.; Plenum: New York, 1986; pp 129–147.
27. Trissl, H.-W. *Photochem. Photobiol.* **1990**, *51*, 793–818.
28. Hong, F. T. In *Proceedings of the 11th School on Biophysics of Membrane Transport*; Kuczera, J.; Przystalski, S., Eds.; Agricultural University of Wrocław: Wrocław, Breslau, Poland, 1992; pp 218–242.
29. Hong, F. T. *IEEE Eng. Med. Biol. Mag.* **1994**, *13(1)*, 75–93.
30. Hong, F. T. In *Biomembrane Electrochemistry*; Blank, M.; Vodyanoy, I., Eds.; Advances in Chemistry. 235; American Chemical Society: Washington, DC, 1994; pp 531–560.
31. Hong, F. T. *Prog. Surf. Sci.*, in press.
32. Hong, F. T.; Mauzerall, D. *Proc. Natl. Acad. Sci. U.S.A.* **1974**, *71*, 1564–1568.
33. Hong, F. T. *Photochem. Photobiol.* **1976**, *24*, 155–189.

34. Hong, F. T.; Montal, M. *Biophys. J.* **1979**, *25*, 465–472.
35. Hagins, W. A.; McGaughy, R. E. *Science (Washington, D.C.)* **1967**, *157*, 813–816.
36. Hong, F. T. In *Molecular Electronics: Biosensors and Biocomputers*; Hong, F. T., Ed.; Plenum: New York, 1989; pp 105–114.
37. Hong, F. T. In *Molecular Electronics: Materials and Methods*; Lazarev, P. I., Ed.; Kluwer Academic: Dordrecht, The Netherlands, 1991; pp 291–310.
38. Deisenhofer, J.; Michel, H. *Science (Washington D.C.)* **1989**, *245*, 1463–1473.
39. Engelman, D. M.; Henderson, R.; McLachlan, A. D.; Wallace, B. A. *Proc. Natl. Acad. Sci. U.S.A.* **1980**, *77*, 2023–2027.
40. Henderson, R.; Baldwin, J. M.; Ceska, T. A.; Zemlin, F.; Beckmann, E.; Downing, K. H. *J. Mol. Biol.* **1990**, *213*, 899–929.
41. Hong, F. T. In *Biomedical Engineering in the 21st Century*; Wang, C.-Y.; Chen, C.-T.; Cheng, C.-K.; Huang, Y.-Y.; Lin, F.-H., Eds.; Center for Biomedical Engineering, National Taiwan University College of Medicine: Taipei, Taiwan, 1990; pp 85–95.
42. Nagle, J. F.; Morowitz, H. J. *Proc. Natl. Acad. Sci. U.S.A.* **1978**, *75*, 298–302.
43. Honig, B. In *Electrogenic Ion Pumps: Current Topics in Membranes and Transport*; Bronner, F.; Slayman, C., Eds.; Academic: Orlando, FL, 1982; Vol. 16, pp 371–382.
44. Hong, F. T. *Bioelectrochem. Bioenerg.* **1978**, *5*, 425–455.
45. Hong, F. T. In *Bioelectrochemistry: Ions, Surfaces, Membranes*; Blank, M., Ed.; Advances in Chemistry 188; American Chemical Society: Washington, DC, 1980; pp 211–237.
46. Okajima, T. L.; Hong, F. T. *Biophys. J.* **1986**, *50*, 901–912.
47. Ikonen, M.; Sharonov, A. Yu.; Tkachenko, N. V.; Lemmetyinen, H. *Adv. Mater. Opt. Electron.* **1993**, *2*, 211–220.
48. Trissl, H.-W.; Montal, M. *Nature (London)* **1977**, *266*, 655–657.
49. Hong, F. T.; Okajima, T. L. In *Biophysical Studies of Retinal Proteins*; Ebrey, T. G.; Fraunfelder, H.; Honig, B.; Nakanishi, K., Eds.; University of Illinois: Urbana-Champaign, IL, 1987; pp 188–198.
50. Michaille, S.; Hong, F. T. In *Proceedings of the 11th Annual International Conference of the IEEE Engineering in Medicine and Biology Society*; Kim, Y.; Spelman, F. A., Eds.; The Institute of Electrical and Electronics Engineers, Inc.: New York, 1989; pp 1333–1335.
51. Michaille, S.; Hong, F. T. *Bioelectrochem. Bioenerg.* **1994**, *33*, 135–142.
52. Okajima, T. L.; Michaille, S.; McCoy, L. E.; Hong, F. T. *Bioelectrochem. Bioenerg.* **1994**, *33*, 143–149.
53. Hong, F. T. *J. Electrochem. Soc.* **1987**, *134*, 3044–3052.
54. Drachev, L. A.; Kaulen, A. D.; Skulachev, V. P. *FEBS Lett.* **1978**, *87*, 161–167.
55. Hong, F. T. In *Protein Engineering: Protein Design in Basic Research, Medicine, and Industry*; Ikehara, M.; Titani, K.; Oshima, T., Eds.; Japan Scientific Societies: Tokyo, Japan, 1990; pp 235–242.
56. Hong, F. T.; Hong, F. H.; Needleman, R. B.; Ni, B.; Chang, M. In *Molecular Electronics—Science and Technology*; Aviram, A. Ed.; American Institute of Physics: New York, 1992; pp 204–217.
57. Hong, F. H.; Chang, M.; Ni, B.; Needleman, R. B.; Hong, F. T. *Bioelectrochem. Bioenerg.* **1994**, *33*, 151–158.

58. Birge, R. R.; Cooper, T. M. *Biophys. J.* **1983**, *42*, 61–69.
59. Cooper, A. *Nature (London)* **1979**, *282*, 531–533.
60. Matthews, R. G.; Hubbard, R.; Brown, P. K.; Wald, G. J. *Gen. Physiol.* **1963**, *47*, 215–240.
61. Váró, G.; Lanyi, J. K. *Biochemistry* **1991**, *30*, 5016–5022.
62. Cafiso, D. S.; Hubbell, W. L. *Biophys. J.* **1980**, *30*, 243–264.
63. Hong, F. T. J. *Molec. Electron.* **1989**, *5*, 163–185.
64. Shevtchenko, T. F.; Kalamkarov, G. R.; Ostrovsky, M. A. *Sens. Syst.* **1987**, *1*, 117–126 (in Russian).
65. Ostrovsky, M. A. In *Molecular Electronics: Biosensors and Biocomputers*; Hong, F. T., Ed.; Plenum: New York, 1989; pp 381–384.
66. Bolshakov, V. I.; Kalamkarov, G. R.; Ostrovsky, M. A. *Dokl. Akad. Nauk USSR* **1978**, *240*(5), 1231–1244 (in Russian).
67. Emeis, D.; Kühn, H.; Reichert, J.; Hofmann, K. P. *FEBS Lett.* **1982**, *143*, 29–34.
68. Wilden, U.; Kühn, H. *Biochemistry* **1982**, *21*, 3014–3022.
69. Drain, C. M.; Christensen, B.; Mauzerall, D. *Proc. Natl. Acad. Sci. U.S.A.* **1989**, *86*, 6959–6962.
70. Drain, C. M.; Christensen, B.; Mauzerall, D. In *Proceedings of the 11th Annual International Conference of the IEEE Engineering in Medicine and Biology Society*; Kim, Y.; Spelman, F. A., Eds.; The Institute of Electrical and Electronics Engineers, Inc.: New York, 1989; p 1336.
71. Hara, M.; Majima, T.; Miyake, J.; Ajiki, S.; Sugino, H.; Toyotama, H.; Kawamura, S. *Appl. Microbiol. Biotechnol.* **1990**, *32*, 544–549.
72. Michaile, S.; Duschl, A.; Lanyi, J. K.; Hong, F. T. In *Proceedings of the 12th Annual International Conference of IEEE Engineering in Medicine and Biology Society*; Oranal, B.; Pedersen, P. C., Eds.; The Institute of Electrical and Electronics Engineers, Inc.: New York, 1990; pp 1721–1723.
73. Lanyi, J. K. *Physiol. Rev.* **1991**, *70*, 319–330.
74. Cone, R. A. *Science (Washington, D.C.)* **1967**, *155*, 1128–1131.
75. Hong, F. T.; Mauzerall, D. *J. Electrochem. Soc.* **1976**, *123*, 1317–1324.
76. *The Concept of Intelligent Materials and the Guidelines on R&D Promotion*; Takagi, T., Ed.; Science and Technology Agency, Government of Japan: Tokyo, Japan, 1989.
77. Hong, F. T. *Nanobiology* **1992**, *1*, 39–60.
78. Hong, F. T. *Intell. Mater. (Intell. Mater. Forum: Tokyo)* **1992**, *2*(2), 15–18.

RECEIVED for review June 3, 1992. ACCEPTED revised manuscript April 5, 1993.

Photodiodes Based on Bacteriorhodopsin

George W. Rayfield

Physics Department, University of Oregon, Eugene, OR 97403

Photodiodes constructed from bacteriorhodopsin (BR), a material of biological origin, are reviewed. The origin of the photoelectrical signal from illuminated BR is discussed. BR photodiodes have unique photoelectrical-response characteristics due to the complex photophysics of BR. For example, BR photodiodes that give a photoelectrical response only when there is a change in light intensity have been demonstrated. The photoelectrical response (polarity and spectral response) of the diode can be optically programmed and altered in real time. Also, depending on how the BR photodiode is constructed, its response time can be very fast (<5 ps). Several optical devices based on these features are reviewed. The construction of an ultrafast BR photodiode is described in detail. Methods used to modify BR for application to BR photodiodes are also briefly reviewed.

THE USE OF BACTERIORHODOPSIN IN PHOTOELECTRIC DEVICES, particularly photodiodes, is the focus of this chapter. Photoelectric signals are observed when an oriented sample of BR is illuminated by light. A review by Trissl (1) discusses in detail the biophysical origin of the photoelectric signals from BR and the implications they have on the biological function of BR. This chapter concentrates primarily on device applications of the photoelectric effect in BR. Device applications based on the photochromic properties of BR have been recently reviewed by Oesterhelt et al. (2).

Several features unique to BR make this material attractive for photoelectric devices. First, the photoresponse is very fast, probably less than 1 ps. Second, light of various colors can be used to control the photoelectric response. Third, the photoresponse of BR can be tailored by genetic engineering. Finally, BR or genetically engineered BR is

0065-2393/94/0240-0561\$08.00/0
© 1994 American Chemical Society

readily produced in quantity, robust in laser light, and stable over long periods of time.

Background

Structure and Function. BR is a light-active material of biological origin. It is a protein found in the cell membrane wall of *Halobacterium halobium*, where it functions as a light-driven proton pump. A single BR molecule, or monomer, consists of two main parts: the opsin and a retinal. The opsin is a seven- α -helical array of 248 amino acids and has a molecular weight of 26,000. Each of the seven-linked- α -helices spans the membrane and is roughly perpendicular to it. The retinal is responsible for visible-light absorption by BR. It is located within a pocket of the opsin and is bound via a protonated Schiff base (PSB) to a lysine in the amino acid chain forming the opsin.

In the cell wall BR is found in the form of a two-dimensional crystalline sheet called "purple membrane" (pm). Each pm sheet is approximately 1 μm in diameter and 45 \AA thick. A single pm contains about 10^5 individual BR molecules. Each molecule is vectorially oriented to pump protons in the same direction across the pm. The BR molecules in the pm are located on a triangular lattice with three BR molecules—a trimer—on each lattice site. The spacing between trimers is 60 \AA . The region between trimers is filled with lipid, which accounts for about 15% of the pm by weight (3).

The pm structure of BR is retained after it is isolated from the bacteria and suspended in distilled water, and it is still functional in the aqueous suspension. Thus, illumination of the aqueous pm suspension causes the BR to pump protons across the pm. In distilled water with a pH near 7, the pm has both a net negative charge and a large intrinsic-dipole moment (4). This dipole moment is important for device applications because it allows the orientation of the pm to be controlled by electric fields.

Light Absorption. An aqueous suspension of pm has a peak in its absorbance at 570 nm. Retinal is responsible for the absorption of visible light by BR. The electric dipole moment of the retinal lies nearly in the plane of the pm so that light incident normal to the plane of the pm is strongly absorbed. Interaction between the retinal and the opsin causes the absorption spectrum of the retinal to be strongly red shifted from that of free retinal.

Isomerization. The retinal chromophore of BR may exist in either an all-*trans* or 13-*cis* conformation. Absorption of light by retinal results in a photoinduced isomerization between the conformational states. An

aqueous suspension of pm that has been kept in the dark has an equal mixture of each conformational state. Exposure of the solution to continuous light results in the "light-adapted state" in which all retinal chromophores are in the *trans* conformation. After about one-half hour in the dark, the original "dark-adapted state" (i.e., the 1:1 mixture of conformational states) is recovered. Dark-adapted BR (i.e., the 13-*cis* chromophore) has a peak absorption at 554 nm, whereas the light-adapted BR has a peak absorption at 568 nm. Only the all-*trans* conformational state is active for light-driven proton pumping.

Photocycle. Flash illumination of an aqueous suspension of light-adapted pm causes a transient change in its absorbance spectrum. The different transient absorbance states or photointermediates comprise a photocycle and have characteristic rise and fall times that vary from less than 1 ps to more than 1 ms. Although the photocycle is complex (5), its main features are illustrated by the simplified photocycle shown in Figure 1. The photocycle consists of three intermediates BR570, K610, and M410. Before absorption of a photon, the BR molecule is in state BR570, which has an absorbance maximum of 570 nm. Absorption of a photon causes a *trans-cis* isomerization of the retinal (recall that light-adapted BR has only all-*trans* retinal). The K610 photointermediate with an absorbance maximum of 610 nm and a 13-*cis* retinal is formed in about 1 ps. The subsequent steps in the photocycle are thermally driven.

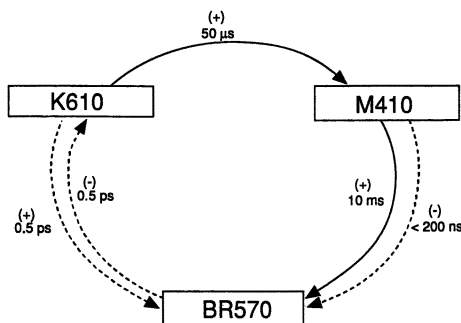


Figure 1. A simplified photoreaction cycle consisting of only 2 intermediates and the initial (BR570) state. The full photocycle consists of 7 intermediates and the initial (BR570) state. Absorption of a photon by BR in the initial state creates K and starts the photocycle. Both intermediates, K and M, may be photoconverted to the BR state. However, neither K nor BR can be photoconverted directly to M. The formation of M only occurs through thermal processes from K. Thermal-driven transitions are shown as solid lines; photodriven transitions are shown as dotted lines. The polarity of the photoelectric response corresponding to each transition is indicated by the sign in parentheses.

Deprotonation of the Schiff base causes a blue shift of the retinal-absorbance maximum to 412 nm. The last step in the photocycle (back to BR570) involves reprotonation of the Schiff base and reisomerization of the retinal. The complete cycle takes about 10 ms.

At low temperature (77 K) the photocycle terminates at K610 because later steps in the cycle are thermally driven. However, K610 can be photoconverted back to BR570 by red light (1, 6). Thus, at low temperature, the BR molecule is a two-state system. Green light shifts the absorbance to 610 nm, and red light shifts it back to 570 nm. Other photocycle intermediates are also light active. For example, blue light will photoconvert M410 back to BR570. Different photocycles are observed if the retinal begins in the 13-*cis* conformation (dark adapted), if retinal analogs are used in place of the retinal (7, 8) or if amino acids in the opsin are substituted (1, 9, 10).

Proton Translocation and Charge Movement. Flash illumination of a pm suspension (light adapted) also causes a transient release of protons to the bathing solution followed by a slow uptake. Uptake and release occur on opposite sides of the membrane. Thus, absorption of a photon of light by the BR molecule causes it to pump a proton across the pm. The photocycle and proton pumping are correlated (11, 12). Proton release takes place with the rise of M410, and proton uptake occurs with the decay of M410.

Photoelectric Signal

Experimental Arrangement and Measurements. The movement of charges within the pm following a light flash can be detected electrically (1). This detection is done by attaching the pm sheets in an oriented arrangement to a supporting substrate, for example, a black lipid membrane (BLM), colloidal film, or thin Teflon film, separating two chambers filled with electrolyte. A light flash produces a photovoltage or photocurrent between electrodes immersed in each electrolyte solution. Figure 2 shows a typical photovoltage response. The log time plot shows three main components in the photovoltage response. The initial negative polarity component (labeled 1 and not time resolved) is followed by two positive polarity components (labeled 2 and 3) with time constants of about 20 μ s and 20 ms, respectively. The photovoltage ultimately decays to zero after several seconds depending on the permeability of the substrate supporting the pm and the external circuit parameters (1). Positive components in the photovoltage correlate with proton release and uptake during the photocycle (13).

If a very low impedance ammeter is used in place of the high impedance voltmeter, a photocurrent is measured. If the substrate has low

proton permeability, the photocurrent measures the capacitive charging currents, which is the derivative with respect to time of the photovoltage (*I*). However, if the substrate supporting the oriented pm is permeable to protons, continuous illumination generates a continuous photocurrent (*14, 15*).

Other photocycle intermediates also exhibit a photoelectric response. Illumination of the K610 intermediate with red light produces a fast photoelectric response signal with a positive polarity (i.e., of opposite polarity to that observed coincident with the BR570 to K610 transition) (*1, 6*). Illumination of the M410 intermediate with blue light produces a photoelectric response of negative polarity (*16*). The photoelectric activity of the photocycle intermediates is important for device applications to be discussed in the next section.

Flash illumination of dark-adapted BR also produces a photoelectric response (*17*). None of the device applications discussed in this chapter is based on the photoelectric response of dark-adapted BR.

Orientation of pm. Near pH 7, a pm sheet has both a net charge (negative) and an electric dipole moment (*4*). Therefore, pm in an aqueous suspension can be orientated by applying a modest (20 V/cm) electric field (*18*). This orientation persists for several tenths of a second after the field is turned off but ultimately the orientation is lost due to Brownian motion. Illumination of the suspension produces a photovoltage between two electrodes suspended in the suspension while the orientation persists (*18*). The electric-field induced orientation of the pm can be preserved by freezing it by using dried films (*19, 20*) or hydrogels (*21–23*) to immobilize the pm.

Because the purple membranes carry a negative charge, they also move in the electric field used for orientation. Thus, after several minutes, the positive electrode used to establish the electric field in the pm suspension becomes coated with a film of oriented pm (*19*). The pm film remains intact and oriented when the coated electrode is removed from solution and dried. A photodiode is formed by covering the film with a second electrode. The diode gives a photovoltaic response similar to that shown in Figure 2 in response to a flash of light.

We use the following procedure to form BR photodiodes. First, the pm sample is washed in ultrapure distilled water and is resuspended at about 4 mg/mL. A drop of this solution (30 μ L) is then placed between two transparent electrodes [indium tin oxide (ITO)-coated glass] with a separation of 1 mm. The pm drop forms a bridge between the electrodes so that a current flows between the electrodes when a voltage is applied. Usually 2–3 V are applied for 2 or 3 min. When the transparent electrodes are separated, it is found that the negative-biased electrode (cathode) has only clear water attached to it, whereas the positive elec-

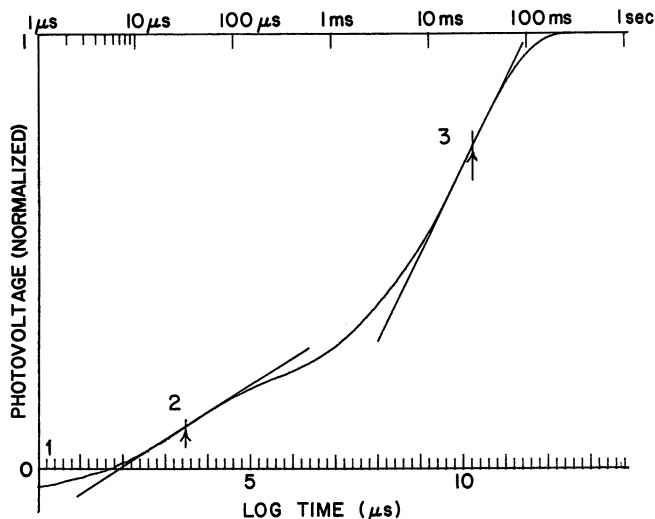


Figure 2. The photovoltage response of oriented pm sheets attached to a supporting Teflon film is shown. A 1- μ s laser-light flash (590 nm) was used to illuminate the pm sheets. Three components to the photovoltage exist. The initial negative component (1) in the photoresponse is not time resolved. The slow decay of the photovoltage to the baseline is not shown.

trode (anode) has all of the pm on its surface. This electrode is then dried under vacuum and covered with a counterelectrode. The active area of the resulting photodetector is about 0.25 cm². Care must be taken in drying because extensive vacuum drying will completely dehydrate the BR and will change the photoresponse (24).

Following the literature (21, 23), we also used oriented pm immobilized in a hydrogel for BR photodiodes. Typically, polyacrylamide is used for the hydrogel. The oriented pm gel is formed by first forming an aqueous suspension of pm and monomer. An electric field is then applied and polymerization is initiated. Some care must be taken because the gel-forming solution increases the ionic strength of the solution and interferes with the electric-field orientation of the pm. Also the polymerization must be rapid because the pm sheets drift in the applied electric field. A photodiode is formed by sandwiching the oriented pm gel between two transparent electrodes.

Photodiodes have also been prepared by using the Langmuir-Blodgett (25–29) technique. This technique is complicated and requires both a Langmuir trough and computer-controlled instrumentation. It relies on the fact that a pm monolayer spread at the air–water interface is oriented. This orientation occurs because the surface of the pm that has the greater negative charge is attracted to the water substrate. After

spreading, the oriented pm film on the surface of the water is transferred to a solid substrate. This is done by passing the substrate vertically through the surface. More than 100 layers must be deposited on the substrate to produce an optically thick film. Each pm layer transferred must be dried before depositing the next layer. About 15 min are required to deposit a single pm layer on the substrate. The process of forming an oriented pm film with this method is tedious and time-consuming.

We prefer to form BR photodiodes by using the dried film approach for several reasons. The film forming process is fast and simple, the films formed are both optically dense and thin, and the films can be left exposed to air without changing their properties.

Origin of Photoelectric Signal. The displacement of a charge between two parallel conducting plates causes a voltage to appear across the plates (30, 31). The rise time of the voltage is limited only by the time required to displace the charge. As discussed in the next paragraph, the magnitude of the voltage depends on the magnitude of the charge, the distance it is displaced, and the capacitance of the plates.

Suppose a charge q is located between two parallel conductor plates of area A and separation d . The distance between the charge and one of the plates is x . If the plates are connected by a conducting wire, they are at the same potential. Boundary conditions require that the plate a distance x from the charge has an induced charge $-q(x/d)$ on it. The other plate has an induced charge $-q(1 - x/d)$ on it. If the charge q is now displaced a distance δx , then the induced charges on the plates change. A charge $q(\delta x/d)$ moves through the wire to maintain the proper induced charge on each plate. The response time depends on how fast the necessary charge can be moved through the circuit (wire) connecting the plates. If the plates are not connected by a wire, then, when q is displaced, the charge induced on the plates cannot be redistributed between the plates. A voltage equal to $q\delta x/(Cd)$ develops between the plates where C is the capacitance of the plates. This voltage appears instantaneous with the displacement of q because in this "open-circuit" configuration no other charges move (i.e., no conduction path connects the plates).

The previous discussion assumes that only the charge q is displaced in the region between the conducting plates. However, the displacement of q changes the electric field in the region near q . Thus, in the more general case, other charges in the vicinity of q may move in response to the displacement of q . Each of these charge movements will contribute to the voltage appearing across the plates. If their response time is fast compared to the time required to displace q , then the voltage appearing across the plates will not follow the displacement of q . In this case, the

rise time of the photovoltage will depend on the polarization response time, that is, on the dielectric response function of the medium surrounding q . Although the dielectric response function of dried PM has not been measured, it is unlikely that the polarization response time is faster than 20–40 ps (32). Thus, on the picosecond time scale, the kinetics of the photovoltage should still follow the kinetics of the displacement of q .

Devices Based on the Photoelectric Effect in BR

Ultrafast BR Photodetector. The initial negative component in the photovoltage (Figure 2) appears to be associated with the initial light-induced conformational change of the retinal (1, 33). If so, the rise time of this negative component should be about 1 ps. The possibility of a 1 ps response time suggest the use of BR photodiodes as ultrafast photodetectors.

Detection of the Fast Picosecond Signal. Two approaches were considered for measuring the fast rise time of the photovoltage from BR photodiodes. The first was based on electrooptic (EO) sampling and the second on Josephson junctions.

EO Sampling. In the past few years a technique called EO sampling has been developed (34). This technique is capable of resolving picosecond photoinduced electrical transients. In EO sampling a 1 ps light pulse from a laser is first split into two light pulses that traverse different optical paths. One light pulse is used to excite the diode. The voltage produced is impressed across an EO crystal that responds by rotating polarized light passing through it. The second pulse of light passes first through a polarizer and then through the crystal. If the voltage signal and the second light pulse arrive at the same time in the crystal, the polarization of the light is rotated and it can pass through an analyzer and be detected. The rise time of the photovoltage is resolved by varying the arrival time of the voltage signal at the crystal. This is done by varying the optical path length in the apparatus. Thus the time dependence of the voltage signal appearing across the crystal is sampled by the picosecond light pulse passing through the sample.

We encountered three difficulties in using this approach. First, the responsivity of our BR photodiode is not large (about 0.35 mV/ μ J). Second, the cycling time of BR is slow (about 10 ms). Third, the voltage response of the BR photodetector is the integral of the picosecond light pulse. These difficulties along with the complexity of the EO sampling technique led us to temporarily abandon this technique. EO sampling is still most attractive for measuring the rise time with subpicosecond resolution.

Josephson Junction Oscilloscope. Josephson junctions are capable of resolving voltage rise times with picosecond resolution (35). An ultrafast digital sampling oscilloscope that uses a Josephson junction and superconducting input circuitry is commercially available (model PSP-1000; Hypres Inc., Elmsford, NY). This oscilloscope is capable of measuring voltage transients with a time resolution of a few picoseconds. Sampling rates of 10 Hz can be used, and signals of 10-mV amplitude can be resolved. With this instrument, it is possible to measure the photovoltage rise time of BR photodiodes with picosecond resolution despite their slow recovery time and low responsivity. Although a Josephson junction is capable of resolving voltage rise times with 1-ps resolution, the input circuitry of the Hypres oscilloscope limits it to 5- to 8-ps resolution.

Photodetector Construction. Figure 3 shows a BR photodiode. A dried oriented BR film is deposited on an ITO-coated glass support. A thin 6- μm Teflon film separates the BR film from the center electrode of the diode. Light-induced charge displacements within the BR film generate a voltage between the ITO-coated glass and the center electrode, which form a planar waveguide. The voltage (electromagnetic) wave first travels radially outward and then along the coaxial waveguide formed by the center electrode and the outer wall of the diode. The diode attaches directly to the input connector of the oscilloscope.

Picosecond Measurement. Figure 4 shows the photovoltage rise time of the BR photodiode in response to a 3-ps light pulse (36). A dye laser synchronously pumped by an Argon ion mode locked continuous-wave laser was used as a source of the picosecond light pulse. A longi-

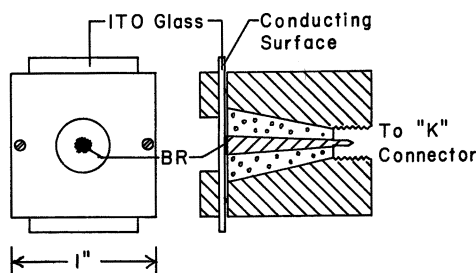


Figure 3. An ultrahigh-speed BR photodiode. The center conductor and outer housing form a coaxial waveguide that connects directly to the input "K" connector of the oscilloscope. The BR film is sandwiched between the end of the center conductor and a sheet of ITO glass that forms a transparent electrode. The voltage wave produced by illumination of the BR film first travels radially outward and then along the coaxial waveguide of the diode.

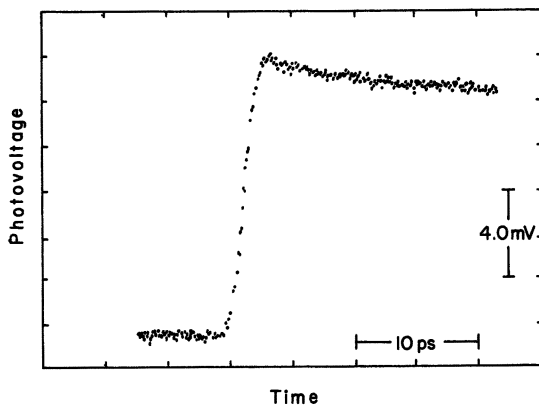


Figure 4. The photovoltage rise time of the BR photodiode in response to a 3-ps light pulse. As discussed in the text, the shape of the response suggests an “overshoot” in the input voltage signal to the oscilloscope.

tudinal pumped three-stage dye amplifier chain was built to amplify the pulses from the dye laser. Output light pulses at a wavelength of 595 nm, with 300 μJ of energy, a pulse width of 3 ps, and a repetition rate of 10 Hz were produced by the apparatus.

The rise time of the photovoltage shown in Figure 4 appears to be about 4 ps. However, the “K” connector of the oscilloscope attenuates high-frequency components in the input signal due to a 40-GHz high-frequency roll off. Thus, a step function voltage input signal should be recorded by the oscilloscope as a signal with a rise time of 8 ps. However, if the voltage input signal to the oscilloscope has an overshoot, then the response recorded on the oscilloscope will appear to have a faster rise time. There are two possible sources of the overshoot. First, the overshoot in the input signal may be an experimental artifact associated with ringing, that is, wave reflections in the BR photodiode. Second, the overshoot might also be intrinsic in the BR photovoltage caused, for example, by the retinal transient dipole moment in response to a light flash (1, 33).

The time constant of the decay of the photovoltage signal is about 250 ps. This decay is due to input impedance of the oscilloscope (50 Ω) and the capacitance of the BR photodiode, which is 4–5 pF.

It has been suggested that the initial negative component in the photovoltage is probably associated with light-driven formation of the K610 photointermediate in the photocycle (1). Recall that this is a picosecond event and is associated with the *trans-cis* isomerization of the retinal. This isomerization causes a displacement of the PSB away from its negative counterion on the opsin. In support of this idea, Trissl et al. (6) have shown that irradiation of the K610 intermediate generates

BR570, a *cis-trans* isomerization and a photovoltage opposite in sign to that generated in the BR570 to K610 photoconversion. However, it is not yet clear that the direction of such a charge movement is consistent with the observed signal magnitude and polarity. Estimates of a charge displacement in excess of 10 Å (*I*) are much larger than the small distance the PSB moves during the isomerization. Also, to account for the sign of the photovoltage, the movement of the PSB has to be in the opposite direction from proton translocation by the pump.

If the observed photovoltage signal has an intrinsic overshoot, it may be due to a redistribution of electronic density on the retinal (*I*, 33). The resulting dipole moment would be transient and last only for the lifetime of the electronic excited state. Two-photon absorption (37) measurements and second-harmonic generation (38) measurements are consistent with a large dipole moment associated with the electronic excited state of retinal. One problem with this proposal is the very short (femtosecond) lifetime of the electronic excited state.

BR Photodiode Limitations. An ideal photodiode has fast response, broad spectral response, high sensitivity, and fast recovery. Ideally, the time dependence of the photodiode's output follows the light intensity changes of the incident light. The photodiode should also be inexpensive.

Although the BR photodiode has very rapid response, is simple, is cheap to produce, and has broad response in the visible spectral region, it has significant limitations. First, the responsivity is low, only about 0.35 mV/ μ J. Second, the diode integrates the light signal, and third, its recovery time is slow. The recovery time could be reduced by using a background red light to photoinitiate the K-to-BR transition and quickly return the K610 state back to the initial BR570 state.

In "Photoelectric Signal", it was mentioned that charge movement within the pm is correlated with the proton pumping cycle and the photocycle (*13*). The BR photodiode described previously uses the very fast, negative polarity, photoelectrical response coincident with the photoinitiated BR-to-K transition. The input impedance of the oscilloscope and capacitance of the BR photodiode function as a high-pass filter. This prevents interference due to photoelectric effects associated with slower charge displacements that occur during the photocycle.

Other BR-Photodiode Devices. Photoelectric effects unique to BR photodiodes have begun to be exploited for other device applications (*16*, *39*, *40*). Two important effects are to be exploited. First, BR photodiodes can be photoelectrically interrogated to determine the number of BR molecules in a particular photocycle intermediate state. Second, BR photodiodes have a memory capability.

BR photodiodes can be photoelectrically interrogated because some photocycle intermediates are photoelectrically active. For example, the

illumination of the K610 intermediate with red light generates a photovoltage of opposite polarity (i.e., positive) to that generated when the initial BR570 state is illuminated with green light (6). Thus, the number of BR molecules in the K610 state of the photodiode can be measured by the photoresponse of the diode to red light. The M410 intermediate of the photocycle is also photoactive. Illumination of the M410 intermediate with blue light generates the BR570 state and a photoelectrical response that is proportional to the number of molecules in the M410 state (16).

Photoelectric measurements can be made on molecules in the BR570 state without affecting the population of the M410 state. The population of the M410 state is not affected because photoconversion of BR570 or K610 does not directly affect the number of molecules in the M410 state of the diode. Recall that M410 is only the result of thermal processes. So that if K610 is photoconverted by red light back to BR570 before it thermally decays to M410, then the population of M410 will not be affected. Thus, it is possible to read the "state" of the diode without erasing (16).

The memory capability of BR photodiodes depends on the lifetime of the photocyclic intermediates. In an aqueous suspension of pm at room temperature, K610 has a lifetime of a few microseconds. The corresponding lifetime of M410 is about 10 ms. The lifetime of these photointermediates can be extended by lowering the temperature, chemical treatment, genetic modification, or the replacement of retinal with retinal analogs (1, 3). For example, lowering the temperature to 77 K traps the K610 intermediate. The BR molecules can exist only in two states, BR570 and K610. Different colored light is used to convert BR molecules between the two memory states. Thus, the photoresponse of the diode is reprogrammable with light (16). Similarly, the lifetime of the M410 intermediate can be extended. This provides the BR photodiode with additional memory capability and programmability.

Several device applications of BR photodiodes have been demonstrated that take advantage of the unique features of the BR photodiodes discussed previously. Haronian and Lewis (16) have investigated a neural-network architecture based on a BR photodiode synapse. Several unique properties of a BR photodiode were used to implement a four-element synaptic matrix. First, light incident on a BR photodiode can be used to program the diodes photoelectric response. Thus, each element of an array of BR photodiodes can be individually programmed with a different photoresponse. Second, the photocurrent from a BR photodiode depends on the load connected to the diode. Thus, one element in the array can control the response of another element by varying the load resistance connected to it.

Miyasaka et al. (41) demonstrated a BR photodiode with differential responsivity to light. The photodiode consists of a transparent electrode, an oriented pm layer, an aqueous electrolyte gel, and a counter electrode. The diode responds only to changes in light intensity (>50 Hz). No photocurrent is produced by constant illumination. An array of these BR photodiodes is capable of detecting a mobile object in an input scene.

Takei et al. (39) used the unique photoresponse of the BR photodiode to simulate the properties of the ganglion receptive field found in the retina. Groma et al. (40) demonstrated that photoinduced electric-field patterns can be stored in a film of BR.

Future Work

More improved BR diodes will result from genetic engineering of the material and the use of retinal analogs in place of retinal in the protein.

Genetic Engineering of BR. A number of different mutant BR genes have been expressed in *Escherichia coli*. The resulting BR variants have altered photoelectric properties (1, 9, 42, 43). For example, the variant D96N has a very long-lived M410 intermediate (42, 43). Another variant, D85N, has an initial component in the photoresponse that is much larger in amplitude than is wild-type BR (9). These results suggest that BR variants have the potential to produce BR photodiodes with properties superior to diodes produced with wild-type BR.

The practical use of genetically engineered BR for device applications (i.e., BR photodiodes) will require that the material is available in quantity. The recent development of an expression system for modified BR in *H. halobium* makes this possible (44). What now needs to be done is to screen a large number of different BR variants for optimized photoelectric response.

Retinal Analogs. A number of different retinal analogs can be substituted for retinal in BR (45, 46). Several of these retinal-analog BRs have altered photoresponse, particularly those with substitutions at the C13 of the retinal (46). Although potentially useful for BR photodiodes, retinal-analog BR is more difficult to produce in quantity than is genetically engineered BR. Therefore, from a practical point of view, retinal-analog BR may not be as attractive for BR photodiodes as genetically engineered BR.

References

1. Trissl, H.-W. *Photochem. Photobiol.* **1990**, *51*(6), 793–818.
2. Oesterhelt, D.; Bräuchle, C.; Hampp, N. *Quarterly Rev. Biophys.* **1991**, *24*(4), 425–478.

3. Henderson, R.; Baldwin, J. M.; Ceska, T. A.; Zemlin, F.; Beckmann, E.; Downing, K. H. *J. Mol. Biol.* 1990, 213(4), 899–929.
4. Papp, E.; Fricsovszky, G.; Meszena, G. *Biophys. J.* 1986, 49, 1089–1100.
5. Váró, G.; Lanyi, J. K. *Biochemistry* 1991, 30(20), 5008–5015.
6. Trissl, H.-W.; Gärtner, W.; Leibl, W. *Chem. Phys. Lett.* 1989, 158(6), 515–518.
7. Gärtner, W.; Oesterhelt, D.; Vogel, J.; Maurer, R.; Schneider, S. *Biochemistry* 1988, 27, 3497–3502.
8. Eremin, S. V.; Mitsner, B. I.; Danshina, S. V.; Drachev, L. A.; Kaulen, A. D.; Khitrina, L. V. *Bioorg. Khim.* 1989, 15(11), 1484–989.
9. Otto, H.; Marti, T.; Holz, M.; Mogi, T.; Stern, L. J.; Engel, F.; Khorana, H. G.; Heyn, M. *Proc. Natl. Acad. Sci. U.S.A.* 1990, 87, 1018–1022.
10. Thorgeirsson, T. E.; Milder, S. J.; Miercke, L. J. W.; Betlach, M. C.; Shand, R. F.; Stroud, R. M.; Kliger, D. S. *Biochemistry* 1991, 30(38), 9133–9142.
11. Mitchell, D. C.; Rayfield, G. W. *Biophys. J.* 1986, 49, 563.
12. Grzesiek, S.; Dencher, N. A. *FEBS Lett.* 1986, 208(2), 337–342.
13. Drachev, L. A.; Kaulen, A. D.; Skulachev, V. P. *FEBS Lett.* 1984, 178, 331–335.
14. Liu, S. Y. *Biophys. J.* 1990, 57(5), 943–950.
15. Eisenbach, M.; Weissmann, C.; Tanny, G.; Caplan, S. R. *FEBS Lett.* 1977, 81(1), 77–80.
16. Haronian, D.; Lewis, A. *Appl. Opt.* 1991, 30(5), 597–608.
17. Drachev, L. A.; Kaulen, A. D.; Skulachev, V. P.; Zorina, V. V. *FEBS Lett.* 1988, 239(1), 1–4.
18. Keszthelyi, L.; Ormos, P. *Biophys. Chem.* 1983, 18, 397–405.
19. Varo, G. *Acta Biol. Acad. Sci. Hung.* 1981, 32(3), 301–310.
20. McIntosh, A. R.; Boucher, F. *Biochim. Biophys. Acta* 1991, 1056(2), 149–158.
21. Dér, A.; Hargittai, P.; Simon, J. J. *Biochem. Biophys. Meth.* 1985, 10, 295–300.
22. Liu, S. Y.; Ebrey, T. G. *Biophys. J.* 1988, 54(2), 321–329.
23. Kunugi, S.; Kusano, T.; Yamada, H.; Nakamura, Y. *Polymer Bull.* 1988, 19, 417–421.
24. Kovács, I.; Váró, G. J. *Photochem. Photobiol.* 1988, 1, 469–474.
25. Korenbrot, J. I.; Hwang, S.-B. *J. Gen. Physiol.* 1980, 76, 649–682.
26. Furno, T.; Takimoto, K.; Koyama, T.; Ikegami, A.; Sasabe, H. *Thin Solid Films* 1988, 160, 145–151.
27. Lukashev, E. P.; Zaitsev, S. Y.; Kononenko, A. A.; Zubov, V. P. *Stud. Biophys.* 1989, 132(1–2), 111–118.
28. Sasabe, H.; Furuno, T.; Takimoto, K. *Synth. Met.* 1989, 28(1–2), C787–C792.
29. Maksimychev, A. V.; Charmorvskii, S. K.; Kholmanskii, A. S.; Erokhin, V. V.; Levin, E. V.; Chekulaeva, L. N.; Kononenko, A. A.; Rambidi, N. G. *Biol. Membr.* 1991, 8(1), 15–29.
30. Läger, P.; Benz, R.; Stark, G.; Bamberg, E.; Jordan, P. C.; Fahr, A.; Brock, W.; *Q. Rev. Biophys.* 1981, 14(4), 513–598.
31. Rayfield, G. W. *Biophys. J.* 1983, 41, 109–117.
32. Grant, E. H.; Sheppard, R. J.; South, G. P. *Dielectric Behaviour of Biological Molecules in Solution*; Oxford University: Oxford, England, 1978; Chapters 5 and 6.
33. Kononenko, A. A.; Lukashev, E. P.; Chamorovsky, S. K.; Maksimychev, A. V.; Timashev, S. F.; Chekulaeva, L. N.; Rubin, A. B.; Paschenko, V. Z. *Biochim. Biophys. Acta* 1987, 892, 56–67.

34. Valdmanis, J. A.; Mourou, G. J. *Quantum Electron.* **1986**, QE-22(1), 69–78.
35. Tuckerman, D. B. *Appl. Phys. Lett.* **1980**, 36(12), 1008–1010.
36. Simmeth, R.; Rayfield, G. W. *Biophys. J. Biophys. Soc.* **1990**, 57, 1099–1101.
37. Birge, R. R.; Zhang, C.-F. *J. Chem. Phys.* **1990**, 92(12), 7178–7195.
38. Huang, J. Y.; Chen, Z.; Lewis, A. *J. Phys. Chem.* **1989**, 93, 3314–3320.
39. Takei, H.; Lewis, A.; Chen, Z.; Nebenzahl, I. *Appl. Opt.* **1991**, 30(4), 500–509.
40. Groma, G. I.; Varo, G.; Keszthelyi, L. *J. Mol. Electron.* **1991**, 7(2), 75–77.
41. Miyasaka, T.; Koyama, K.; Itoh, I. *Science (Washington D.C.)* **1992**, 255, 342–344.
42. Butt, H. J.; Fendler, K.; Bamberg, E.; Tittor, J.; Oesterhelt, D. *EMBO J.* **1989**, 8(6), 1657–1663.
43. Holz, M.; Drachev, L. A.; Tatsushi, M.; Otto, H.; Kaulen, A. D.; Heyn, M. P.; Skulachev, V. P.; Khorana, H. G. *Proc. Natl. Acad. Sci. U.S.A.* **1989**, 86, 2167–2171.
44. Baofu, N.; Chang, M.; Duschl, A.; Lanyi, J.; Needleman, R. *Gene* **1990**, 90(1), 169–172.
45. Fendler, K.; Gärtner, W.; Oesterhelt, D.; Bamberg, E. *Biochim. Biophys. Acta* **1987**, 893, 60–68.
46. Trissl, H.-W.; Gärtner, W. *Biochemistry* **1987**, 26, 751–758.

RECEIVED for review March 12, 1992. ACCEPTED revised manuscript February 17, 1993.

Author Index

- Albrecht, O., 343
Birge, Robert R., 1, 131
Bohn, Paul W., 475
Brüchle, Christoph, 511
Conrad, Michael, 43
Di Bella, Santo, 223
Dvornikov, A. S., 161
Eguchi, K., 343
Fendler, Janos H., 413
Fragalá, Ignazio L., 223
Fujihira, Masamichi, 373
Gorman, Christopher B., 179
Hampp, Norbert, 511
Hong, Felix T., 527
Hosoda, Masahiro, 303
Kamath, M., 395
Kaplan, D., 395
Kumar, J., 395
Lanyi, Janos K., 491
Lawrence, Albert F., 131
Lim, J. O., 395
Marder, Seth R., 179
Marks, Tobin J., 223
Martynski, T., 439
Marx, K. A., 395
Matsuda, H., 343
Metzger, Robert M., 81
Nafie, Laurence A., 63
Nakagiri, T., 343
Oesterhelt, Dieter, 511
Olinger, Jill M., 475
Ottova-Leitmannova, A., 439
Pierce, Brian M., 243
Ratner, Mark A., 223
Rayfield, George W., 561
Reed, Mark A., 15
Rentzepis, P. M., 161
Sakai, K., 343
Samuelson, L. A., 395
Sasabe, Hiroyuki, 303
Schnur, J. M., 455
Seabaugh, Alan C., 15
Sengupta, S., 395
Shashidhar, R., 455
Sligar, Stephen G., 475
Sponsler, Michael B., 321
Stayton, Patrick S., 475
Takimoto, K., 343
Thoma, Ralph, 511
Tien, H. T., 439
Tripathy, S. K., 395
VanDoremale, Gerard H. J., 179
Wada, Tatsuo, 303
Wardak, A., 439
Wollman, Susan T., 475
Zeisel, Dieter, 511
Zhang, Jian, 321

Affiliation Index

- California Institute of Technology, 179
Canon Research Center, 343
Hughes Aircraft Company, 243
Max-Planck Institute of Biochemistry, 511
Michigan State University, 439
Molecular Technologies Inc., 395
Naval Research Laboratory, 455
Northwestern University, 223
RIKEN, 303
Syracuse University, 1, 63, 131, 321, 413
Texas Instruments Inc., 15
Tokyo Institute of Technology, 373
U.S. Army Natick Research, 395
University of Alabama, 81
University of California, 161, 491
University of Illinois at Urbana-Champaign, 475
University of Massachusetts at Lowell, 395
University of Munich, 511
University of Oregon, 561
Wayne State University, 43
Wayne State University School of Medicine, 527
Yale University, 15

Subject Index

A

- Absorption
 - light, bacteriorhodopsin, 562–563
 - two-photon, 267
- Absorption probability, uncertainty and, 147–148
- Absorption probability distribution
 - mean for, 145
 - standard deviation for, 145
- Absorption probability matrix, 139
- Absorptivities, nonlinear refractive index coefficient and, 248–249
- Acceptors, donors and, *See* Donor–acceptor processes
- Adenosine cyclic 3',5'-phosphate (cAMP) cascade, M-m communication links, 50–51
- AlAs tunnel barriers, negative differential resistance and, 25–27, 26*f*
- Al BDDAP-C-BHTCNQ Al fingers with low overlap, rectification experiment, 119
- Algorithms, learning, 54–55
- Amino acid sequences, 47–48, *See also* Proteins
- Analog error tolerance, 12
- Anisotropic properties, materials with, fabrication with tubules, 466*f*, 466–468, 467*f*
- Ansatz of Aviram and Ratner, *See* Aviram–Ratner organic unimolecular rectifier
- Antenna complexes, reaction center, 374
- Antenna molecules, triad molecules and, simulation of primary process in photosynthetic RC with mixed monolayer with, 384*f*, 384–385, 385*f*
- Applied bias, quantum dots and, 34*f*, 34–35, 35*f*
- Architectures, 3*t*, 7
 - fault-tolerant, 11–12
 - M-m, 49–51, 50*f*, *See also* Macroscopic–microscopic communication links
 - with large second-order optical nonlinearities, computational design, 223–239
- Asymmetric donor–acceptor complexes, 2:1, 237, 238*t*
- Asymmetry, donors and acceptors, 183*f*, 183–185, 184*f*
- Atomic hydrogen, orbital wave functions, 69
- Automation, LB film and, 360

- Aviram–Ratner organic unimolecular rectifier, 91–92, 92*f*, 97–118
 - crystal structures of model molecules, 111–112, 112*f*–114*f*
 - cyclic voltammetry, 104–109, 106*t*–107*t*, 109*f*
- D- σ -A monolayers, Fourier transform infrared spectra, 116
- donors and acceptors
 - electron affinities, 100*t*
 - ionization potentials, 99, 100*t*
 - practical criteria, 101–102
 - electronic and synthetic criteria, 99–101, 100*t*, 101*f*
 - energy level diagram, 101*f*
 - metals, work functions, 100*t*
 - molecular orbital calculations, 112, 114*f*–118*f*, 114–116
- NLO data, 116–118
- PL and LB films, 109–111, 110*t*, 111*f*
- synthesis, 102–104
- Azobenzene isomerization, holographic recording media based on, 327–329, 329*f*

B

- Bacterial photosynthetic reaction center, structure, 96
- Bacteriorhodopsin (BR)
 - biochemical properties, 512*t*
 - films
 - Fourier polarization holograms in, 517–519, 518*f*, 519*f*
 - holographic properties, 514–517, 516*f*, 517*t*
 - photochemical reaction cycle, 503–504
 - genetic engineering, 573
 - light absorption, 562–563
 - membranes, fast photovoltaic signal from, 540–543, 543*f*
 - optical RAM based on, reliability calculations, 150–151
 - photochemical properties, 513*f*, 513–514
 - photochemical reaction cycle
 - grid-search, 498–500
 - in films, 503–504
 - kinetics, 492–494, 500–503, 501*f*, 502*f*
 - optical multichannel spectroscopy, 494–498, 495*f*, 497*f*
 - transport mechanism and thermodynamics, 504–507, 506*f*

- Bacteriorhodopsin (BR)**—*Continued*
 photochromic molecular switch,
 132–133
 two-photon 3D optical memories and,
 152–155, 153*f*
 photodetector, ultrafast, 568–571,
 569*f*, 570*f*
 photodiodes based on, 561–573, *See also* Photodiodes
 photoelectric effect in, devices based
 on, 568–573, 569*f*, 570*f*
 photophysical properties, 512*t*,
 513–514
 modification, 514
 proton pump in, 504–507, 506*f*, 564
 photoinduced proton transfer in LB
 films as simple model of, 390–391,
 391*f*
 real-time holographic correlator based
 on, experimental implementation,
 521–522, 522*f*, 523*f*
 rhodopsin versus, 546–547
 structure and function, 562
 variants for holographic pattern
 recognition, 511–523
- Band gap, quantum well**, 20–24, 21*f*, 23*f*,
 24*f*
- Band-gap-engineered tunneling transistor
 structures**, 16, 27, *See also*
 Resonant-tunneling transistors
 (RTTs)
- Band-gap engineering, colloid chemical
 approach to**, 413–436, *See also*
 Colloid chemical approach
- Base–collector tunnel barrier, negative
 differential resistance and**, 27
- BDDAP-C-BHTCNQ**, scanning tunneling
 microscopy on, 119
- BDDAP-C-HETCNQ**, scanning tunneling
 microscopy on, 120, 120*f*, 122
- Benzenes, donor–acceptor-substituted**,
 184–185
- β , *See* First hyperpolarizability
- Bilayer lipid membranes (BLM)**
 connection to unimolecular device, 88
 generation of particulate films at,
 414–415
 self-assembling, on solid support,
 439–452, *See also* Supported
 bilayer lipid membranes
- Bilayer lipid membranes (BLM)-ES
 junctions, particulate films**,
 428–432, 429*f*, 430*f*
- Binomial probability distribution**,
 140–141
- Biological polymers, information-
 processing capabilities of**, 46–49
- Biomaterials**, *See also specific type*
 electrooptical, protein engineering for,
 475–489
 intelligent, based on LB monolayer
 films, 395–411
- Biomimetic D– σ -A photosynthetic
 reaction center, progress toward**,
 96–97
- Biomolecular electronics, defined**, 2
- Biosensing, membrane-based**, 48, *See also*
 Supported bilayer lipid membranes
- Biotechnological infrastructure,
 development**, 59–60
- Biotin lipid–streptavidin-conjugated
 phycoerythrin monolayers, LB
 trough formation of**, 401–402,
 402*f*, 403*f*
- Biotinylated lipid–streptavidin
 recognition, incorporating
 photodynamic proteins**, 395–411
- Biotinylated polymers–streptavidin
 recognition, incorporating
 photodynamic proteins**, 395–411
- Bipolar quantum-well resonant-tunneling
 transistor (BiQuaRTT)**, 21*f*, 22–23,
 23*f*, 24, 24*f*
 room-temperature size-quantization
 effects, 25, 25*f*
- Bipolar transistor, resonant-tunneling**, 17,
 21*f*, *See also* Resonant-tunneling
 transistors (RTTs)
- BiQuaRTT**, *See* Bipolar quantum-well
 resonant-tunneling transistor
- Bisphosphinehaloplatinum aryl
 complexes, donor–bridge–acceptor
 molecules**, 185
- Bit size, trends in**, 6, 6*f*
- Bleaching rate, bacteriorhodopsin film**,
 515–517
- BLM**, *See* Bilayer lipid membranes
- Bonding networks**
 conjugated π -electron molecules for
 third-order NLO applications,
 293–294
 polarizabilities, 258–259
- Born–Oppenheimer approximation**,
 Zeroth-order, 263
- BR**, *See* Bacteriorhodopsin
- Bulk molecular devices**, 84–87, 85*f*

C

- Calixarenes, connection to unimolecular
 device**, 89
- cAMP cascade, M-m communication links**,
 50–51
- Carbamates, Aviram–Ratner organic
 unimolecular rectifier and**,
 synthesis, 104

- Carbon
 in computing, 43–60
 future, 59–60
 intelligent particles versus digital switches and, 43–44
 learning algorithms and, 54–55
 macroscopic–microscopic communication links and, 49–51, 50*f*
 self-assembly model, 51–53, 52*f*
 shape-based information processing and, 46–49
 silicon versus, 44–46, 55–56
 low reactivity of, 44
 Carbon–silicon synergy, 56–59, 57*f*
 Carrier confinement, 16
 Charge movement, bacteriorhodopsin, 564
 Charge quantization, 38–39
 Charge-transfer molecular gates, optically coupled, 2, 4*f*, 5
 Charging effects, single-electron, 16
 Chemical contamination, LB films and, 356–357
 Chemical generation, of particulate films, at monolayers, 415–416, 416*f*
 Chirality, NLO crystals and, optimization, 197–198, 198*f*
 $C_{16}H_{33}OQ3CNQ$, scanning tunneling microscopy on, 120–122, 121*f*
 Chromophores, organic, structure–property relationships for NLO response in, 180–194
 Circuits, *See also specific type*
 resonant-tunneling transistor, 27–30, 28*f*, 29*f*
 Clean rooms, LB films and, 355–356
 Cleaved edge overgrowth, 38
 Coatings, optical, LB films, 344–345
 Colloid chemical approach
 particulate film electronic behavior, 424–435, 425*f*, 427*f*, 429*f*, 430*f*, 433*f*–435*f*
 particulate film generation at bilayer lipid membranes, 414–415
 particulate film generation at monolayers, 415–417, 416*f*–418*f*
 to band-gap engineering and quantum-tailored devices, 413–436
 Combinatorial variability of structure–function relations, 47–48
 Communication links
 LB film, 350–351
 macroscopic–microscopic, 49–51, 50*f*
 Compressed function logic, resonant-tunneling transistor, 28
 Computers
 bit size and, 6, 6*f*
 carbon in, 43–60, *See also* Carbon
 Computers—*Continued*
 human–machine interface, 59
 intelligent particles versus digital switches, 43–44
 Condensation reactions, Diels–Alder, 89
 Condensed phase, molecules in, calculation of, 271–273
 Conditional probability
 continuous case, 141
 discrete case, 139–140
 joint, 147
 Conducting polymers
 molecule-based transistor using, 86
 synthesis and characterization, 397–400, 398*f*, 399*f*
 Conductivity, LB films, change due to light-induced conformational change, 94
 Confinement, quantum, 16, 31–32, *See also* Quantum *entries*
 future prospects, 37–38
 Conformational change
 light-induced, conductivity change in LB films due to, 94
 potential systems, 94
 Conformational switching, 47
 Confusion matrix, 142
 Conjugated π -electron organic molecules, *See also specific type*
 third-order NLO applications, 246–247, 291–297, *See also* Third-order optical nonlinearities
 Contamination, chemical, LB films and, 356–357
 Continuity equation, 68
 Continuous case, analysis of probabilities, 140–148
 Continuous film balance, 359
 Controlled release applications, tubules for, 469–470
 Conventional film balance, 358–359
 Conventional transistor, RTD integration into heterostructures, 22
 Core antenna, 374
 Correction factor, binomial probability distribution, 141
 Coulomb blockade, 38–39
 Coupled Hartree–Fock method, third-order polarizability, 265
 Covalent attachment, of chromophores to polymer, 207
 Cross-linking, poled polymer films, 208–210, 209*f*
 Crossing spectra, 0D–0D tunneling, 36–37
 Crystal(s)
 liquid, as holographic recording media, 321–338

Crystal(s)—*Continued*

NLO

- characterization, 195–196
- chirality, 197–198, 198*f*
- control of structure, 196–197
- hydrogen bonding, 198*f*, 198–199, 199*f*
- inclusion complexes, 199–200
- optimization, 195–202, 198*f*–202*f*
- organic photorefractive, 201–202, 202*f*
- N-oxides, 201, 201*f*
- salts, 200*f*, 200–201

Crystal structures, model donor, acceptor, and D- σ -A molecules, Aviram–Ratner rectifier, 111–112, 112*f*–114*f*

Crystalline polymers, liquid, 207, 208*f*

Current density, transition, *See* Transition current density (TCD)

Current–voltage (*I*-*V*) characteristics quantum dot

- 1D–0D tunneling, 32–34, 33*f*
- 0D–0D tunneling, 36, 36*f*
- resonant tunneling, 18*f*, 18–19, 19*f*

CV, *See* Cyclic voltammetry

Cyanines, *See also* Phthalocyanine-based optoelectronics

linear

- calculated versus measured nonresonant γ_s , 277*t*, 277–278
- comparison of calculated $\gamma_r(0; 0, 0, 0)$ s, 278*f*, 278–279
- important $1\pi^0$ states defining $\gamma_r(0; 0, 0, 0)$, 279–283, 280*f*–282*f*
- molecular geometries, 276
- polarizability dependence on geometry and protonation, 287–289, 288*t*
- SOS terms important to $\gamma_r(0; 0, 0, 0)$, 283–287, 284*t*, 285*f*, 286*f*
- structures, 275*f*
- third-order NLO applications, 273–297

Cyclic voltammetry (CV), Aviram–Ratner unimolecular organic rectifier, 104–109, 106*t*–107*t*, 109*f*

Cyclodextrins, connection to unimolecular device, 89

D

- D- π -A electron transfer molecules, 94–95, 97
- D- σ -A monolayers, Fourier transform infrared spectra, 116
- D- σ -A unimolecular rectifiers, 81–122, *See also* Unimolecular devices

D- σ -A- σ -D molecules, 97

D- σ -A molecules, 97

DANS, *See* 4-Dimethylamino-4'-nitrostilbene

Defects, LB film

- control, 361–362
- identification, 362–363
- visibility, 363–364

Density function, 63, *See also* Transition current density (TCD)

Deposition process, materials and, LB films, 360–364

Diels–Alder condensation reactions, 89

Differential resistance, negative, *See* Negative differential resistance (NDR)

Digital error correction, 12

Digital switches, intelligent particles versus, computers and, 43–44

Dimensionality, low, *See* Quantum dots

Dimer clusters, 226–233, 227*f*, 228*t*, 229*f*, 229*t*, 231*f*, 233*f*

4-Dimethylamino-4'-nitrostilbene (DANS), 182*f*, 182–183

Diode, *See also* Photodiodes

Esaki, 17

resonant-tunneling, 17, *See also* Resonant-tunneling transistors (RTTs)

Discrete case, analysis of probabilities, 138–140

Dissipation, carbon versus silicon and, 48

Dithiolyldienemethyl, 184, 184*f*

DNA, shape-based information processing and, 49

Domain synergy, human–machine interface, 59

Donor–acceptor complexes asymmetric 2:1, 237, 238*t* 1:1, 233–236, 235*f*, 236*f*

Donor–acceptor processes, *See also*

Unimolecular devices

asymmetry, 183*f*, 183–185, 184*f* switching and, carbon in, 46

Doping

resonant-tunneling transistor, 22 spin-coated polymer films, 309, 311, 311*f*

Dual-axis joint Fourier transform correlator, mathematical description, 519–521

Dual trough, LB film and, 360

Dynamic processes, informationally significant, 48

E

EDA complexes, *See* Donor–acceptor complexes

- EFISH (electric field-induced second-harmonic generation) technique, 181–182
- Electric field(s)
 conjugated π -electron molecules for third-order NLO applications, 294–296
 effect on tubules, 462–463
 external, polarization response and, 260
- Electric field-induced second-harmonic generation (EFISH) technique, 181–182
- Electric properties
 anisotropic, tubules in fabrication of materials with, 466*f*, 466–468, 467*f*
 protein, manipulation, 484–486
- Electric susceptibility, third-order NLO applications and, 245, *See also* Third-order optical nonlinearities
 molecular polarizability and, 251–256, 256*t*
 nonlinear refractive index coefficient and, 248
- Electrical double layer, photoinduced electron transfer kinetics and, LB film, 380–384, 381*f*–383*f*
- Electrochemical generation, of particulate films, at monolayers, 417, 417*f*, 418*f*
- Electron affinities, donor and acceptor, in Aviram–Ratner organic unimolecular rectifier, 100*t*, 106*t*–107*t*
- σ -Electron bonding networks, 258–259
- π -Electron bonding networks, conjugated, 293–294
- Electron current density, 63–64, *See also* Transition current density (TCD)
 nonstationary states, 67
 stationary states, 66
- Electron donor–acceptor (EDA) complexes, *See* Donor–acceptor complexes
- π -Electron organic molecules, *See also specific type*
 third-order NLO applications, 245, 291–297, *See also* Third-order optical nonlinearities
- Electron potential energy surface, 3D screening problem and, 34, 34*f*
- Electron probability density, 63
 conservation, 67–68
 nonstationary states, 66–67
 stationary states, 65–66
- Electron system, length and nature of, effect on optical nonlinearity, 185–188, 186*f*–188*f*, 188*t*
- Electron transfer
 particulate films, 424–432, 425*f*, 427*f*, 429*f*, 430*f*
 photoinduced
 in LB films, 373–391
 kinetics, 380–384, 381*f*–383*f*
- Electron transfer molecules, D– σ -A and D– π -A, 94–95, 97
- Electron tunneling, *See* Tunneling
- Electronic structure, third-order polarizability and, 269–273, 272*t*
- Electronic switches, *See* Switches
- Electrooptical biomaterials, protein engineering for, 475–489
- Electrostatic switches, reliability calculations, 149–150, 150*f*
- Emitter subband level, crossings with quantum dot levels, 34–35, 35*f*
- Emitter tunnel barrier, negative differential resistance and, 27
- Energy band profiles, resonant-tunneling transistor, 20–24, 21*f*, 23*f*, 24*f*
- Energy second-derivative matrix, 269
- Energy transfer
 bacteriorhodopsin, 505–507, 506*f*
 photoinduced, in LB films, 373–391
 quenching of pyrene-substituted fatty acid, by photooxidized product, 386–390, 387*f*–390*f*
- Ensembles
 averaging, reliability and, 10–12
 dynamics, probabilistic analysis and, 136–138, 138*f*
 size, effect on device reliability, 150, 150*f*
 with known starting states, calculations for, 143–145
 with unknown starting states, calculations for, 147–148
- Enthalpy cycle, bacteriorhodopsin, 505–507, 506*f*
- Entropy cycle, bacteriorhodopsin, 506*f*, 506–507
- Enzymes, *See also specific type*
 shape-based pattern recognition by, 47
- EO sampling, 568
- Epitaxy, molecular beam, *See* Molecular beam epitaxy (MBE)
- Equilibrium conditions, analysis of probabilities, 142–143
- Error
 correction, digital, 12
 origins, reliability calculations and, 133–138, 138*f*
 probability, 140
 read operations at multiple wavelengths, 146
 tolerance, analog, 12

- Esaki diodes, 17
 Esters, Aviram–Ratner organic unimolecular rectifier and, synthesis, 104
 Excited-state molecular geometries, 268–269
 Exclusive-NOR gate, resonant-tunneling transistor, 28, 28*f*

F

- Fabrication, molecular devices using LB films, 354–355
 Fast photovoltaic signal, from bacteriorhodopsin membranes, component analysis of, 540–543, 543*f*
 Fast picosecond signal, detection, ultrafast BR photodetector, 568–569
 Fatigue, D memory devices, 172–175, 173*f*
 Fatty acid, pyrene-substituted, energy-transfer quenching by photooxidized product, 386–390, 387*f*–390*f*
 Fault-tolerant architectures, 11–12
 Feature size, high-speed semiconductor devices, 8
 Femtosecond responses, VOPc(*t*-bu)_n thin films, 312–315, 313*f*, 315*f*
 Fermi level pinning value, 34
 Ferrocene, donor–bridge–acceptor molecules, 185
 FF method, *See* Finite field method
 Film(s)
 bacteriorhodopsin
 Fourier polarization holograms in, 517–519, 518*f*, 519*f*
 holographic properties of, 514–517, 516*f*, 517*t*
 photocycle in, 503–504
 LB, *See* Langmuir–Blodgett films
 LS, *See* Langmuir–Schaefer film
 MBE, 311–312, 312*f*
 particulate, *See* Particulate films
 PL, *See* Pockels–Langmuir film
 polymer
 poled, 202–210, 203*f*, 205*f*, 206*f*, 208*f*, 209*f*
 spin-coated doped, 309, 311, 311*f*
 thin
 MPc, 305*f*–308*f*, 305–312, 310*t*, 311*f*, 312*f*
 protein, 477–483, 478*f*, 480*f*–482*f*, 483*t*, 484*f*
 vacuum-deposited, 305*f*–308*f*, 305–309, 310*t*
 VOPc(*t*-bu)_n, femtosecond responses, 312–315, 313*f*, 315*f*
 Film balance
 continuous, 359
 conventional, 358–359
 Film lift system, 358
 Finite-field (FF) method, optical nonlinearities
 second-order, 181
 third-order, 265
 First hyperpolarizability (β), 180, *See also* Polarizability
 computational and experimental methods for, 180–182, 225
 electron system and, 185–188, 187*f*
 Hammett parameters and, 183, 183*f*
 molecular orbital analysis, 188–194, 189*f*–191*f*, 192*t*, 193*f*, 194*f*
 Fluorescence spectroscopy, intelligent biomaterials based on LB films, 406–409, 407*f*–409*f*
 f_{max} (maximum frequency of operation), device speed and, 5
 Folded-type S–A–D triads, LB photodiodes, 377–380, 378*f*, 379*f*
 Force-constant matrix, 269
 Fourier polarization holograms, in bacteriorhodopsin films, 517–519, 518*f*, 519*f*
 Fourier transform correlator, dual-axis joint, mathematical description, 519–521
 Fourier transform infrared spectra, D– σ –A monolayers, 116
 Franck–Condon factors, 268
 Free energy, bacteriorhodopsin, 505–507, 506*f*
 Fulgides, 3D storage using, 169–170, 170*f*
 Full adder, using RTTs, 29*f*, 30

G

- Gallium arsenide (GaAs) semiconductors, heterojunctions in, 16
 Gas phase, molecules in, calculation of, 269–271, 272*t*
 Gates, *See* Molecular gates
 Gaussian distributions, convolution of, 143–144
 read operations at multiple wavelengths, 147
 General transition continuity equation, 68
 Genetic engineering, 8–9
 of bacteriorhodopsin, 573
 Geometries, third-order optical nonlinearities, 267–269
 conjugated π -electron molecules for, 293
 linear cyanines and polyenes, 276, 287–289, 288*t*

- Grid-search, photochemical reaction cycle of bacteriorhodopsin, 498–500
 Ground-state molecular geometries, 267–268
 Guest-host systems, poled polymer, 206f, 206–207

H

- H, *See* Hydrogen
 Hammett parameters, β and, 183, 183f
 Hartree-Fock method
 coupled, third-order polarizability, 265
 polysilane linear polarizability, 258
 time-dependent, third-order polarizability, 265–266
 Heisenberg's uncertainty principle, 5
 state assignment error and, 134–136
 Helical structures, formation mechanism, 463–465, 464f
 Heme proteins, *See also* Proteins
 pocket alterations, 486–488, 487f
 Henderson's thesis, 44
 Heteroepitaxial technology
 future quantum device prospects and, 38
 resonant tunneling and, 17
 Heterogenous A/S/D Langmuir-Blodgett films, 374–377, 375f
 Heterojunctions
 bipolar transistor, AlAs tunnel barriers and, 25–27, 26f
 future quantum devices and, 37, 38
 p-n junctions versus, 16, *See also* p-n junctions
 High-speed semiconductor devices, feature size, 8
 Holography
 azobenzene isomerization-based recording media, 327–329, 329f
 bacteriorhodopsin film properties, 514–517, 516f, 517t
 bacteriorhodopsin variants for pattern recognition, 511–523
 basics, 322f, 322–323, 323f
 instantaneous media, 326–327, 327f
 liquid crystals and
 advantages and disadvantages, 332–334
 in recording media, 324–336
 molecular electronics, 337
 non-recording uses, 336–337
 postirradiation filling with, 329–330, 330f
 switching characteristics, 335–336
 synergy, 323–324, 324f
 pattern recognition, 519–523, 522f, 523f

- Holography—*Continued*
 photopolymerization media, 330–332, 331f, 332f
 Hot electron transistor, resonant-tunneling, 17, 21f, *See also* Resonant-tunneling transistors (RTTs)
 Human-machine interface, domain synergy, 59
 Hydrogen, atomic, orbital wave functions, 69
 Hydrogen atom transfer switch, 93
 STM on, 119
 Hydrogen bonding, NLO crystals, 198f, 198–199, 199f
 Hyperpolarizability, first, *See* First hyperpolarizability (β)

I

- I-V* characteristics, *See* Current-voltage characteristics
 Implementation of molecular electronics, advantages and disadvantages, 2, 3f
 Inchworm memory, LB films, 364–366
 Inclusion complexes, NLO crystals, 199–200
 Indium phosphide (InP) semiconductors, heterojunctions in, 16
 Industrial applications, LB film, 348
 Inelastic tunneling current, *See* Leakage
 Information processing, *See also* Computers
 LB films and, 354
 shape-based, 46–49
 self-assembly model and, 51–53, 52f
 Information storage functions, in biology versus computing, 49
 Infrared phosphors, 3D storage using, 169–170
 Infrared spectra, Fourier transform, D- σ -A monolayers, 116
 Infrastructure, biotechnological, development, 59–60
 Insulation, LB film, 345–346
 Integrated circuits (ICs)
 slow progress in, reasons for, 30
 transistor-based, scaling of, 15
 very large scale, 39
 Intelligent biomaterials, based on LB monolayer films, 395–411
 methods, 397–400, 398f, 399f
 results, 400–410, 402f–411f
 Intelligent particles, digital switches versus, computers and, 43–44
 Intensity-dependent refractive index, 248
 VOPc(*t*-bu)_n, optical waveguide, 315–317, 316f, 317f

- Intercircuit connections, thiophene, spiro-linked, 89
- Intermolecular interactions, 223–239
 computational methods, 225–226
 dimer and trimer clusters, 226–233, 227f, 228t, 229f, 229t, 231f, 233f
 EDA complexes
 asymmetric 2:1, 237, 238t
 1:1, 233–236, 235f, 236f
- Intramolecular electron transfer, 95–96
- Intramolecular rearrangements, light-induced, 94
- Intrinsic parameters, tubule formation dependence on, 458–465, 460f, 461f, 464f
- Ionization potentials, in Aviram–Ratner organic unimolecular rectifier, 99, 100t
 gas-phase vertical potentials, 106t–107t, 108
- Isomerization
 azobenzene, holographic recording media based on, 327–329, 329f
 bacteriorhodopsin, light absorption and, 562–563

J

- Joint conditional probability, 147
- Joint Fourier transform correlator, dual-axis, mathematical description, 519–521
- Josephson junction oscilloscope, 569

K

- Kerr effect
 magneto-optical, 434–435
 optical, 248
- Kogelnik's formula, 515, 516

L

- Langmuir–Blodgett (LB) films, 84–85, 85f
 advantages, 343
 alternatives to, 348–349
 changing properties, 361
 conductivity change, due to light-induced conformational change, 94
 connection to unimolecular device, 88
 Aviram–Ratner organic unimolecular rectifier, 109–111
- defects
 control, 361–362
 identification, 362–363
 visibility, 363–364
- deposition process, 360–364
- disadvantages, 343–344

- Langmuir–Blodgett (LB) films—

Continued

- folded-type S–A–D and linear-type A–S–D triads, 377–380, 378f, 379f
- formation and characterization, 400
- heterogenous A/S/D, 374–377, 375f
- highly conducting, 87
- materials, 360–364
- molecular devices using, 341–369
 attempts, 364–368
 communication, 350–351
 fabrication, 354–355
 information movement, 354
 structure, 352–353, 353f
- monolayer, intelligent biomaterials based on, 395–411
- order within, 351, 352f
- photoinduced electron and energy transfer in, 373–391
 kinetics and effect of electrical double layer, 380–384, 381f–383f
 molecular photodiodes and, 374–380, 375f, 378f, 379f
 proton transfer as model of proton pump in bacteriorhodopsin, 390–391, 391f
 quenching of pyrene-substituted fatty acid, 386–390, 387f–390f
 simulation of primary process, 384f, 384–385, 385f
- problems with applications, 355–357
- proposed applications, 344–348
- second-order NLO activity, 210–212, 211f, 347–348
- spin transitions in, 87
- technology, means of improvement, 357–360
- trough, 400–401
 dual, 360
 formation of biotin lipid–Str-PE monolayers, 401–402, 402f, 403f
 use of, 352
- Langmuir–Blodgett (LB) monolayer Hg, rectification experiment, 118–119
- Langmuir–Blodgett (LB) organic rectifiers, multilayer, 85–86
- Langmuir–Blodgett (LB) photodiode, 93–94, 374–380, 375f, 378f, 379f
- Langmuir–Blodgett (LB) technique, 8
- Langmuir–Schaefer (LS) film, 84, 85f
 connection to unimolecular device, 88
 rectification curve and, 122
- Laser power, fatigue as function of, 172–173, 173f
- LB devices, *See* Langmuir–Blodgett entries
- Leakage, resonant tunneling, 18
 suppression of, 20, 21

Learning algorithms, 54–55
 Light, differential responsivity to, BR photodiode with, 573
 Light absorption, bacteriorhodopsin, 562–563
 Light-induced functions, *See* Photoinduced *entries*
 Linear absorptivity, nonlinear refractive index coefficient and, 249
 Linear conjugated π -electron organic molecules, outlook for, 297
 Linear cyanines, third-order NLO applications, 273–297
 Linear polarizability
 conjugated π -electron molecules for third-order NLO applications, 293
 Hartree–Fock, polysilane, 258
 Linear polyenes, third-order NLO applications, 273–297
 Linear-type A–S–D triads, LB photodiodes, 377–380, 378*f*, 379*f*
 Lines, molecular, connection to unimolecular device, 89
 Lipid, *See also* Phospholipids
 biotinylated, streptavidin recognition incorporating photodynamic proteins, 395–411
 Lipid membranes, bilayer, *See* Bilayer lipid membranes (BLM)
 Lipid–streptavidin-conjugated phycoerythrin monolayers, biotin, LB trough formation of, 401–402, 402*f*, 403*f*
 Liquid crystalline polymers, 207, 208*f*
 Liquid crystals, as holographic recording media, 321–338
 Lithography, 9
 Logic functions, resonant-tunneling transistor, 28*f*, 28–30, 29*f*
 Lorentzian distribution functions, 156
 Low dimensionality, *See also* Quantum dots
 future quantum device prospects and, 38–39
 LS film, *See* Langmuir–Schaefer (LS) film

M

M-m architecture, *See* Macroscopic–microscopic communication links
 Macromolecules, *See also specific type* conformational switching by, 47
 shape-based pattern recognition by, 47
 structure–function relations, combinatorial variability of, 47–48
 Macroscopic connections to unimolecular device, 88–89
 Macroscopic–microscopic (M-m) communication links, 49–51, 50*f*
 carbon switches and, 55
 Macroscopic susceptibility, molecular polarizability and, 251–256, 256*t*
 Macroscopic tests, rectification experiments, 118–120
 Magnetic domains, particulate film, 434*f*, 434–435, 435*f*
 Magnetic fields, effect on tubules, 462–463
 Magnetic particulate films, generation, at bilayer lipid membranes, 414–415
 Magnetic properties, anisotropic, tubules in fabrication of materials with, 466*f*, 466–468, 467*f*
 Materials, *See specific type or application*
 Matrix exponentials, read operations at multiple wavelengths, 146
 Maximum frequency of operation (f_{max}), device speed and, 5
 MBE, *See* Molecular beam epitaxy
 MECI (monoexcited configuration interaction), 225
 Membrane-based biosensing, 48, *See also* Supported bilayer lipid membranes
 Membrane separation, LB films in, 347
 Memory
 BR photodiode, 572
 inchworm, LB films, 364–366
 optical, *See* Optical memory
 photochromic, reliability calculations, 130–158
 terabit, LB films, 366–368, 367*f*
 Memory densities, bit size and, trends, 6, 6*f*
 Mesoscopic connections to unimolecular device, 89
 Metalized tubules, devices and systems using, 468–469, 469*f*, 470*f*
 Metallic particulate films, generation at bilayer lipid membranes, 414–415
 at monolayers, 415–417, 416*f*–418*f*
 Metallophthalocyanines (MPcs)
 optoelectronics based on, 303–319
 thin films, 305*f*–308*f*, 305–312, 310*t*, 311*f*, 312*f*
 Microscopy, scanning tunneling, *See* Scanning tunneling microscopy (STM)
 Minimum device geometries, downscaling of, 15–16
 MO calculations, *See* Molecular orbital calculations
 Mode-lines measurement, VOPc(*t*-bu)_n optical waveguide, 317–319, 318*f*
 Molecular beam epitaxy (MBE), 16
 future quantum device prospects and, 38

- Molecular beam epitaxy (MBE) films, 311–312, 312*f*
- Molecular computers, *See* Computers
- Molecular electronic devices, *See also specific type or feature*
 architecture, 3*t*, 7
 based on photovoltaic effect, 552–554, 553*f*
 nanoscale engineering, 3*t*, 8–9
 nonlinear properties, 3*t*, 10
 quantized behavior, 3*t*, 7
 reliability, 3*t*, 10–12
 reliability calculations, 130–158
 speed, size and, 2, 3*t*, 4*f*, 5–6, 6*f*
 stability, 3*t*, 9–10
 using LB films, 341–369
- Molecular electronic structure, third-order polarizability and, 269–273, 272*t*
- Molecular electronics
 defined, 1–2, 81
 broad versus narrow definitions, 82–84
 implementation, advantages and disadvantages, 2, 3*t*
- Molecular gates, optically coupled, 2, 4*f*, 5
 reliability calculations, 150
- Molecular geometry, *See* Geometries
- Molecular lines, connection to unimolecular device, 89
- Molecular orbital (MO) calculations
 Aviram–Ratner organic unimolecular rectifier, 112, 114*f*–118*f*, 114–116
 β , 188–194, 189*f*–191*f*, 192*t*, 193*f*, 194*f*
 molecules in gas phase, 269–271, 272*t*
- Molecular parameters, tubule formation dependence on, 458–465, 460*f*, 461*f*, 464*f*
- Molecular polarizability, *See* Polarizability
- Molecular switch, *See* Switches
- Molecular wires, connection to unimolecular device, 89
- Molecule-based transistor, using conducting polymers, 86
- Monelectronic devices, reliability calculations, 155–156
- Monoexcited configuration interaction (MECI), approximation, 225
- Monolayer(s), particulate film generation at, 415–417, 416*f*–418*f*
- Monolayer films
 LB, *See also* Langmuir–Blodgett (LB) films
 intelligent biomaterials based on, 395–411
 protein, single-component, 477–482, 478*f*, 480*f*–482*f*
- Monomolecular devices, *See* Unimolecular devices
- MOPAC software, 268
- MOPCs, *See* Metallophthalocyanines
- Multichannel spectroscopy, optical, photochemical reaction cycle of bacteriorhodopsin and, 494–498, 495*f*, 497*f*
- Multicomponent assemblies, protein thin films, 482–483, 483*t*, 484*f*
- Multilayer structures, second-order NLO activity, 212–213, 214*f*
- Multiple wavelengths, read operations at, 145–147
- Mutagenesis, site-directed, 8–9
- Mutation, point, effect on photoelectric signal, 543–546, 544*f*, 545*f*
- N
- NAND gates, *See* Not And gates
- Nanofabrication, 17
- Nanoscale devices, 3*t*, 8–9
- Nanosopic connections to unimolecular device, 89–91
- Nanosopic tests, rectification experiments, 119, 120*f*, 120–122, 121*f*
- NDR, *See* Negative differential resistance
- Negative differential resistance (NDR), 17, *See also* Resonant-tunneling transistors (RTTs)
 AIs tunnel barriers and, 27
- Negative transconductance (NTC), BiQuaRTT, 22
- Network dynamics, shape-based information processing, 48
- Neurons, self-assembly model and, 53
- p*-Nitroaniline (PNA), 182*f*, 182–183
- Nonlinear materials, 3*t*, 10, *See also*
 Nonlinear optical (NLO) materials
- Nonlinear optical (NLO) D– σ -A and D– π -A molecules, 97
- Nonlinear optical (NLO) data, D– σ -A system, 116–118
- Nonlinear optical (NLO) materials, 10, *See also specific materials*
 second-order, 179–214
 crystalline, 195–202, 198*f*–202*f*
 future outlook, 213
 LB films, 210–212, 211*f*, 347–348
 optimization, 194–213
 poled polymer films, 202–210, 203*f*, 205*f*, 206*f*, 208*f*, 209*f*
 structure–property relationships for response in organic chromophores, 180–194
 third-order, 247–251

- Nonlinear optical (NLO) responses
 in organic chromophores, structure–
 property relationships for,
 180–194
 intermolecular interactions and,
 223–239
 second-order, 256*t*, *See also* Second-
 order optical nonlinearities
 third-order, 256*t*, *See also* Third-order
 optical nonlinearities
- Nonlinear refractive index coefficient,
 248
- Nonresonant γ_r component, third-order
 molecular polarizability, 262–266
- Nonresonant γ_s component, linear
 polyenes and streptocyanines,
 calculated versus measured, 277*t*,
 277–278
- Nonresonant γ_{rs} component, third-order
 molecular polarizability, 262
- Nonstationary-state wave function, 66
- Nonstationary states, transition current
 density and, 66–67
- Normal distribution, 140
- Not And (NAND) gates, optically
 coupled, reliability calculations,
 150
- NOTSCAN output, optical multichannel
 spectroscopy, 496
- NTC (negative transconductance),
 BiQuaRTT, 22

O

- Optical applications, phthalocyanine and,
See Phthalocyanine-based
 optoelectronics
- Optical biomaterials, electrooptical,
 protein engineering for, 475–489
- Optical coatings, LB films, 344–345
- Optical D– σ -A and D– π -A molecules,
 nonlinear, 97
- Optical data, nonlinear, D– σ -A system,
 116–118
- Optical interfacing, carbon versus silicon,
 48
- Optical Kerr effect, 248
- Optical memory
 energy-transfer quenching of pyrene-
 substituted fatty acid by its
 photooxidized product, 387–390,
 388*f*–390*f*
 phase-change, 86–87
 3D, 161–176, *See also* Two-photon
 three-dimensional optical memory
 reliability calculations, 151–155,
 153*f*

- Optical multichannel spectroscopy,
 photochemical reaction cycle of
 bacteriorhodopsin and, 494–498,
 495*f*, 497*f*
- Optical nonlinearities, *See also* Nonlinear
 optical (NLO) *entries*
 second-order, computational design of
 architectures with, 223–239
 third-order, *See* Third-order optical
 nonlinearities
- Optical properties, protein, manipulation,
 486–488, 487*f*
- Optical random access memory, based on
 bacteriorhodopsin, reliability
 calculations, 150–151
- Optical waveguide
 LB film, 345
 VOPc(*t*-bu)_n, implementation, 315–319,
 316*f*–318*f*
- Optically coupled gates, 2, 4*f*, 5
 reliability calculations, 150
- Optoelectronics, based on
 phthalocyanine, 303–319
- Orbital calculations, *See* Molecular orbital
 (MO) calculations
- Orbital transitions
 densities, 68–76, 70*f*, 71*f*, 73*f*–75*f*, 77*f*
 simple, 63–79
- Orbital wave functions, 72
- Organic chromophores, NLO response in,
 structure–property relationships
 for, 180–194
- Organic molecules, π -electron, third-
 order NLO applications, 245, *See*
also Third-order optical
 nonlinearities
- Organic photonics, 303
- Organic photorefractive crystals,
 201–202, 202*f*
- Organic rectifiers
 bulk, 84
 LB, multilayer, 85–86
 unimolecular, 97–118, *See also*
 Unimolecular devices
- Organic salts, as NLO chromophores, 185
- Organic switch, phase-change, 86
- Organic synthesis, 8
- Oscilloscope, Josephson junction, 569
- Overlap probability density, 67
- N-Oxides, NLO crystals, 201, 201*f*

P

- p-doping, resonant-tunneling transistor,
 22
- p–n junctions
 heterojunctions versus, 16
 resonant-tunneling transistor, 20, 21*f*

- Parallel systems, programmability, 55
- Particulate films
- characterization, 418–424, 419*f*–422*f*, 421*t*
 - electron transfer and junctions, 424–432, 425*f*, 427*f*, 429*f*, 430*f*
 - electronic behavior, 424–435, 425*f*, 427*f*, 429*f*, 430*f*, 433*f*–435*f*
 - generation
 - at bilayer lipid membranes, 414–415
 - at monolayers, 415–417, 416*f*–418*f*
 - semiconductor, preparation-dependent rectification behavior, 432–434, 433*f*
- Pattern recognition
- holographic
 - bacteriorhodopsin variants for, 511–523
 - experimental implementation of bacteriorhodopsin-based real-time correlator, 521–522, 522*f*, 523*f*
 - mathematical description of dual-axis joint Fourier transform correlator, 519–521
 - learning algorithms and, 54
 - shape-based, 47
- Peak-to-valley current ratio (PVR), 19, 19*f*, 22
- Pentacarbonyltungsten-pyridine, donor–bridge–acceptor molecules, 185
- Peripheral antenna, 374
- Perturbation methods, *See also specific methods*
- third-order polarizability, 265–266
- pH adjustment, conjugated π -electron molecules for third-order NLO applications, 296–297
- Phase-change optical memories, 86–87
- Phase-change organic switch, 86
- Phase shift, refractive index and, 247
- Phospholipids, self-assembling tubules
- from, 455–471, 456*f*
 - dependence of formation on intrinsic parameters, 458–465, 460*f*, 461*f*, 464*f*
 - electric field effects on, 462–463
 - for controlled release applications, 469–470
 - formation, 457*f*, 457–465, 460*f*, 461*f*, 464*f*
 - in fabrication of materials with anisotropic electric and magnetic properties, 466*f*, 466–468, 467*f*
 - magnetic field effects on, 462–463
 - mechanism of formation, 463–465, 464*f*
 - metalized, 468–469, 469*f*, 470*f*
- Phospholipids, self-assembling tubules from—*Continued*
- potential applications, 465–470, 466*f*, 467*f*, 469*f*, 470*f*
 - structure, 459–462, 460*f*, 461*f*
- Phosphors, infrared, 3D storage using, 169–170
- Photobiological membranes, reconstituted, photovoltaic effect in, 551–552
- Photochemical reaction cycle, bacteriorhodopsin, 491–507, *See also* Bacteriorhodopsin (BR)
- Photochemical stability, 9–10
- Photochromic memories, *See also* Two-photon three-dimensional optical memory
- reliability calculations, 130–158
- Photoconductivity; intelligent biomaterials based on LB films, 409–410, 410*f*, 411*f*
- Photocycle, photodiodes based on bacteriorhodopsin and, 563*f*, 563–564
- Photodetector, construction, 569, 569*f*
- Photodiodes
- based on bacteriorhodopsin, 561–573
 - background, 562–564
 - charge movement, 564
 - devices, 568–573, 569*f*, 570*f*
 - future work, 573
 - isomerization, 562–563
 - light absorption, 562–563
 - limitations, 571
 - photocycle, 563*f*, 563–564
 - photoelectric signal, 564–568, 566*f*
 - proton translocation, 564
 - structure and function, 562
 - LB, 93–94, 374–380, 375*f*, 378*f*, 379*f*
- Photodynamic proteins, biotinylated polymers–streptavidin and biotinylated lipid–streptavidin recognition incorporating, 395–411
- Photoelectric effect, in bacteriorhodopsin, devices based on, 568–573, 569*f*, 570*f*
- Photoelectric signal
- photodiodes based on bacteriorhodopsin, 564–568, 566*f*
 - point mutation effect on, 543–546, 544*f*, 545*f*
- Photoinduced electron transfer and energy transfer, in LB films, 373–391
- Photoinduced intramolecular rearrangements, 94

- Photoinduced proton transfer, in LB films, as simple model of proton pump in bacteriorhodopsin, 390–391, 391*f*
- Photoinduced refractive index changes, *See* Refractive index, light-induced changes
- Photonics, organic, 303
- Photooxidized product, energy-transfer quenching of pyrene-substituted fatty acid by, 386–390, 387*f*–390*f*
- Photopolymerization media, holography and, 330–332, 331*f*, 332*f*
- Photoreceptor membranes, visual, photovoltaic effect in, 546–551, 550*f*–551*f*
- Photorefractive crystals, organic, 201–202, 202*f*
- Photorefractive polymers, 210
- Photosynthetic reaction center, 373–374, *See also* Langmuir–Blodgett (LB) films, photoinduced electron and energy transfer in antenna complexes, 374 bacterial, structure, 96 biomimetic D– σ –A, progress toward, 96–97 LB films and, 374 primary process in, simulation, 384*f*, 384–385, 385*f*
- Photovoltaic devices, retinal proteins in, 527–556 perspectives, 554–556 point mutation and, 543–546, 544*f*, 545*f*
- Photovoltaic effect in other reconstituted photobiological membranes, 551–552 in visual photoreceptor membranes, 546–551, 550*f*–551*f* molecular devices based on, 552–554, 553*f* molecular mechanisms of signal generation and, 530–540, 531*f*–533*f*, 535*f*, 537*f*–539*f*
- Photovoltaic signal, fast, from bacteriorhodopsin membranes, 540–543, 543*f*
- Phthalocyanine-based optoelectronics, 303–319, *See also* Cyanines MPc thin films, 305*f*–308*f*, 305–312, 310*f*, 311*f*, 312*f* VOPc(*t*-bu)_{*n*} thin films, 312–319, 313*f*, 315*f*–318*f*
- Picosecond measurement, 569–571, 570*f*
- PL films, *See* Pockels–Langmuir film
- Planarity, polarizability and, 259
- PNA (*p*-nitroaniline), 182*f*, 182–183
- Pockels–Langmuir (PL) film, 84, 85*f* Aviram–Ratner organic unimolecular rectifier, 109–111, 110*t*
- Point mutation, effect on photoelectric signal, 543–546, 544*f*, 545*f*
- Polar solvents, stability and, 175
- Polarizability, *See also* First hyperpolarizability (β); Linear polarizability Hartree–Fock, polysilane, 258 linear cyanine, dependence on geometry and protonation, 287–289, 288*t* macroscopic susceptibility and, 251–256, 256*t* third-order, 261–267, *See also* Third-order optical nonlinearities molecular electronic structure and, 269–273, 272*t* molecular geometry and, 267–269
- Polarization holograms, Fourier, in bacteriorhodopsin films, 517–519, 518*f*, 519*f*
- Polarization response, third-order, 251–256, 256*t* maximization, 256–260
- Poled polymer films, 202–203 chromophore attachment to, covalent, 207 chromophore modification, 208 cross-linking, 208–210, 209*f* developments, 206*f*, 206–210, 208*f*, 209*f* guest-host systems, 206*f*, 206–207 liquid crystalline, 207, 208*f* photorefractive, 210 poling methods, 205*f*, 205–206 poling procedure, 203*f*, 203–205 thermal history, relaxation behavior and, 207–208
- Polyenes, linear calculated versus measured nonresonant γ_s , 277*t*, 277–278 comparison of calculated $\gamma_r(0; 0, 0, 0)$ s, 278*f*, 278–279 important ${}^1\pi^*$ states defining $\gamma_r(0; 0, 0, 0)$, 279–283, 280*f*–282*f* molecular geometries, 276 SOS terms important to $\gamma_r(0; 0, 0, 0)$, 283–287, 284*t*, 285*f*, 286*f* structures, 275*f* third-order NLO applications, 273–297
- Polymacromolecular structures, network dynamics and, 48
- Polymer(s) biological, information-processing capabilities of, 46–49

- Polymer(s)**—*Continued*
 biotinylated, streptavidin recognition incorporating photodynamic proteins, 395–411
 conducting
 molecule-based transistor using, 86
 synthesis and characterization, 397–400, 398f, 399f
 liquid crystalline, 207, 208f
 photorefractive, 210
 poled, 202–210, 203f, 205f, 206f, 208f, 209f
 spin-coated doped films, 309, 311, 311f
 spiropyran in, *See also* Spiropyran stability, 171–172, 174t, 175t, 175–176
- Polymer–streptavidin–biotinylated protein monolayers**, formation, 402–404, 404f–406f
- Polysilane**, Hartree–Fock linear polarizability, 258
- Postirradiation filling**, holographic, with liquid crystal, 329–330, 330f
- Potential well**, quantum well and, 18
- Probabilistic analysis**, 136–138, 138f
- Probabilities**, analysis of, 138–148
 continuous case, 140–148
 discrete case, 138–140
- Probability density**, *See* Electron probability density
- Probability distribution**
 absorption, 145
 binomial, 140–141
- Programmability**
 parallel systems, 55
 serial systems, 55
- Pronation**, linear cyanine, polarizability dependence on, 287–289, 288t
- Property density functions**, 64, *See also* Transition current density (TCD)
- Proteins**, *See also specific type*
 conformational switching, 47
 electrical properties, manipulation, 484–486
 engineering for electrooptical biomaterials, 475–489, 477f
 low dissipation, 48
 membrane-based biosensing, 48
 optical properties, manipulation, 486–488, 487f
 photodynamic, biotinylated polymers–streptavidin and biotinylated lipid–streptavidin recognition incorporating, 395–411
 reconstitution with new optical centers, 488
- Proteins**—*Continued*
 retinal, in photovoltaic devices, 527–556
 shape-based pattern recognition, 47
 structure–function relations, combinatorial variability of, 47–48
 thin films, assembly, 477–483, 478f, 480f–482f, 483t, 484f
- Proton pump**, in bacteriorhodopsin, 504–507, 506f, 564
 photoinduced proton transfer in LB films as simple model of, 390–391, 391f
- Proton transfer switch**, 93
- Pt C₁₆H₃₃-Q3CNQ Mg Al**, rectification experiments, 120
- Pt DDOF-C-BHTCNQ Mg Al**, rectification experiments, 119
- Purple membrane**, *See also* Bacteriorhodopsin orientation, photodiodes and, 565–567, 566f
- PVR (peak-to-valley current ratio)**, 19, 19f, 22
- Py-C-HETCNQ**, scanning tunneling microscopy on, 120–122, 121f
- Pyrene-substituted fatty acid**, energy-transfer quenching of, by photooxidized product, 386–390, 387f–390f

Q

- Quantex Q-phosphors**, 3D storage using, 169–170
- Quantum devices**, 3t, 7–8, 15–40, *See also specific type*
 colloid chemical approach to, 413–436, *See also* Colloid chemical approach
 dot structures, *See* Quantum dots
 future prospects, 37–39, 39f
 tunneling in, 16, 17–30, *See also* Resonant-tunneling transistors (RTTs)
- Quantum dots**, 30–37
 anchoring onto, unimolecular device, 89
 1D–0D tunneling, 32–35, 33f–35f
 transport in, 32–37, 33f–36f
 0D–0D tunneling, 35–37, 36f
- Quantum well**, band gap, 20–24, 21f, 23f, 24f
- Quantum-well excited state tunneling transistor (QuEST)**, 20, 21f
 bipolar, 21f, 22–23, 23f, 24, 24f

- Quantum-well resonant-tunneling transistor, 18, *See also* Resonant-tunneling transistors (RTTs); *specific type*
 scaling, 23
 superlattice, 24–25
- Quenching, energy-transfer, of pyrene-substituted fatty acid by photooxidized product, 386–390, 387*f*–390*f*

R

- Random access memory (RAM), optical, based on bacteriorhodopsin, 150–151
- Reaction center (RC), *See* Photosynthetic reaction center
- Reaction cycle, photochemical, bacteriorhodopsin, *See also* Bacteriorhodopsin (BR)
- Read operations
 at multiple wavelengths, 145–147
 conditional probability, 141
 in 3D memory, 164–167, 165*f*, 166*f*
 probabilistic analysis, 137
- Reading, state, 12
- Real-time holographic correlator, bacteriorhodopsin-based, experimental implementation, 521–522, 522*f*, 523*f*
- Recording media, holographic, 321–338
- Rectification behavior, preparation-dependent, of semiconductor particulate films, 432–434, 433*f*
- Rectification experiments, 118–122, 120*f*, 121*f*
- Rectifiers
 organic
 bulk, 84
 multilayer LB, 85–86
 unimolecular, 97–118
 unimolecular, 81–122, *See also* Unimolecular devices
- Redox center reconstitution, protein, 485–486
- Redox potentials, protein, 484–485
- Refractive index
 intensity-dependent, 248
 VOPc(*t*-bu)_n optical waveguide, 315–317, 316*f*, 317*f*
 light-induced changes, 248
 phase shift and, 247
- Relaxation behavior, poled polymer film, thermal history and, 207–208
- Reliability
 calculations, 130–158
- Reliability—*Continued*
 analysis of probabilities and, 138–148, *See also* Probabilities for electrostatic switches, 149–150, 150*f*
 for monoelectronic and monomolecular devices, 155–156
 for optical RAM based on bacteriorhodopsin, 150–151
 for optically coupled NAND gates, 150
 molecular switch dynamics and, 132–133
 origins of error and, 133–138, 138*f*
 for specific devices, 148–156
 for 3D optical memories, 151–155, 153*f*
 carbon versus silicon, 47
 device, 3*t*, 10–12
- Resistance, differential, negative, *See* Negative differential resistance (NDR)
- Resistive summing network, resonant-tunneling transistor, 28, 28*f*
- Resonant γ_* component, third-order molecular polarizability, 266–267
- Resonant peak voltage, 18
- Resonant-tunneling bipolar transistor (RTBT), 17, 21*f*, *See also* Resonant-tunneling transistors (RTTs)
- Resonant-tunneling diode (RTD), 17, *See also* Resonant-tunneling transistors (RTTs)
- Resonant-tunneling hot electron transistor (RHET), 17, 21*f*, *See also* Resonant-tunneling transistors (RTTs)
 room-temperature exclusive-NOR gate, 28, 28*f*
- Resonant-tunneling transistors (RTTs), 17
 circuits, 27–30, 28*f*, 29*f*
 current-voltage characteristics, 18*f*, 18–19, 19*f*
 device physics, 19–24, 21*f*, 23*f*, 24*f*
 recent device results, 24–27, 25*f*, 26*f*
 transfer characteristic, 24, 24*f*
- Retinal analogs, 573
- Retinal proteins, *See also* Bacteriorhodopsin (BR)
 in photovoltaic devices, 527–556, *See also* Photovoltaic *entries*
- RHET, *See* Resonant-tunneling hot electron transistor
- Rhodopsin, bacteriorhodopsin versus, 546–547
- Room-temperature exclusive-NOR gate, RHET, 28, 28*f*

Room-temperature operation, *See also*
 Temperature
 future quantum device prospects and,
 39
 Room-temperature size-quantization
 effects, BiQuaRTT, 25, 25f
 RTBT, *See* Resonant-tunneling bipolar
 transistor
 RTD, *See* Resonant-tunneling diode

S

SA layers, *See* Self-assembled layers
 Salts
 NLO crystals, 200f, 200–201
 organic, as NLO chromophores, 185
 Scalar fields, transition current density,
 64–65
 Scale factor, 9
 Scaling, quantum-well resonant-tunneling
 transistor, 23
 Scanning tunneling microscopy (STM)
 connection to unimolecular device, 91
 on BDDAP-C-BHTCNQ, 119
 on BDDAP-C-HETCNQ, 120, 120f
 on C₁₆H₃₃-Q3CNQ, 120–122, 121f
 on H atom switch, 119
 on Py-C-HETCNQ, 120–122, 121f
 Schrödinger equation, time-dependent,
 65
 Second-messenger system, self-assembly
 model and, 53
 Second-order optical nonlinearities
 important responses, 256t
 large, computational design of
 architectures with, 223–239
 optimization of materials for
 applications, 179–214, *See also*
 Nonlinear optical (NLO) materials,
 second-order
 Self-assembled (SA) layers, LB films
 versus, 349
 Self-assembly, 8–9
 BLM, on solid support, 439–452, *See*
also Supported bilayer lipid
 membranes
 future of computing based on, 59–60
 model, 51–53, 52f
 carbon–silicon synergy and, 58–59
 reliability and, 47
 stability and, 47
 structures based on trichlorosilane
 derivatives, second-order NLO
 activity, 212
 tubules, from phospholipids, 455–471
 Semiconducting switches, carbon versus
 silicon in, 45–46

Semiconductor devices, *See also specific*
type
 high-speed, feature size, 8
 quantum, 15–40, *See also* Quantum
 devices
 Semiconductor particulate films
 generation
 at bilayer lipid membranes, 414–415
 at monolayers, 415–417, 416f–418f
 rectification behavior, preparation-
 dependent, 432–434, 433f
 Sensors, LB films in, 346–347
 Serial systems, programmability, 55
 Serpentine transfer characteristic, RTT,
 logic functions and, 28–30, 29f
 Shape-based information processing,
 46–49
 self-assembly model and, 51–53, 52f
 Signal generation, molecular mechanisms
 of, photovoltaic effect and,
 530–540, 531f–533f, 535f,
 537f–539f
 Signal processing, optical, materials
 requirements for, 247–251
 Signal propagation times, size of
 molecular gates and, 5
 Silicon
 carbon and, synergy, 56–59, 57f
 carbon versus, 44–46, 55–56, *See also*
 Carbon
 Silyl bridge, 88–89
 Simple orbital transitions, 63–79
 Single-component monolayers, protein
 thin films, 477–482, 478f,
 480f–482f
 Single-electron charging effects, 16
 Site-directed mutagenesis, 8–9
 Size of molecular scale, speed and, 2, 3t,
 4f, 5–6, 6f
 Size quantization, room-temperature,
 BiQuaRTT, 25, 25f
 Solar energy conversion, artificial
 photosynthetic systems, 374, *See*
also Langmuir–Blodgett (LB) films,
 photoinduced electron and energy
 transfer in
 Solid support, self-assembling bilayer
 lipid membranes on, 439–452, *See*
also Supported bilayer lipid
 membranes
 Soliton switch, 93
 Solution half-wave potentials, Aviram–
 Ratner unimolecular organic
 rectifier, 106t–107t, 108
 Solvents, polar, stability and, 175
 SOS method, *See* Sum-over-states method

- SPARKLES option, MOPAC software, 268
- Spatial structure, self-assembly model and, 51
- Spectroscopy
 fluorescence, intelligent biomaterials based on LB films, 406–409, 407*f*–409*f*
 multichannel, optical, 494–498, 495*f*, 497*f*
- Speed
 molecular size and, 2, 3*t*, 4*f*, 5–6, 6*f*
 procedure, LB film applications and, 357
- Spin-coated doped polymer films, 309, 311, 311*f*
- Spin transitions, in LB films, 87
- Spiro-linked thiophene intercircuit connections, unimolecular device and, 89
- Spiropyran, 3D storage using, 167–169, 168*t*, 170
 fatigue, 172–175, 173*f*
 stability, 171–172, 172*f*, 173*f*, 174*t*, 175*t*, 175–176
- Spontaneous assembly, *See* Self-assembly
- Stability
 carbon versus silicon, 47
 D memory devices, 170–172, 172*f*, 173*f*, 174*t*
 polymer effect on, 174*t*, 175*t*, 175–176
 photochemical, 9–10
 thermal, 9–10
- State assignment error, Heisenberg's uncertainty principle and, 134–136
- State reading process, 12
- Static field derivative, 265–266
- Stationary states, transition current density and, 65–66
- Stilbenes, donor–acceptor-substituted, 184–185
- STM, *See* Scanning tunneling microscopy
- Streptavidin, biotinylated polymers and biotinylated lipid recognition, incorporating photodynamic proteins, 395–411
- Streptocyanines, *See* Cyanines
- Structure–function relations, combinatorial variability of, 47–48
- Structure–property relationships, for NLO response in organic chromophores, 180–194
 asymmetry, 183*f*, 183–185, 184*f*
 basic features, 182*f*, 182–183
 computational and experimental methods, 180–182
- Structure–property relationships, for NLO response in organic chromophores—*Continued*
 electron system length and nature, 185–188, 186*f*–188*f*, 188*t*
 molecular orbital analysis of β , 188–194
- Subband spacing, emitter, 35
- Substrates, 47
- Sum-over-states (SOS) method
 intermolecular interactions and, 225
 NLO materials and, structure–property relationships, 181
 terms important to $\gamma_r(0; 0, 0, 0)$, linear cyanines and polyenes, 283–287, 284*t*, 285*f*, 286*f*
 third-order polarizability and, 263–264, 265–266
- Superlattice, quantum-well resonant-tunneling transistor, 24–25
- Supported bilayer lipid membranes, 439–452, *See also* Bilayer lipid membranes (BLM)
 experiments, 441*t*
 materials, 440–442
 methods, 442
 results, 444–450, 445*f*, 446*t*, 448*f*–450*f*
 spontaneous assembly, techniques, 442–444, 443*f*
- Surface modification, LB films in, 346
- Susceptibility, electric, *See* Electric susceptibility
- Switches
 carbon, silicon versus, 44–46, 55–56
 digital, intelligent particles versus, 43–44
 electrostatic, reliability calculations, 149–150, 150*f*
 H atom transfer, 93
 molecular, photochromic, 132–133
 organic, phase-change, 86
 proton transfer, 93
 soliton, 93
- Switching, conformational, 47
- Switching power
 downscaling of, 15, 16
 third-order NLO materials, 250
- Synergy
 carbon and silicon, 56–59, 57*f*
 holography and liquid crystals, 322*f*, 322–323, 323*f*
- T**
- Tactilization
 learning algorithms and, 54–55
 M-m scheme, 51
 self-assembly model and, 51–53, 52*f*

- Taylor-series expansion, 252, 265
 TCD, *See* Transition current density
 TCNQ, *See* Tetracyanoquinodimethane
 TDHF method, *See* Time-dependent Hartree-Fock method
 Temperature, *See also* Room-temperature entries
 fatigue as function of, 172-173, 173*f*
 quantum dot current-voltage characteristics and, 32, 33*f*
 Temporal structure, self-assembly model and, 51-52
 Terabit memory, LB films, 366-368, 367*f*
 Tetracyanoquinodimethane (TCNQ)
 Aviram-Ratner organic unimolecular rectifier and, synthesis, 103
 phase-change organic switch and, 86
 Tetrathiafulvalene (TTF)
 Aviram-Ratner organic unimolecular rectifier and, synthesis, 102-103
 highly conducting LB films and, 102-103
 Thermal history, poled polymer film, relaxation behavior and, 207-208
 Thermal stability, 9-10
 Thermodynamics, bacteriorhodopsin, transport mechanism and, 504-507, 506*f*
 Thin films
 MPc, 305*f*-308*f*, 305-312, 310*t*, 311*f*, 312*f*
 protein, 477-483, 478*f*, 480*f*-482*f*, 483*t*, 484*f*
 Thiophene intercircuit connections, spiro-linked, unimolecular device and, 89
 Third-order optical nonlinearities, 243-297
 conjugated π -electron molecules for alignment of molecular units, 292-293
 design, 291-297
 electric fields and, 294-296
 geometries, 293
 linear molecular units with conjugated π -electron bonding networks, 293-294
 linear polarizabilities, 293
 number density of molecular units, 292
 pH adjustment, 296-297
 important responses, 256*t*
 linear cyanines and polyenes and, 273-297
 materials requirements, 247-251
 molecular polarizability, 261-267
 macroscopic susceptibility relation to, 251-256, 256*t*
 Third-order optical nonlinearities—
 Continued
 molecular electronic structure and, 269-273, 272*t*
 molecular geometry and, 267-269
 MPc systems, 303-319
 polarization response maximization, 256-260
 Three-dimensional images, holographic, liquid crystals as recording media, 321-338
 Three-dimensional optical memory, two-photon, 161-176
 reliability calculations, 151-155, 153*f*
 Three-dimensional screening problem, solution, 34, 34*f*
 Three-terminal devices
 quantum mechanical tunneling and, 16, *See also* Quantum devices
 switches, *See* Switches
 transistor, 7
 Threshold switching, carbon versus silicon in, 46
 Time-dependent Hartree-Fock (TDHF) method, third-order polarizability, 265-266
 Time-dependent Schrödinger equation, 65
 Trade-off cube, carbon-silicon synergy, 56-58, 57*f*
 Transconductance, negative, BiQuaRTT, 22
 Transfer characteristics, RTT, 24, 24*f*
 circuits and, 28-30, 29*f*
 Transistor
 conventional, RTD integration into heterostructures, 22
 molecule-based, using conducting polymers, 86
 resonant-tunneling, *See* Resonant-tunneling transistors (RTTs)
 three-terminal, 7
 Transistor-based integrated circuits, scaling of, 15
 Transition continuity equation, general, 68
 Transition current density (TCD), 63-79
 classifications, 65
 defined, 67
 nonstationary states and, 66-67
 orbital, 68-76, 70*f*, 71*f*, 73*f*-75*f*, 77*f*
 probability density conservation and, 67-68
 stationary states and, 65-66
 theory, 65-68
 Transition matrices, 142-143
 for simultaneous exposure to wavelengths, 146

- Transition-metal moieties, as donors and acceptors, 185
- Transition probability density, 67
- Transitions, spin, in LB films, 87
- Triacyanovinyl, 184, 184*f*
- Triad molecules, antenna molecules and, simulation of primary process in photosynthetic RC with mixed monolayer with, 384*f*, 384–385, 385*f*
- Trichlorosilane derivatives, second-order NLO activity, 212
- Trimer clusters, 226–233, 227*f*, 228*t*, 229*f*, 229*t*, 231*f*, 233*f*
- Trissl–Montal method, 540
- Trough, LB film, 400–401
dual, 360
formation of biotin lipid–Str-PE monolayers, 401–402, 402*f*, 403*f*
- TTF, *See* Tetrathiafulvalene
- Tubules, self-assembling, from phospholipids, 455–471
- Tunneling, *See also* Scanning tunneling microscopy (STM)
nonclassical, 16
quantum mechanical, 16, *See also* Quantum dots; Resonant-tunneling transistors (RTTs)
- Two-dimensional electron gas (2DEG) systems, 16, 37–39
- Two-photon absorption, 267
- Two-photon three-dimensional optical memory, 161–176
fatigue, 172–175, 173*f*
materials, 167–170, 168*t*, 170*f*
reliability calculations, 151–155, 153*f*
stability, 170–172, 172*f*, 173*f*, 174*t*
polymer effect on, 174*t*, 175*t*, 175–176
two-photon mechanism, 162–164
writing and reading in, 164–167, 165*f*, 166*f*
- Two-state formula, 181
- U**
- Ultrafast bacteriorhodopsin photodetector, 568–571, 569*f*, 570*f*
- Uncertainty
analysis of probabilities, 147–148
Heisenberg's principle, 5, 134–136
- Unimolecular devices, 81–122, *See also specific type*
Aviram–Ratner organic unimolecular ratifier, 91–92, 92*f*, 97–118
conductivity change in LB films due to light-induced conformational change, 94
- Unimolecular devices—*Continued*
connections to, 87–91, 90*f*
Fujihira's LB photodiode, 93–94
light-induced intramolecular rearrangements, 94
potential conformational change systems, 94
proposed D– σ –A rectifier, 91–92, 92*f*
proposed H atom and proton transfer switches, 93
proposed soliton switch, 93
rectification experiments, 118–122, 120*f*, 121*f*
reliability, 10–12
calculations, 155–156
- V**
- Vacuum-deposited films, 305*f*–308*f*, 305–309, 310*t*
- Valley current, peak current ratio to, 19, 19*f*, 22
- Vanadylphthalocyanine (VOPc), *See also* Metallophthalocyanines (MPcs)
VOPc(*t*-bu)_n optical waveguide, implementation, 315–319, 316*f*–318*f*
VOPc(*t*-bu)_n thin films, femtosecond responses, 312–315, 313*f*, 315*f*
- Vector field, transition current density, 64
- Very large scale integrated (VLSI) devices, 9
- Vibronic coupling effects, 269
- Visual photoreceptor membranes, photovoltaic effect in, 546–551, 550*f*–551*f*
- Voltage
current and, *See* Current–voltage (*I*–*V*) characteristics
operating temperature and, quantum devices and, 39, 39*f*
- Voltammetry, cyclic, Aviram–Ratner unimolecular organic rectifier, 104–109, 106*t*–107*t*, 109*f*
- VOPc, *See* Vanadylphthalocyanine
- W**
- Waveguide
LB film, 345
VOPc(*t*-bu)_n implementation, 315–319, 316*f*–318*f*
- Wavelengths, multiple, read operations at, 145–147
- Wires, molecular, connection to unimolecular device, 89
- Write operation
in 3D memory, 164–167, 165*f*, 166*f*
probabilistic analysis, 136–137

Z

Zeolites, connection to unimolecular device, 89

Zero-dimensional quantum dots, *See* Quantum dots

Zeroth-order Born–Oppenheimer approximation, 263

ZINDO model, 225

Zirconium phosphonate layers, second-order NLO activity, 213, 214*f*

Production: Margaret J. Brown

Acquisition: Barbara C. Tansill

Indexing: Barbara Farabaugh

Cover design: Amy Hayes

Typeset by TAPSCO

Printed by United Book Press, Inc., Baltimore, MD

Bound by American Trade Bindery, Baltimore, MD